Processus photophysiques de molécules organiques fluorescentes et du kérosène applications aux foyers de combustion : applications aux foyers de combustion

Björn Rossow

UNIVERSITÉ PARIS-SUD 11

THÈSE

pour obtenir le grade de

DOCTEUR de l'université Paris-Sud 11

ÉCOLE DOCTORALE DE CHIMIE

Institut des Sciences Moléculaires d'Orsay
(préparée à l'ONERA)

Spécialité : Chimie-Physique

présentée et soutenue publiquement
par

Björn ROSSOW

le 27/09/2011

Processus photophysiques de molécules organiques fluorescentes et du kérosène – applications aux foyers de combustion

Directrice de thèse : Prof. Dolorès GAUYACQ
Encadrant à l'ONERA: Prof. Frédéric GRISCH

Jury :

Prof. Hélène MESTDAGH	Présidente
Dr. Pascale DESGROUX	Rapporteur
Prof. Christof SCHULZ	Rapporteur
Dr. Brigitte ATTAL-TRETOUT	Examinateur
Prof. Abdelkrim M. BOUKHALFA	Examinateur
Dr. Gilles BRUNEAUX	Examinateur
Prof. Dolorès GAUYACQ	Directrice de thèse
Prof. Frédéric GRISCH	Encadrant à l'ONERA

UNIVERSITÉ PARIS-SUD 11

THÈSE

pour obtenir le grade de

DOCTEUR de l'université Paris-Sud 11

ÉCOLE DOCTORALE DE CHIMIE

Institut des Sciences Moléculaires d'Orsay
(préparée à l'ONERA)

Spécialité : Chimie-Physique

présentée et soutenue publiquement
par

Björn ROSSOW

le 27/09/2011

Photophysical processes of organic fluorescent molecules and kerosene – applications to combustion engines

Directrice de thèse : Prof. Dolorès GAUYACQ
Encadrant à l'ONERA: Prof. Frédéric GRISCH

Jury :

Prof. Hélène MESTDAGH	Présidente
Dr. Pascale DESGROUX	Rapporteur
Prof. Christof SCHULZ	Rapporteur
Dr. Brigitte ATTAL-TRETOUT	Examinateur
Prof. Abdelkrim M. BOUKHALFA	Examinateur
Dr. Gilles BRUNEAUX	Examinateur
Prof. Dolorès GAUYACQ	Directrice de thèse
Prof. Frédéric GRISCH	Encadrant à l'ONERA

Remerciements

Je voudrais exprimer mes remerciements à toutes les personnes qui m'ont d'une manière ou d'une autre accompagné lors de mes travaux pour cette thèse. Mes remerciements vont à …

… tous les membres de mon jury : Madame Mestdagh, Madame Desgroux, Monsieur Schulz, Monsieur Boukhalfa et Monsieur Bruneaux pour leur regard critique, leurs questions et les discussions lors de ma soutenance.

… ma directrice de thèse, Dolorès Gauyacq, pour son accueil chaleureux, sa supervision et les discussions engagées sur mon travail. Je te remercie aussi pour ton indulgence, ta confiance et ton investissement personnel qui m'ont permis de faire aboutir mon projet de thèse.

… mon encadrant à l'ONERA, Frédéric Grisch, désormais Professeur à l'INSA Rouen, pour son accueil chaleureux, sa supervision, le suivi direct de mon travail à l'ONERA et les discussions très enrichissantes tout au long de mon travail. Tu as su créer une atmosphère de travail toujours agréable. Pour ta gentillesse, la façon dont tu m'as guidé et suivi dans mes idées et ta patience à les voir se réaliser, je te suis très reconnaissant.

… Pierre Touboul pour m'avoir accueilli à l'ONERA au sein du département Mesures Physiques (DMPH), ainsi qu'à Brigitte Attal-Tretout et Michel Lefebvre pour leur chaleureux accueil au sein de l'unité Diagnostic Optique et Plasma (DOP), maintenant devenue Systèmes Lasers et Métrologie (SLM).

… tous mes collègues de l'ONERA, avec qui j'ai eu le plaisir de partager mon quotidien pendant les trois ans que j'ai passé au DOP. Vous avez été mes premiers collègues en France… merci de votre accueil. Les doctorants – Sara Abbate, Philippe Barranger, Antoine Berrou, Olivier Carraz, Renée Charrière, Isabelle Debecker, Guy-Alexandre Grandin, Perrine Jaffrenou, Constantin Ledier, Fabien Lienhart, Jean-Michel Melkonian, Dominique Messina, Michèle Packan, Myriam Raybaut, et tous les autres collègues de l'ONERA – Florence Baumgartner, Yannick Bidel, Jean Bonnet, Alexandre Bresson, Christophe Brossard, Nelly Dorval, Paul-Quentin Elias, Jean-Pierre Faléni, Pierre Gicquel, Antoine Godard, Eric Jourdanneau, Ajmal Mohamed, Mikaël Orain, Denis Packan, Thomas Schmid, Nassim Zahzam – et tous ceux que j'ai oublié de mentionner.

Meinen ehemaligen Kollegen vom LTFD aus Aachen möchte ich ebenfalls meinen Dank aussprechen ! Die Jahre mit Euch waren im Rückblick nicht nur fachlich interessant, sondern vor allem eine Menge Spaß ! Grüße aus Paris an Andreas Greis, Christoph Pauls, Julia Rösing, Peter Wieske, Stefan Wissel, Frau Plagge und Gerd Grünefeld !

Ich danke besonders meinen Eltern, meiner Familie in Deutschland und meinen Freunden : ohne Eure Unterstützung hätte ich diese Arbeit nie geschafft !

Danke für Euer Vertrauen.

Je remercie tout spécialement ma femme et ma fille, toute ma famille en France, ainsi que mes amis : sans votre soutien je n'aurais jamais pu y arriver !

Merci pour votre confiance.

A ma fille Zoé et ma femme Carole

Résumé

Les diagnostics lasers sont devenus des outils de recherche indispensables à l'étude expérimentale de la dynamique des fluides réactifs. Contrairement aux sondes de mesures mécaniques « intrusives » ne permettant pas d'accéder à une fine compréhension des processus physiques et chimiques de ces écoulements, l'imagerie de fluorescence induite par laser (PLIF) permet de répondre à ces besoins. Couplée à des caméras CCD, cette technique donne accès à des mesures bidimensionnelles instantanées sur une grande variété de paramètres scalaires comme la concentration de vapeur de carburant et de radicaux, la température, la richesse locale… Notamment, ces données sont vitales pour le dimensionnement des processus d'atomisation et d'évaporation du carburant liquide dans des chambres de combustion. Une optimisation de la mesure par fluorescence induite par laser est alors dictée sur la sélection d'un traceur chimique fluorescent aux propriétés spectroscopiques permettant une quantification de sa fluorescence. Ainsi, il est nécessaire que les traceurs chimiques possèdent une transition moléculaire accordée sur la fréquence d'une source laser impulsionnelle de grande énergie et délivrant un fort rendement quantique.

Les stratégies de mesures pour la PLIF appliquée aux carburants en phase vapeur ainsi que leurs applications à des foyers de combustion sont initialement détaillées dans une revue bibliographique. Les traceurs fluorescents les plus usités sont issus des familles des cétones aliphatiques et d'aromatiques ayant pour chromophores le carbonyl et le benzène. Ces espèces chimiques sont caractérisées par une affinité chimique aux carburants dérivés du pétrole, ce qui permet de mesurer

des concentrations de carburants liquides et gazeux en sortie des systèmes d'injection. Pour cela, le traceur est soit ensemencé dans un carburant de substitution non-fluorescent, soit il est naturellement présent dans le carburant.

Dans cette thèse, les processus photophysiques de fluorescence des molécules organiques et du kérosène sont analysés dans le domaine spectral UV. Le choix des molécules organiques est justifié car entrant dans la composition chimique du kérosène et par leurs propriétés attractives permettant de les tracer dans de nombreux types d'écoulements. Selon la littérature, les espèces sélectionnées font partie du groupe des cétones aliphatiques ainsi que des aromatiques mono- et bicycliques simples et substitués, qui possèdent des transitions électroniques accessible dans le domaine UV.

La fluorescence en régime linéaire rend proportionnel le signal S_f avec la concentration χ de l'espèce fluorescente via le nombre de densité N_1^0. Dans la phase vapeur, ce dernier permet de mesurer la concentration que dans le cas où la température et la pression ainsi que leurs variations spatiales et temporelles sont connues. L'interprétation directe des signaux de fluorescence en termes de concentration se limite alors à des systèmes homogènes en température et pression. En situation hétérogène, la connaissance des champs de température et pression ne suffit cependant pas à la quantification du signal de fluorescence. Les variations de température et pression n'influencent pas seulement le nombre de densité, mais également le bilan des processus photophysiques intrinsèques à la molécule. C'est la raison pour laquelle une étude exhaustive des ces effets est nécessaire. Outre la température et la pression, le choix du bain de molécules dans lequel est plongé le traceur entraîne des interactions sur la production de fluorescence. Les collisions entre la molécule traceur excitée et le gaz subsidiaire entraîne une baisse d'énergie interne du traceur. Ceci se passe à l'intérieur de l'état singulet excité, ce qui a pour conséquence de changer le bilan des processus photophysiques qui dé-

pendent pour la plupart de l'énergie vibrationnelle en excès. En outre, par des collisions avec certaines espèces chimiques, la molécule traceur se désexcite par des réactions de quenching électronique directement ou via l'état triplet, vers l'état électronique fondamental. Les collisions avec l'oxygène triplet sont souvent les plus efficaces pour le quenching électronique de ces traceurs organiques.

L'étude photophysique a nécessité la réalisation d'une cellule un acier inoxydable. Dans cette cellule optique, des mesures à des températures comprises entre 300 et 900 K et des pressions entre 1 et 30 bar ont été réalisées, ce qui s'approche des conditions opératoires rencontrées dans des foyers de combustion. La chambre dispose de trois fenêtres en silice UV, permettant le passage d'un faisceau laser d'excitation à 266 nm et la détection de l'émission de fluorescence par un système optique associant un télescope, un spectrographe et une caméra CCD intensifiée. L'ensemencement du traceur fluorescent dans le flux de gaz porteur entrant dans la chambre est contrôlé et piloté par ordinateur. La conduite des expériences est facilitée par une programmation sous LabVIEW, ce qui améliore la reproductibilité des mesures. Différentes concentrations d'oxygène peuvent être injectées dans le gaz subsidiaire en mélangeant un flux pur d'azote avec un flux d'air.

L'étude spectroscopique de la fluorescence des cétones aliphatiques, des aromatiques et du kérosène comprend l'évaluation des effets de la température et de la pression sous un environnement d'azote (absence de quenching) et l'effet du quenching par l'oxygène. Les mesures sont comparées aux résultats de la littérature scientifique décrivant les processus importants pour la désactivation de l'état excité rentrant en compétition avec l'émission de fluorescence.

Parmi les cétones, l'acétone et le 3-pentanone sont étudiés. Les mesures expérimentales sont en accord avec des mesures publiées par [Thurber 1998 et Koch 2003b] et de simulations de rendement de fluorescence. La fluorescence diminue modérément avec l'augmen-

tation de la température, alors qu'un accroissement de la pression entraîne une augmentation de la fluorescence. L'influence de l'oxygène sur le quenching électronique est peu significative, comme c'est généralement le cas pour les cétones aliphatiques.

Pour les espèces aromatiques monocycliques, le toluène et le 1,2,4-triméthylbenzène sont abordés. La fluorescence de ces deux molécules révèle de fortes similitudes par rapport à l'influence des paramètres étudiés. Sous azote, une augmentation de la température cause une très forte diminution du signal de fluorescence. Prenant en compte l'effet de la température sur la section efficace d'absorption, le rendement de fluorescence décroit exponentiellement de trois ordres de grandeur dans le domaine de température entre 300 et 900 K. Ceci concorde avec les observations de [Koban 2004] pour le toluène. A notre connaissance, le présent travail est le premier à considérer également l'effet de la pression en environnement sous azote (absence de quenching). Pour la même longueur d'onde d'excitation, l'effet stabilisateur produit sur la fluorescence des cétones aliphatiques par une augmentation de la pression se révèle être atténuateur pour la fluorescence des aromatiques monocycliques. L'effet collisionnel sur la fluorescence dépend du bilan entre l'excès en énergie d'excitation photonique (par rapport à l'origine de l'état excité) et la différence des énergies thermiques des états excités et fondamental. Pour le quenching par l'oxygène, les résultats pour le toluène sont comparables à ceux décrits par [Koban 2005a]. Le quenching suit une loi de type Stern-Volmer. Ce quenching diminue lorsque la température augmente.

Le naphtalène est choisi parmi les aromatiques bicycliques pour l'étude spectroscopique. Sous azote, la fluorescence diminue modérément en cas d'augmentation de la température et augmente modérément avec la pression. Ces constats rappellent le comportement observé pour la fluorescence des espèces cétoniques. Le quenching par l'oxygène suit une loi de Stern-Volmer. Le quenching du naphtalène est

beaucoup plus grand que pour les monocycliques étudiés et diminue également avec une augmentation de la température.

En parallèle de cette étude expérimentale, un modèle de simulation du rendement de fluorescence du naphtalène est développé. Les processus physiques intervenant dans le bilan énergétique par voie non-radiative sont abordés. Leurs taux sont simulés sous forme paramétrique en fonction de l'énergie vibrationnelle en excès, déduites des données acquises dans des conditions de basse pression (domaine torr) et recensées dans la littérature scientifique. A l'issue d'une procédure d'optimisation non-linéaire, un jeu unique de paramètres décrivant les taux de désactivation ainsi que le transfert d'énergie par collision est alors trouvé. Les effets du quenching de l'oxygène sont également intégrés dans le modèle numérique. Une distinction en termes d'efficacité de quenching permet de séparer les collisions intramoléculaires entre le naphtalène et l'oxygène (relaxation vibrationnelle) et les collisions intermoléculaires (quenching électronique). Les relations de Stern-Volmer sont simulées en fonction de la température. Le modèle de fluorescence numérique calcule les rendements de fluorescence en excellent accord avec les résultats expérimentaux obtenus dans la présente étude sur la gamme de température, pression et concentration d'oxygène.

Dans le cas du toluène, un modèle numérique de fluorescence similaire à celui du naphtalène est établi qui permet de décrire l'effet de la température sur sa fluorescence. Le développement de ce modèle est réalisé en analogie avec celui du naphtalène.

Pour permettre une comparaison des propriétés spectroscopiques des traceurs cétoniques et aromatiques, un étalonnage des spectres des différentes molécules est réalisé sous azote à 1 bar et 450 K (absence de quenching). L'utilisation combinée de ces données et des spectres de fluorescence enregistrés dans les conditions étendues de température, pression et teneur en oxygène précitées, permet alors d'obtenir une quantification relative des rendements de fluorescence de

ces espèces, ce qui n'existe pas actuellement dans la littérature scientifique.

Suite à ces travaux, la fluorescence du kérosène (Jet A1) qui, rappelons le, est un produit multi-composant a été analysé dans les mêmes conditions de température, pression et teneur en oxygène. Le spectre de fluorescence du kérosène excité à 266 nm affiche deux bandes spectrales distinctes. La bande à haute fréquence est le résultat de la fluorescence d'une fraction des espèces aromatiques monocycliques constituant le kérosène. La bande à basse fréquence provient de l'émission des constituants aromatiques bicycliques.

Grâce aux spectres de fluorescence des traceurs pré-étudiés, un mélange de plusieurs traceurs aromatiques a été déterminé pour reproduire un spectre de fluorescence identique à celui du kérosène et cela dans nos conditions expérimentales. Un calcul du spectre de fluorescence du kérosène avec les spectres des traceurs composant ce mélange permet également de reproduire les changements du spectre de fluorescence du kérosène en fonction des variations de la température, la pression et la concentration d'oxygène. Cette approche synthétique est applicable à l'avenir à l'analyse des lots de kérosène présentant des compositions chimiques différentes selon le procédé de distillation utilisé.

Le comportement des aromatiques dans le kérosène nous permet d'établir une stratégie de mesure de la concentration de la phase vapeur du kérosène dans des environnements où la teneur en oxygène est importante. Dans ces conditions, cette stratégie est justifiée par notre modèle de fluorescence du naphtalène qui indique que le rendement de fluorescence est gouverné principalement par le quenching de l'oxygène. Les collisions avec l'azote causent une relaxation vibrationnelle intramoléculaire dont l'effet sur le rendement de fluorescence est négligeable. Appliquée aux autres traceurs aromatiques étudiés, les lois de Stern-Volmer peuvent être étendues à des pressions élevées (i.e. 30 bar). Pour le kérosène, l'utilisation directe de ces évolutions

étant impossibles (recouvrement partiel des deux bandes de fluorescence), un filtrage spectral de la fluorescence du kérosène permet d'établir différentes bandes spectrales avec des lois de Stern-Volmer physiquement décorrélées. L'analyse conjointe de ces lois de Stern-Volmer évoluant différemment avec la température et la teneur en oxygène permet alors de déduire les paramètres de température, de concentration d'oxygen χ_{O_2} et de concentration de carburant χ_{fuel} par une procédure d'analyse employant un algorithme itératif. Ceci nécessite l'hypothèse d'une conservation des produits chimiques dans notre écoulement ce qui est parfaitement justifié dans les zones non-réactives. L'étalonnage absolue des lois de Stern-Volmer est quant à lui assuré par l'enregistrement des signaux de fluorescence dans un mélange gazeux kérosène/air aux propriétés thermodynamiques connues. Expérimentalement, la définition de filtres optiques pour la détection du signal de fluorescence du kérosène permet d'établir d'enregistrer simultanément deux bandes spectrales sur deux caméras ICCD, et ainsi de réaliser des mesures bidimensionnelles de signaux de fluorescence possédant des évolutions différentes avec les conditions de température et teneur en oxygène.

Le travail de cette thèse débouche sur l'application de la technique PLIF-kérosène en combinaison avec la technique PLIF du radical OH en sortie d'un injecteur multi-point intégré dans une chambre de combustion aéronautique. Plusieurs conditions de fonctionnement sont réalisées avec des températures de préchauffage d'air maximales de 800 K et des pressions maximales atteignant 22 bar. Il est mis en évidence dans des conditions de combustion que le couplage des deux techniques permet de visualiser simultanément la structure de la flamme et la distribution de la vapeur de kérosène en amont de la zone de flamme. Une distinction de la fluorescence du kérosène par le filtrage optique des signaux correspondant aux mono- et di-aromatiques est démontrée. Ceci donne accès à une quantification en termes de température et de richesse locale (rapport de la concentration du combustible

sur la concentration d'oxygène). La comparaison des images de fluorescence du kérosène et du OH montre que les aromatiques contenus dans le kérosène disparaissent à l'endroit où les radicaux OH sont produits. La fraction des aromatiques naturellement présents dans le kérosène est ici utilisée comme un traceur et se montre alors représentative du comportement de la concentration du carburant.

La comparaison des propriétés photophysiques des traceurs étudiés et des résultats obtenus pour le kérosène est une opportunité de définir de nouvelles stratégies de mesure par fluorescence induite par laser adaptées au traçage de la concentration des carburants multi-composant existants (diesel…) ou nouveaux (biocarburants, esters, …). La différence de comportement de fluorescence avec la température et la concentration d'oxygène entre les cétones et les aromatiques peut ainsi servir dans des applications du type FARLIF (« fuel-air-ratio » LIF). Notons cependant que l'écart significatif des rendements de fluorescence de ces espèces nécessite une concentration en cétones importante pouvant alors modifier le comportement chimique du carburant. Une alternative consistera à privilégier l'utilisation de mélanges de produits aromatiques (mono- et di-aromatiques, di- et multi-aromatiques…).

Abstract

Laser diagnostics based on fluorescence tracer has become a key tool for the experimental study of fluid dynamics in reactive flows. A spectroscopic fluorescence study was performed for a number of tracers from aliphatic ketones and mono- and bicyclic aromatics. The results allow a better understanding of the influence of temperature, pressure and oxygen concentration on the fluorescence photophysics in the UV/visible domain. In consequence, a model could be developed for the simulation of the fluorescence yield of aromatic species (naphthalene and toluene), producing results very close to the data measured within this work.

To develop a technique for planar laser induced fluorescence (PLIF) diagnostics on the vapour phase of a multi-component fuel, the spectroscopic study has been extended to kerosene (Jet A-1). Comparing the fluorescence properties of kerosene to those of the aromatic tracers studied before allows then to define a measurement strategy for detection of kerosene vapour concentration at variable oxygen concentration. The fluorescence signals from mono- and di-aromatic species in the kerosene highlight different evolutions with temperature and oxygen concentration. With appropriate optical filters applied to two ICCD cameras, a two-dimensional measurement of temperature and concentration of the kerosene vapour phase is then possible. Finally, the thesis work leads to the application of this kerosene PLIF technique at the exit of a innovative multi-point industrial injection system integrated to high-pressure combustor test rig, combined to probing of the OH radical, which is also detected by PLIF.

Table of contents

Chapter 1 Motivation and background

The oil crisis from the early 1970s made transport related fuel consumption a serious concern of cost and supply. Fuel consumption represents a large part of the direct operating costs of aeronautic aircrafts. Next to engine performance, technical reliability and durability, fuel efficiency became a high priority for the development of new engine designs to both airlines and manufacturers. Next to commercial aspects like the payload and the flight range of the fleet, the aim of a better specific fuel consumption was also important to improve the emission performance of aircraft combustion.

Aviation stands for only two to three percent of the worldwide petroleum fuel consumption. This low participation should, however, not serve as an argument to neglect its role to pollutant emissions related to the overall combustion of fossil fuels. Following common forecast scenarios, the high growth rates of aviation transport throughout the past decades are likely to be maintained or even exceeded in the future. Furthermore, aircrafts have long life cycles within all stages, 5-10 years of technology development, 15-20 years of production run followed by 25-35 years of service to the fleet until retirement [Penner 1999]. Thus, ignoring the impact of today's aircraft transport creates a potential emission burden for the future.

For aviation transport, the concerns about pollution were initially focussed to the vicinity of airports. With the Clear Air Act the U.S.A. provided first legislative regulations in the 1970s. These were subsequently followed by international standards fixed by the ICAO (International Civil Aviation Organisation). In the framework of the CAEP meetings (Committee on Aviation Environmental Protection, established in 1983) recommendations for aircraft emission limits below 3000 feet for carbon monoxide (CO), unburned hydrocarbons (UHC), nitrogen oxides (NO_x) and smoke were made to the ICAO. Since the publication of the first report CAEP/1 in 1986, these recommendations have become more and more stringent. A new report is currently underway with the CAEP/8 meeting in February 2010.

The important role of aircraft related pollution was addressed throughout several European research programs with the aim to assess the global effects on climate and ozone layer resulting from increasing air traffic [Amanatidis 2001]. After several national activities, with the AERONOX program for the first time research on these topics was integrated on the European level in 1992. Since then, many programs have followed, and recently, European and national activities have been bundled under the CORSAIRE (Coordination of Research

for the Study of Aircraft Impact on the Environment) cluster, aiming to provide a solid scientific basis for any future policy or regulatory action.

The formation of pollutants in turbine combustion is primarily determined by the temporal and spatial distributions of temperature, pressure and species concentration throughout the engine cycle. In the case of liquid fuel combustion, the efficiencies of fuel atomisation and evaporation affect the local species concentration and residence time. These properties are specific functions of the combustion process, and thus vary for different designs of combustor and engine cycle.

1.1 Pollutant formation in turbine combustion

The transition from simple turbojet engines to engines with low bypass ratio during the 1960s and further to engines with high bypass ratio during the 1970s and 1980s improved the engine cycle properties in terms of higher operating temperature and pressure. This resulted in better thermal and propulsive efficiencies, and thus, in better specific fuel consumption (SFC) [Brasseur 1998], i.e. the ratio of mass of fuel burnt per unit time to unit thrust. The benefit was more than 40 % SFC reduction for bypass ratios of 6:1 and another 10 % for bypass ratios of 9:1. Engine designs with even higher bypass ratio would mean further fuel economy, but are up to now difficult to realise due to major technology problems. However, based on thermodynamic considerations, possible further improvements are restricted to a maximum of 65 to 70 % compared to the SFC of 1960s turbojet generation.

An improved SFC due to a better design of the engine cycle essentially limits the amount of the unavoidable primary products of the combustion reaction, carbon dioxide (CO_2) and water (H_2O). Next to the primary, secondary products of combustion are carbon monoxide (CO), unburned hydrocarbons (UHC), nitrogen oxides (NO_x) and soot or particulate matter (PM), and their specific emission levels are mainly determined by the design of the combustion chamber.

Due to its influence to the pollutant formation, the change of adiabatic flame temperature with the (fuel-to-air) equivalence ratio plays an important role for the understanding of the combustion mechanism. The raise in flame temperature is maximum at stoichiometric conditions. For both leaner and richer conditions the temperature raise decreases. Thus, temperature driven mechanisms like the formation of nitrogen oxides tend to be most efficient at stoichiometric conditions and to have a steep fall to fuel lean and fuel rich conditions.

The formation of CO and UHC is primarily a problem for combustion at low engine loads, i.e. low equivalence ratio and thus low temperature. In contrast, NO_x and soot formation is favoured for high engine loads, i.e. high equivalence ratio and thus high temperature, as well as for high pressure [Brasseur 1998].

The technology development towards engines with increasingly high bypass ratio was beneficial for fuel efficiency and the output of CO and UHC. However, the necessary higher internal temperatures and pressures increased the pollutant emissions of NO_x and smoke [Brasseur 1998, Lefebvre 1999]. New engine designs are under investigation, which provide a better balance between the various pollutant emissions. The tradeoff between high emissions of carbon monoxide and nitrogen oxide is currently the main target for advances in combustor technology, aiming to maintain the benefits from high bypass ratios, while reducing the emissions of NO_x.

The combustion of a petroleum fuel such as kerosene produces primarily carbon dioxide and water. These emissions are undesirable but unavoidable by-products of the reaction, and their amount depends on the fuel composition and the specific fuel efficiency of the engine cycle. For the special case of complete combustion under stoichiometric condition the reaction is

$$C_xH_y + \left(x + \frac{y}{4}\right)O_2 + \frac{79}{21}\left(x + \frac{y}{4}\right)N_2 \Rightarrow xCO_2 + \left(\frac{y}{2}\right)H_2O + \frac{79}{21}\left(x + \frac{y}{4}\right)N_2 \tag{1.1}$$

The general case of combustion of a long-chain hydrocarbon fuel as a function of the equivalence ratio ϕ and the fraction of fuel burnt η_c may be represented by [Lefebvre 1999]

$$\begin{aligned}\phi \cdot C_xH_y + \left(x + \frac{y}{4}\right)O_2 + \frac{79}{21}\left(x + \frac{y}{4}\right)N_2 \Rightarrow\ & \eta_c\phi\left(xCO_2 + \frac{y}{2}H_2O\right) + \frac{79}{21}\left(x + \frac{y}{4}\right)N_2 \\ & + (1 - \eta_c\phi)\left(x + \frac{y}{4}\right)O_2 + (1 - \eta_c)\phi \cdot C_xH_y\end{aligned} \tag{1.2}$$

The reaction (1.1) represents thus a special case of the general term (1.2) for completely burnt fuel $\eta_c = 1$ and stoichiometric ratio $\phi = 1$, i.e. both the amount of remaining fuel $(1 - \eta_c)$ and remaining oxygen $(1 - \eta_c\phi)$ equal zero. The general case of reaction (1.2) is describing the combustion in most practical combustors, where the combustion efficiency is less than unity and the fuel-to-air ratio varying with the engine load.

For fuel rich combustion, i.e. $\phi > 1$, there is a lack of oxygen to complete the reaction to carbon dioxide (CO_2). Therefore, large amounts of carbon monoxide (CO) will occur as secondary products. Fuel rich combustion is either due to the current operating condition under high engine load, but may also be the result of insufficient fuel preparation (homogenisation). If the atomisation and evaporation process of the liquid fuel is not efficient, fuel rich pockets will form and be the source of incomplete oxidation. The incomplete combustion due to poor fuel preparation will further lead to the occurrence of unburned hydrocarbons (UHC), which mainly consist of thermal degradation products from remaining fuel. UHC may also form as a consequence of local flame extinction, e.g. at walls [Brasseur 1998]. For fuel lean combustion, i.e. $\phi < 1$, there is excess air of $\varepsilon = (1 - \phi)/\phi > 0$, and thus, oxi-

dation should exclusively result in the formation of CO_2. The role of equivalence ratio to the CO formation is characterised by slow rates of oxidation associated with low combustion temperatures. The rate of oxidation raises with flame temperature, and thus with increasing equivalence ratio for sub-stoichiometric conditions. For temperatures over 1800 K, chemical dissociation of CO_2 to CO becomes relevant. Consequently, low levels of CO formation are found only in a narrow range of equivalence ratio around 0.8 [Lefebvre 1999]. The high-temperature dissociation is, however, not significant, because in most cases, CO is oxidised later in cooler air-rich downstream zones [Wulff 1997]. Increasing the combustion pressure is beneficial to the emission of carbon monoxides at low equivalence ratios, because conversion reactions from CO to CO_2 are favoured. At high equivalence ratios, increased pressure reduces chemical dissociation [Lefebvre 1999]. The main emissions of UHC and CO can thus be assigned to the low power (idle) engine loads.

The formation of nitrogen oxides NO_x (i.e. NO and NO_2) is, as seen from the mechanism (1.2), not directly involved to the combustion reaction. NO_x formation is a side phenomenon, which is mainly explained by four mechanisms, the thermal NO, the nitrous oxide, the prompt NO and the fuel NO mechanism [Lefebvre 1999]. Without going into further detail of these mechanisms, their participation to the formation of nitrogen oxides in combustors can be summarised as follows [Wulff 1997]. For high combustor inlet temperatures NO_x emissions are dominated by the thermal mechanism. Prompt NO becomes a relevant mechanism for low temperature, where the formation of thermal NO is of limited importance.

For a lean premixed flame at 1900 K it is estimated that 60 % of nitrogen oxides occur via the thermal NO and 30 % via the prompt NO mechanism [Wulff 1997]. Technical efforts to the reduction of nitrogen oxides are therefore mostly concentrated on the thermal mechanism. The thermal NO mechanism consists in the oxidation of atmospheric nitrogen in the post flame gases. The oxidation to NO is most active in the presence of O and OH radicals, i.e. high temperatures and long residence times are favouring this mechanism.

The formation of soot is primarily a problem of fuel rich conditions and extinction. These are causing hydrocarbons to be not completely cracked to C_1 and C_2, and thus lead to formation of soot precursors like acetylene (C_2H_2). Acetylene then reacts with CH and CH_2 radicals to C_3H_3, from which benzene is produced by recombination and rearrangement [Brasseur 1998]. Further addition of C_2H_2 to the ring finally leads to soot formation, which is generally favoured for high temperatures and pressures. In current engines, good fuel preparation in particular using air blast atomisers leads to a homogeneous fuel distribution. Thus, fuel rich pockets are avoided, which generally reduces the soot formation to negligible levels.

1.2 Low emission engine design

Understanding the mechanisms of pollutant formation in turbine combustion clearly changed the concepts for engine development. Staying with the conventional combustor design, further increase of temperature and pressure by means of bypass ratio beyond 9:1 promises better specific fuel consumption, but this is unfortunately more than counterbalanced by higher NO_x levels.

1.2.1 The conventional combustor and its emission problems

In contrast to piston engines, turbines release their heat of combustion continuously. Wall cooling is therefore a serious issue of turbine design, and the maximum feasible load of the engine is mainly determined by the cooling capacities.

The wide operating range between low power idle and high power take-off settings would be unfeasible if the whole available air was taken for the combustion process. Thus, the conventional approach is a combustor design, which introduces only a part of the available air into a primary zone, where the fuel is injected and burned (cf. figure 1, top). In this way, the equivalence ratio is raised (compared to the overall equivalence ratio without air split) to approximately stoichiometric conditions for high engine loads and values sufficiently above the lean extinction limit at idle settings. Due to a fixed geometry, the air split between the primary zone, the downstream secondary zone and the dilution zone is constant. This makes lean combustion unfeasible for high power operation [Wulff 1997].

The bottom figure 1 shows the CO and NO_x emissions of a conventional combustor as a function of the primary-zone temperature. The range of temperature from 1670 K to 1900 K could be characterised as a low-emission window. This corresponds roughly to intermediate power settings, e.g. under cruise conditions. Including idle and take-off power settings, the temperature in the primary-zone ranges from 1000 to 2500 K. Especially for the engine emission test, which corresponds to a weighted cycle of landing/take-off (LTO), conventional combustors show therefore a relatively high level of pollutant emission (obscuring the better emission levels at cruise).

An improvement of conventional combustors was achieved by a better fuel preparation (more homogeneous fuel-air mixture by use of air blast atomisers) and the shortening of the combustor length. The former helped to optimise the fuel-air mixing, which limits the necessary time to burn out CO and UHC. The latter reduces the residence time, favouring the limitation of NO_x formation.

The ongoing demand for further reduction of the NO_x levels leads to new engine concepts. The control of the combustion process and the fuel injection must imply an adapta-

tion of the equivalence ratio in order to avoid extinction problems and high emissions of UHC and CO for low temperatures at idle as well as high levels of NO_x formation for high temperatures at take-off.

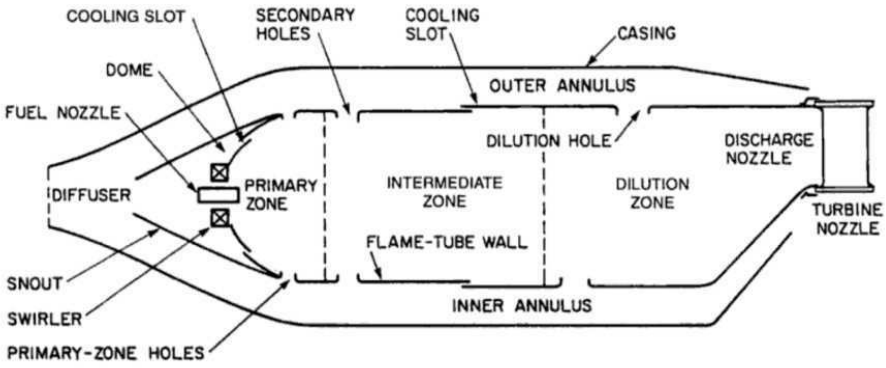

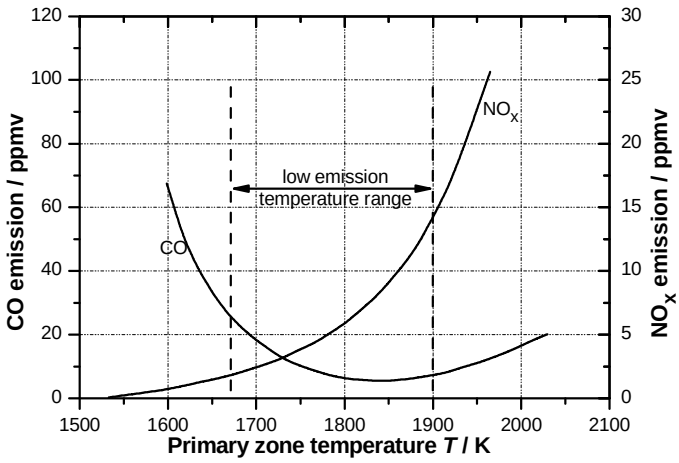

Figure 1: From [Lefebvre 1999].

Top figure: principle design of the conventional combustor. The air is split up between the primary-zone and the downstream intermediate or secondary zone and the dilution zone. The split is constant due to a fixed geometry, which makes lean combustion at high power settings unfeasible.

Bottom figure: influence of primary zone temperature on CO and NO_x emissions. This is only a cut-off from the conventional combustor temperature, which can range from 1000 K (low power) to 2500 K (high power).

1.2.2 Fuel staging

The main problem of the conventional combustor design is the unchangeable split of air between its zones. The equivalence ratio cannot be adapted for different engine loads in order to stay under conditions of low-emission. Lean combustion at high power take-off settings is therefore unfeasible. Variable geometry concepts regulating the air split have been discussed, but were not pursued due to reliability problems. Another possibility to adapt the equivalence ratio is fuel staging. This concept was initially applied to conventional combustors: by turning on and off of the individual burners placed on the perimeter around the

combustor axis both satisfactory lean extinction limits and a reduction of pollutant emissions were achieved [Wulff 1997].

Today's fuel staging is basically following the same concept, but is realised by means of two separated combustors in a single casing, the first called the pilot and the second the main. Different geometries are possible, tandem, axial (series) or radial staging. All geometries have specific benefits and weaknesses (e.g. the ignition reliability and the combustion efficiency of the main profiting from the heat released in the pilot or the limited length combined to the smallest cooling surface for axial staging; the largest cooling surface versus better constructive integration of pilot and main for radial staging). The first staged combustors supplied to the fleet of Airbus A320 and Boeing 777 were the General Electric CFM 56 and GE 90, both certified in 1995. With these dual-annular combustors (DAC), 35 % lower CO and UHC and 45 % lower NO_x emissions were achieved compared to the corresponding single-annular version [Lefebvre 1995].

The principle of the lower emission levels achieved by staged combustion lies in the operating of pilot and main over the range of engine loads. At idle condition, the fuel is solely burned by the pilot combustor, allowing to double the equivalence ratio compared to a conventional combustor under the same load, and thus to start in the range of low-emission (cf. bottom figure 1). Equivalence ratio (and temperature) increases with engine power until the upper limit of the low-emission window is reached. At this so-called staging point, the fuel is redistributed to both the pilot and the main combustor in order to return to the lower equivalence ratio limit of the low-emission window in the primary-zone [Wulff 1997].

Comparing engines with and without fuel staging, complexity and weight are clearly increased for staged combustors. Further, the application of staged combustors requires a stronger effort to maintain the levels of engine reliability. A somehow limiting factor is also the amount of available air, which has to be split into surface cooling and combustion control between the pilot and main zone. The greater cooling surfaces especially in the case of radial staging are thus limiting the flexibility of combustion control and therefore the efficiency of emission reduction. Besides, at high engine load (beyond the staging point) staged combustors have higher emissions of UHC and CO than conventional combustors.

1.2.3 Injection strategies for lean combustion (LPP, LP and LDI)

For liquid fuel combustion, the flame stability is prone to inhomogeneities of the fuel distribution. Especially near to the lean extinction limit, the existence of locally fuel rich pockets next to fuel lean zones increases the risk of flame extinction. In the conventional combustor, only a part of the overall available air is used in the primary-zone. For low engine loads, this allows to increase the equivalence ratio to acceptable values above the lean extinction limit. If inhomogeneities could be avoided, leaner combustion very close to the extinction limit

would be feasible, resulting in lower temperatures and substantial further reductions of NO_x emissions.

A promising concept to reach ultra lean combustion conditions is to improve the fuel preparation by means of fuel premixing and prevaporisation in order to provide a fully homogenised fuel-air mixture to the combustor. This concept is commonly referred to as lean premixed prevaporise (LPP) combustion and is an issue of actual research for further reduction of pollutant emissions.

A typical LPP combustor is subdivided into three sections, the first of which is designed for fuel injection, vaporisation and fuel-air mixing, taking special care to obtain complete evaporation and homogeneous mixing. The lean premixed prevaporised fuel-air mixture is then provided to the second zone, where combustion is carried out at the smallest possible margin to the lean extinction limit and the flame is stabilised by means of recirculation zones. The exhaust is provided to a third zone for dilution [Lefebvre 1999].

The design of the LPP combustor implies major conceptual problems. The minimum length of the premix duct is designed to achieve a fully evaporated well homogenised fuel-air mixture prior to the combustion zone. At high temperatures associated with high power settings autoignition or flashback from the combustion zone might occur in the premix duct if the residence time of the fuel-air mixture exceeds its autoignition delay time. Further, operating the LPP combustor with lean fuel-air mixtures at high power settings comes at the price of very low equivalence ratios at idle conditions (the same as for the conventional combustor), and thus, the risk of flame extinction.

A common technique to reduce the risk of flashback and flame extinction was found with fuel injection into shear layers [Wulff 1997]. Future applications of the LPP concept to aeroengines will certainly need some type of fuel staging to overcome the drawbacks of this technique. An alternative approach is investigated, which is less difficult to handle. The concept of this so-called lean premixed (LP) or partially evaporation and rapid mixing (PERM) injection consists of premixing primary air with liquid fuel and entering the combustion chamber at incomplete evaporation. The LP concept reduces the risk of flashback and instabilities compared to the LPP technique.

Next to LP and LPP approaches, lean direct injection (LDI) is another concept to achieve lean combustion mixtures. LDI is avoiding autoignition and flashback problems by directly injecting the liquid fuel into the combustion zone. Rapid mixing allows for a very homogeneous fuel distribution. This is realised by multipoint injection systems. As the fuel is not premixed and prevaporised, it is important to achieve fine atomisation and mixing of the fuel and air quickly and uniformly so that flame temperatures are low and NO_x formation levels near those of LPP systems [Tacina 2002].

Lean combustion concepts based on LP, LPP or LDI (multipoint) injection are operating in a narrow window of equivalence ratio in order to achieve low NO_x emissions for all engine power settings. As mentioned earlier, an adaptation of the equivalence ratio to this low emission window is also possible by fuel staging, i.e. variable fuel splitting over the engine load between a pilot and a main combustor. DAC technology applying injection strategies for lean combustion is addressed by the CLEAN combustor approach (SNECMA, MTU and Avio), featuring an axially staged combustor, whose main dome is provided with an LPP injection system. An alternative fuel staging concept is the direct integration of the pilot and main stage to the level of fuel injection, which allows for reduction of weight and complexity. Fuel staged injectors can thus be integrated into single annular combustors (SAC). Further, bundling of both lean injection and fuel staging is possible. The staging might help to overcome the weaknesses of the lean injection concept providing adaptability of the equivalence ratio to the engine load.

An example of SAC technology integrating fuel staging to a lean injection of LP type is the GEnx (General Electric next generation) engine with the Twin Annular Premixing Swirler (TAPS) from General Electric, planned for Boeing 787 and Airbus A350 aircraft. A similar concept is pursued by Rolls Royce plc with the ANTLE technology, also applying a fuel staged LP injection strategy to a SAC. An approach followed by SNECMA realises lean fuel-air premixing by means of a multipoint injector, which could by categorised as LDI type.

1.3 European research on lean combustion technology

The Advisory Council for Aeronautic Research in Europe (ACARE) has released a Strategic Research Agenda (SRA) fixing further reduction targets of 50 % in CO_2 and 80 % in NO_x for the year 2020 (compared to 2000). As already stated, CO_2 reductions are mainly achieved by increasing fuel efficiency and aircraft performance. In contrast, for the reduction of secondary pollutant emissions such as UHC, CO and NO_x, manufacturers have to focus upon the development of the combustor technology. New injection concepts enabling lean combustion like LP, LPP and LDI (multipoint) are particularly promising to reach the ACARE targets for NO_x emissions. Their application was studied throughout a series of research projects within European Framework Programs (FP), such as LowNOx III (FP4), LOPOCOTEP (FP5) and TLC (FP6).

The LowNOx III project concentrated on LPP injection systems covering overall pressure ratios (OPR) from 15 to 40. The LPP technique showed promising results for small engines with low OPR, achieving substantial NO_x reductions. However, applying the LPP technique to large engines with axial or radial staging, the high OPR increased the risk of auto-ignition and lead to a propensity for instability. Pursuing the work in the LOPOCOTEP program, the industrial partners concentrated on different aspects of performance improve-

ment, such as emission levels, stability limit and operating range. Fuel staged injection concepts for lean combustion were further studied for SAC engines like the ANTLE combustor by Rolls-Royce plc and the first implementation of LPP technique to a SAC via fuel staging by SNECMA and Rolls-Royce Deutschland.

With the knowledge gained within the previous EC funded and national projects, the most promising among the concepts to meet the challenging ACARE objectives were considered to be the fuel staged lean injection systems mounted to single annular combustors. The development was carried on within the project "Towards Lean Combustion" (TLC), again uniting the five main European manufacturers (SNECMA, Rolls-Royce Deutschland, MTU aero-engines, Avio and Turbomeca). Further participants were the two main European national research centres in aeronautics (ONERA, DLR) and many of the universities and laboratories in the field of measurement techniques and computation. The objective of TLC was to obtain sufficient technological maturity on fuel staged lean injections systems designed for SAC, using design optimisation procedures, i.e. genetic algorithms. Advanced experimental diagnostics and computational fluid dynamics (CFD) helped to access key issues like the fuel distribution, and thus contributed largely to define the fuel injection design. The emission performances, the risk of auto-ignition and flash-back and the stability of combustion were investigated for fuel staged LP or LPP injection systems and OPR from 15 to 35.

1.4 Physical parameters to be experimentally and computationally accessed

The design process and the control of fluid-thermal systems like combustors, furnaces and reactors requires quantitative data on the actual flow field, such as temperature, pressure, species concentration and velocity [Knight 2006]. Better knowledge and dimensioning of current and new engine concepts is provided by accessing the combustion process via computational and experimentation tools. In many situations, very limited access to the flow domain is available and strong constraints are thus placed on the experimental data that can be obtained through non-intrusive (e.g. optical) and intrusive techniques [Jaluria 2010]. Some non-intrusive optical diagnostic techniques have become very important to research in the field of combustion engines due to their capability of providing instantaneous information on physical properties of interest from the inside of the combustor. With the necessary input and feedback of experimentation, numerical simulations are a main tool for the development of new engine concepts. Under conditions not easily accessed experimentally, numerical tools are of utmost importance to obtain the necessary information on the flow field.

Commonly, numerical simulation tools such as Computational Fluid Dynamics (CFD) are applied. Experimental data are valuable in solving complex practical problems that involve thermal transport processes and are often critical to obtain accurate, valid, physically

realistic and dependable numerical results [Jaluria 2010]. CFD calculations can only be successful if the boundary conditions are well defined, which is often not the case due to lack or inaccuracy of experimental data. Sometimes, coupling of the experimentation with the simulation data is appropriate. Genetic algorithms are an innovative approach to engineering research based upon the synergistic interaction between experiment and simulation.

CFD computation designed for an overall process description integrates various submodels. For the development of model subclasses, experimental data is required as well as for its validation. [Dreizler 2002] present an exemplary overview of requirements for submodel development and validation in the field of turbine combustor technology. An integrated model for a fluid-thermal system like a combustor is composed of subclasses representing turbulence models, chemistry-turbulence interaction models, reduced reactions models, detailed chemistry models, spray models and radiation and heat transfer models. A number of laser-based techniques are suitable for the specific needs involved in the process of model development and validation.

Diagnostics are targeting principle problems of the combustion process, such as the NO formation as a function of fuel richness and the safety and reliability of ignition, involving the description of combustion chemistry and the phenomena of turbulent combustion. Trying to give a response to these problems, the development and validation of specific designs in industrial applications such as IC engines and gas turbines needs a number of diagnostic features for charge visualisation (fuel concentration and fuel-air mixture), visualisation of residual burned gas, droplet and vapour-liquid phase characterisation and pollutant and temperature measurements [Kohse-Höinghaus 2005].

1.5 Implication to the "Towards Lean Combustion" (TLC) project

For the aircraft combustor concepts described earlier, the equivalence ratio was shown to be of primary influence for the formation of pollutant emissions due to its link to the combustion temperature. The sensing of the fuel-air mixture by means of laser diagnostics applied to the SNECMA multipoint fuel staged injector was part of this thesis work embedded to the TLC project and realised within the laser diagnostics group at the Physics Sensing and Instrumentation Department of ONERA. The results were later used by other project participants as input data for genetic design optimisation algorithms and for validation of CFD calculations.

The present work was mainly motivated by the need for the planar laser-induced fluorescence (PLIF) technique capable of the analysis of kerosene-air mixture after fuel injection into the combustion chamber of an aeroengine. Fluorescence photophysics of kerosene fuel

had to be studied in a laboratory environment in order to achieve maturity of the kerosene PLIF diagnostics with regard to its application to high-temperature and high-pressure conditions. Temperatures and pressures were extended from 300 to 900 K and from 1 to 30 bar. A diagnostics strategy for kerosene PLIF was derived, which allows for the analysis of kerosene-air mixtures under conditions realistic for different engine loads. The kerosene PLIF technique was then applied to thorough investigations of a SNECMA multipoint injector, a single of which was mounted to a single sector combustor test rig, which was then implemented to the ONERA M1 test bench.

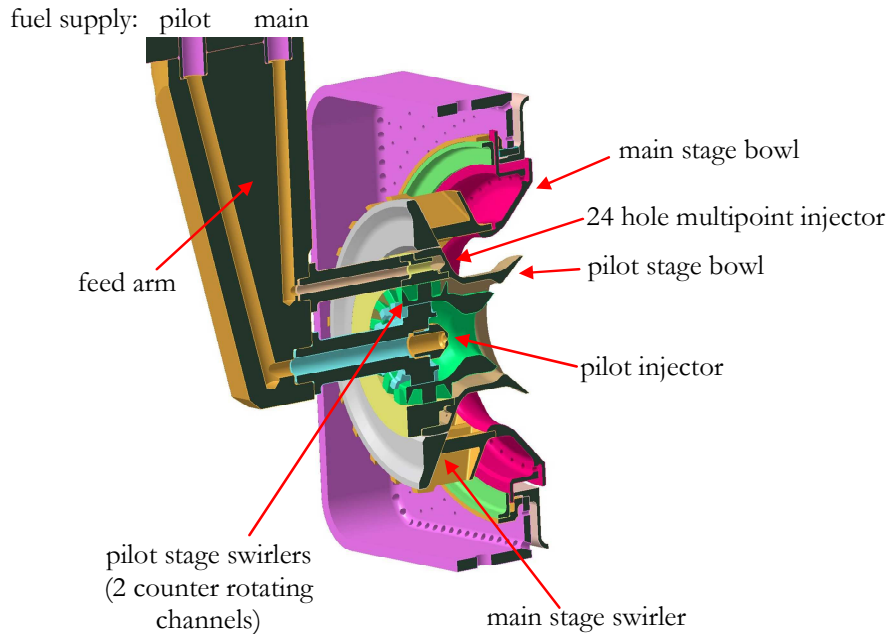

Figure 2: Cutaway model of the SNECMA multipoint fuel staged injector.

Figure 2 contains a cutaway model of the SNECMA injector, about 20 of which are typically mounted in an annular combustion chamber of an aeroengine. At the axis of an inner bowl, the pilot stage is placed. The main stage is formed by a 24 hole multipoint injection into an outer bowl, which serves for fuel-air premixing. The bowl length has short design in order to avoid the risk of autoignition and flashback, which is an issue for LP and LPP concepts. Turbulent premixing is provided by means of swirlers around the pilot and main stage injectors.

In order to complete the set of acquired information for an easier data evaluation and interpretation, the sensing of equivalence ratio was accompanied by PLIF measurement of the OH radical. OH occurs near to the flame front, where the kerosene fluorescence signal should vanish, and thus indicates the reaction zone location downstream from the injectors.

1.6 Use of non-intrusive laser diagnostics in combustion media

Laser light provides remote access for non-intrusive measurements even under extreme physical conditions. Coherent laser light can be focussed and is hence able to deliver the energy where it is needed for local "in situ" sensing. Due to short nanosecond pulse durations of commercial laser sources, combustion processes can be "frozen". Modern sheet forming optics and the accessible high repetition rates of today's lasers allow for spatially and temporally precise measurements. Dependent on the choice of the application, inelastic laser techniques like Raman scattering or laser-induced fluorescence yield the possibility of species resolved sensing for local physical quantities like concentration and temperature. The knowledge of the molecule's intrinsic structure with its various internal states of energy is thereby a key for the studying of thermodynamic properties. Lasers are spectrally narrowband and therefore the most adapted devices for resonant excitation of single transitions (spectral lines). Very short pico- to femtosecond laser pulses give access to study the processes of inter- and intramolecular energy transfer.

The interaction of polarisable media with the electromagnetic light wave is at the source of all laser diagnostics. For references see textbooks dealing with fundamentals of electrodynamics, photonics and laser diagnostics ([Griffiths 1999], [Saleh 2001] and [Eckbreth 1996]).

1.6.1 Geometric arrangement

Generally, incoherent diagnostics techniques are characterised by a geometric arrangement different to the coherent case (cf. figure 3). For incoherent processes, a single laser beam is scattered by molecules in each point of the beam path. The intensity of the scattering light varies with the angle of observation and is detected over a solid angle by means of collection optics. Mostly, large solid angles and hence wide collection optics are necessary to reach satisfying signal-to-noise levels or sensitivity. For coherent techniques the signal originates from the intersection volume of crossing laser beams. The signal presents as the modulation of one of the original beams or as a newly generated signal beam.

Coherent techniques are generally limited to point measurements, whereas the incoherent approach allows for line sensing or even two-dimensional imaging diagnostics. The strong signal intensities of coherent techniques are clearly an advantage. However, one has to pay for this with the need for a free line-of-sight due to its double ended arrangement. Incoherent techniques can be single ported when performed in backscatter. In the linear regime, the incoherent signal intensity depends linearly on the laser fluence, while its spectral shape and position do not. Hence, signals are likely to be normalised to the laser intensity in many practical applications.

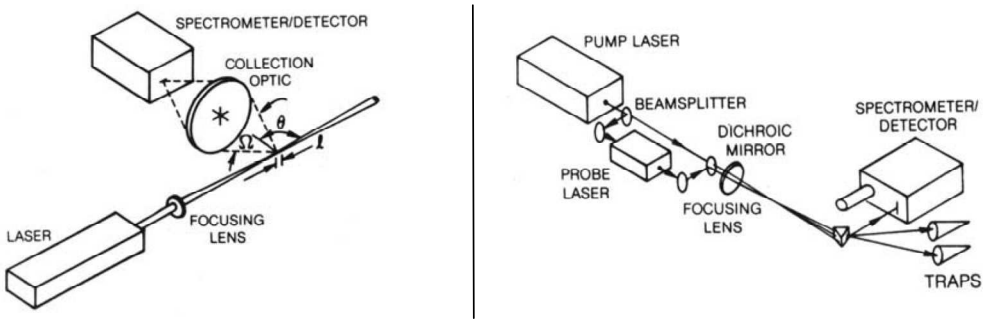

Figure 3: Geometric arrangements of incoherent (on the left) and coherent (on the right) techniques from [Eckbreth 1996].

The main criterion for the origination of a coherent process is the nonlinearity of the medium, which shows for the higher orders of susceptibility under the coercive condition of strong laser irradiance. The laser-like signals of coherent techniques allow for application to highly interfered environments, e.g. as found in combustion chambers, but for the prize of complicated line shapes, because these processes, intrinsically dependent on laser intensity, show nonlinear behaviour with species concentration, which complicates normalisation and calibration procedure [Eckbreth 1996].

1.6.2 Application to turbulent combustion

Combustion in internal combustion engines and turbines practically always involves turbulent flow fields. Turbulence increases the mixing of fuel and oxidiser and thus enhances the combustion reaction. In turn, the combustion itself releases heat, which generates flow instabilities, favouring the turbulence [Peters 2006]. Hence, diagnostics applied to combustion engines has to cope with turbulent fluid dynamics coupled to the chemical kinetics of the combustion reaction. Each consecutive observation of the field of flow and scalars is different from the previous and none is identical to the average [Kohse-Höinghaus 2005]. This specific background explains, why optical diagnostics employing pulsed laser sources and fast gated detectors are such valuable. Especially the simultaneous acquisition of multiple quantities within instantaneous single-shot measurements are of great interest for the development and validation of submodels such as the chemistry-turbulence interaction.

(a) Combustion engines

A large number of combustion diagnostics applied to piston and turbine engines is motivated by the challenging regulations concerning the air quality, limiting the pollutant emissions of future engine designs. The combustion process has to become "cleaner", while not less efficient. Laser diagnostic techniques provide evidence directly from the combustion

process. Concepts are evaluated on carefully designed test systems, where the impact of design variations on key parameters such as fuel-air mixing, spray formation and evaporation or pollutant emission can be observed straightaway. Prior to application, modern combustion concepts like the homogeneous charge compression ignition (HCCI) engine or the lean-premixed prevaporised (LPP) gas turbine need for experimentally validated models.

Practical combustion engines yield challenges for laser diagnostic measurements within the pre-combustion, combustion and post-combustion phases. The engine configuration of piston engines is largely different from turbine engines. In face of the different technology aspects, many laser diagnostic techniques are applied similarly to both, because they need for the same type of information. At a distinct observation point of the engine, the continuous combustion in turbines results in a constant pressure, whereas the cylinder pressure of piston engines changes specifically for each cycle with the crank angle. In order to successfully provide the sought information, laser diagnostics have to be adapted to the operating conditions of the specific engine type.

For a constant engine load, in internal combustion (IC) piston engines the local parameters change continuously with the crank angle, which means a real challenge for diagnostics, especially if the temporal development of combustion in a single engine cycle may need to be followed. An estimate of the average cylinder temperature is commonly derived from the cylinder pressure trace assuming adiabatic compression. The cycle variation of temperature and pressure induces a change in species number densities, and therefore, in-cylinder diagnostics are commonly calibrated to the crank angle. This is usually done providing a homogeneous fuel-air mixture to the cylinder. For various laser diagnostics, e.g. like laser-induced fluorescence, the intensity of the radiative emission depends on the number density, not only of the emitting species, but further of other species, potentially being partners for collisional quenching and chemical reactions. These non-radiative processes are playing the role of competing events in the rate-equation balance for the emission. Whenever competing events are highly efficient, signal quantification might provide ambiguous data. The fluorescence emission of many aromatic species are most efficiently quenched by collisions with oxygen. Crank angle calibrations with homogenous charge have thus to be repeated for different fuel-to-air ratios in order to account properly for the quenching influence referred to the local oxygen concentration. Laser-induced fluorescence measurements are mostly performed using non-fluorescent alkane surrogates doped with fluorescence tracers. Choosing a tracer species, which is practically insensitive towards oxygen quenching, allows to circumvent the otherwise challenging signal quantification.

Turbine engines work under temporally nearly constant temperature and pressure conditions for a given engine load, which should in principle simplify the application of laser diagnostics compared to piston engines. However, so far only few studies report from laser diagnostics in turbine combustion, whereas examples for piston engines are quite numberless. The large dimension of real-size turbine combustor test rigs and their high operating cost are

certainly main reasons for this. Besides, piston engines are often operated with simple alkane surrogate fuels, providing nearly the same combustion properties, while substantially simplifying the high complexity of laser diagnostic application compared to the use of real petroleum type fuels. Surrogate fuels designed for turbine engines generally need a large number of chemical species to achieve high real fuel analogy within engine operation. This complicates the application of laser diagnostics. Methods making use of UV or visible laser pulses suffer from interferences and signal cross-talk, induced by simultaneous excitation of multiple species.

(b) Non-premixed and premixed combustion

The study of combustion media must account for the rate of turbulent mixing between fuel and oxidiser, which determines largely the reaction rate. Two limiting cases exist, the non-premixed and the premixed combustion. Chemical reaction can only occur if the mixing is complete to the molecular level. For non-premixed combustion the location of the reaction zone is determined by the turbulent mixing field. For the premixed case, the reactants are already mixed to the molecular level. Therefore, the combustion is not longer bound to the stoichiometric level, but controlled by the propagation of an ignition front from the hot product zone to the cold reactants [Bilger 1989] (remember: premixed combustion was already mentioned to be prone to flashback). For scalar data in non-premixed (diffusion) flames sensed by means of incoherent laser diagnostics, signal intensities depend on both, the local instantaneous composition and the progress of reaction. Both effects must be considered by simultaneous measurements in order to obtain a closure relation, enabling sustainable data interpretation [Kohse-Höinghaus 1994].

1.6.3 Fundamental issues for laser diagnostics in combustion media

Intrusive techniques using physical probes have lost much of their importance for diagnostics in combustion media, which must be seen as a consequence of their inferiority compared to non-intrusive laser-based methods. However, all types of laser diagnostics present next to specific advantages also limitations, especially with respect to signal quantification. Effectively, there is no simple approach for the measurement of all needed quantities satisfying at the same time the various constraints met within the observation of such a complex process like combustion. Rather, different diagnostic techniques have to be applied in a complementary way. The choice of the technique depends on the quantity to be sensed, the species and the specific environmental conditions. If possible, different quantities are measured simultaneously to obtain the largest possible data base for submodel development and validation.

A number of reviews has been published in the field of laser diagnostics applied to combustion media (e.g. [Kohse-Höinghaus 1994], [Wolfrum 1998], [Wolfrum 2000], [Hassel

2000]). [Kohse-Höinghaus 2002] presented a large assembly of contributions from different experts, addressing the main available diagnostic methods along with their typical applications in the field of combustion. To become familiar with the fundamental principles of laser-based combustion diagnostics, [Eckbreth 1996] is an excellent standard, more concentrating on background issues of specific techniques.

A large number of references testify to the combined use of different laser diagnostics in combustion media. For distinct examples refer to the reviews of [Wolfrum 2000] and [Kohse-Höinghaus 2002]. The quantities and information sought within combustion diagnostics are typically resumed as follows:

- temperature, concentrations of major and minor constituents and velocity (often needed along with local gradients or spatial and temporal variations)
- concentration and distribution of soot particles or droplets
- information about fuel atomisation and evaporation, ignition, localisation of the flame front, flame propagation, heat release and flame extinction.

A number of laser diagnostic techniques was developed to meet these needs. An incomplete list might look as follows:

- absorption techniques: Fourier transform infrared (FTIR) and UV/vis absorption spectroscopy, cavity ringdown spectroscopy (CRDS)
- laser extinction: (Beer-Lambert law, scattering and absorption of particles leading to attenuation) diagnostics of combustion-generated soot
- laser-induced incandescence (LII)
- particle sizing and velocimetry techniques: Mie scattering imaging (MSI or ILIDS), laser Doppler velocimetry (LDV), phase Doppler anemometry (PDA), particle imaging velocimetry (PIV), gaseous image velocimetry (GIV), laser flow tagging (LFT)
- incoherent molecular scattering techniques (major species concentrations): laser-induced Rayleigh scattering (LRS), filtered Rayleigh scattering (FRS), spontaneous Raman scattering (SRS), near resonant Raman scattering
- incoherent linear spontaneous fluorescence techniques: laser-induced fluorescence (LIF), laser-induced exciplex fluorescence (LIEF)
- nonlinear coherent techniques: coherent anti-Stokes Raman scattering (CARS), degenerate four-wave mixing (DFWM)
- other seldom applied techniques: laser-induced grating spectroscopy (LIGS), laser-induced breakdown spectroscopy (LIBS), resonance-enhanced multi-photon ionization (REMPI).

In the following, some basic issues concerning these methods will be presented. Restriction is made to the detection of minor and major concentration of gases, vapours and soot. Particle sizing and velocimetry approaches will not be considered.

(a) Chemiluminescence emission

Despite emission following absorption, luminescence might also occur from chemical reactions. This can be of interest for diagnostics. Chemiluminescent species like the free radicals OH, CH and C_2 allow for qualitative observation of flames, helping to assess information on the combustion process, useful to improve the design of practical combustors [Caldeira-Pires 2001].

(b) Laser-induced incandescence (LII)

The blackbody radiation of soot particles allows to study the soot production in practical combustors by laser-induced incandescence (LII). Soot particles absorbing a laser light pulse are heated well above the flame temperature, followed by total evaporation and cooling. Under these circumstances, the resulting blackbody radiation is blue-shifted compared to the flame emission. Applying a specific calibration procedure, the soot volume fraction can be quantitatively derived from the LII signal.

First observations contributing to the development of this method were made during Raman measurements by [Eckbreth 1977], who noticed that the Raman probe laser heated the soot particles well above the ambient flame temperature, thereby producing a broadband signal interfering with the Raman signal. [Dasch 1984] vaporised soot particles by a strong laser beam and sensed the absorption reduction by means of a weak probe beam in order to measure local soot concentrations. [Melton 1984] was the first to provide theoretical and experimental demonstrations of laser-induced incandescence as a diagnostic method for soot concentration sensing. A thorough review of recent trends of the LII method is given by [Schulz 2006].

As a part of the TLC project, [Geigle 2008] performed LII soot measurements on the SNECMA multipoint fuel staged injector mounted to a single sector combustor test rig implemented to the ONERA M1 test bench.

(c) Absorption techniques

One of the most reliable methods for the detection of trace species is the laser absorption spectroscopy. The absorption process is practically immediate (approx. $10^{-15}\,\mathrm{s}$), and thus, competition with other pathways is generally not relevant. Absorption measurements can

provide unambiguous information on both species concentration and temperature if the absorption scheme of the respective molecule is well-understood. Absorption spectroscopy is therefore a standard for calibration purposes, even though it has some principal drawbacks. As a line-of-sight technique with limited spatial resolution it is restricted to homogeneity of the absorber distribution and temperature along the laser beam. Further, for many species the sensitivity is too poor for detection at very low concentration levels. Absorption techniques are distinguished by wavelength range into UV/visible spectroscopy and Fourier transform infrared (FTIR) spectroscopy.

Another absorption technique is the cavity ring-down spectroscopy (CRDS). Rather than working on the absolute absorbance, this method is based on the decay rate of a laser pulse due to absorption and scattering when trapped in a cavity with highly reflective mirrors. If the cavity is entirely filled by the sensed species, the absorption can be determined from the ring-down time, i.e. the time constant of the signal decay. Knowledge of the ring-down time for the empty cavity allows to correct for mirror losses and other scattering/refraction phenomena, not related to the sensed species. The decay rate is independent from the laser intensity, which is clearly an advantage of CRDS. Further, the multiple passage of the cavity enables very high species sensitivity. A principle weakness of CRDS is the need to homogeneously fill the cavity with the sensed species, which makes it unsuitable for in-situ detection in combustion chambers. Moreover, acquisition of CRDS spectra is time consuming due to the use of a monochromatic laser source. CRDS techniques avoiding spectral scanning by use of broadband sources and grating detection are currently under investigation.

Due to its high sensitivity, CRDS is a valuable method for calibration of other techniques like laser-induced fluorescence (LIF) or incandescence (LII). Further, CRDS is a highly sensitive method for sensing of toxic emission sampled in the exhaust gas of combustion engines, especially for non-fluorescent species.

(d) Scattering techniques

If the dielectric medium consists of molecules much smaller than the wavelength of the incident laser light, the incoherent emission of radiating dipoles linearly and instantaneously induced by the incident electric field through their time-invariant molecular polarisability (susceptibility) is called Rayleigh scattering.

The elastic Rayleigh scattering is illustrated together with the inelastic Raman effect in figure 4. In the case of Rayleigh scattering, the molecule passes via a virtual energy level and returns immediately to the initial state. Rayleigh scattering is not tied to molecular resonance frequencies, and thus occurs at any frequency of the incident light. Since there is no energy exchange between the incident photon and the scattering molecule, the Rayleigh emission says nothing about the molecule's structure, i.e. Rayleigh scattering is not species selective.

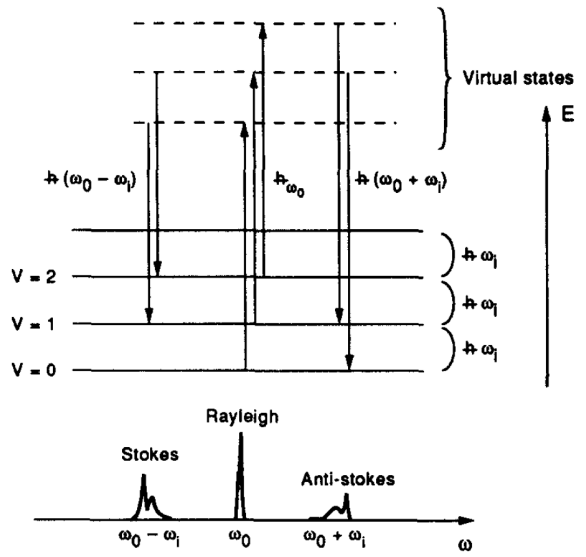

Figure 4: Schematic (virtual) energy state illustration of scattering processes. Taken from [Stepowski 1992].

Rayleigh scattering: no Raman effect, molecule does not change energy.

Raman scattering: (Stokes and Anti-Stokes) at any frequency of the incident light, i.e. non-resonant; molecule photon energy exchange equal to the differences of the vibrational and rotational energy-levels.

The moment of each oscillating dipole contributes not only microscopically to the elastic Rayleigh scattering at the incident wavelength, but further to inelastic scattering. This effect occurs via weak oscillating terms of the polarisability due to the molecule vibration and rotation. If the incident light has a frequency, which does not significantly perturb the molecular oscillations, the associated effect is called spontaneous Raman scattering (SRS). The Raman emission occurs Stokes shifted (to the red from the incident light) or Anti-Stokes shifted (to the blue). The latter is the case if molecules are in an excited state prior to scattering. For the Stokes shift, the molecule makes a transition to a higher state by transfer of some energy from the scattered photon to the molecule oscillation in terms of rotational, vibrational or electronic energy. The molecule passes by a virtual state, corresponding to the sum of initial state energy and the energy of the incident photon. This virtual state becomes an actual state only for resonant Raman scattering, where it coincides with a real molecule energy state.

The Rayleigh scattering cross-section scales with the forth power of the laser frequency, increasing considerably towards the ultraviolet. Within UV laser-induced fluorescence measurements, Rayleigh signals may therefore present a source of disturbing interferences, and they are generally suppressed by filters. Since the Rayleigh scattering is not species selective, its intensity depends on total number density of particles in the probe volume. In case the pressure is known, this enables thermometric sensing of the gas phase, given that the ideal gas law can be assumed.

The Rayleigh cross-section is very low ($\approx 10^{-27}\,\mathrm{cm}^2/\mathrm{sr}$), and high excitation intensities are needed to achieve a sufficient signal-to-noise (SNR) ratio. Rayleigh detection suffers from many interference sources, such as fluorescence and incandescence induced through the strong irradiation. In combustion media, the Rayleigh signal competes further with Mie scat-

tering at dust particles and surfaces, ambient light and flame emission. Whereas the two latter are largely suppressed by gated intensified detectors, spurious (stray) light from parasitic laser reflections can neither be filtered in time nor frequency domain. Laser-induced Rayleigh scattering (LRS) is applied as point, line or planar diagnostic tool, preferably to non-sooting combustion media.

A thorough review of Rayleigh scattering techniques was presented by [Miles 2001]. For unfiltered detection and use of standard lasers, the signal collection will comprise not only the elastic Rayleigh scattering (Cabannes lines), but also rotational and vibrational Raman lines. The contribution from the vibrational Raman scattering is very small, and thus negligible. The Cabannes lines span over a narrow frequency domain of a few hundredths of cm^{-1}. They are reflecting the translational motion of the molecules through Doppler and collisional shift causing temperature and pressure broadening. Collective scattering from many anisotropic molecules leads to partially depolarisation of the Rayleigh signal due to orientational averaging of the polarisability. Diagnostic approaches are possible either for recording the rotational Raman lines by filtering the Cabannes lines (used for species and temperature measurements) or by resolving the Cabannes line profile by means of narrow linewidth lasers (enabling pressure, temperature and velocity measurements of the gas from scattering strength, linewidth and frequency).

An example for an application of planar LRS for quantitative fuel vapour imaging under non-fired and fired conditions in a Diesel engine was presented by [Espey 1997]. They prevented fluorescence interferences from the fuel vapour by operating with mixtures of n-hexadecane and heptamethylnonane as Diesel reference fuels. Mie scattering from fuel droplets was avoided by restriction to zones of entirely evaporated fuel, scattering from surfaces by confinement of the laser sheet. Air and fuel were filtered to avoid scattering on dust particles. For fired operation, flame emission was eliminated by means of camera gating and spectrally filtering (10 nm bandpass).

First applied by [Miles 1992], the filtered Rayleigh scattering (FRS) is a spectral filtering approach designed to cut out the scattering light from slowly moving particles (Mie scattering) and multi-scattering from optics and surfaces by a super narrow atomic (or molecular) filter mounted in the detection path of the Rayleigh signal. This requires a narrowband laser with a linewidth much smaller than the temperature and pressure broadening, tuneable to the wavelength of the atomic filter. At the Division of Combustion Physics at Lund university, [Zetterberg 2008] applied FRS for 2D thermometry measurements in sooty premixed and non-premixed flames showing that the spurious scattering light can be sufficiently eliminated, enabling good SNR ratios. Implicated to the TLC program, the same research group was charged to adapt the FRS technique to the scattering from vaporised liquid fuels for application in a new burner facility with the possibility to investigate combustion/vaporisation phenomena at high pressure up to 16 bar with a maximum air flow rate of 1.3 kg/s and preheating of 800-900 K.

Spontaneous Raman scattering (SRS) emission is much weaker than laser-induced fluorescence. Comparable signals can only be obtained for near-resonant Raman scattering, enhancing the Raman cross-section up to six orders of magnitude [Eckbreth 1996]. For many molecules of practical interest in combustion diagnostics, there are unfortunately no electronic resonance frequencies in the vicinity of strong UV laser sources, and therefore, near-resonant SRS has not gained much importance in the past.

SRS applications allow for species selective sensing. Within the domain of UV excitation, primarily the vibrational Raman effect is occurring. Compared to Rayleigh scattering, the Raman scattering cross-section is about three orders of magnitudes smaller ($\approx 10^{-31}\,\mathrm{cm}^2/\mathrm{sr}$). For reasonable SRS signal intensities, strong laser irradiation is required, and detection is limited to majority species.

Almost all molecular species exhibit active Raman vibrational modes allowing for detection by SRS. A restriction to point or line measurements enables the collection of the Raman signal with spectral dispersion by line array detectors or charged coupled devices (CCD). Spectral analysis of the SRS signal yields the possibility to simultaneously detect the concentration of diatomics (e.g. H_2, N_2, O_2, etc.) and other simple molecules (e.g. CO_2, H_2O, etc.) in gas mixtures. If different large organic molecules are present, e.g. as in the vapour of petroleum type fuels, similarity and spectral overlap of the Raman bands complicate the determination of species concentration. However, the CC, CH and CH_3 bands scatter into specific spectral modes, and the intensity of these modes can be associated with fuel concentration.

Heteronuclear molecules systematically present infrared (IR) active vibrational modes, and thus generally allow for Fourier transform infrared (FTIR) spectroscopy. In contrast, homonuclear molecules like H_2, N_2 or O_2 do not show any IR absorption schemes in lack of a permanent dipole moment, and moreover, for some of them, electronic absorption bands exist only at high energies in the vacuum ultraviolet (VUV). Since Raman transitions are allowed, homonuclear molecules can be detected by SRS diagnostics.

In-cylinder SRS measurements have been realised in IC engines, sensing simultaneously for majority species like oxygen, fuel, nitrogen and water [Grünefeld 1994]. The use of an optical multichannel analyser (OMA) enables spatially (one-dimensional) resolved SRS approaches. Unfiltered detection of Raman scattering is highly suffering from interferences, which are generally unpolarized. In contrast, the Raman scattering itself is highly polarised. This allows for elimination of the broadband laser-induced fluorescence interfering with the Raman signal within the combustion of hydrocarbons. Grünefeld et al. demonstrated substantial improvements of the SRS signal-to-noise ratio enabling (even single-shot) measurements in spray flames and in areas contaminated by fuel droplets. SRS temperature measurements are precise, because the temperature information is obtained from the ratio of Stokes and anti-Stokes lines, which is generally unaltered, even under these difficult conditions.

(e) Laser-induced fluorescence

The basic principles of the underlying photophysics for electronic transitions are resumed in Chapter 2, where also a more detailed description of the nature of spontaneous fluorescence emission is presented.

Absorption of photons with appropriate energy promotes molecules to an excited electronic state. The change of the electronic configuration is ultrafast ($\sim 10^{-15}$ s), and is concluded, long before the vibrational excess energy has been distributed to a new nuclear configuration, which depends on the new electronic charge field. From the excited state configuration, a number of non-radiative and radiative deactivation pathways occur on competitive time scales. The radiative electronic transition from an excited state of singlet multiplicity back to the ground state is called fluorescence, i.e. the emission of a photon, whose frequency is defined via the quantum energy corresponding to the energy gap between the electronic states.

Whereas spontaneous Raman scattering is observed regardless of the used wavelength, fluorescence scattering only occurs if the photon energy matches the energy gap of the electronic transition. Since the state energies are characteristic, both absorption and fluorescence emission are species selective. Only for small symmetric molecules, transition lines are observed. For large molecules, absorption and fluorescence emission occur on extended spectral bands. Within the linear regime, the fluorescence emission depends on the laser irradiation and further on local environmental conditions such as temperature, pressure and gas composition.

The main drawback of spontaneous Rayleigh and Raman techniques was their poor scattering cross-sections, not allowing for detection of minor species in the ppm range. Secondary by-products such as CO and NO in hydrocarbon fuel combustion are thus practically out of range. Another disappointing feature was the restriction to point or line measurements. This is, where the laser-induced fluorescence (LIF) technique has its strengths: very small concentrations of the probed molecule can be detected (e.g. ppm or even sub-ppm of some radical species concentrations in flames). The high fluorescence cross-sections allow further for two-dimensional detection schemes referred to as planar laser-induced fluorescence (PLIF). Often, planar detection is feasible even in single shot acquisition mode, which has made PLIF a very important technique for the characterisation of turbulent combustion.

The laser-induced fluorescence method has, the same as all other techniques, important weaknesses. A main issue are non-radiative events such as collisional quenching competing with the fluorescence within its rate-equation balance. If collisional quenching plays an important role, a proper fluorescence quantification needs a thorough analysis of the collisional energy transfer. Further, the relevant quenching species concentration must be detected si-

multaneously to the fluorescence or a priori known. Sometimes, spontaneous Raman scattering (SRS) seems to be a better choice, despite its low cross-section [Mokhov 2005].

Next to the linear regime, fluorescence measurements can also be performed under saturated conditions. Then, the emission intensity does not change with the laser irradiation, and further, the fluorescence becomes practically independent from collisional quenching. However, saturation is difficult to ensure at the outer wings of the laser beam. Widening of the beam by means of an expander is a solution, which comes at the prize of minor spatial resolution.

The hydroxyl radical OH is often used for the characterisation of flames, where it is formed in high concentrations (percent level). This intermediate mirrors relatively well the transition from unburnt to burnt parts of the flame, and is thus a good marker for the flame front localisation, more stable (long-living) than the CH radical, which only occurs in zones with high reaction rates. Nitrogen monoxide (NO) and carbon monoxide (CO) are major pollutants occurring within the combustion of hydrocarbon fuels, typically with concentrations depending on stoichiometry (temperature) and fuel preparation.

In the field of turbulent combustion, species like OH, NO, CH and CO can quantitatively be probed by LIF [Hassel 2000], since their molecular structure and collisional energy transfer are relatively well known. In order to probe these combustion species, they need to have an accessible electronic transition band. Fluorescence detection of the OH intermediate has practically become a standard, since this species is relatively well understood. Excitation is usually done near 284 nm. For lower excitation wavelengths, such as provided by a KrF excimer laser, OH radicals are produced by dissociation of water molecules, and thus measured OH concentrations will not be representative for the amount of OH radicals produced by the flame. For NO, different excitation schemes exist, all presenting specific difficulties. An excitation near 225 nm is possible, but due to saturation effects the detection is limited to about 10 ppm. High-pressure combustion environments become opaque at 225 nm. Alternatively, NO can be excited near 248 nm, producing a vibrationally excited population, but only for elevated temperatures. NO PLIF is often used for mixing visualisation in flames, but only if no relevant concentrations of water and carbon dioxide are present, because these are most effective quenchers. CO has VUV electronic transitions and LIF measurements must therefore be performed by two-photon excitation. The fluorescence is rather weak compared to OH, and for excitation with two photons of 230.1 nm the signal suffers from interferences with the C_2 Swan bands (430 – 700 nm) [Linow 2000].

The quantification of the fluorescence signal needs for calibration to the detection efficiency of fluorescence photons, which depends on the observed solid angle, the transmission of the optical system and the detector response. Using identical excitation and detection paths for a known number density in the probe volume, correction for the detection efficiency can be done by calibration to Rayleigh or Raman scattering. However, if for the fluo-

rescence detection specific optical filters have to be used, it is most advantageous to use a calibration cell filled with a known homogeneous gas mixture comprising the fluorescing species. This is mostly done for stable species, whereas for transient intermediates, such as radicals in flames, calibration to standard flames is used, where species concentration and temperatures are well known.

For some radical species such as OH, O_2 and NO temperature information can be obtained from simultaneous excitation of two rotational lines, separated by an appropriate energy difference in the ground state [Wolfrum 2000]. If the two lines are ideally chosen, such that identical levels are populated by excitation through either laser photon, the depopulation processes from the excited state are common, and thus cancel out, making this method insensitive to quenching or rotational energy transfer (RET).

Many organic molecules exhibit a considerable temperature-induced (generally bathochromatic) shift for both, the absorption and fluorescence spectrum. At different positions of the absorption spectrum, the temperature dependence is thus not the same, which enables ratiometric methods using two-line excitation two-channel detection schemes for temperature measurements. This has been successfully applied to several ketones for two-dimensional temperature sensing in inhomogeneous concentration fields. Other ratiometric techniques benefit from a large temperature shift of the emission spectrum at a single excitation wavelength by two channel detection of the different parts of the emission spectrum. Simple benzene derivatives have been proposed for this. Approaches for ratiometric fluorescence measurements will be discussed more precisely in section 4.6.4.

(f) Signal interferences

A principal problem occurring for laser diagnostics are spectral interferences leading to ambiguity of the signal origin. This might be caused by large polycyclic aromatic molecules (PAH) absorbing in the UV and subsequently emitting background fluorescence in the UV and visible domain. The line emission spectra of small molecules like CN, CH, C_2, OH, NO and O_2 also interfere with some diagnostic methods [Kohse-Höinghaus 2005]. In preparation of laser diagnostic measurements, often excitation-emission spectra (EES) are recorded for identification of possible interferences.

Soot particles generated in fuel rich flames emit blackbody radiation, which is subject to a hypsochromic shift with increasing temperature following Wien's displacement law. This phenomenon, well known as the yellow-orange emission in many flames, is a source of background emission, and thus quantification of weak signals might suffer from it for wavelengths longer than 450 nm in the vicinity of flames. Although sometimes beneficial within LII soot diagnostics, the laser vaporisation of C_2 from soot can be a further interference source.

(g) Competition with non-radiative events

Diagnostic approaches based on the detection of radiative emissions must account for competing collisional events, which results in either intra- or intermolecular energy transfer. Intramolecular collision-induced vibrational relaxation changes the spectral emission, whereas intermolecular collisional quenching decreases the overall signal intensity. Radiative transitions occur between electronic states, whose energy gap has significant influence on the quenching efficiency. This shows for many aromatic molecules quenched very efficiently by molecular oxygen, making their use as tracers for laser-induced fluorescence (LIF) diagnostics a challenge, especially in combustion engines. The signal quantification becomes complicated and thorough studying of the collisional events is necessary.

Examples are rare, for which the radiative and collisional events have been decrypted to a degree enabling detailed rate-equation modelling. Such a case is found for the OH radical. The prediction of its state-specific fluorescence decay and spectral structure allows hence for quantitative temperature measurements in combustion environment [Kohse-Höinghaus 1994].

(h) Non-linear techniques

The nonlinearity of a medium shows for higher orders of the susceptibility only in case of strong laser irradiance. Non-linear coherent laser techniques have thus not been feasible until strong tuneable laser sources had been developed.

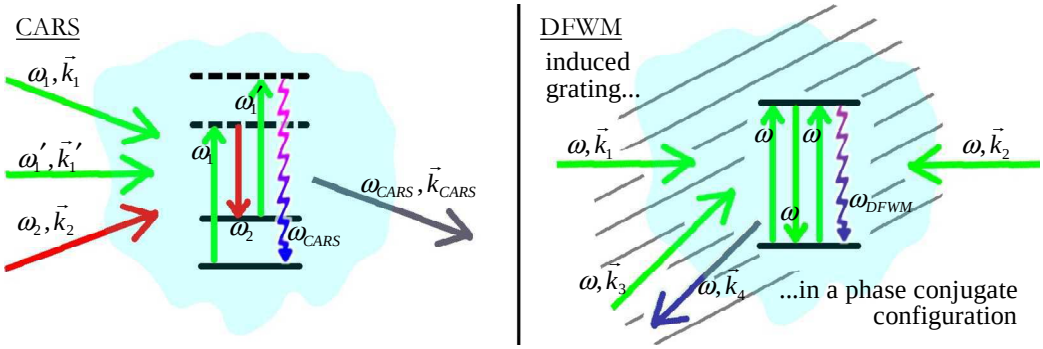

Figure 5: Four-wave mixing processes. Left: coherent anti-Stokes Raman scattering (CARS). The difference of $\omega_1 - \omega_2$ corresponds to an allowed transition. Right: degenerated four-wave mixing (DFWM) can be seen as a scattering from an induced grating (here in a phase conjugate configuration), formed between the probe wave with $\vec{k}_3$ and one of the pump waves ($\vec{k}_1$ or $\vec{k}_2$).

While sensing important combustion intermediates by means of fluorescence scattering, collisional quenching is a serious issue for signal quantification. Insensitive to quenching processes, coherent non-linear techniques such as coherent anti-Stokes Raman spectroscopy

(CARS) and degenerated four-wave mixing (DFWM) have become quite important. An illustration of these four-wave mixing techniques is given in figure 5.

In the CARS configuration, two laser beams of frequencies ω_1 and ω_1' are focussed in the probe volume together with a third beam, which has the Stokes frequency ω_2. If the frequency difference $\omega_1 - \omega_2$ corresponds to an allowed transition of the molecule, a forth and new wave with anti-Stokes frequency $\omega_{CARS} = \omega_1 + \omega_1' - \omega_2$ is generated, the direction of which is determined by the phase matching condition $\vec{k}_{CARS} = \vec{k}_1 + \vec{k}_1' - \vec{k}_2$ [Eckbreth 1996]. Variation of the frequency difference $\omega_1 - \omega_2$ allows hence for scanning of molecular energy levels, e.g. all transitions of a vibrational-rotational band. This results in a temperature dependent CARS spectrum. Using a broadband Stokes wave instead of a monochromatic wave, many resonance lines can be scanned simultaneously, which is of great interest for temperature measurements, e.g. in turbulent combustion media. Temperature is derived from measured CARS spectra by comparison to a simulated spectrum. Hence, temperature information can only be precise if the CARS spectra are numerically well described. The CARS technique is by definition a pointwise method. One drawback is its spatial resolution, roughly defined by the geometrical overlap of the input laser beams, and sometimes exceeding the turbulence length scales, which might e.g. happen if the probe volume contains a flame front. The good sensitivity of the CARS method for major species even in hostile environments with large amounts of particles and soot is owed to the coherence of the signal and its small divergence. Light scattering on particles in the probe volume decreases with the square of the distance to the detector, whereas the intensity of the coherent CARS beam rests the same.

The DFWM technique presents the major advantage to employ only a single, tuneable laser source in the setup, instead of two or three required for CARS measurements. Two pump laser beams are propagating in opposite direction. A third beam called probe beam crosses the pump beam axis forming an angle θ. If all beams have parallel polarisation, the wave of the probe beam forms with the waves of each pump beam an interference pattern with fringe spacing $d = \lambda / [2\sin(\theta/2)]$. The sinusoidal intensity variation of the interference pattern forms a refractive index grating if the three input beams with same frequency are turned to an electronic resonance of the molecule species in the probe volume. This grating coherently scatters the other pump beam (similarly to Bragg diffraction in a crystal), forming a signal beam in counter direction to the probe beam. In concurrence to the refractive index grating, thermal gratings can form through collisional quenching of the pumped, upper electronic states, especially for higher pressures. Thermal gratings also produce radiation obscuring the DFWM signal, but they can be eliminated by crossed probe and pump beam polarisation (accepting a significant loss of signal intensity). Also, thermal gratings can be used within laser-induced grating spectroscopy (LIGS), but this leads back to the issue of collisional quenching, the same as for the quantification of LIF measurements [Eckbreth 1996].

The pressure dependence of the DFWM technique can be significantly reduced if the excited state populations are saturated for high pump laser intensity (this is called saturated DFWM, quite similar to saturated fluorescence).

Other non-linear techniques exist such as the polarisation spectroscopy (PS), sum frequency generation (SFG) or resonance enhanced multiphoton ionisation (REMPI), the latter providing detection limits of even ppb with molecular beam sampling [Wolfrum 2000]. In combustion media, however, CARS and DFWM are so far the only coherent techniques having found wide application, although practically limited to point resolution. This is mainly due to the phase matching condition, which has to be largely respected in order to obtain high signal levels. Two-dimensional approaches are principally possible for DFWM, but in practice, to maintain the phase matching and the necessary pump energy, the spatial extension has been limited to several millimetres, see e.g. [Nyholm 1994]. A review of the non-linear coherent techniques with practical considerations for the measurement of species with intermediate concentrations and an outlook for future applications is given by [Dreier 2002].

1.7 Motivation of fluorescence tracer studying and roadmap through this thesis

Among the laser diagnostic techniques presented so far, laser-induced fluorescence is recognised as one convenient technique for single-shot planar temperature and species concentration measurements. PLIF is currently applied in various combustion conditions occurring in aeronautic and automobile combustion chambers. Furthermore, this technique offers the ability to give precious information on physical processes governing combustion like fuel vapour distribution, flame structure, mixing and pollutant formation.

Commonly, the fluorescence signal from the excitation of one specific molecular species offers good SNR assuming the use of wide collection optics. Quantification of the fluorescence signal remains, however, a complicated task, when competing events such as collisional quenching or chemical reactions occur on relevant time scales. Next to intermolecular processes, another key limitation is the change of energy distribution by means of intramolecular events, e.g. internal vibrational redistribution (IVR), which tends to be very fast.

Obtaining absolute concentration measurements from fluorescence signals needs a precise knowledge of the nature and relevance of these competing events, including its behaviour with varying environmental conditions. An example of success of quantitative measurements is the one obtained on OH. Environmental effects on the fluorescence signal can be predicted from spectroscopic simulations, which allows the investigation of this radical in many experiments, especially for species concentration and sometime temperature measurements. However, OH is a transient intermediate species, which is mainly present in the vicin-

ity of hot reaction zones. Other molecular species such as stable inorganic molecules (NO) can also be used for temperature measurements in the major part of combustion chambers.

Concentration and temperature distributions in the mixing zone of fuel and oxidiser downstream from the injection system is mostly known by probing the fuel vapour. At the present time, organic molecules offer a good alternative, see for instance the abundant literature on acetone for the characterisation of mixing layers in heated nonreactive flow fields. When such tracers are applied to more stringent environments, the fluorescence measurements on these molecules are generally no longer quantitative, but rather qualitative. To prevent this limitation and avoiding time-consuming spectroscopic studies on the tracer photophysics, simplifying assumptions are often proposed. Relevant physical processes such as the evolution of temperature or the impact of collisional quenching on fluorescence signals are studied within a restricted range of thermodynamic conditions. Afterwards, the fluorescent tracer is used for fuel concentration measurements, while these physical processes are completely or partially neglected.

Numerous references report applications of laser-induced fluorescence diagnostics with these organic molecules, but only few provide insight to their underlying photophysics. Photophysics is rather related to fundamental spectroscopic studies, which are performed, quite unrepresentative for combustion diagnostics, in closed vessels at low pressure, limiting then collisional interactions with the environment. Ambient or low temperature conditions are also chosen to avoid any chemical reactions in the vessel.

Under these conditions, the variation of physical parameters deliver significant influence on the energy redistribution subsequently to electronic absorption. The amount of vibrational excess energy depends on temperature of the ground state molecules and the energy of the exciting photons. Vibrational excess energy favours non-radiative deactivation pathways, which leads to a fall-off in fluorescence quantum yield. An increase in pressure enhances collisional interactions, leading either to vibrational relaxation within the excited singlet state or to bimolecular quenching. Low temperature and pressure conditions also display weak impact on the fluorescence quantum yield, but unfortunately all these thermodynamic conditions are not representative for combustion experiments.

Fundamental spectroscopic studies covering the thermodynamic conditions typically encountered within combustion diagnostics are then required to access to relevant information about the energy transfer under these conditions, along with the sensitivity towards quenching. Most of the molecular species studied under such conditions belong to two specific groups of species. Being mainly insensitive towards oxygen quenching, carbonyl species were proposed in non-fluorescing (e.g. isooctane) surrogate fuels, providing temperature and/or concentration measurements under specific conditions. Aromatic species, mainly simple benzene derivatives like toluene or bicyclic aromatics (naphthalenes), were studied in order to propose experimental strategies for concentration and even fuel-to-air ratio measurements.

The latter stands to benefit from the characterisation of oxygen quenching behaviour, and its application is limited to the coercive condition of quenching dominated deactivation.

The study presented in this thesis contributes to the continuing efforts to reinforce our knowledge on the photophysics of organic molecular species for their application as fluorescence tracers to combustion diagnostics. The role of temperature, pressure and oxygen concentration on the behaviour of the fluorescence quantum yield is systematically studied within the range of thermodynamic conditions encountered for engine applications.

Within **Chapter 2**, the **"Photophysical processes"** following the absorption to an excited electronic state are discussed. Elementary concepts like the Born-Oppenheimer approximation are presented to detail the nature of electronic transitions and selection rules invoked in laser-induced fluorescence. The relevant radiative and non-radiative pathways occurring on competitive time scales are also discussed in front of the Jablonski diagram.

The **Chapter 3** exposes the **"Experimental techniques"** applied to the spectroscopic setup used within this work. Laser absorption and spectral fluorescence measurements on selected fluorescent tracers are performed in a flow cell, carefully designed for reliable operation under high-temperature and high-pressure conditions. The conditioning of the fluorescent tracer in the test cell depends on the accurate control of tracer seeding, temperature and pressure, enabling the correction of the laser irradiance for beam attenuation. The fluorescence signal is corrected for the intensity response and the apparatus function of the optical detection path. Error influences are discussed together with the reliability of environmental parameter control. The reproducibility of the measurement is enhanced by the integration of timing and acquisition schemes to an automated processing. Low-to-high temperature and pressure variation is presented and the resulting fluorescence spectra compared when possible to data from other research groups.

In **Chapter 4**, strategies and applications for laser-induced fluorescence measurements in the field of combustion engines are presented within a "**Review of fuel tracer vapour fluorescence diagnostics**". Most of the fluorescence tracers belong to the group of aliphatic ketones and aromatics, featuring carbonyl and benzene chromophores easily excited by UV laser sources and a pronounced chemical affinity to petroleum type combustion fuels, which makes them well-suited to represent the fuel fraction. Measurements are either performed on fluorescence tracers doped to non-fluorescing surrogates or directly from the emission of petroleum based real fuels. References are synthesized, either being of exemplary nature or providing key knowledge for the common measurement strategies.

The approach followed within this thesis for the measurement of fuel-to-air ratio downstream from an innovative SNECMA multipoint injector (TLC European project) is then detailed: recording of spectrally separated patterns of the kerosene fluorescence spectrum was the solution adopted. When these patterns behave independently different on changing environmental parameters like temperature, pressure and oxygen concentration, ratiometric

measurement strategies become possible, in case when the knowledge of kerosene photophysics is sufficiently valuable.

Chapter 5 summarises the state of the art of the knowledge about photophysics of aliphatic ketone and aromatic tracers. A study of "**Spectroscopic fluorescence of organic fuel tracers**" is performed with the experimental setup described in Chapter 3 for acetone, 3-pentanone, toluene, 1,2,4-trimethylbenzene and naphthalene. The impact of temperature, pressure and oxygen concentration on the fluorescence quantum yield of these molecular tracer species is observed for 266 nm excitation wavelength within a thermodynamic range, relevant for diagnostics in combustion. When feasible, the data from measurements are compared with modelling simulations.

Chapter 6 describes the results obtained for the "**Spectroscopic fluorescence of kerosene fuel**" studied under the same conditions as the organic species in Chapter 5. The analysis of the aromatic species is beneficial for the interpretation of the kerosene emission changing on temperature, pressure and oxygen concentration. An "optical fuel" displaying similar spectroscopic behaviour can be determined from the aromatic species studied in Chapter 5. Finally, the experimental strategy for kerosene PLIF quantification in terms of temperature and fuel-to-air ratio is developed.

Chapter 7 details the application of "**Kerosene and OH PLIF in a high-pressure combustor**". The kerosene vapour fluorescence is detected to characterise the efficiency of an innovative SNECMA multipoint injector in a high-temperature and high-pressure combustor test rig. The operating conditions in the test rig correspond to various engine loads of real turbine engines (maximal pressure: 25 bar). The spectral detection of fluorescence signals by means of appropriate optical and temporal filters enables a ratiometric measurement strategy, which is based on the data recorded during the spectroscopic study described in Chapter 6. In addition to the detection of kerosene, OH radical is also probed by PLIF, providing valuable information about the localisation and the structure of the flame front. Correlation between the OH and kerosene images is finally presented to highlight the performances of PLIF diagnostic in real combustion systems.

Chapter 2 Photophysical processes

This chapter gives a theoretical overview of photophysical processes with special regard to organic molecules.

The phenomenon of light absorption and emission can be rated via the Einstein coefficients. The Schrödinger equation describes the molecule's equilibrium energy state when the Hamiltonian operator contains only an unperturbed part. The perturbation part of the Hamiltonian represents the interaction of the molecule's dipole with photon energy brought to the molecule via a light wave. Solving the Schrödinger equation of the perturbed system yields a probability expression for the molecule being promoted from an initial to a final state of energy. This is the squared matrix element, also called the transition dipole moment, which is deduced by operating the Hamiltonian on the initial and final wave functions.

Each molecular energy state consists of an electronic, a nuclear and a spin part of motion. An analytical solution of the wave function is found only by simplification of the system description. Since there is a great difference between the mass of an electron and the nuclei, acceleration takes place on very different time scales. The change in electronic configuration will therefore be completed, while the position of the nuclei is still unchanged due to their great mass inertia. The Born-Oppenheimer approximation proposes to separate electrical and vibrational molecular motions, which thereby leads to a resolvable expression for the matrix element.

The following sections give a closer look to the nature of the transition dipole moment, the selection rules governing over the effective transition strengths within the Born-Oppenheimer zero order approximation, and the breakdown of this approximation, leading to first order coupling interactions of the motions via mixing of the initial and final energy states. Thus, getting knowledge of terms like electronic interaction, vibronic or spin-orbit coupling is elucidating the existence of the numerous pathways of deactivation, being of either radiative or non-radiative, intra- or intermolecular nature, with specific rates all in competition.

The different sections of the present chapter are following several textbooks. In terms of reference for this chapter and for further reading see the following references: [Bernath 1995], [Gilbert 1991], [Eckbreth 1996], [Klessinger 1995], [Atkins 2008] and [Turro 1991].

2.1 Absorption, stimulated and spontaneous emission

Molecules (as atoms) have discrete energy levels, and it is known from Planck that the energy transfer between these levels is quantised. As outlined in the previous chapter, light waves are susceptible to polarise molecules, and under specific conditions, a transfer of the photon energy takes place. The photon energy might be absorbed in case it matches the energy condition $h\nu_{10} = \hbar\omega_{10} = E_1 - E_0$ between a fundamental state E_0 and an excited state E_1.

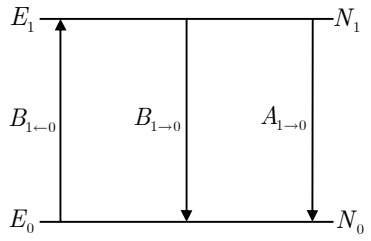

$$B_{1\leftarrow 0} \Leftrightarrow M^* \leftarrow M + h\nu_{10}$$
$$B_{1\rightarrow 0} \Leftrightarrow h\nu_{10} + M^* \rightarrow M + 2\cdot h\nu_{10}$$
$$A_{1\rightarrow 0} \Leftrightarrow M^* \rightarrow M + h\nu_{10}$$

Figure 6: Energy transfer between light and matter based on a two-level scheme. Transfer rates are described by the Einstein coefficients.

Having a look on a simple two-level scheme for a molecule in equilibrium (see fig. 6), the energy balance between ground and excited level reveals the absorption rate to equal the summation of stimulated and spontaneous emission rates. Described as a closed scheme, the sum of ground level and excited level populations is constant and the whole system is thermally equilibrated, following the Boltzmann distribution

$$N_1 = N_0 \cdot \exp\left(-h\nu_{10} / kT\right) \tag{2.1}$$

Absorption and stimulated emission are physically different, but somehow equivalent processes, since they are only possible via the interaction with the radiation density $\rho_\nu(\nu_{10})$ of appropriate frequency. The Einstein B coefficients for absorption and stimulated emission are hence analogue, reading as rate constants

$$\frac{dN_1}{dt} = B_{1\leftarrow 0}\rho_\nu(\nu_{10})N_0 \quad \text{and} \quad \frac{dN_1}{dt} = -B_{1\rightarrow 0}\rho_\nu(\nu_{10})N_1 \tag{2.2}$$

The spontaneous emission takes place independently from radiation density, and the emission rate is therefore described by the Einstein A coefficient as follows

$$\frac{dN_1}{dt} = -A_{1\rightarrow 0}N_1 \tag{2.3}$$

Planck has given an expression for the radiation density of a black body

$$\rho_\nu(\nu_{10}) = \frac{8\pi h\nu_{10}^3}{c^3}\frac{1}{\exp(h\nu_{10}/kT - 1)} \tag{2.4}$$

Combination of equations (2.2) and (2.3) with equation (2.4) and doing the rate balance leads to the relation between the Einstein A and B coefficients [Bernath 1995]

$$\frac{A_{1\to 0}}{B_{1\leftarrow 0}} = \frac{8\pi h\nu_{10}^3}{c^3} \quad \text{with } B_{1\leftarrow 0} \equiv B_{1\to 0} \tag{2.5}$$

The natural lifetime τ_{sp} for spontaneous emission can be found from a measurement of absorption:

$$\frac{1}{\tau_{sp}} = A_{1\to 0} = \frac{8\pi h\nu_{10}^3}{c^3} B_{1\leftarrow 0} \tag{2.6}$$

Several conclusions are made from equation (2.6). Spontaneous emission from excited states bridging a large energy gap to the ground state level has high Einstein coefficients and takes place on short time scales. Due to the dependence on cubic frequency, spontaneous emission is dominant compared to stimulated emission, and grows rapidly towards shorter wavelength. It is therefore more easily detected in the UV-visible than in the infrared domain.

2.2 Electronic transitions

In quantum mechanics, each quantum mechanical system is represented by a wave function $\Psi(\vec{x}, t)$, describing the state of the system at any time, the wave function itself being not directly measurable. The average value $\langle \mathbf{P} \rangle$ of an observable $\mathbf{P}$ of an arbitrary state ψ is evaluated by computation of the matrix element $\int \psi_n^* \mathbf{P} \psi_m \, d\tau \; / \int \psi_n^* \psi_m \, d\tau$, also written as $\langle \psi_n^* | \mathbf{P} | \psi_m \rangle \; / \; \langle \psi_n^* | \psi_m \rangle$ [Atkins 2008].

2.2.1 Schrödinger equation – unperturbed molecule's energy balance

The different energy states E_n of a molecule are expressed as wave functions Ψ_n, which are solutions of the time-independent Schrödinger equation, representing the energy balance for the unperturbed molecule

$$\left[-\frac{\hbar^2}{2m_e}\nabla^2 + U\right]\Psi = i\hbar\frac{\partial \Psi}{dt} \quad \Rightarrow \quad \hat{H}_0\Psi = E\Psi \tag{2.7}$$

Thereby, the term in brackets is the sum of kinetic and potential energy, which is the total energy of the molecule also defined as Hamiltonian operator $\hat{H}_0$. The expression containing the time derivative on the right side is called the energy operator E. Solutions for the unperturbed molecular system are found as

$$\Psi_n = \psi_n \exp(-iE_n t/\hbar) = \psi_n \exp(-i\omega_n t) \quad \ldots n = 0,1 \tag{2.8}$$

2.2.2 Including dipole interaction with electromagnetic radiation by perturbation

The molecule in equation (2.7) was described as an unperturbed system. If the molecule interacts with electromagnetic radiation, the system becomes perturbed. The net dipole moment $\boldsymbol{\mu}$ of the whole molecule is then affected by the time-dependent electric field $\mathbf{E}(t)$ of the wave. Due to the perturbation of the molecular dipole, a fraction of the ground state population N_0 is promoted to a higher state. The transition probability between the states E_0 and E_1 is found by computing the matrix element over the molecule's net dipole moment. This is the so-called transition dipole moment $\mathbf{M_{01}} = \int \psi_1^* \boldsymbol{\mu} \psi_0 \, d\tau$, often written as $\langle \psi_1^* | \boldsymbol{\mu} | \psi_0 \rangle$. The net dipole moment of the entire molecule is the sum of the individual dipole moments of any of its charged particles (nuclei or electrons) $\boldsymbol{\mu} = \sum_i \mathbf{r_i} \cdot q_i$, $\mathbf{r_i}$ being the positions of the individual charges q_i relative to the mass centre of the molecule.

To introduce the interacting wave into the state description of the molecule, the unperturbed (time-independent) Hamiltonian operator is completed with a time-dependent perturbation part. The total Hamiltonian operator is then $\hat{H}_{total} = \hat{H}^0 + \hat{H}'(t)$, with the perturbation part $\hat{H}'(t) = -\boldsymbol{\mu} \cdot \mathbf{E}(t) = -\mu \cdot \mathrm{E}_0 \cos(\omega t)$. The dipole of the molecule is clearly modified via the scalar product with the electric field. The total Hamiltonian is applied to the Schrödinger equation

$$\left[\hat{H}^0 + \hat{H}'(t)\right]\Psi = i\hbar \frac{\partial \Psi}{\partial t} \tag{2.9}$$

The perturbed system's wave function is calculated by linear combinations of the wave functions of the unperturbed system prior to and after the transition, each weighted with a time-dependent coefficient $a_i(t)$ [Bernath 1995]

$$\Psi(t) = a_0 \psi_0 \exp(-i\omega_0 t) + a_1 \psi_1 \exp(-i\omega_1 t) \tag{2.10}$$

Before the perturbation, a_0 equals unity and a_1 is zero, which means that the molecule is still in the lower state and the transition has not yet occurred. After the perturbation, when the transition has taken place, the coefficients are inverted. During the transition process a_0 decreases while a_1 is increasing.

2.2.3 Definition of the transition dipole moment

A differential equation system is found for operating the perturbed Hamiltonian on the wave function of the perturbed system from equation (2.10) via the time-dependent Schrödinger equation (2.9). Multiplication with ψ_0^* or ψ_1^* from the left, integration and replacing $\langle \psi_1^* | \mu_x | \psi_0 \rangle$ by $M_{01,x}$ leads to

$$\dot{a}_0 = -\frac{i}{\hbar} a_1 M_{01,x} E_x \, \mathrm{e}^{-i\omega_{10}t} \cos(\omega t) \quad \wedge \quad \dot{a}_1 = -\frac{i}{\hbar} a_0 M_{10,x} E_x \, \mathrm{e}^{i\omega_{10}t} \cos(\omega t) \tag{2.11}$$

Solutions are found for the initial conditions before transition, a_0 equals unity and a_1 is zero at $t = 0$. In order to simplify the expressions, equation (2.11) and the following equations are all written for a unidirectional (planar) electromagnetic wave. To obtain the total transition dipole moment, the squared contributions in direction of the three spatial axes have to be summed

$$\left|\mathbf{M_{01}}\right|^2 = \left|M_{01,x}\right|^2 + \left|M_{01,y}\right|^2 + \left|M_{01,z}\right|^2 \tag{2.12}$$

Restriction to resonance or near resonance, i.e. ω equals or is near to the Bohr frequency $\omega_{10} = (E_1 - E_0)/\hbar$, a somehow more accessible expression for (2.11) can be given:

$$\begin{gathered} \dot{a}_0 = \frac{a_1}{2} i\omega_R \, \mathrm{e}^{i\Delta\omega t} \quad \text{and} \quad \dot{a}_1 = \frac{a_0}{2} i\omega_R \, \mathrm{e}^{-i\Delta\omega t} \\ \text{with } \omega_R = \frac{M_{10}E}{\hbar} \qquad \Omega = \sqrt{\omega_R^2 + \Delta\omega^2} \qquad \Delta\omega = (\omega - \omega_{10}) \end{gathered} \tag{2.13}$$

The probability that the molecule energy state is actually the state Ψ_1 at a time t is proportional to the squared transition dipole moment, or more precisely [Bernath 1995]

$$P_{1\leftarrow 0}(t) = \left|a_1(t)\right|^2 = \sin^2\left(\frac{\omega_R t}{2}\right) \text{(resonance)} \quad = \frac{\omega_R^2}{\Omega^2} \sin^2\left(\frac{\Omega t}{2}\right) \text{(near resonance)} \tag{2.14}$$

where the so-called Rabi frequency ω_R and Ω cancel out for the resonance case.

2.2.4 Relating the Einstein coefficients to the transition dipole moment

The actual case for linear regime of fluorescence is the weak excitation, i.e. the majority of the population rests in the lower state. The time dependent coefficients then become $a_1 \approx 0$ and $a_0 \approx 1$. Differential equation (2.13) is solvable by means of simple integration

$$\begin{aligned} a_1 &= \frac{1}{2} i\omega_R \int_0^t \exp(-i\Delta\omega t)dt \\ \Rightarrow \quad P_{1\leftarrow 0}(t) &= \left|a_1(t)\right|^2 = \frac{\omega_R^2}{\Delta\omega^2}\sin^2\left(\frac{\Delta\omega t}{2}\right) = \frac{E_0^2 M_{10}^2}{\hbar^2}\frac{\sin^2(\Delta\omega t/2)}{\Delta\omega^2} \end{aligned} \tag{2.15}$$

This term might be explained as the probability of a state-to-state electronic transition, i.e. from a single initial to a single final vibrational level, being the result of a perfectly monochromatic excitation. In practice, the radiation source line shape must be assumed to be rather large, i.e. having a hardly varying radiation density $\rho = \varepsilon_0 E^2/2$ for near resonance frequencies. With some trigonometric simplifications, the absorption rate per molecule is derived as

$$\frac{d}{dt}P_{1\leftarrow 0} = \frac{\pi M_{10}^2}{\varepsilon_0 \hbar^2}\rho_\nu(\omega_{10}) \tag{2.16}$$

The transition dipole moment can be related to the Einstein A and Einstein B coefficients if equation (2.16) is compared to equation (2.2), assuming $N_0 \approx N$ for the case of weak excitation. Equation (2.2) was derived for isotropic radiation, whereas equation (2.16) was written for a planar wave. Hence, a factor three must be inserted to equation (2.16),

$$\frac{d}{dt}P_{1\leftarrow 0} = \frac{1}{3}\cdot\frac{\pi\left|M_{10}\right|^2}{\varepsilon_0\hbar^2}\rho_\nu(\omega_{10}) = \frac{dN_1/N}{dt} = B_{1\leftarrow 0}\rho_\nu(\nu_{10}) = 2\pi\cdot B_{1\leftarrow 0}\rho_\nu(\omega_{10}) \tag{2.17}$$

Thus, with help from equation (2.5), the Einstein A and B coefficients are related to the transition dipole moment by [Bernath 1995]

$$A_{1\to 0} = \frac{16\pi^3\nu^3}{3\varepsilon_0 hc^3}\left|M_{10}\right|^2 g(\nu-\nu_{10}) \quad \text{and} \quad B_{1\leftarrow 0} = \frac{2\pi^2}{3\varepsilon_0 h^2}\left|M_{10}\right|^2 g(\nu-\nu_{10}) \tag{2.18}$$

with $g(\nu-\nu_{10})$ being the absorption line shape, which has to be considered for the losses from the upper state by relaxation through spontaneous emission or collisions. This is the fundamental equation connecting macroscopic (measured) transition rates to the microscopic transition dipole moment of a tracer molecule. The transition rates for absorption and spontaneous emission are proportional to the squared transition dipole moment. As seen earlier for equation (2.5), the rate of spontaneous emission is dependent on the cubic frequency of

the electromagnetic wave, whereas the absorption is frequency independent. Remember that the probability to find a molecule in the state Ψ_1 at a time t for weak excitation was given by equation (2.15). For the near resonance case, i.e. $\omega \approx \omega_{10}$, $\Delta\omega$ becomes very small, the sinus-function can be approximated by its argument. Thus, the probability is written as a proportionality function [Gilbert 1991]

$$P_{1\leftarrow 0}(t) \propto \frac{|M_{10}|^2 E^2}{\hbar^2} t^2 \tag{2.19}$$

Next to the squared dipole moment, the transition is also proportional to the square of the time and the amplitude of the electric field. Experimental control over the transition strength is possible only by a change of the electric field amplitude, i.e. a variation of the radiation intensity of the laser light. The transition dipole moment is, however, an intrinsic property of the studied molecule and may change for the variation of external conditions like temperature, pressure and collisional environment.

2.3 Absorption cross-section and Beer-Lambert Law

Think of a volume of length l with a section of $1\ \mathrm{m}^2$ filled with a number N_0 of molecules in the ground state and N_1 in the excited state. A photon flux $F = I_0 / h\nu$ passes the volume along l. If the transition dipole moment is non-zero and the light frequency fulfils Planck's law, some photons will be absorbed, while others will lead to stimulated emission. The number balance for the excited level is then $dN_1/dt = -B_{1\to 0}\rho N_1 + B_{1\leftarrow 0}\rho N_0$. With the radiation intensity being $\rho = I_0 / c = Fh\nu / c$, using the relation (2.18) between Einstein coefficients and the transition dipole moment, the number balance can be rewritten as

$$\frac{dN_1}{dt} = \frac{2\pi^2\nu}{3\varepsilon_0 hc}|M_{10}|^2 F(N_0 - N_1) g(\nu - \nu_{10}) = \sigma_\nu F(N_0 - N_1) g(\nu - \nu_{10}) \tag{2.20}$$

An "effective area", which captures photons from the flux F, is defined for the molecule as the absorption cross-section [Bernath 1995]

$$\sigma_\nu = \frac{2\pi^2\nu}{3\varepsilon_0 hc}|M_{10}|^2 g(\nu - \nu_{10}) \tag{2.21}$$

The absorption was related to the effective lifetime of spontaneous emission by equation (2.6). With $\nu = c/\lambda$ and equation (2.18) the absorption cross-section can be written as a function of the lifetime of the spontaneous emission [Bernath 1995]

$$\sigma_\nu = \frac{\lambda^2}{8\pi} A_{1\to 0} = \frac{\lambda^2}{8\pi} \cdot \frac{1}{\tau_{sp}} \tag{2.22}$$

The Beer-Lambert law as known from practical measurement is more likely to be written in another form, which can be deduced from the loss of flux dF/dx as [Bernath 1995]

$$\int_{F_0}^{F} \frac{1}{F} dF = -\sigma_\nu (N_0 - N_1) \int_0^l dx \quad \Rightarrow \quad \ln\left(\frac{F}{F_0}\right) = \ln\left(\frac{I}{I_0}\right) = -\sigma_\nu (N_0 - N_1) l \tag{2.23}$$

2.4 The Born-Oppenheimer "zero order" approximation

The wave function Ψ was introduced in equation (2.7) and (2.9) in order to describe the energies of initial and final states of a transition. An observable property is obtained for computation of the matrix element $\langle \psi_n^* | \mathrm{P} | \psi_m \rangle$ with P being a mathematical operator. For example, using the Hamiltonian operator $\hat{H}$, the matrix element yields the average system energy. In order to compute the matrix element, the wave functions of the initial and final energy states of the system must be determined. This is in an analytical way, most unfortunately, not possible even for simple molecules. Thus, to make the matrix element accessible, the system has to be simplified by approximations.

Born and Oppenheimer took a most important step towards the solution of the matrix element proposing the use of an approximate wave function. Profiting from the rapidity of orbital electron motion compared to the relative slow nuclear vibrations, the Born-Oppenheimer approximation splits the true wave function into separate parts, describing independently the electronic charge distribution and the vibrating nuclei. Further, for most organic molecules, electron motions do not impact on spin motions, because the former depend on electronic and the latter on magnetic interactions. Thus, spin motions can be separated from electron and nuclear motions. An approximation of the true wave function is found as the product of an orbital, a nuclear and a spin wave function [Turro 1991]

$$\begin{array}{ccccccc} \Psi \sim & \phi & \cdot & \chi & \cdot & \mathrm{S} & \\ & \text{orbital...} & & \text{nuclear...} & & \text{spin...} & \text{wave function} \end{array} \tag{2.24}$$

The Born-Oppenheimer approximation simplifies the determination of the transition moment $\mathbf{M_{01}} = \int \psi_1^* \boldsymbol{\mu} \psi_0 \, d\tau = \langle \psi_1^* | \boldsymbol{\mu} | \psi_0 \rangle$, ψ_i being the molecular wave function for the initial and final states. The net dipole moment $\boldsymbol{\mu}$ implies all nuclear and electronic charges, hence

$$\boldsymbol{\mu} = -|e| \sum\nolimits_i \mathbf{r_i} + |e| \sum\nolimits_A Z_A \mathbf{R_A} \tag{2.25}$$

where $|e|$ is the electronic charge at $\mathbf{r_i}$, $|e|Z_A$ the nuclei charge at $\mathbf{R_A}$, with Z_A being the atomic number. Taking benefit from the Born-Oppenheimer approximation, the transition between energy states E_0 and E_1 is now divided into separate parts for an orbital and a nuclear wave function. Introduction of the net dipole moment to the matrix element leads then to the following expression for the transition moment (for transitions without change of multiplicity, i.e. singlet-singlet or triplet-triplet) [Klessinger 1995]

$$\begin{aligned}\mathbf{M}_{\mathbf{m}\nu\to\mathbf{n}\nu'} &= \left\langle \phi_n^* \chi_{\nu'}^* \middle| -|e|\sum\nolimits_i \mathbf{r_i} + |e|\sum\nolimits_A Z_A \mathbf{R_A} \middle| \phi_m \chi_\nu \right\rangle \\ &= \left\langle \phi_n^* \middle| \phi_m \right\rangle \left\langle \chi_{\nu'}^* \middle| |e|\sum\nolimits_A Z_A \mathbf{R_A} \middle| \chi_\nu \right\rangle + \left\langle \phi_n^* \middle| -|e|\sum\nolimits_i \mathbf{r_i} \middle| \phi_m \right\rangle \left\langle \chi_{\nu'}^* \middle| \chi_\nu \right\rangle\end{aligned} \tag{2.26}$$

The electronic charge distribution operates on the orbital, the nuclear charge distribution on the nuclear wave function. The first summand of equation (2.26) vanishes for orthogonality of ground and excited state wave functions for fixed nuclear configuration

$$\mathbf{M}_{\mathbf{m}\nu\to\mathbf{n}\nu'} = \left\langle \phi_n^* \middle| -|e|\sum\nolimits_i \mathbf{r_i} \middle| \phi_m \right\rangle \left\langle \chi_{\nu'}^* \middle| \chi_\nu \right\rangle = \mathbf{M}_{\mathbf{mn}} \left\langle \chi_{\nu'}^* \middle| \chi_\nu \right\rangle \tag{2.27}$$

Hence, the electronic transition dipole moment $\mathbf{M}_{\mathbf{mn}}$ determines the overall intensity of the transition $\mathbf{M}_{\mathbf{m}\nu\to\mathbf{n}\nu'}$, whereas the so-called Franck-Condon overlap integrals $\left\langle \chi_{\nu'}^* \middle| \chi_\nu \right\rangle$ stand for the vibrational energy distribution in the initial and final electronic energy states, therefore representing the vibrational structure of the absorption band.

An expression similar to equation (2.27) can be derived for the case of change in multiplicity of the spin, i.e. singlet-triplet or triplet-singlet transitions

$$\mathbf{M}_{\mathbf{m}\nu J\to\mathbf{n}\nu' J'} = \mathbf{M}_{\mathbf{mn}} \cdot \left\langle \chi_{\nu'}^* \middle| \chi_\nu \right\rangle \cdot \left\langle S_{J'}^* \middle| S_J \right\rangle \tag{2.28}$$

2.5 From atomic orbitals to orbital configurations of spin-orbitals

One-electron atomic orbitals (AOs) χ_μ are described with respect to a vector $\mathbf{r_\mu}$ starting from a centre, on which generally a nucleus is placed, pointing to the one-electron. Molecular orbitals (MOs) ψ_k are commonly constructed via linear combinations of these AOs χ_i by application of the "Linear Combination of Atomic Orbitals" (LCAO) method

$$\psi_k = \sum_i c_{ik} \chi_i(\mathbf{r_i}) \tag{2.29}$$

Spin-orbitals are defined as the product of the MOs with the spin functions α and β with respect to the combined spin and space coordinates, here indicated as $\mathbf{x}_j$ [Klessinger 1995]

$$\psi_k^\alpha = \psi_k(\mathbf{x}_j)\cdot\alpha(\mathbf{x}_j) \equiv \phi_k \quad \wedge \quad \psi_k^\beta = \psi_k(\mathbf{x}_j)\cdot\beta(\mathbf{x}_j) \equiv \bar{\phi}_k \tag{2.30}$$

Possible selections from occupied molecular spin-orbitals combine as orbital configurations. Since electrons are fermions, orbital configurations are antisymmetric with respect to exchange of the coordinates of two electrons.

The spin state for a closed-shell configuration is a singlet state, i.e. all the contributions from α and β spins are paired and cancel due to spin correlation as a consequence of the Pauli principle. The closed-shell singlet state is called the ground state with multiplicity $2S+1=1$. Free radicals have an odd number of electrons, therefore presenting as open shell configurations, having a spin quantum number $S=1/2$, i.e. a doublet spin state. By exposure to electromagnetic radiation with energy $h\nu_{10} = \hbar\omega_{10} = E_1 - E_0$ matching an electronic transition, closed shell systems produce excited states with either singlet or triplet multiplicity for paired or parallel spin orientation. The singlet state is higher in energy as the corresponding triplet state, since electron-electron repulsion is reduced.

For a singlet state with $S=0$, an antisymmetric spin function is imposed, and hence, the orbital wave function must be symmetric to produce an antisymmetric overall wave function. In contrast, for triplet states with $S=1$, the spin function is symmetric, and therefore the orbital wave function antisymmetric. For a two-electron molecule, the excited singlet and triplet state is hence [Levine 2000]

$$^1\Psi_1 = \underbrace{\frac{1}{\sqrt{2}}\left[\psi_1(\mathbf{x_1})\psi_2(\mathbf{x_2}) + \psi_2(\mathbf{x_1})\psi_1(\mathbf{x_2})\right]}_{\text{symmetric orbital wave function}} \cdot \underbrace{\frac{1}{\sqrt{2}}\left[\alpha(\mathbf{x_1})\beta(\mathbf{x_2}) - \beta(\mathbf{x_1})\alpha(\mathbf{x_2})\right]}_{\text{antisymmetric spin function}} \tag{2.31}$$

$$^3\Psi_1 = \underbrace{\frac{1}{\sqrt{2}}\left[\psi_1(\mathbf{x_1})\psi_2(\mathbf{x_2}) - \psi_2(\mathbf{x_1})\psi_1(\mathbf{x_2})\right]}_{\text{antisymmetric orbital wave function}} \cdot \underbrace{\begin{cases} \alpha(\mathbf{x_1})\alpha(\mathbf{x_2}) \\ \frac{1}{\sqrt{2}}\left[\alpha(\mathbf{x_1})\beta(\mathbf{x_2}) + \beta(\mathbf{x_1})\alpha(\mathbf{x_2})\right] \\ \beta(\mathbf{x_1})\beta(\mathbf{x_2}) \end{cases}}_{\text{symmetric spin function}} \tag{2.32}$$

The three different symmetric triplet state spin functions are hence $\alpha\alpha$, $\alpha\beta+\beta\alpha$ and $\beta\beta$, and the z component of the total spin M_s equals $\hbar$, zero or $-\hbar$, respectively. They are degenerate, i.e. they have the same energy, for absence of an external magnetic field. If in contrast there is an exposure to an external magnetic field, the spin magnetic moments cause a slight energy splitting as illustrated in figure 7.

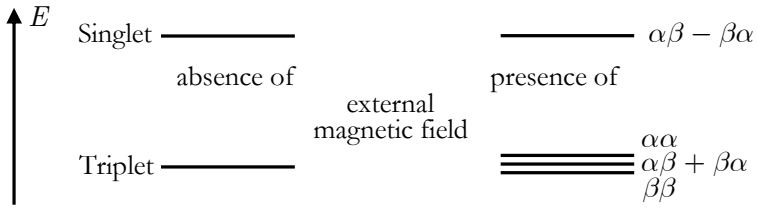

Figure 7: Energy levels for singlet and triplet states of Helium. Degeneracy of triplet levels $\alpha\alpha$, $\alpha\beta + \beta\alpha$ and $\beta\beta$ for absence and slight energy splitting for presence of an external magnetic field. Taken from [Lowe 2006].

2.6 Calculation of the electronic wave function

Analytic solutions of the Schrödinger equation exist only for one-electron atoms without electron-electron interaction. Within the exact formulation, the wave function of the Schrödinger equation writes as function of both electron and nuclei coordinates, $\hat{H}\Psi(\mathbf{r},\mathbf{R}) = E\Psi(\mathbf{r},\mathbf{R})$ with $\hat{H} = T_e + T_N + V$ being the sum of kinetic energies of the electrons and nuclei and potential energy of the system. As shown above, the Born-Oppenheimer approximation allows to separate the wave function to an orbital and a nuclear part, i.e. $\Psi(\mathbf{r},\mathbf{R})$ is replaced by $\phi(\mathbf{r},\mathbf{R})\chi(\mathbf{R})$, and therefore, the Schrödinger equation can be expressed as the electronic Schrödinger equation [Atkins 2008]

$$H\phi(\mathbf{r},\mathbf{R}) = (\mathrm{T}_e + V)\cdot\phi(\mathbf{r},\mathbf{R}) = E_e(\mathbf{R})\phi(\mathbf{r},\mathbf{R}) \tag{2.33}$$

with $E_e(\mathbf{R})$ representing the electronic contribution to the total energy of the molecule plus the potential energy from internuclear repulsion for fixed nuclear configuration, the electronic wave function $\phi(\mathbf{r},\mathbf{R})$ being a solution. By reinsertion of $\mathbf{E}_\mathbf{e}(\mathbf{R})$, the Schrödinger equation for the vibrational motion of the nuclei is obtained as $(\mathbf{T}_\mathbf{N} + \mathbf{E}_\mathbf{e})\boldsymbol{\chi} = \mathbf{E}\boldsymbol{\chi}$. This expression yields the potential energy of the molecule when plotted against the nuclear positions as exemplary shown for a diatomic molecule in figure 8.

Applying the Born-Oppenheimer approximation, the Hamiltonian is the sum of kinetic energy of the electrons and potential energies from nucleus-nucleus and electron-electron repulsions. For simplification, the nucleus-nucleus repulsions are conventionally neglected within molecular structure calculations and considered afterwards in an averaged form. Different ab initio and semiempirical methods exist to find a solution for the electronic wave function. The main difficulty for all these methods lies in the respect of the potential energy from electron-electron repulsion, which is of critical importance for obtaining accurate electronic structures.

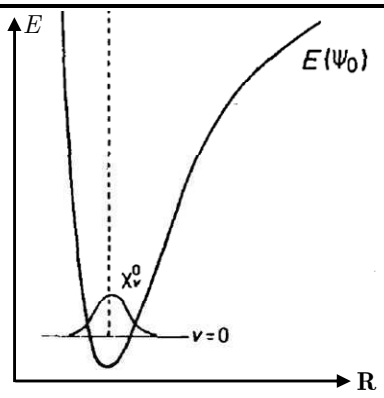

Figure 8: Potential energy curve plotted against the nuclear positions for the ground state Ψ_0 of a diatomic molecule with its fundamental vibrational level χ_ν^0 for $\nu = 0$. Taken from [Klessinger 1995].

2.6.1 Singlet-Triplet energy gap – the repulsion potential in context of the Pauli principle

As an initial step towards a solution for the electronic wave function, the repulsion can be extracted from the Hamiltonian formulation by separation to a sum of one-electron core Hamiltonians and a supplemental term $\hat{g}_{i,j}$ for Coulomb electron repulsion [Klessinger 1995]

$$\hat{H}^0(1,\ldots n) = \sum_i^n \hat{h}_i + \sum_j^n \sum_{i<j} \hat{g}_{i,j} \tag{2.34}$$

Neglecting the repulsion term, potential energies would be the same for both singlet and triplet states. The repulsion term depends on the charge interactions of the electrons within the fixed nuclear framework, which has its classical representation with the Coulomb integral J. The classical repulsion approach must further be corrected for the quantum mechanical effect of spin correlation (Pauli principle) by introduction of the exchange integral K.

The probabilities of finding a first electron in an orbital Ψ_a and another electron in an orbital Ψ_b, each multiplied with the electron charge $-e$, read as the Coulomb integral J when expressed as follows [Atkins 2008]

$$J = \frac{e^2}{4\pi\varepsilon_0} \int \Psi_a^*(1)\, \Psi_b(2) \left(\frac{1}{\mathbf{r_{12}}}\right) \Psi_b^*(2)\, \Psi_a(1)\, \mathrm{d}\tau_1 \mathrm{d}\tau_2 \tag{2.35}$$

This integral corresponds to the average potential energy of repulsion between an electron in Ψ_a and an electron in Ψ_b, due to the Coulomb interaction between the orbital charge distributions $-|e|\left|\Psi_a(1)\right|^2$ and $-|e|\left|\Psi_b(2)\right|^2$. With the electrostatic self-interactions of the overlap charge distribution, i.e. the overlap densities $\Psi_a^*(1)\Psi_b(1)$ and $\Psi_b^*(2)\Psi_a(2)$, the exchange integral K is given as [Atkins 2008]

$$K = \frac{e^2}{4\pi\varepsilon_0} \int \Psi_a^*(1)\, \Psi_b^*(2) \left(\frac{1}{\mathbf{r_{12}}}\right) \Psi_a(2)\, \Psi_b(1)\, d\tau_1 d\tau_2 \tag{2.36}$$

This integral is a pure quantum mechanical representation and has no classical counterpart. However, looking at equation (2.32), the amplitude of a triplet wave function vanishes when the coordinates of two electrons become very close ($\mathbf{x_1} \rightarrow \mathbf{x_2}$), which means, corresponding to the Pauli principle, two electrons of parallel spin cannot occupy the same orbital. This probability sink for $\mathbf{x_1} \rightarrow \mathbf{x_2}$ is called Fermi hole. In contrast, for the singlet state expressed by equation (2.31) the amplitude of the wave function is maximal for $\mathbf{x_1} \rightarrow \mathbf{x_2}$ (the electrons have antiparallel spin). Thus, the energy of the singlet state is found as the sum of Coulombic potential J and exchange term K, whereas the triplet state energy is obtained by subtraction of K. The potential energy difference ΔE_{ST} between singlet and triplet state (E_0 being the zero order one-electron excited state energy) is given as [Turro 1991]

$$\left.\begin{aligned} E_S &= E_0 + J + K \\ E_T &= E_0 + J - K \end{aligned}\right\} \Rightarrow \Delta E_{ST} = E_S - E_T = 2 \cdot K \tag{2.37}$$

The transition dipole moment $\mathbf{M_{m \rightarrow n}}$ of a purely electronic transition is obtained for operating the electronic charge distribution on the orbital wave function, i.e. $\langle \phi_n^* | -|e| \sum_i \mathbf{r_i} | \phi_m \rangle$ (cf. section 2.4). Like for the Franck-Condon overlap integral $\langle \chi_\nu^* | \chi_\nu \rangle$, an analogous integral $\langle \phi_n^* | \phi_m \rangle$ can be defined for the orbital wave functions, which then corresponds to the spatial overlap of the orbital wave functions. Also known as electronic overlap integral, this term is then proportional to the exchange integral K [Turro 1991]

$$K \sim \langle \phi_m^* | \phi_n \rangle \tag{2.38}$$

Spatial overlaps are graphically illustrated for $n \rightarrow \pi^*$ and $\pi \rightarrow \pi^*$ transitions by means of molecule orbitals (cf. figure 9). The poor spatial overlap of the $n \rightarrow \pi^*$ transition is found to have a major part of responsibility for the much lower absorption of carbonyl compounds compared to their benzenoid relatives.

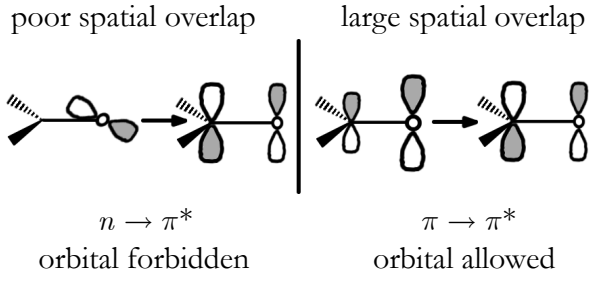

Figure 9: Orbital overlap illustration for $n \rightarrow \pi^*$ and $\pi \rightarrow \pi^*$ transitions. Taken from [Turro 1991].

Since the exchange term is further linked to the singlet-triplet energy gap, this gap is generally much smaller between two (n,π^*)-states than between two (π,π^*)-states

$$\begin{array}{lll} \Delta E_{ST}[^1(n,\pi^*) - {}^3(n,\pi^*)] & < \Delta E_{ST}[^1(\pi,\pi^*) - {}^3(\pi,\pi^*)] & \\ \text{Formaldehyde} \quad 10 & \text{Benzene} & 40 \\ \text{Acetone} \quad 7 & \text{Naphthalene} & 35 \\ \text{Benzophenone} \quad 7 & \text{Anthracene} & 35\,kcal/mole \end{array} \tag{2.39}$$

The size of the singlet-triplet energy gap has a very important role for intersystem crossing (ISC), the ISC rate increasing with the square of the decreasing energy gap. Further, the amount of gap energy can potentially be transferred to another molecule, e.g. within a quenching reaction with oxygen, the mechanism then called catalysed or "assisted ISC". If the energy gap is large enough to supply with the energy needed for the excitation of triplet state oxygen into its singlet state, this sensitising process opens another very efficient quenching channel, which is predominant within the strong quenching of aromatic compounds.

2.6.2 Antisymmetric orbital configurations

J.C. Slater proposed a simple way to express wave functions being antisymmetric for interchange of electronic space and spin coordinates by writing them as a (normalised) "Slater determinant" [Foldy 1962]. This determinant automatically produces an antisymmetric orbital configuration composed of the spin-orbitals $\phi_a, \phi_a, \ldots$ containing N electrons

$$\Psi(1,2,\ldots N) = \left(\frac{1}{N!}\right)^{1/2} \det\left|\phi_a(1)\phi_b(2)\cdots\phi_z(N)\right| \tag{2.40}$$

The exchange of a pair of rows of the determinant corresponds to the interchange of two electrons. If there are two rows the same, which means putting two electrons into identical spin-orbitals, the determinant vanishes, which is known as the Pauli principle.

Within a configuration interaction (CI) calculation, a ground or excited state wave function Ψ_k is noted as a linear combination of n-electron Slater determinants

$$\Psi_k = \sum_i C_{ik}\phi_i \tag{2.41}$$

The coefficients C_{ik} are determined using e.g. the Hartree-Fock method using a variational minimisation approach (cf. section 2.6.3).

Singlet and triplet states of n-electron molecules are then expressed by singly excited configurations [Klessinger 1995]

$$ {}^1\Psi_{if} = \frac{1}{\sqrt{2}}\left(\left|\phi_1\bar{\phi}_1 \ldots \phi_i\bar{\phi}_f \ldots\right| + \left|\phi_1\bar{\phi}_1 \ldots \phi_f\bar{\phi}_i \ldots\right|\right) \quad \wedge \quad {}^3\Psi_{if} = \begin{cases} \left|\phi_1\bar{\phi}_1 \ldots \phi_i\phi_f \ldots\right| \\ \frac{1}{\sqrt{2}}\left(\left|\phi_1\bar{\phi}_1 \ldots \phi_i\bar{\phi}_f \ldots\right| - \left|\phi_1\bar{\phi}_1 \ldots \phi_f\bar{\phi}_i \ldots\right|\right) \\ \left|\phi_1\bar{\phi}_1 \ldots \bar{\phi}_i\bar{\phi}_f \ldots\right| \end{cases} \tag{2.42} $$

2.6.3 Hartree-Fock (HF) based ab initio methods

The Hartree-Fock (HF) method primarily neglects the repulsion term of equation (2.34). The overall n-electron wave function $\Psi^0(\mathbf{x},\mathbf{R})$ is then an eigenfunction of $\sum_i \hat{h}_i \cdot \Psi^0 = \sum_i E_i \cdot \Psi^0$ with eigenvalue $E = \sum_i E_i$ ($\mathbf{x_i}$ represent the joint spin space coordinates of electron i and $\mathbf{R}$ the fixed nuclear configuration). The wave function $\Psi^0(\mathbf{x},\mathbf{R})$ is obtained as product wave function of one-electron spin-orbitals from the Slater determinant in equation (2.40). The initially neglected electron-electron repulsions are then considered by treating them in an average way: each electron is considered to be moving in the electrostatic field of the nuclei and the average field of the remaining $n-1$ electrons [Atkins 2008]. The best solution for the product wave function is found for minimisation of the energy expectation value, the so-called Rayleigh ratio $\mathcal{E}$

$$ \mathcal{E} = \frac{\int \Psi^* \hat{H} \Psi \mathbf{dx}}{\int \Psi^* \Psi \mathbf{dx}} \tag{2.43} $$

For insertion of the true ground-state wave function, $\mathcal{E}$ corresponds to the ground-state energy, whereas for all other wave functions, $\mathcal{E}$ is larger. The HF method finds the best n-electron determinant by the variational method for minimisation of the Rayleigh ratio $\mathcal{E}$ [Atkins 2008]. Once the optimised set of m spin-orbitals has converged to a self-consistent field (SCF), the orbitals are arranged by energy order, the lowest in energy representing the n occupied, the remaining $m-n$ the virtual orbitals. The Slater determinant over the n occupied spin-orbitals is the HF ground state wave function ϕ_0 of the molecule.

The self-consistent field Hartree-Fock method is an approach taking into account electron interaction in closed-shell ground states in a reasonable way. However, in order to obtain wave functions for excited states, configuration orbital interaction (CI) must be included. Based on the set of spin-orbitals found by use of the Hartree-Fock approach, ab initio semiempirical calculations are chosen like the PPP method (developed by Pariser, Parr and

Pople, see [Pariser 1953] and [Pople 1953]). Introducing the zero differential overlap (ZDO) approximation and further working with empirical values of electron-repulsion integrals, the PPP method alleviates the complexity of the repulsion treatment of the Hartree-Fock (HF) method, leading to more accurate results for the open shell excited states.

Within a configuration interaction (CI) calculation (cf. equation (2.41), a ground or excited state wave function Ψ_k is noted as a linear combination of n-electron Slater determinants, each being solution sets of the HF method [Atkins 2008]. The expansion coefficients C_{ik} have to be determined by minimisation of the Rayleigh ratio $\mathcal{E}$ using Ψ_k as basis set. Equation (2.41) is summing over the ground configuration ϕ_0, singly, doubly, triply … excited configurations (i.e. a single, two, three … electrons are promoted from a ground state spin-orbital to a virtual spin-orbital).

For most organic molecules, the ground state is reasonably described by the ground configuration ϕ_0. The first excited singlet and triplet state descriptions yield mainly singly and sometimes doubly excited configurations. Transitions from the highest occupied MO (HOMO) to the lowest unoccupied MO (LUMO) are frequently approximated by just one singly excited configuration, which yields the possibility of drastic simplifications, e.g. as taken benefit for the Hückel MO method (HMO), which does not take into account any electron repulsion [Klessinger 1995].

2.7 Selection rules

The Born-Oppenheimer approximation describes a spatially "frozen" situation of the nuclei. Following this approximation, the overall transition moment vanishes if the matrix element operation on either of the orbital, nuclear or spin wave functions of equation (2.24) results in a zero argument for the orbital, nuclear or spin wave contribution in equation (2.28). These cases are generally described as the selection rules.

2.7.1 Spin selection rule

For spin allowed electronic transitions, the spin multiplicity does not change, because the electric dipole (and quadrupole) moment operators do not operate on spin. Due to the so-called "spin selection rule", based on the orthonormal properties of the spin wave function, the integration over $\langle S_{J'}^* | S_J \rangle$ results in zero elements whenever spin functions are different, and therefore, the overall transition strength is zero or "spin forbidden".

2.7.2 Spatial symmetry selection rule

Following the "symmetry selection rule", spatial charge integration over the electron coordinates may also cause the transition moment to vanish. This will be the case if the integrand of the matrix element is antisymmetric with respect to at least one symmetry operation of the point group of the molecule. Looking at $\langle \psi_n^* | \mathbf{P} | \psi_m \rangle$, the integrand of the matrix element is a product of three functions, each of them having a particular irreducible representation. The triple product $\psi_n^* \mathbf{P} \psi_m$ belongs to the direct product representation, which has to be tested in the direction of the Cartesian coordinates $\alpha = x, y, z$ to form a basis for the totally symmetric irreducible representation or a reducible representation that contains the totally symmetric irreducible representation. The transition moment vanishes in any coordinate direction, in which such a basis could not be found. If this happens in all three directions, the transition is said to be "symmetry forbidden".

2.7.3 Orbital overlap selection rule

A further selection rule exists for the spatial overlap of the initial and final orbitals of a transition. This is expressed by the overlap charge distribution $-|e| \phi_f^* \phi_i$ [Klessinger 1995]. The differential overlap $\phi_f^* \phi_i$ leads to vanishing transition moments only within the ZDO approximation, and therefore, this is a rather weak selection rule. However, if the wave function of the initial orbital has large amplitudes only where the wave function of the final orbital is weak and vice versa, the overall transition moment can be very small.

2.8 "First order" coupling interactions — mixing of wave functions

For any transition between two electronic states, energy and momentum have to be conserved. Conservation is performed by intramolecular coupling interactions via mixing of different states, by intermolecular exchange with other molecules or by radiative exchange with an electromagnetic field.

The Born-Oppenheimer approximation is a zero order approximation. The zero order Hamiltonian does not include coupling between different energy states, because of the separation of electronic, nuclear and spin motion. However, by perturbation theory it is possible to introduce the so-called first order interactions, i.e. mixing between e.g. the electronic motion of different electrons (electronic interactions), between the electron orbital and the magnetic spin motion (spin-orbit coupling) or between vibrational and electron orbital motion (vibronic coupling).

2.8.1 Spin-orbit coupling

Strictly following the spin selection rule, transitions from singlet to triplet states and vice-versa should be practically unobservable. However, the spin magnetic and orbital magnetic moments are not independent, i.e. spin-orbit coupling occurs between them.

The interaction energy of the magnetic dipole $\mathbf{m}$ and the magnetic field $\mathbf{B}$ is represented by the spin-orbit Hamiltonian $\hat{\mathbf{H}}'_{\mathbf{so}} = -\mathbf{m} \cdot \mathbf{B}$. An electron moving with velocity $\mathbf{v}$ in the presence of an electric field $\mathbf{E}$ (due to an isotropic electric potential ϕ) is subject to a magnetic field $\mathbf{B} = -(1/rc^2) \cdot (d\phi/dr) \cdot \mathbf{r} \times \mathbf{v}$. The orbital angular momentum is defined as the cross product of the position vector from the nucleus to the electron and the linear momentum, thus $\mathbf{l} = \mathbf{r} \times \mathbf{p} = m_e \cdot \mathbf{r} \times \mathbf{v}$. Hence, for an atom the spin-orbit Hamiltonian is written as [Atkins 2008]

$$\hat{\mathbf{H}}'_{\mathbf{so}} = -\frac{e}{m_e^2 r c^2} \frac{d\phi}{dr} \cdot \mathbf{s} \cdot \mathbf{l} = \xi(\mathbf{r}) \cdot \mathbf{s} \cdot \mathbf{l} \tag{2.44}$$

with ξ being the spin-orbit coupling constant. The Coulombic electric potential of an electron in an atom with nucleus charge $Z \cdot e$ is $\phi = Ze/(4\pi\varepsilon_0 r)$. The spin-orbit Hamiltonian for a molecule is computed as a summation term running over all electrons j and nuclei μ [Klessinger 1995]

$$\hat{\mathbf{H}}'_{\mathbf{so}} = \frac{e^2}{8\pi\varepsilon_0 m_e^2 c^2} \sum_j \sum_\mu \frac{Z_\mu}{\left|r_j^\mu\right|^3} \cdot \mathbf{s_j} \cdot \mathbf{l_j^\mu} \tag{2.45}$$

The matrix element $\langle \psi_n^* | \hat{\mathbf{H}}'_{\mathbf{so}} | \psi_m \rangle$ represents the interaction energy, which potentially induces intersystem crossing. Irrespective of the amount of this coupling energy, the system's total angular momentum, i.e. the momentum from orbit plus spin must be conserved.

A simplifying model might describe the electron motion in a p-orbital as a figure-eight orbit around the nucleus, with the electron velocity strongly accelerating to near light speed close to the nucleus due to the nucleus charge, cf. figure 10. The magnetic field induced by the electron motion represents a magnetic torque on the electron spin magnetic moment μ_s. The maximum torque is found for the electron passing nearby the nucleus, and precisely at this moment the spin might be flipped if there is a possibility that the change in spin momentum μ_s is compensated by a change in orbital angular momentum l (dotted lines in the middle sketch). This is the case if the initial and the final orbital are orthogonal, e.g. the transition from a p_y to a p_x-orbital.

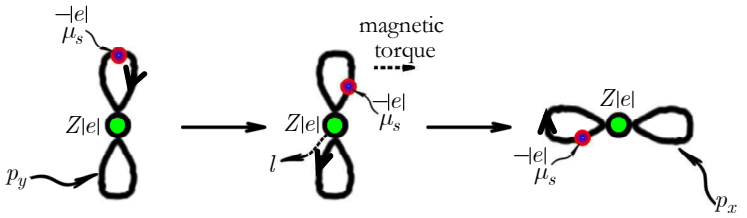

Figure 10: Simplified model of an electron motion in a p-orbital generating a magnetic torque, which might induce a spin flip if there is a possibility for compensating for the change in spin momentum, e.g. by an electron jump from a p_y to a p_x-orbital. From [Turro 1991]

Hence, for intersystem crossing, the spin flip corresponds to a change of the spin function from α to β and induces an angular momentum change, which may be compensated by an orbital transition from a p_x to a p_y-orbital. If such an orbital jump during intersystem crossing is possible, spin-orbit coupling is most effective.

Two major effects promoting the strength of spin-orbit coupling can readily be read from equation (2.45), the "heavy atom" effect and the "one-centre" effect.

Firstly, as to the "heavy atom" effect, the spin-orbit coupling is strongly promoted by a heavy atom with high atom number Z (strong nuclear charge) if accessible to the electron whose spin is to be flipped. More precisely, the orbital magnetic momentum of an electron is proportional to its velocity, i.e. coupling of the spin and orbital magnetic moments will be maximal when the electron is accelerating near the nucleus of charge Ze. This "heavy atom" effect exists not only as intramolecular (internal) effect, i.e. within the molecular structure one ore more hydrogen atoms are replaced by e.g. bromine atoms, but also as intermolecular (external) effect, i.e. the molecule is dissolved in a heavy-atom solution.

Secondly, as to the "one-centre" effect, if the transition from p_x to p_y, i.e. the electron jump compensating the momentum change due to the spin flip, occurs at the same atom (centre) as the spin flip, the latter can be connected to the electron jump and is most likely to occur. This is the case for non-saturated carbonyl compounds, where the intersystem crossing ${}^1(n,\pi^*) \rightarrow {}^3(\pi,\pi^*)$ is triggered via a one-centre $p_x \rightarrow p_y$ interaction, cf. figure 11. The enhancement of intersystem crossing due to the "one-centre" effect is represented by the position vector in the denominator of equation (2.45), which is naturally smaller and makes $\hat{\mathbf{H}}'_{\mathbf{so}}$ increase compared to the two-centre orbital jump.

Further looking on ${}^1(n,\pi^*) \rightarrow {}^3(n,\pi^*)$ and ${}^1(\pi,\pi^*) \rightarrow {}^3(\pi,\pi^*)$ intersystem crossing, it can be stated that neither for the n- nor for the π^*-orbital a spin flip generates orbital angular momentum along the bond axis, i.e. no $p_x \rightarrow p_y$ electronic jump is involved. This will

later be referred as the El-Sayed's rules, qualifying an intersystem crossing without $p_x \rightarrow p_y$ electron jump as forbidden.

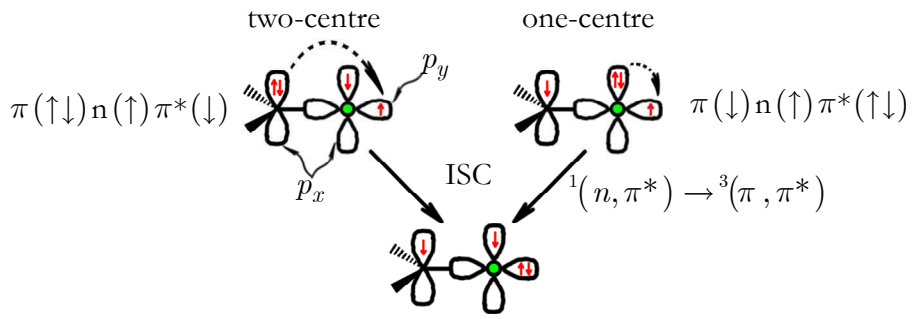

Figure 11: Illustration of possible electron configurations for intersystem crossing (ISC) of a carbonyl compound. The so-called "one-centre" effect is likely to be the most probable case.

2.8.2 The Franck-Condon principle

Recalling the Born-Oppenheimer approximation, it was stated that the vibration of the nuclei is much slower (> 100 times) than the electronic motion, which is due to the higher inertia of the nuclei. This means that the change in electronic configuration will take place while the nuclear configuration remains unchanged. The global strength of the transition dipole moment is given by the electronic transition moment. After the electron has "jumped" to the new electronic configuration, the vibrational motion will change as a function of the squared overlap integrals of the vibrational wave functions, the so-called Franck-Condon factors $\left\langle \chi_{\nu'}^* \mid \chi_\nu \right\rangle^2$, representing the transformation efficiency between the vibrational modes of the initial and final state. The nuclei are reacting to the newly established electronic force field, to which the nuclei find themselves exposed.

Due to the "frozen" nuclear configuration, the electron "jump" reads as a vertical line from the initial to the final electronic state in the potential energy (PE) diagram. It is immediately clear, that the shape and position (equilibrium nuclear separation) of the initial and final state PE surfaces have a major impact on the amount of excess vibrational energy to be produced in the final state, once the vibrational motion has adapted to the new electronic configuration. The excess energy is determined by the intersection point of the vertical electronic transition with the PE curve of the final state, which is the "turning point" of the vibration (cf. figure 12).

In the case of similar shape and position, the electronic force field after the electron jump will not have changed very much, and therefore, the vibrational motion will nearly remain unchanged. The $n \rightarrow \pi^*$ transition is an example of this particular case, since the electron configuration of the (n_0^2)-state is very similar to the (n,π^*)-state. For proof see e.g. the

vibrational modes of acetone in the ground state and the first excited state, being very much alike [Angeli 2005].

An increasing difference in the equilibrium separation of the initial and final state PE curves entails significant changes in the electronic configuration. Intermediately shifted PE curves are found for $\pi \rightarrow \pi^*$, largely shifted PE curves for $n \rightarrow \sigma^*$ transitions.

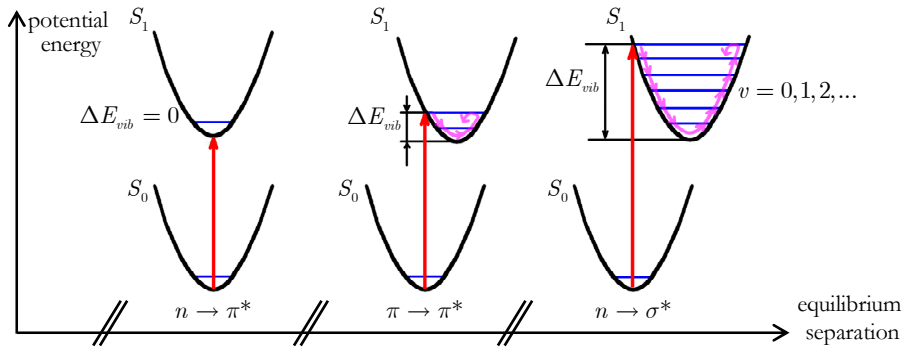

Figure 12: Franck-Condon principle. The difference in equilibrium separation between initial and final state potential energy curve is directly linked to the amount of vibrational excess energy produced in the final state. Adapted from [Turro 1991].

If the initial and final states PE curves have identical shape and equilibrium separation (the rather improbable case), the vibrational wave functions are orthonormal, i.e. only vibrational transitions from modes $0 \rightarrow 0$, $1 \rightarrow 1$, $\ldots \nu \rightarrow \nu$ can be observed, and the transition is said Franck-Condon allowed. In the general case, the PE curves differ in form and equilibrium geometry, and the Franck-Condon factors reflect the relative intensity of the transition between the nonorthogonal vibrational wave functions χ_ν^i and $\chi_{\nu'}^f$, i.e. between the vibrational modes ν and ν' of the initial and final states.

2.8.3 Vibronic coupling

The separation of the transition dipole moment into a product of the electronic transition moment representing the global strength of the transition and the overlap of the vibrational wave functions, see equation (2.27), was justified by the Born-Oppenheimer approximation. Following strictly this approximation of fixed nuclear configuration, symmetry forbidden transitions should never by observable. In practice, however, these transitions often show finite (albeit mostly small) oscillator strengths, which must be seen as the breakdown of the Born-Oppenheimer approximation, or in other words, as the change from zero order approximation to first order coupling, i.e. mixing of the wave functions.

A first order perturbation approach for the vibronic coupling of a state b close-lying to the final state f, where the symmetry forbidden transition $i \rightarrow f$ "borrows" intensity from an allowed transition $i \rightarrow b$, might look as follows [Klessinger 1995]

$$\begin{aligned} \mathbf{M}_{\mathbf{i}\nu\rightarrow\mathbf{f}\nu'} &= \mathbf{M}_{\mathbf{if}} \left\langle \chi_{\nu'}^{*}(\mathbf{Q}) \middle| \chi_{\nu}(\mathbf{Q}) \right\rangle \\ &+ \sum_{k=1}^{3N-6} \left\langle \chi_{\nu'}^{*} \middle| \left\langle \phi_b \middle| (\partial \hat{H}_{el} / \partial Q_k)_{Q_k=0} \middle| \phi_f^{*} \right\rangle \mathbf{Q_k} \middle| \chi_{\nu} \right\rangle \mathbf{M_{ib}} / (E_b - E_f) \end{aligned} \tag{2.46}$$

The first summand corresponds to the zero order description of the transition moment of equation (2.27) for fixed nuclear configuration $\mathbf{Q}$, i.e. for the purely electronic Hamiltonian. The second summand stands for the participation of an expanded Hamiltonian depending on vicinity geometries $\mathbf{Q_k}$, which are slightly varying from the equilibrium geometries $\mathbf{Q_i}$ and $\mathbf{Q_f}$ of the initial and final state. The summation runs all over the normal modes of vibration. This second term represents the mixing of intensity from the allowed transition $i \rightarrow b$ to the forbidden transition $i \rightarrow f$, assuming the state b being energetically close to the final state f. The vibronic perturbation operator $\hat{\mathbf{H}}'_{\mathbf{vib}}$ is obtained from the expansion of the electronic Hamiltonian into a power series and truncation to terms linear in $\mathbf{Q_k}$, hence $\hat{\mathbf{H}}'_{\mathbf{vib}} = \sum_k (\partial \hat{H}_{el} / \partial Q_k)_{Q_k=0} \mathbf{Q_k}$.

2.9 Transition pathways

The zero order Born-Oppenheimer approximation does not allow radiationless transitions from one energy surface to another. First order interactions between electronic states have to be introduced by use of time dependent perturbation theory. For the theoretical case of a direct state-to-state transition, equation (2.15) stands for the transition probability and its time derivative for the respective transition rate. However, in practice, the more general case is represented by a transition from an initial state to a band of final states with closely spaced energy levels, the number of levels per unit energy being characterised by the density of states $\rho_n = dn / dE$. Thereby the transitions are radiative with a vertical energy change $h\nu$ or non-radiative, i.e. horizontal isoenergetic transitions. The probability $P_{if}^{\rho_n}$ of transition to ρ_n states can be expressed by integration of the state-to-state probability P_{if} weighted by the density of states ρ_n over the energy band E [Gilbert 1991]

$$P_{if}^{\rho_n} = \int P_{if} \cdot \rho_n dE = \hbar \int \frac{4E_0^2 M_{fi}^2}{\hbar^2} \frac{\sin^2(\Delta\omega t/2)}{\Delta\omega^2} \cdot \rho_n d\omega = \frac{2\pi E_0^2 M_{10}^2}{\hbar} t \cdot \rho_n \tag{2.47}$$

with $dE = \hbar d\omega$ and substitution of $\Delta\omega t / 2$. The time derivative

$$k_{if,rad} = \frac{d}{dt}\left(P_{if}^{\rho_n}\right) = \frac{2\pi}{\hbar}\left(E_0 M_{fi}\right)^2 \rho_n \quad \text{radiative transition} \qquad \ldots \qquad k_{if,nr} = \frac{d}{dt}\left(P_{if}^{\rho_n}\right) = \frac{2\pi}{\hbar}\hat{H}_{fi}^2 \rho_n \quad \text{non-radiative transition} \tag{2.48}$$

is known as Fermi's (second) golden rule, which corresponds to the rate of electronic transitions between an initial quantum state Ψ_i and a final quantum state Ψ_f, depending on the density of states ρ_n in the final state Ψ_f at the energy of the initial state E_i. For radiative transitions, the perturbation part of the Hamiltonian is defined as the scalar product of electric field and dipole moment vectors [Gilbert 1991]. For the non-radiative case, there is generally no electric field involved in the transition, which is therefore driven by a perturbation part $\hat{H}_{fi}$ internal to the molecular Hamiltonian.

As the density of states is strongly increasing with the vibrational energy, non-radiative electronic transition rates are much faster in downward direction than vice-versa. This is after all the main reason for the low rates of inverse intersystem crossing found for most organic molecules. Often fast vibrational relaxation follows the non-radiative transition making it practically irreversible [Klessinger 1995].

2.9.1 Kinetics

A fully allowed "pure" electronic transition between two states Ψ_0 and Ψ_1 would have an approximate rate of $10^{15} - 10^{16}\,/\mathrm{s}$ if nuclear and spin configuration remain unchanged. In practice, this high rate of pure electronic transition will be always a hypothetical case, real rates being much smaller. Yet, taking into account the time it takes to establish the vibrational motion in the final state after the "pure" electronic transition, non-radiative transitions between two excited electronic states have a maximal rate of $k_{\max} = 10^{13} - 10^{14}\,/\mathrm{s}$ in case of no change in spin multiplicity [Turro 1991]. This may be called the zero point motion limit for the vibration of the nuclei. But this rate will never be practically measured, since it is conceived for the case of very similar wave functions having a minimal energy gap. Measurable rates differ from this maximal rate by a prohibiting factor f, varying between zero and unity for fully forbidden to fully allowed transitions. For separation of f to prohibiting factors f_e, f_v and f_s with respect to the changes in electronic, nuclear and spin configuration during a transition, the observable transition rate k_{obs} is written as follows [Turro 1991]

$$k_{obs} = k_{\max} \cdot f = k_{\max} \cdot \left(f_e \cdot f_v \cdot f_s\right) \tag{2.49}$$

The prohibiting factors represent the selection rules for electronic transitions and the first order state mixing as described in the previous sections. The prohibiting factor f is propor-

tional to the square of the matrix element of the transition and inversely proportional to the energy gap between the initial and final state [Turro 1991]

$$f_{if} \propto \left[\frac{\left\langle \Psi_f^* \middle| \mathrm{P}_{if} \middle| \Psi_i \right\rangle}{\Delta E_{fi}} \right]^2 \tag{2.50}$$

Introducing state mixing, i.e. allowing coupling of electron, nuclear and spin motions, equation (2.49) modifies to [Turro 1991]

$$k_{obs} = k_{\max} \cdot \left[\frac{\left\langle \psi_n^* \middle| \hat{\mathbf{H}}'_{\mathbf{vib}} \middle| \psi_m \right\rangle}{\Delta E_{nm}} \right]^2 \left[\frac{\left\langle \psi_n^* \middle| \hat{\mathbf{H}}'_{\mathbf{so}} \middle| \psi_m \right\rangle}{\Delta E_{nm}} \right]^2 \left\langle \chi_{\nu'}^* \middle| \chi_\nu \right\rangle^2 \tag{2.51}$$

taking into account vibronic and spin-orbit coupling. The Franck-Condon factor $f_v = \left\langle \chi_{\nu'}^* \middle| \chi_\nu \right\rangle^2$ can be approximated by the energy gap law

$$f_v = \alpha \cdot \exp(-\Delta E_{nm}) \tag{2.52}$$

if neither f_e nor f_s are limiting factors for the decay kinetics, α being a proportionality constant.

2.9.2 Pathways

A simple illustration of the numerous pathways between electronic states of organic molecules can be realised by means of a Jablonski diagram as in figure 13, showing the possible radiative and non-radiative transitions. The straight arrows correspond to radiative, the wavy arrows to non-radiative processes.

Here, the Jablonski diagram is drawn for the case of high vibrational relaxation (VR) rates, i.e. radiative emissions have no time to occur before thermalisation is completed, which is the most common case for the liquid or the high pressure gas phase. In the gas phase of medium pressure, however, VR might be in competition with other pathways. For large organic molecules, VR can then be thought as a cascading deactivation process over the vibrational levels, see [Thurber 1999b] and 5.3.2. At each step of the cascade, the collisional relaxation competes with specific radiative and non-radiative rates, which are functions of vibrational excess energy. An extreme point is the collisionless condition, i.e. for either very low pressure and/or very low temperature. Practically no collisions occur any more, and hence, all deactivation pathways have their starting point at the vibrational levels, to which the molecules were initially promoted by absorption.

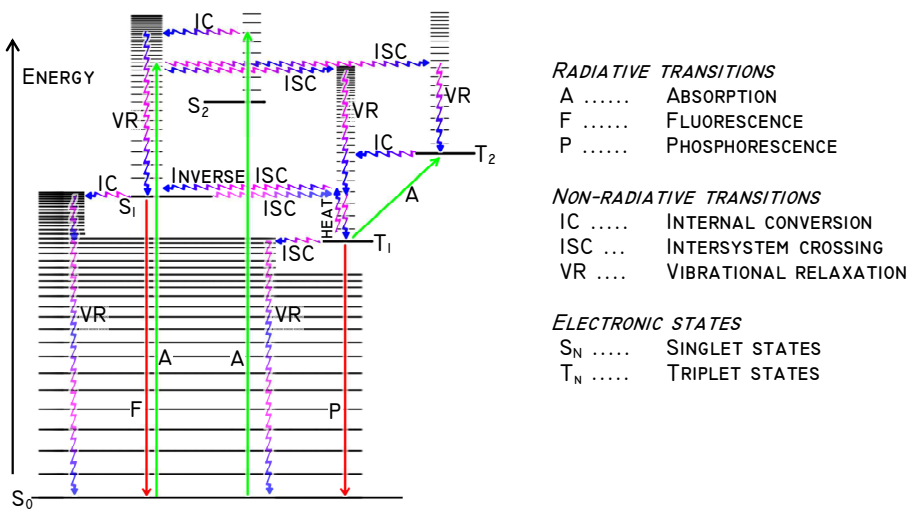

Figure 13: Jablonski diagram. Straight arrows correspond to radiative, wavy arrows to non-radiative processes. Only intramolecular processes are show here. Depending on the photon energy, $h\nu$ absorption from the singlet ground state leads to either the first excited or a higher excited singlet state. Another excitation scheme is given for triplet-triplet absorption.

Within the zero-order approximation of Born-Oppenheimer, the separation of the wave function into a nuclear, vibrational and spin part leads to the selection rules. Vibronic coupling and spin-orbit coupling are the first-order processes for mixing of initial and final states, i.e. the breakdown of the Born-Oppenheimer approximation. The Hamiltonians for the vibronic and spin-orbit interactions are molecule specific and further depend on the environmental conditions, e.g. the properties of the solvent when in solution.

The transition rates depend on the energy gap, the coupling Hamiltonians, the Franck-Condon factors, see equation (2.51), and further on the spatial overlap of the initial and final electronic states. The energy gap between higher electronic levels is relatively small, leading to very fast internal conversion (IC) from S_2 to the first excited state. Between the first excited singlet and the ground state, the energy gap is generally high and IC from the S_1 to S_0 therefore negligible. Hence, the sum of quantum yields of fluorescence and intersystem crossing is nearly unity in most cases.

An ultrafast return from the lowest excited states to the ground state might occur via IC at conical intersections (called "funnel") behind small energy barriers. This might be referred to the onset of what is known as the "third channel", which is observed as a sudden increase of the radiationless decay for vibrationally highly excited aromatic molecules [Bernardi 1996].

2.9.3 Yield formulations

Generally, a quantum yield of a reaction is defined as the number of molecules undergoing a specific process divided by the number of absorbed light quanta. However, sometimes it is more useful not to refer to the total number of absorbed quanta, but to the number of molecules in a given state. The efficiency η_i is defined as the ratio of the number n_i of molecules undergoing a specific reaction i to the number of molecules n_A in the precursor state A of the reaction, $\eta_i = n_i / n_A$, or in term of rates $\eta_i = k_i / \sum_j k_j$, the sum running over all processes of consideration.

The quantum yield of a multi-step reaction is the product of the efficiencies of each single step. For example, a specific reaction depopulating a single state is the phosphorescence from the vibrational ground level of T_1. Due to the spin selection rule, the triplet state is practically never populated by direct absorption from S_0, but rather by intersystem crossing from S_1 due to spin-orbit coupling, the populating efficiency being the triplet formation yield $\phi_T = k_{ST} / \left(k_f + k_{IC} + k_{ISC}^{ST}\right)$. Neglecting possible population from higher triplet states as well as quenching or photochemical reaction pathways, the phosphorescence quantum yield might then be formulated as product of populating and depopulating efficiencies

$$\phi_{ph} = \eta_{pop} \cdot \eta_{depop} = \frac{k_{ST}}{k_f + k_{IC} + k_{ISC}^{ST}} \cdot \frac{k_{ph}}{k_{ph} + k_{ISC}^{TS}}$$

Dependent on exclusive conditions limiting the rate balance of populations and depopulations to a state, the yield definition of a specific reaction might have different formulations, e.g. the quantum yield of phosphorescence will not be the same, once quenching and photochemical reactions are included.

2.9.4 Lifetimes

Two major expressions have to be distinguished for the description of the lifetime of excited states. The first is the experimentally accessible effective fluorescence lifetime $\tau_{eff} = \tau_f = 1/k_{tot}$. The second is the radiative lifetime (also lifetime of spontaneous emission), which is the time within the population of the excited molecules decays from 1 to $1/e$, $\tau_{rad} = 1/k_f$, being related to the transition dipole moment via the equations (2.6) and (2.18).

In practice, from fluorescence quantum yield measured data the fluorescence decay rate follows by

$$k_f = \frac{\phi_f}{\tau_f} \tag{2.53}$$

and in consequence, the non-radiative rate of intramolecular decay can be derived from

$$k_{nr} = \frac{(1-\phi_f)}{\tau_f} \tag{2.54}$$

2.10 Radiative deactivation – Fluorescence and Phosphorescence

Luminescence is the radiative deactivation of electronically excited states to the ground state through photon emission. It is distinguished between fluorescence and phosphorescence dependent on whether the emissive transition is spin-allowed or spin-forbidden, i.e. fluorescence occurs for the deactivation of singlet and phosphorescence for the deactivation of triplet states, provided that the ground state is a singlet state.

Radiationless deactivation rates are very fast for the higher excited electronic states. Thus, generally luminescence occurs mainly from the first excited singlet and triplet states, where the radiative emission rates are in competition with the non-radiative pathways.

Except for a resonance excitation, the fluorescence emission is Stokes shifted from the excitation wavelength towards longer wavelengths due to the dissipation of energy into non-radiative decay channels. For the liquid phase, vibrational relaxation (VR) leads to a very fast thermalisation. Thus, in this case fluorescence occurs mainly from the vibrational ground state and the emission spectrum becomes independent from the excitation wavelength. However, in the medium and low-pressure gas phase the VR rate becomes competitive to fluorescence and other non-radiative pathways, and therefore the emission spectrum is dependent on both excitation wavelength and environmental conditions like pressure and temperature.

As mentioned above, the radiative lifetime of an emission shortens with the squared transition dipole moment, i.e. a transition is fast if it is allowed and the slower the more forbidden. Because phosphorescence is a spin-forbidden triplet-singlet deactivation, it is generally much longer-lived than the spin-allowed fluorescence. Fluorescence lifetimes are found from one to hundred nanoseconds, whereas the lifetime of phosphorescence emission is from milliseconds to seconds.

The radiative lifetimes of different species are very much depending on the selection rules. If e.g. both the spatial symmetry and the orbital overlap selection rules are violated like in ketones, the radiative lifetime can be of microsecond duration. However, the (observed)

effective fluorescence lifetime of ketones is only of the order of nanoseconds due to a very fast rate of intersystem crossing.

2.10.1 Fluorescence signal

The laser-induced fluorescence signal can be derived from a two-level energy scheme including the rate constants of absorption, stimulated and spontaneous emission, quenching, photoionisation and predissociation, cf. figure 14.

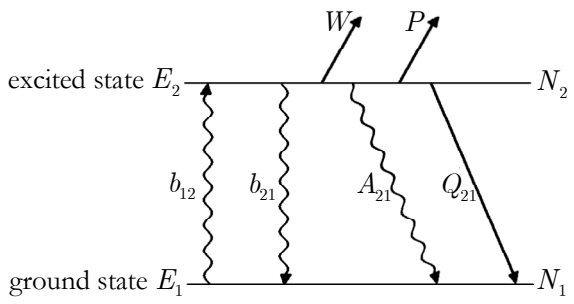

Figure 14: Two energy level diagram for laser induced fluorescence modelling [adapted from Eckbreth 1996]. b_{12} and b_{21} are the rate constants for absorption and stimulated emission, related to the Einstein coefficient by $b = BI_\nu / c$. A_{21} and Q_{21} are the rate constants of spontaneous emission and bimolecular deactivation via quenching. W and P are the rate constants for photoionisation and predissociation.

The absorbed energy corresponds to the energy of a photon with the laser frequency $h\nu_L$. The rate constants of absorption and stimulated emission are related to the Einstein coefficient by $b = BI_\nu / c$, I_ν being the spectral irradiance of the laser source. More accurately, the spectral distribution has to be taken into account, and hence the rate constant for absorption and stimulated emission becomes

$$b = B / c \cdot \int_\nu I_\nu(\nu)\, g(\nu)\, d\nu \tag{2.55}$$

where $I_\nu(\nu)$ and $g(\nu)$ are the laser and absorption line shapes. The fluence of the laser pulse is defined as $I_L = \int_\nu I_\nu d\nu = \int_t I_\nu \, \Delta\nu_L dt = I_\nu^0 \, \Delta\nu_L$, product of the normalised spectral irradiance I_ν^0 and the laser profile FWHM $\Delta\nu_L$. Assuming a broad $\Delta\nu_L$, the laser spectral distribution $L(\nu)$ is merely varying over the absorption lineshape $g(\nu)$, and therefore $I_\nu(\nu) \approx I_\nu^0$. Hence the averaged absorption cross-section can be written as

$$\sigma_\nu = \frac{h\nu_L}{I_L} \int_\nu b \, d\nu = \frac{h\nu_L}{c} \frac{B_{12}}{\Delta\nu_L} \tag{2.56}$$

From figure 14, the fluorescence signal power is seen to be proportional to $N_2 A_{21}$, product of the species population N_2 of the excited state and the rate constant of spontaneous emission A_{21}. Being $\Omega/4\pi$ the observed solid angle, $h\nu_{LIF}$ the energy of a fluorescence photon and V the observed volume, the fluorescence power is

$$F_{LIF} = h\nu_{LIF} N_2 A_{21} \frac{\Omega}{4\pi} V \tag{2.57}$$

Considering ionisation and dissociation being insignificant processes and the initial excited state population N_2^0 negligible, it follows for the state populations $N_1 + N_2 = const = N_1^0$, i.e. the two-level scheme is a closed system without any loss of population. The species population N_2 can then be expressed as a function of the ground state initial population N_1^0 or number density of absorbing molecules $N_2 = N_1^0 B_{12} / [(B_{12} + B_{21}) \cdot (1 + I_{sat}^{\nu} / I_{\nu})]$, the saturation spectral irradiance defined as $I_{sat}^{\nu} = (A_{21} + Q_{21}) \cdot c / (B_{12} + B_{21})$.

(a) Linear fluorescence regime for low laser irradiance

For the case of low laser irradiance excitation, i.e. $I_{\nu} \ll I_{sat}^{\nu}$ the fluorescence power is found as

$$F_{LIF} = \frac{h\nu_{LIF}}{c} \frac{\Omega}{4\pi} V N_1^0 B_{12} I_{\nu} \phi \tag{2.58}$$

where ϕ is defined as the fluorescence quantum yield $\phi = A_{21} / (A_{21} + Q_{21})$. The number of fluorescence photons N_{LIF} emitted within a time period t can be deduced by integration of equation (2.58)

$$N_{LIF} = \int \frac{F_{LIF}}{h\nu_{LIF}} dt = \frac{\Omega}{4\pi} V \frac{N_1^0 \sigma_{\nu} \phi}{h\nu_L} \int_t I_{\nu} \Delta\nu_L dt = \frac{\Omega}{4\pi} V N_1^0 \sigma_{\nu} \phi \frac{I_L}{h\nu_L} \tag{2.59}$$

using the definition of the absorption cross-section from equation (2.56). Finally, being η_D the efficiency of the detection system, the detected fluorescence intensity is derived as

$$S_f = \eta_D \cdot N_{LIF} = \eta_D \frac{\Omega}{4\pi} V N_1^0 \sigma_{\nu} \phi \frac{I_L}{h\nu_L} \tag{2.60}$$

(b) Saturated fluorescence regime for high laser irradiance

For the case of high laser irradiance excitation, i.e. $I_\nu \gg I_{sat}^\nu$ the fluorescence power is found as

$$F_{LIF} = h\nu_{LIF} \frac{\Omega}{4\pi} V N_1^0 \frac{B_{12}}{B_{12} + B_{21}} A_{21} \tag{2.61}$$

The rates of absorption and stimulated emission are dominating the state-to-state energy transfer, and thus the fluorescence power is independent of the laser irradiance and the quenching.

2.11 Non-radiative intramolecular deactivation

Non-radiative deactivation channels, where the energy is transformed within the molecule itself are called intramolecular. Thus, for these isoenergetic pathways the vibrational excess energy after the electronic transition must be transformed to the vibrational modes of the final state. In practice, isoenergetic internal conversion (IC) and intersystem crossing (ISC) are followed by vibrational relaxation, fast dissipating the vibrational energy into heat of thermalisation.

2.11.1 Internal conversion – energy gap law

The term "internal conversion" is referred to the radiationless transition between electronic states of the same spin multiplicity, i.e. singlet-singlet or triplet-triplet transitions between isoenergetic vibrational levels. Mostly, internal conversion is directly followed by vibrational relaxation (VR). If the VR rate is dominated by the rate of collisional events, VR is proportional to the number density of colliders and to the Lennard-Jones collision frequency.

Radiationless deactivation from higher excited states to the first excited state is usually so fast, that in most cases radiative emission is observed only from the lowest excited state. This is what is known as "Kasha's rule", i.e. the rate of radiationless transfer depends on the energy gap between the electronic states, which is much smaller between higher electronic states compared to the gap between the lowest excited state and the ground state. The cascading of non-radiative transitions therefore normally ends at the thermalised level of the first excited state. Exception from Kasha's rule is observed for e.g. azulene, presenting fluorescence emission from the second excited singlet state.

The rate of internal conversion is estimated to be an exponential decrease with the energy gap between the S_1 and S_0 state (by estimation of Franck-Condon factors through the energy-gap law in equation (2.52))

$$k_{ic} = 10^{13} \cdot f_v = 10^{13} \exp(-\alpha \cdot \Delta E) \tag{2.62}$$

the proportionality constant α being $4.85\,\mathrm{eV}^{-1}$ for e.g. benzenoid aromatics.

2.11.2 Intersystem crossing – El Sayed's rules

Electronic transitions from singlet to triplet multiplicity or vice-versa are called "intersystem crossing" (ISC) and are forbidden by the spin selection rule. They become possible via first order mixing through spin-orbit coupling, i.e. the angular momentum change induced by the necessary spin flip is compensated by an orbital transition, e.g. by an orbital jump from a p_x to a p_y-orbital, see section 2.8.1. This is generally known as the El Sayed's rules

$$\text{ISC allowed:} \quad {}^1(n,\pi^*) \rightleftarrows {}^3(\pi,\pi^*) \quad \text{and} \quad {}^1(\pi,\pi^*) \rightleftarrows {}^3(n,\pi^*) \tag{2.63}$$

$$\text{ISC forbidden:} \quad {}^1(n,\pi^*) \rightleftarrows {}^3(n,\pi^*) \quad \text{and} \quad {}^1(\pi,\pi^*) \rightleftarrows {}^3(\pi,\pi^*) \tag{2.64}$$

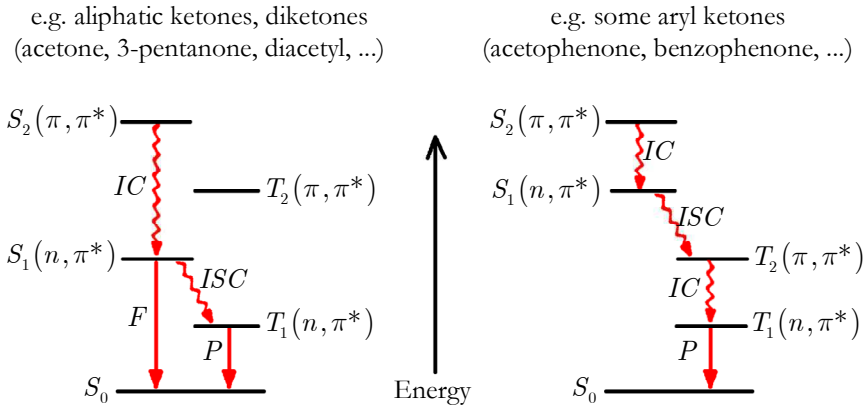

Figure 15: Luminescence types for molecules containing both (n,π^*) and (π,π^*)-states (adapted from [Malkin 1992]). The left side sequence corresponds e.g. to aliphatic ketones. The right side disposition is typical for some aryl ketones. The ISC rate of aliphatic ketones is small due to El Sayed's rule (2.64) allowing fluorescence to be competitive to the non-radiative decay. The ISC rate of most aryl ketones is very fast, with almost unity yield for benzophenone, the gap of S_1 and T_2 being very small and the transition allowed according to El Sayed's rule (2.63). This is why practically no fluorescence is seen for this molecule.

Thus, for aromatic molecules without n-orbital there is no accessible orbital jump to compensate for the spin flip, the ISC transition is then said forbidden. Similarly for aliphatic ketones, due to the energy sequence of singlet and triplet states allowed ISC transitions as in El

Sayed's rule (2.63) are not available. The disposition of the lowest singlet and triplet states of either (n,π^*) or (π,π^*)-type is molecule specific and may further change on solvent effects. The knowledge of this state disposition is a key to classification in luminescence types.

The above figure 15 shows the state dispositions for two different luminescent types as usually found for the case of aliphatic ketones (left side) and aryl ketones (right side).

It was mentioned in section 2.9.1 that the rate of electronic transitions does not only increase with the squared dipole moment, but also it decreases with the square of the energy gap between the electronic states. The singlet-triplet energy gap ΔE_{ST} was shown to be the consequence of the spin correlation postulated by the Pauli principle, ΔE_{ST} being just twice the exchange integral K, see equation (2.37) section 2.6.1. Thereby K is generally smaller for (n,π^*)-states than for (π,π^*)-states, and therefore, ΔE_{ST} of simple ketones is much lower than for benzenoid compounds, see equations (2.38) and (2.39) in section 2.7.3. Thus, intersystem crossing of e.g. acetone is about 500 times faster than for naphthalene [Turro 1991].

2.11.3 Intramolecular vibrational redistribution

The vibrational relaxation of organic molecules with excess vibrational energy in the ground state or in the excited state occurs for a part on fast ($10^{11}-10^{13}\,s^{-1}$) internal vibrational redistribution (IVR) and for a second part on slower ($10^{9}-10^{11}\,s^{-1}$) vibrational energy transfer (VET) to the solvent (gas or liquid) bath molecules.

IVR is the redistribution of vibrational energy from optically active to inactive modes. For large organic molecules, optically active modes overlap more and more with inactive vibrational modes, because the density of states increases exponentially with the excess in vibrational energy. Thus, the IVR rate is dominated by the density ρ_n of vibrational states.

2.12 Bimolecular deactivation processes

In addition to monomolecular pathways through radiative emissions and non-radiative deactivation channels, also bimolecular events might be of major importance for the population rate balance of electronically excited states. If excitation energy is transferred between molecules, this is referred to as a quenching process. Further this is called luminescence quenching if the transfer suppresses a part of the possible radiative emission. Sometimes a quenching process assists a specific transfer reaction, otherwise impossible or having only a minor rate, e.g. like the benzophenone-sensitised phosphorescence of naphthalene.

2.12.1 Vibrational relaxation (VR) in collisional cascade

As mentioned in the previous section, apart from intramolecular vibrational redistribution (IVR) the excess vibrational energy can be transferred to other molecules in the bath gas through collisions, i.e. by intermolecular vibrational energy transfer (VET). IVR and VET both contribute to what is generally known as vibrational relaxation (VR), i.e. the vibrational excess energy is dissipated until the vibrational level of thermalisation is reached. In the literature, often the term of VR is used instead of VET to address the intermolecular collisional process, which here will be done as from now.

Within the kinetic gas theory the nature of a collisional event is characterised by the Lennard-Jones collision frequency Z_{coll}, inherent property of the colliding couple. The collision rate is generally related to the collision frequency by the number density of the colliding species M in the bath gas, $k_{coll} = Z_{coll} n_M$. Due to the proportionality to the number density of species M the intermolecular loss of vibrational energy in the liquid and high-pressure gas phase is ultrafast.

The relaxation rate for the intermediate pressure gas phase is much smaller and depends on the pressure. The fluorescence rate might then become competitive to all other deactivation processes. In this case the fluorescence yield of large organic molecules might be computed via a scheme of stepwise deactivation within a vibrational cascade, the rate of each deactivation channel depending on the excess vibrational energy of the cascade steps. For extremely low gas pressures or temperatures near to zero point of the Kelvin scale, collision rates become very small, i.e. this condition is said "collisionless".

2.12.2 Collisional quenching

The properties of the collisional partners as well as the surrounding environment govern over the possible mechanisms and rates of intermolecular collisional energy transfer. A potentially fluorescing molecule might be transferred from the excited singlet state to the triplet state or return to the ground state through a quenching event. Thus, quenching reactions open another channel of non-radiative deactivation responsible for the decrease of the fluorescence quantum yield. The fluorescence quantum yield in presence of a quenching collision partner is

$$\phi_f^q = \frac{k_f}{k_{tot} + \tilde{k}_q \cdot n_q} \tag{2.65}$$

k_{tot} being the sum of the fluorescence rate and the non-radiative deactivation rates, $k_f + k_{NR}$. The efficiency of the quenching reaction can be rated by the quotient of signal intensity S_f^0

without quenching influence to the intensity S_f^q under respect of the quenching influence. This is generally expressed via the Stern-Volmer coefficient $k_{SV} = \tilde{k}_q / k_{tot}$, which is the slope of the ratio of S_f^0 and S_f^q, plotted as a function of the number density of the quencher

$$S_f^0 / S_f^q = k_{SV} n_q + 1 \tag{2.66}$$

With the definition of the Stern-Volmer coefficient k_{SV} the fluorescence quantum yield ϕ_f^q for quenching can be written as a function of the yield without quenching ϕ_f^0

$$\phi_f^q = \frac{k_f / k_{tot}}{1 + k_{SV} n_q} = \frac{\phi_f^0}{1 + k_{SV} n_q} \tag{2.67}$$

The intensity of the fluorescence emission is proportional to the number density n_{abs} of the absorbing species as well as to the fluorescence quantum yield. Equation (2.67) yields a particularly interesting feature for the condition that the quenching is the dominating deactivation process, i.e. $k_{SV} n_q \gg 1$, that is the signal intensity of fluorescence will become a proportionality function like

$$S_f^q \propto n_{abs} \sigma_{abs} \phi_f^q \approx n_{abs} \sigma_{abs} \cdot \frac{\phi_f^0}{k_{SV} n_q} = g(T,P) \cdot \boxed{\frac{n_{abs}}{n_q}} \searrow \text{FAR} \tag{2.68}$$

Thus, the fluorescence signal of a molecule mainly deactivated by quenching potentially yields an expression corresponding to the equivalence or fuel-to-air ratio (FAR). The absorption cross-section, the quantum yield without quenching and the Stern-Volmer factor are potentially dependent from temperature and pressure, but can sometimes be separated via a calibration function $g(T,P)$. In this case, the equivalence ratio can be inferred from the fluorescence intensity.

2.12.3 Accounting for the efficiency of quenching collisions

If the quenching interaction between a molecule and a quencher is assumed to be due to short-range collisional energy transfer, the rate coefficient $\tilde{k}_q$ stands for the effective quenching collision frequency, i.e. not all but only a fraction of the collisional events leads to quenching, whereas the rest is likely to produce vibrational relaxation. A quenching efficiency or probability of effective collision $\langle P \rangle$ is then defined as being the ratio of the rate coefficient $\tilde{k}_q$ to the Lennard-Jones collision frequency Z_q, or involving the Stern-Volmer coefficient

$$\langle P \rangle = \frac{\tilde{k}_q}{Z_q} = \frac{k_{SV} k_{tot}}{Z_q} \tag{2.69}$$

With the quenching efficiency the collision rate may now be separated in a part of effective quenching k_q^{quench} and a part of vibrational relaxation k_q^{VR}

$$k_q^{total} = k_q^{quench} + k_q^{VR} = \langle P \rangle Z_q n_q + \left(1 - \langle P \rangle\right) Z_q n_q \tag{2.70}$$

Introducing k_q^{quench} into equation (2.67) for the fluorescence quantum yield leads to

$$\phi_f^q = \frac{k_f}{k_{tot} + k_{SV} n_q k_{tot}} = \frac{k_f}{k_f + k_{NR} + k_q^{quench}} \tag{2.71}$$

This is the quantum yield for the thermalised vibrational level, the population efficiency of the latter assumed to be unity due to the presence of either liquid or high-pressure gas phase. As mentioned earlier, for intermediate gas pressures the average time between consecutive collisional events is much longer and the vibrational excess energy dissipation via a collisional cascade is now slow enough to be in competition with other decay channels like fluorescence, quenching and non-radiative pathways. The population efficiency of a specific single step of the cascade is the product of population efficiencies of all previous steps, the step positions defined by the amount of energy lost via each individual step. Think now of a bath gas consisting of non-quenching and quenching species, e.g. dry air containing nitrogen and oxygen, with collision rates accounting for both. The non-quenching collisional events with nitrogen will lead to vibrational relaxation and population of the next lower step of the cascade with the rate $k_{N_2}^{VR} = Z_{N_2} n_{N_2}$. The collisions with the quenching species do both populate the next lower cascade step via VR with the rate $k_{O_2}^{VR} = (1 - \langle P \rangle) Z_{O_2} n_{O_2}$ and the triplet state via assisted ISC with the rate $k_{O_2}^{quench} = \langle P \rangle Z_{O_2} n_{O_2}$. Thus, a balance for the fluorescence quantum yield of a specific cascade step i will now look like

$$\phi_{f,i}^q = \underbrace{\frac{k_{f,i}}{k_{f,i} + k_{NR,i} + k_{N_2}^{VR} + k_{O_2,i}^{VR} + k_{O_2,i}^{quench}}}_{\text{fluorescence efficiency from i}} \cdot \underbrace{\prod_{j=1}^{i-1} \frac{k_{N_2}^{VR} + k_{O_2,j}^{VR}}{k_{f,j} + k_{NR,j} + k_{N_2}^{VR} + k_{O_2,j}^{VR} + k_{O_2,j}^{quench}}}_{\substack{\text{population efficiency} \\ \text{from upper cascade steps}}} \tag{2.72}$$

The above expression looks very much like the cascading fluorescence yield model formulated for ketones by [Thurber 1999b] and [Koch 2005]. The major difference from Thurber's and Koch's description is here the distinction between intra- and intermolecular events for collisions with the quencher molecule, which leads to the supplementary participation of the rate $k_{O_2}^{VR}$ in the numerator and denominator of equation (2.72). As will be shown later within the discussion of section 5.4.2, for the case of low quenching efficiency the original

model of Thurber and Koch is sufficient to well predict the fluorescence yield of ketones. However, for an initial increase of total pressure of pure oxygen, yield stabilisation has been observed for 3-pentanone fluorescence, which is probably due to a non-negligible rate $k_{O_2}^{VR}$, cf. section 5.3.4. The distinction of the quenching rate in an intra- and intermolecular part is a result of our adaptation of the model in order to predict the fluorescence yield of strongly quenched naphthalene, cf. section 5.3.

2.12.4 Quenching mechanisms

A quenching reaction is commonly referred to as a photophysical interaction of the excited state M* of a molecule with the quencher Q, leading to either the ground state M or another excited state M′. If the quencher is of the same type as the molecule M, this is called concentration or self-quenching. If the quencher is of some other chemical species, one says impurity quenching.

Most intermolecular deactivation processes are subject to collisional quenching. Next to long-distance electron and energy-transfer mechanisms the bimolecular deactivation occurs via the apparition of an intermediate species. This can either be an encounter complex $(M^*..Q)$, an exciplex $(MQ)^*$ or an excimer $(MM)^*$.

Quenching mechanisms involving a simultaneous transfer of the electronic energy of the quenched molecule to the quencher are referred to as electronic energy transfer. The quenched molecule is often called the donor D*, the quencher molecule the acceptor A, and the mechanism is generally expressed as

$$D^* + A \rightarrow D + A^* \tag{2.73}$$

The excitation of A is due to either radiative or non-radiative energy transfer from D*. As to the radiative transfer, a photon is emitted from the donor, which is than captured by the acceptor molecule. This process called the "trivial" transfer will be efficient if there is a sufficient spectral overlap between the emission spectrum of the donor and the absorption spectrum of the acceptor molecule. However, in most cases the non-radiative energy transfer is much more efficient. Two important non-radiative mechanisms are to be considered, the Coulomb or Förster mechanism and the exchange mechanism.

The non-radiative energy transfer of mechanism (2.73) corresponds to isoenergetic transitions $D^* \rightarrow D$ and $A \rightarrow A^*$, coupled by a donor-acceptor interaction. The energy transfer of both transitions are vertical processes following the Franck-Condon principle, and hence the spectral overlap J of donor emission and acceptor absorption is related to the number of resonant transitions between emission and absorption spectrum. The spectral overlap is a distribution quantity like the Franck-Condon factor. The relation to the oscillator strengths

of the coupled transitions is given by the interaction integral $\beta = \left\langle \Psi_f \middle| \hat{H}' \middle| \Psi_i \right\rangle$, the Hamiltonian respecting all electrostatic electron and nucleus interactions between donor and acceptor, Ψ_i and Ψ_f being the antisymmetrised wave functions of the initial and final state, i.e. corresponding to the left and the right side of the mechanism (2.73). The interaction integral is found to be the sum of the Coulomb term β_C and the exchange term β_E, with respect to Ψ_D and Ψ_A using the definitions in equation (2.35) and (2.36) section 2.6.1.

The Coulomb mechanism is referred to the coupling between the donor and acceptor transition, which is dominated by the interaction of the charge distributions. In order to produce a non-vanishing Coulomb integral, the single transitions $D^* \rightarrow D$ and $A \rightarrow A^*$ must follow the spin selection rules. Thus, allowed Coulomb mechanisms are

$$^1\mathrm{D}^* + {}^1\mathrm{A} \rightarrow {}^1\mathrm{D} + {}^1\mathrm{A}^* \tag{2.74}$$

$$^1\mathrm{D}^* + {}^3\mathrm{A} \rightarrow {}^1\mathrm{D} + {}^3\mathrm{A}^* \tag{2.75}$$

whereas the triplet-triplet energy transfer $^3\mathrm{D}^* + {}^1\mathrm{A} \rightarrow {}^1\mathrm{D} + {}^3\mathrm{A}^*$ is a forbidden mechanism. As a long-range process the Coulomb term may be written as a function of the allowed transition moments M_D and M_A and the separation R_{AD} between the molecules (dipole-dipole interactions are dominating), $\beta_C \propto M_D M_A / R_{AD}^3$.

The exchange mechanism is a short-range mechanism, the exchange term decreasing exponentially with the separation R_{AD}. Further, since the exchange term is of pure quantum mechanical nature, the oscillator strengths of the donor and acceptor transitions are not involved. The exchange integral represents the interaction of the overlap densities, and thus vanishes if the wave functions Ψ_{D^*} and Ψ_{A^*} (or Ψ_D and Ψ_A) contain different spin functions. The exchange mechanism occurs via the formation of an encounter complex $(\mathrm{D}^*\ldots\mathrm{A})$ and is subject to the Wigner-Witmer spin selection rules, i.e. the total spin of the reaction must not change. Thus, allowed processes are

$$^1\mathrm{D}^* + {}^1\mathrm{A} \rightarrow {}^1\mathrm{D} + {}^1\mathrm{A}^* \tag{2.76}$$

$$^3\mathrm{D}^* + {}^1\mathrm{A} \rightarrow {}^1\mathrm{D} + {}^3\mathrm{A}^* \tag{2.77}$$

referred to as singlet-singlet and triplet-triplet energy transfer.

The electronic energy transfer follows the Fermi golden rule for non-radiative transitions, see equation (2.48), with the Hamiltonian corresponding to the interaction integral β and the density of states related to the spectral overlap J of donor emission and acceptor absorption. [Förster 1951] and [Dexter 1953] derived expressions for the rate constants for non-radiative energy transfer via the Coulomb mechanism, $k_C \propto f_D f_A / R_{AD}^6 \cdot J$, and via the exchange mechanism, $k_E \propto e^{-2R_{AD}/L} J$.

2.12.5 Fluorescence quenching by triplet oxygen

Collisions of molecules with a quencher may lead to the formation of a short-lived singlet exciplex $^1(MQ)^*$. Quenching mechanisms due to a heavy-atom effect are enhancing the ISC of this singlet exciplex to the triplet state $^3(MQ)^*$.

Oxygen molecules occur naturally with a triplet ground state. In the case of triplet oxygen as the quencher, the diffusion-controlled quenching mechanism occurs via a highly excited triplet exciplex $^3(MO_2)^{**}$, followed by internal conversion to $^3(MO_2)^*$ and decay into $^3M^*$ and $^3O_2$. Because the net reaction presents as a catalysed intersystem crossing, it is spin allowed in contrast to the simple ISC from $^1M^*$ to $^3M^*$. Thus, the fluorescence quenching of a molecule in the first excited singlet state $^1M^*$ with oxygen as a quencher molecule has the net mechanism

$$^1M^* + {}^3O_2 \rightarrow {}^3M^* + {}^3O_2 \tag{2.78}$$

A special case is given for collisions with molecules having a singlet-triplet energy gap ΔE_{ST} exceeding the energy for the excitation of oxygen into the singlet state, the underlying mechanism being

$$^1M^* + {}^3O_2 \rightarrow {}^3M^* + {}^1O_2 \tag{2.79}$$

The excitation energy of $^1O_2^*$ is $0.98\,\text{eV}$ $(22.6\,\text{kcal/mol})$ [Kikuchi 1993] and is exceeded by ΔE_{ST} of most aromatic compounds. The important electronic overlap between (π,π^*)-states, see equation (2.39) section 2.7.3, leads to gap energies higher than $30\,\text{kcal/mol}$. For aliphatic ketones ΔE_{ST} does not exceed $10\,\text{kcal/mol}$, and therefore oxygen quenching is mainly attributed to (catalysed) enhanced intersystem crossing following the mechanism (2.78), the mechanism (2.79) being not accessible [Nau 1996]. Thus, the high singlet-triplet energy gap of aromatic compounds is the main reason to be most efficiently quenched in the presence of oxygen, in contrast to aliphatic ketones exhibiting only negligible quenching behaviour.

Chapter 3 Experimental techniques

The aim of this thesis was to perform fluorescence measurements from the excitation of aromatic species naturally present in kerosene fuel. The operating of the kerosene-fuelled aircraft engine yields high-temperature and pressure conditions. Knowing about the influence of changing temperature, pressure and concentration parameters is crucial to correctly interpret the fluorescence signals. Hence, spectroscopic study was done for various tracers. In order to meet the aircraft engine operating conditions, a flow cell has been developed in which high levels of temperature and pressure could be attained.

3.1 Flow cell

The stainless steel test cell shown in figure 16 allows observation of tracer vapour fluorescence at temperature between 300 and 900 K, pressure from 0.1 to 3.0 MPa after laser excitation in the UV domain. The outer cell dimension is 190 × 145 × 120 mm with 15 mm overall minimal wall thickness and its inner volume is approximately 230 cm^3. Figure 17 describes the entire experimental set-up.

3.1.1 Tracer seeding to the flow cell

For each measurement the needed concentration of tracer vapour that pours into the cell is produced from a "controlled evaporator and mixer" (CEM, Bronkhorst). This apparatus guarantees well-defined molar fractions of the tracer vapour / N_2 buffer gas mixture. Continuous and constant evaporation of the liquid tracer to the buffer gas is achieved in a steadily heated capillary (less than 200 °C).

All gas flows are regulated by mass flow controllers (MFC) from Bronkhorst. The liquid tracer flow is controlled by a liquid flow meter (LFM) and the intake needle valve of the CEM. The value read out and value setting of the flow signals is done by a LabView routine via a data acquisition board from National Instruments (NI). The error influence from the flow regulation on the vapour concentration obtained in the test cell defines flow operating conditions and will be discussed later.

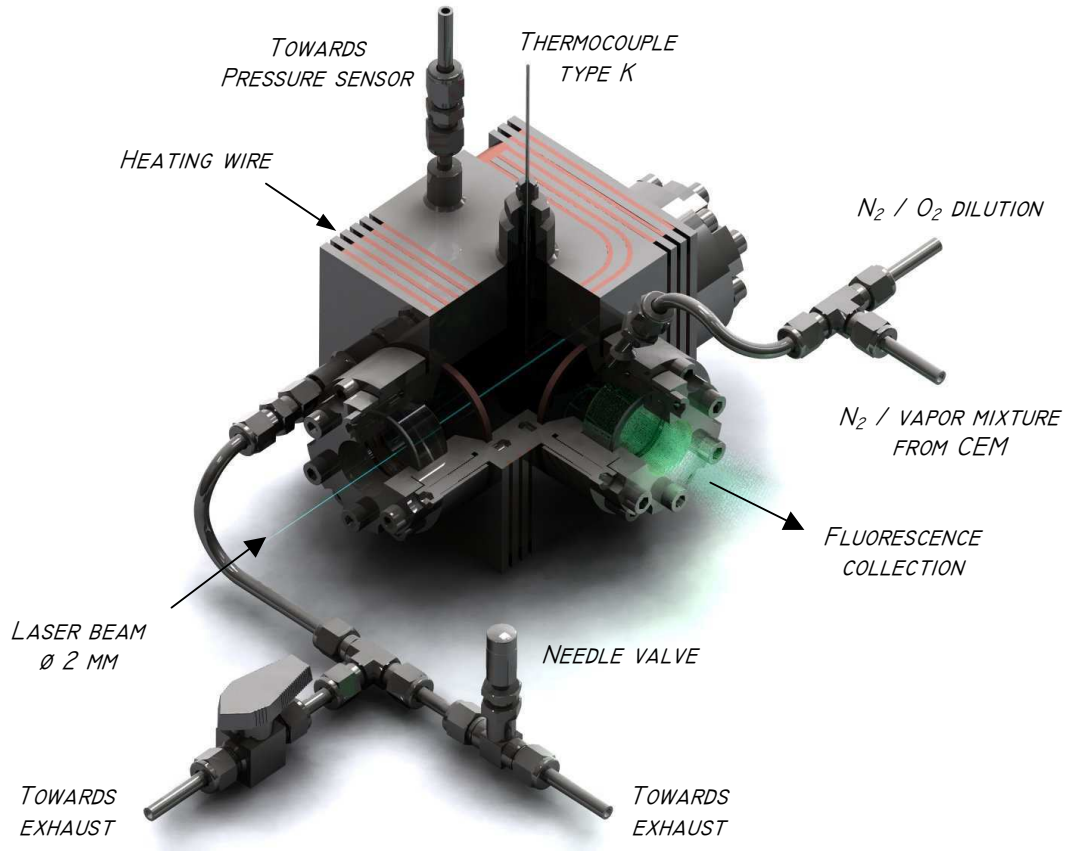

Figure 16: Flow cell for high-temperature and high-pressure spectroscopic fluorescence measurements. The absorbent tracer is evaporated in N_2 buffer gas by the CEM system. Dilution can be obtained from mixture with N_2 / O_2 (industrial air) to produce the needed oxygen concentration before the final vapour / gas mixture pours in the test cell. Flange-mounted UV-transparent silica windows allow optical access for laser excitation and fluorescence detection.

In the test cell, oxygen concentration between 0 and 16.7 % is controlled by dilution with a N_2 / O_2 gas mixture (industrial air) at the exit of the CEM capillary. Dilution is done as short as possible before the inlet to the test cell in order to minimize the length of flow contact between tracer and oxygen and hence to limit effects of tracer oxidation or pyrolysis. An air-like 21 % oxygen concentration can be obtained from dilution with pure oxygen instead of industrial air.

In some cases, the tracer is solid under normal conditions (e.g. naphthalene). For safety reasons tracer dilution was preferred to tracer sublimation by heating of the reservoir. A sample of the civil kerosene jet fuel "Jet A1" fuel used in this work was analysed by the French Institute of Petroleum (IFP), revealing that the (non-absorbing) alkane fraction has an amount of about 80 % by mass of the total fuel. Whenever necessary, the studied tracer was therefore diluted to an alkane solvent like n-undecane, in order to match a similar com-

position as found in the "Jet A1" fuel. However, an absence or a change of the solvent species did not affect the fluorescence results recorded within this study.

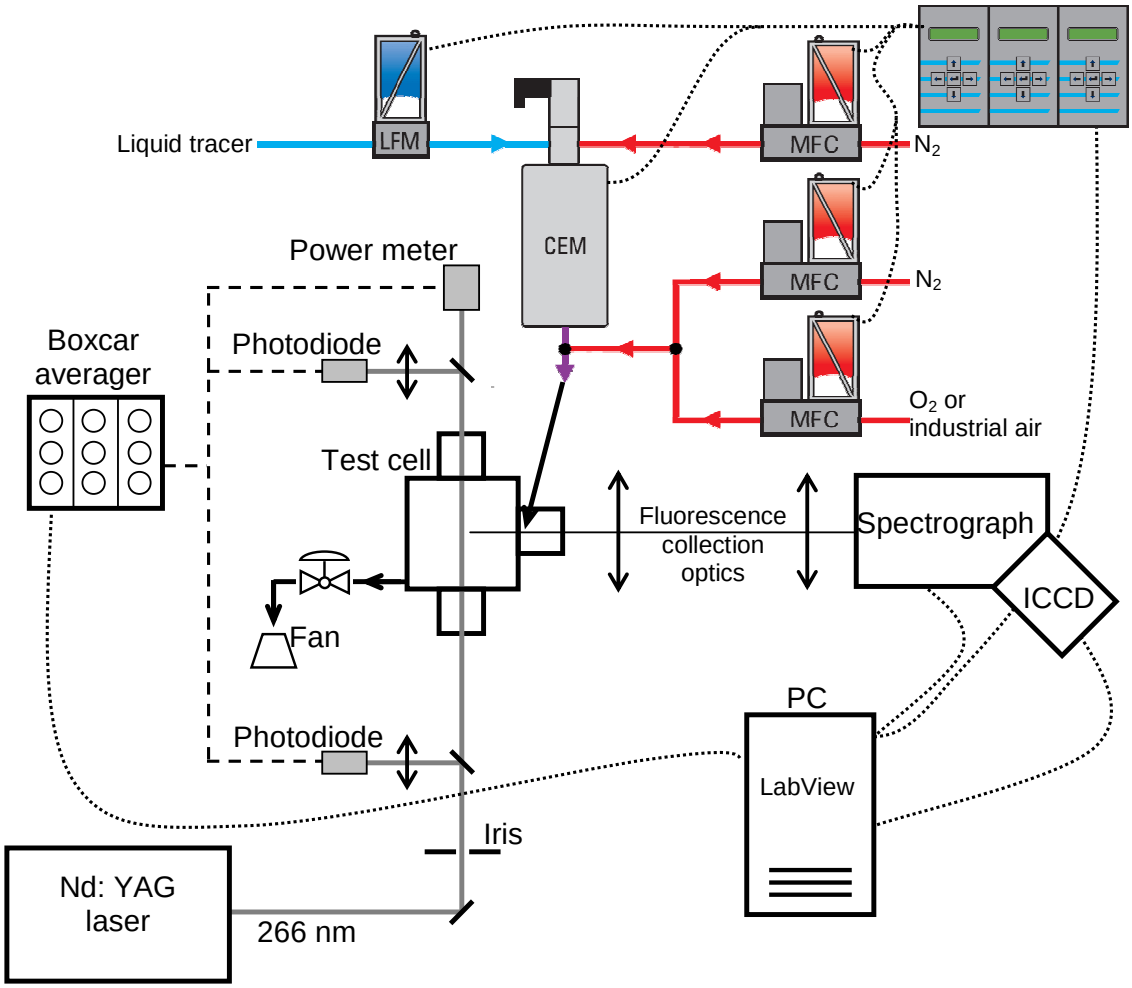

Figure 17: Experimental set-up for high-temperature and high-pressure spectroscopic fluorescence measurements. The laser beam intensity is measured with photodiodes prior to and after the cell passage in order to correct fluorescence spectra from laser energy and Beer-Lambert absorption. Caloric energies of the laser pulses are obtained from a laser power meter behind the test cell. Diode and power meter signals are integrated on a boxcar system and collected by a National Instruments (NI) data acquisition board to a PC running a LabView routine. LabView also controls the position of the spectrograph grating and acquires the spectra from the ICCD.

3.1.2 Temperature and pressure control

The test cell is heated with a 2-m long 2 kW heating wire (Thermocoax SEI type with Inconel alloy sheath) embedded into grooves. A PID temperature control is applied. The temperature of the gas inside the cell is controlled by means of a type K thermocouple placed a

few millimetres above the laser probe volume. Pressure between 0.1 and 3.0 MPa can be obtained inside the cell and measured with a pressure transducer (Tb244, JPB).

Temperature and pressure values are read out via the NI data acquisition board to a LabView routine. Semi-automatic PID pressure regulation can be obtained for the test cell by the feedback of the measured pressure values to the gas flow regulation. This is done for manual control of the needle valve position at the test cell exhaust. Cautious manipulation of the needle allows for pressure-regulated stabilisation to the needed flow values.

3.1.3 Optical access and pressure sealing

Optical access is provided by three UV-transparent silica windows, two of which were used for laser access and one on the spectrograph side to record fluorescence emitted by the tracer vapour. The windows are all flange-mounted to allow for operation under high-pressure and high-temperature conditions. Pressure sealing between window and flange is obtained using Supranite gaskets, between flange and test cell using annealed copper seals.

3.1.4 UV laser excitation, beam energy and absorption control

In each experiment, the tracer / N_2 / O_2 gas mixture is excited by UV pulses from the frequency-quadrupled output of a Nd:YAG laser (YG780, Quantel) at 266 nm. The laser beam used in the probe volume of the test cell is limited by an iris aperture to a size of 2 mm from close to the centre of an originally 9 mm beam and therefore has a top-hat rather than Gaussian intensity profile. The beam energy in the probe volume is always kept below 0.5 mJ per pulse to ensure weak (linear) excitation (cf. figure 18).

The incident beam intensity and the beam attenuation by the absorbent vapour in the test cell are recorded with two photodiodes (DET210, Thorlabs) placed prior to and after the cell passage of the beam. Direct comparison to a calorimetric measurement of the pulse energy can be obtained from a laser power meter placed behind the test cell.

The high temperature span of the experiments carried out in the test cell is somehow complicating the beam intensity detection of the photodiodes. The cell heating causes a thermal dilatation leading to loose in flange bolting tension. Compensation is necessary by retightening the screws of the window-sealing flange, which implies a compression of the Supranite gaskets inducing slight angular and axial window displacements. While these displacements are of no consequence for the fluorescence measurements, it must be paid attention with regard to the photodiodes. However, a simple solution to avoid a displacement impact to the diodes is the beam collimation to the photodiode sensitive surface. To stay in the photodiode dynamic detection range, the beam intensity has to be sufficiently lowered.

An UV-transparent silica window is used under 45° to use the weak intensity front face reflection (approx. 5 %), further attenuated by an UG11 Schott filter.

The beam intensity is measured on a shot-to-shot basis, while the number density of absorbent vapour pouring into the test cell is controlled by the CEM device. The fluctuations of temperature, pressure and flow signals are taken into account for the calculation of molecular cross-sections from the beam absorption.

The Beer-Lambert law describes the phenomenon of light absorption due to its passage through an absorbent medium. Light intensity $I_{L,0}$ diminishes due to the absorption A to the intensity I_L after the path length d_{absorb}. For a frequency ν of incident light, the molecular absorption cross-section σ_ν is derived from number density N_1^0 at pressure P and temperature T for absorbent species partial pressure P_{absorb}

$$\sigma_\nu = \frac{A}{N_1^0 \cdot d} = \frac{\ln\left(I_{L,0} / I_L\right)}{N_1^0 \cdot d} \tag{3.1}$$

$$\chi = \frac{\dot{n}_{absorb}}{\dot{n}_{absorb} + \dot{n}_{gas}} \tag{3.2}$$

$$P_{absorb} = P \cdot \frac{\dot{n}_{absorb}}{\dot{n}_{total}} = P \cdot \frac{\dot{n}_{absorb}}{\dot{n}_{absorb} + \dot{n}_{gas}} = P \cdot \chi \tag{3.3}$$

Flows in $\mathrm{mol/h}$ are calculated from liquid mass and gas volumetric flows as follows

$$\begin{aligned} \dot{n}_{absorb} &= \frac{\dot{m}_{absorb}}{M_{absorb}} && \text{with } \left[\dot{m}_{absorb}\right] = \mathrm{g/h} \\ \dot{n}_{gas} &= 60 \cdot \frac{\rho_{gas} \cdot \dot{v}_{gas}}{M_{gas}} && \text{with } \left[\dot{v}_{gas}\right] = \mathrm{ln/min} \\ & && \text{and } [M] = \mathrm{g/mol} \end{aligned} \tag{3.4}$$

For the ideal gas law, the number density of absorbent species in the test cell is

$$N_1^0 = \frac{T_0}{T} \cdot \frac{P_{absorb}}{P_0} \cdot Lo = \frac{T_0}{T} \cdot \frac{P}{P_0} \cdot Lo \cdot \chi \tag{3.5}$$

with Loschmidt number $Lo = 2.69 \cdot 10^{19}\ \mathrm{molecules/cm^3}$ and T_0 and P_0 the temperature and pressure at standard condition.

Combining (3.1) and (3.5), the molecular absorption cross-section results in

$$\sigma_\nu = \frac{\ln\left(I_{L,0}/I_L\right)}{d} \cdot \frac{T \cdot P_0}{T_0 \cdot P \cdot Lo} \cdot \frac{1}{\chi} \qquad \ldots\left[\mathrm{cm}^2\right] \tag{3.6}$$

Knowing the cross-section of the absorbent on a real time scale allows for the instantaneous correction of the beam attenuation in the test cell. The beam energy in the probe volume is then

$$\begin{aligned} I_L &= I_{L,0} \cdot \mathrm{e}^{-A} = I_{L,0} \cdot \exp\left(-\sigma_v\, n\, d\right) \\ E_L &= \left\{E / I\right\}_{calibration} \cdot I_L \end{aligned} \tag{3.7}$$

where d is the beam path length on the inner side of test cell up to the probe volume centre and the beam energy is derived by the photodiode intensity from calibration of the photodiodes to the laser power meter as $\left\{E / I\right\}_{calibration}$.

3.1.5 Fluorescence linearity with excitation energy

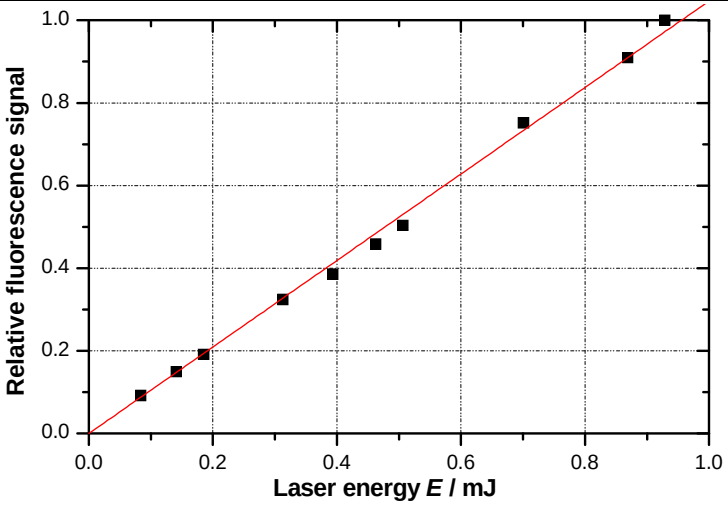

Figure 18: Naphthalene fluorescence after 266 nm laser excitation; integrated signal as a function of incident laser energy. Normalised to maximum. Pure nitrogen atmosphere at 350 K and ambient pressure. The beam size was approx. 2 mm.

Concentration and temperature values are simple to evaluate from laser-induced fluorescence signals if the laser beam intensity is restricted to the condition of linear excitation. In other words, the fluorescence intensity has to show as a linear function of the beam energy. This is the case for weak excitation limited to a small fraction of the population in the absorbing ground state. To ensure this condition, fluorescence spectra were measured for a constant seeding of naphthalene vapour while increasing the beam energy. The result is shown in figure 18, revealing the expected linearity up to two-times the maximum beam energy of 0.5 mJ/pulse realised within all spectroscopic measurements.

The linearity test shown here for the naphthalene case was repeated in a similar way for all other probed tracers. Within the probed energy range from 0.1 to 1 mJ/pulse linear fluorescence response was found for all of them.

3.1.6 Fluorescence detection

The fluorescence collection optical set-up is illustrated in figure 19. The fluorescence light from part of the illuminated tracer vapour in the probe volume is collected at right angle to the laser beam via a telescope-like combination of two UV achromatic doublets ($f_1 = 160\,\mathrm{mm}$ and $f_2 = 100\,\mathrm{mm}$) by a spectrograph (Jobin Yvon, SPEX 270M). The light dispersed by the grating is recorded with a 16-bit intensified CCD camera (Princeton Instruments, model HSICCD-576G/BT) with an intensifier gate width of 500 ns. The CCD array is 576 by 384 pixels (Thomson, THM 576×384, 0.0225 μm per pixel) and the framing rate of the system is fixed to the 10 Hz repetition rate of the laser. The spectrograph and the ICCD camera are connected to a personal computer, which is used for device control and acquisition of the spectra.

Fluorescence spectra are measured over a wavelength range from 240 to 540 nm. Thereby the focal lengths of the lenses and hence of the telescope are underlying a chromatic shift Δf, illustrated in figure 20.

However, the focal shift influences only slightly the magnification of the telescope. The probe volume is magnified on the telescope focal plane by 0.788 ± 0.005 between 240 and 540 nm (calculated with ZEMAX software).

The light entering the spectrograph has to be limited to avoid possible overfill of the spectrograph maximum aperture $f/4$, which could otherwise lead to photon loss and stray light. Therefore, a circular aperture of diameter D_{stop} is used between the two lenses to reduce illumination of the second doublet to $f_2/D_2 > 4$.

The rectangular spectrograph entrance slit is parallel to the laser beam and of variable width and fixed height. The width is stepper motor controlled by 12.5 μm steps in perpendicular direction to the laser beam (spectral dimension). In the laser beam direction (spatial dimension), the slit height is 15 mm. The distance between the telescope and the entrance slit is optimised in order to find the sharpest shape of the ICCD image in the detector focal plane of the spectrograph. In the present case, the telescope magnification results in a probe volume image of 1.6 mm in the telescope focal plane exhibiting a quite flat intensity profile, since the exciting laser beam is cut-off close to the centre of an originally larger beam by an iris diaphragm.

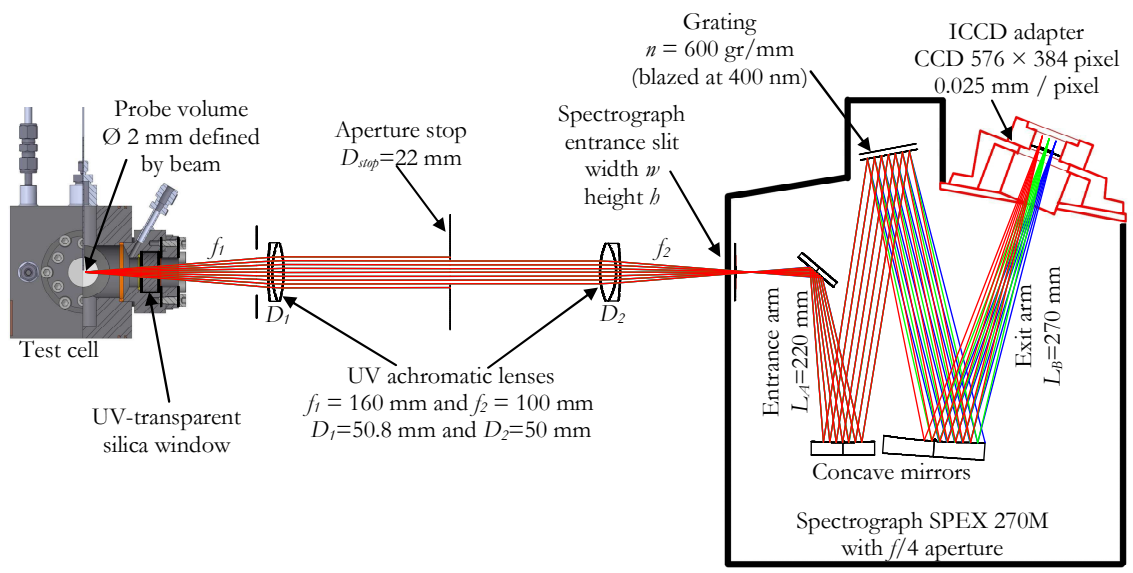

Figure 19: Fluorescence collecting optics. The fluorescence light of the excited vapour is collected by a telescope system of two achromatic lenses. The spectrograph entrance slit is parallel to the laser beam. The Czerny-Turner SPEX 270M spectrograph has an aperture of f/4.

The spectrograph entrance slit has to be varied for changing operating conditions, e.g. when the fluorescence signal becomes very weak or too strong for camera detection. This might be the case when changing from one type of tracer species to another or for measurements in atmospheres partially containing oxygen. However, all individual measurements series are referred to the variation of only one physical parameter (temperature, pressure or oxygen concentration) and the slit width is always kept constant. To be able to compare between individual series with different slit widths, particular effort is done to consider the slit influence on the fluorescence signal strength by means of a calibration measurement (see fig. 21). The slit width maximally varies between 100 and 1000 μm. The influence of the slit width on spectral resolution will be discussed later in this paragraph.

Within the experiments undertaken for the present work, the fluorescence light from the probe volume is always cut-off perpendicularly to the laser beam by the entrance slit. Working in this way guarantees the slit width being the governing parameter for the spectrograph wavelength resolution. In contrast to spectrometer set-ups, the multichannel detection method has no exit slit, and hence the light is directly diffracted from the grating to the detector focal plane. For a not entirely light-filled entrance slit, the spectral resolution would be dependent on the unbounded size of the fluorescence light entering the spectrograph slit.

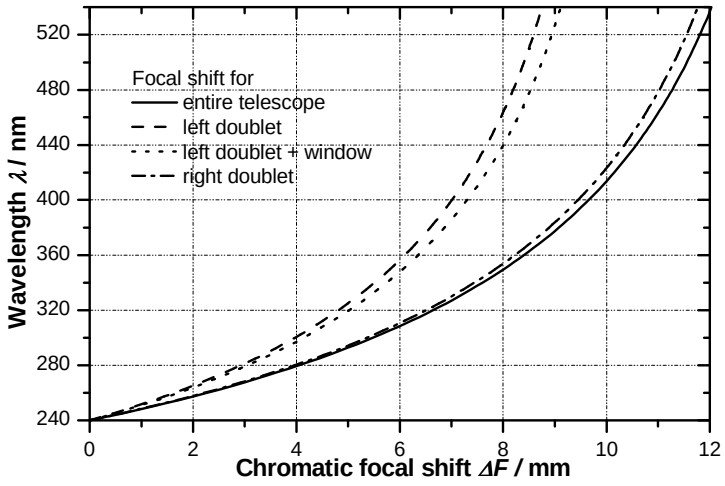

Figure 20: Chromatic focal shift of the fluorescence collection telescope.

The SPEX 270M is built as a Czerny-Turner configuration providing two concave mirrors of 220 mm (entrance) and 270 mm (exit) focal length. The angle geometry of a flat reflection grating as used in the spectrograph is shown in figure 22. The deviation angle D_V is an instrument constant, while the incident angle α and the diffraction angle β change with the grating tilt. The entrance and exit arm lengths L_A and L_B are given by the foci of the concave mirrors. Their quotient $L_B/L_A = 270/220 = 1.23$ stands for the mirror magnification of the spectrograph.

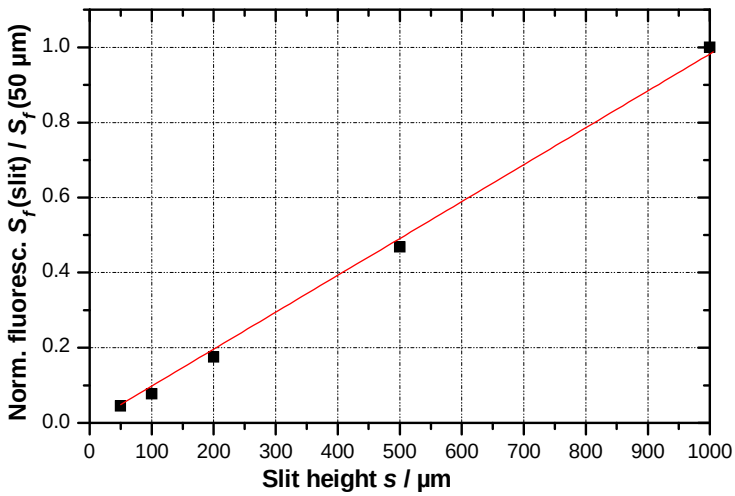

Figure 21: Influence of spectrograph slit aperture on fluorescence signal intensity. Illustrated for naphthalene flow at constant number density, 450 K in ambient pressure nitrogen atmosphere.

The spectrograph was provided with a 600 grooves/mm ruled grating blazed at 400 nm (Jobin Yvon, grating model 510 12 330) of 50 mm × 50 mm blank size. The dependence of the incident and diffracted light waves is basically described by the grating equation

$$\sin(\alpha) + \sin(\beta) = 10^{-6} \cdot kn\lambda \tag{3.8}$$

where k is the diffraction order, n the groove density in grooves per mm and λ the wavelength in nm. By derivation of λ with respect to the diffraction angle β, the angular dispersion $d\beta/d\lambda$ is obtained. The angular dispersion is linked to the linear dispersion $d\lambda/dx$ by the exit arm length L_B.

$$\frac{d\beta}{d\lambda} = 10^{-6} \cdot \frac{k \cdot n}{\cos(\beta)} \qquad \text{and with } L_B \cdot d\beta = dx \tag{3.9}$$

$$\frac{d\lambda}{dx} = 10^{6} \cdot \frac{\cos(\beta)}{k \cdot n \cdot L_B} \tag{3.10}$$

The graph in figure 22 shows the dependence of the linear dispersion from the centre wavelength on the detector focal plane for first order diffraction of the applied grating. In contrast to spectrometer applications, for spectrograph use, the term bandpass does not refer to the exit slit but to the entire wavelength range in the long strip output to the detector. Calculating for an wavelength of 500 nm, the angular dispersion of the grating is of 0.034°/nm, while the linear dispersion is 6.17 nm/mm. The detector size in the sense of diffraction is 576 pixels. With a pixel size of 22.5 µm /pixel this results in a spectral bandpass of 576 pixels × 22.5 µm × 6.17 nm/mm ≈ 80 nm on the ICCD (slightly changing from 79.43 to 79.97 nm with $\cos(\beta)$ between 240 and 540 nm).

As mentioned above, the mirror magnification is determined by the quotient of the entrance and exit arm lengths. This is only the diffractionless part of magnification. Except for the case where the incident angle α equals the diffraction angle β, the anamorphic magnification due to the grating tilt has to be taken into account. The derivation of the above grating equation (3.8) to α and β leads to the expression

$$\cos(\alpha)\, d\alpha + \cos(\beta)\, d\beta = 0 \tag{3.11}$$

This implies the magnification in the dispersion direction of the grating

$$r = -d\beta/d\alpha = \cos(\alpha)/\cos(\beta) \tag{3.12}$$

Therefore, the entrance slit width w is projected on the focal plane to the anamorphic slit width

$$w' = w \cdot \frac{L_B}{L_A} \cdot \frac{\cos(\alpha)}{\cos(\beta)} \tag{3.13}$$

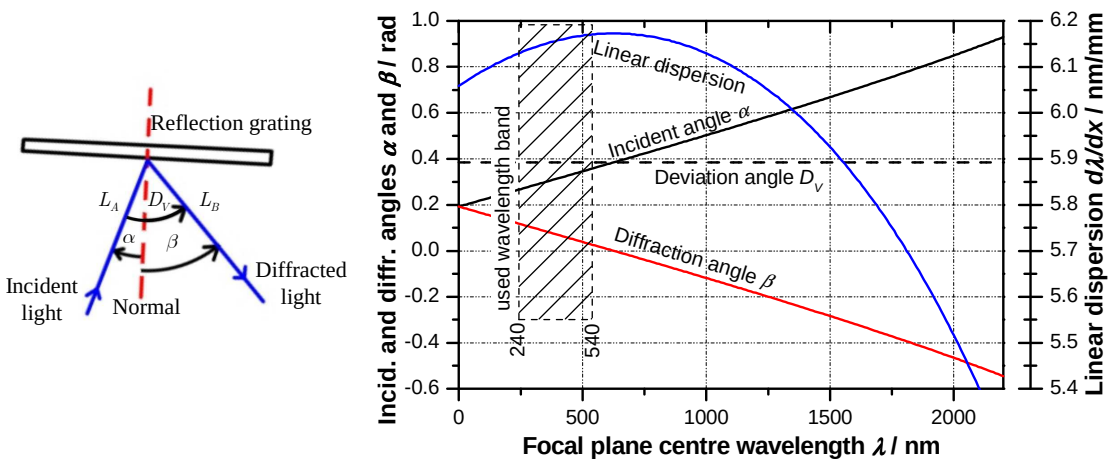

Figure 22: Angle geometry of light diffraction on a reflection grating. Incident and diffraction angles α and β are measured relative to the normal of the grating (same sense of rotation). The linear dispersion is a function of cos(β) changing with the focal plane centre wavelength.

The wavelength resolution $d\lambda$ of a spectrometer device is given as the product of the linear dispersion and either the exit slit width or the projection size of the entrance slit (which corresponds to the anamorphic magnification), depending on which is larger

$$d\lambda = 10^6 \cdot w \cdot \frac{\cos(\alpha)}{k \cdot n \cdot L_B} \cdot \frac{L_B}{L_A} \tag{3.14}$$

This equation is suitable for spectrometer use, where the wavelength part falling on the detector is determined by the exit slit. For spectrograph applications, the exit slit width has to be replaced by the width of a single detector pixel, i.e. the maximal resolution is the bandpass over a single pixel. The practical resolution is indicated as the bandpass over at least three adjacent pixels, since two adjacent peaks must have an intermediate pixel in-between with lower value in order to be distinguished (cf. figure 23).

To give an impression of the actual spectral resolution for the test cell experiments carried out within this work, a ray tracing image simulation was done by ZEMAX software for the detector focal plane of the spectrograph. The calculation was based on a synthetic long cylindrical Gaussian light source of 2 mm diameter representing the laser beam in the probe volume. This cylinder source was assured to exceed the aperture of the collection optics in the direction of the laser beam.

Simulation results are presented in figure 24 for the lower and upper wavelengths used in the experiments, 240 and 540 nm. The simulated image equals the ICCD detector in size corresponding to 80 nm spectral bandpass in horizontal direction (perpendicular to the laser beam) and 8.64 mm spatial extension in vertical direction (parallel to the laser beam). The

projection of the entrance slit on to the detector plane is shown for several entrance slit widths w from 100 to 2000 µm.

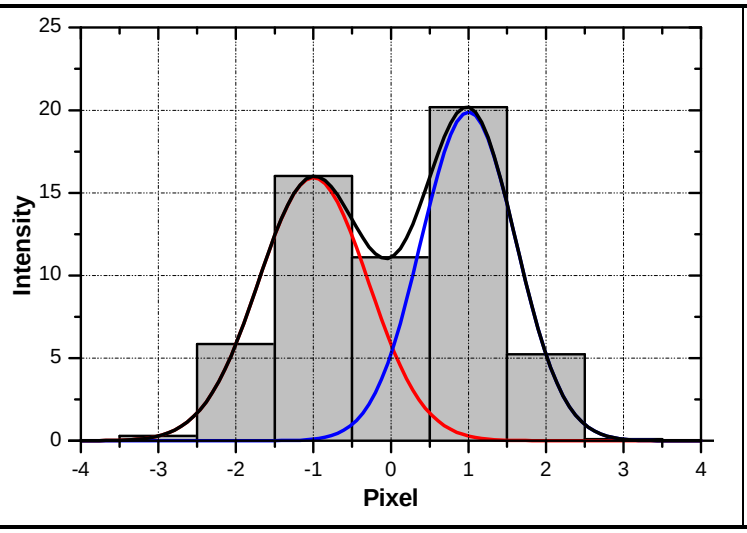

Figure 23: The resolution of two adjacent peak signals is possible if at least one pixel with lower value is located between them.

The magnification of the slit height h on the detector focal plane underlies only the mirror magnification, since its orientation is parallel to the grooves. The spatial extension of the slit projection is evidently greater than the vertical detector size. Actually, the vertical detector size corresponds to 8.9 mm probe volume extension in the beam direction, hence smaller than the limiting aperture diaphragm diameter placed in between the achromatic doublets. The signal intensity shows as a homogeneous distribution all-over the spatial extension of the detector (laser beam attenuation is neglected for this simulation). However, this allows for vertical binning of the detector signal over its entire height, which is done most timesaving in the hardware mode for acquisition rates beyond 100 Hz, by far fast enough for an acquisition timing triggered to the 10 Hz frequency of the laser.

In the spectral image direction, the spread from the entrance slit width w to w' in the detector plane is described by equation (3.13) as the combined mirror and anamorphic magnification. It is clearly seen how spectral resolution is affected while increasing the entrance slit. Up to entrance slits of 1000 µm, w' is growing linearly with w following equation (3.13), whereas for 2000 µm, w' begins to level off. This is the result of slit width w exceeding the size of the probe volume projection on to the entrance slit (1.6 mm). Further opening of the slit ends the cut-off of the light cone entering the spectrograph. The total amount of collected fluorescence signal is proven to be linear with the entrance slit width w between 50 and 1000 µm (cf. figure 21).

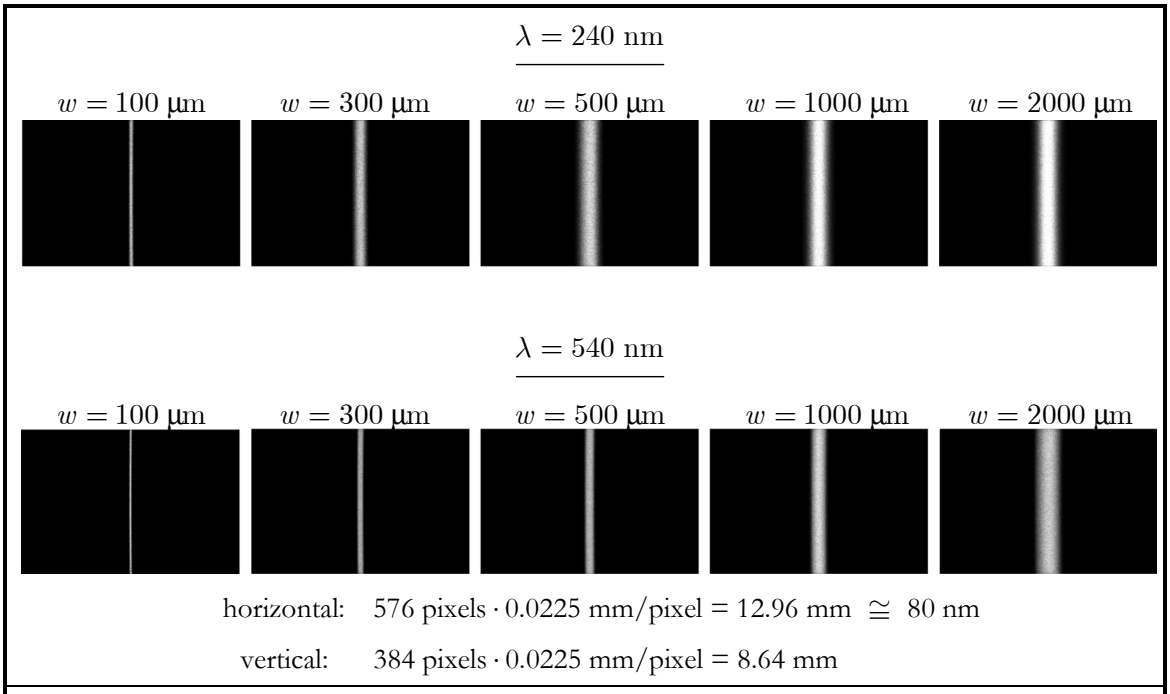

Figure 24: Spread of slit image *w'* on the detector focal plane as function of slit width *w*. The slit height *h* is magnified only by the mirror magnification, since it is parallel to the grating grooves. Slit height is 15 mm and slit width varies from 100 µm to 2000 µm. Focal plane image analysis was done with ZEMAX software for the whole collecting optics, which implies the telescope in front of the spectrograph. The two columns correspond to different central wavelengths on the detector focal plane, thus to different incident and diffraction angles.

There are obviously only small differences between the 240 nm and the 540 nm simulations. This becomes clear when looking at the linear dispersion of the grating in this spectral band (cf. figure 22): the grating is used only in a very small spectral zone where dispersion is almost constant (between 6.13 to 6.17 nm/mm from 240 to 540).

The linearity of the total amount of fluorescence signal with the entrance slit width up to 1000 µm allows for adapting the actual measured fluorescence signal level to improve the use of the camera detection dynamic range. However, increasing the entrance slit width means also sacrificing spectral resolution. Therefore, increasing the gain factor of the image intensifier seems to be the primary technique to enhance signal levels. The use of intensifier gain levels up to 9 was always preferred to increasing the entrance slit width of the spectrograph. Figure 25 shows the intensifier gain calibration curve allowing correction for the gain factor.

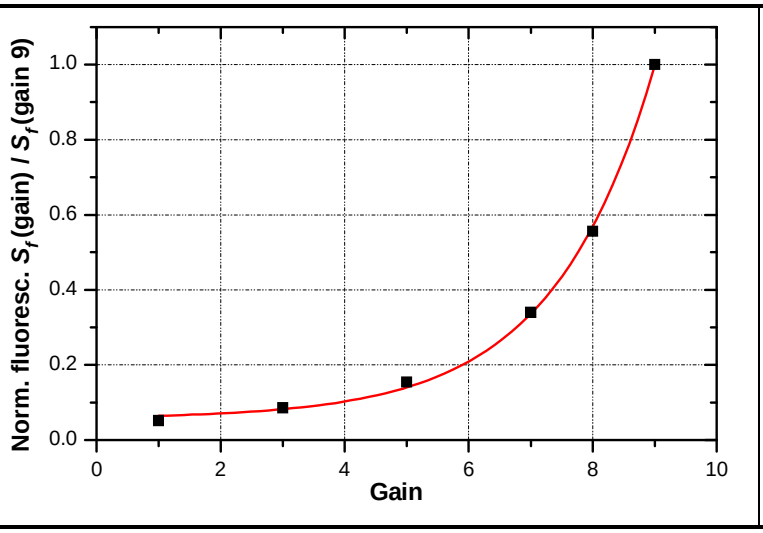

Figure 25: Influence of the gain of the camera on the fluorescence signal intensity. Illustrated for naphthalene flow at constant number density, 450 K in ambient pressure nitrogen atmosphere.

3.2 Correction and reconstruction of fluorescence spectra

The detection of fluorescence spectra with the presented set-up composed of telescope, Czerny-Turner spectrograph and ICCD detector needs for subsequent correction and data processing. The ICCD detector has to be corrected for its inhomogeneous intensity distribution as response on a homogeneous illumination. Furthermore, the spectral response of the entire optical set-up has to be determined by means of calibration to well-known lamp sources. Finally, the algorithm used for combining individual overlapping spectra in order to obtain a single large spectrum is described.

3.2.1 Intensity response function

A frequent method for ICCD detector signal intensity calibration is to generate a very homogeneous and uniform illumination using a Lambert diffuser and a discharge lamp (e.g. a Xe lamp). This approach is often difficult, particularly with regard to the need of an (achromatic) objective in front of the camera, since for this method the spectrograph has to be put aside. As a result, the absence of the concave spectrograph mirrors also necessitates the removal of the telescope.

To avoid complex and laborious changes of the spectroscopic optical set-up, a simple incandescence lamp is used as a stable continuous spectrum light source placed in the probe volume of the test cell. LabView control of the set-up allowed for regular signal shifts of 1 nm by changing the grating tilt of the spectrograph. The left graph in figure 26 shows the result. The presented signal pattern consists of 41 spectra shifted by 1 nm to each other. The

individual spectrum consists of 576 pixels and has a spectral bandpass of 80 nm (vertical on-chip binning of 384 lines yields average over 8.9 mm in probe volume).

The determination of the "best" intensity correction function is possible by computing a simple optimisation algorithm (non-linear least-squares), hence the shape of the uncorrected lamp signal pattern in the left graph of figure 26 can be transformed to the corrected regular pattern in the right graph. The algorithm converges to the correction function shown in the bottom graph of figure 26.

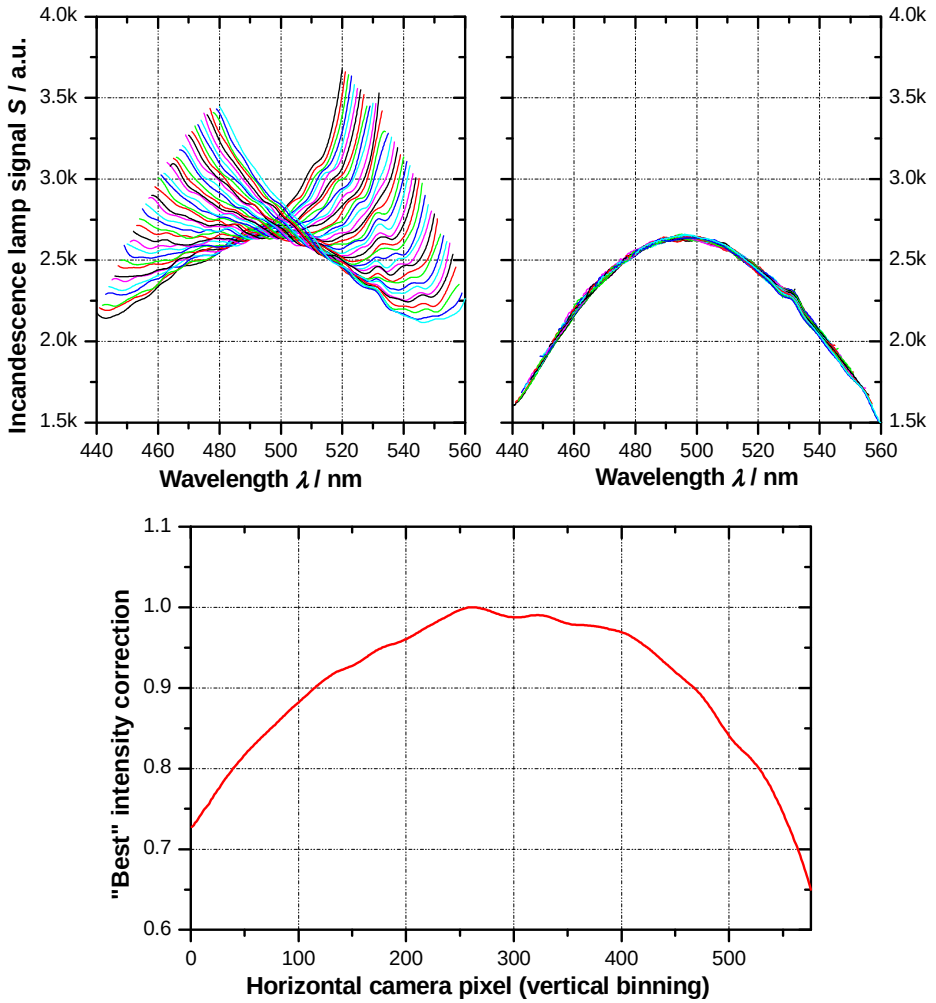

Figure 26: Graphs on the top: Incandescence lamp signal without (left side) and with camera intensity correction (right side). The signal pattern consists of 41 spectra of 80 nm width shifted by 1 nm to each other. Bottom graph: "Best" intensity response correction function transforming uncorrected spread signal pattern to regularly signal pattern. Evaluated by simple optimisation algorithm (non-linear least-squares method).

3.2.2 Spectral response function

The devices of optical set-ups have specific spectral response patterns, often referred to as their "apparatus function". For the interpretation of spectrally resolved measurements, it is important to know these responses, if not for each single component, at least for the assembly of the entire optical path from the source to the detector. For this purpose, the system response is compared to predefined spectra of well-known light sources.

Two main questions may be posed with regard to experimental spectra. Firstly, does the signal pattern appear at the right spectral position, and if not, is the signal simply shifted or even stretched? Secondly, does the spectral intensity distribution of the measured signal correspond to the "real" distribution of the source?

To answer to the first question, the atomic line spectra of mercury and cadmium calibration lamps are used to correct for the spectral position of the spectra obtained with the presented optical set-up. The spectral bandpass of the detector is thereby approved to be of 80 ± 1 nm.

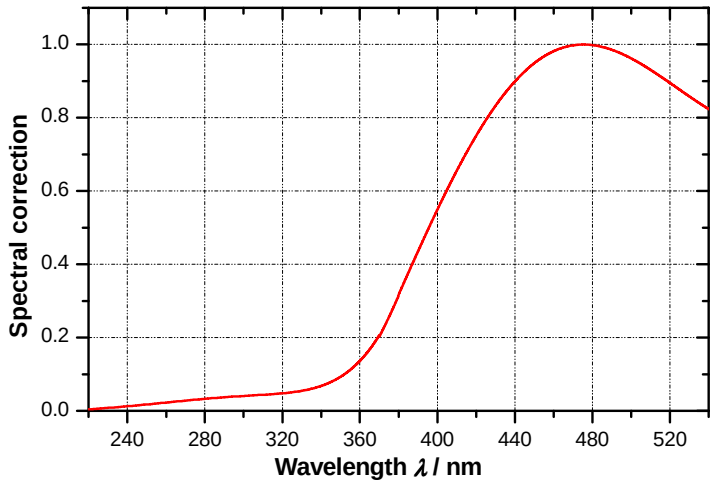

Figure 27: Spectral response function. A deuterium lamp (200 to 400 nm) and a tungsten lamp (400 to 540 nm) were used as calibration light sources.

The spectral intensity response of the optical set-up is found by the use of two calibration lamps producing broadband spectra. From a deuterium lamp, the correction for the near ultraviolet domain could be obtained (220 – 400 nm). For the visible domain (400 – 540 nm), a tungsten filament incandescence source was used, generating a light spectrum depending on its operating temperature. The figure 27 presents the apparatus function of the optical set-up resulting from the calibration procedure.

3.2.3 Gluing algorithm for overlapping spectra

As discussed earlier, individual fluorescence images are projected to the ICCD detector with a spectral bandpass of 80 nm and 8.9 mm spatial extension. Averaging is done over the spatial pattern of the image by vertical hardware binning. The resulting single line spectrum is multiplied by the intensity and the spectral response functions.

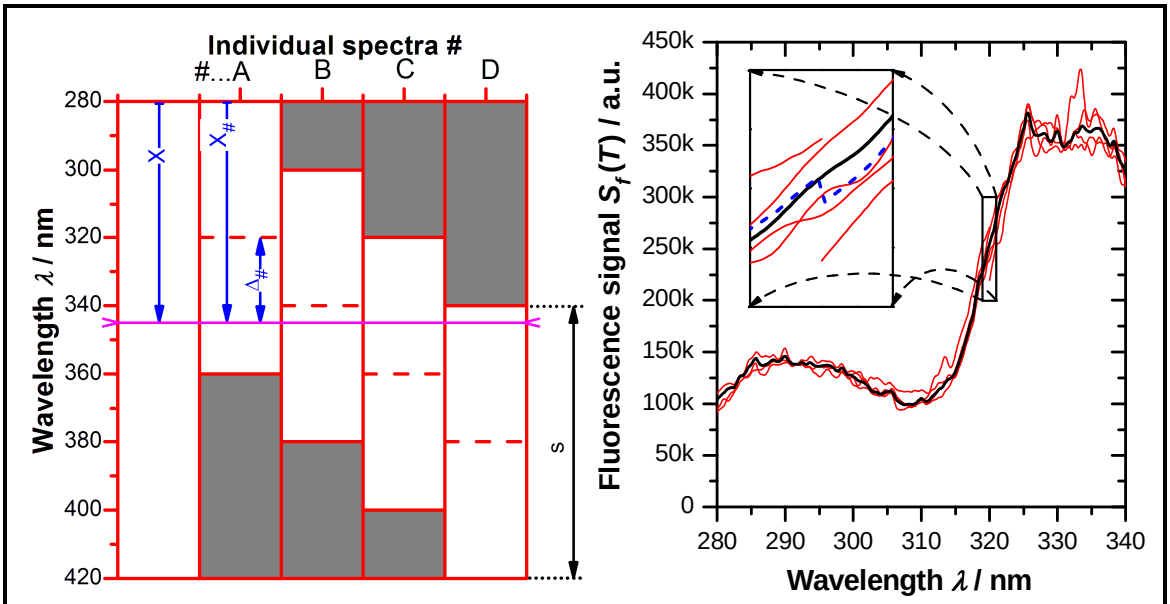

Figure 28: Left side: Illustration of gluing algorithm. Several overlapping spectra are "glued" together with respect to a weight function accentuating the spectra pixel when moving towards the detector centre. Right side: Cutout from the fluorescence spectrum of kerosene; red lines are individual spectra each of 80 nm size, black line is the spectrum glued by the described algorithm. The further detailed sketch shows the difference of the weighted algorithm to a simple unweighted average, shown as the dashed blue line here.

To enhance the readability of diagrams and the comfort of data processing, it is chosen to join overlapping individual spectra after the corrections mentioned above have been effectuated. Gluing has thereby to be done with care, since it is important to keep the representative structures of the individual spectra while reducing the statistical noise to an average. This is achieved by the implementation of a weight function to each spectrum accentuating pixels closer to the detector centre. On the left side of figure 28, an illustration is shown for this method, assuming the position of the actually gluing pixel to be at $X = 345\,\mathrm{nm}$, marked as the flashed horizontal line. With a weight function as described by

$$weight_{\#} = 1 - \frac{\Delta_{\#}}{s/2} \quad \text{for } \# \rightarrow A, B, C, D \ldots \tag{3.15}$$

the weight coefficients of the individual example spectra A to D calculate as follows

$$weight_A = 1 - {}^{25}\!/_{40} = 0.375 \qquad weight_B = 1 - {}^{5}\!/_{40} = 0.875$$
$$weight_C = 1 - {}^{15}\!/_{40} = 0.625 \qquad weight_D = 1 - {}^{35}\!/_{40} = 0.125$$

The resulting intensity $Y(X)$ is normalised to the sum of weight coefficients

$$Y(X) = \frac{\sum_{\#} Y_{\#}\left(X_{\#}\right) \times weight_{\#}}{\sum_{\#} weight_{\#}} \tag{3.16}$$

In the right graph of figure 28, the result for the application of this gluing method is shown for a cutout of the kerosene fluorescence signal. Red lines are representing the individual spectra measured with an overlap of 60 nm. The black line shows the glued spectrum obtained from application of (3.15) and (3.16).

The weighted algorithm enhances the gluing quality especially at zones, where individual spectra start or end. The detail sketch in the right graph shows the difference between the weighted algorithm and a simple unweighted average, depicted as the dashed blue line.

3.3 Detection error

Nowadays high quality in optical sensing is reached by use of photomultiplier tubes (PMT), charged-coupled devices (CCD), photodiodes and other opto-electronic devices. For optical measurements, the error is never negligible. By its physical nature, the measured object might be itself already the source of intrinsic noise such as for quantum mechanical events like photon observation. Furthermore, all devices are participating in the measurement noise due to their imperfections depending on the operating conditions.

The discussion will concentrate on the assumption of photon arrival on the detector surface at a constant generation rate. The photon detection includes the intrinsic "shot noise", which is often assumed to be the dominating noise source, especially if signal-to-noise ratio (SNR) is high due to spatial or temporal signal averaging. When SNR becomes small, further imperfections of the detector device emerge. In the case of a CCD, the most important are thermal noise, read-out noise and A/D converter noise.

For our application, only the shot noise and the thermal noise are considered. This seems to be justifiable, since spatial and temporal averaging allows for SNR enhancement, and therefore, mostly the signal dependent shot noise is of importance.

The subsequent noise discussion is referring to different textbooks, e.g. [Tkachenko 2006], [Eckbreth 1996], Pawley in [Stevens 1994].

3.3.1 Shot noise limited optical measurements

In any case, even the best detector is affected by shot noise (also known as quantum or "Poisson" noise), the intrinsic noise of the light caused by its quantum mechanical nature.

The probability of N_{Ph} photons coming from a source with generation rate k to be observed in an observation time interval Δt follows a Poisson distribution

$$P_{N_{Ph}}(k,\Delta t) = \frac{(k\Delta t)^{N_{ph}} \cdot e^{-k\Delta t}}{(N_{Ph})!} \tag{3.17}$$

The Poisson distribution is unlike the Gaussian distribution an asymmetric probability function. Due to the nature of the photon generation, the mean number of observations is found as the product of rate and observation time (cf. figure 29)

$$\langle N_{Ph} \rangle = k\Delta t \tag{3.18}$$

For a very large number of observations (i.e. either high count rate or long observation time), the Poisson distribution converges to the symmetric Gaussian form.

A very important property of Poisson distributions is called the square root law, i.e. the average of the square deviation is equal to the average value

$$\sqrt{\langle \Delta N_{Ph}{}^2 \rangle} = \sqrt{\langle N_{Ph} \rangle} \tag{3.19}$$

In practice, this is used to determine the standard deviation of detection for an observation of an average number of photons N_{Ph}

$$\sigma = \sqrt{N_{Ph}} \tag{3.20}$$

The square root law describes the minimal intrinsic noise representing the "best" case for "shot noise limited" optical measurements. This detected noisy signal S_{noise} is

$$S_{noise} = S \pm \sigma = \eta \cdot N_{Ph} \pm \sqrt{\eta \cdot N_{Ph}} \tag{3.21}$$

written as the number of photon electrons with η being the quantum efficiency of the conversion.

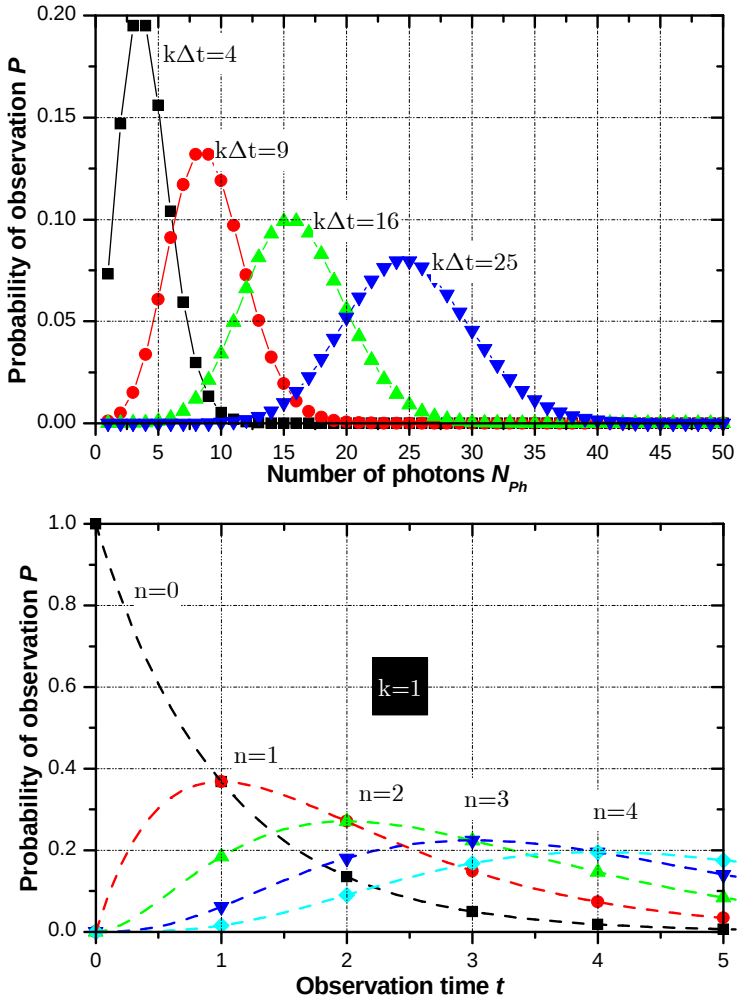

Figure 29: Upper plot: Poisson distribution for different generation rates $k\Delta t$ as function of the number of photons N_{Ph}. As $k\Delta t$ increases, the distribution becomes more and more symmetric and Gauss-like. Bottom plot: Poisson distribution for different $n = k\Delta t, k = 1$ as function of observation time t.

The detection noise is often specified by the signal-to-noise ratio (SNR), which is defined as the reciprocal of the relative detection error

$$SNR = S/\sigma \tag{3.22}$$

and hence, for shot noise limited measurements,

$$SNR = N_{Ph}/\sqrt{N_{Ph}} = \sqrt{N_{Ph}} \tag{3.23}$$

3.3.2 Averaging

Single shot measurements for the observation of processes, which generate only small numbers of photons, are often critical due to low SNR levels. To raise the SNR level of our spectroscopic study, spatial averaging by on-chip hardware binning in vertical direction is done as well as time averaging by accumulation of up to 400 laser shots within the same camera frame.

Repeating M-times the same measurement under identical conditions, each single measurement follows a distribution $p_i(X_i)$. The mean values $\langle X_i \rangle$ have their own distribution, leading to the average mean value of the M-times series

$$P(\langle X \rangle_M) = \prod_{i=1}^{M} p_i(X_i) \tag{3.24}$$

p_i is likely to be a Gaussian distribution. Hence, one may write for the series of $\langle X \rangle_M$

$$P(\langle X \rangle_M) \sim \exp\left[\frac{-(X - X_0)^2}{2\sigma^2}\right]^M = \exp\left(\frac{-(X - X_0)^2}{2\sigma_M^2}\right) \tag{3.25}$$

The standard deviation of a series of M measurement is related to the individual measurement by $\sigma_M = \sigma / \sqrt{M}$. This is again the square root law.

Accumulation of 400 shots on the same camera frame enhances the SNR of the measurement by a factor 20. Equation (3.25) is valid also for spatial signal averaging. Binning over the vertical CCD extension of 384 lines further enhances the SNR by a factor $\sqrt{384} \approx 19.6$.

3.3.3 Thermal noise (dark current)

Thermal noise is originated by thermal charge fluctuations. Since electrical charges follow also a quantum mechanical description, thermal noise can be thought as quantum noise in the low frequency band. Applied to electrical circuits it is known as Johnson noise, where the fluctuating charges in a range Δf induce voltage and current noise, presenting a resistance independent noise power

$$\left.\begin{aligned} \langle U^2 \rangle &= 4kT \cdot R \cdot \Delta f \\ \langle I^2 \rangle &= \frac{4kT}{R} \cdot \Delta f \end{aligned}\right\} \Rightarrow P = \sqrt{\langle U^2 \rangle \langle I^2 \rangle} = 4kT\Delta f \tag{3.26}$$

The thermal noise shows as dark current for CCD arrays. Even with the camera closed, electrons are freed and stored to the pixel well. Since thermal noise is dependent on tempera-

ture, cooling of the camera chip is a convenient solution to reduce the dark current. This can be done by water cooling or flushing with liquid nitrogen.

With CCD cooling, in the configuration of this work, a typical dark current signal D has a standard deviation of only a few counts over the CCD array with a mean value offset of typically about 100 counts, depending on the cooling temperature. Sampling of D and subtraction from the measurement signal S' is done. Subtraction assumes dark current and measured signal to be statistically correlated. This is not the case, since the sampling periods are not the same. Thus, enhancement of the dark current error takes place when subtracting the uncorrelated dark current D. The "true" signal depends on a dark current participation of $2N_{dc}$ [Eckbreth 1996]

$$S = S' - D = \eta N \pm \sqrt{\eta N + 2N_{dc}} \tag{3.27}$$

Generally, with recent CCD arrays, even for low SNR levels, cooling reduces the dark current sufficiently to allow measurement with high quality.

3.4 Reliability of physical parameter control

The previous section concentrated on the detection error for a given number of photons arriving at the detector surface. However, the error sources lie not only in the detection part of the experiment, but are also found upstream in the control of the physical parameters leading to the generation of fluorescence photons. Before the fluorescence will be reviewed more precisely in order to define the uncertainty of the number of generated fluorescence photons in section 3.5, all parameters having influence on the number density of tracer will be discussed. Evidently, the control of the laser irradiance in the probe volume has to be rated, but as well the temperature and pressure reliability for constant setpoints, and likewise, the fluid control of buffer gas and liquid tracer flow rate.

3.4.1 Reliability of laser energy detection

As a consequence of the restriction to unsaturated linear excitation, the fluorescence signal can be normalised to the measured laser beam energy, or more precisely, to the laser irradiance. The quality of this correction depends on the reliability of the energy detection. In order to determine the error of energy correction, the fluorescence signal of a constantly seeded naphthalene atmosphere was acquired simultaneously to photodiode signals for beam energy detection. The graph in figure 30 illustrates the dependence of the beam energy and the uncorrected "raw" fluorescence signal on a shot-to-shot base. The time scale is 100 ms per shot or 10 Hz. The laser energy level was the same as for all later measurement series.

From an analysis of 9000 consecutive laser shots, the photodiode signal is found to be correlated to the fluorescence signal by a factor of 98 %. The correlation error $(S_{Diode} - S_{ICCD})/S_{Diode}$ of 2 % is due to the uncorrelated shot noises of photodiode and camera detection, and further implies the inhomogeneities of vapour concentration over the probe volume.

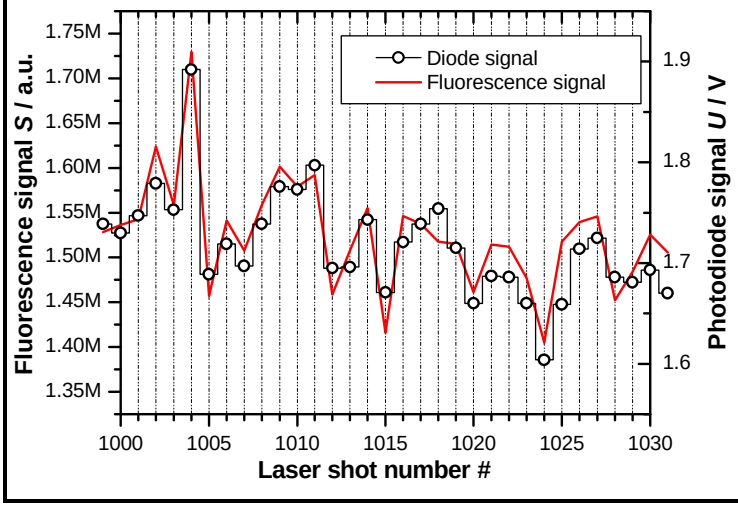

Figure 30: Reliability of correction of fluorescence signal by measured laser energy. This figure illustrates the dependence of laser energies measured with photodiodes and recorded "raw" fluorescence signal on a shot-to-shot base.

The strong correlation between photodiode and fluorescence signals simplifies the estimation of the uncertainty number of fluorescence photons, normalising the number of fluorescence photons with respect to the laser energy (cf. section 3.5.2).

3.4.2 Reliability of temperature and pressure control

Via the gas law, the temperature and the pressure have direct impact on the number density of molecules in the probe volume. Hence, errors in the control of these parameters have also to be analysed. Since the expression for the number density from equation (3.5) displays the pressure in ratio to the temperature, the relative number density error is derived from the sum of relative pressure and temperature errors.

The reliability of temperature and pressure constancy for given setpoints are controlled for a time series corresponding to several hundred laser shots (e.g. 4-times 400 shots). Resulting relative errors are shown in figure 31 for constant gas flow rate of 2 ln/min. For the relative temperature error, a maximum error bound of $3.66 \cdot FS/RD^{1.88}$ is found, where $FS = 1372\,°\mathrm{C}$ is the fullscale of the thermocouple temperature range and RD is the actual readout. The relative pressure error can be described as $2.2\,\% FS/RD$. The fullscale of the pressure transducer is 5 MPa.

The little deviation of the relative pressure error from a hyperbolic function stands in contrast to the spread distribution of the relative temperature error. This is due to the regulation of temperature, which is not as direct as for the pressure case. While the pressure transducer feeds back directly to the flow control by PID regulation (as a part of the LabView routine), the PID temperature control is linked to the temperature of the test cell walls. The fluctuations of the probe volume temperature are hence temporally uncorrelated with the PID regulation.

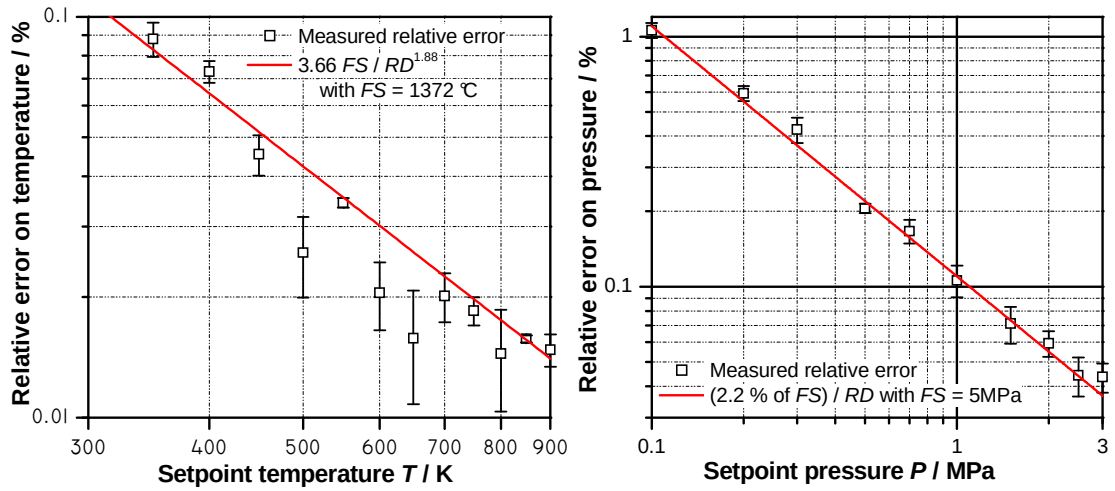

Figure 31: Graph on left side: Reliability of PID regulated temperature control (measured with constant total gas flow of 2 ln/min). Graph on right side: Reliability of pressure control (semi-automatic PID pressure regulation can be obtained for the test cell by the feedback of the measured pressure values to the gas flow regulation).

3.4.3 Reliability of fluid flow control

The molar fraction of absorbent tracer is defined mainly by the flow rates of buffer gas and tracer containing liquid applied to the CEM unit (cf. section 3.1.1). In section 3.1.4, the molar fraction is defined by equation (3.2) as function of the respective flow rates. The equation (3.4) shows the relation of flow rates to liquid mass and gas volumetric flows, which are the primarily controlled parameters.

The liquid flow control is split up to a Bronkhorst sensor model LIQUI-FLOW L1-F A and the 3-way mixing valve of the CEM unit (model series W-202). The gas flow is controlled by Bronkhorst controller (model EL-FLOW series L-201C). The respective flow controls range from 0.2 to 10 g/h for the liquid flow (for acetone - conversion factor for other liquids) and from 0.2 to 10 ln/min for the gas flow (for nitrogen - conversion factor for other gases).

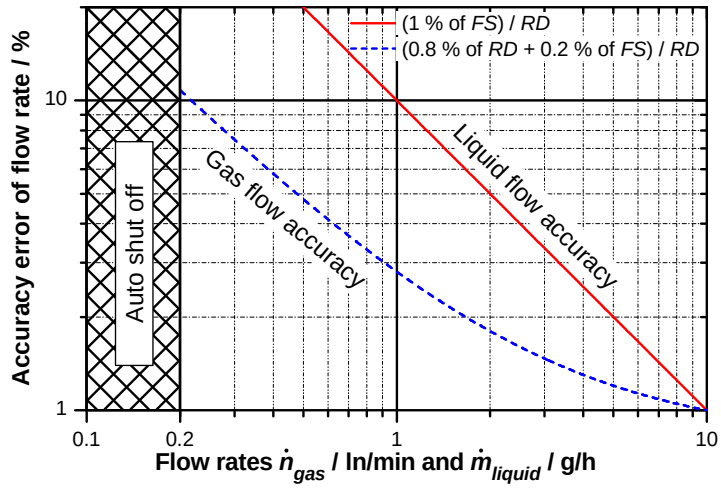

Figure 32: Relative accuracy error of fluid flow controls as specified by Bronkhorst. The error of liquid flow is given as 1 % of the fullscale of 10 g/h divided by the actual readout. For the gas flow, the error is determined from the sum of a constant part of 0.2 % of the fullscale of 10 ln/min and a variable part of 0.8 % of the readout, divided by the readout.

The Bronkhorst devices are supplied with a specification of the accuracy of the respective flow controls. Figure 32 shows the trend of accuracy as a function of the actual readout values. Liquid flows below 2 g/h are avoided for all measurements done within this work, because single parameter inaccuracies beyond 5 % were judged as too high. For the single case of measurement series to evaluate the fluorescence dependence from oxygen quenching and specifically for the ketone tracers, the gas flow rate was decreased down to 0.33 ln/min, leading to an inaccuracy of 6.9 % for this parameter. For temperature series, the lowest flow rate is found for ketone as 0.5 ln/min corresponding to 4.8 % inaccuracy. For aromatic tracer, the minimum flow was always 2 ln/min, which limits the inaccuracy to 1.8 %.

3.4.4 Flow rate impact on local number density in probe volume

The homogeneity of the vapour distribution in the test cell is directly impacting as the local mole fraction on the fluorescence intensity. Differences in vapour density over the probe volume might arise from recirculation and dead zones in the test cell, which are formed differently in strength and position when varying the flow structure by the change of the inlet gas velocity. An exact study of this phenomenon would need accurate, space and time resolving planar imaging methods like Rayleigh scattering or laser-induced fluorescence (PLIF) for the vapour phase concentration, combined with flow field techniques like particle image or gaseous imaging velocimetry (PIV or GIV). This would displace completely the actual objective of the spectroscopic study, which is to learn for different tracer species about the photophysical fluorescence response on the variation of physical parameters like temperature, pressure and oxygen molar fraction. For reasons of simplicity, it was decided to analyse homogeneity indirectly by the detection of fluorescence spectra with the actual set-up.

As mentioned earlier, the acquisition of fluorescence spectra is fast, since spatial averaging is realised over the beam path of the probe volume by hardware binning. The choice of

flow rates has a direct impact on the accuracy of the tracer mole fraction at the outlet of the CEM as shown in the previous section. Further, the local mole fraction in the probe volume is influenced by the flow pattern in the test cell. In order to illustrate the flow pattern influence, fluorescence spectra were studied for varying liquid and gas flow rates, while all other parameters like laser energy, pressure and temperature in the probe volume were kept to constant values.

The results are presented in figure 33, where the flow rate impact on the local number density in the probe volume is proven by means of the trend observed for the integrated fluorescence signal for atmospheric pressure and 450 K with naphthalene tracer. The upper plot shows the influence of variable liquid flows for constant gas flow and the bottom plot the influence of variable gas flow for constant liquid flow. For the variation of liquid flow, the normalised fluorescence error is following the limits given by the manufacturer. The flow range below 2 g/h is clearly to avoid due to the large inaccuracies. For variation of the gas flow, the trend of normalised fluorescence error is also quite well described by the manufacturer accuracy limit for medium gas flow rates. For low gas flow rates, it clearly deviates, probably as a reason of unmixedness of the vapour phase in the probe volume due to the low gas velocity. Hence, gas flows below 2 ln/min are used only if unavoidable under specific experimental conditions.

In addition to the effect of individual variation of the liquid or the gas flow, it is quite interesting to learn about the coupled effect of a simultaneous variation of both, liquid and gas flow rates. To give an example of application used within this work, the constancy of tracer number density cannot be realised unlike increasing gas flow while liquid flow decreases for rising pressure conditions over a range of factor 30. The pressure range is clearly exceeding the dynamics of factor 5 of the liquid (or the gas) flow control when the flow range is limited between 2 and 10 g/h (2 to 10 ln/min) as just described for accuracy reasons.

Figure 34 presents the fluorescence error for a coupled variation of the liquid and gas flow rates. The individual manufacturer accuracy limits for both flow controls are combined as the square root of the sum of the squares. The measured accuracy error seems to follow sufficiently this trend to allow for combined variation of both flow rates.

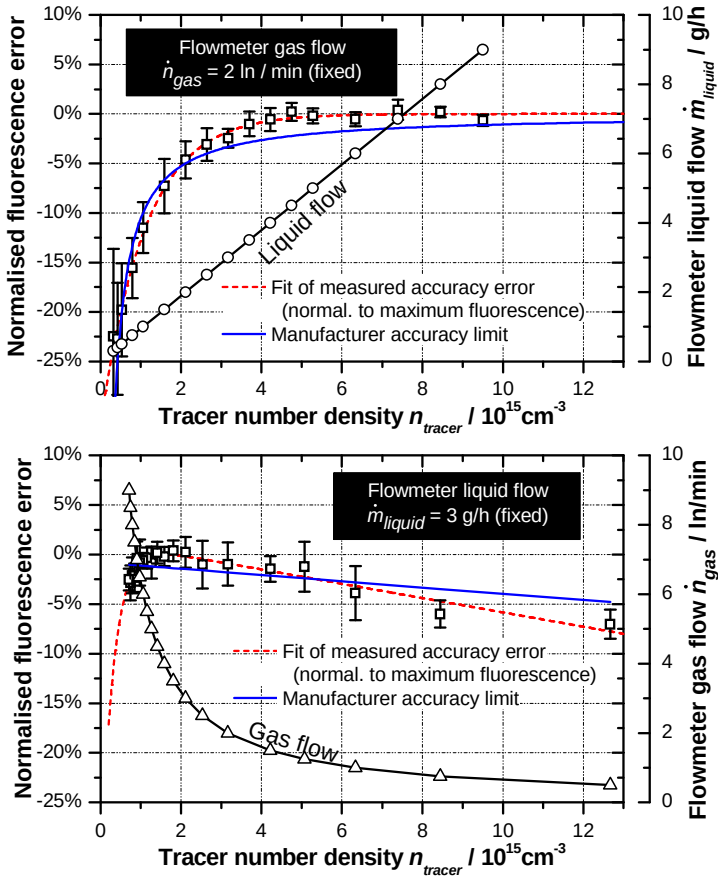

Figure 33: Flow rate impact on local number density in the probe volume as proven by means of integrated fluorescence for atmospheric pressure and 450 K with naphthalene tracer. Top figure: influence of liquid flow variation for fixed gas flow. Bottom figure: influence of gas flow variation for fixed liquid flow.

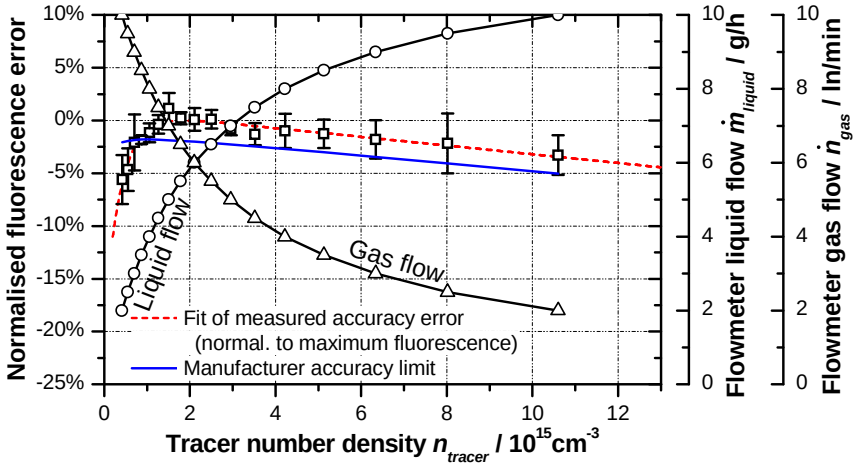

Figure 34: As in previous figure, but here for simultaneous variation of liquid and gas flow (e.g. as it is needed to produce constant number densities over a pressure range of factor 30). Manufacturer limits of liquid and gas controls are derived as square root of the sum of the squares.

3.5 Fluorescence error including the preparation and control of physical parameters

In section 3.3, the noise sources were discussed for the detector based on a constant rate of photon arrival. It was concluded that for the present application, the detection error is dominated by shot noise, since SNR levels are high as a consequence of spatial and temporal signal averaging.

The shot noise is a signal-dependent noise and depends therefore on the number of photons N_{Ph} arriving at the detector surface. Now, N_{Ph} will not be defined by a constant rate anymore, but by the number of fluorescence photons N_{LIF}. Therefore, it is important to determine, how N_{LIF} can be expressed as a function of experimental parameters (for the derivation of the following expressions refer to [Eckbreth 1996]).

3.5.1 Analytical number of fluorescence photons

Remember, the number of fluorescence photons within a time period t was expressed in chapter 2.10.1 as

$$N_{LIF} = \frac{\Omega}{4\pi} V N_1^0 \sigma_\nu \phi \frac{I_L}{h\nu_L} \qquad \text{see equation (2.59)}$$

assumed as constant		variable parameters	
Ω …	collection solid angle	I_L …	laser fluence
V …	probe volume	N_1^0 …	number density of tracer molecule
$h\nu_L$ …	energy of absorbed photon		

laser parameters		molecule intrinsic parameters	
I_ν …	laser lineshape	σ_ν …	absorption cross section of tracer
$\Delta\nu_L$ …	laser profile FWHM	ϕ …	fluorescence quantum yield

Some of the parameters are assumed to be constant values, such as the collection angle or the probe volume size. $h\nu_L$ is the energy of a single absorbed photon with the excitation frequency ν_L of the laser source.

3.5.2 Uncertainty number of fluorescence photons

Equation (2.59) is valid only for fluorescence in the linear regime at low laser irradiance. The number of fluorescence photons N_{LIF} is then direct proportional to the laser fluence I_L and the number density of tracer molecules N_1^0.

The absorption cross-section σ_ν and the fluorescence quantum yield ϕ characterise as intrinsic properties the photophysical response of the tracer molecule on laser excitation. They are hence not directly impacting the error of N_{LIF}.

However, for the calculation of the laser beam attenuation, the absorption cross-section is needed as well as the number density of tracer molecules (see equation (3.7)). Thus, the absorption cross-section has indirect influence on the error.

The number of fluorescence photons from equation (2.59) is rewritten with proportionality factors only, with A as absorption of the laser irradiance in the probe volume

$$N_{LIF} \propto I_{L,0} \cdot \exp(-A) \cdot N_1^0 = I_L \cdot \exp\left(-\sigma_\nu N_1^0 d\right) \cdot N_1^0 \tag{3.28}$$

Applying equations (3.1) to (3.7) to equation (3.28), the number of fluorescence photons can be expressed as proportionality function of directly measured parameters like

$$N_{LIF} \propto I_{L,0} \exp\left(-\underbrace{\boxed{\frac{\ln(I_{L,0}/I_L)}{d} \cdot \frac{T}{T_0} \cdot \frac{P_0}{P} \cdot \frac{1}{Lo\chi}}}_{\Rightarrow \sigma_\nu} * \underbrace{\boxed{\frac{T_0}{T} \cdot \frac{P}{P_0} \cdot Lo\chi}}_{\Rightarrow N_1^0} * d \right) \cdot \underbrace{\boxed{\frac{T_0}{T} \cdot \frac{P}{P_0} \cdot Lo\chi}}_{\Rightarrow N_1^0} \tag{3.29}$$

$$N_{LIF} \quad \propto I_L \frac{P}{T} \chi = I_L \frac{P}{T} \cdot \frac{\dot{n}_{absorb}}{\dot{n}_{absorb} + \dot{n}_{gas}} \tag{3.30}$$

It can be seen from (3.29) that for the absorption A many parameters cancel. Thus, parameter uncertainties do the same. It is reminded from equation (3.7), that the laser fluence in the probe volume I_L is not measured directly, but implies the calculation of absorption by the tracer in the flow cell from $\ln\left(I_{L,0}/I_L\right)$.

In section 3.4.1 it was shown for steady seeding conditions, that the measurement of the laser fluence by the photodiodes is strongly correlated to the detected fluorescence signal. The number of fluorescence photons will thus be normalised with respect to I_L

$$\frac{N_{LIF}}{I_L} \quad \propto \frac{P}{T} \chi = \frac{P}{T} \cdot \frac{\dot{n}_{absorb}}{\dot{n}_{absorb} + \dot{n}_{gas}} \tag{3.31}$$

Generally, if a function q consists of a number i of independent quantities x_i measured each with a small uncertainty Δx_i, the relative uncertainty for q is given as

$$\frac{\Delta q}{|q|} = \sqrt{\sum_i \left(\frac{\Delta q_{x,i}}{x_i} \right)^2} = \sqrt{\sum_i \left(\frac{\partial q}{\partial x_i} \frac{\Delta x_i}{x_i} \right)^2} \tag{3.32}$$

see e.g. [Taylor 1997]. Further, the error is limited by an upper bound of uncertainty to

$$\frac{\Delta q}{|q|} \leq \sum_i \left| \frac{\partial q}{\partial x_i} \cdot \frac{\Delta x_i}{x_i} \right| \tag{3.33}$$

which is always true and which has moreover to be chosen if quantities are dependent. Since the measurement parameters in equation (3.30) are all independent, the relative error or the uncertainty number of fluorescence photons is derived as follows

$$\begin{aligned} \frac{\Delta\left(N_{LIF} / I_L\right)}{\left(N_{LIF} / I_L\right)} &= \sqrt{\sum_i \left(\frac{\partial\left(N_{LIF} / I_L\right)}{\partial x_i} \frac{\Delta x_i}{x_i} \right)^2} \\ &= \sqrt{\left(\frac{\left(S_{Diode} - S_{ICCD}\right)}{S_{Diode}} \right)^2 + \left(\frac{\Delta P}{P} \right)^2 + \left(\frac{\Delta T}{T} \right)^2 + \alpha^2 \left(\frac{\Delta \dot{n}_{absorb}}{\dot{n}_{absorb}} \right)^2 + \alpha^2 \left(\frac{\Delta \dot{n}_{gas}}{\dot{n}_{gas}} \right)^2} \end{aligned} \tag{3.34}$$

$$\alpha = \dot{n}_{gas} / \left(\dot{n}_{gas} + \dot{n}_{absorb} \right) \tag{3.35}$$

Due to the normalisation of the number of fluorescence photons with respect to the laser fluence, the correlation error $\left(S_{Diode} - S_{ICCD}\right) / S_{Diode}$ of 2 % induced by the uncorrelated shot noises of photodiode and camera detection has to be considered (cf. section 3.4.1). This error is added in square under the square root of equation (3.34).

With known values of T, P, $\dot{n}_{absorb}$ and $\dot{n}_{gas}$, the relative error of number of fluorescence photons can be derived for each individual experimental condition. The uncertainties of temperature $\Delta T / T$ and pressure $\Delta P / P$ are derived from experimental observations as shown in section 3.4.2. The maximum uncertainty is reached for atmospheric conditions with $\Delta T / T \cong 0.11\%$ and $\Delta P / P \cong 1.1\%$.

The accuracy of the initial tracer mole fraction χ as obtained at the exit of the CEM capillary is strongly influenced by the choice of liquid flow rate and gas flow rate. The regulation quality of the flow controls is dependent on the respective control range. The uncertainties of the buffer gas flow rate $\Delta \dot{n}_{gas} / \dot{n}_{gas}$ and the liquid absorbent flow rate $\Delta \dot{n}_{absorb} / \dot{n}_{absorb}$ are defined in the flow control manuals from Bronkhorst (cf. section 3.4.3).

Series for studying of fluorescence temperature dependence are all done with fixed gas flow rate of 0.5 ln/min for ketone tracers and 2 ln/min with aromatic tracers. Liquid flow rates are adapted to the temperature condition to keep number density constant, for instance 3.5 g/h for 350 K to 9 g/h for 900 K. The relative error of the number of fluorescence photons $\Delta(N_{LIF}/I_L)/(N_{LIF}/I_L)$ is less than 6 % for ketones and less than 4 % for aromatics.

Series for studying of fluorescence pressure dependence are also done with constant number density, but it is necessary to vary gas and liquid flow rates at the same time, since the dynamics of either gas flow or liquid flow is limited to a factor of 10. Starting from atmospheric pressure with 2 ln/min gas flow and 10 g/h liquid flow, gas flow is increased and liquid flow is reduced while pressure is raised. At 2.5 MPa, the maximal gas flow rate of 10 ln/min is reached and liquid flow rate is 2 g/h. The only pressure condition with changed number density is realised for 3 MPa with flow rates equal to 2.5 MPa. This is done, because liquid flow rates below 2 g/h are avoided due to the strongly increasing inaccuracy. The relative error of the number of fluorescence photons $\Delta(N_{LIF}/I_L)/(N_{LIF}/I_L)$ varies from 3 to 5.5 % increasing pressure from 0.1 to 3 MPa.

The investigations of the fluorescence dependence on oxygen quenching are all done with maximal liquid flow rate of 10 g/h. In order to realise the different oxygen concentrations the nitrogen gas flow rate is varied from 0.33 to 2 ln/min for ketone tracers and from 2 to 10 ln/min for aromatic tracers. The flow rate of dilution air is calculated as the difference of total gas flow rate and nitrogen flow rate. Total gas flow rate is of 2 ln/min for ketones and 10 ln/min for aromatics. Equation (3.34) has to be slightly modified for mixtures of air and nitrogen. The term for the gas flow rate uncertainty is replaced by an expression for the errors of nitrogen and air flow rate. The factor α is replaced by individual coefficients β_i considering the respective air, nitrogen and liquid absorbent flow rates.

$$\frac{\Delta(N_{LIF}/I_L)}{(N_{LIF}/I_L)} = \sqrt{\left(\frac{(S_{Diode}-S_{ICCD})}{S_{Diode}}\right)^2 + \left(\frac{\Delta P}{P}\right)^2 + \left(\frac{\Delta T}{T}\right)^2 + \beta_1\left(\frac{\Delta\dot{n}_{absorb}}{\dot{n}_{absorb}}\right)^2 + \beta_2\left(\frac{\Delta\dot{n}_{N2}}{\dot{n}_{N2}}\right)^2 + \beta_3\left(\frac{\Delta\dot{n}_{air}}{\dot{n}_{air}}\right)^2} \tag{3.36}$$

$$\beta_1 = \frac{\dot{n}_{N2}+\dot{n}_{air}}{\dot{n}_{N2}+\dot{n}_{air}+\dot{n}_{absorb}} \quad \Leftrightarrow \beta_2 = \frac{\dot{n}_{N2}}{\dot{n}_{N2}+\dot{n}_{air}+\dot{n}_{absorb}} \quad \Leftrightarrow \beta_3 = \frac{\dot{n}_{air}}{\dot{n}_{N2}+\dot{n}_{air}+\dot{n}_{absorb}} \tag{3.37}$$

The relative error of the number of fluorescence photons $\Delta(N_{LIF}/I_L)/(N_{LIF}/I_L)$ is less than 3.2 %. As an exemplary case the calculation of the relative error for the 3-pentanone tracer is shown in table 1 for a series studying the quenching effect at 450 K under atmospheric pressure.

— Species: 3-pentanone

— Molar mass: 86.31 g/mol

— Temperature: 450 K

— Pressure: 0.1 MPa

— Liquid flow rate: 10 g/h 3-pentanone

Table 1: Example of error calculation for 3-pentanone tracer with equations (3.36) and (3.37). Series studying the fluorescence dependence on oxygen quenching. *) is correlation error $(S_{Diode} - S_{ICCD}) / S_{Diode}$.

$\dot{m}_{absorb}$ $\frac{\text{g}}{\text{h}}$	$\dot{v}_{N2}$ $\frac{\text{ln}}{\text{min}}$	$\dot{v}_{air}$ $\frac{\text{ln}}{\text{min}}$	β_1 /	β_2 /	β_3 /	*) %	$\frac{\Delta T}{T}$ %	$\frac{\Delta P}{P}$ %	$\frac{\Delta \dot{m}_{absorb}}{\dot{m}_{absorb}}$ %	$\frac{\Delta \dot{m}_{N2}}{\dot{m}_{N2}}$ %	$\frac{\Delta \dot{m}_{air}}{\dot{m}_{air}}$ %	$\Delta \frac{\frac{N_{LIF}}{I_L}}{\frac{N_{LIF}}{I_L}}$ %
10	2.00	0.00	0.98	0.98	0.00	2	0.1	1.1	1	1.8	0.0	3.0
10	1.80	0.20	0.98	0.88	0.10	2	0.1	1.1	1	1.9	10.8	3.2
10	1.71	0.29	0.98	0.84	0.14	2	0.1	1.1	1	2.0	7.7	3.2
10	1.52	0.48	0.98	0.74	0.23	2	0.1	1.1	1	2.1	5.0	3.2
10	1.30	0.70	0.98	0.64	0.34	2	0.1	1.1	1	2.3	3.7	3.2
10	1.09	0.91	0.98	0.53	0.44	2	0.1	1.1	1	2.6	3.0	3.1
10	0.89	1.11	0.98	0.43	0.54	2	0.1	1.1	1	3.0	2.6	3.1
10	0.69	1.31	0.98	0.34	0.64	2	0.1	1.1	1	3.7	2.3	3.2
10	0.51	1.49	0.98	0.25	0.73	2	0.1	1.1	1	4.7	2.1	3.2
10	0.33	1.67	0.98	0.16	0.82	2	0.1	1.1	1	6.9	2.0	3.2

3.6 Measurement timing and acquisition mode

The fluorescence measurement is triggered to the Q-switch 10 Hz frequency of the laser. Beam energies from photodiodes are integrated by a boxcar averager system (SR250, Stanford Research Systems) to 30 laser shots. The boxcar averager is driven with double frequency at 20 Hz in order to subtract a baseline signal, which is derived from the diode signal measured in-between two consecutive laser shots.

Temperature and pressure signals are detected simultaneously to each laser shot. They are acquired together with the beam energies by a National Instruments (NI) data acquisition board, installed on a PC running a LabView routine.

The ICCD images are captured to the PC. Dependent on the fluorescence signal intensity, spectra accumulation of 100 to 400 laser shots is performed. The spatial extension (direction parallel to the laser beam) of the probe volume corresponds to the vertical, the spectral bandpass to the horizontal direction of the detector. Fast hardware binning in vertical direction transforms the spatially resolved fluorescence images into single line spectra. The camera acquisition and the grating tilt of the spectrograph are both LabView controlled.

A main source of inaccuracy of laboratory measurements is due to the human handling. To guarantee a reproducible test cycle for the acquisition of fluorescence spectra with fixed physical parameters, the whole measurement procedure is LabView controlled. A measurement interface was programmed for systematic influence on all relevant physical parameters, which can be preset via an event scheme on a laser shot count time basis. The event schemes are stored to ASCII files and allow for repetition of the same measurement under "nearest the same" conditions.

Figure 35 presents a typical fixed measurement cycle. The probe volume in the test cell is alternately filled with the tracer / buffer gas mixture and purged by flushing with nitrogen to measure the beam absorption and to check for vapour accumulation within the purge periods. Measurements of 80 nm large spectra are realised with 60 nm overlap in order to obtain sufficient information and to reduce boundary effects for the "gluing" process. The spectra are accumulated over 100 to 400 laser shots, dependent on the tracer species fluorescence signal intensity. Repeated dark image correction is realised by changing the spectrograph grating tilt to the 100 nm position. Since the ICCD entrance window does not capture in the far ultraviolet, this grating position reproduces nearly the "closed camera" condition. Comparison to a "real dark image" with closed camera revealed similar results and it was assured, that stray light is not of importance when taking dark images at 100 nm tilt angle.

The acquired spectra are corrected for tracer number density and beam energy in the probe volume. Beam attenuation by absorption is accounted for.

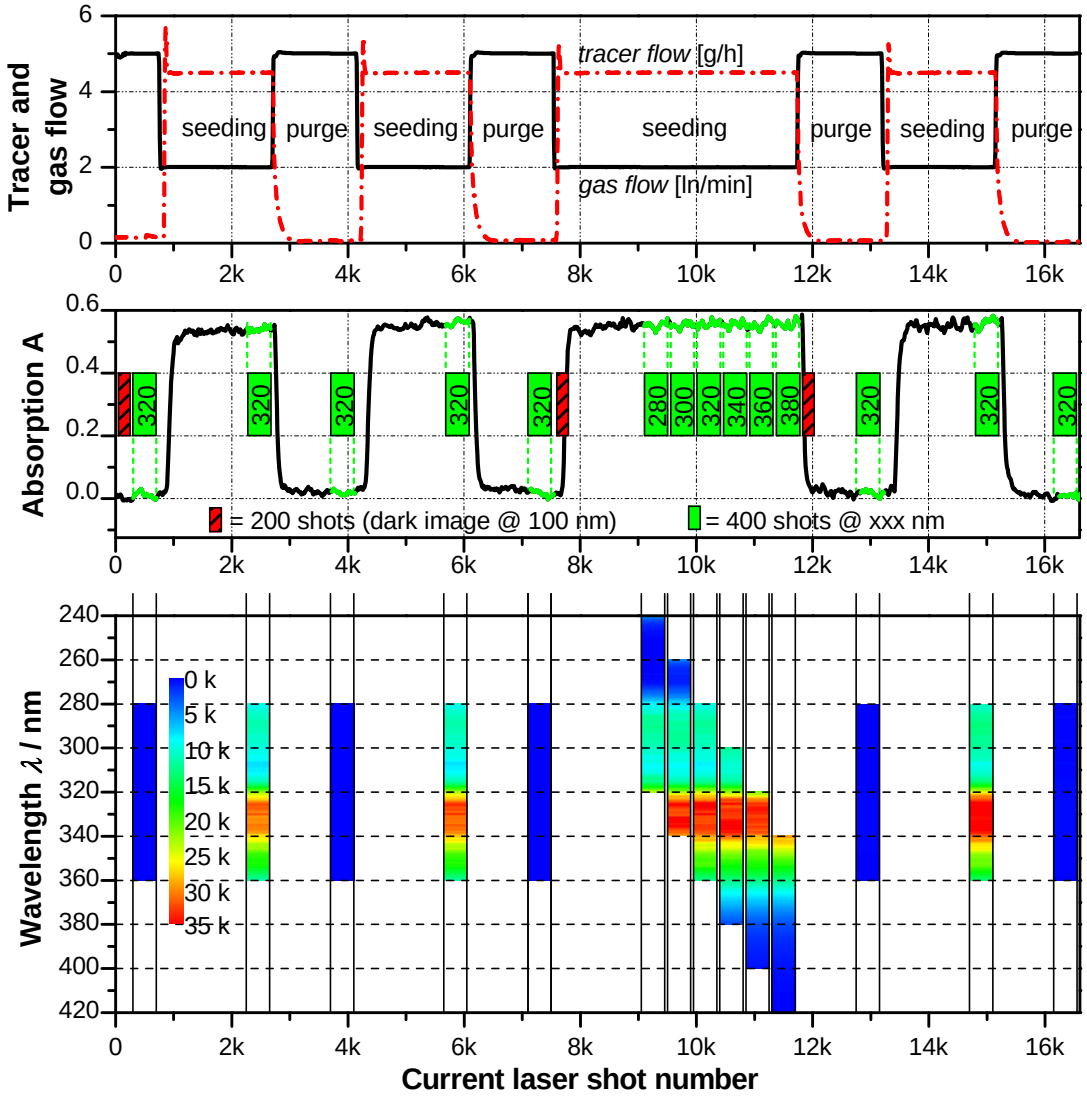

Figure 35: Typical fixed measurement cycle for study of a physical parameter, which is kept constant within the cycle duration. A measurement interface was programmed for systematic influence on all relevant physical parameters, which can be preset via an event scheme on a laser shot count time basis. Refer to the text.

3.7 Reliability of measured fluorescence spectra

As mentioned earlier in sections 3.2.1 and 3.2.2, the fluorescence spectra measured with the present spectroscopic set-up are corrected for the intensity and for the spectral response functions. Although the acquisition and the succeeding corrections are performed most care-

fully, it might be insightful to check the reliability of the set-up comparing the measured spectra to results from other scientific groups who performed their work under similar conditions.

3.7.1 Shape and intensity

To judge the measured spectra on their shape and intensity qualities, they shall be compared for both a ketone and a monocyclic aromatic tracer to results from several other research groups.

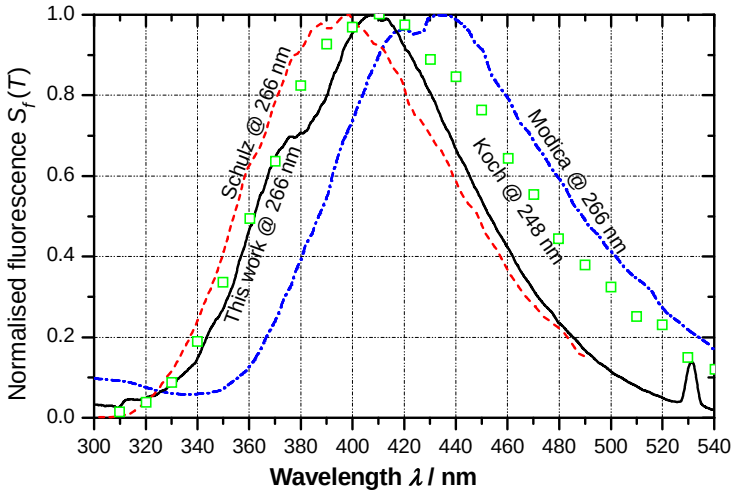

Figure 36: Spectral and intensity reliability: 3-pentanone fluorescence spectrum measured with spectroscopic set-up of this work (continuous black line) compared to measurements from [Schulz 2005] (dashed red line), from [Koch 2003b] (green square dots) and from [Modica 2007] (dash-dot blue line). Atmospheric pressure pure nitrogen.
Schulz: 295 K with 13 mbar tracer at 1 atm, pure N_2. This work: 350 K with 32 mbar tracer at 1 atm, pure N_2. Koch: (with 248 nm excitation) 298 K with 4 mol % tracer (~ 40 mbar) at 1 atm, pure N_2. Modica: 473 K with less than 2.96×10^{18} cm^{-3} tracer (~ 193 mbar !) at 1 atm, pure N_2.

Figure 36 shows the emission fluorescence spectrum of 3-pentanone from this work measured in pure nitrogen atmosphere for 350 K at 1 atm after a 266 nm laser excitation for 32 mbar tracer concentration. Closest to this work's result is the spectrum from [Schulz 2005], which was measured for slightly lower temperature at 295 K and less than the half of the tracer concentration. However, the spectral shift from the maximum position is less when comparing to [Koch 2003b], whose spectrum is reported for a 248 nm excitation (at 298 K with a 4 % molar tracer fraction). The rising slope of Koch's spectrum describes quite well the result from our set-up, whereas the falling slope is shifted to the red by 20 nm. When looking at Koch's result it must not be forgotten the difference in excitation wavelength. Another spectrum from the same work of Koch (not shown here) for 308 nm excitation differs

only little from that for 248 nm excitation. However, the spectrum presented in the work of [Modica 2007] is located approximately 25 nm to the red and the profile of the falling slope is slightly shallower, as it also can be seen for Koch's result.

To summarize, it might be retained that the spectral shapes of the spectra from the four work groups are quite different, although measured for similar tracer concentrations in pure nitrogen atmosphere. The slightly pronounced double peak feature revealed in our spectrum shows only in the work of Modica.

The shape differences between the 3-pentanone spectra are much more reasonable, when looking at the quite small fluorescence quantum yield (0.8 to 1.0×10^{-3} from Rayleigh-calibrated measurements of [Koch 2004]) and the relatively low tracer concentrations.

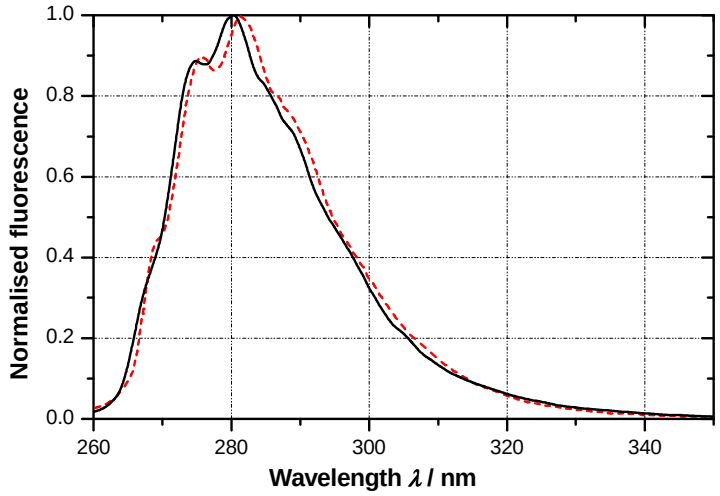

Figure 37: Spectral and intensity reliability: toluene fluorescence spectrum measured with spectroscopic set-up of this work (continuous line) compared to measurement from [Koban 2004] (dashed line). Atmospheric pressure pure nitrogen. This work: 350 K with 7.7 mbar tracer (1.59×10^{17} cm^{-3}), 1 atm, pure N_2. Koban: 296 K with 5 mbar tracer, 1 atm, pure N_2.

For further evaluation of the correctness of the spectral shape, in figure 37 a toluene fluorescence spectrum measured with the set-up of this work is confronted to the work of [Koban 2004]. Apart from the slightly higher temperature condition for this work, the spectra were taken under similar conditions (with respect to Koban's comment to the identical shapes of emission spectra for 248 and 266 nm excitation at room-temperature). The results show good agreement with a minimal shift of 0.8 nm to the red for Koban's spectrum. It shall be noted that the molar tracer concentration is even less than for the 3-pentanone spectra. The better concordance for the toluene tracer comes along with its larger absorption cross-section (toluene: 1.9×10^{-19} cm^2 [Koban 2004], 3-pentanone: 4.6×10^{-20} cm^2 [Koch 2003b]) and its higher fluorescence quantum yield (0.3 for room temperature reported by Burton and Noyes [Burton 1968]). This leads to better SNR levels as well for the measurement of the laser beam attenuation by the photodiodes as for the ICCD camera detection.

3.7.2 Physical parameter variation

So far, the reliability of the detection part of the set-up has been discussed, based on a given tracer concentration for fixed temperature and atmospheric pressure. However, the principal aim of the spectroscopic set-up is to show how fluorescence and absorption depend on temperature, pressure and concentration changes. The preparation of the physical parameters in the probe volume is realised prior to and is kept constant during each measurement.

All parameters having influence on the tracer number density of the mixture pouring into the test cell and its distribution to the probe volume are essential for the measured fluorescence signal intensity. These are primarily the flow rate of the liquid phase containing the tracer molecule and the flow rate of the buffer gas. Moreover, the global number density of tracer rises with increasing pressure and drops with increasing temperature as known from the ideal gas law.

The local number density in the probe volume is further influenced by the flow pattern in the test cell, which depends principally on the gas flow rate. If the gas flow rate is very low, homogenisation of the tracer concentration in the test cell is not possible, since the gas phase is not sufficiently mixed to disperse the tracer everywhere in the cell. On the other hand, too high gas flow rates might lead to unsteady vortices and turbulences hindering the tracer homogenisation.

Anyway, the exact knowledge of the flow structure inside the test cell is not the aim of the experimental study performed with this set-up. Sufficient control of the seeding process can also be obtained from the absorption of the laser beam passing through the probe volume. Figure 38 shows the time response of the tracer distribution after starting tracer seeding to a prior purged test cell. The homogenisation of the tracer concentration over the probe volume is not an immediate process, which is clearly observed from the absorption feature. This time delay to reach tracer homogenisation varies with the tracer type, since volatility class and molar weight are of importance. Raising the temperature in the test cell shortens, rising the pressure stretches the time delay to reach tracer homogenisation, because the saturation pressure is changed.

Another important concern is the average time of presence of an individual tracer molecule in the probe volume. Recirculation of the gas flow is a relevant phenomenon, often encountered for test cells similar to the present geometry. It can lead to multiple excitation of the same tracer molecule re-entering into the laser beam and should therefore be avoided to limit the probability of photochemical reactions, especially in the case of higher temperatures and present oxygen.

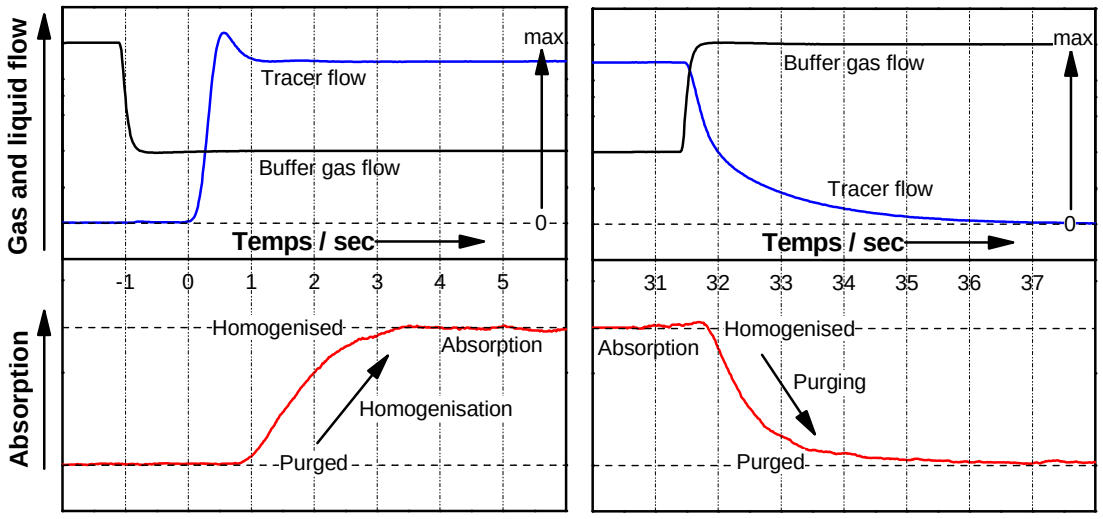

Figure 38: Left part: Homogenisation of tracer molecule over the probe volume after start of seeding process. The time delay to reach homogenised situation is exemplarily shown on the stabilisation of the laser beam absorption after several seconds. Right part: Purging of tracer from the test cell after seeding period.

The construction of a test cell is somewhat a tradeoff between more or less stringent requirements such as good optical accessibility and homogeneous heating of the probe volume, high pressure resistance, limitation of tracer wall adsorption and beneficial flow characteristics leading to homogenous distribution and limited residence time of the tracer molecules. High cell mass and a high cell volume might be favoured to achieve a homogeneous temperature field in the probe volume, whereas a small cell volume with simpler geometry is certainly advantageous for a better control of the flow field and the tracer seeding.

For spectroscopic fluorescence measurements with a multichannel array detector coupled to an imaging spectrograph, it is important to collect a high number of fluorescence photons from the probe volume for a low noise detection quality. This leads to detection optics with large solid angles and hence justifies the use of bigger test cells. If in contrast spectral resolution is not needed, the fluorescence signal can be spectrally integrated by means of a photomultiplier tube allowing for smaller solid angles and hence a decrease of cell size.

In order to concentrate on beneficial flow characteristics, it is sometimes chosen to separate the heating from the cell construction by placing the whole test cell in a muffle furnace (e.g. experimental set-ups of [Thurber 1998] and [Koban 2004]). The solid angle for the fluorescence detection optics is then evidently much reduced, since lenses have to be placed outside the muffle furnace.

With the present test cell geometry used for this work, the cell heating is integrated to the cell, and furthermore, the cell construction is rather thick-walled to allow also for high-pressure use. For each type of tracer molecule and each temperature / pressure condition,

the gas flow rate is adapted to guarantee sufficient tracer mixing while preventing from recirculation potentially causing a prolonged residence time or even tracer accumulation. This can be done by the observation of the laser beam absorption, which is fast converging to a constant level of homogenised tracer concentration (cf. figure 38).

The temperature influence on the tracer homogenisation is found to be of minor importance. Thus, working with the same constant gas flow rate for all temperatures at a fixed pressure allows for eliminating the influence of the flow conditions to the measurement. Furthermore, the flow rate of the tracer containing liquid is adapted to keep the tracer number density in the probe volume to the same level when changing the temperature condition, which simplifies considerably the evaluation of the experimental results. Absorption and fluorescence signal then change with the temperature condition only due to intrinsic phenomena caused by the tracer molecule's photophysics. Hence, the photodiode signals underlie only small changes, because the absorption is only moderately dependent on the temperature (e.g. rarely changes more than one order of magnitude for a temperature shift of several hundred K). For the fluorescence detection, it is possible to work with fixed intensifier gain and spectrograph entrance slit for all temperatures of a series, the dynamic range of the detector being wide enough to resolve the fluorescence with sufficient SNR even for the highest temperatures (~ 900 K).

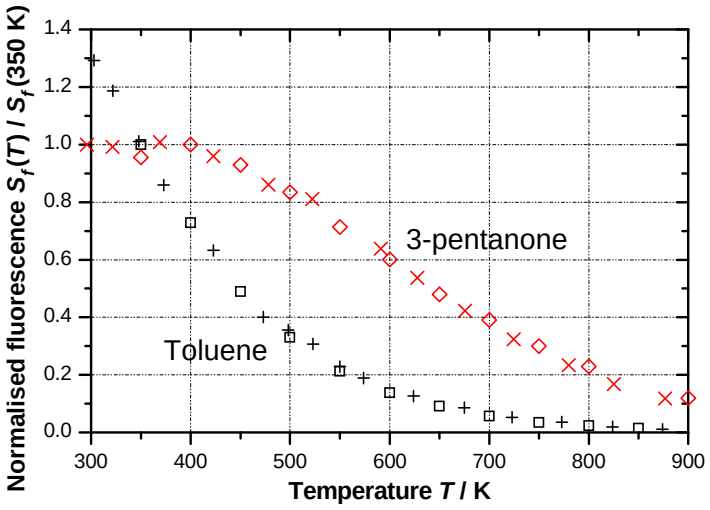

Figure 39: Temperature sensitivity: fluorescence measurements with spectroscopic set-up of this work compared to measurements from [Koch 2003b] and [Koban 2004]. Atmospheric pressure pure nitrogen.
Toluene:
□ this work, + Koban.
3-pentanone:
◇ this work, × Koch.

The reliability of the fluorescence measurements done with the spectroscopic set-up with regard to the change of temperature condition is compared to results from other research groups for the 3-pentanone and the toluene tracer molecules. Figure 39 shows the relative fluorescence temperature dependence for 3-pentanone [Koch 2003b] and toluene [Koban 2004] from ambient temperature to 900 K for atmospheric pressure and pure nitrogen. The data obtained from our set-up is in very good agreement. As mentioned above, within temperature series, the number density of the tracer is kept constant. When discussing

the results in more detail in Chapter 5, this clearly presents as advantage for the quality of the fluorescence signal at high temperature conditions.

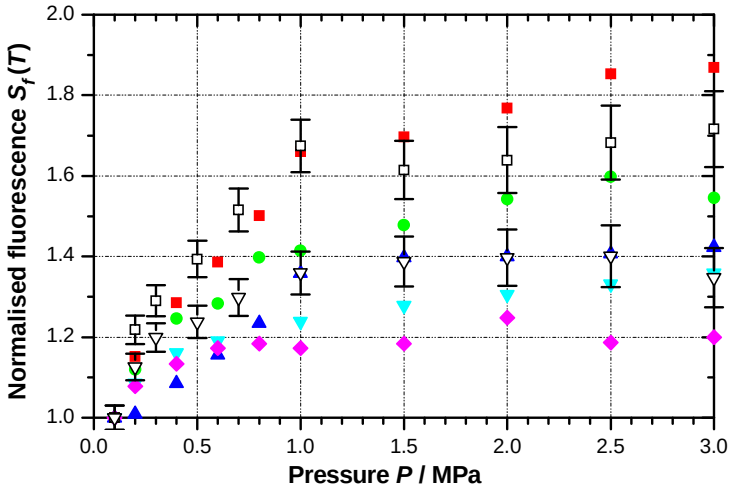

Figure 40: Pressure sensitivity: fluorescence measurements with spectroscopic set-up of this work compared to measurements from [Modica 2007].

This work: □ 550 K, ▽ 450 K.

Modica: less than 2.96×10^{18} cm^{-3} tracer in pure N_2, ■ 573 K, ● 523 K, ▲ 473 K, ▼ 423 K, ◆ 373 K.

In contrast to the temperature influence, for aromatic tracers, the pressure dependence was merely studied so far. Hence, for the variation of pressure, the reliability of the set-up will only be controlled by comparison to measurements from [Modica 2007] for 3-pentanone. Modica detected relative fluorescence signal as function of the pressure up to 4 MPa as shown in figure 40 (cut to 3 MPa). Five temperature levels from 373 to 573 K are presented with pure nitrogen as buffer gas. Data points obtained with our set-up presented for 450 and 550 K fit very well in Modica's plot.

Chapter 4 Review of fuel tracer vapour fluorescence diagnostics

The fluorescence emission of molecular organic species in the vapour and liquid phases can be used as a powerful tool for physical parameter sensing in combustion environments. In contrast to minor species the density of states is very high, and thus absorption is congested to large spectral bands. Large band absorption enables the use of standard laser sources in contrast to the excitation of small inorganic molecules, for which tunability to distinct absorption lines is necessary. Thus, the use of organic tracers considerably eases the measurement requirements.

Electronic transitions reach from the far-UV to the infrared domain. However, practically excitation is limited downwards due to the sudden loss of transmittance of quartz glasses and the strong increase of extinction by oxygen and water molecules below 200 nm. The minimal energy necessary to promote unsaturated organic molecules to an electronic excited state is met for photons of about 700 nm. Fortunately, for saturated organic molecules the transition strength of absorption is very low between 200 and 700 nm. These species can therefore be used as optically transparent solvents doped with unsaturated organic molecules serving as fluorescence tracer. Different groups from organic molecules will be discussed along with their electronic transitions in section 4.3. Some of them are especially relevant to fluorescence diagnostics, because they contain specific chromophores like C=C or C=O or aromatic groups.

Most combustion fuels like gasoline, kerosene and Diesel are mixtures from a very large spread of organic species. A great number of unsaturated fuel constituents might exhibit fluorescence when excited in the near UV/visible domain. Therefore, the fuel emission potentially consists of the superimposed fluorescence from multiple species. Generally, the fuel composition is not known exactly, i.e. it changes considerably from bulk to bulk. Standard regulations specify lower and upper limits of specific constituents or chemical groups.

Only in some special cases and for a limited number of organic species the photophysics is known to a point where parameters like temperature, concentration or pressure might be inferred from the fluorescence signal. In practical fuels, however, phenomena like signal cross-talk between the multiple fluorescing species are likely to be a problem. A reasonable method is therefore to replace the fuel with a non fluorescing surrogate chosen from satu-

rated organic species, and to dope with small amounts of a fluorescence tracer with well-known photophysics. The chemical affinity of many tracer substances to commercial fuels allows many applications, where the replacement of the real fuel by a surrogate with a fluorescence tracer seeded to it has only minor influence to the physical and chemical phenomena to be observed.

Attention has to be paid when tracer species are detected near to flame fronts. On the one hand, well-chosen tracer substances disappear close to the parent fuel and thus can be good markers of the flame front. On the other hand, getting close to the flame front, the surrogate fuel seeded with tracer will in many cases behave very differently from the real multicomponent fuel, which is likely to react in a more step-wise manner. It is thus difficult to say if a surrogate/tracer couple is still a good representative for the real fuel then, and in many cases, restriction is made to measurements under either unfired conditions or to exclusion of the reaction zone from quantification.

With commercial UV laser sources the energy necessary for promotion to an electronic excited state is easily provided. The possibility to confine the laser light to extended planar sheets of thickness in the mid-range of the micrometer scale enables two-dimensional parameter sensing referred to as planar laser-induced fluorescence (PLIF).

The spectral domain from the near UV to the visible is preferable for detection with regard to both, the sensitivity of most CCD cameras and the fluorescence emission of organic species, providing strong absorption bands in the UV. Further, compared to fluorescence signals in the infrared, the fluorescence intensity is rather high due to its cubic dependence on the light frequency. This allows in many cases for non-intensified fluorescence detection and the observation of two-dimensional probe volumes.

In various practical applications, however, SNR levels are low, e.g. due to minor quantum yields or when a high time resolution is required. Thus, multichannel plate (MCP) intensifiers are used with the cameras, and the wavelength sensitivity of the detection path is defined by the phosphor screen of the intensifier device. In addition to the enhancement of the signal level, MCPs have excellent electronic gating time properties as a result of ultra fast (several nanoseconds) voltage switching applied between the photocathode and the front end of the multiplier section, see [Eckbreth 1996].

4.1 Accessing the individual parameters influencing the fluorescence signal

As mentioned in section 2.10.1, the intensity of the fluorescence emission in the linear regime is proportional to the number density of the fluorescing species, the absorption cross-section and the fluorescence quantum yield

$$S_f \propto N_1^0 \sigma_\nu \phi \propto \left[\frac{P}{T}\right] \sigma_\nu(\lambda, T)\, \phi(\lambda, T, P, \chi_i) \cdot \chi_{tracer} \tag{4.1}$$

For most measurement applications, mainly the local mole fraction χ_{tracer} of the tracer species is of interest, and not its number density N_1^0 itself. Thus, the fluorescence signal increases with the ratio pressure/temperature for a given tracer mole fraction. In addition to its dependence on the photon energy via the wavelength, the absorption cross-section is also a function of the vibrational excess energy in the excited state via the temperature. The pressure is usually believed to have negligible impact on the absorption process, because for the gaseous phase absorption occurs much faster than collisions. The fluorescence quantum yield is the balance of fluorescence to the non-radiative deactivation pathways. In the low and medium pressure gas phase these pathways occur on competitive timescales, all of them being dependent on temperature and pressure. Chemical or quenching reactions might become effective deactivation channels via the respective mole fractions χ_i of other species.

(i) Parameter restriction

In order to enable a direct link between the fluorescence signal and the specific parameter of interest, e.g. the local tracer concentration or the local temperature, the number of physical parameters influencing the fluorescence signal must be reduced. A possible approach is to make restrictions to special conditions, for which the tracer fluorescence is known to be invariant to the change of one or more of the parameters at least within the experimental conditions. This might be simply the choice of a non-quenching environment or quenching insensitive species. Also, it can be related to a specific tracer property, e.g. the quasi temperature independent fluorescence signal of 3-pentanone for 308 nm excitation below 600 K [Koch 2005]. Thus, in such a case the concentration field can be directly inferred from the fluorescence signal.

Generally, even if the absorption and quantum yield behaviour with temperature, pressure and species concentration is well known, the number density remains a source of measurement ambiguity coupling the temperature and pressure to the fluorescence signal. Thus, except the isothermal case or the homogenously seeded isobaric case, the measurement of the local tracer concentration requires the knowledge of the temperature field and vice-versa.

(ii) Multiply variable scalar quantities

It is quite intuitive to search a number of independent simultaneous equations corresponding to the number of variables, when solving a system of equations. This simple approach is successfully transferred to fluorescence diagnostics. Generally, each unknown parameter with impact on the fluorescence signal must be represented by simultaneous detection of an individual fluorescence feature depending on this parameter. This might be performed by separating the wavelength dependent photophysical emission behaviour of the tracer molecule

into different channels of simultaneous observation. Sometimes independent fluorescence features are accessible for a single wavelength excitation. Then, the separation of the detection pathway into several spectral domains covering the individual features by use of appropriate optical filters might be a promising strategy. However, often the wavelength dependent fluorescence features are not sufficiently uncorrelated or separable with respect to the parameters to be inferred from. Then, two-channel excitation with different laser wavelengths eventually leads the way to a measurement strategy.

(iii) Complexity of real fuel systems

Promising techniques to infer the local tracer concentration or temperature from the fluorescence signal are mostly known for simple systems, consisting of one or two different fluorescing species with a photophysical behaviour well-studied under the relevant experimental conditions. Otherwise, reciprocal influences like signal cross-talk, e.g. by reabsorption or quenching reactions between species, might lead to complicated and thus uncontrollable conditions. Most petroleum type real fuels fluoresce when excited in the ultraviolet due to the amount of aromatic species contained in their mixture composition. The interpretation of real fuel fluorescence is very complex, and if the species at the origin of the emission have not been identified, rather inaccessible. Thus, the direct use of the fluorescence of real fuels for quantitative interpretation is rather discouraging. For ultraviolet excitation, the by far most applications of quantitative fluorescence measurements are consequently based on the use of fluorescence dopants (tracer) with well-known photophysical properties. Often the tracer molecules are dissolved to surrogate fuels, which are transparent to the ultraviolet laser source. One typical example is the use of 3-pentanone as fluorescence tracer dissolved in isooctane. Exhibiting nearby the same boiling point as isooctane, 3-pentanone has become a standard fluorescence tracer in isooctane, which is the mostly used alkane surrogate for gasoline real fuel.

4.2 Small inorganic tracer molecules

"Quantitative minor species concentration measurements are a prerequisite for understanding combustion processes and pollutant formation. They are also necessary to validate and optimise reaction mechanisms and models in combustion research" [Brockhinke 2006]. The fluorescence of small inorganic di- and tri-atomic molecules is often exploited in combustion diagnostics. Small and unstable molecules like OH, CH and C_2-radicals are generated within the combustion reaction and can be used as a proof to localise the flame front or for the study of flame structure (often in combination to other diagnostics, e.g.: simultaneous CH-PLIF and PIV in a non-premixed turbulent jet flame [Carter 1998]; CH and OH-PLIF in turbulent partially premixed methane/air flames [Kiefer 2008]; OH and fuel PLIF for flame structure and direct proof of NO-concentration by NO-LIF in a LPP combustor test rig

[Hicks 2005]; OH and acetone PLIF for quantitative imaging of species concentration and temperature in subsonic and supersonic flames [Grisch 2001]; simultaneous kerosene PLIF and OH PLIF in a multipoint injection system of a fired high-pressure combustor [Grisch 2008]). Well-understood photophysics as in the case of NO permits the use as a tracer seeded to gaseous fuels, e.g. to measure temperature profiles [Fuyuto 2006]. Thereby toxicity can be quite a problem working with tracers from oxides and dioxides of sulphur and nitrogen like NO or SO_2. Sometimes, LIF quantification is complicated, because fluorescence competes with electronic quenching, which is a function of excited state quantum numbers and number density of collision partners, e.g. see [Brockhinke 2006] for C_2, [Rao 1969] for SO_2.

The absorption features of small inorganic molecules are generally narrow-band, and therefore tuneable laser sources are needed to promote them to electronic excited states. For measurements aiming the study of the mixing zone before the onset of combustion, organic tracer molecules are much more suited, especially when featuring accessible electronic transitions like the $\pi \rightarrow \pi^*$ transition of aromatics and the $n \rightarrow \pi^*$ transition of carbonyl compounds in the middle ultraviolet.

4.3 Organic fluorescence tracers for the vapour phase

Compared to atoms and small inorganic species, organic molecules have a high density of vibrational states leading to broadband absorption. The excitation energy for a molecule promoted from the ground state to an excited electronic state is transition-specific, and can be provided in many cases via absorption of photons of wavelength from 200 to 700 nm [Turro 1991].

Generally, for molecules exhibiting broadband absorption spectra, near resonance excitation is possible, and hence the fluorescence emission is red-shifted from the excitation wavelength due to the loss of excitation energy into radiationless deactivation pathways. This turns out to be an advantage for the detection of the fluorescence emission, making its separation from Mie and Rayleigh scattering easier.

Fluorescence diagnostics are performed on various organic tracer molecules. The choice of a tracer is motivated by the molecule's photophysics and is a trade-off between e.g. oscillator strength of the absorption feature and the accessibility of the transition by an excitation (laser) source.

For many organic molecules, strong absorption bands are found for orbital and symmetry-allowed transitions in the vacuum UV. However, the absorption of oxygen grows strongly for wavelengths below 200 nm (see [Frederick 1982] and [Gibson 1983]). In air, the excitation (and detection) is normally limited to longer wavelengths. To access absorption features be-

low 200 nm, the entire light path has to be evacuated from air, e.g. by flooding with nitrogen and/or vacuum pumping. For the purpose of combustion related diagnostics, this is practically never seen. In the middle UV, excitation of organic hydrocarbons leads to rather weak absorption features if the transition is (partially) violating a selection rule.

4.3.1 Electronic excitation of different groups of organic molecules

The theory of photophysical processes given in Chapter 2 assists the comprehension of electronic absorption transitions observed for different groups of organic molecules. The organic molecules are classified by the type of promotion between the molecular orbitals within their valence shell. This section uses the information supplied for different chemical groups of organic molecules following different textbooks, see e.g. [Rohatgi-Mukherjee 1978], [Silverstein 1998] and [Valeur 2007].

The description should help to distinguish organic molecule groups for the use as a fluorescence tracer with regard to the possibility of excitation in the middle UV. Interesting spectroscopic properties of specific groups from organic molecules have motivated their use as fluorescence tracers within the last decades. For instance, the properties of benzene and carbonyl chromophore make aromatic species and aliphatic ketone molecules the so far most relevant organic tracers for quantitative combustion related fluorescence diagnostics.

Ketone molecules contain the carbonyl functional group providing the electronic $n \rightarrow \pi^*$ transition, which is accessible by photon absorption near to 280 nm. Due to a poor spatial overlap between the initial and final n and π^*-MOs, the dipole moment is very low, and the transition is said orbital overlap forbidden. Furthermore, the wave functions of the ground and excited state have different symmetry, and this transition is said symmetry forbidden. However, as the result of a breakdown of the Born-Oppenheimer approximation the $n \rightarrow \pi^*$ transition in ketones is clearly observed. Symmetry forbidden transitions might become partially allowed by coupling the electronic wave function to the vibrational motion of the nuclei. This vibrational-electronic coupling is called vibronic interaction. Due to the periodical symmetry changes caused by the not totally symmetric vibrational motions of the nuclei, the electrons have to adapt themselves instantaneously, following the Franck-Condon principle.

Within combustion diagnostics accessible vibronically allowed and hence weak transitions are preferred to strong symmetry allowed, but inaccessible transitions. This applies also for the symmetry forbidden $\pi \rightarrow \pi^*$ transitions of aromatic compounds exhibiting intermediate oscillator strength due to a spatial orbital overlap better than for ketones. For benzene, the lowest energy transition band occurs at 256 nm. The number of methyl substitutions leads to a continuous bathochromic (red-) shift of the transition, see table 3 in chapter 4.3.1.

(a) Molecule orbitals derived from Hückel's LCAO method

Referring to Kasha's notation, electronic transitions in molecules are generally described by the involved molecular orbitals (MO) and can be classified by transition energy. Following Hückel's molecular orbital method ([Hückel 1931]), molecular orbitals arise from linear combinations of the participating atomic orbitals (LCAO method), see sections 2.5 and 2.6. Symmetric combinations lower the orbital energy, therefore leading to binding MOs, whereas antisymmetric combinations raise the orbital energy, therefore producing antibonding MOs.

Strong axial symmetric single bonds called σ-MOs are formed between the combining atoms (i.e. in the direction of the bond, there is no node) by overlap of s or p_z or hybridised sp, sp^2 and sp^3 atomic orbitals. Combination of p_x, p_y or hybridised orbitals of similar symmetry leads to so-called π-MOs, participating in double and triple bonds with a pair of antiparallel spin electrons. Less strong than the σ-bonds, the π-bonds allow for orbital delocalisation, e.g. as found in conjugated systems of double bonds like the linear butadiene or the cyclic benzene molecule. Remaining atomic orbitals not used for MO-construction and occupied by lone pair electrons are called n or nonbonding orbitals. The antibonding π^* and σ^*-MOs are the antibonding equivalents for the respective antisymmetric combinations of the atomic orbitals.

(b) Highest occupied and lowest unoccupied molecule orbitals

The lowest energy transition typically occurs from the highest occupied molecular orbital (HOMO) to the lowest unoccupied molecular orbital (LUMO). Thereby the HOMO level consists of binding σ or π-MOs or non-binding n-MOs, whereas the LUMO level is represented by antibonding π^* or σ^*-MOs. The HOMO-LUMO transition is crucial for photophysical and photochemical processes of organic compounds and depends mainly on the type of chromophoric group contained in the molecules.

Since the absorption cross-section is wavelength dependent and the photon energy is proportional to its frequency, not all possible electronic transitions are accessible via excitation in the middle UV or visible range. Generally, the different electronic transitions can be classified by energy as follows:

$$\begin{gathered}\sigma \rightarrow \sigma^* > \sigma \rightarrow \pi^* > n \rightarrow \sigma^* > \pi \rightarrow \pi^* > n \rightarrow \pi^* \\ \text{far (vacuum) UV} \cdots\cdots\cdots\cdots\cdots\cdots \text{middle UV}\end{gathered} \tag{4.2}$$

(c) Far-UV absorption of saturated molecules with only σ-MOs

Saturated molecules like paraffin, which is an alkane representative from aliphatic hydrocarbons, consist exclusively of methyl (RC–H) and ethyl (RC–C) groups. These groups have only σ-MOs, and in the absence of double bonds or lone pair electrons, promotion to excited states is only possible following the $\sigma \rightarrow \sigma^*$ transition, which can be accessed with high-energy photons for vacuum UV wavelength below 180 nm. For these compounds, the electronic transition is not followed by fluorescence, but by photodissociation. A major part of most combustion fuels consists of such saturated aliphatic hydrocarbons, and is therefore transparent for light in the near UV/visible spectrum. Therefore, alkanes can be used as transparent solvents when probing organic tracer molecules with excitation wavelengths in the middle UV.

Table 2: Electronic transitions of alkanes, alcohols, alkenes and dienes. (a)=[Lee 2001]; (b)=[Cheng 2002]; (c)=[Orkin 1997]; (d)=[Lu 2004]; (e)=[Fahr 1994]; λ_{max} defined as the maximum of the absorption band.

Group	Molecule	Functional group		Transition	λ_{max} / nm	σ_ν / 10^{-20} cm^2
Alkanes	Methane	Methyl	RC–H	$\sigma \rightarrow \sigma^*$	<130 (a)	2000 (a)
	Ethane	Ethyl	RC–C	$\sigma \rightarrow \sigma^*$	132 (a)	2800 (a)
Alcohols	Methanol	Hydroxyl	ROH	$n \rightarrow \sigma^*$	183 (b)	62 (b)
Alkenes (olefins)	Ethylene	Vinyl	RC=C	$\pi \rightarrow \pi^*$	160-180 (c,d)	≈4000 (c,d)
Dienes (diolefines)	1,3-Butadiene	conjugated linear	RC=C–C=C	$\pi \rightarrow \pi^*$	200-220 (e)	≈10000 (e)

(d) Vacuum UV absorption of saturated molecules containing n-MOs

Saturated molecules containing n-MOs besides the σ-bonds allow for $n \rightarrow \sigma^*$ transitions of lone pair electrons. This transition, e.g. found for the hydroxyl group (ROH) of alcohols, requires less energy than the $\sigma \rightarrow \sigma^*$ transition. However, absorption is significant only for wavelength below 200 nm (e.g. methanol, having a maximum absorption at 183 nm, cf. figure 42 and table 2). Alcohols can be used as solvents for fluorescence tracers, but it must be kept in mind the extent of their absorption feature up to wavelength of 220 nm.

(e) Vacuum to middle UV absorption: unsaturated molecules with σ and π-bonds

Unsaturated molecules contain in addition to σ-MOs also π-MOs, leading to double bonds. Thus, between two neighbouring carbon atoms a vinyl group (RC=C) is formed, characteris-

tic of molecules belonging to the group of alkenes (olefins). The π-MO of the vinyl group is responsible for strong (allowed) $\pi \rightarrow \pi^*$ transitions in the vacuum ultraviolet, e.g. for ethylene between 160 and 180 nm, cf. figure 42.

(f) Electron delocalisation in conjugated π-bonds: bathochromic shift

For dienes (diolefines), two double bonds alternate with a single bond to form a conjugated double bond system (RC=C–C=C). Because of the possible electron delocalisation in π-bonds, the presence of a second π-MO allows for additional combinations, generating two binding orbitals π_1 and π_2 with the corresponding antibonding orbitals π_3^* and π_4^*. Compared to the $\pi \rightarrow \pi^*$ transition in alkenes, the $\pi_2 \rightarrow \pi_3^*$ transition of dienes lies lower in energy, leading to a bathochromic (red) shift of the absorption feature.

The bathochromic shift increases with the number of conjugated π-MOs, the wavelength of the corresponding absorption band becoming more and more large. This is true not only for linear conjugated systems (polyenes), but also for cyclic conjugated systems (aromatic molecules). A classic example of absorption red-shift is a series from ethylene over 1,3-butadiene to 1,3,5-hexatriene, presenting a bathochromatic shift of about 40 nm for each added conjugated double bond, whereas the strength of the absorption feature more than doubles at each step.

Due to the bathochromic shift, aliphatic non-saturated molecules with extended conjugated systems could have interesting spectroscopic properties for fluorescence diagnostics. Unfortunately, long chains molecules tend to polymerisation, which makes them unsuitable for diagnostic applications.

(g) Aromatic chromophore – electron delocalisation in cyclic conjugated π-bonds

Hydrocarbons forming a cycle of conjugated p-orbitals without interruption are called aromatic hydrocarbons or arenes if the cycle follows the Hückel rule, i.e. the number of its π-electrons equals $4n+2$, $n = 0,1,2,\ldots$. The simplest arene is the benzene molecule, which is the base of larger aromatic hydrocarbons. The benzene ring owes its stability to resonance structures (Kekulé structures). The energy of the molecule is lowered by the amount of the resonance or delocalisation energy, corresponding to the decrease in repulsion for electrons, which are the farther apart the more delocalised. The p-orbitals form six π-MOs, three of which are binding and three antibonding. The HOMO level consists of two degenerated π-MO, completely filled with electrons.

Table 3: (g)=[Shama 1991]; (h)=[Koban 2004]; (i)=[Bolovinos 1982]; (k)=[Etzkorn 1999]; (l)=[Gattermann 1977]; (m)=[George 1968] ; λ_{max} defined as the maximum of the absorption band.

Group	Molecule	Functional group		Transition	λ_{max} / nm	σ_ν / 10^{-20} cm^2
Aromatics	Benzene	Cyclic	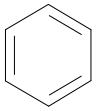	$\pi \rightarrow \pi^*$	179 (i)	31810 (i)
				$\pi \rightarrow \pi^*$	200 (i)	2363 (i)
				$\pi \rightarrow \pi^*$	253 (i)	133 (i)
	Toluene	cyclic, substituted	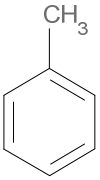	$\pi \rightarrow \pi^*$	184 (g)	17800 (g)
				$\pi \rightarrow \pi^*$	204 (g)	2430 (g)
				$\pi \rightarrow \pi^*$	260 (h)	64 (h)
	1,2,4-Trimethyl-benzene	cyclic, substituted	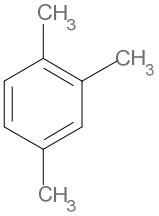		189 (i)	17350 (i)
				$\pi \rightarrow \pi^*$	211 (i)	2563 (i)
				$\pi \rightarrow \pi^*$	275(i, k)	130 (i)
	Naphthalene	Bicyclic	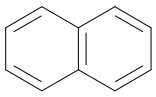	$\pi \rightarrow \pi^*$	210 (l)	54000 (m)
				$\pi \rightarrow \pi^*$	278 (l)	2140 (m)
				$\pi \rightarrow \pi^*$	312 (l)	543 (m)

Benzene has three absorption bands corresponding to three $\pi \rightarrow \pi^*$ transitions at 184, 204 and 256 nm, see table 3. The first transition at 184 nm is a symmetry allowed transition, therefore exhibiting very high transition strength. The other two weak transitions are symmetry forbidden. However, due to vibronic coupling the perfect symmetry is broken by partially violation of the Born-Oppenheimer approximation introducing non-zero contributions to the integral dipole moment of the transition.

(h) Carbonyl chromophore

In figure 41 an approximate orbital correlation diagram is shown for formaldehyde, the simplest molecule containing a carbonyl group. In the outermost shell, the valence electrons, consisting of four electrons from the oxygen and two electrons from the carbon atom, form the binding σ and π-MOs and the non-binding n-MO. In principle, if the radiation matches the energy gap for the electronic transition from a binding to an antibonding orbital, an electron of any of these MOs might be excited. Obviously, the transitions in the absorp-

tion band are classified by the size of the energy gap, i.e. transitions with lower energy gap are found at higher wavelength.

Table 4: (n)=[Appuhn 1997]; (o)=[Limão-Vieira 2003]; (p)=[Nobre 2008]; (q)=[Koch 2008]; (r)=[Koch 2008]; (s)=[Horowitz 2001] ; λ_{max} defined as the maximum of the absorption band.

Group	Molecule	Functional group		Transition	λ_{max} / nm	σ_ν / 10^{-20} cm^2
Carbonyls	Acetaldehyde	Aldehyde	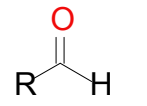	$\pi \rightarrow \pi^*$	166 (n)	6634 (n)
				$n \rightarrow \sigma^*$	182 (n)	3971 (n)
				$n \rightarrow \pi^*$	290 (o)	5.0 (o)
	Acetone	Ketone	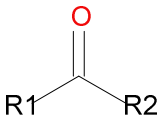	$\pi \rightarrow \pi^*$	153 (p)	6680 (p)
				$n \rightarrow \sigma^*$	195 (p)	2843 (p)
				$n \rightarrow \pi^*$	278 (q)	4.9 (q)
Diketones	Diacetyl	Two conjugate acetyl groups	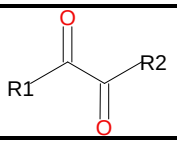	$n \rightarrow \pi^*$	275 (s)	
					450 (s)	

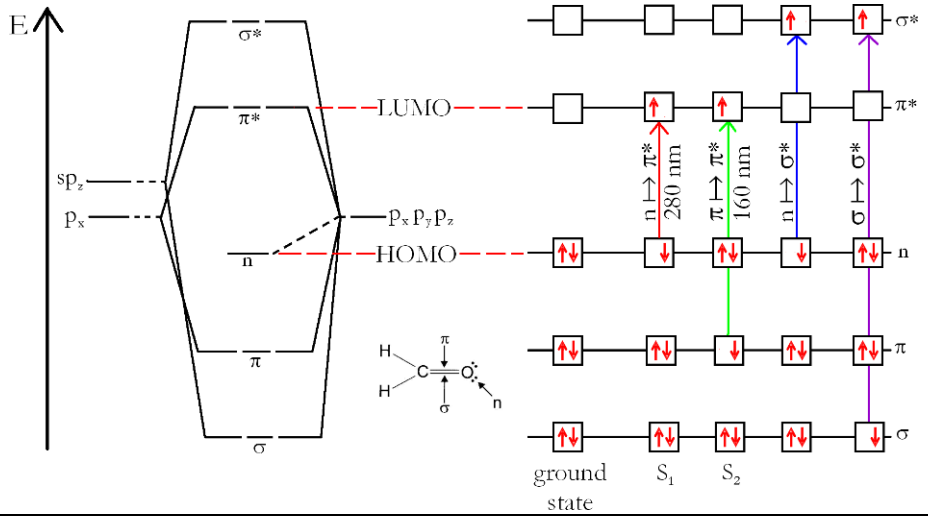

Figure 41: Approximate orbital correlation diagram and possible transitions of formaldehyde as example of molecule with a carbonyl group. The lowest-energy promotion to an electronic excited state is the HOMO-LUMO $n \rightarrow \pi^*$ transition with a maximum cross-section at 280 nm, leading to the first excited singlet state S_1. Only accessible in the vacuum UV is the second excited singlet state with a maximum cross-section at 160 nm. Adapted from [Rohatgi-Mukherjee 1978].

Various electronic transitions exist for the carbonyl group. As for the group of alkanes, $\sigma \rightarrow \sigma^*$ transitions are only to be reached by radiation in the far-UV. The π-MO responsible for the double bond might be accessed for a $\pi \rightarrow \pi^*$ transition at wavelength around

160 nm. However, under practical conditions, radiation below 200 nm is strongly absorbed by air. For molecules from the carbonyl group, the HOMO-LUMO transfer is the $n \rightarrow \pi^*$ transition. A lone pair electron of the n-MO is promoted to the first excited singlet state S_1 for wavelength of about 280 nm.

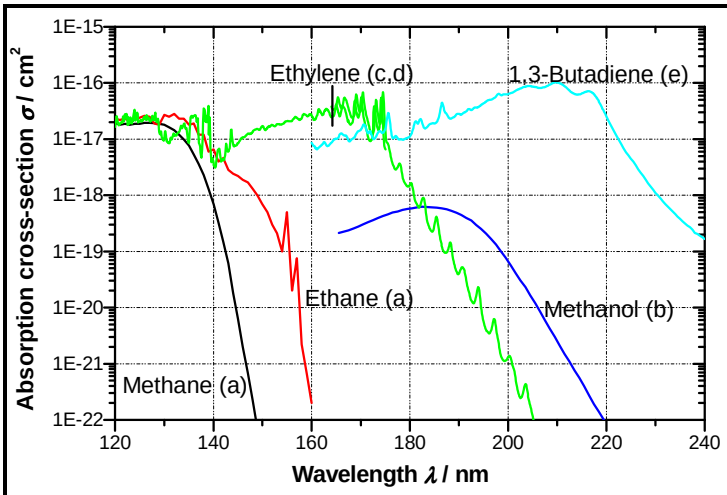

Figure 42: Absorption spectra of gaseous alkanes, alcohols, alkenes and dienes, illustrated by the example of methane, ethane, methanol, ethylene and 1,3-butadiene. Literature references refer to the indices in table 2. All spectra are taken near to room temperature.

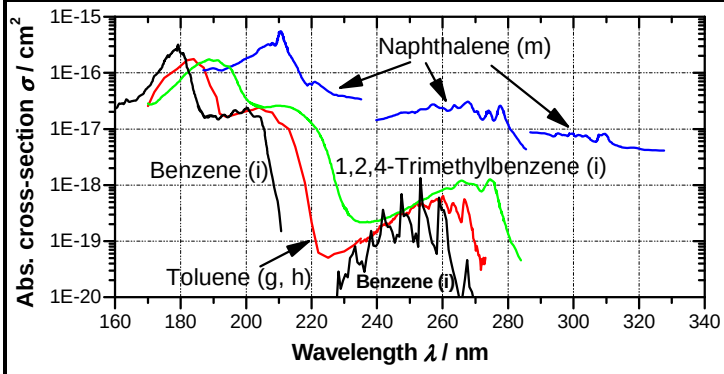

Figure 43: Absorption spectra of gaseous aromatic molecules. Benzene, toluene and 1,2,4-trimethylbenzene from monocyclic aromatics, naphthalene from bicyclic aromatics. All spectra are taken near to room temperature. Literature references refer to the indices in table 3.

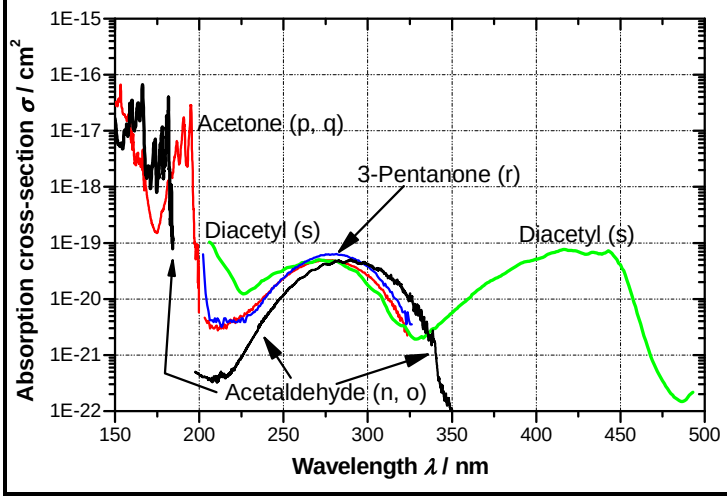

Figure 44: Absorption spectra of gaseous molecules containing the carbonyl group. Acetaldehyde from aldehydes, acetone and 3-pentanone from aliphatic ketones, diacetyl from diketones. All spectra are taken near to room temperature. Literature references refer to the indices in table 4.

4.4 Petroleum-based combustion fuel types

The main combustion fuel types are obtained from petroleum oil refinery products: aviation fuels (kerosene/jet fuel), Diesel fuels (mainly Diesel No. 2), heating oil (mainly fuel oil No. 2), heavy industry and marine oils (mainly fuel oil No. 6) and motor gasoline. Petroleum fuels consist nearly entirely of hydrocarbon molecules, next to small quantities of impurities and additives. The heat of combustion is very high compared to their average molecular mass.

The carbon number range of the chain or ring hydrocarbon molecules contained in different fuels is very instructive, because of its relationship to the distillation curve. Except for the gaseous fuels within the range of C_1 (methane) to C_4 (Butane), higher carbon number fuels present in liquid form under normal conditions. Gasoline (petrol, mogas) is found in the C_4 to C_{12} carbon number range, whereas kerosene globally falls in the range of C_6 to C_{16}, see [Collins 2007]. Depending on the kerosene subtype, more volatile kerosene types like JP-4 are settled between carbon numbers of C_4 to C_{16}, less volatile kerosene types like JP-5 between C_{10} and C_{19}. JP-8 kerosene, further known as the Jet A1, is also a less volatile kerosene type, mainly developed for commercial use. Diesel fuels with carbon numbers from C_8 to C_{21} are quite similar to fuel oils used for heating, which are less refined, hence containing heavier hydrocarbons from C_{15} to C_{22}. Oils with carbon numbers from C_{18} to C_{34} are used for lubrication as motor oils, still higher carbon numbers oils as hydraulic fluids.

4.4.1 Chemical affinity between organic tracers and commercial fuel types

For combustion processes related to transport, the fuel mostly used for aviation is the commercial kerosene "Jet A1", for automobiles and trucks the medium volatile "Diesel No. 2" or gasoline and for railway and ship transport the low volatile "Diesel No. 4". All of these fuels are mixtures of several hundreds of species, and the exact composition is often varying from one lot to the next or even within a specific lot with time, when exposed to light and oxygen. Global values and constituents are regulated by fabrication norms, e.g. the ASTM D 1655 for Jet A1 fuel. Standard procedures for the identification of the fuel constituents are the PONAU and the PIANO methods (acronyms of the first letter of detected hydrocarbons from paraffins, olefins, naphthenes, indanes, aromatics and unknowns), both using gas chromatography.

Table 5 shows a comparison for the main characteristics of kerosene JP-8/Jet A1, Diesel no. 2 and gasoline. These three fuel types nearly deliver the same combustion heat. Since kerosene JP-8/Jet A1 is a less wide cut than Diesel No. 2, the distillation curve of the Diesel fuel ends at higher temperature. Gasoline is much more volatile as the boiling point range is shifted to lower temperatures due to the carbon number range limited to C_{14}.

All of these fuels contain a quite large amount of aromatic compounds. Aromatic molecules directly present in the fuel or generated as products by the combustion process may cause toxicity problems during fuel handling as well as for the health impact of the exhaust gases. Exposure and toxicity studies for JP-8 kerosene and Diesel No. 2 are reported by [Topal 2004].

Many of the aromatic constituents of commercial fuels are excitable via the $\pi \rightarrow \pi^*$ electronic transition in the middle UV (section 4.3.1), therefore often called naturally present tracers.

Table 5: Properties and chemical composition of petroleum based combustion fuels: kerosene, Diesel and gasoline. (a)=[Rakopoulos 2004]; (b)=[Spadaccini 1982]; (c)=[Topal 2004]; (d)=[Edwards 2001]; (e)=[Faiz 1996]; (f)=[Burri 2004]

Property	Kerosene JP-8 / Jet A1	Diesel No.2	Gasoline
Approx. Formula	$C_{11}H_{21}$ (a)	$C_{12}H_{26}$ (a)	~ C_8H_{18}
Cetane number	47 (a)	52 (a)	0 – 5 (e)
Research octane number	–	–	92 – 98 (e)
Boiling point range / K	432 – 538 (b)	428 – 622 (b)	310 – 478 (e)
Net heating value / kJ/kg	43217 (d)	42500 (a)	44000 (e)
Stoichiometric fuel-to-air ratio	12 (c)	14.7 (c)	14.7 (e)
Density range / kg/l (c)	0.75 – 0.84 (c)	0.82 – 0.86 (c)	0.72 – 0.78 (e)
Aromatics /vol. %	18 (d)	27.5 (b)	36.2 (f)
Naphthenes / vol. %	20 (d)	15.3 (b)	4.8 (f)
Paraffins / vol. %	60 (d)	54.8 (b)	42.0 (f)
Olefins / vol. %	2 (d)	2.4 (b)	12.1 (f)

4.4.2 Difficulties of interpretation of the fluorescence of mixture fuels

Unfortunately, the direct use of fuel fluorescence from naturally present fluorescence tracers is not straight forward. For multicomponent fuels like kerosene, Diesel and gasoline, the fluorescence signal comes as overlaid signal pattern from the emission of different types of simultaneously excited aromatic species, each presenting individual photophysical behaviour. In the gas phase, the radiative emission competes with radiationless deactivation pathways like internal conversion (IC) and intersystem crossing (ISC), where the rates of IC and ISC are intrinsic properties of each species and the external environmental conditions. The local temperature in combustion chambers is strongly affected by the heat of adiabatic compres-

sion as well as of the chemical reaction. The non-radiative depopulation rates often change with the quantum number of the vibrational state, from which the deactivation occurs. Higher vibrational states are populated for higher temperatures, coupling the efficiency of IC and ISC to the local temperature condition. Further, radiationless deactivation occurs from collisional quenching. The quenching efficiency strongly depends on the gas composition and on the pressure having impact on the number density of collisional partners. Oxygen quenching is known to be very efficient for the deactivation of aromatic molecules, very much limiting the fluorescence yield to low levels, especially under engine relevant pressure conditions.

4.5 Surrogate mixtures: representation for real fuels

The weak point of fluorescence experiments based on real fuel is generally the poor knowledge of the exact fuel composition. Thus, surrogate mixtures are composed to replace the real fuel by a well-composed mixture having similar properties.

For the case of aviation or rocket fuels, [Edwards 2001] distinguished between physical and chemical types of surrogates fuel. Physical surrogates are designed to be representative of the physical fuel properties of interest for the respective experimental study. Sometimes it is possible to work with a very limited surrogate composition, e.g. dodecane and JP-7 have similar density, viscosity, thermal conductivity and heat capacity over a temperature range from about 100 to 650 °C.

If the volatility and evaporation behaviour of the real fuel is the property under investigation, the surrogate fuel is usually multicomponent in order to represent the individual volatility classes, for which vaporisation occurs on different time scales. An example for such a surrogate design is given in [Wood 1989]. A surrogate comprised of 14 pure hydrocarbons was formulated based on the distillation curve and compound class composition of the real fuel petroleum-derived JP-4. Similar behaviour between the surrogate and the JP-4 fuel was achieved for non-reacting droplet size and velocity measurements as well as for the atomisation characteristics. Nowadays, standardised physical property codes are used to generate surrogate compositions valuable over a wide range of temperature and pressure.

Chemical surrogates are referred to compositions characteristic of the main chemical properties of the real fuel, e.g. in order to simulate the combustion properties. The real fuel chemical-class composition and average molecular weight is therefore respected. Besides, the proportions of organic groups like aromatics, naphthenes and paraffins are reproduced from the real fuel to the surrogate.

[Edwards 2001] qualified the suitability of surrogates to the different fields of applications. They noted that single-component surrogates are at most adapted to trace the heat

transfer of a single phase by representation of the critical temperature. Physical multicomponent surrogates, fitting the distillation curve of the real fuel, might represent the behaviour of vaporisation, injection and mixing in non-reacting environments. Chemical surrogates matching the major chemical classes of the real fuel are, however, dedicated to simulate properties like the fuel heat release, the flame speed, the ignition and the thermal oxidation. A major problem of the surrogates is the difficulty to include the enhancing and damping effects of additives used in the real fuel. Real limitations are further found for modelling thermal depositions and soot formation from combustion, since these processes are driven by trace fuel species, which cannot be captured in any accurate form by a surrogate. In contrast, NO_x emissions might be traced if the surrogates are matching important temperature driving chemical classes, the emissions of polycyclic aromatic hydrocarbons (PAH) by matching major and minor classes contributing to molecular growth.

Several references are found for surrogate fuel definitions and their applications, e.g. the study of oxidation and low to medium temperature reactivity of jet and Diesel fuels [Lenhert 2007, Natelson 2008], the study of jet fuel detonation [Strelkova 2008], the measurement of jet fuel ignition delay times [Vasu 2008]. A surrogate fuel blend comprising a paraffin and a mono-aromatic representative was chosen to imitate the sooting behaviour of kerosene [Moss 2007]. A wide review of earlier studies of ignition, oxidation, and combustion behaviour of kerosene by means of surrogates is given in [Dagaut 2006].

4.6 Fluorescence experiments on tracers doped to surrogates

The complexity of real fuel fluorescence is linked to the multiplicity of compounds being at its origin. The complex interpretation of the fluorescence signal requires the identification of the fluorescing species and their individual photophysical properties, which are dependent on temperature, pressure and species concentration. Instead, the common method is to replace the real fuel by a non-fluorescing surrogate, which is then doped with a fluorescence tracer of well-known photophysical behaviour. Often, the surrogate is mono-component from the group of alkanes, e.g. dodecane or isooctane, transparent for ultraviolet excitation. Within such a configuration, the interpretation of the fluorescence signal is simplified and enables strategies to infer the species concentration or temperature from the measured signal. The "tracer seeded to surrogate fuel" concept seems to have imposed itself upon fluorescence diagnostics, when applied to numerous applications with all types of flows, jets, sprays or flames in research of fundamental and/or industrial interest, e.g. the fuel evaporation and mixing in combustion engines.

4.6.1 Single-tracer techniques for vapour concentration

A wide variety of fluorescing species has been used as tracer for concentration measurements. For applications to internal combustion engines, these tracers are usually added to an alkane surrogate fuel. The tracer species are chosen with regard to the engine operating conditions mostly from species containing either the carbonyl or the single-ring aromatic chromophore. The simplest measurement strategies are relying on the fluorescence signal of only one tracer species. This implies, that maximal one single parameter can be inferred from the fluorescence signal, whereas the other parameters of virtual impact on the signal must be known from other sources. A large number of studies thus obtain the tracer concentration based on simplifications made for the temperature correction, while eventual quenching influences are often excluded via the choice of a ketone tracer.

Early work reported on measurements with carbonyl tracers was of more or less qualitative nature. Even if in some cases many photophysical properties were known [Lozano 1992], research often concentrated on practical problems like toxicity, boiling point, thermal stability or simply the strength of fluorescence signal.

Acetaldehyde has been used as marker for the fuel distribution up to the flame front, e.g. seeded to stoichiometric propane/air mixtures in an internal combustion engine simulator [Arnold 1990b] or to laminar and turbulent methane flames [Tait 1992], both using 308 nm excitation wavelength. Arnold did not try to further quantify the fluorescence signal, because they assumed independence from pressure due to complete relaxation of vibrational states for a pressure range relevant to combustion engines. For the case of acetaldehyde vapour, Tait observed negligible temperature dependence with excitation at 308 nm, whereas the fluorescence of acetone vapour increased by a factor of more than 1.5 from 300 to 800 K.

Because of the significant toxic and carcinogenic properties of acetaldehyde, biacetyl was proposed as alternative tracer, e.g. to represent the fuel distribution of gasoline in SI engines [Baritaud 1992]. They seeded biacetyl to isooctane fuel to study the mixing behaviour in an engine with optical access, exciting the tracer at 355 nm. Only a minor quenching influence of oxygen was reported, after observation of 8 % loss of fluorescence signal measured in air compared to data obtained in pure nitrogen atmosphere. The fluorescence temperature dependence was studied up to 425 K. The application of the biacetyl PLIF method to the model engine produced results, which were "quantitative in relative value". As a disqualifying property of biacetyl for the use with isooctane the chemical decomposition of the tracer was observed, once seeded to the host, exceeding 11 % of loss in fluorescence signal per hour, even if kept under ambient conditions.

[Lozano 1992] studied possible candidates presenting high vapour pressures as possible tracers in PLIF concentration measurements with gaseous flows. They compared the properties of acetaldehyde, biacetyl and acetone and summarised the relevant characteristics for

their use as tracers. Acetone was found to be the most suitable tracer for concentration measurements in gaseous flows, based on its low toxicity, high vapour pressure and the strongest fluorescence signal. Biacetyl seemed less attractive due to its absorption feature settled between 340 and 470 nm, more difficult to access by commercial lasers, and due to its smell. Since then, acetone has been frequently used as marker suited for gaseous flows ([Lozano 1994], [Bryant 1997], [King 1997]).

When, like in the study of Baritaud, a fluorescence tracer is added to isooctane for the purpose of studying the gasoline fuel mixing in internal combustion engines, biacetyl is the better choice from the point of view of the boiling point (BP), the biacetyl BP (88 °C) much nearer to the BP of isooctane (100 °C) than those of acetone (56 °C). However, 3-pentanone is even more suitable with its BP of 101 °C. [Arnold 1993] and [Neij 1994] seemed to be the first to apply 3-pentanone as tracer in internal combustion engines.

[Arnold 1993] studied fuel distributions and the combustion process in a four cylinder, 16-valve spark-ignition engine. They observed the fluorescence of commercial gasoline to be not quantifiable due to its multicomponent aspect. Hence, they used isooctane as fuel seeded with 3-pentanone as fluorescence tracer excited at 308 nm. From their own, not reported spectroscopic measurements they believed the fluorescence quantum yield of 3-pentanone to be independent from pressure and temperature at least for the engine operating conditions. Quenching was assumed to be not important. The fuel intake was studied for different equivalence ratios simultaneously to the distribution of hydroxyl radical (non resonant excitation at 248 nm).

Many single-tracer methods can be found, see the literature examples given in table 6. Not all of these studies truly infer the measured tracer fluorescence to its local concentration with respect to the necessary corrections to be made for varying local temperature and pressure. Thorough parameter studies like [Smith 2007] for biacetyl are quite exceptional cases. Thus, some references must be said to be rather examples of fuel visualisation, primarily taking profit of the insensitivity of oxygen quenching on ketone tracer fluorescence. This enables, in contrast to the direct use of strongly quenched real fuels like gasoline, the possibility of fuel distribution visualisation under engine conditions, e.g. [Arnold 1993, Neij 1994 and Johansson 1995]. A further (but somehow prevalent) approach is to proof the negligibility of a scalar parameter for the range of interest ([Baritaud 1992, Tait 1992 and Lawrenz 1992] for the neglect of temperature and/or pressure) or for the field of observation ([Herold 2007] for the neglect of temperature) within the measurement. Finally, the engine operating conditions are often reproduced in a test cell with homogeneous tracer concentration in order to find a point of calibration to each specific condition, i.e. changing parameters of temperature and pressure for different crank angles ([Lawrenz 1992, Yan 2007, Herold 2007) and/or different overall equivalence ratios ([Neij 1994 and Johansson 1995] relating exhaust gas analysis to equivalence ratio fed to the engine operated under homogeneous fuel distributions, [Hishinuma 1996 and Sercey 2005] using a look-up-table relating equivalence

ratio to averaged LIF intensity obtained from calibration by operating the engine with uniform mixture concentration). It must be clearly stated, that local parameter fluctuations are lost when averaging of the fluorescence data over the image is performed within the calibration procedure. This type of calibration implies the assumption that the local parameter variations may be the same for the measurement and the calibration cycle. When sometimes the influence of the local parameter variation is explicitly meant to be included to the calibration procedure, however, in the end this parameter is often not accessed via local measurement, but instead only calculated. Iterative approximations starting from a first guess are forced to converge towards an averaged condition known from boundary values. A procedural example is the fit of local temperature to the actual crank angle using a polytropic exponent derived from the pressure-volume relationship $p_1 v_1^{\alpha} = p_2 v_2^{\alpha}$ and the inlet conditions by $pv = nRT$ with respect to the measured cylinder pressure trace (e.g. [Berckmüller 1994] using the temperature dependence of 3-pentanone measured on their own or [Salazar 2009] using the temperature dependence of acetone studied by [Thurber 1998] to correct for the local temperature).

Table 6: Single-tracer methods based on a single fluorescing dopant added to a surrogate or parent fuel

Tracer	Mixed to fuel	Exc.	Application / observed effect / remarks	Reference
Acetaldehyde	Stoichiometr. propane/air mixture in internal combustion simulator	308 nm	Assumption of pressure independent fluorescence due to complete relaxation of vibrational states for the relevant pressure range of combustion engines.	Arnold 1990b
Acetaldehyde	Pure or added to parent fuels like methane or propane	308 nm	Measurement of parent fuel fraction in laminar and turbulent methane flames seeded with acetaldehyde; assumption of negligible fluorescence temperature dependence.	Tait 1992
Acetone	5 vol.-% tracer in isooctane	266 nm	Mixing process of air and fuel in DI gasoline engine based on fluorescence intensities changing with temperature and pressure on crank angle; calibration to known fuel-to-air ratios for homogeneous charge.	Sercey 2005
Acetone	Below 1 vol-% in hydrogen	266 nm	Single-cylinder research engine operated with hydrogen; in-situ calibration and correction for the effect of local temperature on the fluorescence measurement.	Salazar 2009

Tracer	Mixed to fuel	Exc.	Application / observed effect / remarks	Reference
Biacetyl	2 vol.-% in isooctane	355 nm	Visualisation of gasoline distribution in port injection SI engines; assumed less than 8 % of the LIF quenched by air; temperature dependence smaller than 1.6 % per 10 °C; negligible pressure dependence.	Baritaud 1992
Biacetyl	10 vol.-% in isooctane	355 nm	High-speed measurement of fuel concentration for varying pressure and temperature conditions, quantitative equivalence ratio maps for fuel injection within single cycle in a SI direct-injected engine; thorough study of LIF signal strength of biacetyl varying substantially over a wide range of temperatures and pressures.	Smith 2007
2-butanone	Pure as fluorescing surrogate for gasoline	308 nm	Fuel-to-air ratio throughout the intake and compression stroke in a transparent SI Engine calibrated to data from bomb experiments; tracer chosen for vapour characteristics similar to gasoline, but insensitive to oxygen quenching; insensitivity to pressure changes in the range of interest for engine applications.	Lawrenz 1992
3-pentanone	6 vol.-% in isooctane	308 nm	Fuel distributions and combustion process in a four cylinder, 16-valve Otto engine (simultaneous to LIF of hydroxyl radical); pure visualisation and qualitative results, no correction for temperature or pressure.	Arnold 1993
3-pentanone	25 vol.-% in isooctane	308 nm	Imaging the in-cylinder fuel concentration in a firing SI engine for different crank angles in the inlet and compression stroke; prior study of relative fluorescence for six aldehydes and ketones from 300 to 900 K shows acetone, butanone and pentanone linear dependent from T.	Berckmüller 1994
3-pentanone	2 vol.-% in isooctane	248 nm	Imaging of the fuel distribution within an operating SI engine; calibration of LIF signal to images of known (homogeneous) fuel concentration; signal attenuation of 3-pentanone/isooctane mixtures over several hours attributed to the decomposition of 3-pentanone.	Neij 1994 and Johansson 1995
3-pentanone	20 vol.-% in isooctane	266 nm	Quantify the unmixedness of the in-cylinder fuel distribution in a gasoline HCCI engine; fluorescence temperature dependence was ignored due to isothermal probe volume; LIF from port injection related to average LIF (known number density) from homogeneously fuelled case at same crank angle.	Herold 2007

Tracer	Mixed to fuel	Exc.	Application / observed effect / remarks	Reference
3-pentanone	20 vol.-% in isooctane	266 nm	Planar fuel distribution in a direct injection SI engine; the high 3-pentanone concentration was chosen with respect to the results from [Davy 2003] (3-pentanone in low concentrations has faster evaporation rate than isooctane when the two are mixed); calibration for quantification of molecular concentration inside the cylinder to LIF image by generating a homogeneous fuel-air mixture in the cylinder.	Yan 2007
Dimethyl-aniline (DMA)	0.2 vol.-% in isooctane	248 nm	Mixture distribution of fuel in a single cylinder SI engine; boiling point of DMA corresponds to 60 % distillation temperature of gasoline; calibration of LIF signal to images of known (homogeneous) fuel concentration for different equivalence ratios and crank angles; results were related to fuel-to-air ratio.	Hishinuma 1996

4.6.2 The non-ideal tracer …

Besides for favourable fluorescence photophysical properties, the choice of a specific tracer is often motivated by nearby boiling points of tracer and fuel. The use of fluorescence tracers for fuel diagnostics is then questioned about several issues:

- Is the tracer representative of the fuel properties/behaviour of interest?
- Does the tracer impact the quantities/phenomena under investigation?
- Is a tracer/surrogate mixture stable during storage?

(a) Are tracers representatives for the evaporation of real fuels?

The evaporation of fuel droplets might be characterised by the Peclet number (compare [Han 2002a]), i.e. the ratio of surface regression to liquid-phase mass diffusion. Two general domains may be distinguished, the first of which is the limit for high Peclet number with evaporation too fast to allow for efficient mixing, the droplet thus being frozen in composition. In this case, the tracer could be freely chosen without looking for volatility differences, coevaporation being guaranteed. The second domain, however, applies for a large number of situations, especially for lower temperature conditions or compression rates, where the limit for low Peclet number is relevant. For this case, there is sufficient time for mixing, leading to preferential evaporation of the more volatile components due to an equilibrium established at the phase interface as described by Raoult's law.

Motivated by the subject of preferential evaporation for applications with low Peclet number, [Han 2002b] focussed on mixtures of 3-pentanone and isooctane. They pointed out, that especially when added in low concentrations to the mixture, 3-pentanone evaporates significantly faster than isooctane, which is in contradiction to what might be assumed with regard to their similar boiling points and vaporisation heats. Of course, representation of spray evaporation and of fuel-air mixing within engine applications by inferring the fuel concentration from the tracer fluorescence signal would become problematic.

Using an apparatus designed for slow evaporation of liquid mixtures, Han et al. correlated the measured vapour phase fluorescence signal from isooctane and several ketones to the remaining liquid mass fraction. In this way they were able to propose a ternary mixture, for which a heavier ketone like 3-hexanone, when added to the mixture of 3-pentanone and isooctane, might to some extent compensate for the early evaporation of the lighter 3-pentanone.

In a further study, [Han 2002a] showed, using the same apparatus, how cautious choice of components and molar fractions allows the design of tracer surrogate mixtures with respect to a fluorescence signal tracing correctly the total evaporation of the mixture. They found a mixture of cyclohexane and isooctane (representatives for different fractions of gasoline) with three ketones (2-butanone, 3-pentanone and 3-hexanone) to be such a well-designed mixture to a large extent.

But apart from the boiling points of the individual components, their specific fraction in the mixture was of utmost importance. This might lead, as for the case of a 9/1 mixture of cyclohexane and 3-pentanone, to an azeotropic composition, even for quite different boiling points. There is, after all, a principle problem for the use of azeotropic mixtures for the condition of coevaporation, the azeotropic composition being clearly dependent on temperature. The mixture is prepared, generally in atmospheric environment, and must be azeotropic for the operating temperature during the measurement. This temperature should thus not change in order to stay within azeotropic conditions.

The same research group reported in [Davy 2003], that the 3-pentanone mole fraction corresponding to the azeotropic point in a mixture with isooctane changes with temperature from 0.367 at 300 K to 0.64 at 500 K. Except for the case of diffusion-limited evaporation, where non-ideal effects of mixture behaviour have no impact, the liquid will rapidly decrease in its concentration of 3-pentanone due to preferential tracer evaporation if the 3-pentanone mole fraction in the mixture is less than 0.367 at 300 K. As a consequence, the new 3-pentanone mole fraction will be even farther from the azeotropic point, and the preferential tracer evaporation thus be reinforced.

Many of the studies using 3-pentanone as fuel tracer in isooctane are restricting the tracer concentration to a limit of less than 10 % by volume in order to avoid strong attenuation of the laser light over the pathway in the probe volume. This is, however, a necessary

provision to guarantee a good signal-to-noise ratio and dynamic range, both suffering within strongly attenuated regions. Further, as also mentioned by Davy et al., if the mixture is prepared with respect to the azeotropic point, the high tracer concentration alters substantially other physical properties like the surface tension and the viscosity compared to pure isooctane. Consequently, the behaviour of liquid atomisation and break-up will be modified due to a change of mean droplet diameters.

Apart from the coevaporation of tracer and surrogate, doing diagnostics based on tracer/surrogate mixtures might be problematic with regard to combustion conditions implying to a large degree the low-temperature chemistry of the fuel. [Sick 2009] presented results from a computational model studying the fuel consumption within the combustion of tracer/fuel mixtures like biacetyl/isooctane in situations similar to homogeneous charge compression ignition (HCCI) or Diesel engines. Tracer and fuel actually turned out to have unproportional consumption rates, even if the delay of total disappearance was almost the same.

The impact of tracer adding on the combustion performance was checked by [Zhang 2004] using isooctane with either 3-pentanone or toluene as fluorescence dopant in a direct injection spark ignition gasoline engine operated with nearly homogeneous charge. For the tested tracer concentrations (5 or 15 % by volume for 3-pentanone and 3 % by volume for toluene), no significant negative impact was found with regard to parameters like peak pressure, location of peak pressure, indicated mean effective pressure and peak burn rate, when compared to pure isooctane for various equivalence ratios.

[Zhang 2006] tested the stability of tracer/fuel mixtures (either 15 % by volume 3-pentanone or 10 % by volume biacetyl in isooctane) during storage in ambient atmosphere and at about 50 °C. From their investigations it was concluded that preferential evaporation is the mechanism causing the observed decrease in fluorescence signal, and not chemical decomposition, in contrast to what was supposed by e.g. [Johansson 1995].

4.6.3 Fuel-to-air ratio laser-induced fluorescence (FARLIF) measurements

It is important to state, that one can modify the equivalence ratio in two different ways: either the fuel or the oxygen concentration can be varied, while the respective other quantity is kept fixed. Above in table 6, many of the cited studies report from local equivalence or fuel-to-air ratio measurements by means of tracer PLIF. However, for all these studies, the oxygen concentration did not substantially change from a known level, i.e. the local equivalence ratio was practically inferred from the measured fuel concentration.

Carbonyl tracers are almost insensitive to oxygen quenching. Therefore, single-tracer diagnostics based on the fluorescence of ketones will not be sufficient if the oxygen concen-

tration underlies significant variations throughout the measurement. A typical engine example for substantially changing oxygen partial pressure is given for exhaust gas recirculation (EGR).

Aromatic tracers are subject to very efficient oxygen quenching, especially if the size of their singlet-triplet energy gap ΔE_{ST} exceeds the energy needed to promote triplet oxygen to its excited singlet state (cf. section 2.12.5). Being a natural constituent of gasoline and, in addition, much less hazardous to health than benzene, toluene is a quite obvious choice, when looking for potential tracers capable of oxygen sensing.

In this context, at room temperature and for 248 nm excitation [Reboux 1994] observed the increase of toluene fluorescence signal being proportional to the fuel-to-air ratio, and furthermore, the slope staying the same for all pressures higher than 3 bar, i.e. quenching through oxygen then becomes the dominating channel of deactivation. This corresponds to $S_f^0 / S_f^q = k_{SV} n_q + 1$ becoming $S_f^q \propto n_{abs} / n_q$ for $k_{SV} n_q \gg 1$ (cf. section 2.12.2). For lower pressures, the oxygen quenching competes with other non-radiative pathways and the slope depends on the pressure.

Regarding more precisely, the predominantly quenched fluorescence is not simply proportional to the fuel-to-air ratio, but depends further on a function $g(T,p) = \sigma_{abs} \phi_f^0 / k_{SV}$. With $k_{SV} = \tilde{k}_q / k_{tot}$ and $\phi_f^0 = k_f / k_{tot}$, this leads to $S_f^q \propto \sigma_{abs} \left[k_f / \tilde{k}_q \right] \cdot n_{abs} / n_q$, the bracketed term being the ratio of the fluorescence rate to the quenching rate coefficient. The absorption cross-section depends mainly on temperature and is rather independent from pressure. Fluorescence rate and quenching rate coefficient may both individually depend on temperature and pressure condition. Reboux et al. assumed that the fuel-to-air ratio could be inferred from the quenched toluene signal at least for engine relevant pressures by separating the influence of temperature via an experimentally accessible function $g(T)$. They obtained such a calibration from a measurement of the mean fluorescence signal over the crank angle within the compression stroke of their engine.

The method proposed from Reboux et al. fast became popular, known as the toluene fuel-to-air ratio FARLIF concept, and the assumption, that temperature influence was separable via calibration, covered the lack of virtual high temperature verification. Thus, the concept was applied, as e.g. by [Sacadura 2000], without challenging its validity. In fact, as later analysed by [Koban 2005b], the FARLIF concept fails at increased temperature and only seemingly worked well for applications, where equivalence ratio was essentially varied via the fuel concentration, while the oxygen concentration remained nearly unchanged. This is not truly astonishing since a simple ketone tracer would have done the same, namely measure the concentration of the fuel. [Kaiser 2003 and Kaiser 2005] proposed the use of 1-methylnaphthalene as a tracer working with the FARLIF concept. Natural constituent at a level of 5 % in the target jet fuel JP-8, 1-methylnaphthalene has a boiling point near to that

of the chosen surrogate n-dodecane. The same as for Sacadura et al., Kaiser et al. varied the fuel-to-air ratio via the tracer concentration with oxygen partial pressures remaining nearly unchanged.

The work of [Koban 2005d] can be understood as an answer to the remaining questions related to the non-validated high-temperature behaviour of toluene fluorescence quenching and the applicability of the FARLIF concept as proposed by Reboux et al. An extensive study of the temperature influence was realised both in pure nitrogen and for variable oxygen partial pressures under ambient total pressure for 248 and 266 nm excitation. The results allowed for defining a semi-empirical fluorescence model, which was presented in [Koban 2005c and Koban 2005b] with the following results. In case the vibrational excitation is high, quenching does not remain the dominant deactivation mechanism of the excited toluene. Consequently, for high vibrational excitation (248 nm and 650 K) the fluorescence intensity was shown to level off for rising fuel-to-air ratio, the latter varied by changing the oxygen concentration, whereas for low vibrational excitation (266 nm and 325 K) the FARLIF condition was fulfilled. The misjudgement of Reboux et al. was due to the neglect of the increasing efficiency of intramolecular deactivation pathways for higher vibrational excitation.

An experimental check of the FARLIF validity for 248 nm excitation was reported by [Frat 2004 and Frat 2007], and for 266 nm excitation by [Scholz 2006], both carrying out cell studies similar to [Reboux 1994]. As well Frat et al. as Scholz et al. changed the fuel-to-air ratio via the fuel concentration, i.e. these studies were unsuitable as tests for the FARLIF concept towards applications with significant variation of the oxygen concentration. Frat et al. showed, that the pressure limit reported by Reboux et al. was chosen too low for higher temperatures. Scholz et al. proved, just as predicted by [Koban 2005b], that the FARLIF validity is extended towards higher temperatures for 266 nm excitation compared to the results of Frat et al. for 248 nm. Furthermore, Scholz positively tested the applicability of the FARLIF concept to "colourless" gasoline (near-standard gasoline without yellow-brown bitumen components) up to 500 K for $p \geq 1\,\mathrm{bar}$ and fuel-air mixtures of $\lambda > 0.1$.

Table 7: Single-tracer methods dealing with fuel-to-air ratio LIF (FARLIF)

Tracer	Mixed to fuel	Exc	Application / observed effect / remarks	Reference
Toluene	5 vol.-% in isooctane	248 nm	Spectroscopic study of the mixture isooctane/toluene in a cell; the fluorescence signal increases linearly with fuel-to-air ratio for all the pressures from 0.5 to 8 bar, and further the slope stays always the same for pressures higher than 3 bar; the cell study from Reboux was done for ambient temperature; the FARLIF concept was extrapolated to engine relevant conditions based on a temperature calibration over crank angle within the compression stroke of the engine.	Reboux 1994
Toluene	5 vol.-% in isooctane	248 nm	Two-dimensional visualisation in optical direct injection SI engine using the FARLIF concept as proposed from [Reboux 1994]; characterisation of the fuel-air distribution during the compression stroke and the combustion phase; the concept is followed without challenging its validity to higher temperature conditions.	Sacadura 2000
1-methyl-naph-thalene	5-10 vol.-% in dodecane (JP-8 surrogate)	266 nm	As FARLIF tracer dominated by oxygen quenching used in a catalytic mesoscale burner operating with the electrosprayed surrogate.	Kaiser 2003 and Kaiser 2005
Toluene	vapour (about 5 mbar) seeded to flow through heated test cell	248 and 266 nm	Study of fluorescence dependence on temperature and oxygen concentration for quantitative fuel tracer imaging and development of a semi-empirical fluorescence model; toluene is strongly quenched by oxygen; FARLIF concept as proposed by [Reboux 1994] breaks down, since oxygen quenching is not dominant at elevated temperatures; corrected signal interpretation is demonstrated for various practical cases.	Koban 2005c and Koban 2005b
Toluene or gasoline	5 vol.-% in isooctane or pure gasoline	266 nm	FARLIF-concept holds for exc. wavelength of 266 nm for fuel-air mixtures with $\lambda \geq 0.2$ at pressures between 1.5 bar and 10 bar and temperatures at least up to 433 K; as well for a near-standard gasoline for $\lambda \geq 0.1$, $p \geq 1$ bar and temperatures at least up to 500 K; longer wavelength excitation at 266 nm is the better choice for FARLIF with toluene-isooctane as predicted by [Koban 2005b].	Scholz 2006
Toluene	0.3 vol.-% in isooctane	248 nm	Extension of [Frat 2004]; the validity of the FARLIF technique is checked for applications to engine studies for extend temperature range in heated cell from 373 – 523 K and 0 to 10 bar; for temperatures higher than room temperature FARLIF condition is fulfilled only for higher pressures than expected from [Reboux 1994].	Frat 2007

The semi-empirical fluorescence model described in [Koban 2005c] relies on cell experiments studying the wavelength, temperature and oxygen quenching influence exclusively for atmospheric pressure. [Devillers 2009] tested the behaviour of toluene fluorescence in air and nitrogen with 248 nm excitation in an optical engine. Temperature and pressure increased simultaneously within an adiabatic compression stroke from 20 °C and 1 bar to 500 °C and 23.6 bar. Similarly, [Wermuth 2005] made an exhaustive study for the combined temperature and pressure dependence of the absorption and fluorescence of toluene, acetone, 3-pentanone, and biacetyl within adiabatic compression from about 1bar and 300 K to about 8 bar and 700 K.

4.6.4 Ratiometric measurements in inhomogeneous flows

The measured tracer fluorescence signal is a function of instrumentation properties from both the detection and the excitation channel, compare equation (2.60). For single-wavelength measurements, a number of disturbing influences must be accounted for by calibration, such as the non-uniformities of the CCD response or the inhomogeneous intensity distribution of the excitation source. Further, the fluorescence intensity is directly proportional to the local number density of the fluorescence tracer. It was shown in equation (4.1) that the number density can be separated to a temperature and a pressure trace if the molar fraction of the fluorescence tracer is the property of interest.

Although several arguments like the minimisation of instrumentation costs and the simplicity of the optical setup are clearly in favour of single-wavelength fluorescence techniques, sometimes a ratiometric detection strategy is indicated. This might be the case for inhomogeneous conditions, i.e. the tracer concentration and the temperature are both locally variant parameters within the measurement volume. Another relevant case is the dynamical change of pressure and temperature, e.g. for adiabatic compression.

Following a ratiometric approach, two fluorescence images are acquired simultaneously covering the same measurement volume via individual detection channels, see equation (4.3). The measured signal ratio is a function, which can be split into several parts.

$$\frac{S_{f,\alpha}}{S_{f,\beta}} = \frac{\{\eta_D \Omega V\}_\alpha}{\{\eta_D \Omega V\}_\beta} \cdot \frac{\{P/T\}_\alpha}{\{P/T\}_\beta} \cdot \frac{\{\lambda_L I_L\}_\alpha}{\{\lambda_L I_L\}_\beta} \cdot \frac{\{\chi\}_\alpha}{\{\chi\}_\beta} \cdot \frac{\{\sigma_\nu(\lambda,T)\}_\alpha}{\{\sigma_\nu(\lambda,T)\}_\beta} \cdot \frac{\{\phi(\lambda,T,P,\chi_i)\}_\alpha}{\{\phi(\lambda,T,P,\chi_i)\}_\beta} \tag{4.3}$$

signal ratio | detection constant C_{det} | thermo-dyn. | excitation | tracer | absorption | quantum yield

The two detection channels have different detection efficiencies, depending on individual elements used within the optical pathways between probe volume and detectors, and further on the wavelength dependent detector sensitivity. Also, the collection solid angle and the

probe volume will slightly differ, which complicates the alignment of the two detectors. The optical alignment of two-channel techniques is indeed very time consuming and prone to systematic error if the two detection channels are not adjusted to observation of identical pixels. If the alignment process succeeded and the position of the detectors are stabilised to relative shifts in the subpixel domain, all parameters of the detection pathway can be factored out to a detection constant C_{det} via a calibration measurement. A very efficient method avoiding alignment problems is to use a single detector for both channels, capable of short delayed acquisition of two frames on the same chip. Interline transfer CCD are often applied for this purpose.

One main advantage of the ratiometric approach is that the tracer number density cancels out (the ratio will still depend on the inherent fluorescence behaviour of the tracer on pressure and temperature). This is valid, if an observation of identical pixels can be guaranteed by careful detectors alignment.

The other parts of the equation above are linked to the excitation energy applied to the measurement volume, the tracer mole fraction, the absorption and the fluorescence quantum yield. Generally, calibration can be obtained for ratios of the product of absorption and quantum yield $\sigma \cdot \phi$. A ratiometric approach is successful if this calibration results in a single valued function $f(\xi)$ of the property to be derived from the measurement, which is most often the local temperature value. The inverse function f^{-1} then directly provides the wished property, see equation (4.4).

$$\frac{\{\sigma_\nu(\lambda,T)\}_\alpha}{\{\sigma_\nu(\lambda,T)\}_\beta}\cdot\frac{\{\phi(\lambda,T,P,\chi_i)\}_\alpha}{\{\phi(\lambda,T,P,\chi_i)\}_\beta}=\underbrace{\left(\frac{S_{f,\alpha}}{S_{f,\beta}}\right)^{-1}\cdot {C_{\mathrm{det}}}^{-1}\cdot\frac{\{\lambda_L I_L\}_\alpha}{\{\lambda_L I_L\}_\beta}\cdot\frac{\{\chi\}_\alpha}{\{\chi\}_\beta}}_{*}=f(\xi)\quad\Rightarrow\quad\underline{\underline{\xi=f^{-1}(*)}}\tag{4.4}$$

Different sub-cases of the ratiometric approach exist. Their specific features and application examples are subject of the following paragraphs.

(a) Dual wavelength excitation – dual tracer method

This case illustrated in equation (4.4) is the most general, and that one, for which the largest experimental effort and equipment are required. Two individual excitation wavelengths are used to excite two different tracer species. The energy of both excitation sources brought into the probe volume must be sensed individually throughout the measurement. The sensing error of both excitation energies relative to each other has direct impact on the measurement precision, inversing the wanted quantity, e.g. the temperature, as described above. In addition, the ratio of mole fraction from both tracer molecules has to be known precisely. This is given for either coevaporation from a liquid phase both tracers were added to or for the use

of totally pre-evaporated tracer. However, for the choice of the coevaporation assumption one might expose to the risk of non-ideal mixture evaporation, cf. section 4.6.2. In practice, at least for a pair of tracers from organic molecules, such measurements have been so far reserved to theoretical discussions. [Frieden 2003] used the couple 3-pentanone/toluene with 248 nm excitation for combined fuel and oxygen concentration measurements in a spatially homogeneous temperature field (this technique benefits from the difference in behaviour with oxygen present, i.e. quasi non-quenched ketones versus strongly quenched aromatics, see method (c) below). They proposed to further chose a second excitation channel for the 3-pentanone to extend the applicability of the method to engine conditions with spatial temperature variations. So far, an example of such a technique was not realised or at least, to our knowledge, not reported.

(b) Dual wavelength excitation – single tracer method

Like for the previous method, the sensing error of laser energies limits the precision of this technique. A substantial advantage of this technique is that the ratio of tracer mole fraction in equation (4.4) cancels out. In general, fluorescence spectra will recover to a large degree if both excitations are followed by the same electronic transition. This means no harm to the technique, which is based on the ratio of fluorescence signals changing differently on temperature for the two excitation wavelengths. However, in order to distinguish the overlapping emissions, a temporal separation must be realised between the two laser pulses. This time shift must be larger than the emission duration. For organic tracers, fluorescence lifetime is of several to hundreds of nanoseconds. If a single detector is used, a much larger time shift is forced by the repetition rate of the camera in full-frame mode (rather seconds) or in interline transfer mode (microseconds). The reduction of necessary experimental equipment and the relief of alignment between two detectors has thus to be traded-off against loss of temporal resolution.

In the past, especially the ketone tracers acetone and 3-pentanone have been proposed and applied to this type of measurement. Restricting to high-energy pulsed commercial UV lasers and avoiding further application of dye lasers, the optimal choice for the combination of excitation wavelengths is reported as 248 and 308 nm for both acetone [Thurber 1998] and 3-pentanone [Koch 2003b], producing the single valued ratio of fluorescence signals, which is most dependent on temperature. For 3-pentanone, the signal ratio is more sensitive to temperature than for acetone. Seeded to isooctane, the choice of 3-pentanone has further the advantage of nearer boiling points between tracer and parent fuel compared to the use of acetone. Moreover, the use of short wavelengths with acetone tracer might lead to an important photobleaching effect caused by the increasingly important role of photolysis if the same molecules are repeatedly excited (e.g. for a low gas exchange rate), see section 5.2.5.

Practical applications of this two-line excitation single tracer method for investigation of temperature fields in IC engines are reported for 3-pentanone from [Einecke 2000], for toluene from [Fujikawa 2006] in air.

(c) Single wavelength excitation – dual tracer method

The choice of this technique largely simplifies the experimental set-up, since the excitation energy cancels from equation (4.4). The single valued function, from which the wanted parameter, e.g. the temperature is derived, is obtained from the fluorescence ratio of two different tracer species. This implies, that both tracer species have sufficiently overlapping absorption spectra. Furthermore, the fluorescence pattern of both species must be spectrally separable, e.g. by means of dichroic mirrors or a colour glass filter.

Different species, which are subspecies of the same molecular family, are most likely to exhibit overlapping fluorescence spectra, as it can be observed for the simple aliphatic ketones as well as for the derivatives of benzene. However, choosing one tracer from aliphatic ketones and the other from benzene derivatives, combinations are possible, which share a common domain of absorption and avoid exhaustive spectral overlap of the emission.

Ketones and benzene derivatives behave most differently, when oxygen is present, the ketone fluorescence being rather unchanged, whereas the emission of benzene derivatives is strongly quenched. Thus, if the temperature parameter is the quantity of interest, for the present oxygen concentration a calibration curve must be known and the oxygen concentration has to be necessarily constant. This situation is rather seldom to be met. Albeit, it is possible to find an application reported from [Kakuho 2006], who combined alternatively TEA or toluene with 3-pentanone in order to derive temperature information, but it must said, that these results were based on the assumption, that the influence of temperature and quenching on the fluorescence have multiplicative character, i.e. quenching behaviour of TEA or toluene does not change on temperature. This is, however, clearly violating the findings obtained from [Koban 2005a], showing that for 266 nm excitation toluene followed a linear Stern-Volmer relation, but the quenching efficiency was strongly decreased with increasing temperature.

The other way round, for a constant temperature environment, the different sensitivity towards oxygen quenching can be used for determination of oxygen concentration. In the past this method has been repeatedly proposed for the tracer pair 3-pentanone/toluene due to the newly gained insight to toluene photophysics through the thesis work of [Koban 2005d]. Basically, this concept corresponds to the application of toluene as a FARLIF tracer (see section 4.6.3), expanded by the simultaneous use of a non-quenched species like 3-pentanone. The fluorescence signal of 3-pentanone thus yields information about the fuel concentration (assuming coevaporation of the tracers with the parent fuel, e.g. isooctane).

With known fuel concentration, the oxygen concentration is derived from the toluene fluorescence following equation (2.68) section 2.12.2, assuming that the condition $k_{SV} n_q \gg 1$ is fulfilled, i.e. quenching by oxygen is the dominating deactivation process.

A first applications of this technique has been demonstrated for observation of a turbulent mixing processes of interacting air and nitrogen jets seeded with a mixture of 3-pentanone/toluene for atmospheric pressure room temperature by [Koban 2002]. A signal cross talk between the two tracers was also discussed. The toluene fluorescence was observed to be quenched by 3-pentanone, which could not be neglected for low oxygen concentration. Through the energy transferred during the quenching process, the fluorescence signal of 3-pentanone was even shown to enhance. [Frieden 2002] and [Frieden 2003] have adopted the same method to an application in a single-cylinder optical direct injection SI engine for motored, skip-fired and continuous fired operating. As mentioned above in the discussion of method (a), Frieden et al. restricted to homogeneous temperature environment, because otherwise, further information would have to be acquired, e.g. through another excitation wavelength for 3-pentanone (to resolve the ambiguity of fluorescence signal depending on both concentration and temperature).

(d) Single wavelength excitation – single tracer – dual channel detection method

By means of appropriate filters, different parts of a single fluorescence spectrum can be separated to individual detection channels. A single valued function is obtained from the ratio of two channels if each varies differently on temperature. If this is achieved using a single wavelength exciting a single tracer, both the ratios of excitation energy and tracer concentration cancel from equation (4.4).

For many aromatic compounds, a bathochromatic shift is observed with increasing temperature at the long-wavelength tail of the fluorescence spectrum. Several studies report from the possibility to exploit the spectral red-shift by means of appropriate filters in order to provide a single tracer ratiometric LIF thermographic method based on a single excitation wavelength. [Koban 2004] discussed the application of toluene as such a tracer excited at either 248 or 266 nm for nitrogen atmosphere and inhomogeneous tracer concentration. The fluorescence signal was separated by means of Schott filters. For 266 nm excitation, the ratio of these channels provided a single valued function with a temperature sensitivity comparable to two-line thermometry on 3-pentanone, whereas signal intensities for the proposed method on toluene should be equal or higher due to the much higher quantum yield and slightly larger absorption cross-sections of toluene. The main benefit is thus the much reduced experimental cost of the toluene method, since a single excitation wavelength is sufficient.

[Luong 2006] tested different filter combinations to separate the toluene spectrum into a "blue" and a "red" channel. Even in air atmosphere, for which the temperature sensitivity of the fluorescence spectrum is much less pronounced than for nitrogen, the application of a single wavelength excitation technique seemed feasible. Thus, later [Luong 2008] applied it to a temperature measurement in a single-cylinder four-stroke DISI engine. The homogeneous mixture of toluene and air from a premixing unit was introduced into the intake air flow. The engine was motored without fuel injection at 2000 rpm, when temperature measurements were performed. A temperature decrease over roughly 200 K from 40 to 90 degree ATDC was measured with a single-shot standard deviation (σ) of 34 K.

[Tea 2010] applied the same technique to sense unburnt gas temperature in an evaporating Diesel spray. They performed measurements in a high-pressure, high-temperature cell capable of reproducing the thermodynamic conditions in the combustion chamber of a Diesel engine during the injection. A calibration was made to toluene-LIF spectra acquired under well-controlled conditions at variable temperatures [Devillers 2009]. Optimisation of the measurement accuracy was achieved by a thorough error analysis and an improved algorithm allowing for precise superposition of the LIF image pair. The sensitivity of the method was best below 700 K ($\sigma = \pm 20$ K). Below this temperature limit, the two-colour LIF thermometry showed clearly limitations.

[Kaiser 2005] discussed the use of naphthalenes as tracer with substantial fluorescence red-shift for increasing temperature. Another source of red-shift was observed with increasing oxygen concentration. This effect, however, saturated for oxygen concentration higher than 10 %. Thus, for air atmosphere, red-shift of the fluorescence spectrum is due to temperature variation only. Similar to the technique proposed from Koban and Luong, spectral filters were applied to separate the emission of 1-methylnaphthalene to a "blue" and a "red" channel of detection. The ratio of red to blue channel was shown to be a single valued function of temperature within 350 to 900 K. Applying this method to a mesoscale burner prototype, they measured temperature fields from this ratio. With the temperature derived in this way, the "red" channel signal was corrected, therefore providing the tracer concentration. The latter was assumed to be proportional to the fuel concentration (dodecane), and hence to the equivalence ratio, since the oxygen concentration was assumed to be constant (air).

(e) Single wavelength – dual channel detection method on kerosene fuel

As noted earlier, real fuels like kerosene are mixtures of a wide spread of organic compounds, containing a considerable amount of aromatic species (in volume from 18 % for kerosene over 27.5 % for Diesel no. 2 to 36.2 % for gasoline, see table 5). As will be discussed later in more detail (section 4.8.1), excitation of kerosene (Jet-A type) at 266 nm produces a double-band fluorescence spectrum. [Baranger 2005] already assigned the lower band of the kerosene emission spectrum to be originated from monocyclic aromatic, the upper

band from bicyclic aromatic species. It was further observed that the temperature dependence of the emission spectrum is not the same for the lower and upper band. Baranger et al. were capable of identifying a number of aromatic species in order to build a surrogate fuel, which produced nearly the same emission spectrum like kerosene.

In principle, if the individual temperature sensitivities of the lower and upper emission band of kerosene are known, a ratiometric strategy can be proposed, which falls under method (c). However, to achieve a single-valued calibration function, the concentration ratio of the species responsible for the lower and upper band emission has to be constant. For kerosene, following the assignment of Baranger et al., coevaporation between the monocyclic and bicyclic aromatic species is necessary.

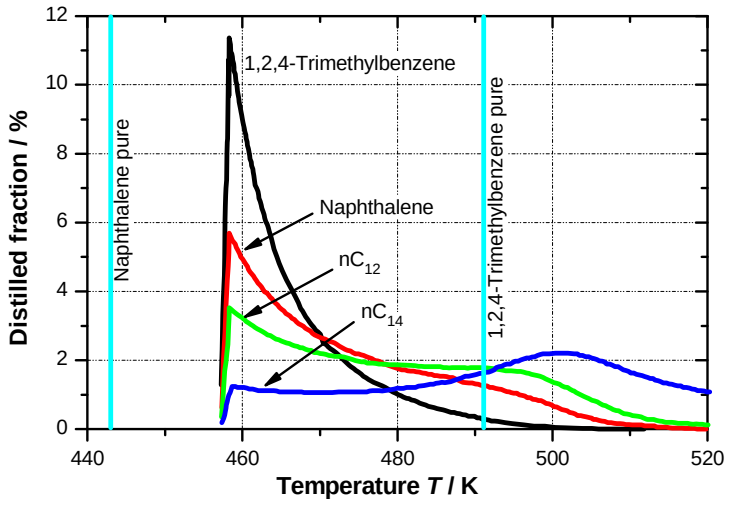

Figure 45: Mixture distillation of BtL- (Biomass to Liquid) fuel. From thermodynamic calculations under atmospheric pressure [Bruneaux 2010]. As pure liquids, monocyclic trimethylbenzene (1,2,4-TMB) and bicyclic naphthalene have largely different boiling points (443 K and 491 K). Mixed with lighter and heavier organic species, such as in BtL fuel, 1,2,4-TMB and naphthalene practically coevaporate.

Recent thermodynamic simulations of fuel mixture evaporation from [Bruneaux 2010] at atmospheric pressure show, that in fuel mixtures such as BtL- (Biomass to Liquid) fuel monocyclic (e.g. 1,2,4-trimethylbenzene) and bicyclic (e.g. naphthalene) aromatic species practically coevaporate, despite their largely different pure liquid boiling points (figure 45). We assume that there should be a similar effect for increased pressure, even though we are in lack of any high-pressure simulations, which are somewhat more difficult to perform. Thus, under typical engine operating conditions, i.e. a high-pressure high-temperature environment, coevaporation of the monocyclic and bicyclic aromatic species enables ratiometric strategies for fluorescence measurements.

4.6.5 Vapour and liquid phase separation by laser-induced exciplex fluorescence (LIEF)

A prevalent issue for diagnostics in IC engines is fuel spray formation and evaporation. These processes occurring on short time scales, fuel is potentially present in both, vapour

and the liquid phase, when the combustion reaction is initiated. Information about the local fuel vapour concentration as well as zones of remaining liquid fuel are of great interest to better understand and improve combustion processes.

Fluorescence diagnostics based on a tracer seeded to the fuel suffer from the problem that the emission of the liquid phase exceeds that of the vapour by up to three orders of magnitude. Naturally, this is problematic with respect to the dynamic range of the detector. If the emission from both phases occur simultaneously, the intensification of the detector has to be adapted to the high signal level of liquid emission in order to avoid detector damage. The acquisition of vapour fluorescence is therefore restricted to relative poor signal-to-noise ratios.

[Melton 1983] proposed an exciplex fluorescence method to overcome the dynamic range issue concerning the simultaneous vapour and liquid phase fluorescence detection. Applications of this approach were later referred to as laser-induced exciplex fluorescence (LIEF). It was mentioned earlier in section 2.12.4 that exciplexes (excited complexes) can be at the outcome of collisional events between monomers of different type. This is when bimolecular deactivation occurs via the reactions

$$\begin{aligned} &\mathrm{M}^* + Q \rightleftarrows (\mathrm{MQ})^* \quad \text{and} \\ &\mathrm{M} + \mathrm{Q}^* \rightleftarrows (\mathrm{MQ})^*, \end{aligned} \tag{4.5}$$

which both are reversible equilibrium reactions in competition to the radiative emissions

$$\begin{aligned} &\mathrm{M}^* \rightarrow \mathrm{M} + h\nu_M \text{ and} \\ &\mathrm{Q}^* \rightarrow \mathrm{Q} + h\nu_Q. \end{aligned} \tag{4.6}$$

The emission wavelength is molecule specific, i.e. $\nu_M \neq \nu_Q$. Further, the exciplex itself can be deactivated via the exciplex fluorescence reaction

$$(\mathrm{MQ})^* \rightarrow (\mathrm{MQ}) + h\nu_{MQ} \tag{4.7}$$

The method proposed from Melton et al. is based on this latter reaction. The complex is lowered in energy by the binding energy, and therefore the excimer fluorescence is red-shifted from the monomer fluorescence. The monomer M is an unsaturated organic molecule, which absorbs the laser light and has an excited state lifetime long enough to allow for collisions with quencher Q. In the liquid phase the free path length of the excited monomer M^* is much smaller than in vapour. In consequence, the probability to encounter a quencher Q within the excited lifetime is much higher, and therefore exciplex formation much more likely. The monomer concentration and excitation wavelength affect the equilibrium constants of mechanisms (4.5). For some couples of M and Q, these parameters can be chosen

such that in the vapour phase emission is dominated by monomer fluorescence and in the liquid phase by exciplex fluorescence.

A configuration with the described behaviour was proposed by Melton et al. consisting of 15 % naphthalene and 1 % N,N,N',N'-tetramethyl-p-phenylenediamine (TMPD) in hexadecane (by weight), excited at 313 nm. The main vapour emission peak was at 380 nm, separated by 90 nm from the emission peak of the liquid at 470 nm.

Since then, many research groups applied the TMPD/naphthalene couple excited by several standard wavelengths of commercial lasers in the UV for LIEF measurements in different alkane fuels. Over the years, the usage of many other exciplex couples was reported, such as

- dimethylaniline (DMA)/naphthalene
- DMA/trimethylnaphthalene (TMN)
- fluorobenzene (FB)/diethylmethylamine (DEMA)
- triethylamine (TEA)/benzene
- TEA/FB.

All these couples have specific properties with regard to such issues as coevaporation with the parent fuel, representation of the fuel boiling point range of interest and liquid-vapour cross-talk, see [Fansler 2009]. The two first are the same as for normal tracer LIF, whereas the latter issue is specific to the LIEF technique. Cross-talk becomes a problem for quantification of the vapour phase fluorescence with the degree of spectral overlap between the emission of the vapour and liquid phase. In principle this is also a general aspect for most of the ratiometric LIF methods discussed in section 4.6.4. However, for the LIEF technique cross-talk can be crucial even for small spectral overlaps, because the emission of the liquid phase is by two to three orders of magnitude stronger than for the vapour. The applicability of this LIEF technique can thus be improved by the choice of appropriate filters.

More challenging than the cross-talk is the oxygen quenching of aromatic species among the LIEF tracer couples, which results in a much reduced emission making detection most difficult. Replacement of the oxygen with inert gases like nitrogen is the usual choice to avoid quenching.

4.7 Fluorescence measurements of petroleum based real fuels

As mentioned earlier, the fluorescence interpretation of a real fuel is a very complicated task. If the knowledge of the photophysics of each participating species is not sufficiently large,

evaluation is not likely to be successful. Nevertheless, various research groups tried to directly exploit the fuel fluorescence, which led to results having more or less qualitative or visualisation character.

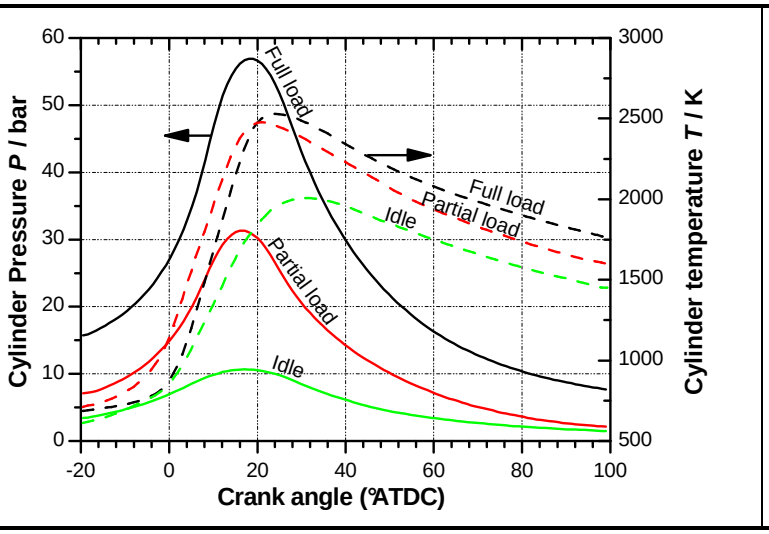

Figure 46: Cylinder pressure and temperature change for different loads of a gasoline spark-ignition engine. Adapted from [List 2008].

Piston engines exhibit particularly difficult conditions with regard to fluorescence measurements. For either spark or compression-ignition engines, within the compression stroke the cylinder pressure and temperature change dramatically (see cylinder pressure curve over the crank angle for a typical spark-ignition engine, fig. 46). This is the consequence of the combustion reaction, but primarily the result of polytropic compression, when the piston is moved in the cylinder. Without knowledge of the self-quenching and oxygen quenching behaviour of the individual fluorescing species in the real fuel in dependence of pressure and temperature, correction for the quenching effect will be rather difficult. Furthermore, the emission from the aromatic species in the real fuel will be quenched to the limit of detection at the high pressures near to top-dead-centre (perhaps the most cited argument against fluorescence diagnostics with real fuels in piston engines). For piston engines, these arguments lead back to the use of surrogate fuels doped with a fluorescence tracer insensitive to oxygen quenching, as discussed in section 4.6. Consequently, few examples are found for the use of real fuel fluorescence of gasoline or Diesel operated in piston engines.

In contrast to the piston engine, the operating conditions in a turbine combustor are rather steady, i.e. pressure and temperature are practically constant values for a given load. As the overall pressure and temperature are high level, the fluorescence signal of the jet fuel will also be strongly quenched, just like for gasoline and Diesel within the compression stroke of a piston engine. A great advantage is, however, the overall steadiness of the turbine operating conditions. A potential strategy inferring the fuel concentration from the fluorescence signal has to cover a limited dynamic range of pressure and temperature compared to piston engines. Therefore, the fluorescence detection can be optimised for acceptable SNR ratios even under the extreme pressure and temperature conditions in the turbine.

4.7.1 Gasoline and Diesel fuel fluorescence

Only few references are available reporting on direct use of gasoline and Diesel fluorescence for the sensing of the fuel concentration.

For gasoline, one example is reported from [Fansler 1995], who used planar LIF images of commercial gasoline in a continuously fired direct-injection stratified-charge (DISC) engine to measure vapour and liquid phase fuel distributions. This study allowed only for qualitative visualisation of the fuel distribution due to the neglect of temperature and pressure effects on the fluorescence. They assumed that the species at the origin of the gasoline fluorescence could be attributed to two different categories of either poorly quenched ketones and aldehydes or strongly quenched polycyclic aromatics and substituted benzenes.

For Diesel fuel, LIF diagnostics are only reported for liquid phase. [Arnold 1990a] demonstrated the principle feasibility of 2-D LIF diagnostics with Diesel fuel spray in a transparent Volkswagen Diesel engine. The fluorescence signal were assumed to be sufficiently high to allow for recording single shot emission spectra after XeCl excimer laser excitation. A major problem was window fouling, which occurred after several seconds and blackened all windows with soot. [Pastor 2002] demonstrated fuel concentration measurements of Diesel sprays under isothermal conditions using PLIF. The commercial Diesel fuel was excited at 355 nm. Special care was taken about correction and calibration procedures including the study of the fluorescence characteristics of the fuel. The fuel concentration was derived from the droplet fluorescence signal measured over a path length relating the volume fuel fraction to the measurement volume.

4.7.2 Kerosene fuel fluorescence

For several years, a number of publications from the NASA Glenn Research Center reported on gas turbine experiments, which were related to the PLIF of kerosene and other minor combustion species. [Hicks 1997] reviewed the impact of the jet fuel fluorescence for the measurements of the combustion minor species NO and OH by PLIF in gas turbine flame tubes with JP-5 and Jet-A fuel. The PAH constituents of the fuel presented large band absorption and emission features with spectral overlap to absorption and emission of combustion species like OH. It was shown, that OH LIF is applicable by use of appropriate interference filters to minimise the disturbing effect of the PAH LIF. Hicks et al. underlined the necessity to gain a better understanding of the spectral dependence from temperature and pressure before attempting to quantify the fuel fluorescence. [Locke 1998] tried to depict the fuel patternation generated from conceptual injectors designed for lean combustion operating under high pressure and temperature by vapour and liquid phase PLIF imaging of JP-8 fuel. Combining the fluorescence maps to Mie imaging and PDPA measurements provided some interesting results, but no relevant quantitative information could be obtained for the

local fuel species concentration. Moreover, the distinction of vapour and liquid was not possible from the fuel PLIF imaging. Later [Locke 1999 and Hicks 2000] avoided this problem by restriction to premixed fuel completely prevaporised prior to reaching the diagnostic zone. The onset of the combustion reaction was localised using a combined technique of fuel vapour and OH PLIF. A pressure limit of 60 bar was exceeded within test series of a LPP injector implemented to a gas turbine combustor. However, as they noted themselves, the fluorescence interpretation was still in lack of quantitative character, mainly due to the uncontrolled influence of fuel quenching.

Other research groups agreed that kerosene PLIF was most suitable for visualisation of the fuel patternation prior to the combustion zone, especially when combined to other diagnostic methods concentrating on the liquid phase. [Greenhalgh 2000] compared PLIF maps of kerosene fuel vapour measured in axial and radial sections of a premixing duct to further measurements repeated for naphthalene (BP 218 °C) and for fluoranthene (BP 380 °C) in order to represent a lighter and a heavier fraction of the kerosene fuel.

The Division of Combustion Physics at Lund University was the first group to study the dependence of kerosene Jet A1 fluorescence on temperature and oxygen quenching. [Löfström 1996] used a combined technique of vapour PLIF for 266 nm excitation and Mie imaging of the liquid fuel. The presence of high quantities of liquid phase was reported to be problematic due to absorption. Some laboratory experiments were carried out to study the kerosene fluorescence. Emission spectra were detected for different temperatures from 500 to 900 K in air. In order to account for oxygen quenching the detection at 700 K was repeated in air. All fluorescence spectra were presented on arbitrary or normalised scales. Thus, only the change of the spectral shape was addressed. The spectral study presented a first insightful view to the photophysics of kerosene. However, restriction to only qualitative analysis was chosen for the results obtained from the measurements applied to the LPP ducts (atmospheric pressure and temperatures from 500 to 900 K). A later application of the same technique with fuel excitation at 290 nm to a LPP combustor is found in [Löfström 2000]. OH PLIF excited at 284 nm was separated by a narrow-band filter. The fluorescence interpretation of the fuel vapour remained qualitative, just as for recently presented measurements, the PLIF/Mie technique this time supplemented by LII measurements to account for the characterisation of soot, see [Seyfried 2007].

The Combustion Research Laboratory from the Paul Scherrer Institute studied the mixture of fuel with air for fuel oil (non-specified commercial brands A, B, C) injection in a gas turbine burner. [Arnold 2000] tried to quantify the fuel concentration by vapour PLIF measurements of these three fuel oil brands. A restriction was made to atmospheric pressure and merely varying temperature conditions (450 - 486 °C). The influence of fuel-to-air ratio on the fuel fluorescence was studied for 450 and 486 °C changing the fuel concentration in air. The fluorescence was nearly linear dependent from the fuel-to-air ratio (7 % error for $1/\lambda$ from 0.25 to 0.5). Further, assuming fluorescence to be approximately independent within

the chosen limits of temperature, they reported the total error for the measured fuel concentration to be less than 25 %. A control for non-evaporated fuel oil was realised by Mie imaging. In a further study, [Gradinger 2001] applied the same PLIF technique to concentration measurements in a full-scale industrial burner at atmospheric pressure, and beyond, to measurements in a reduced scale test burner at pressures up to 15 bar. Apparently no further effort was made to study the high-pressure influence on the fluorescence signal. The fuel quantification error was assigned to be simply higher than 25 % at 15 bar.

4.8 Photophysical study of kerosene fluorescence at ONERA

The review above has shown, that since more than a decade the knowledge of the fluorescence behaviour of real fuels under engine relevant conditions is very limited. The idea of complicated photophysics is a prevalent argument against the feasibility of unambiguous signal quantification. However, replacing the real fuel by a surrogate doped with a fluorescence tracer was shown to be difficult in some cases, the tracer possibly not representative of the fuel concentration due to preferential evaporation, see section 4.6.2. Engine studies using fluorescence tracer doped to a surrogate fuel seem to be limited to piston engines as they cannot be easily applied to industrial scale turbine combustors, mainly due to the overall enormous mass flow. The only reference found for the use of a jet fuel surrogate for fluorescence diagnostics was [Kaiser 2005], using 5 to 10 % by volume of 1-methylnaphthalene as FARLIF tracer in dodecane, surrogate for JP-8. The size of the application was, however, limited and not industrial scale: a catalytic mesoscale burner operating with the electrosprayed surrogate.

Applications of fluorescence measurements with direct use of the real fuels might be beneficial especially for gas turbines. If the study is not restricted to the optical diagnostics of the atomisation and vaporisation behaviour of the injected fuel prior to ignition, the application of real fuel might yield more realistic information on the fuel combustion itself, especially with regard to the pollutants emissions.

4.8.1 Kerosene fluorescence identification – early studies

Progress on the fluorescence interpretation of kerosene vapour was achieved with the study of [Baranger 2005] from the laser diagnostics group at the Physics Sensing and Instrumentation Department of ONERA. The kerosene fluorescence spectrum was first analysed at 450 K with atmospheric pressure nitrogen for three different excitation wavelengths at 266, 282 and 308 nm. For 266 nm, the spectrum clearly exhibited the most structured pattern. The kerosene fluorescence was found to be the overlay of a lower and a higher band of emission apparently originated from two different groups of organic molecules.

For the identification of the individual species contributing to the fluorescence spectrum of kerosene, the excitation at 266 nm was the most suitable. Systematic spectroscopic studies were undertaken for different representatives from mono- and di-aromatics, being all prospects to be at the origin of the observed kerosene fluorescence pattern. Possible candidates were selected from constituents of the kerosene composition analysed by liquid chromatography. A comparison to these measurements allowed for defining a surrogate fuel of only four aromatic compounds dissolved in an alkane majority, which has essentially all spectral properties similar to the fluorescence of kerosene.

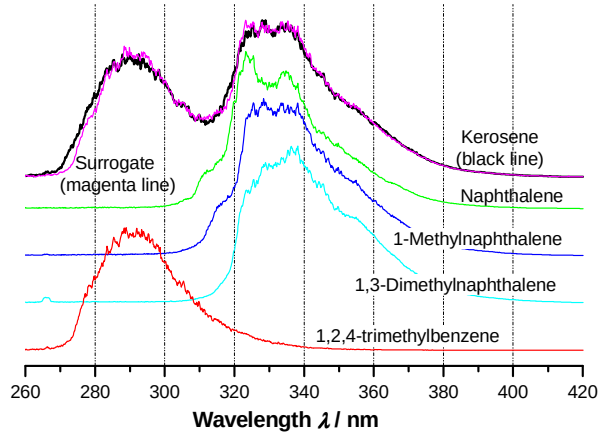

Figure 47: Comparison of fluorescence spectra of the four aromatic surrogate fuel constituents with kerosene as proposed from [Baranger 2005]. Their best fitting composition was recalculated for 82.1 (78.16) % n-undecane to

16.17 (20.02) % 1,2,4-trimethylbenzene

0.63 (0.73) % naphthalene

0.45 (0.47) % 1-methylnaphthalene

0.65 (0.62) % 1,3-dimethylnaphthalene,

completed to 100 mass % (values in brackets are molar %) by n-undecane. 450 K, atmospheric pressure pure nitrogen.

Figure 47 shows the concordance of the surrogate and the kerosene fluorescence spectra. The surrogate constituents are given in mass %. The composition of the surrogate was chosen to fit the kerosene fluorescence from the respective lot used for the measurements. Repeating the measurements with kerosene from another lot would lead to slight changes in the surrogate composition (especially the ratio between mono- and di-aromatics).

Fluorescence spectra of both the surrogate fuel and kerosene were compared at atmospheric pressure for a temperatures between 445 and 670 K and at 445 K for pressures between 1 and 7 bar, with nitrogen as the buffer gas. It could be shown that the surrogate fuel exhibits fluorescence spectra in excellent concordance to the kerosene. The same concordance was found for the influence of oxygen quenching tested under atmospheric pressure at 445 K for both the surrogate and the kerosene fuel.

A strategy was proposed for sensing the kerosene vapour by planar LIF. Due to the limited parameter spread of the spectroscopic study the application was conceived for a kerosene/air jet preheated to 600 K and impinging into atmospheric environment. Restricting the kerosene charge in the exiting jet to less than 0.2 % molar fraction the overall oxygen concentration could be assumed to remain 21 %.

From the spectroscopic study it was known, that the integrated fluorescence of the di-aromatic part of the kerosene fuel varied insignificantly with temperature between 500 and 700 K. In consequence, the di-aromatic fluorescence signal was attributed to the fuel concentration, the fuel assumed to be of invariant composition referred to the chromatographic analysis. With this approach it was possible to derive the local equivalence ratio, i.e. the ratio of kerosene vapour to air, from the simple measurement of the di-aromatic part of kerosene fluorescence.

Further, with knowledge of the individual temperature fluorescence characteristics of kerosene and its di-aromatics constituents, a ratiometric measurement of the kerosene and the di-aromatics fluorescence allowed for qualifying the exiting jet with respect to local temperature variation. For this, a two-camera strategy was necessary to obtain simultaneous information of the kerosene and the di-aromatic fluorescence, the latter separated by means of an appropriate filter, suppressing the lower wavelength band from the kerosene spectrum.

The ratiometric temperature measurement allowed for analysis of temperature gradients in the flow field, but only with restriction to overall similar oxygen concentration. Otherwise, the oxygen quenching of kerosene and di-aromatics fluorescence being different, it is not possible to decide whether the variations in the fluorescence ratio must be attributed to a local change in temperature or oxygen concentration, or even both. Moreover, as this is practically a two-tracer technique with the whole kerosene representing the first and its di-aromatic constituents the second tracer, this method might fail if the evaporation characteristics of the di-aromatic fraction does not sufficiently comply with that of the mono-aromatic fraction, which is at the origin of the lower band of the kerosene fluorescence.

4.8.2 Further studies of kerosene fluorescence in the frame of the present thesis work

The work of [Baranger 2005] contributed largely to the identification of the species at the origin of the kerosene fluorescence emission. However, the spectroscopic fluorescence study was not carried out as largely as would have been necessary to define measurement strategies under the harsh conditions in gas turbines. Further, the parametric spectroscopic fluorescence study suffered from lack of precision, the relative error specified to be about 15 % for fluorescence and 21 % for quantum yield results, see [Baranger 2004]. The major contribution to this imprecision was probably the inaccurate control of the environmental conditions during the measurement.

It was part of the present work to extend the parameter range for the spectroscopic study to high-temperature and high-pressure (300 to 900 K and 1 to 30 bar). In order to improve the accuracy of the spectroscopic fluorescence results, the experiment procedure was changed to a piloted mode, i.e. steering the environmental parameter variation via a LabView

routine on a fixed time scheme allowed for enhancing the reproducibility to a large degree. The construction of the previously used test cell was changed to allow operating at high pressure beyond 30 bar and heating to temperature over 900 K. To guarantee a continuous control of the vapour seeding to the probe volume the absorption was permanently checked and compared to the programmed target value. A detailed description of the revised measurement technique was given earlier in Chapter 3. In addition to the kerosene fuel, several other ketone and aromatic tracers were studied using the same experimental set-up in order to create a wide basis for the definition of possible measurement strategies.

The principal application was a combined kerosene PLIF and OH PLIF measurement of the local equivalence ratio and local flame front structure in a fired high-pressure combustor operating with Jet A1 fuel. With the knowledge of the photophysical properties from the spectroscopic cell study a quantification strategy was defined, and the PLIF techniques could be successfully applied for temperatures between 480 and 730 K and pressures up to 22 bar. A multipoint injection system was operated for various overall equivalence ratios in a combustor connected to the "M1 test bench", which is the high-temperature high-pressure combustion facility from ONERA, dedicated to the investigation of aircraft and helicopter injectors under real operating conditions. Some of the short-term results from these combustor experiments have already been published in [Grisch 2008]. A detailed description of the spectroscopic study of organic tracers is the subject of the next chapter, followed by the study of kerosene in Chapter 6. From the analysis of both, a definition of a strategy for the quantification of kerosene PLIF in terms of temperature and equivalence ratio is then developed. The Chapter 7 addresses kerosene and OH PLIF measurements in a high-pressure combustor under fired conditions realised on the "M1 test bench".

Chapter 5 Spectroscopic fluorescence of organic fuel tracers

This chapter is devoted to the description of the spectroscopic study of various organic molecules with electronic transitions located in the middle UV. All our experiments were performed for a 266 nm excitation wavelength.

Choice of tracer species

The choice of the molecules, which can be used as potential fluorescence tracers, is related to their attractive properties for fluid mechanics experiments and in particular to study the evaporation process of liquid fuels in combustion. The preceding chapter's "review of fuel tracer vapour fluorescence diagnostics" allows to determine several candidates of major interest for our work. Principally, our attention is drawn to two chemical groups of organic molecules, the aliphatic ketones and the aromatics (i.e. mono- and bicyclic).

Selection of best-suited aliphatic ketones and aromatics

From the group of aliphatic ketones, acetone and 3-pentanone were frequently used in the past as fuel tracers. While these harmless species provide high vapour pressures even near room temperature, their fluorescence is almost insensitive to oxygen quenching. This made them the most commonly species used when fluorescence tracer seeding is required.

The group of aromatic tracers can be subdivided into methyl-substituted single-ring aromatics and bicyclic aromatics. Even higher multi-ring aromatics can be of practical interest to simulate lower volatility classes of heavier fuels. The main characteristics of most aromatic tracers is the propensity to produce fluorescence with high fluorescence yield and strong quenching by oxygen. While at first glance, the strong quenching of fluorescence mainly complicates the detection of the fluorescence signal in combustion environments, a specific knowledge about the quenching behaviour provides an unique access to obtain valuable additional information in practical combustion processes. For tracers like toluene and naphthalene, experimental strategies have been proposed in the past to measure key parameters like for instance the fuel-to-air ratio using the FARLIF approach described in section 4.6.3.

We select for our spectroscopic study ***acetone*** and ***3-pentanone*** from aliphatic ketones, as well as ***toluene***, ***1,2,4-trimethylbenzene*** and ***naphthalene*** from monocyclic and bicyclic aromatics.

Literature review for relevant aspects of ketone and aromatic photophysics

Prior to the discussion of our experimental results, key elements on photophysics of organic tracers as well as specific characteristics related to the fluorescence of ketones and aromatics are presented along with a literature review. Next to the fluorescence itself, we focus our attention on competing photophysical processes governing the deactivation of the excited state. These are intramolecular processes such as the isoenergetic internal conversion and intersystem crossing, internal vibrational redistribution and vibrational relaxation through collisional interaction, as well as intermolecular processes like electronic collisional quenching and photochemical reactions such as isomerisation and bond cleavages.

Range and aim of experimental efforts

This experimental work focuses on the effect of physical parameters (temperature, pressure and mixture composition) on the fluorescence and absorption of the tracers. The objective is to obtain data in conditions encountered in practical combustion systems. Temperature is therefore varied within a range of 350 to 900 K and pressure from 1 to 30 bar. Nitrogen is used as buffer gas to either study the effect of temperature or the effect of bath gas pressure to the fluorescence in a non-quenching environment. In addition, different nitrogen/oxygen gas mixtures are used to obtain information about the quenching on the fluorescence of the tracers by oxygen.

Development of a fluorescence-yield model for naphthalene and toluene

The information we gathered about the photophysics of aromatic species allows us to extract data such as decay rates and fluorescence yields, which are required for the simulation of the cascading energy relaxation until the level of thermalisation is reached. In view of the analogies observed for ketones and naphthalene fluorescence in a non-quenching environment, the fluorescence yield simulation of naphthalene, based on an evolution of the cascading ketone yield model proposed by [Thurber 1999b] for acetone and adapted for 3-pentanone by [Koch 2005] is performed. This innovative model includes both intra- and intermolecular relaxation processes in non-quenching and quenching environments. After completing successfully this work, an extension of this model has been performed for toluene.

5.1 Photophysics of organic molecules – general remarks

Based on the presentation of photophysical processes in Chapter 2, we provide some relevant aspects concerning the photophysics of organic molecules of interest. It is useful to

keep in mind the different pathways governing the decay of an electronically excited state population, which can be represented in form of a Jablonski diagram (cf. section 2.9). Very fast processes such as the internal redistribution of vibrational energy occur quasi-instantaneously after absorption. Throughout the subsequent vibrational relaxation towards the Boltzmann distribution, a competition occurs between non-radiative and radiative deactivation processes, presenting different dynamics. Since process rates are also a function of vibrational excess energy, this competition has a strong impact on the fluorescence yield and needs to be known accurately.

5.1.1 Thermalisation of the vibrational population

A raise in temperature of the bath of molecules leads to a thermalisation of the tracer molecule in higher vibrational levels in the electronic ground state. Subsequent laser excitation promotes the molecule to higher vibrational levels in the $S_i\,(i \geq 1)$ state. Increasing the energy of absorbed photons by use of a shorter excitation wavelengths also populates higher vibrational quantum levels in the excited state. The thermal energy is then calculated from the summation over all N vibrational frequencies ω_i of the respective electronic state

$$E_{th} = \sum_{i=1}^{N} \omega_i / (e^{hc\omega_i / kT} - 1) \tag{5.1}$$

5.1.2 Thermal population of excited states

With the knowledge of the vibrational modes in the ground electronic state, the internal energy distribution of energy E_j of a single molecule in a thermal Boltzmann equilibrium is derived from

$$f_{pop}(E_j) = \frac{N_j}{N} = \frac{g_j \exp(-E_j / kT)}{Q_T} \tag{5.2}$$

g_j is the degeneracy of E_j and Q_T the partition function $\sum_j g_j \exp(-E_j / kT)$, fulfilling the normalisation $\sum_j f_{pop}(E_j) \equiv 1$ [Eckbreth 1996]. Q_T is estimated using an algorithm, e.g. such as of [Beyer 1973].

To analyse the thermal population of an electronically excited state after excitation of an ensemble of molecules in the electronic ground state in Boltzmann equilibrium, the population distribution given in equation (5.2) is evaluated for the relevant temperature range. The population at the moment following absorption of the photon prior to vibrational redistribu-

tion provides insight into the accessibility of the excited electronic states. Further, it helps for the estimation of the amount of vibrational excess energy to be redistributed.

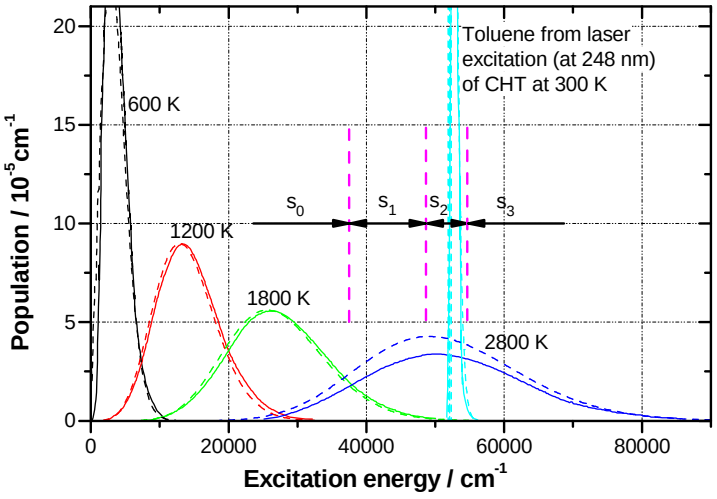

Figure 48: Example for thermal population estimation from [Hippler 1983a] for vibrationally highly excited toluene. The population distribution of toluene in the ground state is calculated for various temperatures (continuous lines from Hippler, dashed lines from this work). Highly excited toluene is obtained from cycloheptatriene at 300 K excited at 248 nm, which transforms to toluene under heat release, just $40323\ \mathrm{cm}^{-1} + \Delta H_f^0 \approx 52000\ \mathrm{cm}^{-1}$ [Ikeda 1985].

For instance, figure 48 shows the vibrational energy distribution calculated for ground state toluene molecules of temperature between 600 and 2800 K. The narrow distribution at about 52000 cm^{-1} corresponds to toluene, which has been rearomatised from 300 K cycloheptatriene (CHT) after excitation at 248 nm (40323 cm^{-1}) [Hippler 1983a]. The difference between the excitation energy and the mean energy of toluene formed from CHT corresponds to the heat of formation dissipated in extra vibrational energy.

5.1.3 Loss of vibrational identity through congestion

In case of low excitation energy, simple molecules might be selectively excited to single vibronic levels under collision-free conditions. For larger organic molecules, the frequency interval between the vibrational modes is so small, that simultaneous excitation of closely spaced "hot bands" becomes significant. Even for the use of an ideally monochromatic excitation source, the molecule is promoted to different electronically excited vibronic modes, defined by the ground state thermal distribution energy. This effect is known as sequence congestion or broadening, see e.g. [Nitzan 1972]. While for low excitation simple molecules show single vibronic level fluorescence spectra, excitation to higher vibrational levels in S_1 results in congestion, sometimes completely obscuring the vibrational structure of the fluorescence spectrum. Such observations are mainly interpreted as an effect of internal vibrational redistribution (IVR), which is at the origin of the loss of vibrational structure prior to the emission [Dolson 1983].

5.1.4 Energy gap law

The transition probability between electronic states is inversely proportional to the squared energy gap between the electronic states, which is also called the energy gap law, see equations (2.50) and (2.52). One consequence of this phenomenon is known as Kasha's rule: for most organic molecules, fluorescence only occurs from the first excited singlet state, subsequently to very fast internal conversion (IC) from S_n to S_1, see section 2.11.1. The large energy gap between the first excited state and the ground state leads to a predominance of fluorescence and ISC compared to IC. Moreover, the ISC rate is favoured for small singlet-triplet energy gaps (e.g. ketones).

5.1.5 Depopulation of single vibrational levels

The depopulation of the vibrational levels excited in the first singlet state is a competition between the fluorescence rate and non-radiative process rates. The rate of each pathway is a function of the environmental conditions, i.e. temperature, pressure and species composition, as well as of inherent energetic molecular structure of the excited molecule. Following the expression of the reaction efficiency defined in section 2.9.3, for each vibrational level n, the respective fluorescence quantum yield is given as the ratio of fluorescence rate $k_{f,n}$ to the sum of all possible radiative and non-radiative decay rates $k_{i,n}$

$$\phi_n = \frac{k_{f,n}}{\sum_i k_{i,n}} \tag{5.3}$$

Within the vibrational population of the excited state, each vibrational level is depopulated by either fluorescence, isoenergetic non-radiative pathways (IC and ISC) or collisional deactivation leading to intramolecular vibrational relaxation or intermolecular quenching reactions.

Since the collisional events are responsible for other pathways of depopulation of the vibrational levels, the denominator of equation (5.3) must be supplemented with the collisional rate and the quenching rate, the latter being the product of a quenching rate coefficient and the number density of quencher molecules $\tilde{k}_q n_q$. The fluorescence quantum yield of the respective vibrational quantum level is then (i.e. neglecting the other photochemical pathways)

$$\phi_n = \frac{k_{f,n}}{k_{f,n} + k_{coll,n} + \tilde{k}_q n_q + k_{NR,n}} \tag{5.4}$$

5.1.6 Changing deactivation rate constants during vibrational relaxation

Thermalisation occurs on time scale function related to the rates of collisions $k_{coll,i}$ with molecules present in the bath gas. This thermalisation is attributed to the vibrational relaxation (VR) (cf. section 2.12.1 with $k_{coll} = k_{VR}$) and ends at E_{th} from the vibrationless energy of the first excited singlet state (see equation (5.1)).

Increasing pressure shortens the average time between collisions, therefore increasing the VR rate (cf. section 2.12.1). The radiative and non-radiative rates both change with the amount of vibrational excess energy. They are thus indirect function of temperature (via the vibrational energy of the thermal ground state population, cf. equations (5.1) and (5.2)).

For a given condition of temperature and pressure, a step-to-step rate balance within a vibrational relaxation cascade towards the thermalised level can be performed. This enables the evaluation of the fluorescence quantum yield dependence on temperature, pressure and bath gas composition. An example of such a step-ladder model of vibrational relaxation is found in [Freed 1974]. Their model is based on the fact that the molecule can be replaced by one n-fold degenerate oscillator and collisions induce transitions to adjacent levels only.

5.1.7 Competition of fluorescence and non-radiative decay

A systematic loss of fluorescence yield with an increase of the excitation energy compared to the fluorescence yield at the (0,0) band might be interpreted as the enhanced influence of non-radiative pathways. Only few aromatic molecules show an absence of any photochemical pathway in exhibiting the same fluorescence yield over an extended range of excitation energy (e.g. for l,2-dihydronaphthalene vapour between 300 and 250 nm [Becker 1969] or for anthracene vapour between 370 and 300 nm [Beddard 1974]). For molecules, which are subject to a loss of fluorescence yield, the competition between isoenergetic pathways and photochemical reactions is mainly depending on the amount of vibrational excess energy.

Internal conversion is favoured by the existence of conical intersections between the potential energy surfaces. For aromatic molecules, this process is considered very fast when the vibrational excess is large [Farmanara 2001]. For a $S_1 \rightarrow S_0$ transition, the electronic energy is transformed into vibrational excess energy, which forms the so-called "hot" molecules in the electronic ground state. These hot molecules favour photochemical reactions [Ikeda 1985], which are likely to occur if their vibrational energy exceeds the level of the energy barrier on the potential energy surface or bond dissociation energies. Recall that the rate of non-radiative transitions was described by the Fermi golden rule (cf. section 2.9.1). With regard to the energy gap between the electronic states, the non-radiative rate is mainly controlled by two factors: the density of vibrational states ρ_n in the final electronic state and the Franck-Condon factors. The greater the energy gap between the electronic states, the higher

the density of vibrational states in the final state, but the smaller the vibrational overlap. Thus, both factors are in opposition, and an increase of ρ_n is generally overcompensated through increasingly unfavourable Franck-Condon factors (compare e.g. [Ashpole 1971, Klessinger 1995]).

Next to the vibronic and spin-orbit couplings, which are represented by their squared Hamiltonian terms in the Fermi golden rule, the relative positions of other electronic states within the range of excitation energy are also important for the effectiveness of non-radiative decay. For ketones, excitation for wavelengths longer than 200 nm is restricted to the first excited state, from which the first and second triplet states can be reached. Despite the collisionless case, vibrational relaxation within the first excited state is very fast, and therefore, the non-radiative decay is likely to occur from the thermalised levels, i.e. limited to $S_1 \rightarrow T_1$ ISC. In contrast to ketones, the energy gap between adjacent singlet states is much smaller for aromatic molecules, and furthermore, the number of accessible triplet states is potentially large (e.g. naphthalene, including six triplet states within an excess energy of 10000 cm^{-1}, cf. [Stockburger 1975]).

5.1.8 Pressure induced fluorescence yield stabilisation effect

For many organic molecules, next to the decrease of the fluorescence yield with vibrational excess energy, the fluorescence yield increases with the pressure of foreign gases. Rapid energy removal by collisionally induced VR lowers the propensity to internal deactivation via radiationless channels such as internal conversion and intersystem crossing, in case these exhibit rates grow with the vibrational energy excess.

[Bowen 1956] studied this phenomenon on perylene to avoid perturbations coming from predissociation and other photochemical effects. For excitation at 405 nm near to the (0,0) band, only a slight dependence on the pressure of added foreign gas (hexamethylbenzene) is observed, the fluorescence levelling off at very low pressure. By contrast, higher energy excitation at 365.5 nm leads to a stabilisation effect, which is not limited to low pressure. The fluorescence enhancement induced by foreign gas pressure is more intensive for large organic molecules with large collisional diameters than for a small inorganic species like nitrogen.

[Archer 1973] discussed extensively the effect of temperature, pressure and excitation wavelength on photoluminescence of acetaldehyde vapours. Compared to perylene, this small molecule becomes easier involved to photodissociation reactions if excitation energy exceeds the (0,0) band energy. However, like for perylene, the fluorescence yield of acetaldehyde showed an increase with rising pressure. The yield stabilisation occurs with different strengths for various foreign gases (acetaldehyde, trans-butene-2 and isobutane). Archer et al. showed further, that even at higher pressure, the absolute yield is considered as a decreasing

function of rising excitation energy. They concluded, that higher vibrational excess increases the probability to populate short-lived vibrational states, which are less sensitive to collisional deactivation.

Measurements of naphthalene fluorescence lifetime and quantum yield in the low-pressure regime (~0 – 160 torr) shows a yield stabilisation effect with increasing foreign gas pressure (argon and methane) for high excitation energies, but not for low excitation energy, where a decrease of lifetime and yield is observed [Beddard 1973]. For further increasing pressure, the lifetime becomes independent from excitation wavelength, converging to the Boltzmann distribution. Longer lifetimes for high excitation energies are attributed to the cooling of the vibrational distribution of naphthalene through collisions with the foreign gas. This is consistent with the idea, that longer lifetimes represent lower internal energies. The shortening of the lifetimes for low excitation energies is interpreted as an opposite effect. Photoexcitation initially cools the molecule, then collisions with the foreign gas heat vibrational levels. Applying the step-ladder model of vibrational relaxation from [Freed 1974], the experimental results are confirmed [Beddard 1974]. The collisionally induced cooling (or heating) of the vibrational population of electronically excited polyatomic molecules was studied in detail by Pollak and co-workers using Gaussian binary collision theory [Wadi 1999]. With their model, they were able to explain the decrease of naphthalene lifetime with argon pressure observed after 310 nm excitation [He 2002].

The experiments of Beddard et al. on naphthalene are performed at pressure lower than 1 bar. However, yield stabilisation of other molecules is also observed for higher pressure. [Thurber 1999a] studied the dependence of the fluorescence quantum yield of room temperature acetone with pressure and composition of the bath gas for various excitation wavelengths. From their measurements performed in nitrogen and a pressure range between 0.5 and 12 bar, Thurber et al. observed a yield stabilisation effect, which is most pronounced for the highest excitation energy at 248 nm and clearly reduced towards lower excitation energies. Similar observations are reported from [Grossmann 1996] and [Koch 2005] for 3-pentanone. A ketone fluorescence yield model developed by Thurber and Koch (cf. section 5.3) explains this behaviour. At high-pressure (~ hundreds of bar), the electronic deactivation via fluorescence occurs after a complete vibrational relaxation of the molecule, i.e. the fluorescence yield is no longer a function of excitation energy. At low-pressure (mbar), electronic deactivation occurs prior to vibrational relaxation. Therefore, the fluorescence occurs from the initially populated vibrational level. The latter is a function of vibrational excess, and thus depends on excitation wavelength. When the rates of non-radiative channels are growing with vibrational excess, the yield stabilisation becomes less intense for a reduction of the excitation energy towards the origin of the (0,0) band.

The opposite effect of the pressure-induced yield decrease observed for naphthalene by Beddard et al. for low excitation energies cannot be explained by the model of Thurber and Koch. This is in part due to the assumption of the unidirectional collisional energy dissipa-

tion from the excited molecules to the bath gas. As noticed by He at al., the observed yield decrease is connected to the initial vibrational cooling by photoexcitation, which occurs for molecules, which have (like naphthalene) vibrational frequencies lower for the excited state than for the ground state. This effect becomes significant in the immediate vicinity (< 500 cm^{-1}) of the (0,0) transition, and is expected to be most intense at ω_{00}.

5.2 Photophysics of ketone tracers

As mentioned in chapter 4.3.1, for carbonyl compounds one of the lone pair electrons of the n-MO is promoted to the π^*-MO by absorption of UV light. For acetone, this transition is both orbital-overlap and spatial-symmetry forbidden. Weak absorption of about $\varepsilon_{\max} = 20\ l\,mol^{-1}cm^{-1}$ is observed as a result of vibronic mixing, i.e. the $S_1(n,\pi^*)$ state is mixed to the second singlet state $S_2(\pi,\pi^*)$.

5.2.1 Distinction between aliphatic and aryl ketones – El Sayed's rules

In contrast to the aliphatic ketones, aryl ketones as benzaldehyde, aceto- and benzophenone are not suitable as fluorescence tracers, because of their weak fluorescence yields. This can be explained from the very fast intersystem crossing (ISC) rate between the (n,π^*) singlet and (π,π^*) triplet state, following the mechanism (2.63), allowed by the El Sayed's rules (cf. section 2.11.2). For aliphatic ketones, this allowed transition is not available due to the specific alternation of the singlet and triplet states (cf. figure 15 section 2.11.2), and hence, ISC occurs via the mechanism (2.64), forbidden by the El Sayed's rules. While the fluorescence is generally of low rate due to the two-fold violation of selection rules mentioned above and due to the lowered ISC rate, fluorescence becomes a competitive pathway.

5.2.2 Absorption studies

A wealth of studies has enlightened the comprehension of ketone photophysics, when excited in the middle UV. Room temperature absorption spectra with UV lamp were reported from [Martinez 1992] for several aliphatic aldehydes and ketones including acetone and 3-pentanone, as well as from [Yujing 2000] for several ketones including acetone. [Grossmann 1996] published normalised absorption spectra for 3-pentanone at 298 and 573 K. A clear red-shift with increasing temperature is systematically observed.

[Grisch 1997] measured the absorption cross-section of acetone for excitation wavelengths between 248 and 320 nm and from room temperature up to 900 K. The results con-

firm the red-shift of the absorption spectra with increasing temperature, and in addition, for fixed temperatures, absolute absorption is found to increase with excitation wavelength. [Koch 2003b] made absorption cross-section measurements of 3-pentanone at 248, 266 and 308 nm and between 300 and 875 K. These measurements were completed by deuterium lamp absorption measurements from room temperature up to 1040 K [Koch 2008]. In order to summarise all previous results, Koch proposed a generalised description for the temperature and the wavelength dependences of the absorption cross-section. Agreement with other published data is sufficient to conclude with the proposal of a general formula, describing the absorption cross-section from acetone and 3-pentanone,

$$\sigma(\lambda,T) = A(T)\exp\left[-\left(\frac{\lambda-\lambda_c(T)}{w(T)}\right)^2\right] \tag{5.5}$$

with the parameter $A(T)$, $\lambda_c(T)$ and $w(T)$ issued from the following table.

Table 8: Fit parameters allowing formula description of absorption cross-section of acetone and 3-pentanone in dependence of temperature and excitation wavelength. From [Koch 2008], valuable from 230 to 330 nm and 300 to 1040 K.

Species	$\frac{w(T)}{\text{nm}}$	$\frac{A(T)}{10^{-20}\ \text{cm}^2}$	$\frac{\lambda_c(T)}{\text{nm}}$
Acetone	$26.8 + 0.00950\,T$ [K]	$3.43 + 0.00482\,T$ [K]	$271.4 + 0.0156\,T$ [K]
3-Pentanone	$25.1 + 0.0101\,T$ [K]	$4.77 + 0.00487\,T$ [K]	$273.7 + 0.0186\,T$ [K]

5.2.3 Deactivation pathways

For aliphatic ketones like acetone and 3-pentanone, the relatively low singlet-triplet energy gap ΔE_{ST} (3200 cm^{-1} or 0.4 eV for acetone [Greenblatt 1984]) allows for very fast depopulation of the singlet state via intersystem crossing (ISC). Practically, the non-radiative decay rate k_{NR} consists of ISC, i.e. $k_{NR} \approx k_{ISC}$, and thus k_{ISC} becomes the limiting factor for the fluorescence yield.

A comparison of photophysical properties like absorption and emission spectral ranges, maximal absorption cross-section, fluorescence yield and decay times was reported for several tracers [Lozano 1992]. [Ghandhi 1996] showed, that the fluorescence yield of acetone and 3-pentanone for 266 nm excitation is subject to a quenching effect when increasing temperature (300 to 600 K). [Grossmann 1996] studied the pressure effect (1 to 26 bar) on the fluorescence for 248 nm excitation at 383 K for both oxygen and synthetic air atmosphere.

The fluorescence signal increases with increasing pressure until the vibrational relaxation is completed. For nitrogen atmosphere, the signal is reported to level off, whereas, for air and oxygen environments, decreases after an initial increase due to collisional quenching. [Ossler 1997] presented fluorescence lifetimes of acetone and 3-pentanone for picosecond laser excitation of 266 nm. The results are concordant with the fluorescence data from Grossmann. [Yuen 1997] measured the pressure dependence of the fluorescence yield of acetone from 1 to 8 bar at 266 nm excitation with nitrogen, air, methane and helium atmosphere. Comparison to [Ossler 1997] shows the same trends for nitrogen and air.

The attenuating effect of the temperature increase on the ketone fluorescence was further studied by [Grisch 1997]. The temperature was varied from 300 to 1000 K for eight excitation wavelengths ranging between 248 and 320 nm. Next to the fluorescence, the absorption cross-section was measured by laser extinction, which allows the determination of the quantum yield over a wide range of wavelength and temperature. Analysing the wealth of data, a ketone fluorescence yield model was proposed, based on a deactivation scheme of the vibrational excess energy via a collisional cascade. Later, [Thurber 1999a] investigated the pressure dependence of acetone fluorescence for 248, 266 and 308 nm excitation and compared the composition dependences for nitrogen, air and oxygen bath gas (0.5 to 8 bar), as well as for nitrogen, methane and helium bath gas (0.5 to 10 bar). All the results are shown to be concordant with their ketone fluorescence yield model. For the 3-pentanone tracer, [Koch 2001] studied the fluorescence and absorption temperature dependence for 248 and 308 nm excitation between 300 and 875 K. In a following study [Koch 2003a], the excitation was extended to 266 nm, and the ketone fluorescence yield model from Thurber was successfully adapted to the case of 3-pentanone. Recently, [Modica 2007] revisited the role of the pressure to the fluorescence of 3-pentanone at 266 nm excitation wavelength. Measurements were performed for pressure between 1 and 40 bar, for temperature from 373 to 573 K and various foreign gases. The results confirm the expectations deduced from Thurber's ketone fluorescence model, which was in the meantime adapted to 3-pentanone by [Koch 2003a] and compared for the pressure data from Grossmann.

5.2.4 Accessibility of electronic states for the studied ketone tracers

The origins of the first excited state of acetone (30435 cm^{-1} [Baba 1985]) and 3-pentanone (30770 cm^{-1} known from [Hansen 1975]) are close. With the knowledge of the vibrational modes in the ground state for acetone [Shimanouchi 1972] and 3-pentanone [Koch 2003a], the population function was calculated for a temperature range from 300 to 1000 K using equation (5.2), cf. section 5.1.1.

Figure 49 depicts the population on the excited states after absorption of a 266 nm photon prior to vibrational redistribution for acetone and 3-pentanone as a function of temperature. Excitation at 266 nm leads to an average vibrational excess energy ranging from 7450 to

12700 cm^{-1} for acetone and from 7600 to 17300 cm^{-1} for 3-pentanone for a change of temperature from 300 to 1000 K. Thus, the population is largely settled above the origin of the S_1 state, but does not reach the energy of the second excited state for both molecules (presuming an S_2 origin of 3-pentanone similar to acetone).

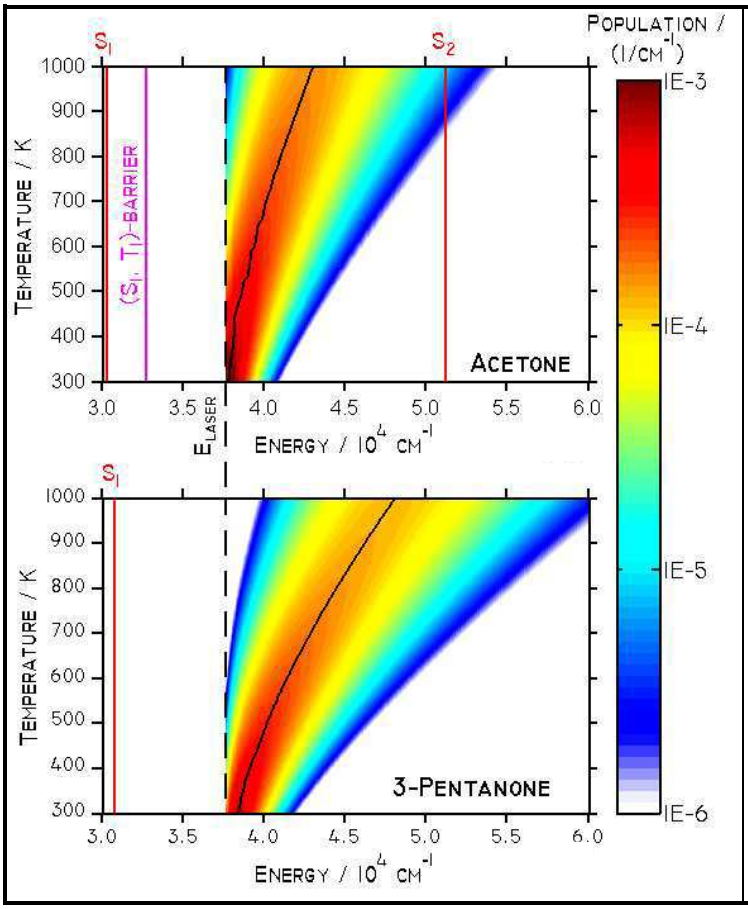

Figure 49: Accessibility of electronic transitions for acetone and 3-pentanone. The ground state populations were evaluated for temperature from 300 to 1000 K from the distribution functions calculated for the vibrational modes of acetone [Shimanouchi 1972] and 3-pentanone [Koch 2003a]. The ground state population is shifted by absorption of the laser energy (266 nm = 37594 cm^{-1}) to the excited state level. This corresponds to the situation prior to the redistribution of the vibrational energy to the modes in S_1 following the Franck-Condon factors. For the origins of the electronic states see for acetone: S_1 [Baba 1985], S_2 [Gaines 1988], (S_1, T_1)-barrier [Zuckermann 1989]; for 3-pentanone: S_1 [Hansen 1975].

The temperature dependence of fluorescence was reported from [Thurber 1998] and [Koch 2003b] to be a strong function of excitation wavelength for both molecules. The increase of the wavelength beyond 300 nm leads to a growing part of the population staying below the origin of the S_1 state for room temperature. Thus, the population excited to the S_1 state becomes a function of temperature. A temperature raise will at the same time modify the population of the excited state and the photophysical processes of the molecule (the rates of fluorescence and non-radiative decay generally vary with the amount of vibrational excess energy).

5.2.5 Reaction pathways

When vibrational excess energy becomes significant, dissociation processes might come into play as additional pathways of deactivation. Thus, we resume relevant information from the

literature about accessible bond-cleavage reactions from the potential energy surface as a function of excitation energy.

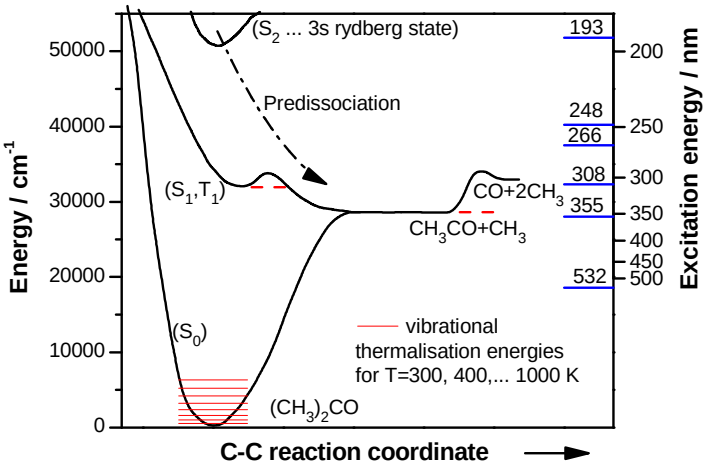

Figure 50: Approximate energy level diagram of acetone adapted from [Trentelman 1989]. An excitation to the predissociative S_2 (3s Rydberg) state is possible for 193 nm. The S_1 state is separated from the T_1 state by an endothermic energy barrier caused by an avoided crossing. Passing over this barrier leads to a first dissociation to acetyl and methyl radicals. A second barrier separates from secondary dissociation of the acetyl radical.

The absorption band corresponding to the $n \rightarrow \pi^*$ transition of the nonbonding electron on the oxygen to the antibonding orbital localised at the C=O group is centred at about 280 nm (cf. figure 44, section 4.3.1). An excitation at this wavelength populates the S_1 adiabatic potential energy surface, which is often depicted together with the first triplet state T_1 separated by a small energy barrier caused by an avoided crossing. Figure 50 shows an approximate energy diagram for acetone over the C-C reaction coordinate. [North 1995] reports a vibrational excess of 2340 cm^{-1} above the S_1 origin to be sufficient to overcome the energy barrier on the (S_1, T_1) surface and to dissociate acetone to an acetyl and a methyl radical

$$CH_3COCH_3 \rightarrow CH_3CO + CH_3 \tag{5.6}$$

A secondary pathway of decomposition is possible, when the energy of the acetyl radical exceeds the dissociation barrier of 6016 cm^{-1}

$$CH_3CO \rightarrow CH_3 + CO \tag{5.7}$$

When ketones like acetone and 3-pentanone are used as fluorescence tracers, special care must be paid to the dissociation characteristics. A strong connection exists with the excitation energy, and thus, even if the absorption increases for shorter wavelength, the fluorescence decreases due to a higher rate of dissociation [Lozano 1992].

Cell measurements with a low gas exchange rate, [Thurber 1999b] show a significant decrease of acetone fluorescence due to laser photolysis for 248 or 266 nm excitation, when

the same molecules are excited repeatedly (thousands of laser shots). For 308 nm excitation, this effect is practically lowered to a negligible extent.

5.3 Ketone fluorescence yield model

A ketone fluorescence yield model was developed for acetone by [Thurber 1999b] and adapted for 3-pentanone by [Koch 2005]. The basic ideas of their approach are described in the following section. The model is used in our study for comparison to our experimental results (cf. section 5.4).

5.3.1 Deactivation rates of fluorescence, ISC and VR as a function of temperature and pressure

For most ketones, the rate of fluorescence is reported to be approximately constant with vibrational energy E, and further rather independent of pressure. [Thurber 1999b] cited several articles reporting a fast increase of the non-radiative decay rate k_{NR} with the vibrational quantum number within the first singlet state for carbonyl compounds as well as for aromatics. Hence, a specific single vibrational level contributes more efficiently to the overall fluorescence quantum yield when the vibrational level is low. The population fast "evacuated" by VR to lower vibrational levels penalises the higher level ISC channels in favour of the less efficient lower lying, yielding an increase of the fluorescence quantum yield efficiency.

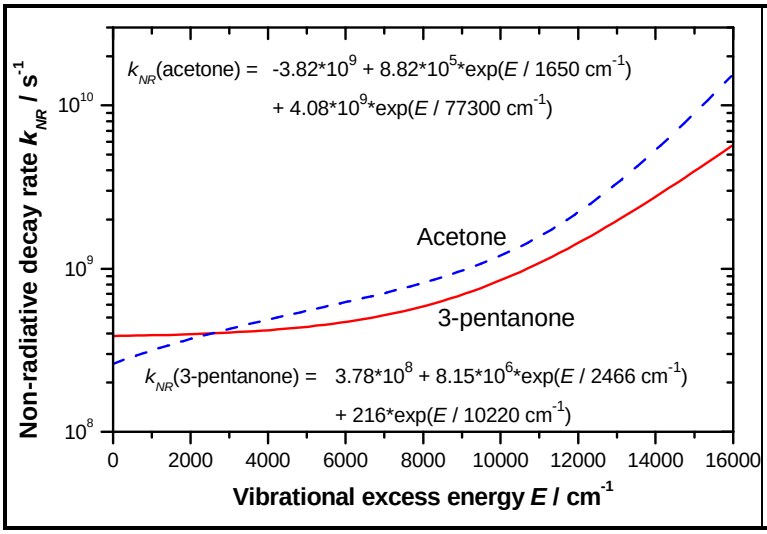

Figure 51: Optimised fit for non-radiative decay rate k_{NR} from experimental data as proposed for acetone and 3-pentanone by [Thurber 1999b] and [Koch 2005]. For both species a double exponential function of vibrational excess energy E was found..

Thurber proposed a double exponential function of vibrational excess energy for the description of k_{NR} as a best fit to experimental data for acetone. Similarly, [Koch 2005] found also a double exponential dependence for 3-pentanone (cf. figure 51).

5.3.2 The cascading approach

Figure 52 illustrates the parameters of the ketone model in a Jablonski diagram. Both Thurber and Koch made several assumptions based on ketone fluorescence literature [Thurber 1999b] and [Koch 2005].

As a consequence of the energy gap law for ketones, the small singlet-triplet energy gap strongly favours ISC compared to IC. The rate of non-radiative isoenergetic decay is therefore $k_{NR} \approx k_{ISC}$. A further consequence (Kasha's rule) is the very fast IC from higher excited electronic states, which therefore restricts the rate balance of the excited population within the fluorescence yield model to the first excited singlet state, cf. figure 52.

The amount of energy brought to the molecule by absorption promotes a molecule from the thermalised energy E_{th} of S_0 to a vibrational level in the excited state S_1 with the vibrational excess energy corresponding to

$$E = E_{th,S_0} + \Delta E_{laser} - E(S_{1,v=0}) \tag{5.8}$$

Collisional and collisionless processes lead to a dissipation of the vibrational excess energy. As mentioned previously, the fluorescence rate k_f is approximately constant with vibrational energy E. The non-radiative decay rate, mostly attributed to ISC, strongly grows with the vibrational excess energy, $k_{NR} \sim E$.

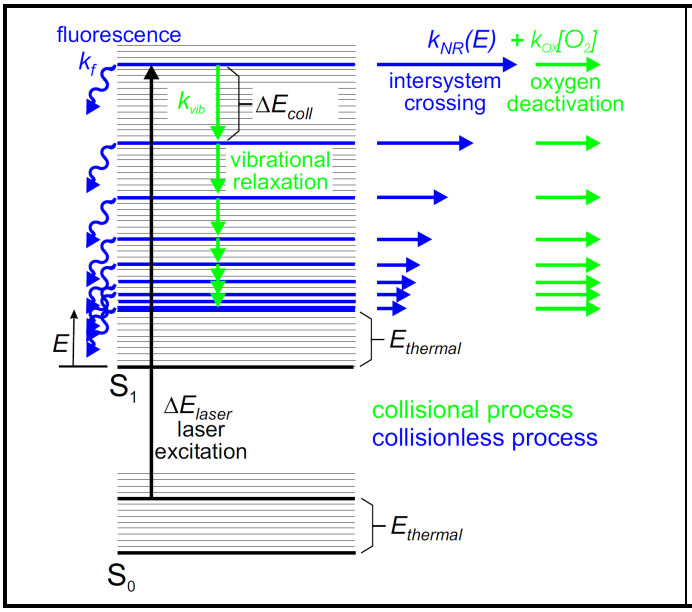

Figure 52: Taken from [Koch 2005]. Jablonski diagram illustrating the model parameters and energy transfer processes involved in the first excited singlet of ketones like acetone and 3-pentanone. $k_{ox}[O_2]$ stands here for $\tilde{k}_{O_2} n_{O_2}$.

Next to IC and ISC, collisional events leading to depopulation by VR are also intramolecular deactivation processes. [Thurber 1999b] studied the rates k_{coll} for acetone collisions with helium, nitrogen and methane as well as for self-collisions with acetone. The collisional model of Thurber is inspired by the results of [Hippler 1989], expecting a linear

proportionality between the vibrational excess energy E and the average energy transferred per collision ΔE_{coll}. The energy decay rate for a molecule at energy E is then given as

$$k_{coll} \cdot \Delta E_{coll} = k_{coll} \cdot \alpha\left(E - E_{thermal}\right) \tag{5.9}$$

The ketone fluorescence yield model developed by Thurber is an energy cascading model, starting from vibrational excess energy E, summing at each level of the collisional cascade the product of the respective probability of fluorescence with the probability of molecules getting to this specific vibrational level. At any step i of the vibrational cascade, the probability of fluorescence occurring from this level is the ratio of the fluorescence rate k_f to the sum of all possible decay rates, whereas the probability of arriving at this level i is the product from all vibrational decay probabilities of levels above i, each being the ratio of the respective vibrational rate k_{coll} to the sum of all possible decay rates. The cascading ends by definition at a minimum distance from the thermalised level. The following expression summarises the cascading algorithm in the following equation

$$\begin{aligned}\phi = \sum_{i=1}^{N} \phi_i = & \quad \frac{k_f}{k_f + k_{coll} + \tilde{k}_{O_2} n_{O_2} + k_{NR,1}} \\ & + \sum_{i=2}^{N-1} \left(\frac{k_f}{k_f + k_{coll} + \tilde{k}_{O_2} n_{O_2} + k_{NR,i}} \prod_{j=1}^{i-1} \frac{k_{coll}}{k_f + k_{coll} + \tilde{k}_{O_2} n_{O_2} + k_{NR,j}} \right) \\ & + \frac{k_f}{k_f + \tilde{k}_{O_2} n_{O_2} + k_{NR,N}} \prod_{j=1}^{N-1} \frac{k_{coll}}{k_f + k_{coll} + \tilde{k}_{O_2} n_{O_2} + k_{NR,j}}\end{aligned} \tag{5.10}$$

5.3.3 Temperature and pressure dependence of the decay rate of VR

The energy decay rate by VR for a molecule at energy E from equation (5.9) is both temperature and pressure dependent via the number density of the collision partner M, relating to the collision rate defined by the Lennard-Jones collision frequency

$$k_{coll} = n_M Z_{coll} \tag{5.11}$$

with Z_{coll} being itself a function of $\sqrt{T}$. Furthermore, equation (5.9) is function of temperature by means of the average energy transferred per collision

$$\begin{aligned}\Delta E_{coll} &= \alpha\left(E - E_{th,S_1}\right) \\ &= \alpha\left[E_{th,S_0} + \Delta E_{laser} - E(S_{1,v=0}) - E_{th,S_1}\right]\end{aligned} \tag{5.12}$$

The thermal energy is defined from equation (5.1) as a function of temperature. The temperature dependence attributed to ΔE_{coll} is inherent to both E_{th,S_0} and E_{th,S_1}. The net influ-

ence is hence small if the vibrational distributions of the ground and excited states are similar.

Within their ketone yield model, Thurber et al. adopted a simplified expression for ΔE_{coll} using exclusively the ground state thermal energy E_{th,S_0}, thus neglecting possible differences between the vibrational mode frequencies in the S_0 and the S_1 states. In the case of acetone, this assumption is justified, since differences are minor, cf. [Liao 1999].

For acetone, Thurber assumes $\alpha_{Ace} = 0.021$ as a simple proportionality constant for collisions with nitrogen. Increasing the pressure, a simple $\alpha_{3P} = 0.05$ allows to achieve good agreement of the quantum yield simulation with experiments for near room temperature for 3-pentanone. For higher temperature (723 K), [Koch 2005] proposes α_{3P} to be further temperature dependent. For nitrogen atmosphere, $\alpha_{3P} = 0.05(T/300)^{-1.2}$ with T in K is suggested to be more adapted to describe the effect of temperature on the pressure dependence of the vibrational relaxation rate.

When quenching reactions are virtually absent, e.g. such as in pure nitrogen, collisions with the bath gas lead exclusively to vibrational relaxation, i.e. intramolecular decay. The fluorescence quantum yield levels off for very low (mbar) and very high (hundreds of bar) pressures. In the first case, the average time between collisional events becomes too large to significantly reduce the non-radiative decay rate. For the latter case, vibrational relaxation becomes dominant over the non-radiative pathways, and therefore fluorescence is occurring only from the thermalised population distribution. For intermediate pressures, vibrational relaxation and non-radiative channels have similar time scales, leading to a competition between the depopulation via collision and intersystem crossing.

5.3.4 Oxygen quenching

The mechanism of fluorescence quenching by triplet oxygen was described earlier in section 2.12.5, pointing out the differences between the quenching efficiency of ketones and aromatic molecules. In contrast to the strong effect on aromatics, which will be detailed in the aromatics section, the quenching effect on ketones is, at least for atmospheric pressure, rather negligible. Nevertheless, for higher pressure, oxygen quenching might compete with vibrational relaxation, and therefore reduces significantly the increase of fluorescence yield observed as a yield stabilisation effect. [Thurber 1999a] studied this behaviour at room temperature for both 248 and 266 nm excitation of acetone vapour. The pressure was varied between 0.5 and 8 bar and pure nitrogen, air and pure oxygen were considered as bath gas. Similarly, for 383 K slightly above the 3-pentanone boiling point, [Grossmann 1996] showed the behaviour of acetone and 3-pentanone fluorescence with pressure up to 26 bar, changing the bath gas between nitrogen, synthetic air and oxygen. For both studies, the fluorescence

signal displayed a decrease with the amount of oxygen present in the bath gas, when pressure is raised to several bar. Thurber referred the oxygen quenching effect to an oxygen-enhanced intersystem crossing as reported by [Nau 1996] for aliphatic ketones and diketones in solution. Nau proposed further processes likely to represent the effect of oxygen quenching, including the electronic energy transfer to the oxygen molecule (resulting in singlet oxygen production) and oxygen-enhanced internal conversion. They reasoned with analogy to the electronic configuration of azoalkanes in which oxygen-enhanced ISC is the dominant quenching process for aliphatic ketones excited to singlet (n,π^*)–states. The quenching induced by ketone-oxygen collisions proceeds via the formation of an intermediate encounter complex. [Thurber 1999b] proposed, according to [Brown 1974], that the overall quenching rate can be handled like a collision frequency if the intermediate formation reaction has a low reverse rate. Thus, Thurber and Koch incorporated the collisional quenching rate directly to the summation of decay rates within the denominator of the model fluorescence yield definition (5.10)

$$k_{O_2} = \tilde{k}_{O_2} n_{O_2} = \langle P \rangle Z_{O_2} n_{O_2} \tag{5.13}$$

Following equation (2.69), the quenching efficiency $\langle P \rangle$ is defined as the ratio of quenching rate coefficient to the Lennard-Jones collision frequency Z_{O_2} for ketone-oxygen collisions.

An interesting result deduced from the measurements of Thurber and Grossmann is the initial fluorescence increase for low pressure under pure oxygen atmosphere, revealing that collisions with oxygen can also lead to vibrational relaxation. However, as a distinction between relaxation and quenching is not accessible, the average energy transferred per collision leading to quenching is calculated with the same proportionality factor α as for the case of nitrogen. Consequently, Thurber and Koch did not account for the $(1-\langle P \rangle)$-proportion of oxygen collisions inefficient for quenching leading to VR and populating the next lower lying vibrational level. This process might be legitimated by the overall low quenching influence for ketones.

For acetone and room temperature, [Thurber 1999a] found a quenching efficiency $\langle P \rangle$ of 0.00399, which lead to the best fit of the model to the experimental results in the presence of oxygen quenching. [Koch 2005] reported the quenching efficiency $\langle P \rangle$ of 3-pentanone with oxygen to be partially defined with a discontinuity at vibrational energy $E = 11000\,\mathrm{cm^{-1}}$, being an exponential function $\langle P \rangle = 0.0023 \exp(5 \cdot 10^{-5} E)$ with E in $\mathrm{cm^{-1}}$ below and jumping to $\langle P \rangle = 0.25$ above that value.

5.4 Fluorescence of aliphatic ketone tracers – acetone and 3-pentanone

The fluorescence spectra measured in this spectroscopic study with a 266 nm excitation for gaseous acetone and 3-pentanone are compared to results obtained from other research groups, cf. figure 53 (for 3-pentanone molecule, refer to chapter 3.7.1). Assessing the spectra found in literature, it must not be forgotten that each result is based on signal correction, e.g. accounting for spectral and intensity sensitivity of the detection optics and devices. Due to the brevity of details in publications, the procedure used to analyse the spectra is often restricted to general terms like "corrected for the detection system transmission and responsivity" [Bryant 2000]. Nevertheless, ignoring this difficulty for comparison between spectral results in figure 53, the shape of the fluorescence spectrum measured within this study for 300 K seems to agree quite well the data of e.g. [Schulz 2005], [Grisch 1997] and [Bryant 2000] under similar conditions, except for the region from 370 to 400 nm, where a double-peak feature showed in our study (as it is the case for 3-pentanone, figure 36, chapter 3.7.1). A similar double-peak feature for acetone was otherwise reported by [Lozano 1992] for 308 nm excitation. Somehow, for the long wavelength tail the spectrum from Bryant differs, which might be related to a very low tracer concentration combined to very high laser intensity.

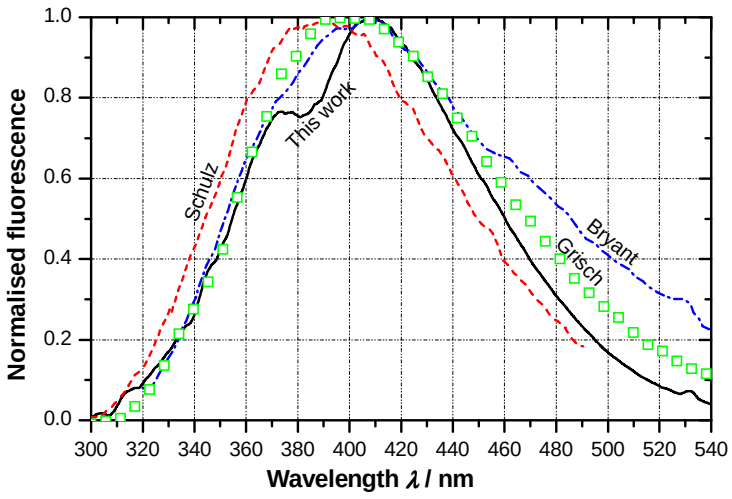

Figure 53: Fluorescence spectra for acetone excited at 266 nm: this work (continuous black line) compared to measurements from [Schulz 2005] (dashed red line), from [Grisch 1997] (green square dots) and from [Bryant 2000] (dash-dot blue line). Atmospheric pressure pure nitrogen.
Schulz: 295 K with 13 mbar tracer at 1 atm, pure N_2. This work: 300 K with 40.6 mbar tracer at 1 atm, pure N_2. Grisch: 290 K with less than 50 mbar tracer at 1 atm, pure N_2. Bryant: 295 K with 2.14×10^{15} cm^{-3} tracer (< 0.1 mbar with 25 mJ/pulse laser energy, 6 mm beam diameter) at 1 atm, dry air.

Altogether, figures 36 and 53 depict the general appearance of the room temperature fluorescence spectra of acetone and 3-pentanone. Without going into details of differences in spectral shape, all spectra are considered as broad-band with a sharp fluorescence increase for the short wavelength tail (~300 nm), and red-shifted from the excitation wavelength. As the underlying electronic transition is an orbital- and symmetry-forbidden $n \rightarrow \pi^*$ transition, the fluorescence quantum yield is low, thus leading to a small signal-to-noise ratio, which evidently turns out to be a disadvantage, especially when looking at spectrally resolved data. It is therefore not surprising to be confronted with the spectral differences for the results of different research teams. Furthermore, the used tracer substances are not always applied with high-grade purity. Thus, impurities might also be at the origin of the different spectral appearances.

5.4.1 Temperature and pressure dependence on acetone and 3-pentanone fluorescence

The temperature dependence of acetone and 3-pentanone fluorescence is studied in this work for nitrogen bath gas at atmospheric pressure, the temperature ranging between 300 and 900 K. In the upper part of figure 54, fluorescence spectra are presented normalised to the one recorded at 400 K. For low temperature, the spectra of acetone and 3-pentanone have almost the same shape, disregarding the lower lying peak at 372 nm being more pronounced for acetone.

With increasing temperature, acetone fluorescence remains spectrally almost unchanged. In contrast, the 3-pentanone spectra are split at about 395 nm to a spectrally changed and unchanged part with increasing temperature. While the long-wavelength tail seems not affected when increasing temperature, the short-wavelength tail presents a hypsochromic (blue) shift, the lower peak increasing more than linearly. Up to now, no explanation for this effect was found due to the lack of references of spectral data for 3-pentanone fluorescence with temperature. To our knowledge, only the Division of Combustion Physics of Lund University published temperature dependent spectra, see [Ossler 1997], which were, however, obtained from excitation with picosecond laser.

The dependence of fluorescence spectra with temperature are integrated from 280 to 520 nm and normalised to the one recorded at 300 K in order to compare to results from [Koch 2003b], see bottom part of figure 54. For both acetone and 3-pentanone, the results are consistent with the data published by Koch. For acetone, the fluorescence yield model from Thurber (multiplied by the absorption cross-section from equation (5.5)) predicts the fluorescence signal with temperature, the proportionality constant for the energy decay rate via vibrational relaxation $\alpha = 0.021$ as chosen by Thurber. In the case of 3-pentanone, three proposals were made for the value of the proportionality constant, one within [Koch 2003a] and two in [Koch 2005], one of which was dependent on temperature. The best α value for

the fluorescence temperature dependence of 3-pentanone is found for $\alpha = 0.050$, at least for atmospheric pressure.

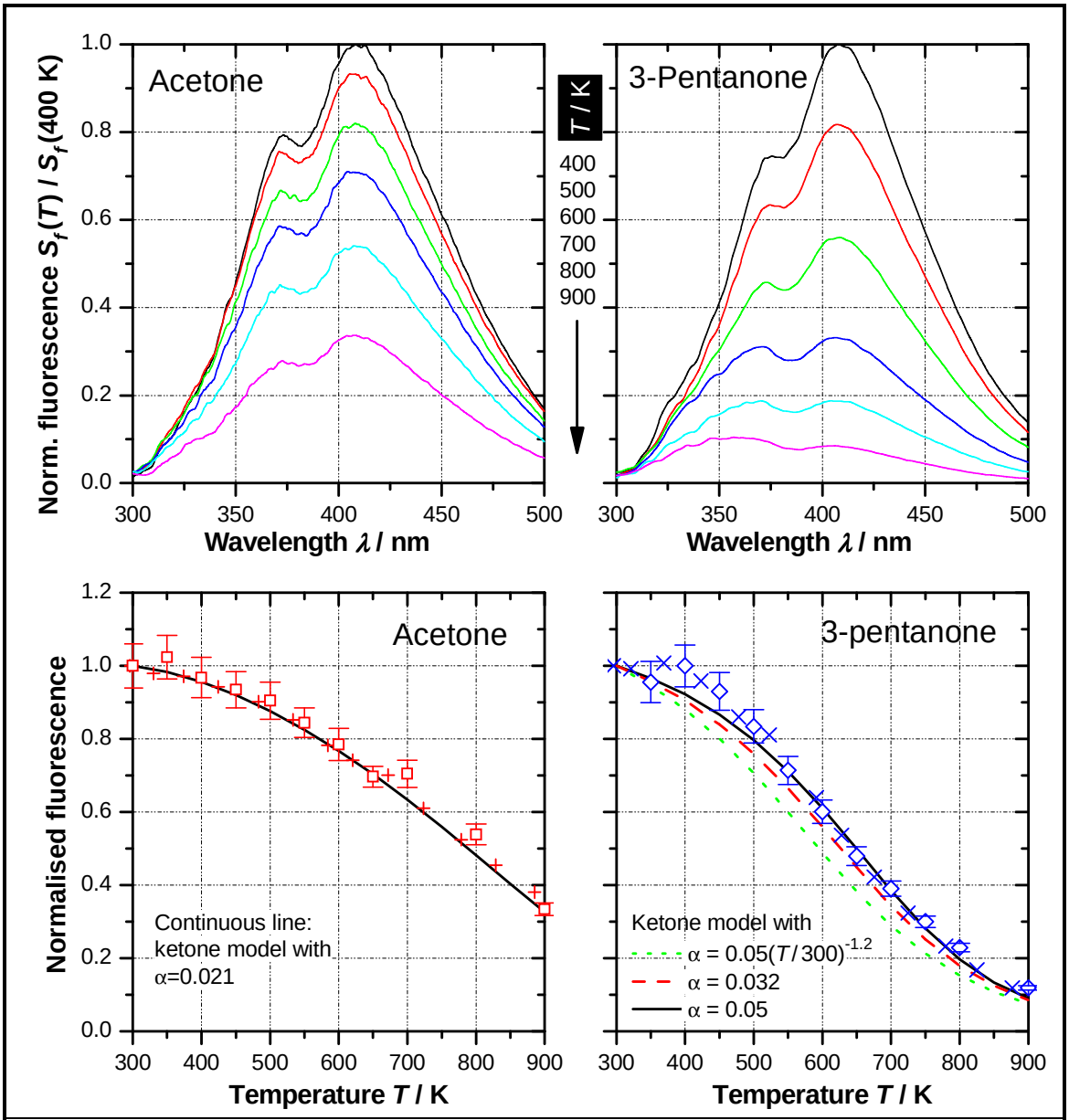

Figure 54: Acetone and 3-pentanone fluorescence after 266 nm laser excitation as a function of temperature. Normalised to the one recorded at 350 K, from integrated fluorescence spectra (280 to 520 nm). Pure nitrogen atmosphere at ambient pressure. The line represents fluorescence yield from [Thurber 1998] with $\alpha = 0.021$ multiplied by the absorption cross-section. Acetone: □ this work, + [Koch 2003b] compared to the model of [Thurber 1998] (multiplied by the absorption cross-section). 3-pentanone: ◇ this work, × [Koch 2003b] compared to the model of [Koch 2005] (multiplied by the absorption cross-section).

As mentioned above, [Koch 2005] reported that the temperature dependent α value gives a better agreement for higher pressure. In order to validate this assumption, experimental data from [Modica 2007] were compared to the fluorescence yield model of Koch. In figure 55, the results from Modica on 50 K temperature steps between 373 and 573 K and data from our work for 450 and 550 K are compared to the simulation for a pressure range between 0.1 and 3 MPa. Very good agreement is obtained with $\alpha(T) = 0.05(T/300)^{-\beta}$, T in K and $\beta = 1.5$ instead of 1.2 as initially proposed by Koch.

Our pressure dependence on fluorescence data as well as the data from Modica agree with the model predictions from Koch, which underlines the reliability of our spectroscopic setup and the fluorescence yield modelling for pressures up to 30 bar.

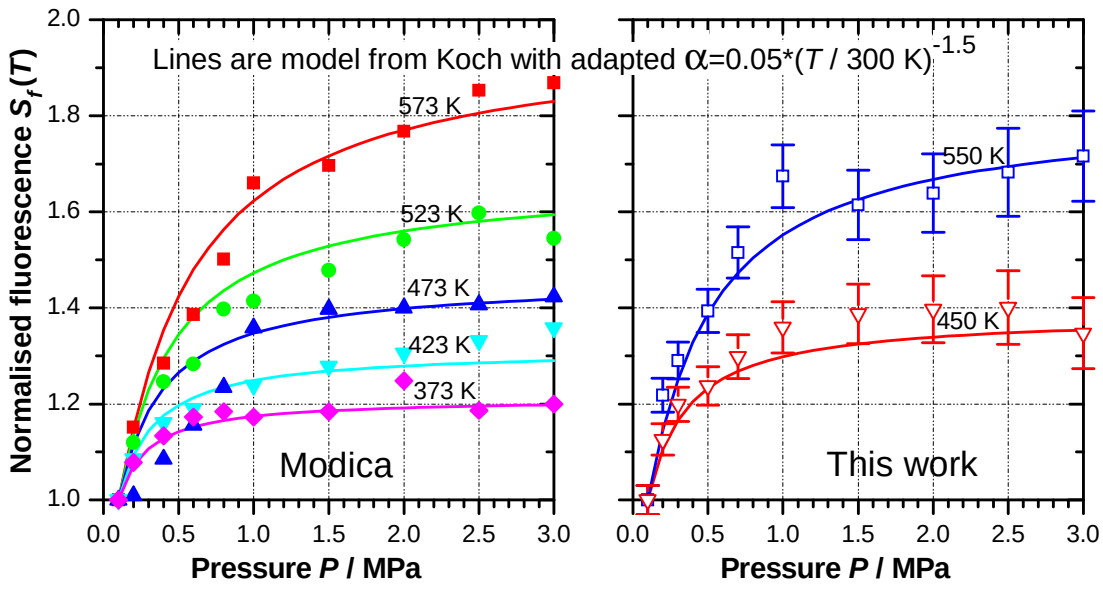

Figure 55: Pressure sensitivity of 3-pentanone fluorescence for various temperatures. Left side: measurements from [Modica 2007], ■ 573 K, ● 523 K, ▲ 473 K, ▼ 423 K, ◆ 373 K, pure N_2. Lines represent model from [Koch 2005] with adapted $\alpha(T) = 0.05(T/300)^{-\beta}$ with T in K and $\beta = 1.5$ instead of 1.2 suggested by Koch. Right side: this work: □ 550 K, ▽ 450 K, pure N_2.

5.4.2 Oxygen dependence on 3-pentanone fluorescence

The influence of temperature and pressure on the fluorescence spectra has been presented for pure nitrogen atmosphere. Thurber and Koch's fluorescence yield model for acetone and 3-pentanone also incorporates ketone-oxygen collisions by means of the quenching rate (5.13). They choose a simplified way to incorporate the quenching rate to the yield model, which is only justified for low quenching efficiency (cf. section 5.3.4). For high quenching

efficiencies, a distinction between intra- and intermolecular collisional events is necessary to take into account the vibrational population distribution of lower levels.

Within this work, the oxygen quenching of 3-pentanone is studied for a temperature from 350 to 550 K (cf. figure 56). Obviously, a Stern-Volmer behaviour is observed only for 350 K. For air, a Stern-Volmer factor of about 1.23 indicates a decrease to 44 % of the signal recorded under pure nitrogen atmosphere.

[Koch 2005] proposed the quenching efficiency $\langle P \rangle$ to be a function of vibrational excess energy and split to a high-value constant part exhibiting a steep fall-off to a low-value, slightly exponential part (cf. section 5.3.4). Koch argued, that the steep fall-off should exist at about 11000 cm^{-1} producing the enhanced intersystem crossing quenching process. This energy roughly corresponds to 600 K at 266 nm excitation. From the quenching efficiency of Koch and the relation $\langle P \rangle = k_{SV} k_{tot} / Z_{O_2}$, Stern-Volmer coefficients are calculated. k_{tot} is the sum of the non-radiative rate (approximated as a bi-exponential function of vibrational excess energy, cf. figure 51) and the fluorescence rate ($k_f = 4.2 \cdot 10^5 / s$, cf. [Koch 2005]). The collision frequency Z_{O_2} for 3-pentanone-oxygen collisions is derived from Lennard-Jones parameters to $Z_{O_2} = 6.858 \cdot 10^{-11}$ $cm^3 s^{-1}$.

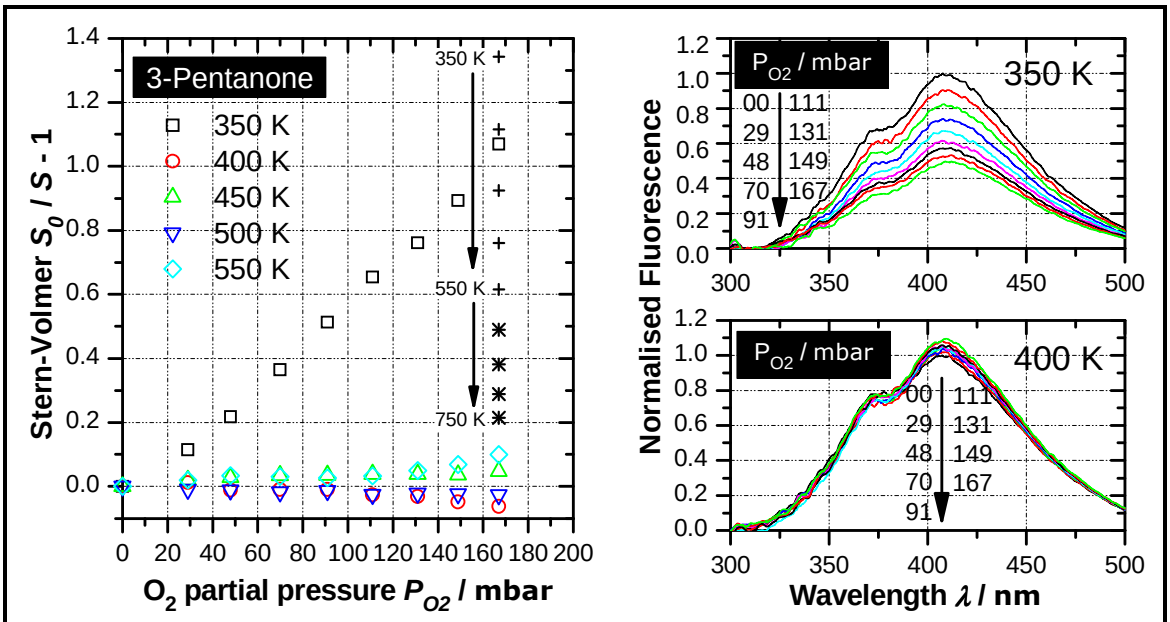

Figure 56: Stern-Volmer plots after 266 nm laser excitation as a function of temperature derived from integrated fluorescence spectra (270 to 340 nm). The maximum oxygen partial pressure for all measurements is 167 mbar for all temperatures. Left figure: 3-pentanone with 23 mbar concentration (evaporated from pure liquid 3-pentanone). Additional points at 167 mbar are calculated from quenching efficiency proposed by Koch (crosses) and Rothamer (asterisks), cf. text. Right figure: Normalised fluorescence spectra as function of oxygen partial pressure for 350 and 400 K. Obviously there is a (weak) quenching influence for low temperatures only.

For comparison with our measurements, values for $k_{SV} \cdot [O_2]$ are calculated using Koch's quenching efficiency and a partial oxygen pressure of 167 mbar, see cross values in Stern-Volmer plot (from the top to bottom: 350, 400, … 550 K).

Our $k_{SV} \cdot [O_2]$ measured at 350 K and 167 mbar is of the same order of magnitude as the values of Koch from 350 to 550 K, nearest to 400 K. Whereas a steep fall-off is observed between 350 and 400 K, the values calculated from the $\langle P \rangle$ expression of Koch decrease more than 50 %. Not shown in this plot is, however, a steep rise of $k_{SV} \cdot [O_2]$ at 600 K to a value larger than 30. We can neither confirm nor rule out the existence of this step, since, unfortunately, no measurements were performed beyond 550 K with oxygen for the 3-pentanone. However, a newer contribution to this subject from [Rothamer 2007] proposes the absence of a step in quenching efficiency as claimed by Koch. Rather, the exponential expression for $\langle P \rangle$ at vibrational excess lower than 11000 cm^{-1} found by Koch extends over the whole energy range. Accounting for this $\langle P \rangle$-function suggested by Rothamer, $k_{SV} \cdot [O_2]$ is found to be a continuously decreasing function (see further values as asterisks in the plot for temperatures from 600 to 750 K).

5.5 Photophysics of aromatic tracers

Aromatic tracers have in common the benzene cycle as a chromophore. The benzene molecule is thus often a base for consideration made about other aromatic species. Substitutions or replacement of a carbon atom of the benzene cycle induces a local change of electronegativity. This modifies the electronic configuration of the whole cycle, which makes the spectrometric parameters of differently substituted benzenes distinguishable.

Benzene has three absorption bands corresponding to three $\pi \rightarrow \pi^*$ transitions. Only the first transition at about 179 nm (E_1 band) is an allowed transition, therefore exhibiting large transition strength. The others are symmetry forbidden transitions and located at about 200 (E_2 band) and 253 nm (B band). The observed weak oscillator strengths come from the vibronic coupling.

5.5.1 Bathochromatic shift through alkyl substitution – hyperconjugation

Alkyl substitution on the benzene ring modifies the absorption spectrum, as shown in figure 43 and table 3 section 4.3.1. The B band (253 nm) absorption is subject to a bathochromatic shift caused by the substitution. This is attributed to the hyperconjugation induced by the substitution group. Hyperconjugation is explained as both an electrostatic effect via an elec-

tron donor effect and a supplemental delocalisation via the conjugation effect [Coulson 1952]. The electrostatic influence is due to the participation of a σ-electron of an alkyl CH bond in resonance with the ring. The substitution group works either as an electron donor (e.g. the methyl group CH_3) or as an electron acceptor (e.g. the carboxyl group COOH). The electronegativity of the C-atom, to which the substitution is attached, is altered through the σ-electron displacement. As a consequence, the π-MOs of the benzene ring will on their part change their energies. If the electrostatic influence was the only relevant effect, the energy shift of the π-MOs should be positive for e.g. methyl substitution, and hence, a hypsochromic shift would be expected. The actual experience of an observable bathochromatic shift of the absorption band is due to the supplemental delocalisation effect generated by the substitution. This is essentially an additional delocalization of the π-electrons of the unsubstituted molecule, which even exists for substitutions with much reduced electronegativity (such as the vinyl group). The supplemental delocalisation effect lowers the π-MO energies and is generally dominant over the electrostatic influence. Among the alkyl substitutions, the methyl group produces an especially strong hyperconjugation effect.

For the di-substituted benzene ring, the wavelength shift caused by the individual substitutions is additive for the ortho and meta substitution, whereas for the para substitution the shift depends on the electronegativity of both substitutions being either electron donating or accepting [Silverstein 1998]. The para isomer generally absorbs at the longest wavelength and exhibits the strongest transition, due to steric interaction between ortho substituents reducing then the effect of hyperconjugation.

5.5.2 Bathochromatic shift of polycyclic (poly-)aromatic hydrocarbons (PAH)

The absorption and fluorescence spectra of polyaromatic hydrocarbons like naphthalene and anthracene do not really have similar spectral structures with the benzene molecule. However, the main absorption bands are shifted to longer wavelengths with the number of condensed rings. For naphthalene, the number of three absorption bands is conserved, just like phenanthrene. For more than two rings the B band of absorption is submerged by the lower lying E band, as can be observed in the spectrum of anthracene [Silverstein 1998].

5.5.3 Absorption studies

Numerous references report photophysical characteristics of simple benzene derivatives for near ultraviolet excitation. Among these, toluene has received considerable attention, because the substitution of a methyl group allows for studying the effect of lowered symmetry. The absence of D_{6h} symmetry in toluene lifts the degeneracy of states compared to benzene,

thus leading to a higher density of vibrational levels. The reduction of symmetry-forbidden interactions is at the origin of higher coupling rates for nonadiabatic transitions [Farmanara 2001].

The singlet-singlet absorption spectrum of toluene in the near ultraviolet was at the origin of many investigations, see e.g. [Ginsburg 1946]. Assignment to individual vibrational frequencies was made by [Bass 1950], comparing vapour absorption and fluorescence spectra. [Sreeramamurty 1951] addressed the trisubstituted 1,2,4-trimethylbenzene (pseudocumene, abbr. 1,2,4-TMB) in the near ultraviolet. They performed vapour absorption spectra and discussed the frequency assignment in front of different symmetries from the 1,2,3 and 1,3,5 isomer and the singly substituted toluene. Near ultraviolet absorption spectra for the 1,2,3 and 1,3,5 isomer were further reported from [Verma 1971]. The study of [Bolovinos 1982] presents vapour absorption spectra from about 135 to 275 nm, which allow for comparison within a wealth of benzene derivatives from benzene to hexamethylbenzene, including toluene and the 1,2,4 and 1,3,5 isomers of trimethylbenzene.

The near UV absorption spectra of naphthalene vapour was also subject to several studies. [Sponer 1955] presented absorption spectra at room temperature 293 K from 250 nm to 290 nm. The second and the third electronic states origin energy could be assigned as well as many vibrational modes. [Ferguson 1957] compared the absorption band of the second naphthalene transition (245 to 285 cm^{-1}) to transitions from anthracene and pyrene near to room temperature (313 K). A decade later, [George 1968] addressed all three $\pi \rightarrow \pi^*$ transitions, measuring the absorption intensity between 30000 and 53000 cm^{-1} (189 to 333 nm). The lowest transition to the first excited state (32020 cm^{-1}) was observed to be 51 times weaker than the middle transition to the second excited state (35910 cm^{-1}), and 650 times smaller than the transition to the third excited state (47530 cm^{-1}).

5.5.4 Deactivation pathways

An investigation of the absorption and the fluorescence behaviour of toluene vapour was performed by [Burton 1968], accounting for the effect of temperature and impurity quenching. A change of excitation wavelengths (240 - 270 nm) or toluene partial pressure (1 – 53 mbar) or temperature (approx. 295 – 450 K) does not affect the mean emission frequencies. The quantum yield was shown to be decreased with increasing temperature. This was assigned to the temperature dependence of a non-radiative channel such as intersystem crossing, being in competition with the radiative emission from the excited state. Toluene fluorescence exhibits quenching behaviour with noble gases like xenon and krypton. This is attributed to collision-induced radiationless transitions induced by the noble gas. The efficiency of quenching is stated to be mainly unity for collisions with triplet oxygen. A possible explanation of this effect comes from the existence of the singlet-triplet energy gap of tolu-

ene, exceeding the energy required for excitation of triplet state oxygen to its singlet state (cf. section 2.12.5).

Other channels of deactivation from the first excited state mentioned by Burton et al. are dissociation, isomerisation and isoenergetic pathways of intersystem crossing and internal conversion. The highest fluorescence yield is reported for excitation at 266.8 nm ((0,0) band) as $\phi_f = 0.3$ for low-pressure toluene (23 mbar) at room temperature, based on a value of 0.18 for benzene under nearby conditions. With increasing excitation energy, the yield continuously decreases, thereby expressing a gain in efficiency for non-radiative channels with rising vibrational excess energy. At 266.8 nm excitation, the yield of fluorescence and intersystem crossover add almost to unity, which means that internal conversion is of negligible importance. A similar finding is reported for jet-cooled toluene from [Dietz 1982], who observed a rate for intersystem crossing of $k_{ISC} = 8.5 \cdot 10^6\ \mathrm{s}^{-1}$ for excitation at the (0,0) band. With the effective lifetime τ_{eff} measured by [Jacon 1977], the rate of the total decay is determined as $k_{tot} = 1.32 \cdot 10^7\ \mathrm{s}^{-1}$. Thus, the quantum yield for intersystem crossing is $\phi_{ISC} = 0.64$ and accounts together with the fluorescence yield from Burton at al. for 94 % of the total decay.

Thereupon, the absence of contribution of the internal conversion to the total depopulation of the S_1 state is confirmed for an excitation near to the (0,0) band. However, [Jacon 1977] reported the existence of a threshold for vibrational excess energy, which, when passed, gives access to another channel of deactivation. This so-called "third channel" of decay or "channel three" was first observed by [Parmenter 1970] for benzene. The fluorescence decay of toluene, simply exponential for low vibrational excess energy, becomes bi-exponential for excitation to energies higher than 2150 cm^{-1} above the (0,0) band. Jacon et al. observed similar behaviour for aniline with a threshold of 3500 cm^{-1}, just as [Loper 1972], who found a threshold of 2500 cm^{-1} for fluorobenzene. For higher aromatic molecules, the appearance of the "third channel" was mentioned, e.g. for naphthalene with a threshold of 10000 cm^{-1} [Fischer 1974b and Huang 1976] and for fluorene with a threshold of 12000 cm^{-1} [Huang 1976]. The "third channel" appears as a classical effect for many aromatic molecules, accompanied by rather similar phenomena. A nearly linear dependence of the non-radiative rate k_{nr} is observed for the low energy excitation, the range of this behaviour being extended to higher energies for increasing size of the molecule. For excitation beyond a threshold, the non-radiative rate increases in an anomalously fast way, defined as an exponential function of vibrational excess energy [Jacon 1977].

In a review article on the dynamics of electronically excited states, [Smalley 1983] reports the threshold of the "channel three" for benzene to be about 3000 cm^{-1}. The decay rate from the S_1 state is shown to be in the range of nanoseconds for excitation to levels below the threshold and in the range of picoseconds for excitation beyond the threshold. In the

case of toluene, [Farmanara 2001] showed, that the decay τ_{IC} from $S_1 \rightarrow S_0$ can be as short as 4.3 picosecond in the case of high vibrational excitation. The opening of the third channel of decay in benzene is attributed to the onset of IVR, redistributing vibrational energy from initially excited spectrally active modes to low frequency modes, at least one of which is strongly promoting internal conversion (IC) from $S_1 \rightarrow S_0$ [Smalley 1983]. In the case of benzene, the effect of the triplet state to the "channel three" phenomenon via an enhanced ISC mechanism is ruled out, since the triplet quantum yield could be shown to drop substantially, which corresponds to an increase of the importance of the IC channel, in lack of any other deactivation pathways for isolated molecules [Otis 1983].

Naphthalene is one of the most intensively studied aromatic molecules throughout the past, providing a wealth of information about its radiative and non-radiative decay characteristics. [Avouris 1977] have presented an exhaustive review of published data, most produced at the beginning of the seventies. Furthermore, the contributions of Lim and co-workers brought insight into the importance of excess vibrational energy dependence of radiationless processes observed for various aromatic molecules. The model from Lim et al. still provides a valuable source of interpretation, as can be seen in the review published more than two decades later [Lim 1997].

[Uy 1970] used their own (low-pressure and room temperature) experiments together with other literature sources to give an explanation of the naphthalene deactivation process from electronically excited states. Like for toluene, the fluorescence spectrum of naphthalene exhibits a bathochromatic (red-)shift increasing with energy of excitation and becoming increasingly diffuse (structureless). The emission of different vibrational levels from the first excited state S_1 underlies large variations. The fluorescence quantum yield for excitation to the second and third excited state decreases smoothly with increasing excitation energy. Absorption to the second or third excited state is followed by very fast internal conversion producing vibrationally "hot" molecules in S_1. The reason for the increase of the red-shift with enhancing vibrational excess in the S_1 can be attributed to large differences in shape and anharmonicity between the potential energy surfaces of the S_1 and the ground state.

Low-pressure fluorescence lifetime measurements of naphthalene for excitation wavelengths ranging between 32500 and 46500 cm^{-1} were initially reported from [Laor 1971]. Unfortunately, Laor et al. did not provide any yield data, thus not allowing for distinction of radiative and radiationless processes. For the total rate of depopulation including all intramolecular decay processes, a linear increase is observed throughout excitation to energies corresponding to the first and second excited singlet states. A sudden change from linear to exponential behaviour then follows when the energy of the third excited state origin is overcome.

In the meanwhile, [Lim 1972] published results on naphthalene lifetimes and associated quantum yields. Following (2.53) and (2.54), the radiative and non-radiative rates are distin-

guished from the fluorescence lifetime. The fluorescence (radiative) rate increases linearly with the energy of excitation, while the rate of the non-radiative decay also increases linearly all-over the first and second excited states, and exponentially for excitation to the third excited singlet state. Lim et al. proposed that the difference in behaviour of the non-radiative decay for low- and for high-energy excitation is related to energy transfer via intersystem crossing (ISC) towards triplet states, which are widely separated in energy. They claim that, for larger Franck-Condon factors within the low-energy excess domain, the crossing to triplet states T_j over a small gap apparently dominates, causing the linearity of non-radiative decay. In contrast, for high excess energy, the crossing over a large gap to T_1 is responsible for an exponential dependence of the non-radiative rate.

The efficiency of the inverse ISC for naphthalene was ruled out by [Soep 1973]. A long lifetime component to the fluorescence decay, which e.g. would have shown as biexponential radiative decay, was not observed, either because inverse ISC is absent or has a weak yield.

A better understanding of the radiationless decay of naphthalene was gained from Lim et al. throughout measurements on lifetime and quantum yield ([Lim 1973 and Hsieh 1974]). Next to the correction of the quantum yield which was four times greater than the one reported in an earlier study (calibration errors), a break of the non-radiative rate at the energy corresponding to the origin of the second excited singlet state was observed. They assumed that, when the energy of the second excited state is reached, the first excited state is populated by direct absorption from the ground state and by IC from S_2. The rate of $S_0 \rightarrow S_1$ absorption is governed by the Franck-Condon matrix, which is necessarily different from the overlap integral dominating the rate of $S_2 \rightarrow S_1$ IC. Further, assuming IVR processes in S_1 to be slow compared to the non-radiative decay (relative low density of vibrational levels in S_1 at the energy corresponding to the S_2 origin), the $S_2 \rightarrow S_1$ IC modifies the vibrational distribution in S_1, i.e. changes both the magnitude and the excess energy dependence of the non-radiative decay rate. [Fischer 1974a] explained the same phenomenon by the change of the distribution of vibrational quanta in S_1 when the energy of the S_2 origin is reached, because the geometry coupling parameters (describing the changes in equilibrium position of the nuclei) $g_j^2(S_0 \rightarrow S_1)$ for the $S_0 \rightarrow S_1$ absorption are different from parameters $g_j^2(S_2 \rightarrow S_1)$ for the $S_2 \rightarrow S_1$ IC.

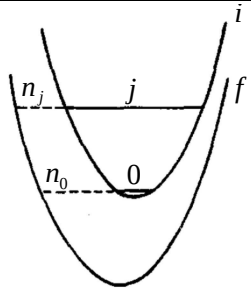

Figure 57: Illustration of the dependence of Franck-Condon overlap factor upon initially populated vibrational level (for non-radiative transitions) by potential energy curves. Adapted from [Hsieh 1974]. , the ratio $k(j)/k(0)$ is defined as the proportionality with the ratio of Franck-Condon factors $k(j)/k(0) \sim \left|\left\langle \chi_j^i(j) \middle| \chi_j^f(n_j) \right\rangle\right|^2 / \left|\left\langle \chi_j^i(0) \middle| \chi_j^f(n_0) \right\rangle\right|^2$.

The model derived from Lim et al. for the description of the rate of non-radiative intramolecular decay (IC or ISC processes) in aromatic molecules is based on Fermi's golden rule (2.48) (cf. section 2.9.1). When the transition rate is once derived for an electronic transition from a higher vibrational level j of the initial state i to an isoenergetic level n_j in the final state f and once for the specific transition from the vibrationless mode "0" to an isoenergetic level n_0, then the ratio of the transition rates, $k(j)/k(0)$ yields an expression depending on vibrational excess. This ratio is partially proportional to the respective Franck-Condon factors as illustrated in figure 57.

For a single transition mode, the energy redistributed to the final state's nuclei vibrations comes from the vibrational energy of the "promoting" mode and from transformation of the electronic energy. The vibrational modes "accepting" this energy can be determined via the energy conservation law $E_i - E_f - \hbar\omega_p = \sum_j \hbar\omega_j \overline{n}_j$. This allows to determine an optimised set $\overline{n}_j$ of distribution of accepting vibrational quanta in the final state. $\overline{n}_j$ is then a function of coupling parameters g_j^2, λ_j^2 and κ_j^2, accounting for the changes in equilibrium position, frequency and anharmonicity of a normal mode j induced by the transition from the initial to the final electronic state.

In order to derive an analytical expression for the ratio of $k(j)/k(0)$, Lim et al. assume, that the energy redistribution in the final state is slow, and thus, extra vibrational quanta m_j of the initial state simply "adds" to the optimum distribution of vibrational quanta of the final state $\overline{n}_j$. This hypothesis holds if there are no relevant changes in frequency and anharmonicity between the initial and final states. The energy conversion is then given by

$$E_i - E_f - \hbar\omega_p = \sum_j \hbar\omega_j \overline{n}_j = \sum_j \hbar\omega_j g_{j(i\to f)}^2 \exp(\omega_j \tau) \tag{5.14}$$

If the vibrational energy of the promoting mode is weak compared to the electronic energy of the transition, then the energy conservation (5.14) increases $\overline{n}_j$. As a consequence, the Franck-Condon factors are decreasing with increasing gap size $E_i - E_f$, overcompensating the increase of state density ρ_n (cf. section 5.1.7). The golden rule formula is rewritten in terms of a single promoting and a set of accepting modes as

$$k_{nr} = \frac{2\pi}{\hbar} \left|V_{if}^p\right|^2 \prod_j F_j \rho(\{\overline{n}_j\}) \tag{5.15}$$

in which $\rho(\{\overline{n}_j\})$ is a Franck-Condon weighted density, cf. [Fischer 1974b]. F_j are the Franck-Condon overlap factors. Applying the assumptions of a slow energy redistribution in the final state, the ratio $k(m_j)/k(0)$ is then ([Fischer 1974b])

$$\frac{k(m_j)}{k(0)} = \prod_j \frac{\left|\left\langle \chi_j^i(m_j) \middle| \chi_j^f(\overline{n}_j + m_j) \right\rangle\right|^2}{\left|\left\langle \chi_j^i(0) \middle| \chi_j^f(\overline{n}_j) \right\rangle\right|^2} \approx \prod_j \frac{(\overline{n}_j + m_j)!}{\overline{n}_j!\, m_j!} \exp(m_j \Delta\omega_j \tau) \tag{5.16}$$

Equations (5.14) and (5.16) represent the basis for the understanding of the non-radiative decay rate dependence in S_1. For a small energy gap ($E_i - E_f \approx 0$), $\overline{n}_j$ is close to zero, and therefore, the ratio before the exponential expression in (5.16) tends to unity. The increase of the decay rate will be only a slowly varying function of vibrational excess. In the opposite case, for a large energy gap, $\overline{n}_j$ increases significantly. This effect impacts on the decay rate of large gap transitions, e.g. as the $S_1 \rightarrow S_0$ IC as well as the $T_1 \rightarrow S_0$ ISC, exhibiting a steeper slope of k_{nr} with vibrational excess than the $S_1 \rightarrow T_1$ ISC, occurring over a small gap.

The model of Lim et al. allows to predict the slopes of k_{IC} and k_{ISC} on the vibrational excess energy, starting from the IC and ISC rates for the vibrationless mode ($k_{IC}(0) = 1.2 \cdot 10^5\ \mathrm{s}^{-1}$ [Fischer 1974b] and $k_{ISC}(0) \approx 5 \cdot 10^6\ \mathrm{s}^{-1}$ [Stockburger 1975]). The two rate functions for IC and ISC are crossing at about 10000 cm^{-1}. Below this, the dominant pathway is ISC, beyond it is IC. The results are in agreement with the assumption for the onset of the "third channel" mentioned in this section (cf. figure 87 section 5.8.1(b)).

5.5.5 Accessibility of electronic transitions for monocyclic and bicyclic aromatic tracers

With respect to the energy provided by the excitation at 266 nm, absorption occurs on the B band, localised between 260 and 280 nm for alkyl substituted benzene derivatives. For the bicyclic naphthalene and its derivatives, the B band is shifted more than 50 nm to the red with respect to the benzene molecule, whereas the E_2 band more than 80 nm. Thus, a 266 nm excitation wavelength will promote the transitions in the B band (~310 nm) and in the E_2 band (~290 nm). An excitation in the E_1 band is out of range.

Table 9: (0,0) band transitions to the first, second and third excited singlet states for benzene derivatives [Bolovinos 1982] and naphthalene [Stockburger 1975]. Bathochromatic shift for methyl substitution. Wavelength in nanometer and corresponding frequency in cm^{-1}. Values reported for ambient temperature gas phase. The position of the (0,0) band for $S_0 \rightarrow S_3$ has been replaced with the $\varepsilon_{\max}$ -position for toluene.

Compound	$S_0 \rightarrow S_1$	$S_0 \rightarrow S_2$	$S_0 \rightarrow S_3$
Benzene	262.6 (38081)	205.6 (48629)	180.5 (55403)
Toluene (Methylbenzene)	266.8 (37476)	212.7 (47016)	182.9 (54677)
Pseudocumene (1,2,4-Trimethylbenzene)	274.5 (36435)	218.3 (45806)	191.4 (52258)
Naphthalene	312.5 (32000)	278.6 (35900)	210.5 (47500)

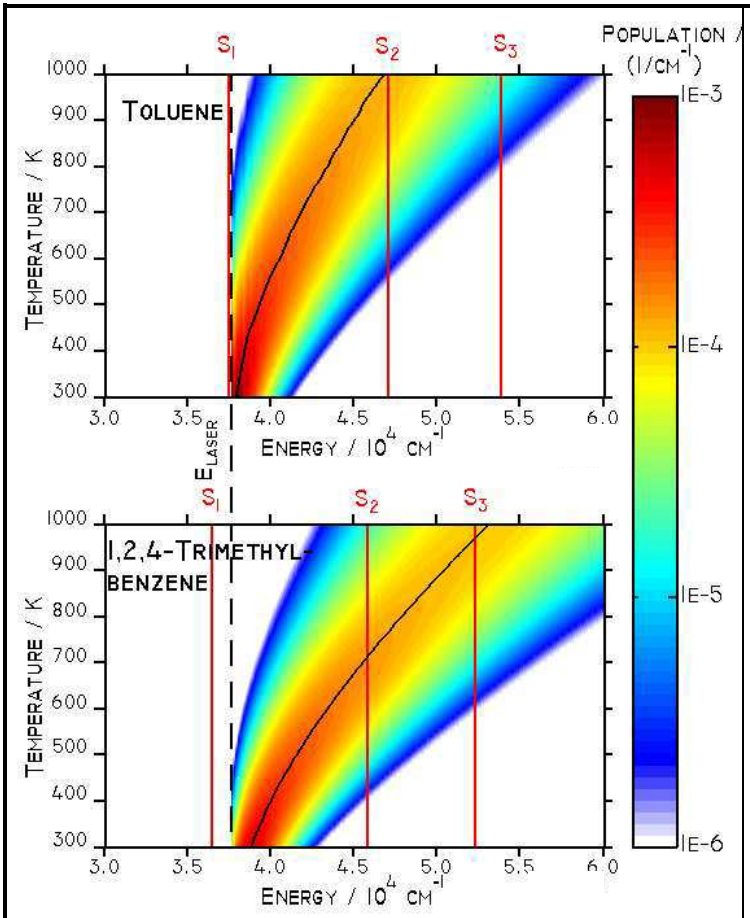

Figure 58: Accessibility of electronic transitions for toluene and 1,2,4-trimethylbenzene. The ground state populations are evaluated for temperature from 300 to 1000 K from the distribution functions calculated for the vibrational modes of toluene [Hickman 1996] and 1,2,4-trimethylbenzene [Draeger 1985]. The ground state population is shifted by absorption of the laser energy (37594 cm^{-1}) to the excited state level. This corresponds to the situation prior to the redistribution of the vibrational energy to the modes in S_1 following the Franck-Condon matrix. For the energies of the electronic states, see the positions of the (0,0) bands in table 9.

The (0,0) band energies corresponding to transitions from the ground state to the first, second and third excited singlet states of benzene, toluene and 1,2,4-TMB [Bolovinos 1982] are given in table 9 together with the values for naphthalene [Stockburger 1975]. The expected bathochromatic shift to longer wavelengths imposed by the methylation is clearly visible. With knowledge of the vibrational modes in the ground state for toluene [Hickman 1996] and 1,2,4-TMB [Draeger 1985], the population function can be calculated for a temperature range from 300 to 1000 K using equation (5.2), cf. section 5.1.1.

Figure 58 depicts the virtual population at the delay just after photon absorption at 266 nm prior to vibrational redistribution for toluene and 1,2,4-TMB with temperature. Figure 59 shows the same information for naphthalene.

For toluene, excitation at 266 nm is located at the red-side wing of the B band in the immediate vicinity of the (0,0) band origin (266.8 nm). Thus, the vibrational excess energy at 300 K is low (581 cm^{-1}) and even for temperature of 1000 K, the maximum of population does not reach the second excited state S_2. With increasing temperature, the thermal population of the ground state shifts to higher vibrational levels, thereby allowing for promotion to the excited state even for photon excitation on the red side of the (0,0) band. This effect

explains the observable broadening of the absorption spectrum with increasing temperature as reported by [Koban 2004].

A comparison between the total vibrational energy of various benzene derivatives reveals an increase with the number of substituents or the substitution chain length. Compared to toluene at a given temperature level, 1,2,4-TMB has thus a higher density of states, and therefore the population function is stretched to higher energies. As a consequence, the second and even the third excited singlet state are thermally populated for 266 nm excitation of high temperature ground state molecules. At the same time, 1,2,4-TMB has excited state origins slightly shifted to the red, which is attributed to the hyperconjugation effect of each methyl substitution.

For naphthalene, a 266 nm wavelength allows an excitation to the second singlet state. Excitation of ground state at temperature beyond 850 K thermally populates the third excited state. As mentioned in the previous section, the population in the second and third excited states is likely to be transformed to highly excited vibrational levels in the first excited singlet state via internal conversion. For the collisionless case, the level of this vibrational level corresponds to the energy of the absorbed photon. A greater vibrational excess leads to a stronger red-shift of the fluorescence emission, whenever the energy surfaces come closer in energy at the transition radius, which depends on whether they have significantly different shapes and anharmonicity in the ground and excited states. In the case of naphthalene, a large red-shift of the fluorescence emission has to be expected for an enhancement of the vibrational excess, either through decreasing excitation wavelength or through increasing temperature of the ground state molecules.

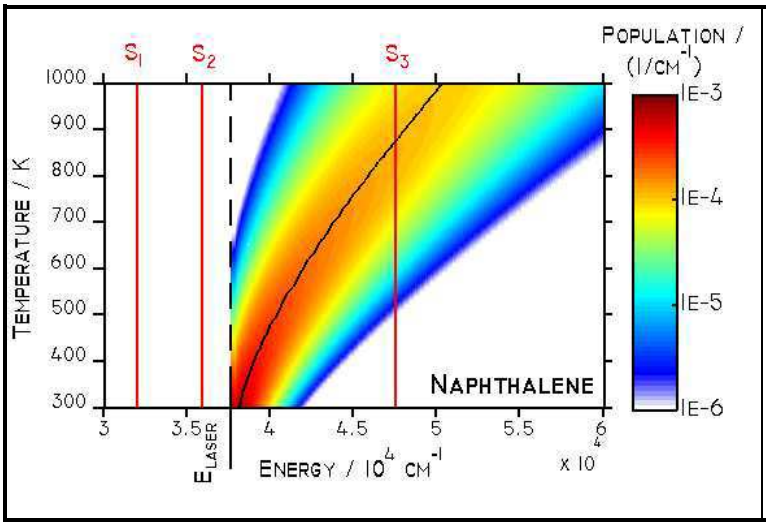

Figure 59: Accessibility of electronic transitions for naphthalene. Compare with figure 58. Vibrational modes of naphthalene from [Beck 1980]. Origins of the electronic states from [Stockburger 1975].

5.5.6 Reaction pathways

As mentioned above, dissociation and isomerisation processes have to be considered to the pathways of deactivation, especially when vibrational excess energy becomes significant. Non-adiabatic transitions via conical intersections could be favoured, producing a population of "hot" molecules, which facilitates the passage over potential energy barriers, thus initiating photochemical reactions. Consequently, we summarise information about accessible isomerisation and bond-cleavage reactions for benzene derivatives like toluene and bicyclic aromatics like naphthalene.

[Burton 1968] assumed, that an increase in vibrational excess energy might produce additional modes of energy dissipation. Rapid isomerisation could then explain to a certain extent the loss of radiative yield with a decrease in excitation wavelength for benzene derivatives, with a tendency to isomer reversion. For o-xylene, an increase of the isomerisation yield is found with a decrease of the excitation wavelength. Further, Burton et al. pointed out that following the ground state conversion, vibrational "hot" molecules might carry enough energy to pass the barrier of CH-cleavage at the methyl group.

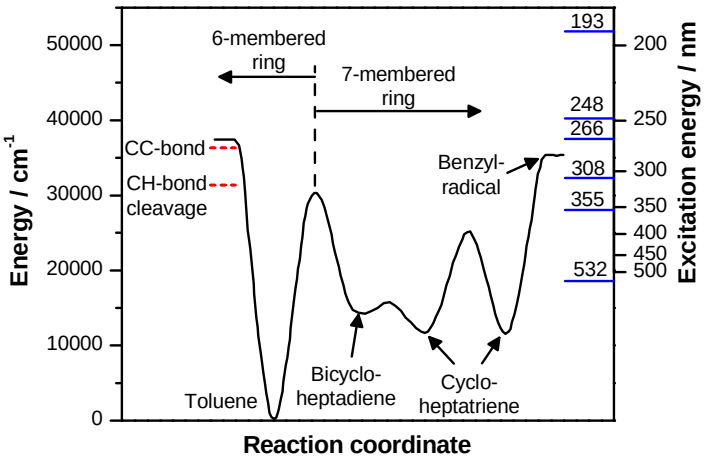

Figure 60: Approximate energy transition state diagram for isomerisation and dissociation reactions of toluene, adapted from [Ni 2004]. The energies were obtained from ab initio calculation. Bond cleavage directly after internal conversion is in competition with isomerisation reactions to seven-membered ring molecules. Rearomatisation and further dissociation are possible.

[Cogan 2007] emphasised that an excitation of the (0,0) transition of toluene (266.8 nm) yields enough energy (37476 cm^{-1}) to induce a bond dissociation (cleavage of CH-bond at 31339 cm^{-1} and of CC-bond at 36254 cm^{-1}) as well as chemical transformation reactions such as ring expansion to cycloheptatriene. The latter is supported by ab initio simulations [Ni 2004]. The barrier height from six-membered to seven-membered ring is reported as 29496 cm^{-1}. This is a value very close to the methyl group bond cleavage energies, and therefore, competition between dissociation and isomerisation is likely to be found. In addition, just as supposed by Burton et al., isomerisation to seven-membered ring is reversible. Internal conversion occurs from the excited state with or without prior isomerisation and rearomatisation, followed by bond dissociation in the ground state. Further, the seven-membered ring

isomers dissociates, forming a benzyl-radical. The accessibility of isomerisation and bond-cleavage reactions for toluene is presented in figure 60.

As to naphthalene, a well known isomer of this molecule is azulene, where a cycle carbon atom is transferred from the first to the second cycle, producing a seven- and a five-membered ring. Photodissociation and isomerisation reactions of azulene after laser excitation at 193 nm have been theoretically studied using ab initio calculations [Dyakov 2005]. Most of the excited azulene population follows fast internal conversion to vibrationally highly excited ground state levels. From there, direct removal of an H-atom or acetylene (C_2H_2) from azulene occurs only on low rates and is thus not significant. The most relevant process is the isomerisation to naphthalene, following the so-called norcaradiene mechanism. This pathway is effective even at lower photon energies such as at 266 nm. In contrast, the inverse rate of isomerisation from naphthalene to azulene is reported to be small for all studied energies.

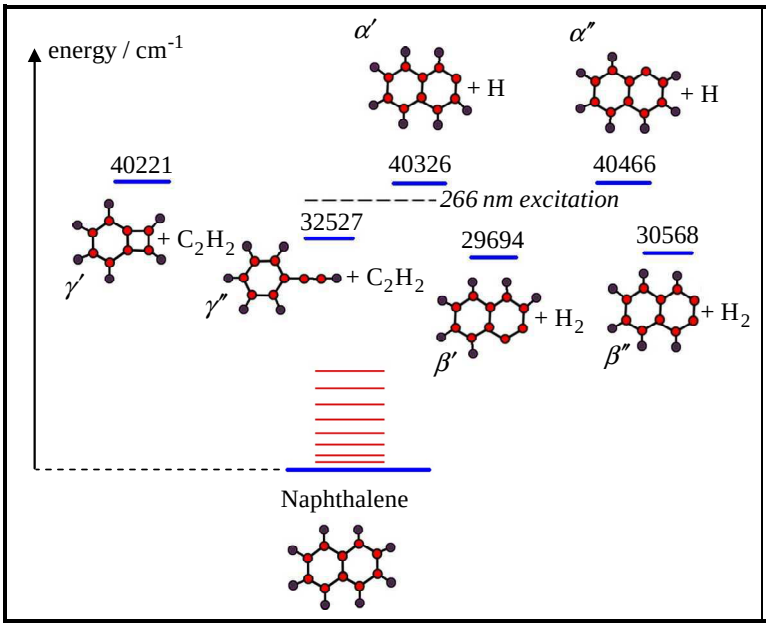

Figure 61: Possible photodissociation products for vibrationally highly excited naphthalene. Adapted from [Dyakov 2005], who presented a scheme for azulene excited at 193 nm. Only steady-state products are presented. The most relevant dissociation reaction occurs through H-atom removal (α), much less important is the removal of H_2 (β) or acetylene (γ).

A reaction scheme presented by Dyakov et al. for azulene can thus be partially applied to evaluate the photodissociation processes of vibrationally highly excited naphthalene. Possible dissociation products are summarised in figure 61. For our purpose, excitation will be at 266 nm. The broken line presents the excitation energy in comparison to the potential energies of the dissociation products. The red lines correspond to vibrational thermalisation energies for ground state molecules at temperature levels from 300 to 1000 K. Only steady-state products are presented. The dissociation reaction producing a $C_{10}H_7$ cation (α) is the most relevant, because the H-atom removal proceeds without further transition states. The removal of H_2 (β) or acetylene (γ) is only reached via successive pathways including transition states of higher energy. The photon energy at 193 nm (51813 cm^{-1}) corresponds quite well to the vibrational energy of hot (1000 K) ground state naphthalene excited at 266 nm

(51283 cm^{-1}). For an 193 nm excitation of azulene, the sum of all products rates of α, β and γ is $6.1 \cdot 10^4\ s^{-1}$, approximately linearly decreasing to $14 \cdot 10^0\ s^{-1}$ for a 266 nm excitation wavelength (37594 cm^{-1}). Isomerisation channels accessible from vibrationally excited naphthalene were also attributed by Dyakov as transition states to the dissociation products (not shown in figure 61). The rates of reverse isomerisation are, however, always higher, which induces steady-state rates much less than unity.

The rates of photodissociation and isomerisation are small compared to the rates of non-radiative decay of excited naphthalene via IC and ISC, as shown in section 5.8.1(b). Naphthalene photodissociation and isomerisation channels will thus not have important influence on the fluorescence quantum yield. Besides, applying the formation rates from Dyakov et al. it must not be forgotten, that these values were reported for hot naphthalene molecules after isomerisation from azulene. Thus, next to the photon energy and the initial thermal energy, the formation heat of isomerisation has to be considered, the latter being approximately 11000 cm^{-1}, cf. [Damm 1991]. Hot naphthalene produced directly from laser excitation of high-temperature ground state naphthalene exhibits much smaller formation rates.

5.6 Fluorescence of monocyclic aromatic tracers – results for toluene and 1,2,4-trimethylbenzene

This section discusses the results of our experimental study on toluene and 1,2,4-trimethylbenzene (pseudocumene, abbr. 1,2,4-TMB) excited at 266 nm. Toluene and 1,2,4-TMB are close relatives, since they are both benzene derivatives which differ only by two additional methyl substitutions at the benzene ring. As discussed earlier, methyl substitution shifts the absorption spectrum to higher wavelength due to the hyperconjugation effect (section 5.5.1). Multiple substitutions either increase or reduce the hyperconjugation effect, which is dependent on the position of their attachments on the benzene ring. [Bolovinos 1982] allows to estimate the bathochromatic shift from benzene to toluene to be between 7 and 8 nm and the one from toluene to 1,2,4-TMB about 10 nm. The (0,0) positions of the electronic transitions were determined slightly less shifted (cf. table 9). With the number of substitutions, the B band ($^1A_{1g} \rightarrow {}^1B_{2u}$) of the absorption spectra becomes more and more structureless, which is, apart from band congestion effects, likely to be caused by its broadening due to an increased rate of the radiationless transitions (figure 62).

5.6.1 Temperature dependence

UV absorption spectra of various polyatomic molecules exhibit a bell-shape form. With increasing temperature, this shape broadens and shifts towards longer wavelengths. This is commonly assigned to the production of a molecular "hot" band, i.e. when the population of excited molecules is increased [Zaslonko 1997].

For toluene, the temperature dependence of the absorption spectrum was investigated by [Hippler 1983a], and the experimental results compared to simulation based on a modified Sulzer-Wieland model. They compared a canonical distribution of toluene heated in a shock wave up to 1800 K to a microcanonical distribution produced by laser excitation of cycloheptatriene at 300 K, which subsequently isomerised to toluene (with average vibrational energy equivalent to 2800 K, cf. figure 48 section 5.1.2). Unfortunately, they did not cover the range of temperatures and excitation wavelengths relevant to our study. At 280 nm, they presented absorption cross-sections, which increase with increasing temperature and fit well with results obtained in shock-wave heated toluene experiments between 296 and 1128 K [Koban 2004].

(a) Absorption

The room temperature absorption spectra of benzene, toluene and 1,2,4-TMB are compared in figure 62 [Bolovinos 1982]. The steep increase of absorption to the short wavelength side marks the transition to the second electronic state ($^1A_{1g} \rightarrow {}^1B_{1u}$).

Excitation of toluene at 266 nm occurs at the red edge of the room temperature absorption spectrum ((0,0) band at 266.8 nm) and produces only small vibrational excess energy in the excited state at room temperature. At 248 nm, the excess energy is of approximately 3000 cm^{-1}, which is redistributed into the vibrational modes of the excited state following the Franck-Condon factors.

With increasing temperature, the thermal population of vibrationally excited ground state levels rises. The population of the excited state by absorption might then be thermally assisted, i.e. energy from high vibrational ground state modes adds to the energy of the exciting photon (cf. figure 58 in section 5.5.5). This leads to a temperature broadening at the long-wavelength tail of the absorption spectrum, which is at the origin of largely increasing absorption cross-section for toluene excited near the (0,0) band. Lamp absorption spectra for toluene from 296 to 1128 K presented by [Koban 2004] confirm this assumption. For 1,2,4-TMB, similar behaviours are expected.

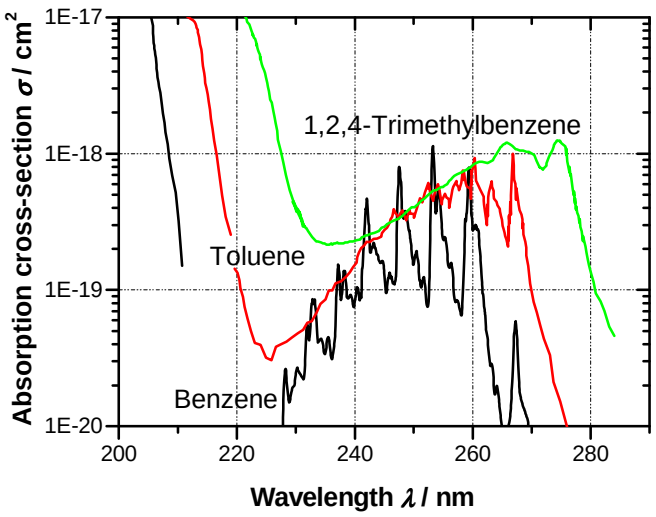

Figure 62: Comparison of absorption spectra of benzene, toluene and 1,2,4-trimethylbenzene from [Bolovinos 1982]. The excitation of toluene at 266 nm is at the red edge of the room temperature absorption spectrum ((0,0) band at 266.8 nm). The spectrum broadens at the long-wavelength tail for increasing temperature as a consequence of increasing population of higher vibrational levels in the ground state (cf. section 5.5.5 and [Koban 2004]). A similar temperature broadening is assumed for the 1,2,4-TMB spectrum.

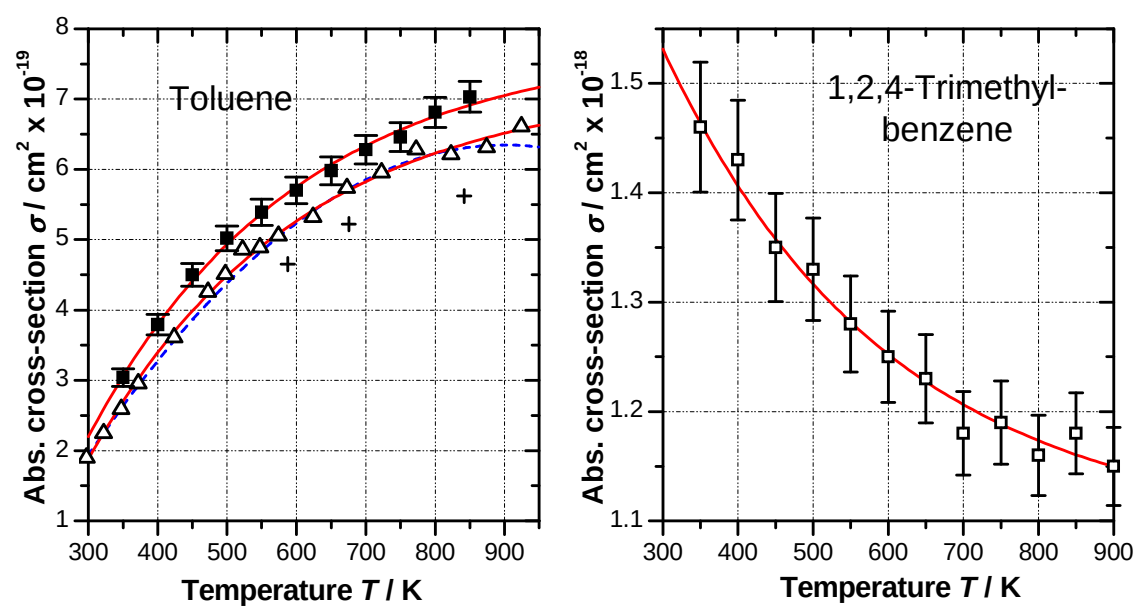

Figure 63: Absorption cross-section at 266 nm laser excitation as a function of temperature in pure nitrogen atmosphere at ambient pressure. Left side: toluene from this work (■), evaporated to constant number density of 1.59×10^{17} cm^{-3} (7.7 to 18.4 mbar from 350 to 850 K). Comparison to data from [Koban 2004] measured in flow cell (△) and shock tube (+). Right side: 1,2,4-TMB, evaporated from liquid mixture of 20 mol % tracer in n-undecane to constant number density of 1.97×10^{16} cm^{-3} (0.95 to 2.44 mbar from 350 to 900 K). Red lines are exponential regressions for the absorption cross-section temperature dependence. The blue broken line is a quadratic approximation from [Koch 2005] for the toluene absorption cross-section.

For excitation of toluene at 266 nm, the change of absorption cross-section with temperature is compared to [Koban 2004], cf. figure 63. As expected, the absorption cross-

section increases with increasing temperature. Our absorption cross-sections are slightly higher (by about $5 \cdot 10^{-20}$ cm^2) than the flow cell data of Koban et al. Lower values (crosses) correspond to their shock tube measurements.

For excitation far above the (0,0) band, the vibrational energy distribution of the ground state molecules becomes insignificant for the population to the first excited state, i.e. thermally assisted population is not relevant. Consequently, for toluene excited at 248 nm, a nearly constant absorption cross-section from room temperature up to 1000 K is observed (cf. figure 4 in [Koban 2004]). The sudden rise of the cross-section, which Koban et al. observed above 1000 K, might be due to thermally assisted population of the second excited state, exceeding the energy of the second state origin (cf. also figure 58, section 5.5.5).

Our absorption cross-section measured for 1,2,4-TMB (right diagram in figure 63) reveals a slight decrease with increasing temperature. Up to 700 K, the decrease of 1,2,4-TMB absorption cross-section is almost linear with temperature. Above 700 K, it becomes appreciably smoother, which we ascribe to coincide with an vibrational excess energy exceeding the origin of the second excited state (cf. also figure 58 section 5.5.5). We assume on closer examination, that the reason of this slight decrease is due to a higher gap between the excitation energy at 266 nm and the (0,0) band position (vibrational excess of about 1160 cm^{-1} for 1,2,4-TMB compared to about 100 cm^{-1} for toluene). The transition at 266 nm is not located at the wing but at a bell-shaped part of the absorption spectrum. Thus, the intensity not necessarily grows in the same way as it does at the wing due to temperature broadening. Examples of combined decrease of absorption cross-section at the bell-shaped part and temperature broadening at the wing are found not only for small molecules like ozone [Astholz 1982] or trifluoroiodomethane [Zaslonko 1997], but also for e.g. azulene [Brouwer 1985].

At the lowest temperature (350 K), the absorption cross-section at 266 nm is $(1.46 \pm 0.05) \cdot 10^{-18}$ cm^2. This is in quite good concordance to an absorption spectrum of $1.36 \cdot 10^{-18}$ cm^2 measured by [Etzkorn 1999] at 298 K. From room temperature absorption spectra of [Bolovinos 1982], a comparable cross-section of about $1.2 \cdot 10^{-18}$ cm^2 is also reported.

The temperature dependence of the absorption cross-sections measured in this work for toluene and 1,2,4-TMB can be fitted as exponential function of T in K

$$\text{Toluene} \quad \sigma(T)_{266nm} = 7.80 \cdot 10^{-19} - 1.5 \cdot 10^{-18} \cdot \exp(-T/300) \qquad (5.17)$$

$$\text{Pseudocumene (1,2,4-TMB)} \quad \sigma(T)_{266nm} = 1.09 \cdot 10^{-18} + 1.2 \cdot 10^{-18} \cdot \exp(-T/300) \qquad (5.18)$$

These expressions will be used to calculate quantum yields from fluorescence results for toluene and 1,2,4-TMB for temperatures between 300 and 900 K. Finally, the absorption

cross-section are found to be quasi-constant with pressure, at least within the range of study performed within this work (1 to 30 bar).

(b) Fluorescence

The dependence of the fluorescence emission on temperature was investigated in nitrogen for atmospheric pressure between 350 and 900 K. Figure 64 presents the evolutions of the normalised fluorescence spectra of toluene and 1,2,4-TMB with temperature. First of all, the pronounced peak at the short-wavelength tail of the spectra comes from the residual Rayleigh scattering and stray light signals at the laser excitation wavelength. Secondly, the signal presented for high temperature for 1,2,4-TMB is observed to suffer from the reduction of the signal-to-noise ratio.

Similar to the absorption spectrum, the fluorescence spectrum of 1,2,4-TMB is red-shifted compared to toluene by about 10 nm (cf. the upper row in figure 64). Further, a strong fall-off of the fluorescence signal is observed with rising temperature for both benzene derivatives over the entire spectral range, somewhat more pronounced for the larger 1,2,4-TMB. For each species, normalisation of the fluorescence spectra reveals a temperature red-shift (cf. the bottom row in figure 64). For toluene, we observe a similar red-shift at the long-wavelength tail as reported for an excitation at 248 nm by [Koban 2004]. At values between 0.4 to 0.6, the averaged shift is of 10.4 nm, increasing the temperature from 350 to 850 K (about 2.1±0.2 nm per 100 K). For 1,2,4-TMB, the shift is slightly more pronounced (14.3 nm from 350 to 750 K, i.e. 3.6±0.6 nm per 100 K).

The spectral shape of toluene fluorescence is in agreement with Koban's room temperature emission spectrum recorded at 248 nm excitation in nitrogen with our result obtained at 350 K and 266 nm excitation (cf. figure 37 section 3.7.1). This result confirms [Burton 1968], who did not observe any effect to the spectral shape of the fluorescence emission for variation of the excitation wavelength between 240 to 270 nm up to 450 K (cf. section 5.5.4).

Integrated fluorescence from the spectra between 270 and 380 nm and quantum yield data are presented as a function of temperature normalised to 350 K for toluene and 1,2,4-MB (cf. figure 65). The fluorescence decrease of toluene is linear up to 500 K, then becoming exponential for higher temperature. Due to the temperature dependence of the absorption cross-section, the quantum yield then reveals a purely exponential decrease. Similarly, the 1,2,4-TMB yield equally exhibits a slightly steeper exponential fall-off with increasing temperature, and corresponds roughly to three orders of magnitude over a range of 600 K.

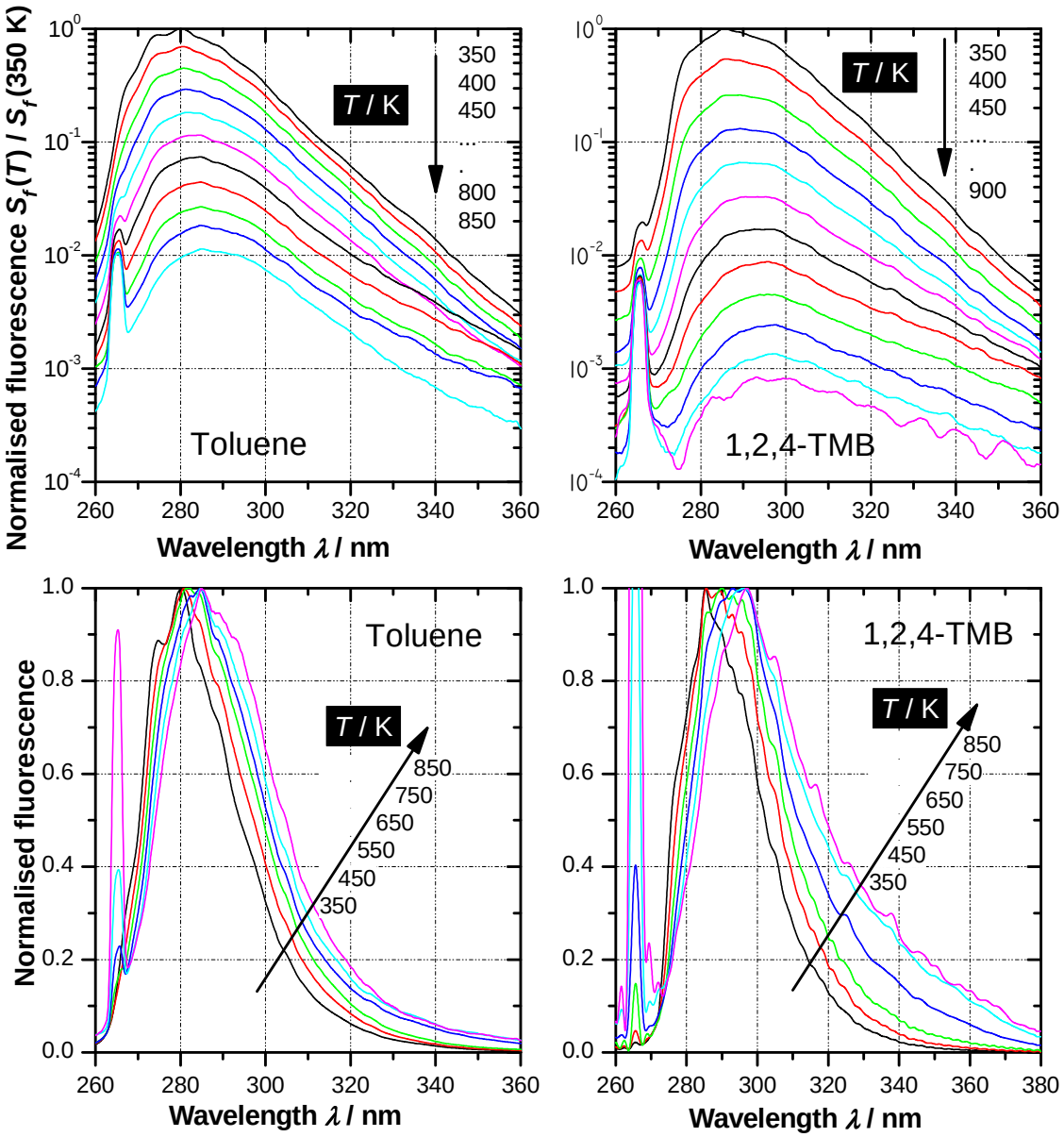

Figure 64: Fluorescence spectra after 266 nm laser excitation as a function of temperature in pure nitrogen atmosphere at ambient pressure (normalised to 350 K). Left side: spectra of toluene, evaporated to constant number density of 1.59×10^{17} cm^{-3} (7.7 to 18.4 mbar from 350 to 850 K). Right side: spectra of 1,2,4-TMB, evaporated from liquid mixture of 20 mol % tracer in n-undecane to constant number density of 1.97×10^{16}cm^{-3} (0.95 to 2.44 mbar from 350 to 900 K). Pure nitrogen atmosphere at ambient pressure. All spectra are first order Savitzky-Golay smoothed with 2.5 nm window size. Bottom row: normalised spectra for illustration of the temperature red-shift.

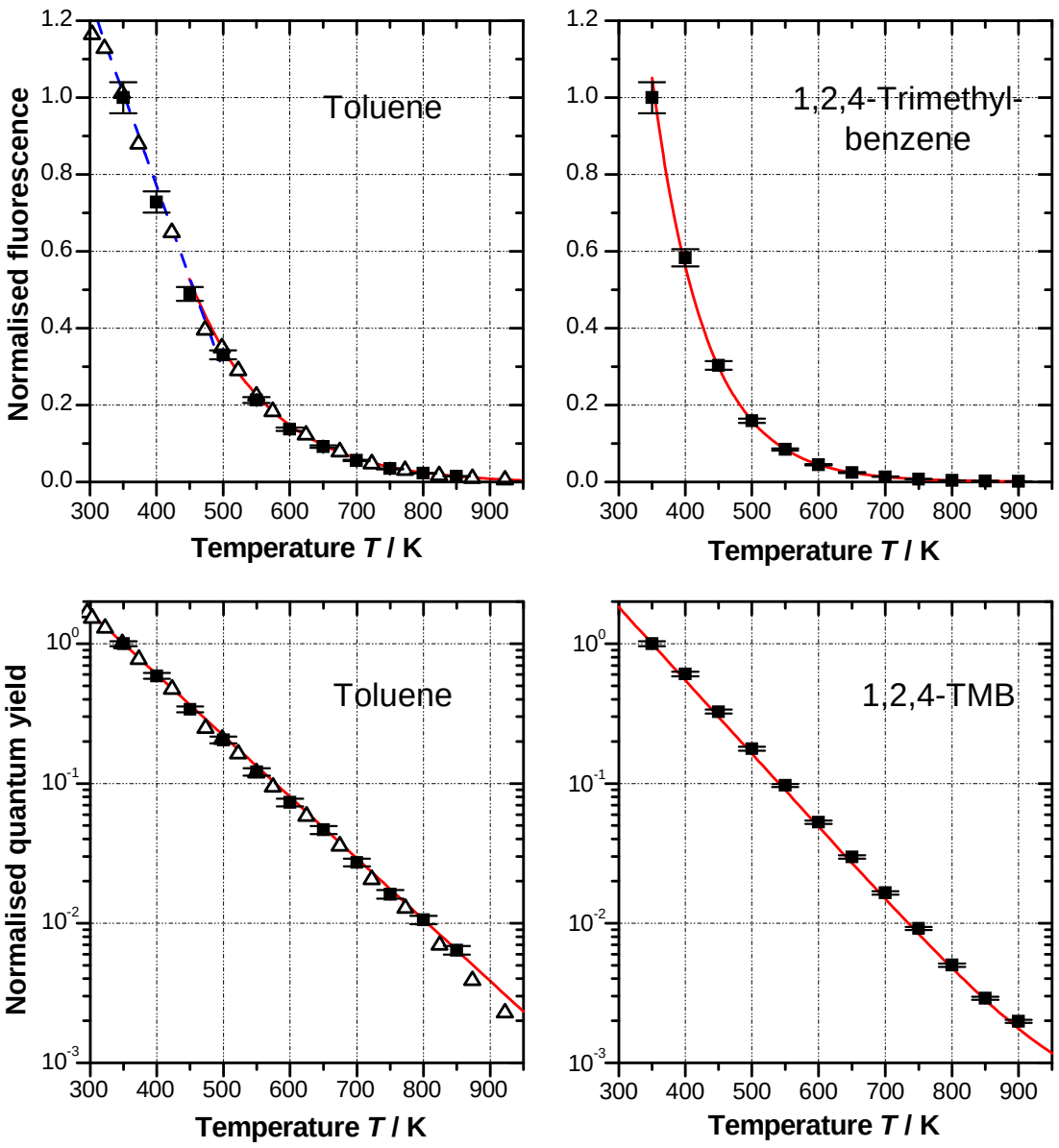

Figure 65: Integrated fluorescence (top diagrams) and quantum yield (bottom diagrams) after 266 nm laser excitation as a function of temperature in pure nitrogen atmosphere at ambient pressure. All red continuous lines represent single exponential decays, the dashed blue line is a linear regression. The diagrams are normalised to 350 K. Left side: Toluene (integrated from 270 to 380 nm). ■ this work, △ [Koban 2004] (flow cell). Right side: 1,2,4-TMB (integrated from 270 to 380 nm).

The temperature dependence of the fluorescence quantum yield measured in this work for toluene and 1,2,4-TMB in nitrogen at atmospheric pressure can be expressed for temperature between 300 and 900 K as exponential regression of T in K

$$\text{Toluene} \qquad \left.\frac{\phi_f(T)}{\phi_f\left(300\,\mathrm{K}\right)}\right|_{266\,\mathrm{nm}}^{\mathrm{N_2}} = 20.7 \cdot \exp(-T/99) \tag{5.19}$$

$$\text{1,2,4-TMB} \qquad \left.\frac{\phi_f(T)}{\phi_f\left(300\,\mathrm{K}\right)}\right|_{266\,\mathrm{nm}}^{\mathrm{N_2}} = 2.59 \cdot 10^{-4} + 37.74 \cdot \exp(-T/82.63) \tag{5.20}$$

The time constant in the exponential term of (5.19) that we found for toluene as a value of 99 is somewhat higher as in [Koban 2004], who reported a value of $1/0.0105 \approx 95.2$.

The observed impact of temperature to the fluorescence yield confirms results from literature, which ascribe this effect to the increase of vibrational excess energy. The temperature quenching of the toluene fluorescence signal was first studied by [Burton 1968] on a limited temperature domain from 296 to 441 K. They used pure toluene at low total pressure between 21 and 25 mbar (15 to 20 torr). [Jacon 1977] performed lifetime measurements of toluene at even lower pressure (0.1 torr). For low excitation energy, the toluene lifetime can be considered as a simple exponential function of excitation energy. In contrast, Burton's yield data measured for similar excitation energies were roughly constant, probably due to an almost complete vibrational relaxation which occurs at high level of pressure.

The yield loss observed by [Burton 1968] and [Jacon 1977] increasing either the energy of photon excitation or the thermal energy (temperature) can be ascribed to non-radiative decay rates being a rising function of vibrational excess. Jacon et al. mentioned, that beyond a threshold level of vibrational energy corresponding to the activation of a "third channel" of decay, the fluorescence lifetime presents a biexponential behaviour, and the non-radiative rate increases in an anomalously fast way (cf. section 5.5.4). This explains the strong fall-off in the yield data from Burton et al. with energies beyond 39500 cm^{-1}. The yield loss observed by Burton et al. with increasing temperature, although measured in low pressure pure toluene, fits quite well in the results reported from [Koban 2004] in atmospheric pressure nitrogen, at least in relative value. Koban's toluene yield data are presented as open triangles in figure 65, showing a good agreement with our measurements.

5.6.2 Pressure dependence

Toluene and 1,2,4-TMB fluorescence spectra were recorded after excitation at 266 nm for nitrogen pressure increasing from 1 to 30 bar, cf. the results in figure 66 for two distinct temperature levels 450 and 700 K. The evolution of fluorescence yields can be inferred from fluorescence intensity, since we do not observe significant changes in absorption cross-section within this pressure domain.

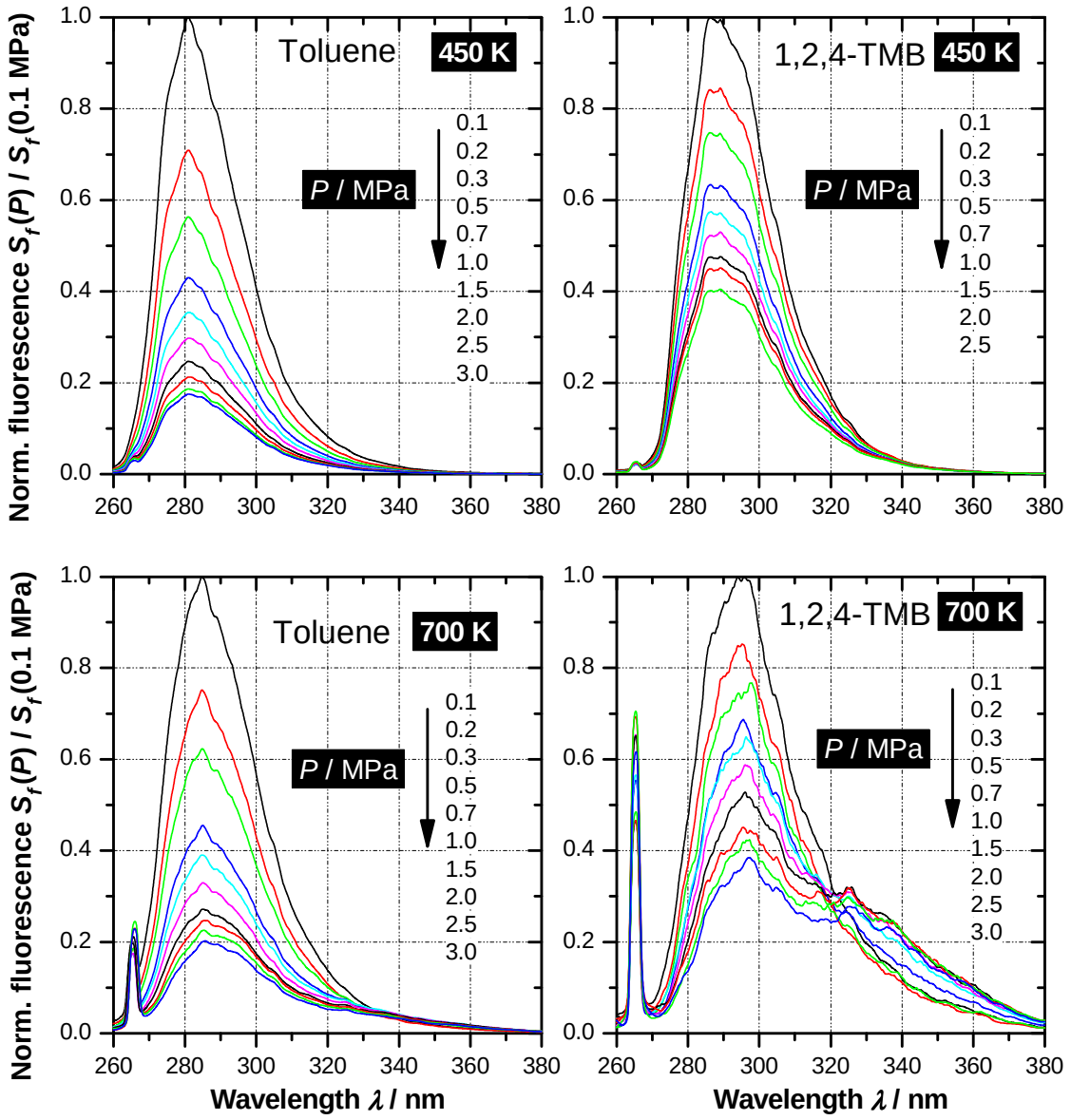

Figure 66: Fluorescence spectra after 266 nm excitation as a function of nitrogen pressure normalised to 1 bar. All spectra are first order Savitzky-Golay smoothed with 2.5 nm window size. Left side: Toluene evaporated from pure liquid to constant vapour number density $n \approx 3.5\times10^{17}$cm^{-3} at 450 K and $n \approx 2.2\times10^{17}$ cm^{-3} at 700 K. Toluene concentration is about 22 mbar. Right side: 1,2,4-TMB evaporated from liquid mixture of 20 mol % 1,2,4-TMB in n-undecane to constant number density $n \approx 4.4\times10^{16}$cm^{-3} at 450 K and $n \approx 2.8\times10^{16}$ cm^{-3} at 700 K. 1,2,4-TMB concentration is about 3 mbar.

The fluorescence yield is observed to significantly decrease with increasing pressure. For toluene, the intensity fall-off is slightly more pronounced than for 1,2,4-TMB. At 450 K, the normalised fluorescence remains spectrally unchanged for both molecules. Compared to 450 K, the signal fall-off is slightly reduced at 700 K. Notably for 1,2,4-TMB, a secondary fluorescence pattern arises from the long wavelength tail ($\lambda \geq 320$ nm). The same effect is ob-

served for toluene, albeit much less pronounced (see the slight change of shape in the vicinity of 330 nm).

For both molecules, the evolution of the integrated fluorescence (from 270 to 380 nm) with pressure is depicted in figure 67 for the two temperature levels.

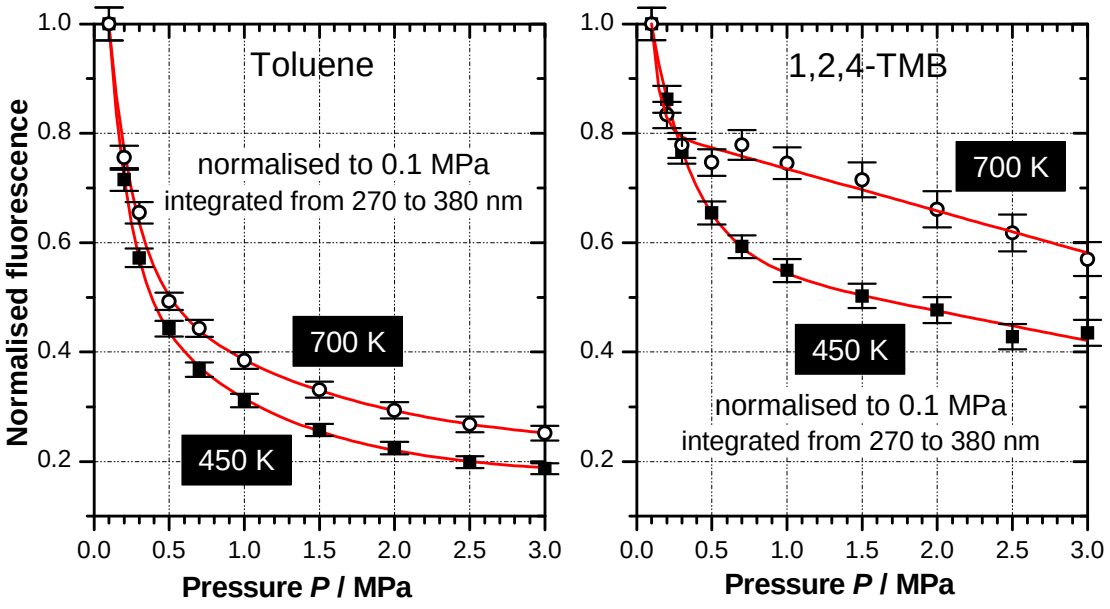

Figure 67: Fluorescence after 266 nm laser excitation as a function of pressure integrated from 270 to 380 nm. Pure nitrogen atmosphere at 450 K and at 700 K. Normalised to 0.1 MPa. Left side: Toluene. Lines represent double exponential decay approximations. Right side: 1,2,4-TMB. Lines represent combination of exponential and linear decay approximations.

In both cases, a strong decrease with increasing pressure is noted, in contrast to our results observed on ketones. This decrease, while surprising, was already highlighted for anthracene vapour. For instance, [Barkova 1987] evidenced a yield decrease of anthracene fluorescence with rising pressure of xenon bath gas at 500 K. Their findings correspond to foreign gas pressures up to 17 bar, in the same range than our experiment. A comparison to the decrease of toluene and 1,2,4-TMB yield excited at 266 nm at 450 K is shown in figure 68. The fall-off of the toluene yield is qualitatively comparable to that of anthracene excited at 365 nm (i.e. close to the (0,0) band), whereas the 1,2,4-TMB yield decreases more like anthracene excited at 296 nm. Barkova et al. thus related the strength of this pressure-induced fluorescence weakening effect to the gap between the excitation energy and the (0,0) band location at (27685 cm^{-1}).

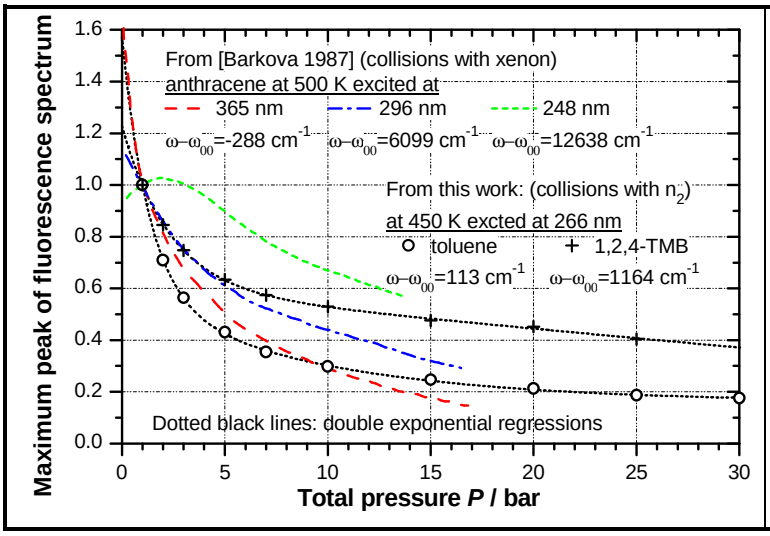

Figure 68: From [Barkova 1987]. Relation of the fluorescence intensity at the maximum of the anthracene spectrum (500 K, 0.27 mbar anthracene) to the Xe pressure for different excitation wavelengths: 365, 296 and 248 nm. Compared to our results with respect to the maximum of the toluene and 1,2,4-TMB fluorescence with nitrogen pressure at 450 K with 22 mbar and 3 mbar toluene and 1,2,4-TMB, respectively, excited at 266 nm.

For toluene, the integrated fluorescence reveals a double exponential decay with increasing pressure (cf. figure 67). In contrast, for 1,2,4-TMB, the initial exponential decrease becomes linear at higher pressure. At the lower temperature level, the signal loss from 1 to 30 bar for toluene and 1,2,4-TMB exceeds 80 and 50 %, respectively. The secondary fluorescence pattern observed at longer wavelengths for 1,2,4-TMB at 700 K partially compensates the intensity loss of the main pattern centred at 295 nm.

Collisional deactivation and excitation energy are key parameters to explain the observed pressure-induced behaviour of the fluorescence emission. Let us recall that fluorescence lifetimes and yields are known to be subject to collisional effects with the bath gas. Collisions govern the intramolecular relaxation down the vibrational manifold within the excited singlet state, while competing with electronic relaxation processes. Alternatively, collisions may also lead to intermolecular electronic deactivation (quenching) reactions.

The stochastic step ladder model proposed by [Freed 1974] allows to study the part of collisions leading to intramolecular vibrational relaxation in a simplistic manner. This model was adapted by [Beddard 1974], and then successfully applied to simulate the pressure-induced stabilisation of fluorescence lifetime and yield experimentally observed for naphthalene in argon and methane gas atmosphere (cf. section 5.1.8). Initially, shifting the excitation wavelength closer to the state origin leads to a reduction of fluorescence stabilisation, until the stabilisation diminishes and finally inverts in the vicinity of the (0,0) band, i.e. we see a weakening effect of fluorescence, which is attenuated with increasing pressure. Similar behaviour was found for the vibrational relaxation of p-fluorotoluene (PFT) by [Brown 1975]. Lifetimes decrease with PFT pressure for excitation energies close to the state origin at 271.2 nm, whereas for higher excitation, a stabilisation effect occurs. [Steer 1978] demonstrated similar behaviour for the relaxation of p-difluorobenzene in parent gas.

The mechanism behind the pressure-induced fluorescence yield and lifetime decrease near the (0,0) band was studied in detail by Pollak and co-workers (cf. [Wadi 1999] and [He

2002]). It was interpreted as a photo-induced cooling of the excited state vibrational distribution, followed by subsequent heating through collisions with the bath gas. The average energy of the initial distribution, where from the Boltzmann distribution is approached after laser excitation, lies either below or above the thermalised level of the excited state. If the vibrational frequencies of the excited state are lower than for the ground state (i.e. higher density of states), more energy is needed per mode to keep the same temperature. A cooling of the nascent distribution takes place, but only if the energy of the laser photon is not too large. To simplify, the excess of energy produced by the laser photon has to be small compared to the difference between the thermalisation energies of the excited and the ground states. Following the cooling of the nascent distribution, the excited molecules are then heated by collisions with bath gas molecules, which causes the observed decrease of lifetime when pressure increases.

By analogy, photo-induced cooling and subsequent heating through collisions with the bath gas molecules might offer a possible explanation for the observed fluorescence decrease with increasing pressure for toluene and 1,2,4-TMB. The PFT absorption spectrum presented by [Brown 1975] fits well with those for substituted benzenes from [Bolovinos 1982], cf. figure 62. The PFT (0,0) band lies in between those of toluene and 1,2,4-TMB, shifted 608 cm^{-1} to the red and 443 cm^{-1} to the blue, respectively. Excitation at 266 nm is thus in the immediate vicinity of the (0,0) band of toluene and still close (1164 cm^{-1}) to that of 1,2,4-TMB. In addition, similarities are observed between the vibrational energy levels of toluene and PFT, which further relates our observations to the findings of [Brown 1975]. The vibrational frequencies published by [Whiteside 2005] for the ground state of toluene and PFT are for instance very similar. While the frequencies of the excited state are only sparsely known, from the few identified frequencies a similar average shift to lower frequencies from the ground to the excited state vibrational mode is deduced. This shift is about 83 cm^{-1} and 70 cm^{-1} for toluene and PFT, respectively. This allows us the approximation of the excited state vibrational modes of toluene and PFT applying this average shift to all ground state frequencies. Using equation (5.1), ground and excited states thermalisation energies are calculated at different temperatures, cf. table 10. Comparing toluene with PFT from 300 to 900 K, the differences between thermalisation energies of excited and ground states are very close, and for both, the energy gap between ground and excited states thermalised distributions increases with increasing temperature. From this point of view, pressure-induced fluorescence yield weakening of toluene excited close (113 cm^{-1}) to the (0,0) band at 266 nm is probable.

Table 10: Thermalisation energies of toluene and PFT ground and excited states (in cm^{-1}). Vibrational frequencies were used from [Whiteside 2005]. The excited state modes were approximated by the average shift from the ground state frequencies deduced from the values reported by Whiteside, refer to our text. The energy gap between ground and excited state thermalised distributions increases with the temperature.

Temperature T / K	Toluene		PFT		Toluene	PFT
	E_{th,S_0}	E_{th,S_1}	E_{th,S_0}	E_{th,S_1}	$E_{th,S_1} - E_{th,S_0}$	$E_{th,S_1} - E_{th,S_0}$
300	580.9	758.4	756.7	944.1	177.5	187.3
400	1291	1571.3	1567.6	1845.5	280.3	277.9
500	2280.4	2660.6	2652.2	3015.9	380.2	363.7
600	3504.3	3975.4	3964.5	4405.3	471.2	440.8
700	4920.3	5472.4	5462	5970.9	552.1	509.0
800	6494.8	7118.6	7111.3	7680.3	623.9	569
900	8201.7	8889.3	8886.5	9508.6	687.6	622.1

While all cited sources reporting from pressure-induced yield weakening refer to lower than atmospheric pressure, the yield stabilisation was also observed at higher than atmospheric pressure (cf. e.g. [Thurber 1999a] for acetone, [Grossmann 1996] and [Koch 2005] for 3-pentanone, [Kühni 2010] for fluoranthene). If we try to explain the yield weakening effect in analogy to the photo-induced cooling and subsequent heating by collisions with the foreign gas, it is therefore necessary to discuss, why the weakening effect might be observable also at this higher pressure level, which we do in the following.

An increase of the vibrational energy transferred within collisions shifts the Boltzmann limit to lower pressure, which implies a faster convergence of the lifetime and yield to a constant value with respect to an unchanged collisional rate. For collisions with parent molecules, the average vibrational energy loss per collision is almost linearly dependent on the number of vibrational modes for benzene derivatives, as shown in [Bae 2000] from 880 cm^{-1} for toluene to 1240 cm^{-1} for mesitylene (1,3,5-trimethylbenzene) at high vibrational excess (25000 cm^{-1}). For collisions with foreign molecules, [Toselli 1991] and [Hippler 1983b] showed at nearby excess energies the average vibrational energy loss to increase with parameters such as the number of atoms, the boiling temperature or the Lennard-Jones well depth.

As can be seen for an mono-aromatic like p-difluorobenzene, the replacement of collisions in parent bath gas by collisions with a much smaller molecule like CF_3H (fluoroform) leads to a tenfold increase in pressure needed for lifetime equilibration (from ca. 20 to 200 torr) [Steer 1978]. From [Hippler 1983b] it is known, that compared to nitrogen, collisions with CF_3H yield an almost threefold toluene vibrational energy loss per collision (at high excess). This is likely to be similar for difluorobenzene, i.e. the tenfold increase from parent gas to CF_3H is likely to be enhanced by a factor three. The lifetime equilibration of difluorobenzene by collisions with nitrogen should thus occur much closer to atmospheric pressure.

In the specific case of toluene, collisions with parent molecules are also almost 6 times more efficient for the energy loss as with nitrogen. Thus, a weakening effect probably observed for toluene/toluene collisions at low pressure should occur at about a pressure six-fold higher, when collisional energy transfer is to nitrogen.

Though we did not excite our tracers at other wavelengths than 266 nm, we presume, that our observations made for toluene and 1,2,4-TMB are in analogy to the effect of yield stabilisation and weakening, depending on the proximity of the excitation wavelength to the (0,0) band and the pressure of foreign gases as described above.

5.6.3 Oxygen dependence

Fluorescence spectra are shown in figure 69 for different oxygen partial pressures at temperature level between 450 and 750 K. As expected, the results of toluene and 1,2,4-TMB are quite similar. As reported from [Koban 2005a], no red-shift of the spectra is observed with oxygen concentration for excitation of toluene at 266 nm. This can be explained by a direct excitation of the (0,0) band located near at 266.8 nm, i.e. all deactivation processes practically start from the vibrationless level. For 1,2,4-TMB, an excitation at 266 nm adds an excess photon energy of 1164 cm^{-1} to the molecule. Despite this vibrational excess, no red-shift with oxygen concentration is observed whatever the temperature explored.

The oxygen quenching of toluene follows, similar as observed by [Burton 1968], a Stern-Volmer evolution, cf. the top diagram in figure 70 (replacing $[O_2]$ with n_{O_2} implies a factor $1.3791 \cdot 10^{-28} \cdot T$ from bar^{-1} to m^3). Temperature implies a strong damping influence on the slope of the Stern-Volmer plots. The bottom diagram of figure 70 shows a comparison with Koban et al.'s measurements at nearby temperature conditions. We notice, that our data are quite close to their results, albeit Koban measured slightly weaker quenching, which results in an apparent shift of 25 to 30 K between their and our data, e.g. at 625 K, their data fall on our 650 K data. From our measurements, a logistic regression for the temperature dependence of the Stern-Volmer factor can be given as

$$k_{SV}(T) = 5.94 + \frac{1469.4 - 5.94}{1 + \left(T / 270.52\right)^{5.93}} \quad \left[\mathrm{bar}^{-1}\right] \tag{5.21}$$

which might be a valuable description from room temperature to about 750 K.

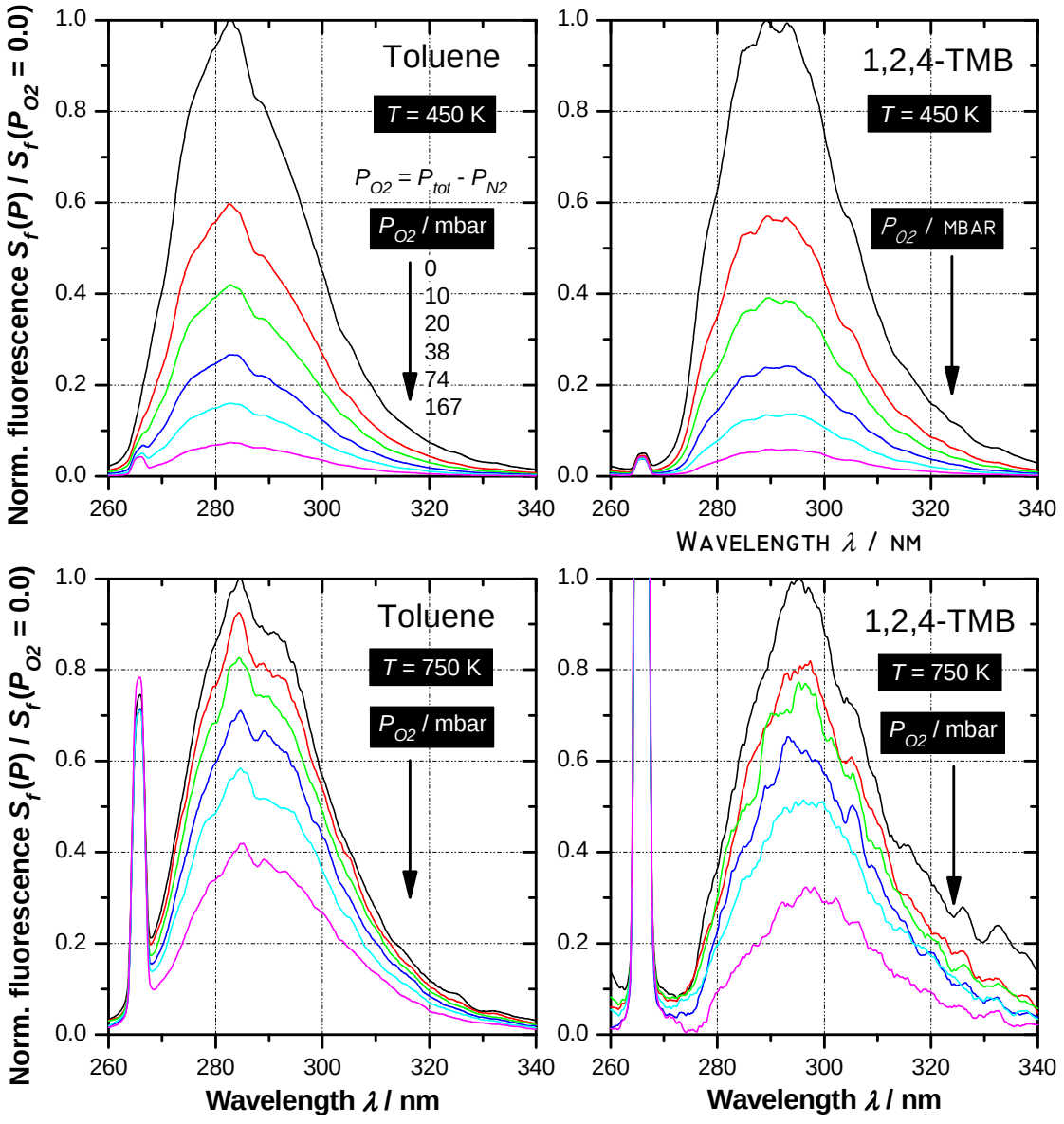

Figure 69: Fluorescence spectra after 266 nm laser excitation as a function of oxygen partial pressure at 450 K (upper figures) and 750 K (lower figures). Normalised to maximum peak under pure nitrogen condition. The maximum oxygen partial pressure for all measurements is 167 mbar. Left side: Toluene with 4.4 mbar concentration (evaporated from pure liquid toluene). Right side: 1,2,4-TMB with 0.55 mbar concentration (evaporated from 20 mol % 1,2,4-TMB in n-undecane).

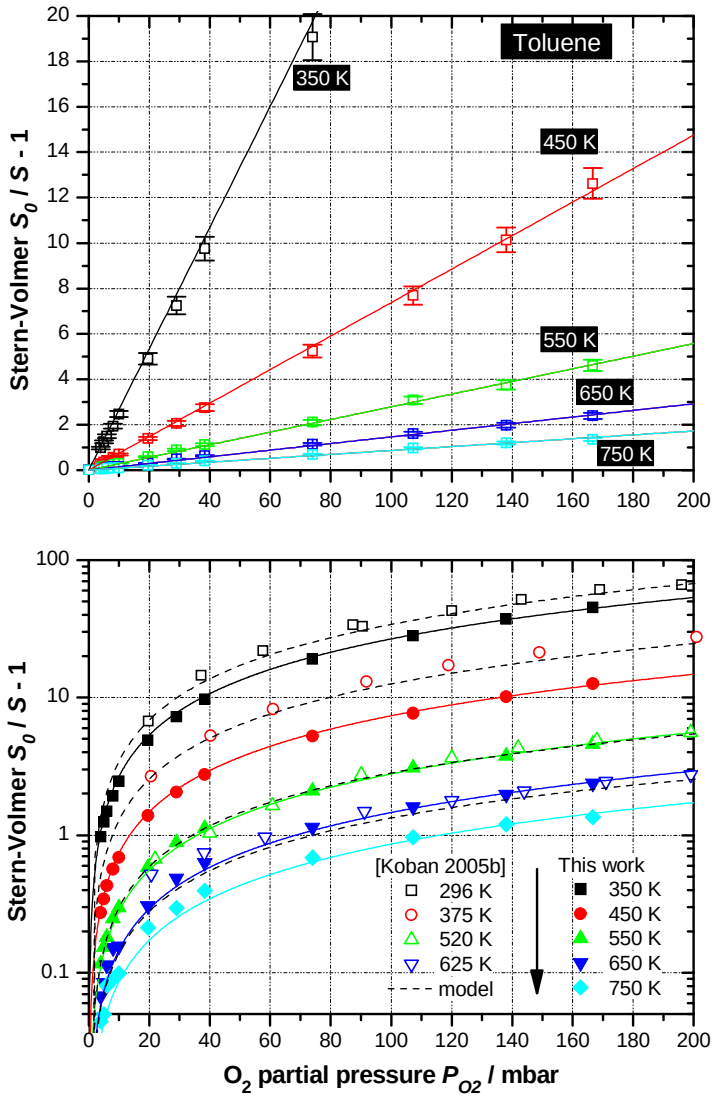

Figure 70: Toluene Stern-Volmer plot for toluene after 266 nm laser excitation as a function of temperature derived from integrated fluorescence spectra (270 to 340 nm). Replacing $[O_2]$ with n_{O_2}. The highest oxygen partial pressure was 167 mbar. Lines are zero-point linear regressions. Data from this work are compared to data from [Koban 2005a] for different temperature levels, cf. bottom diagram. Lines are from Koban's model. Koban et al. measured slightly weaker quenching, which results in an apparent shift of 25 to 30 K between their and our data, e.g. at 625 K, Koban's data fall on our 650 K data (to see in more detail the temperature dependence of the Stern-Volmer coefficient with respect to our and to Koban's data, refer to the curves in figure 74).

With the temperature regressions to the fluorescence yield in non-quenching and quenching environment and to the absorption cross-section, cf. (5.19), (5.21) and (5.17), respectively, the combined temperature and oxygen partial pressure influence to the toluene fluorescence at atmospheric total pressure is predicted (cf. figure 71). The thick black lines mark conditions of pure nitrogen and air. Obviously, the fluorescence intensity reaches a maximum, which changes with increasing oxygen concentration towards higher temperatures, cf. the dash-dotted black line crossing the oxygen isobars. To the lower temperature side from the maximum, the fluorescence loss without quenching is less sensitive to increasing temperature than the damping effect to the oxygen quenching. An extrapolation towards higher oxygen pressure leads to a convergence of the peak of fluorescence towards approximately 550 K (cf. the black plus symbols).

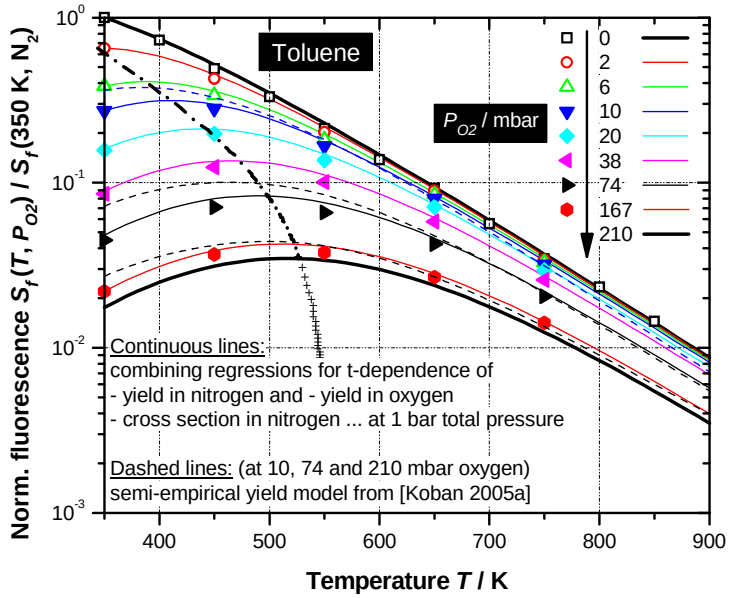

Figure 71: Combined temperature and O_2 influence to toluene fluorescence excited at 266 nm at 1 bar total pressure. Symbols are our experimental data. Lines issue from combined use of the yield regressions for the temperature influence in N_2 atmosphere, cf. (5.19), the O_2 influence, cf. (5.21) and the regression for the temperature influence to the cross-section, cf. (5.17). Broken lines represent fluorescence calculated from semi-empirical model presented by [Koban 2005a] at 10, 74 and 210 mbar oxygen concentration.

Our results are also compared with data calculated from a semi-empirical model [Koban 2005a], cf. the dashed lines for 10, 74 and 210 mbar oxygen concentration. Koban et al.'s model is derived from data obtained for 248 nm excitation, which does not show classical linear Stern-Volmer behaviour, even at room-temperature. The quenching has been found to be damped towards higher oxygen number densities, and the departure from linearity increased with increasing temperature. This non-linearity was also found to be relevant for 266 nm excitation, but only at temperature beyond 625 K and number densities of oxygen higher than $2 \cdot 10^{24}\ \mathrm{m}^{-3}$. From these observations, they relate the strength of the damping of the quenching to the amount of vibrational excitation in the excited state. In reference to this and observations from [Jacon 1977] (cf. section 5.5.4), Koban et al. considered two types of vibrational states with different sensitivities to oxygen quenching. These are represented by states with predominant intersystem crossing and predominant internal conversion. With the respective Stern-Volmer coefficients $k_{SV,1}$ and $k_{SV,2}$, the expression of the quantum yield ϕ_f^q for quenching is written as

$$\phi_f^q = \frac{A_1(\lambda, T)}{1 + k_{SV,1}(T)\, n_{O_2}} + \frac{A_2(\lambda, T)}{1 + k_{SV,2}(T)\, n_{O_2}} \tag{5.22}$$

with the closure relation $\phi_f^0 = A_1 + A_2$. For a given excitation wavelength, A_i and $k_{SV,i}$ depend only on temperature.

No relevant departure from the zero point linear regressions is seen throughout the entire range of our experimental data, even on a logarithmic scale (cf. the bottom diagram of figure 70). Therefore, the temperature regression we proposed with (5.21) readily describes

the combined influence of temperature and oxygen concentration to the fluorescence. Our results are similar to Koban's simulation data, but they do not justify an implementation of an expression such as (5.22) accounting for a possible non-linearity of the Stern-Volmer slope for 266 nm excitation wavelength.

The behaviour of experimental fluorescence data with temperature and oxygen concentration shown in figure 71 are well simulated by combined application of the regressions (5.19), (5.21) and (5.17). The results calculated from the semi-empirical model of Koban (cf. broken lines) are in overall good agreement, despite deviations observed at the low-temperature side.

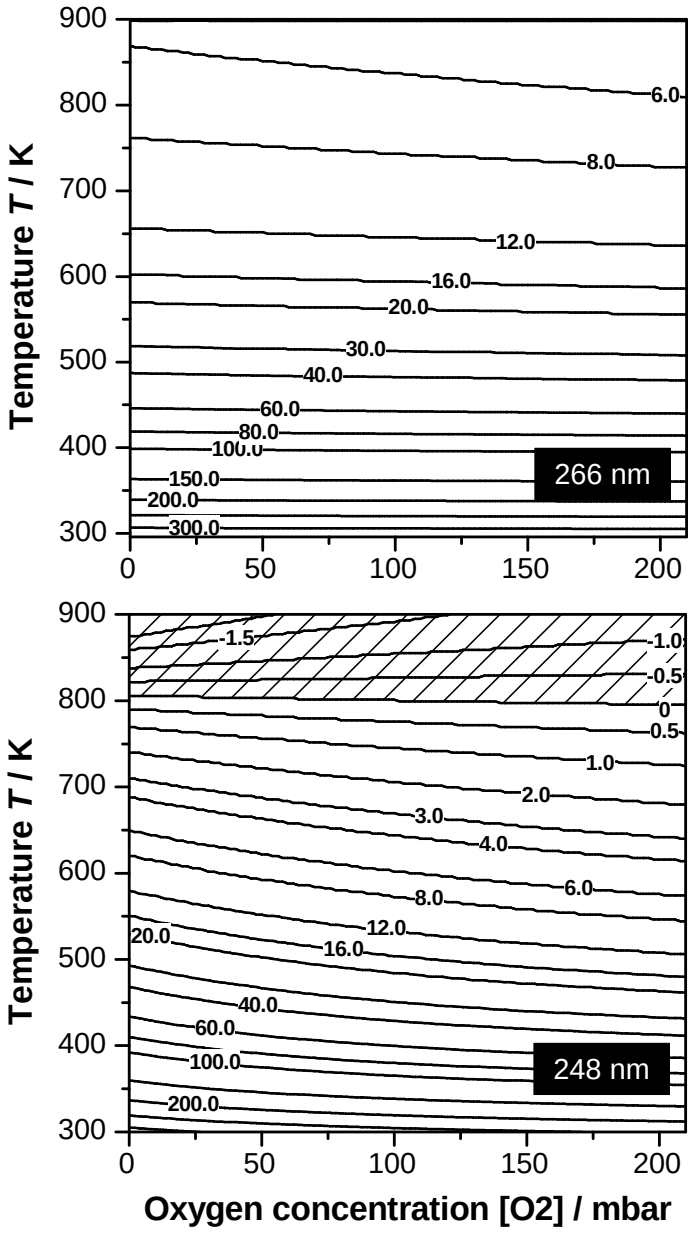

Figure 72: Stern-Volmer factor k_{SV} calculated from the semi-empirical model of [Koban 2005a] (see text for more detail).

The diagram describes, how the semi-empiric model of Koban accounts for the Stern-Volmer factor with temperature and oxygen concentration.

Top diagram: 266 nm excitation. The dependence on oxygen concentration is very limited for low temperatures.

Bottom diagram: 248 nm excitation. The dependence on oxygen concentration is much more pronounced, and moreover, extended to low temperatures.

Koban's semi-empirical model (5.22) of the fluorescence yield for oxygen quenching does somewhat not follow the conventional definition of the Stern-Volmer rule, relating the quenched and unquenched yield by the Stern-Volmer factor. However, an analogy to the conventional expression can be forced, solving (5.22) to k_{SV} by setting it equal to $\phi_f^0 / (1 + k_{SV} n_q)$. This allows a visualisation of their model in terms of a Stern-Volmer factor, which depends on temperature and oxygen number density (cf. the top and bottom diagrams of figure 72 for 266 and 248 nm excitation wavelength, respectively). In contradiction with our own experimental data up to 750 K, extrapolation to higher temperature induces non-linearity of their Stern-Volmer factor. It must be noted, that the validity of Koban's model is only assured for the temperature range of their experimental data (300 to 625 K), therefore representing a limit of applicability of this model.

Like for toluene, the oxygen quenching of 1,2,4-TMB fluorescence also follows a Stern-Volmer relation (cf. the top diagram in figure 73). At 450, 550 and 750 K temperature conditions, oxygen quenching of 1,2,4-TMB fluorescence is stronger, i.e. the Stern-Volmer factors are higher than for toluene (cf. figure 73). Note also on this diagram, that the slope of the 1,2,4-TMB Stern-Volmer plot at 650 K is higher than the slope at 550 K. At this given temperature, the effect of vibrational excess energy to the quenching efficiency is not the same as observed for toluene. However, the Stern-Volmer relation of 1,2,4-TMB is very close with respect to the temperature dependence and even in absolute value to that measured for the fraction of mono-aromatics in kerosene fuel (filtered detection, cf. figures 110 to 112 in section 6.3).

Neglecting the Stern-Volmer plot for 650 K, we obtain an exponential regression for the temperature dependence of the Stern-Volmer factor of 1,2,4-trimethylbenzene

$$k_{SV}(T) = 9.94 + \frac{1849.4 - 9.94}{1 + \left(T / 270.52\right)^{5.93}} \quad \left[\text{bar}^{-1}\right] \tag{5.23}$$

Then, the combined temperature and oxygen partial pressure dependence of the 1,2,4-TMB fluorescence at atmospheric total pressure using equations (5.18), (5.20) and (5.23) is shown (cf. the bottom diagram of figure 73), as earlier for toluene. The tendency of the dependence of the fluorescence signal on temperature and oxygen quenching is globally similar to the results of toluene, excepted the appearance of a fluorescence peak, which, when present, is shifted towards lower temperature.

Finally, a comparison between toluene and 1,2,4-TMB reveals a similar temperature regression for the Stern-Volmer factor, cf. figure 74 and equations (5.21) and (5.23). In addition, a comparison is also performed for toluene with Koban's experimental data. Similar temperature dependence are observed despite a systematic temperature shift by 25 K, maybe induced by an offset in calibration of the thermocouple or by an inappropriate control of the oxygen-free condition. Regressions from Koban's semi-empirical model are shown,

where the Stern-Volmer factor depends on temperature and oxygen concentration, since non-linearity was found within Koban's experimental Stern-Volmer data. The lower green line represents the regression at the low-pressure oxygen limit, the upper green line at air condition. In any case, the regressions provide an overall agreement to our findings.

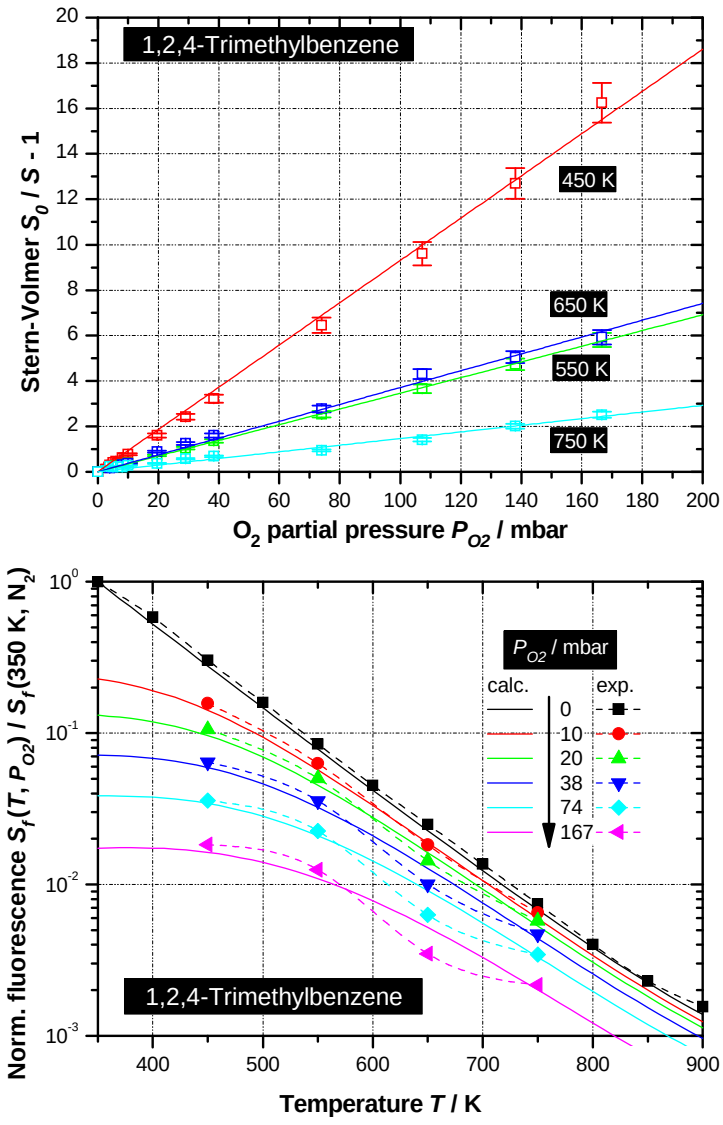

Figure 73: Top diagram: Stern-Volmer plot for 1,2,4-TMB after 266 nm laser excitation as a function of temperature derived from integrated fluorescence spectra (270 to 340 nm). The maximum oxygen partial pressure for all measurements is 167 mbar for all temperatures. Relative errors of S and S_0 add due to the division. 1,2,4-TMB with 0.55 mbar concentration (evaporated from 20 mol % 1,2,4-TMB in n-undecane). Bottom diagram: combined temperature and O_2 influence to 1,2,4-TMB fluorescence excited at 266 nm at 1 bar total pressure. Symbols: our experimental data. Continuous lines: combined use of the yield regressions for the temperature influence in N_2 atmosphere, cf. (5.20), the O_2 influence, cf. (5.23) and the regression for the temperature influence to the cross-section, cf. (5.18). Dashed lines are spline interpolations.

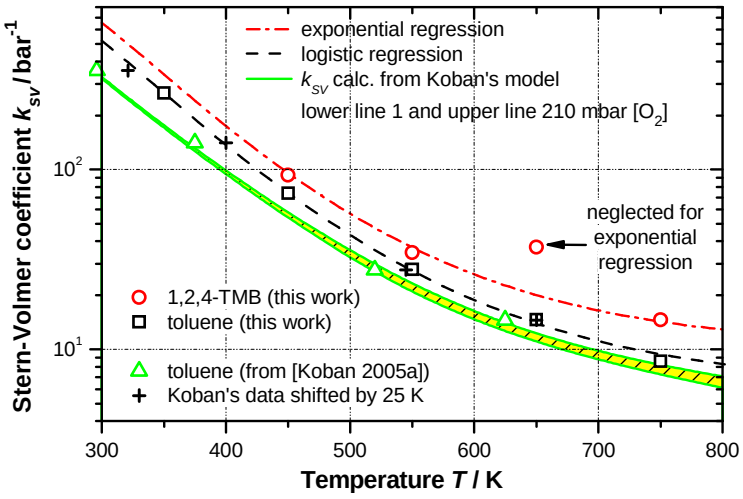

Figure 74: Temperature regressions for the Stern-Volmer factor of 1,2,4-TMB and toluene. For 1,2,4-TMB, the value at 650 K was neglected. For toluene, comparison of our data to data of [Koban 2005a] reveals a shift of approx. 25 K. The regressions of Koban's data shown as green lines correspond to their semi-empirical yield model (refer to text). The lower line is at the low-pressure oxygen limit, the upper line is for oxygen pressure ≥ 210 mbar.

5.7 Fluorescence of bicyclic aromatic tracers – results for naphthalene

In this section, the temperature, pressure and oxygen quenching dependencies of naphthalene fluorescence are detailed.

Excitation at 266 nm (37594 cm^{-1}) promotes the naphthalene molecule ((0,0) band at 32000 cm^{-1}) to the second excited state, which has its origin at 35900 cm^{-1}. Even the third excited state (47500 cm^{-1}) can be thermally populated by the 266 nm excitation wavelength of the ground state at temperature beyond 850 K, cf. section 5.5.5.

Compared to the monocyclic aromatics, the absorption spectrum of bicyclic naphthalene is largely shifted to the red (cf. figure 43). The red-shift caused by the second benzene cycle is much larger than the red-shift for alkyl substitution, cf. [Suto 1992]. Similar results are observed for the emission spectra, which are red-shifted by 40 to 50 nm compared to the monocyclic aromatics studied before. In figure 75, the effect of substitution of one or two methyl groups to the intensity and spectral shape of the naphthalene fluorescence is illustrated in relative value (left hand diagram) and normalised to the peak (right hand diagram). For both methylated naphthalenes, the spectra are similarly broadening to the red side, while a significant intensity gain is only observed for the doubly methylated naphthalene. The central shape of the spectra also changes from a left-hand peak with a right-hand side lobe for naphthalene over a large flattened peak for methylnaphthalene to a right-hand peak with a left-hand side lobe for dimethylnaphthalene.

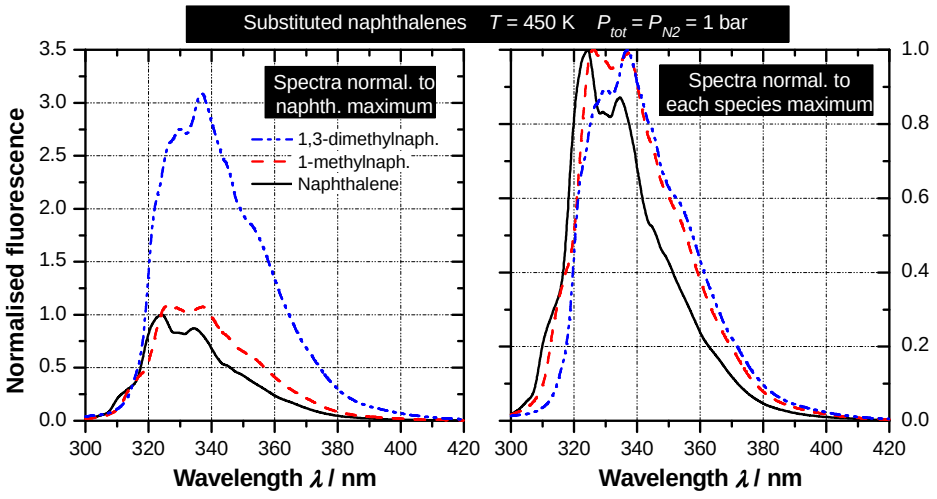

Figure 75: Fluorescence spectra after 266 nm laser excitation as a function of naphthalene methylation in pure nitrogen atmosphere at ambient pressure and 450 K. Naphthalene and 1-Methylnaphthalene are evaporated to 0.3 mbar from 5 mol % solution in n-undecane (number density of 4.8×10^{15} cm^{-3}); 1,3-Dimethylnaphthalene is evaporated to 0.15 mbar from 2.5 mol % solution in n-undecane (number density of 2.4×10^{15} cm^{-3}). Left figure: Spectra are normalised to naphthalene fluorescence maximum. Right figure: Each spectrum is normalised to its own maximum.

Note that the measurements discussed hereafter were also performed for methylated naphthalenes (cf. [Baranger 2004]). Changes to the emission behaviour induced by simple and double methylation are quite small.

5.7.1 Temperature dependence

A comparison of the absorption scheme of benzene derivatives and naphthalene at 266 nm reveals that naphthalene is excited in the middle E_2 band, contrary to toluene and 1,2,4-trimethylbenzene (TMB), which are excited in the B-band. Naphthalene, hereby promoted to the second excited state, is subject to fast internal conversion to the first excited state. This results in a large production of vibrational excess, which largely impacts on the fluorescence emission with change of environmental conditions (temperature, pressure and species concentration).

(a) Absorption

The change of naphthalene absorption cross-section on temperature condition is studied for a 266 nm excitation wavelength in atmospheric pressure nitrogen. To our knowledge, no other published data report the effect of temperature on naphthalene absorption at nearby conditions.

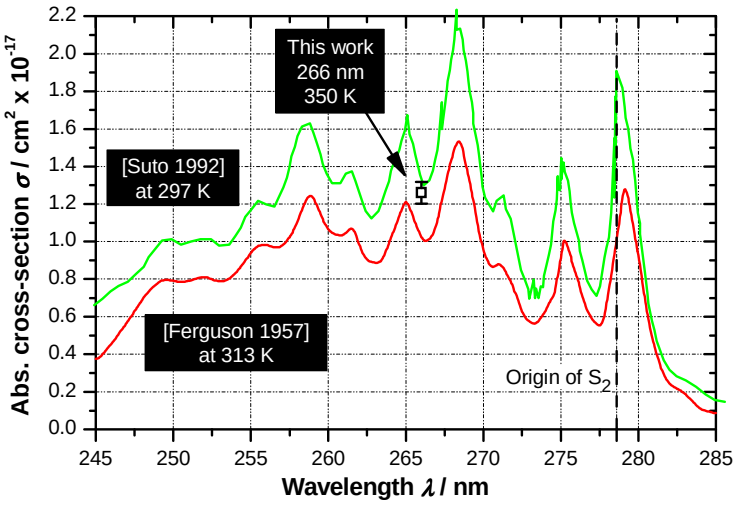

Figure 76: Low-pressure naphthalene absorption cross-section from [Ferguson 1957] at 313 K (lower line) and [Suto 1992] at 297 K (upper line) compared to our measurements performed at 350 K in atmospheric pressure nitrogen.

The lowest studied temperature is chosen as 350 K due to the limited vapour pressure of naphthalene. Near to this value, comparison of our data with absorption spectra from [Suto 1992] at 297 K and from [Ferguson 1957] at 313 K is possible (cf. figure 76). Both reference absorption spectra (measured at several torr) are quite similar. Our absorption cross-section result fits well with the value reported by Suto et al., whereas a difference of $0.2 \cdot 10^{-17}\ \mathrm{cm}^2$ is observed with Ferguson's data.

The effect of temperature on the absorption cross-section is also studied. Results displayed in figure 77 and recorded in the 300 – 900 K range in pure nitrogen show a quasi-flat response with a mean value of $(1.30 \pm 0.04) \cdot 10^{-17}\ \mathrm{cm}^2$. This important feature will then allow to simplify the interpretation of our fluorescence measurements, because a direct relation between the measured fluorescence intensity and its respective yield exists.

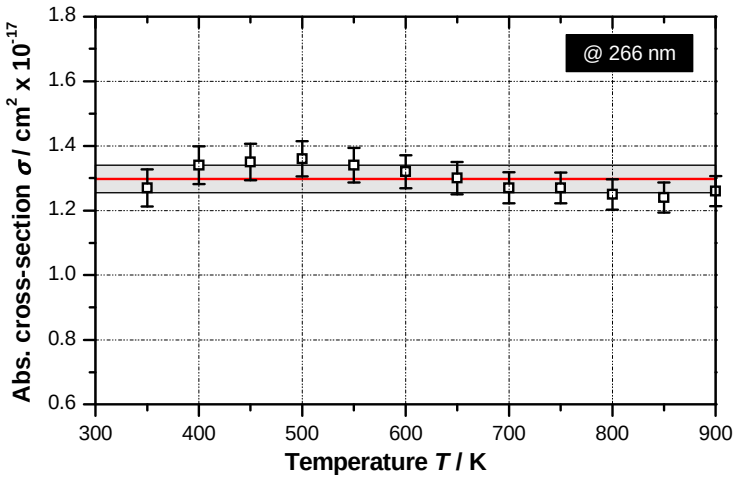

Figure 77: Naphthalene absorption cross-section after 266 nm laser excitation as a function of temperature. Naphthalene was evaporated to constant number density of $4.8 \cdot 10^{15}\ \mathrm{cm}^{-3}$ (0.23 to 0.59 mbar from 350 to 900 K) in pure ambient pressure nitrogen.

(b) Fluorescence

The temperature effect on the fluorescence emission of naphthalene excited at 266 nm is studied from 350 to 900 K in atmospheric pressure nitrogen. Fluorescence spectra, normalised to the fluorescence peak recorded at 350 K, are provided in figure 78.

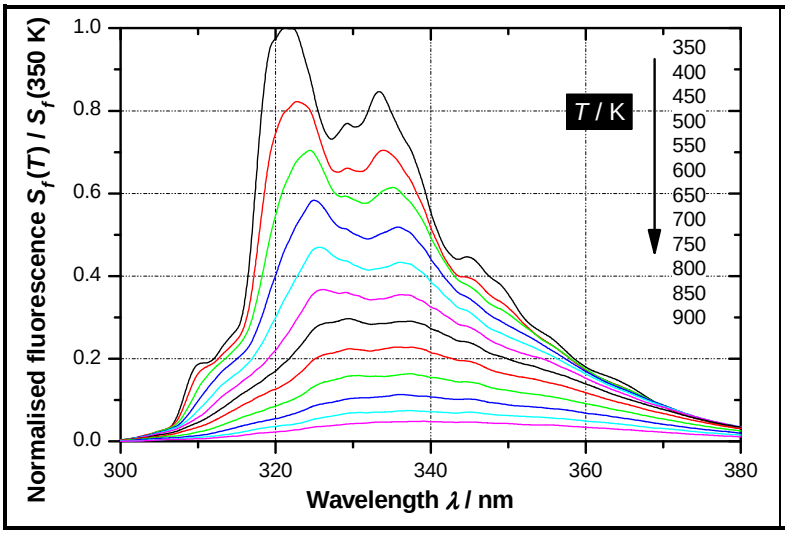

Figure 78: Naphthalene fluorescence spectra after 266 nm laser excitation as a function of temperature. Normalised to 350 K.

Naphthalene was evaporated to constant number density of $4.8 \cdot 10^{15}$ cm^{-3} (0.23 to 0.59 mbar from 350 to 900 K) in atmospheric pressure nitrogen.

Near to the room temperature condition, the spectrum is structured, exhibiting a left-hand peak near 320 nm and a right hand side lobe around 335 nm. With rising temperature, the spectrum broadens to the long wavelength side, while the fluorescence shape becomes structureless. This effect is accompanied by a loss of fluorescence intensity over the entire spectrum. [Kaiser 2005] studied 1-methylnaphthalene under similar conditions and obtained similar results. They notably observed a monotonic loss of fluorescence intensity for an increase of temperature from 400 to 928 K.

The normalised spectra plotted in figure 79 indicate a temperature-induced red-shift of the fluorescence peak accompanied by a spectral broadening. The peak intensity shifts up to 20 nm, whereas the broadening measured at half-maximum is 24 nm when the temperature ranges from 400 to 900 K (i.e. about 4.8±0.4 nm per 100 K). These values are in the same order of magnitude with results from [Kaiser 2005], who records for 1-methylnaphthalene in nitrogen a spectral broadening and a red-shift of about 21.1 nm for temperature between 400 and 928 K (i.e. 4.0 nm per 100 K). Further comparison is also possible to data from [Ossler 2001] which present fluorescence spectra of naphthalene in nitrogen atmosphere after a 266 nm picosecond excitation for temperature from 430 to 980 K. A comparison of their spectra with our data is presented in the bottom diagram of figure 79. Note that their spectra present a lower slope at the rising edge (300 – 330 nm) while the shape is globally similar to our results for nearby temperature. As to the spectral broadening with increasing temperature, a value of about 4.2±0.2 nm per 100 K is estimated.

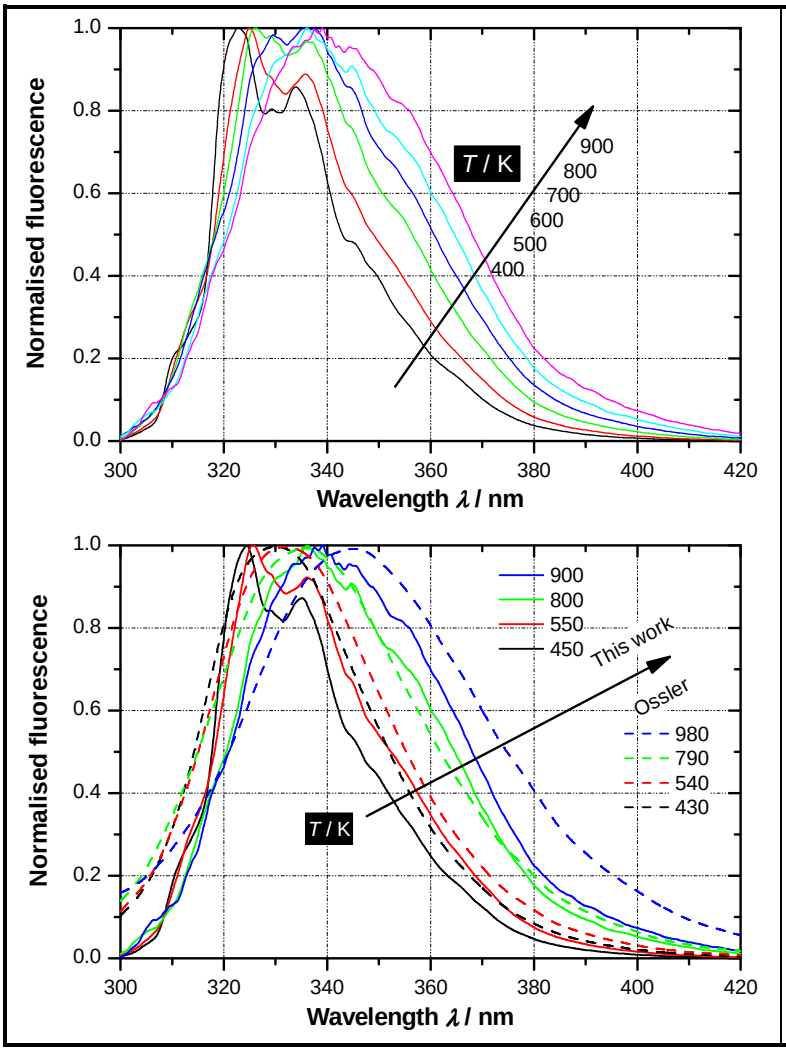

Figure 79: Fluorescence red-shift as a function of temperature for naphthalene in atmospheric pressure nitrogen. Top diagram: fluorescence spectra after 266 nm laser excitation from this work, normalised to maximum peak.. All spectra are first order Savitzky-Golay smoothed with 2.5 nm window size. Bottom figure: as above in comparison to spectra from [Ossler 2001] recorded after picosecond excitation at 266 nm. The straight lines correspond to this work, the dashed lines to Ossler's work.

The origin of the red-shift results from differences in anharmonicity and position of the potential energy surfaces of naphthalene between the ground state and the first excited singlet state. Radiative transitions starting from levels with higher vibrational energy are vertically closer to the ground state than lower lying levels, e.g. following the arguments of [Uy 1970], who observed a naphthalene red-shift increasing with excitation energy.

The naphthalene fluorescence integrated from 300 to 420 nm, i.e. the fluorescence yield shows a monotonic and moderate temperature-induced intensity fall-off compared to the studied mono-aromatic species (cf. figure 80). By contrast, this evolution looks like that observed for ketones (cf. section 5.4.1). The red line in figure 80 corresponds thus to our own yield calculation for the temperature-induced fluorescence of naphthalene, which will be detailed in section 5.8.

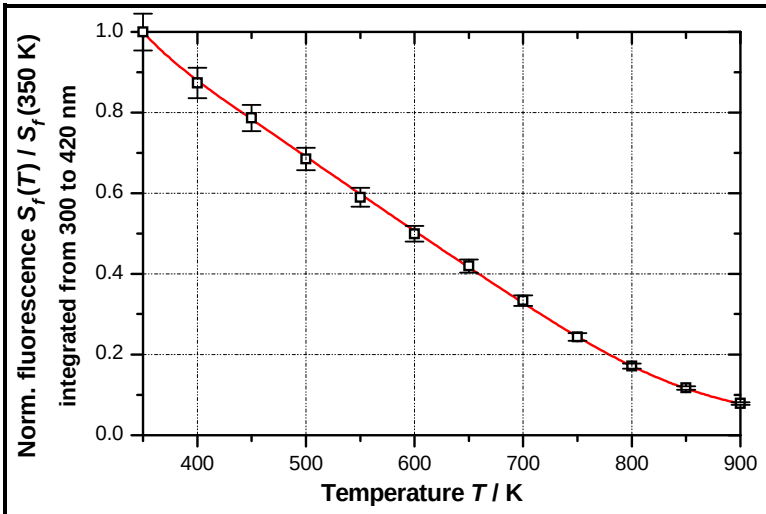

Figure 80: Naphthalene fluorescence after 266 nm laser excitation as a function of temperature. Normalised to 350 K, from integrated fluorescence spectra (300 to 420 nm). Atmospheric pressure nitrogen. Line represents yield from our own model. Absorption cross-section is practically constant with temperature, i.e. $(1.30 \pm 0.04) \cdot 10^{-17}$ cm^2.

5.7.2 Pressure dependence

The pressure effect on the fluorescence emission is measured from 1 to 30 bar in nitrogen atmosphere at two temperatures, 450 and 700 K. Spectral shapes of fluorescence normalised to the fluorescence peak at atmospheric pressure are presented in figure 81.

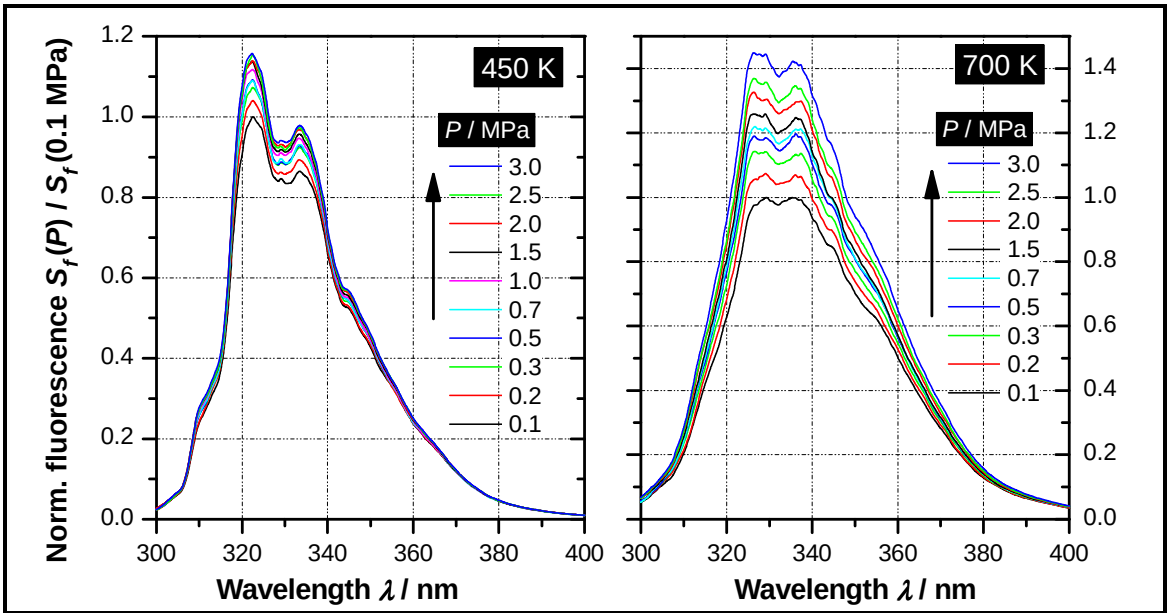

Figure 81: Naphthalene fluorescence spectra after 266 nm laser excitation as a function of pressure. Normalised to 0.1 MPa. Naphthalene was evaporated from liquid mixture of 5 mol % naphthalene in n-undecane to constant number density n. Pure nitrogen atmosphere at 450 K (upper figure) with $n \approx 1.1\times10^{16}$cm^{-3} and at 700 K (lower figure) with $n \approx 6.8\times10^{15}$ cm^{-3}. Naphthalene concentration is about 0.7 mbar. All spectra are first order Savitzky-Golay smoothed with 2.5 nm window size.

Whatever the temperature condition, neither spectral broadening nor red-shift occurs with increasing pressure. The only visible effect is an intensity loss of the spectra, which can be quantified accurately on integrated spectra (from 300 to 420 nm), cf. figure 82.

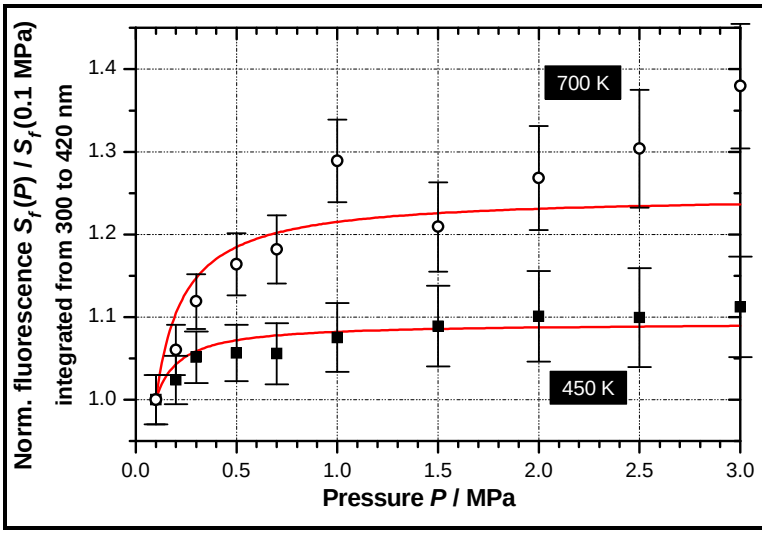

Figure 82: Naphthalene fluorescence after 266 nm laser excitation as a function of pressure. Normalised to 0.1 MPa, from integrated fluorescence spectra (300 to 420 nm). Pure nitrogen atmosphere at 450 K and at 700 K. Red lines represents our own yield model calculation.

For both temperatures, a pressure-induced (yield) stabilisation effect is observed within our experiments. Near atmospheric pressure, the increase of the fluorescence intensity is initially more pronounced than at higher pressure (> 10 bar), where the fluorescence levels off. Contrary to mono-aromatics, where a reduction of fluorescence intensity with increasing pressure is noted, the opposite effect is observed for naphthalene. The occurrence of the stabilisation effect was previously discussed in sections 5.1.8 and 5.6.2. This effect, although reported for various ketones and few aromatic species, is not primarily related to the species, but rather to a physical process, which can be explained in view of the specific absorption scheme and the choice of excitation wavelength. For shorter excitation wavelengths, the increase of the stabilisation effect is likely to be strengthened, whereas it is weakened for excitation closer to the origin of the excited state. At low-pressure, [Beddard 1973 and Beddard 1974] evidenced the influence of argon and methane foreign gas pressure to the fluorescence yield of naphthalene. They observed a stabilisation effect for excitation far from the (0,0) band, which decreases and finally switches to a yield weakening for excitation in the vicinity of the (0,0) band. Pressure equilibration to the Boltzmann limit, however, succeeded well below atmospheric pressure. By contrast, our measurements show, that the fluorescence yield of naphthalene is still enhanced through collisions with nitrogen for pressure larger than atmospheric pressure. This is in analogy to results reported for aliphatic ketones for foreign gas pressure up to 26 bar, cf. [Thurber 1999a], [Grossmann 1996] and [Koch 2003a].

Our results are to our knowledge the first measurement reporting a stabilisation effect to naphthalene fluorescence induced by high-pressure nitrogen gas. Moreover, the stabilisation effect is emphasized for the higher temperature level (cf. figure 82), implying higher yield values at 700 K. This observation is analogous with results from [Thurber 1999a], who evi-

denced a strengthening of the pressure-induced yield increase with increasing temperature for acetone and excitation far from the (0,0) band. Our model developed for the fluorescence yield simulation of naphthalene and detailed later in section 5.8, depicts well the pressure-induced stabilisation effect, including its sensitivity to the temperature level. This can be seen from the red lines in figure 82, fitting quite well into the error limits of our experimental data.

5.7.3 Oxygen dependence

The sensitivity of naphthalene fluorescence towards oxygen quenching was studied at atmospheric pressure. Fluorescence spectra normalised to the condition of pure nitrogen atmosphere are presented in figure 83 for two temperatures, 450 and 750 K.

Contrary to the case of monocyclic aromatics, an increase of the oxygen concentration leads to a spectral broadening of naphthalene fluorescence for both temperature conditions. This effect is characterised by a small red-shift of the peak intensity and the long-wavelength edge of the spectrum (cf. figure 83). The red-shift induced by oxygen concentration is not that regular as the one observed before with temperature (cf. 5.7.1). Increasing the oxygen concentration attenuates the shift. This finding confirms results of [Kaiser 2005], who stated a spectral red-shift saturating at about 10 % oxygen concentration from measurements of 5 % naphthalene in 95 % dodecane at 500 K.

Our results in figure 83 show further, that naphthalene is stronger quenched by oxygen than the studied mono-aromatics, cf. figure 69 in section 5.6.3. An attenuation of the oxygen quenching effect with increasing temperature is then observed. The character of the quenching is best revealed by depicting it as the Stern-Volmer factor with temperature and oxygen concentration. Temperature implies a strong damping influence on the slope of the Stern-Volmer plots, which can be approximated by zero point linear functions. Similar to the other aromatic species, a logistic temperature regression is determined for the Stern-Volmer factor, which writes as follows

$$k_{SV}(T) = 1.68 + \frac{1643.3 - 1.68}{1 + \left(T / 308.12\right)^{3.085}} \quad \left[\mathrm{bar}^{-1}\right] \tag{5.24}$$

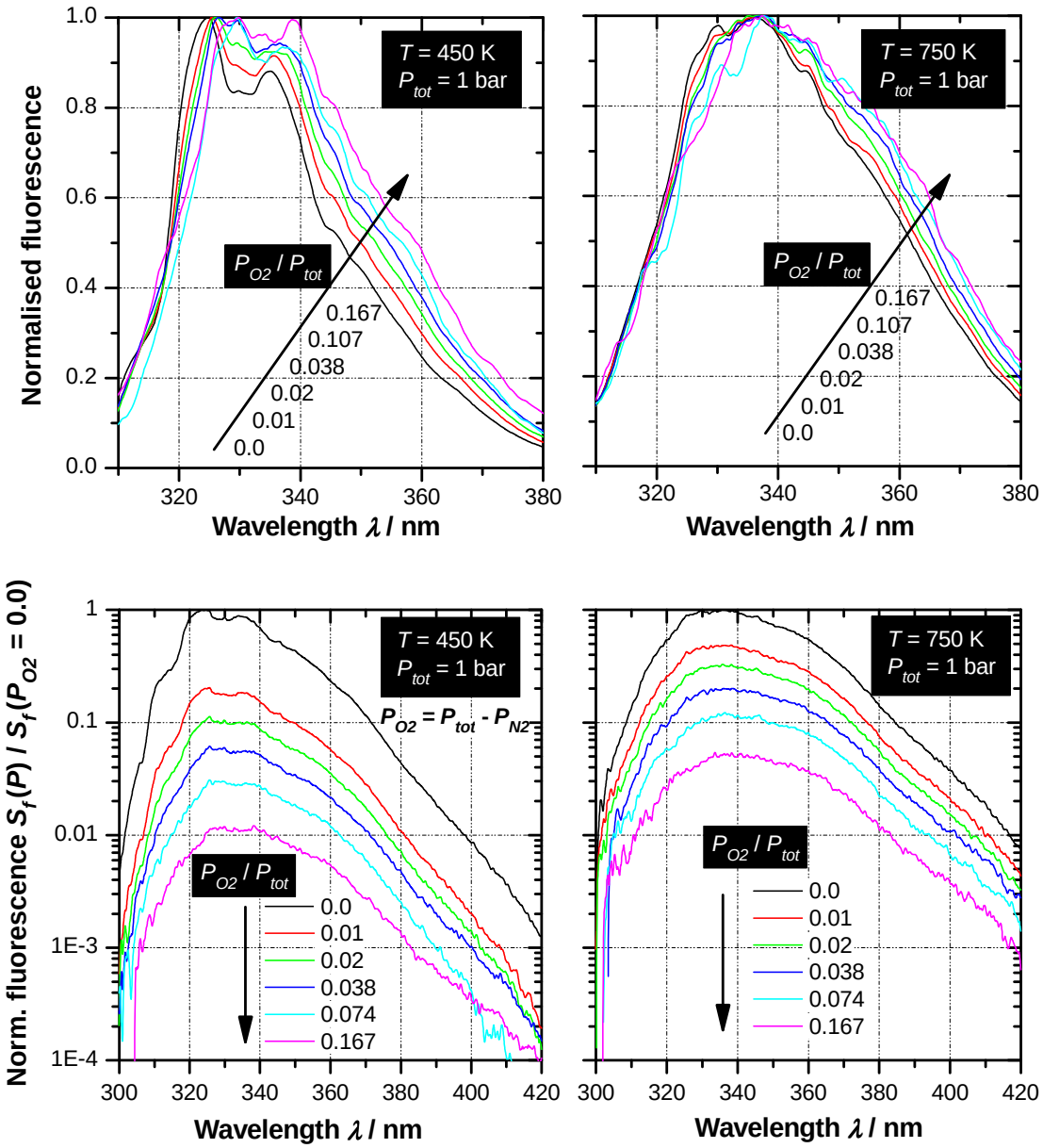

Figure 83: Naphthalene fluorescence spectra after 266 nm laser excitation as a function of oxygen partial pressure at 450 (left hand) and 750 K (right hand). The maximum oxygen partial pressure for all measurements is 167 mbar. Naphthalene with 0.13 mbar concentration (evaporated from 5 mol % naphthalene in n-undecane). All spectra are first order Savitzky-Golay smoothed with 2.5 nm window size. Top diagrams: normalised to peak value at each oxygen concentration for visualisation of spectral broadening and red-shift as a function of oxygen partial pressure. Bottom diagrams: spectra normalised to peak value under pure nitrogen condition.

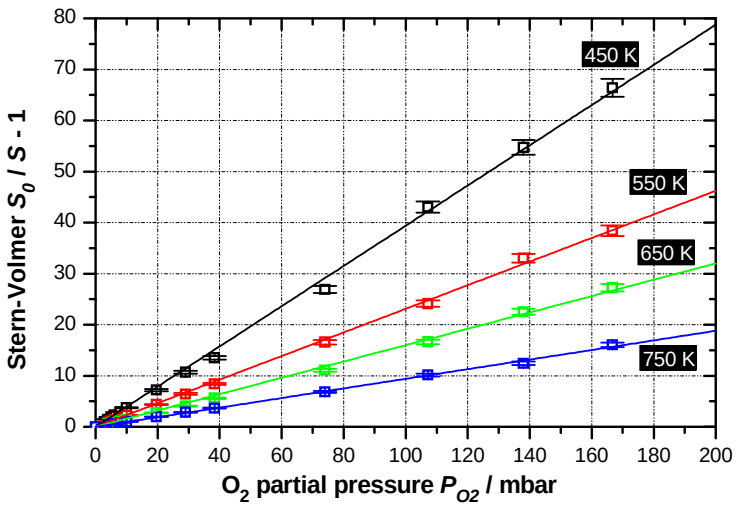

Figure 84: Naphthalene Stern-Volmer plot after 266 nm laser excitation as a function of temperature derived from integrated fluorescence spectra (310 to 420 nm). The maximum oxygen partial pressure for all measurements is 167 mbar for all temperatures. Naphthalene with 0.13 mbar concentration (evaporated from 5 mol % naphthalene in n-undecane). Continuous lines are zero-point linear regressions.

Together with those for 1,2,4-trimethylbenzene (TMB) and toluene, these temperature evolutions are depicted in figure 85. Obviously, the temperature sensitivity of the Stern-Volmer slope is less pronounced for naphthalene compared to the monocyclic aromatics.

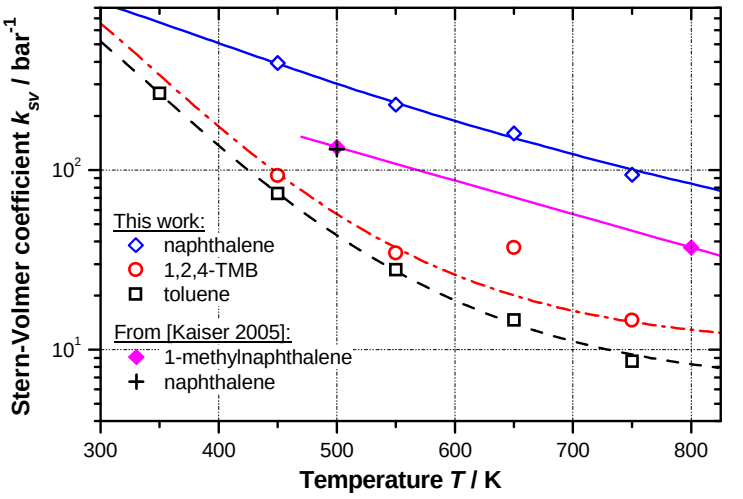

Figure 85: Temperature regressions of the Stern-Volmer factor of oxygen quenching for the aromatics studied in this work: naphthalene compared to 1,2,4-TMB and toluene. For naphthalene the quenching is much stronger, whereas the dependence of the Stern-Volmer factor on temperature is less important. [Kaiser 2005] measured a similar temperature dependence, while the absolute quenching was measured roughly half as strong as in our study.

A comparison of our naphthalene results is performed with naphthalene and methyl-naphthalene data reported from [Kaiser 2005] for 500 and 800 K. Since at 500 K, their results for methylnaphthalene and naphthalene are very close, the naphthalene value at 800 K might then be approximated by that of methylnaphthalene. The naphthalene quenching of Kaiser et al. is roughly half as strong as we found within this work. This difference might be induced by the choice of their experimental approach. They realised measurements in the vicinity of the nozzle exit of a heated fuel–N_2–O_2 jet expanding in ambient air. A few mbar of oxygen entrained to the jet by diffusion may induce a significant change of the absolute

Stern-Volmer value. For instance at 450 K, a concentration of 2.5 per mil of residual oxygen is sufficient to reduce the Stern-Volmer factor by the same order of magnitude.

5.8 Fluorescence yield model: from ketones to aromatics

The ketone fluorescence yield model from Thurber and Koch detailed in section 5.3 is based on the competition of fluorescence with non-radiative depopulation mechanisms by stepwise (or step-ladder) summation of fluorescence quantum yield within a cascade of vibrational relaxation. In principle, it should be possible to adapt this yield model to other organic tracers. For organic molecules, vibrational population is generally congested to a quasi-continuum distribution, followed by vibrational relaxation to a Boltzmann thermalised distribution through collisions with foreign gas. Care should be taken, when congestion becomes less severe, which might be a consequence of a lower density of initially populated levels. A practical example for this is the insufficient yield simulation reported for difluorobenzene by [Steer 1978], where redistribution is not finished before vibrational relaxation comes into play.

In order to develop a yield model for aromatic species, the respective rates of radiative and non-radiative decays are needed as function of vibrational excess energy. These are generally derived from low-pressure yield and lifetime data at room-temperature as a function of excitation energy. These conditions are quite far from those, where the model will be mainly applied. Throughout our fluorescence experiments, the excitation energy is constant, whereas the temperature and the pressure conditions are varied. Assuming the rate data being practically independent from pressure, a transcription to constant excitation energy and variable temperature implies a transformation of the thermal ground state energy of the Boltzmann distribution to vibrational excess energy. The thermal energy adds to the photonic excess energy after the absorption and is then redistributed as a function of Franck-Condon factors.

As a first step, the thermal energy of the ground state room temperature population is included in the excess energy as $\hbar / \lambda_{exc} + E_{th}(T_{ambient})$ when displaying the low-pressure rate data measured for varying excitation energy. Next, the low-pressure rate data is used as an initial guess within a non-linear least-squared optimisation procedure. A set of decay rates dependent on vibrational excess energy is obtained from fitting the modelled yield to our experimental data. This is first performed for data recorded in non-quenching nitrogen atmosphere for variable temperature. The span of vibrational excess energy corresponds to the temperature range of our experiments, applying again $\hbar / \lambda_{exc} + E_{th}(T = 350 \ldots 900\,\mathrm{K})$.

After successful derivation of a first set of rates, collisional parameters have to be derived from fitting the model to our pressure dependent yield results in non-quenching environment. Several iterations are necessary to obtain a good convergence to a single rate set,

which accurately describes temperature and pressure dependencies. When possible, collisional parameters of other bath gases and also different pressure domains are considered.

So far restricted to intramolecular deactivation processes, a further milestone is the opening towards electronic deactivation through intermolecular quenching processes, such as encountered in presence of oxygen. Therein, our approach is innovative compared to the ketone yield model discussed earlier. The ketones correspond to the limit of very low quenching efficiency, which allows the neglect of the $\langle P \rangle$-proportion of collisions efficient for the quenching without drastic changes to the accuracy of the yield modelling. A distinction between intra- and intermolecular processes is thus not necessary. In contrast, most aromatic species are at the limit of very strong quenching, where it is the $(1-\langle P \rangle)$-proportion of inefficient collisions, which is negligible. The $\langle P \rangle$-proportion of efficient collisions has then to be removed from the vibrational cascade to respect the population balance of the next lower cascade level. For the intermediate case of moderate quenching efficiency, the $(1-\langle P \rangle)$-proportion of oxygen collisions leading to vibrational relaxation has to be considered for the population of lower lying levels.

The approach presented above allowed to develop a yield model for naphthalene and toluene. Throughout the following sections, the adaptation of this yield model to these aromatics is detailed. Firstly, intramolecular deactivation in non-quenching environment is considered. As a second step, the implementation of quenching reactions to the model is discussed.

For the sake of completeness, we present some sets of parameters from the optimisation procedures in appendices A-1 and A-1.

5.8.1 Intramolecular deactivation

As a first step, the cascade yield model of vibrational relaxation is adapted to naphthalene and toluene, while excluding electronic quenching reactions. This enables a comparison to our experimental results under nitrogen atmosphere as well as to pure tracer low-pressure yield data from literature references.

(a) Collisional energy transfer

Prior to the discussion of the results obtained for the optimisation of the yield model to naphthalene in the next section, it is noted that a different approach of handling the collisional energy transfer must be applied when approaching the thermalised level. For the ketone model of Thurber and Koch, the energy induced by collision is only transferred from the tracer molecule to the bath gas, and the vibrational modes of the excited state are ap-

proximated by the ground state modes, when calculating the thermal energy. For an excitation in the vicinity of the (0,0) transition, this approach fails. For a complete description of the observed phenomena for the behaviour of the fluorescence yield and lifetime as a function of collisional energy relaxation, bidirectional energy transfer is then necessary.

We discussed the mechanism behind the pressure-induced yield and lifetime decrease near the (0,0) band in section 5.6.2 in terms of photoinduced cooling of the nascent vibrational distribution during excitation close to the (0,0) band. Cooling occurs if the vibrational modes are lower in frequency in the excited state than in the ground state, and cooling is followed by heating through collisions with the bath gas if the photonic excess energy is smaller than the difference in thermal energy between excited and ground states.

For naphthalene, complete sets of vibrational mode frequencies are known for the ground and the first excited states. We implemented the frequencies from [Beck 1980] in our model. Thermal energy differences between the excited and the ground states are calculated applying the mode frequencies to equation (5.1). Results between 300 and 900 K are presented in table 11. Like for toluene, the thermal energy gap between the excited and the ground states grows with increasing temperature (cf. table 10 in section 5.6.2).

As already mentioned, the scale of this energy gap essentially changes the collisional energy transfer within the cascading relaxation of the yield model, cf. equation (5.12) in section 5.3.3. Thurber's and Koch's ketone model neglects the difference in thermal energy (ground state modes are used for the excited state). Thus, relaxation ends, when the condition

$$\left[\Delta E_{laser} - E(S_{1,v=0})\right] - \cancel{\left(E_{th,S_1} - E_{th,S_0}\right)} \geq \varepsilon \text{ with } E_{th,S_1} \approx E_{th,S_0} \tag{5.25}$$

is violated (ε defines the end of the cascade algorithm, which otherwise could turn out to be an endless procedure). Considering the thermal energy gap now leads to a change in the terminating condition, such as

$$\left|\left[\Delta E_{laser} - E(S_{1,v=0})\right] - \left(E_{th,S_1} - E_{th,S_0}\right)\right| \geq \varepsilon \text{ with } E_{th,S_1} > E_{th,S_0} \tag{5.26}$$

ΔE_{coll} becomes a negative energy term if the photonic excess is small compared to the thermal energy gap. In that case, the tracer molecule is heated through collisions with the bath gas. We calculated the excitation wavelengths, below which negative ΔE_{coll} values are obtained for naphthalene, within the temperature range from 300 to 900 K, cf. the last column in table 11 (with 32020 cm^{-1} as state origin).

Table 11: Thermalisation energies of naphthalene ground and excited states (in cm^{-1}). Vibrational frequencies were used from [Beck 1980]. The energy gap between ground and excited state thermalised distributions increases with the temperature. Accordingly, the excitation wavelengths, below which negative values for ΔE_{coll} are obtained, are shown in the last column.

Temperature T / K	E_{th,S_0}	E_{th,S_1}	$E_{th,S_1} - E_{th,S_0}$	$\lambda_{exc} = 10^7 / \Delta E_{laser}$ with negat. ΔE_{coll} $\Delta E_{laser} = E(S_{1,v=0}) + \left(E_{th,S_1} - E_{th,S_0}\right)$
300	871.3	1273.3	402.1	308.4 nm
400	1884.9	2568.6	683.7	305.8 nm
500	3268.4	4225.4	957	303.2 nm
600	4953.5	6164.6	1211.1	300.9 nm
700	6879.4	8326.2	1446.7	298.8 nm
800	8999.4	10666	1666.3	296.9 nm
900	11278	13149	1871.2	295.1 nm

A schema of the energy transfer processes involved in the excitation of naphthalene as handled by our yield model adapted for naphthalene is depicted in figure 86. Since internal conversion from higher excited singlet states is much faster than any collisional event, the cascade relaxation does not occur until the whole distribution has been transferred to the first excited state, even if naphthalene may have been initially promoted to higher excited singlet states.

Neglecting the thermal energy gap between the ground and the excited states, excitation occurs directly to the thermalised level, when the photon energy equals the (0,0) transition, whereas for consideration of this gap, the photon energy has to be $\Delta E_{laser} = E(S_{1,v=0}) + \left(E_{th,S_1} - E_{th,S_0}\right)$. If the photon energy is higher than this term, the energy is transferred by collision from the tracer molecule to the bath gas molecules. In the opposite case, the energy transfer is now from the bath gas to the tracer.

An illustration of this phenomenon is presented for the case of naphthalene at 300 K. The energy, for which the vibrational energy of the molecule is not affected during the promotion to the excited state is defined by equation (5.26). Given the vibrational modes of naphthalene, this occurs for an excitation wavelength of 308.4 nm, i.e. at 402.1 cm^{-1} from the origin of the first excited state (32020 cm^{-1}). Photo-induced cooling is followed by subsequent heating through collisions with the bath gas if the excitation wavelength higher than 308.4 nm is chosen. This result is in good agreement with the data of [He 2002], which reveals photo-induced cooling up to 500 cm^{-1}.

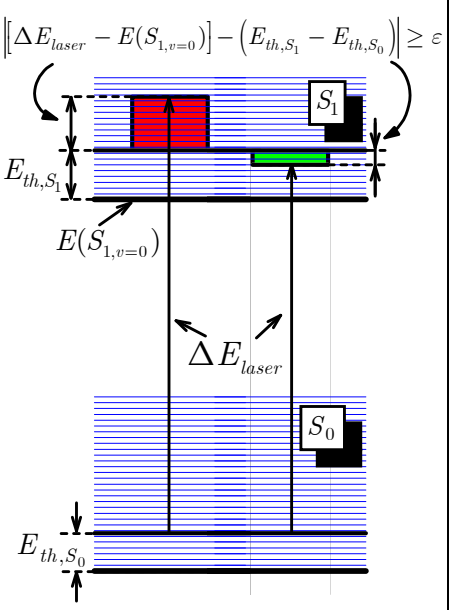

Figure 86: Schema of energy transfer processes involved in the excitation to the excited singlet state as handled by our yield model adapted to naphthalene. For excitation directly to the thermalised level of the excited state, the energy of the laser photon has to be chosen as follows:

excitation directly to the thermalised level:
$$\Delta E_{laser} = E(S_{1,v=0}) + \left(E_{th,S_1} - E_{th,S_0}\right)$$

If the photon energy is higher, the bath gas molecules are cooling the tracer (cf. red surface for cascade in downward direction of vibrational energy), if it is lower, the bath gas molecules are heating the tracer (cf. green surface for upward cascade). The ketone yield model from Thurber and Koch simplifies by neglecting the differences between the thermalisation energies. By setting this gap to zero, excitation to the thermalised level is reached just for $\Delta E_{laser} = E(S_{1,v=0})$.

(b) Naphthalene

Excitation energy dependence of naphthalene radiative and non-radiative decay are depicted in the top diagram of figure 87. As detailed in the previous section, the thermal energy of the ground state room temperature population is considered to the excess energy as $\hbar / \lambda_{exc} + E_{th}(T)$ resulting in a shift of Hsieh's rate data by 839 cm^{-1} (296 K). Continuous lines represent rate functions calculated from the optimisation procedure described in section 5.8. Necessary rates of radiative and non-radiative decay (k_f and k_{nr}) are given from naphthalene lifetime and yield data (τ_f and ϕ_f) low-pressure measurements at room-temperature performed at excitation wavelengths ranging from 308 to 200 nm [Hsieh 1974], see symbols in figure 87. In the same figure are also plotted the rate functions of internal conversion (IC) and intersystem crossing (ISC) from Lim's model (cf. cyan lines), which highlight a crossing at about 10000 cm^{-1}, corresponding to the third channel threshold (cf. section 5.5.4). Above this threshold, the non-radiative rate is dominated by IC, whereas below it is dominated by ISC. For excitation in the first excited state, k_{nr} data stay lower than the estimated rate function for ISC.

An exploitable description of the radiative and non-radiative decay rates as function of excess energy for the decay has to be derived to allow their implementation to the cascade model for the fluorescence yield. The "best" fit for the non-radiative decay is found applying an Edgeworth-Cramer series function, such as

$$k_{nr} = y_0 + \frac{A}{w\sqrt{2\pi}}\left\{\exp(-0.5z^2)\left[\begin{array}{l}1+\frac{a_3}{3!}z(z^2-3)+... \\ ...+\frac{a_4}{4!}(z^4-6z^3+3)+\frac{10a_3^2}{6!}(z^6-15z^4+45z^2-15)\end{array}\right]\right\} \quad (5.27)$$

with the substitution $z = (E - x_c)/w$. The radiative rate is approximated as a modified Boltzmann function

$$\log\left(k_f\right) = \alpha_2 + \frac{\alpha_1 - \alpha_2}{\left[1+\exp\left[(E - \alpha_3)/\alpha_4\right]\right]^{\alpha_5}} \quad (5.28)$$

The rate data from Hsieh shown in figure 87 represent only the low-pressure domain. A direct use of Hsieh's data would possibly restrict the application of the fluorescence yield model to this domain. Therefore, an adaptation of the rate data is necessary to extend the fluorescence yield model to higher pressure. This is realised by determination of a unique set of parameters within the expressions of equations (5.27) and (5.28) using the following procedure.

The fluorescence yields obtained for the application of such unique set of parameters are iteratively fitted to experimental yield data recorded in low (torr) and high (atmospheric) pressure range. Note that the fluorescence yield model uses the assumption of bidirectional collisional energy transfer described in the previous section. Low-pressure fluorescence yields are taken from Hsieh's room temperature data recorded in pure naphthalene at different excitation wavelengths. For the atmospheric pressure case, fitting is done to yield data from our measurements in nitrogen within the temperature range of 350 to 900 K.

The "best" fit results from the optimisation procedure are presented in the appendix A-1, cf. table 13 for the parameters used within the above rate functions and table 14 for the parameters describing the collisional energy transfer.

Compared to our experimental naphthalene fluorescence yield with temperature recorded at atmospheric pressure, the simulation of the fluorescence yield generates highly concordant results (cf. bottom diagram in figure 87). Similarly, the simulated fluorescence yield fits also the low-pressure yield data from [Hsieh 1974] (cf. bottom diagram in figure 87).

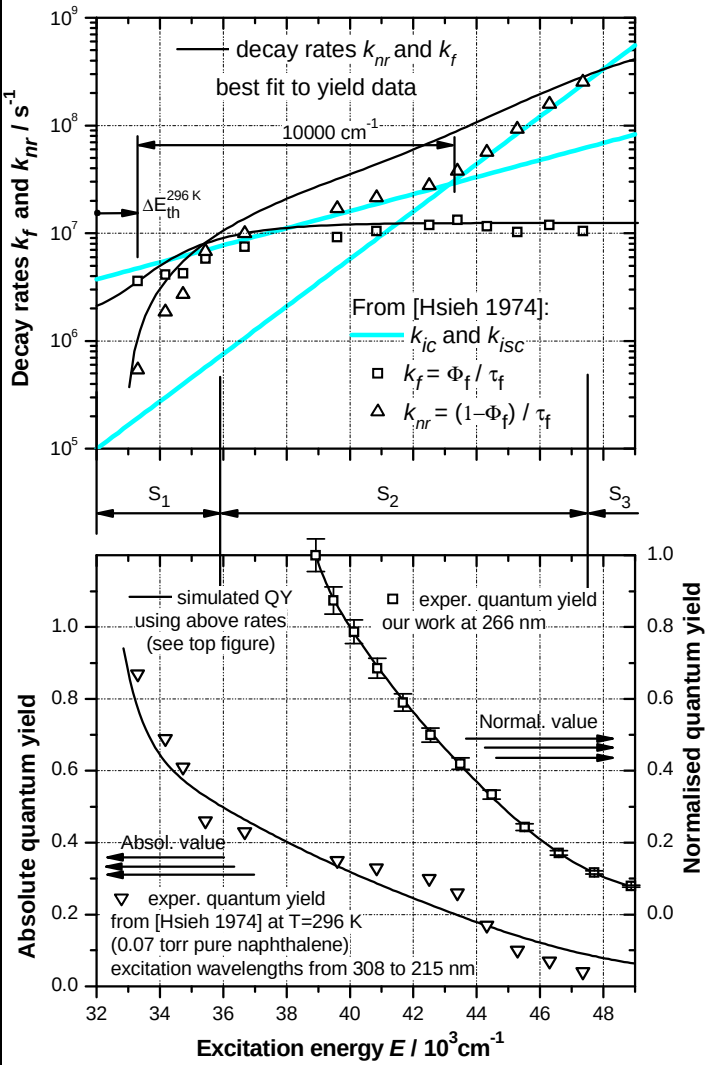

Figure 87: Top diagram: Excitation energy dependence of radiative and non-radiative decay rates for naphthalene. Symbols △ and □ represent k_{nr} and k_f from [Hsieh 1974]. Cyan thick lines are estimated rates of internal conversion and intersystem crossing k_{ic} and k_{isc} with respect to the third channel threshold at 10000 cm^{-1} excess. Line graphs ━ are rates of k_{nr} and k_f, resulting as a "best" fit of our cascade model of vibrational relaxation to the temperature dependence of fluorescence yield measured within this work and absolute yield data from [Hsieh 1974] and [Hall 1976]. Bottom diagram: Comparison of the simulation using the cascade model with the rates from above for k_{nr} and k_f to our yield data for temperatures from 350 to 900 K, normalised at 350 K (symbols □) and to Hsieh's absolute yield data at 296 K in 0.07 torr pure naphthalene for variable excitation wavelengths from 308 to 215 nm (symbols △).

From these results it is noted that the simulation provides accurate fluorescence yields for low (torr) and high (atmospheric) pressures. The resulting rate functions of the radiative and non-radiative decays using the unique set of parameters are shown in the top diagram of figure 87. For the case of the radiative rate, a good agreement to the data of Hsieh is observed. For the case of the non-radiative decay, good agreement to Hsieh's data is also seen for excitation to the first excited state. Towards excitation energies lower than 34000 cm^{-1}, the non-radiative rate exhibits a fast decrease. Negative non-radiative rates arise for energies lower than 32874 cm^{-1}. This non-physical case limits the validity to higher than this value. Fortunately, the thermal energy is readily considered to the excitation energy. Thus, to determine a limiting photon energy, the thermal energy has to be subtracted. At 296 K, the thermal energy, which is equal to 871 cm^{-1}, gives a limiting photon energies of 32003 cm^{-1}, which is very close to the origin of the first excited state (32020 cm^{-1}). The non-radiative rate

is hence valid for equal or higher than room temperature. For higher excitation energy, the non-radiative decay rate deviates from Hsieh's rate data, until coming close again, where the excitation energy corresponds to the origin of the third excited state. The deviation within the second excited state is attributed to the effect of pressure accounted for within our model. Using a non-radiative rate function fitting closely Hsieh's rate data provides a reproduction of their low-pressure yield values, but degrades the agreement between the simulation and the experimental results at atmospheric pressure.

So far, the parameters of the decay rates have been determined by concordance of the modelled fluorescence yield to the experimental data at low (torr) and high (atmospheric) pressure. Additional parameter fitting becomes necessary in order to provide a global solution, which also includes the effect of pressure. A single set will be presented, which allows the yield calculation not only for a change of temperature and excitation wavelength, but further for varying pressure. Therefore, it must be focussed on the transition range between the low-pressure and the Boltzmann limit. In this domain, experimental fluorescence yield data are needed to scale the collisional parameters. The case of collisions with nitrogen has been considered using our fluorescence data recorded between 1 and 30 bar. Methane is also considered due to the available data reported by [Beddard 1973] in the pressure range between 0 and 90 torr and for various excitation wavelengths.

Absolute yield data for the low-pressure and the Boltzmann limit are reported from optic-acoustic measurements in pure naphthalene vapour at 248 nm excitation wavelength [Hall 1976] as 0.35 and 0.79, respectively. We constrain our model to Hall's high-pressure limit, which allows the calculation of absolute fluorescence yields. While the naphthalene model yield is assumed to converge to Hall's Boltzmann limit, we provided it with a free boundary limit towards the low-pressure side. Thus, the optimisation procedure used in our simulation model indirectly determines this limit by fitting the model yield with experimental data within the transition range.

The collisional relaxation of naphthalene is illustrated as a function of pressure for its influence on the simulated fluorescence yield between the low-pressure and the Boltzmann limit and excitation at 248 nm wavelength (cf. figure 88). Three types of collisional interactions are considered: pure naphthalene and naphthalene in methane or nitrogen foreign gases. Further, the effect of napthalene tracer concentration is also examined.

The green, red and black continuous lines in figure 88 represent yield model results for collisions of naphthalene with nitrogen, methane and in naphthalene parent gas, respectively. Essentially, the fluorescence yield describes the conventional shape with pressure, i.e. a constant yield at very low and very high pressure with a transition range in between. For methane and nitrogen, both functions tend to the same low-pressure limit of about 0.21. At first sight, this value seems quite far from Hall's value of 0.35. However, [Beddard 1973] reported a value of 0.17 for nearby excitation at 250 nm, which is close to our result. For the case of

pure naphthalene, the low-pressure limit is determined as 0.27, about in the middle between Hall's value and the limit found for the other colliders. This value corresponds to the absolute yield data reported by [Hsieh 1974] for constant pressure of 0.07 torr (cf. bottom diagram figure 87). The gap between the low-pressure limit for pure naphthalene to the limits for methane and nitrogen are thus ascribed to the error limit of Hsieh's absolute yield values.

Comparison of the transition between the low-pressure and the Boltzmann limit for nitrogen, methane and naphthalene colliders clearly causes a shift in direction of lower pressure. This corresponds to what is expected: the energy transfer per collision is enhanced with growing molecular parameters like size, weight, well depth. Recall that the energy transfer is determined by an expression like $\Delta E_{coll} = \alpha(E - E_{th})$, where the term in brackets represents the excess energy E_{ex}. We can thus compare collisional parameters to literature values. [Kimura 2004] provides with ratios of k_c / Z_{LJ}, where $k_c = k_B T \cdot k_p$ and k_p a deactivation rate of fluorescence for collisions of naphthalene in different foreign gases. This ratio is hence equivalent to our definition of α.

For nitrogen, Kimura obtained an α of 0.0074, which is quite close to our value of 0.01 (cf. appendix table 14). For naphthalene, Kimura reported an α-value of 0.29, where we found a value of 0.20. For methane, Kimura does not provide any data. [Hippler 1983b] reported collisional energy transfer of toluene in a great number of foreign gases including methane. Kimura's α-value change in similar way as Hippler's ΔE-values comparing the same colliders. Observing analogous energy transfer for toluene with methane and CO_2, the α-value of methane is estimated from Kimura's data for carbon dioxide, which is 0.021. In our case, we found a nearby value of 0.03 for methane.

As shown in figure 88, the effect of the tracer concentration on the pressure function of the fluorescence yield function can be quite significant with respect to the foreign gas. 5 % of naphthalene tracer generates a less pronounced shift in methane than in nitrogen. Still at low concentration of 1 % tracer in nitrogen, there is an obvious shift towards lower pressure.

The results previously described for the transition range included the scaling of the collisional energy transfer parameters to methane and nitrogen colliders. For the influence of the excitation energy to the fluorescence yield as a function of foreign gas pressure, it is beneficial to look closer to the results, which we obtain for a simulation of the experimental data reported from [Beddard 1973] for methane collider. This will further allow to see the impact of the application of bidirectional collisional energy transfer within the collisional cascade, as described in the previous section.

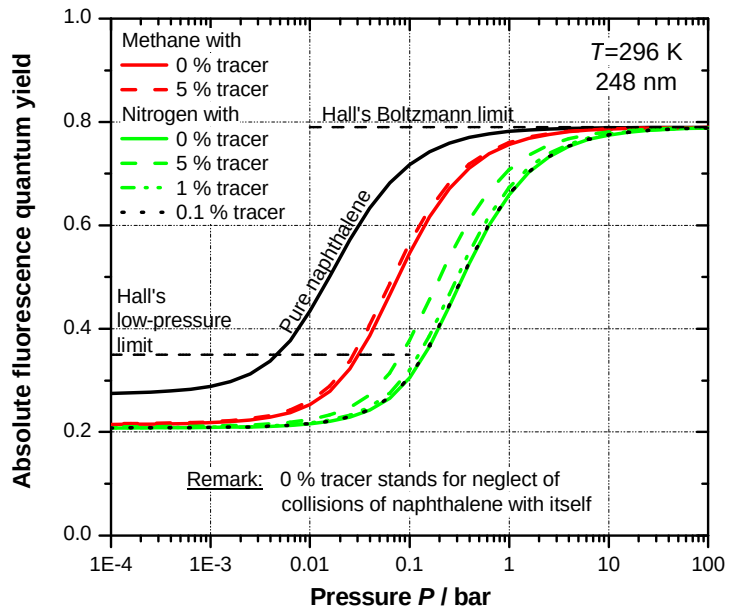

Figure 88: Collisional relaxation of naphthalene as a function of pressure and its influence to the simulated fluorescence yield. The simulated yields are assumed to converge to the Boltzmann limit reported from [Hall 1976].

For nitrogen and methane foreign gas, calibration to pressure dependent data from this work and from [Beddard 1973] leads to the same low-pressure limit for both. This is, however, much lower than predicted by Hall. Refer to the text. The influence of the choice of foreign gas molecule and the concentration of napthalene tracer are illustrated.

Figure 89 depicts our yield simulation compared to results from Beddard between 0 and 90 torr for excitation wavelengths at 250, 260, 270, 280, 290 and 310 nm. The pressure-induced stabilisation effect to the fluorescence yield becomes less important, while the excitation wavelength gets closer to the (0,0) transition. For 310 nm excitation, which is quite close to the (0,0) band at 32020 cm^{-1}, yield weakening is observed for Beddard's data. This is what our previous calculation predicted (cf. table 11 previous section). At 300 K and for excitation below 308.4 nm, the cooling of the nascent vibrational distribution is followed by heating of naphthalene through collisions with the bath gas (cf. the discussion in the previous section). Our yield model with bidirectional collisional energy transfer allows thus to simulate the occurrence of a pressure-induced weakening near to the (0,0) band, although it is observed that the strength of this effect is underestimated.

The naphthalene yield model scaled to the influences of temperature and pressure as described above enables the simulation of the experimental yield data in dependence of nitrogen pressure. The result of this comparison presented earlier in figure 82 section 5.7.2 shows good agreement with respect to the experimental error limits.

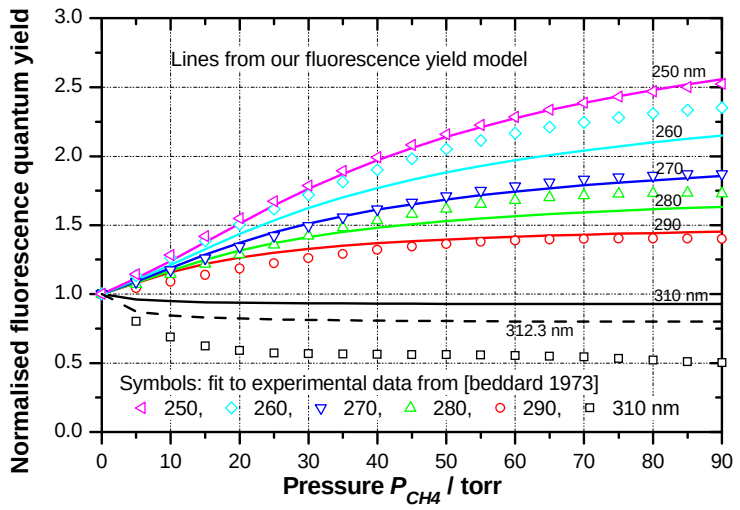

Figure 89: Influence of methane foreign gas pressure to the fluorescence yield of naphthalene at room temperature for various excitation wavelengths. Comparison of our yield simulation to regressions of experimental data from [Beddard 1973]. Yield stabilisation is observed to decrease in strength, when the (0,0) transition is approached. At 310 nm, weakening occurs.

(c) Toluene

The development of a fluorescence yield model for toluene follows to a large extent a similar approach as for the case of naphthalene. A main difference for the toluene case is that the yield model follows the assumption of unidirectional collisional energy transfer (cf. section 5.8.1(a)).

From a combination of low-pressure yield data from [Burton 1968] and low-pressure lifetime measurements from [Jacon 1977], rates of radiative and non-radiative decays are deduced. These rates are depicted as a function of excitation energy for energies up to about 41000 cm^{-1} in the top diagram figure 90. The same as for naphthalene, the thermal energy of the ground state room temperature population is considered to the excess energy as $\hbar / \lambda_{exc} + E_{th}(T)$ resulting in a shift of the rate data deduced from Burton and Jacon by 559 cm^{-1} (296 K). Also in figure 90 are plotted two exponential regression functions to the non-radiative rate data deduced from Burton and Jacon (cf. cyan lines). In analogy to Lim's model for naphthalene (cf. section 5.5.4), these might represent internal conversion (IC) and intersystem crossing (ISC) rates. A crossing is observed at about 2150 cm^{-1}, corresponding to the "third channel" threshold reported by [Jacon 1977]. At vibrational energies below this threshold, it is intersystem crossing, beyond this threshold, it is internal conversion, which dominates the non-radiative deactivation.

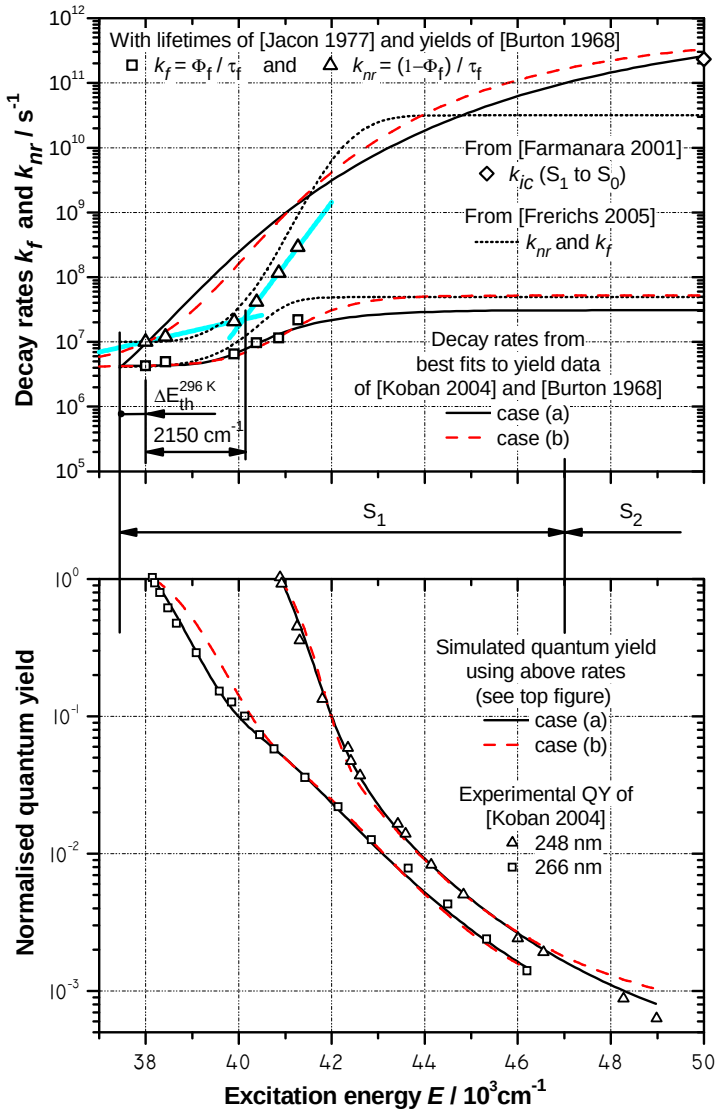

Figure 90: Top diagram: Excitation energy dependence of radiative and non-radiative decay rates for toluene. Symbols △ and □ represent k_{nr} and k_f combining lifetimes from [Jacon 1977] and quantum yields from [Burton 1968]. Cyan thick lines are estimated rates of internal conversion and intersystem crossing k_{ic} and k_{isc} with respect to the third channel threshold at 2150 cm^{-1} excess energy. Symbol ◇ is k_{ic} from S_1 for vibrational excess of 12000 cm^{-1} from [Farmanara 2001]. Dotted black lines levelling off for high excess are estimations for k_{nr} and k_f from [Frerichs 2005]. Lines ━ and ╍ are two cases (a) and (b) of k_{nr} and k_f, resulting as a "best" fit of our cascade model of vibrational relaxation to the temperature dependence of fluorescence yield measured by [Koban 2004] and yield data from [Burton 1968]. Bottom diagram: Comparison of simulation using the cascade model with both rates cases (a) and (b) for k_{nr} and k_f to Koban's yield data normalised at 300 K.

The rate data deduced from Burton and Jacon covers only excitation energies below 41000 cm^{-1}. This corresponds to a toluene temperature of 600 K or to only room temperature when excited at 266 nm or at 248 nm, respectively. The consideration of higher temperatures in the toluene yield model necessitates rate data at higher vibrational energies. These can be derived from a smooth function for the total decay rate of toluene reported by [Lenzer 2000], levelling off at high energy towards a constant value. Fitting of Lenzer's total decay rate to Burton's quantum yield data enables the estimation of the radiative (fluorescence) rate [Frerichs 2005]. Combining of Lenzer's and Frerichs' data yields the non-radiative rate ($k_{nr} = k_{tot} - k_f$). The rates of radiative and non-radiative decay are then shown as black

dotted lines in the top diagram of figure 90. Frerichs further assumes that the rate of total decay should rather converge to a higher value, reported by [Farmanara 2001] as internal conversion rate measured in highly excited toluene and so far unconsidered in Frerichs' total decay rate function. Farmanara's value for τ_{IC} of 4.3 picoseconds corresponds to the rate $k_{ic} = 1/\tau_{ic}$ depicted as the diamond symbol at an excess energy of 12000 cm^{-1} in figure 90.

Based on the available rate data, an optimisation procedure as described in section 5.8 is used to calculate the rate functions of the radiative and non-radiative decays used within the model (cf. continuous and broken lines in the top diagram of figure 90). Firstly, the rate functions are written as a function of excitation energy similar to the case of the naphthalene model. A form similar to the rate functions reported from Lenzer and Frerichs is chosen. The decay rates are approximated by modified Boltzmann functions such as

$$\log(k) = \alpha_2 + \frac{\alpha_1 - \alpha_2}{\left[1 + \exp\left[(E - \alpha_3)/\alpha_4\right]\right]^{\alpha_5}} \tag{5.29}$$

The rate data deduced from Burton and Jacon for toluene shown in figure 90 represent only the low-pressure domain. In order to avoid a restriction to an application of the fluorescence yield model to the low-pressure domain, the rate data has to be adapted. The determination of a unique set of parameters within the expressions of equations (5.29) allows for an extension of the fluorescence yield model to higher pressure. The procedure is analogue to that described for the naphthalene model.

The fluorescence yields obtained for the application of such unique set of parameters are iteratively fitted to experimental yield data recorded in low (torr) and high (atmospheric) pressure range. Note that the fluorescence yield model restricts to the assumption of unidirectional collisional energy transfer. Low-pressure fluorescence yields are taken from Burton's data recorded in pure toluene. Excitation energy is changed either for different constant excitation wavelengths by variation of the temperature or for room temperature and variable excitation wavelength (cf. figure 91). For the atmospheric pressure case, fitting is done to yield data from [Koban 2004] measured for atmospheric pressure as a function of temperature in pure nitrogen at 248 and 266 nm excitation (cf. bottom diagram in figure 90). Our yield data from figure 65 could have been used instead, but we preferred Koban's somewhat more complete set, since it was provided for both 248 and 266 nm excitation wavelengths.

The "best" fits resulting from the optimisation procedure are presented in the appendix A-1, cf. table 15 for the coefficients α_i used within the parameterised rate functions and table 16 for the parameters describing the collisional energy transfer. Two different solutions are proposed. Case (a) produces a better agreement to the experimental yield data when the excitation energy varies with temperature, whereas case (b) agrees better when excitation energy changes with excitation wavelength.

For the high pressure case, the simulation using the rate cases (a) and (b) produces highly concordant results compared to Koban's yield data (cf. line graphs ━ and ╍ in the bottom diagram of figure 90). As observed, the case (a) produces the higher accuracy solution when the energy is varied via the choice of the temperature condition. The comparison of the model result with the low-pressure yield data from Burton in absolute value is shown in figure 91. The yields depending on temperature at different excitation wavelengths are shown in the top diagram, whereas the room temperature yields depending on excitation wavelength are displayed in the bottom diagram. The solution case (a) corresponds better to the yield data when the energy is varied via the temperature. By contrast, the solution case (b) fits better the yield data when the energy changes with the excitation wavelength.

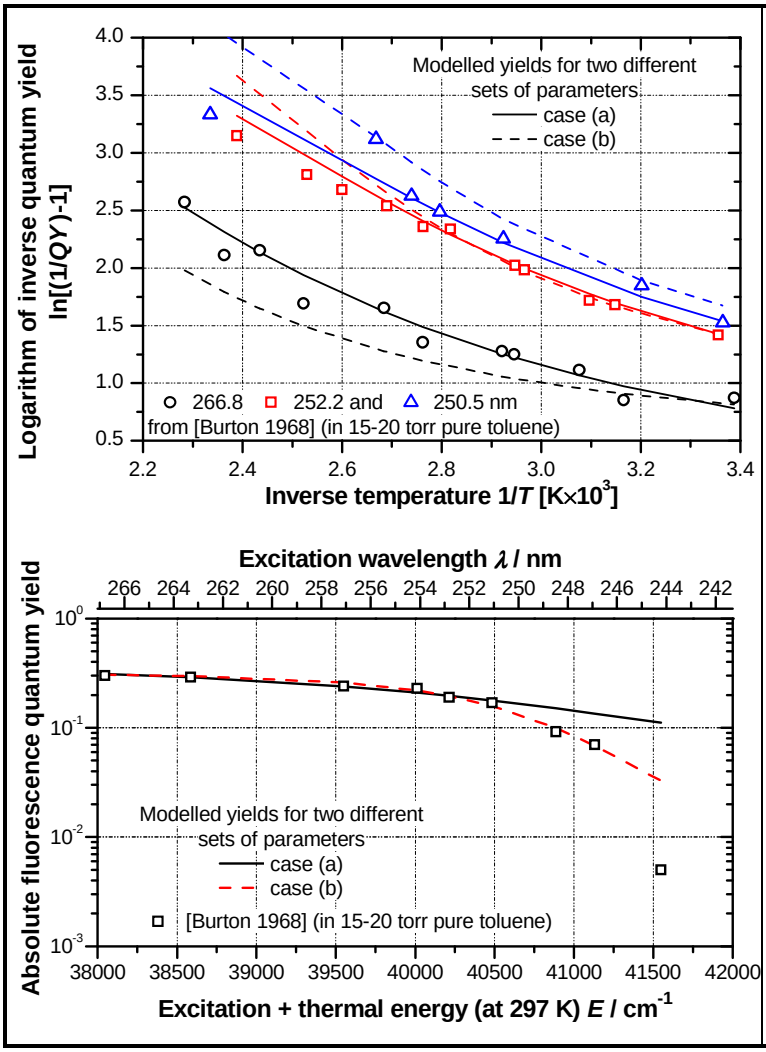

Figure 91: Comparison of toluene yield model results to absolute fluorescence quantum yield data (symbols) from [Burton 1968] measured in pure toluene (approx. 15 to 20 torr). Continuous and broken lines correspond to simulation results obtained from our cascade model of vibrational relaxation using the two rate cases (a) and (b) with the parameter sets presented in table 15 in appendix A-1. The parameters chosen for the collisional energy transfer are given in table 16. Top diagram: temperature dependence of fluorescence quantum yield for different excitation wavelengths 266.8, 252.2 and 250.5 nm. Bottom diagram: dependence from excitation wavelength at 297 K.

The resulting rate functions for k_{nr} and k_f deduced as unique sets of parameters for case (a) and case (b) are depicted in the top diagram of figure 90 (continuous and broken lines). The rates are normalised to the low-pressure rates deduced from Burton and Jacon at

266.8 nm (nearest to the (0,0) band). The two cases (a) and (b) represent quite similar solutions. At low excitation energies, the resulting non-radiative rates show a gap to the low-pressure rate deduced from Burton and Jacon. This might be attributed to differences in temperature and pressure conditions between the experimental yield data from Burton and Koban. Both resulting cases for the fluorescence rate fit well the rate data deduced from Burton and Jacon. At higher excitation energy, case (b) is somewhat closer to the fluorescence rate proposed by Frerichs. Calculation of the fluorescence yield from the rates initially proposed by [Frerichs 2005] for energies higher than 43000 cm^{-1} leads to a small constant yield value (about 0.002). This would be however contradictory to what can be observed in the bottom diagram of figure 90, where the yields for both excitation wavelengths exhibit a continuous decrease with excitation energy far beyond 43000 cm^{-1}. Assuming the fluorescence rate to level off at a constant value, the non-radiative rate then has to be an increasing function of excitation energy up to these high amounts of excess energy. This is the reason why we have chosen to let converge the non-radiative rate to the internal conversion rate reported from Farmanara. Note that this procedure corresponds to the suggestion emitted in [Frerichs 2005].

The validation of the toluene yield model developed here is restricted to the pressure domain between the low-pressure and the atmospheric pressure cases. In contrast to the naphthalene yield model, no pressure dependent yield data was accessible for higher than atmospheric pressures. Our own yield measurements in dependence of the nitrogen pressure with excitation at 266 nm wavelength could have been used. However, the proximity of the excitation to the (0,0) band of the toluene molecule prevents any accurate simulation result, because of probable cooling of the nascent population followed by heating through collisions with the bath gas (cf. the discussion on naphthalene). The inclusion of this effect would necessitate additional pressure dependent series with yield data measured at an excitation wavelength far from the (0,0) band.

5.8.2 Oxygen quenching

Compared to ketones species, aromatics behave very different with respect to collisional fluorescence quenching by triplet oxygen (cf. section 2.12.5). As introduced at the top of this modelling section, the simulation of the oxygen effect to the yield of the aromatic species will be now included by distinction between efficient and non-efficient collisional events.

(a) Adaptation of the population transfer from higher levels

Within the ketone yield model, the product term $\prod_j^{i-1} k_{coll}/(k_f + k_{coll} + \tilde{k}_{O_2} n_{O_2} + k_{NR,j})$ in equation (5.10) describes the probability of population transfer to a specific level i from all

higher levels j in the vibrational cascade. An adaptation to the yield model of strongly quenched aromatics needs to include the effect caused by the $\langle 1-P\rangle$ part of inefficient aromatic-oxygen collisions, which might instead lead to intramolecular events like vibrational relaxation. A new expression for the probability of population transfer accounts now for the inefficient part of collisions

$$\prod_{j}^{i-1}\left(k_{N_2}^{VR}+k_{O_2,j}^{VR}\right)\ /\ \left(k_{f,j}+k_{NR,j}+k_{N_2}^{VR}+k_{O_2,j}^{VR}+k_{O_2,j}^{quench}\right). \tag{5.30}$$

With the definition for the fluorescence efficiency the balance for the fluorescence quantum yield of a specific cascade step i is now defined as

$$\phi_{f,i}^{q}=\underbrace{\frac{k_{f,i}}{k_{f,i}+k_{NR,i}+k_{N_2}^{VR}+k_{O_2,i}^{VR}+k_{O_2,i}^{quench}}}_{\text{fluorescence efficiency from i}}\cdot\underbrace{\prod_{j=1}^{i-1}\frac{k_{N_2}^{VR}+k_{O_2,j}^{VR}}{k_{f,j}+k_{NR,j}+k_{N_2}^{VR}+k_{O_2,j}^{VR}+k_{O_2,j}^{quench}}}_{\substack{\text{population efficiency}\\ \text{from upper cascade steps}}} \tag{5.31}$$

(b) Rates of oxygen collisions leading to VR and quenching

Generally, the oxygen quenching rate from the relation $k_{O_2}^{quench}=\langle P\rangle Z_{O_2}n_{O_2}$ can be derived from the quenching efficiency $\langle P\rangle$, assumed to be a function of excess energy. The part of efficient quenching collisions is however not known by default. Rather, this information is obtained from experiments studying the quenching effect and reporting it as Stern-Volmer relation. The quenching rate is then defined as $k_{O_2}^{quench}=k_{SV}k_{tot}n_{O_2}$, where the Stern-Volmer factor k_{SV} is $S_0/S-1=k_{SV}[O_2]$. Results for the Stern-Volmer relation of toluene and naphthalene were presented earlier (figure 70 section 5.6.3 and figure 84 in section 5.7.3). The inefficient part of quenching collisions leading to intramolecular events like vibrational relaxation is easily derived from $k_{O_2}^{VR}=\langle 1-P\rangle Z_{O_2}n_{O_2}$. Finally, the total decay rate k_{tot} needed in $k_{O_2}^{quench}=k_{SV}k_{tot}n_{O_2}$ is calculated from the sum of non-radiative deactivation rate k_{nr} and fluorescence rate k_f. The decay rates are obtained from the results of the decay rate functions applied to the yield model, cf. equations (5.27) and (5.28) for naphthalene and equation (5.29) for toluene.

(c) Evolution of Stern-Volmer factor with temperature

The population efficiency from upper cascade steps described above contains the Stern-Volmer factor via $k_{O_2,j}^{quench}=k_{SV,j}k_{tot,j}n_{O_2}$ and $k_{O_2,j}^{VR}=\left(1-k_{SV,j}k_{tot,j}\right)n_{O_2}$. However, the exploitation of the Stern-Volmer plot only provides a k_{SV}-factor, which is a temporally integrated

value from $k_{SV,j}$ over the whole cascading process. k_{SV} is thus not always an adapted form for application to our yield calculation.

For the implementation of the oxygen quenching to the naphthalene yield model, the introduction of a correction factor is needed, which accounts for the actual change of the $k_{SV,j}$ factor over the cascade levels. This can be derived from a comparison of our experimental Stern-Volmer data with yield values modelled under identical conditions. Therefore, a parameterised correction function has been implemented to the model, which allows different types of mathematical corrections. The optimal fit to our measurement data is then obtained when k_{SV} is corrected by a factor γ, which depends on the oxygen molar fraction such that the initial Stern-Volmer temperature regression from equation (5.24) becomes

$$\hat{k}_{SV}(T,\chi_{O_2}) = k_{SV}(T)\cdot\gamma\left(\chi_{O_2}\right) = \left\{30.16 + 4382\cdot\exp(-T/180.5)\right\}\cdot\gamma\left(\chi_{O_2}\right) \quad [\text{bar}^{-1}] \qquad (5.32)$$

The resulting expression for $\gamma\left(\chi_{O_2}\right)$ is an exponential function such like

$$\gamma\left(\chi_{O_2}\right) = \left[\gamma_1 + \gamma_2\exp(-\frac{\chi_{O_2}}{\gamma_3})\right] \quad \leftrightarrow \quad \chi_{O_2} = \frac{n_{O_2}}{Lo}\frac{TP_0}{T_0P} \qquad (5.33)$$

$$\Rightarrow \gamma_1 = 0.632 \quad \gamma_2 = 0.2639 \quad \gamma_3 = 0.01678$$

A comparison between the experimental Stern-Volmer data and the yield model accounting for the correction $\hat{k}_{SV}(T,\chi_{O_2})$ is shown in figure 92.

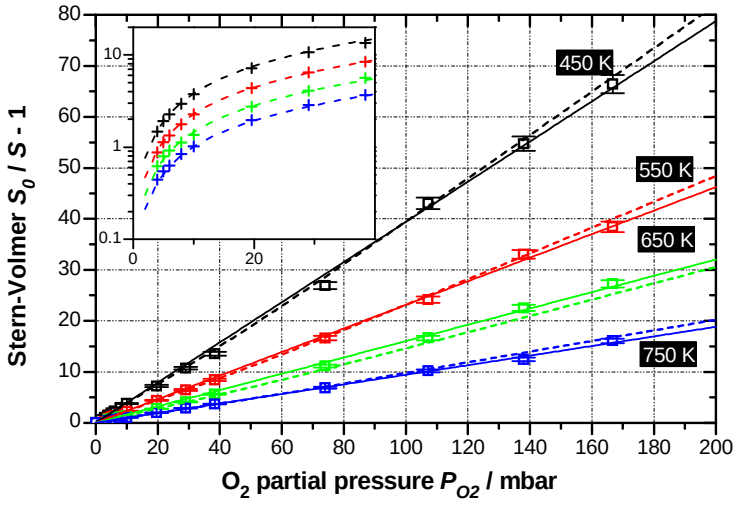

Figure 92: Naphthalene Stern-Volmer plot after 266 nm laser excitation as a function of temperature derived from integrated fluorescence spectra (310 to 420 nm). Continuous lines are zero-point linear regressions; dashed lines are calculated from our own yield model.

In contrast to the findings for naphthalene, oxygen quenching is successfully implemented to the toluene yield model without the need of a correction factor accounting for the actual change of the $k_{SV,j}$ factor over the cascade levels. A comparison between the experi-

mental Stern-Volmer data and the yield model accounting for the uncorrected $k_{SV}(T)$ from equation (5.21) in section 5.6.3 is shown in figure 93.

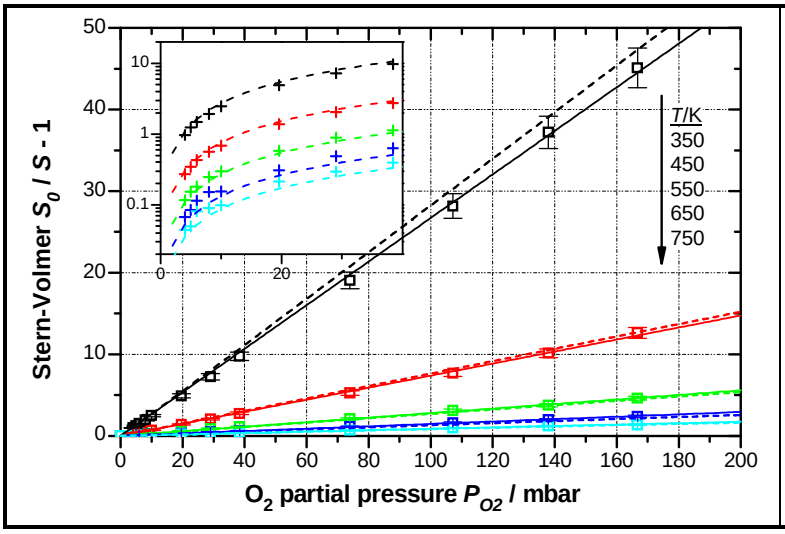

Figure 93: Toluene Stern-Volmer plot after 266 nm laser excitation as a function of temperature derived from integrated fluorescence spectra (270 to 340 nm). Continuous lines are zero-point linear regressions; dashed lines are calculated from our own yield model.

When accounting for the oxygen quenching in both yield models, the collisional energy transfer parameters for naphthalene and toluene have to be determined. This was part of the respective optimisation procedures. The energy transferred per collision with oxygen $\Delta E_{coll} = \alpha_{O_2}(E - E_{th}) \cdot (T/300)^{\beta_{O_2}}$, T in K is then defined by the parameters $\alpha_{O_2} = 0.0488$ and $\beta_{O_2} = 1.86$ for collisions between naphthalene and oxygen or by the parameters $\alpha_{O_2} = 0.473$ and $\beta_{O_2} = 2.49$ for collisions between toluene and oxygen. The energy transfer per collision with oxygen has to be weighted with other types of collisions based on the collisional rates and the frequencies described in tables 14 and 16 of appendices A-1 and A-2. The Lennard-Jones parameters for oxygen are reported in [Reid 1977] as $\sigma_{O_2} = 3.467$ Å and $\epsilon_{O_2}/k_B = 106.7\,\mathrm{K}$ for the collisional diameter and the well depth, respectively.

5.8.3 Application of the naphthalene yield model

So far, we presented simulation results for intramolecular deactivation in section 5.8.1. Now, intermolecular deactivation by means of oxygen quenching will be included to the model as discussed in section 5.8.2.

For the combined influence of temperature and oxygen concentration to the naphthalene fluorescence at atmospheric pressure, our experimental data presented in section 5.7 is compared in relative value to simulated yields, cf. figure 94 (normalised to 350 K). It is reminded, that the absorption cross-section of naphthalene was in good approximation to a constant value over the temperature range from 350 to 900 K, cf. section 5.7.1(a).

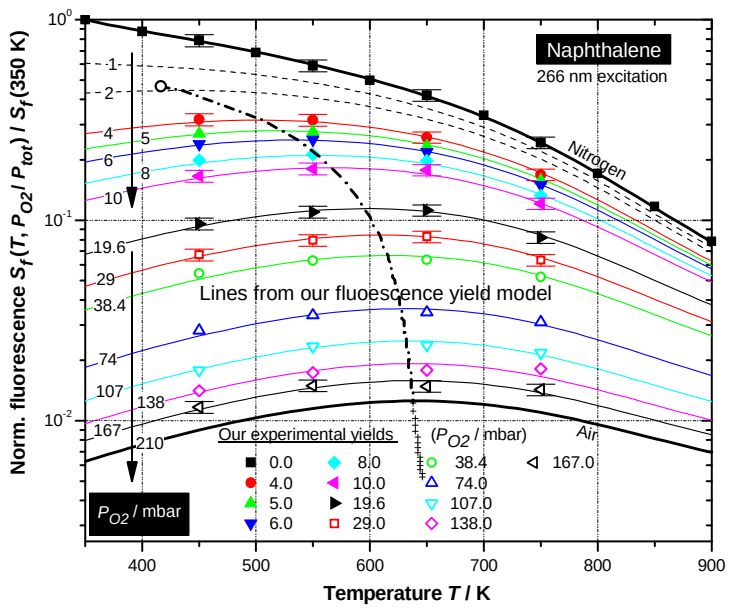

Figure 94: Combined temperature and oxygen influence to naphthalene fluorescence excited at 266 nm at 1 bar total pressure. Normalised to 350 K. Lines are from our own yield model with oxygen partial pressures from pure nitrogen to air.. Symbols are our experimental data. The dash-dotted line shows the temperature of the maximum yield as a function of oxygen concentration.

The overall high concordance between experimental data and simulation demonstrates the capabilities of our yield model to predict naphthalene fluorescence in a large range of thermodynamic conditions. The thick black lines mark the conditions of pure nitrogen and air, respectively. The same as for toluene, the fluorescence intensity passes by a maximum, which moves with increasing oxygen concentration towards higher temperatures, cf. the dash-dotted black line crossing the oxygen isobars. This signifies a competition between the temperature sensitivity of intramolecular and intermolecular deactivation. Increasing oxygen to concentration higher than in air, the temperature, at which the maximum fluorescence is reached, levels off towards about 650 K, cf. the plus symbols.

Similar as presented in [Thurber 1999a] for acetone, the naphthalene model enables to predict the yield behaviour with pressure. We show this for nitrogen foreign gas for two temperature levels, cf. the top and the bottom diagram in figure 95, for 450 and 700 K, respectively. Since we know the Stern-Volmer behaviour at 266 nm, oxygen quenching can also be included at this wavelength. The yield curves at other wavelengths depicted in the figure correspond to pure nitrogen. The relaxation of naphthalene in parent gas is neglected.

The yield values in figure 95 are absolute with respect to the reliability of the high pressure limit reported from [Hall 1976]. The use of a different limit would have lead to shifted values. It is reminded, that the absolute naphthalene yield was forced to converge to Hall's high-pressure limit of 0.79 reported for 296 K from optic-acoustic measurements at 248 nm excitation. In the transition range, the model yield is fitted in relative value to our experiments at 266 nm excitation with nitrogen foreign gas pressures between 1 and 30 bar at 450 and 700 K.

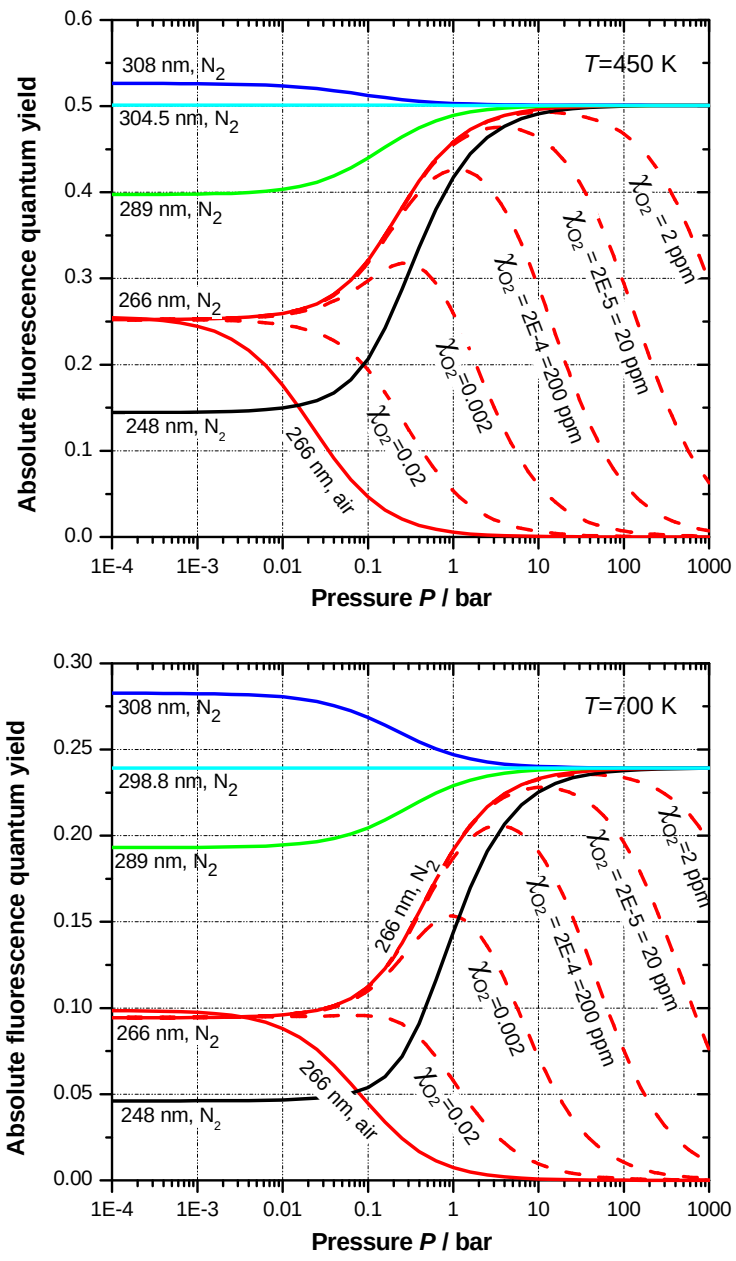

Figure 95: Naphthalene model prediction for the yield at 266 nm excitation with nitrogen pressure at 450 K and 700 K, see the top and the bottom diagrams.

These yield values are absolute with respect to the reliability of the high-pressure limit for the fully relaxed naphthalene reported by [Hall 1976]. Naphthalene collisions in parent gas were neglected for this diagram.

The influence of oxygen quenching leads to quite similar yield curves at both temperature levels, showing the higher quenching efficiency at the lower temperature.

The change of the yield in pure nitrogen with the wavelength of excitation evidences the stabilisation effect far from the (0,0) transition, which diminishes and finally switches to a yield weakening, getting close to the state origin. The wavelength, for which pressure does not affect the yield, corresponds to the values calculated in the last column of table 11 in section 5.8.1(b).

Increasing temperature has obviously a diminishing effect to the yield in pure nitrogen and mixtures of nitrogen and oxygen. The influence of oxygen quenching leads to comparable yield behaviour for both temperatures, with somewhat higher quenching efficiency at the lower temperature. It is interesting to note that for lower oxygen mole fractions, the intramolecular effect of pressure-induced stabilisation is in competition with the intermolecular quenching effect. For example, at 700 K and for an oxygen mole fraction of 2 per mil, the yield passes through a maximum, which is localised at about 1 bar pressure. For mole fractions at the percent level, oxygen quenching then clearly dominates.

The fluorescence yield is subject to the collisional relaxation in nitrogen foreign gas, and therefore strongly dependent on the excitation energy with respect to the (0,0) transition. A yield stabilisation effect is observed to enhance with growing photonic excess. Just where the photonic excess equals the gap between the thermal energy of the excited state and the ground state, the pressure does not affect the fluorescence yield. This corresponds to the wavelengths calculated in table 11 in section 5.8.1(b). To the red side from this, yield weakening occurs.

To a large part, the pressure range in the diagrams of figure 95 is larger than encountered in combustion systems. We will therefore concentrate on simulation results for a more relevant pressure range from 0.1 to 45 bar, cf. figure 96. The coloured line graphs represent different temperature levels of 300, 450, 700 and 850 K. The diagram presented above in figure 94 inserts as vertical plane at atmospheric pressure perpendicularly to the paper plane.

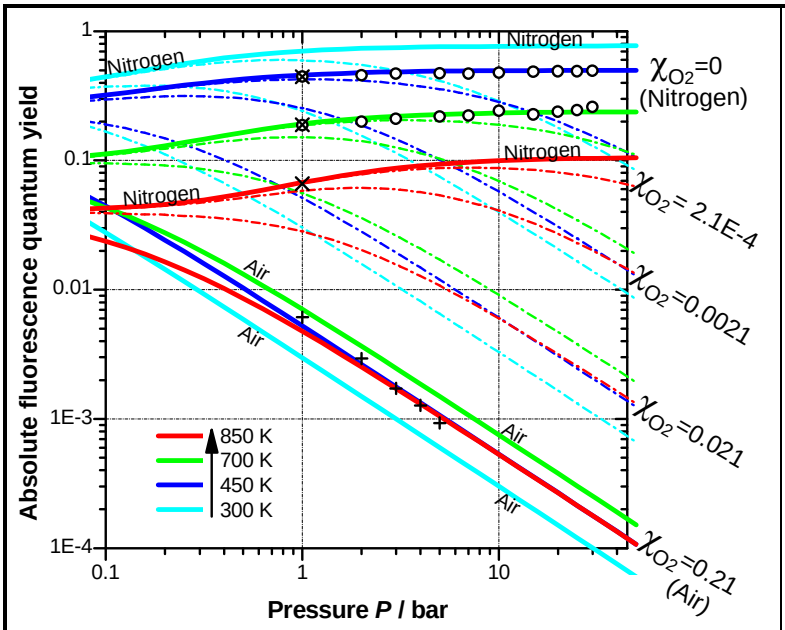

Figure 96: Naphthalene model prediction for the yield at 266 nm excitation with total pressure at 300, 450, 700 and 850 K. The bath gas is completed with N_2 to a molar fraction of 100 % from a given molar fraction of oxygen.

The symbols represent data from our measurement in relative value scaled to the absolute yield ordinate.

There are several insightful observations to be made from the diagram in figure 96. As expected, for pure nitrogen atmosphere, an increase in pressure involves a yield stabilisation effect, which is increasingly pronounced towards higher temperature. The partial pressure of oxygen can be increased by two different means: either at isobaric total pressure by an increase of the oxygen molar fraction or at constant oxygen molar fraction by an increase of the total pressure. For oxygen partial pressure below 0.2 bar, a competition between the intramolecular stabilisation effect and the intermolecular quenching is observed. For a further increase of the oxygen partial pressure, the decreasing effect to the yield becomes more and more the same, whether the oxygen partial pressure was increased by oxygen molar fraction or by total pressure. For high oxygen partial pressures, a tenfold increase in total pressure leads close to tenfold decrease of the fluorescence yield. Thus, we find here the power-law,

which is inscribed to the Stern-Volmer relation of oxygen quenching. Simply expressed, the yield decreases with $1 / P_{O_2}$.

For oxygen molar fractions close to air, the quenching is the dominating path of deactivation. Eventually, this enables a simplified method of fluorescence yield estimation, doing extrapolation of the Stern-Volmer relation to higher air pressure. This is what [Koban 2005a] did, when they applied their semi-empirical toluene yield model. The possible effect of stabilisation or weakening to the yield through collisional energy transfer between tracer and nitrogen is neglected therein.

The error induced when accounting only for the part of oxygen partial pressure (neglecting collisions of naphthalene with nitrogen) can be studied by means of our yield model, setting the proportionality parameter α_{Naph} for the average energy transferred per collision between naphthalene and nitrogen to zero.

The result is shown in figure 97. We have chosen the same temperature levels and three oxygen molar fractions of 0.15, 0.20 and 0.25. With exception of 850 K, the error stays within a band of about 5 %.

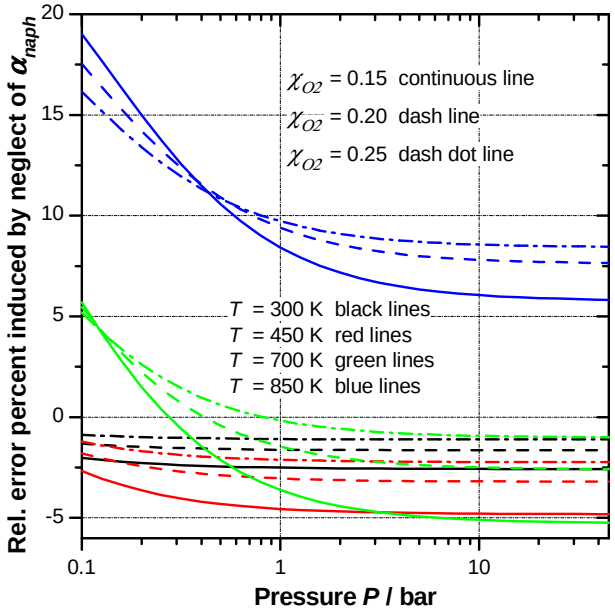

Figure 97: Naphthalene model prediction for the yield error, which is made, when the stabilisation effect through collisions of naphthalene in nitrogen is neglected by setting α_{Naph} to zero. 266 nm excitation and different temperature levels of 300, 450, 700 and 850 K. The error is calculated as

$$\left(\phi_{\alpha_{Naph}} - \phi_{\alpha_{Naph}=0}\right) / \phi_{\alpha_{Naph}}$$

5.8.4 Application of the toluene yield model

Based on the decay rates proposed as case (a) in section 5.8.1(c), the toluene fluorescence yield model is used to predict the absolute fluorescence yields of toluene in an atmospheric pressure of nitrogen. The toluene molar fraction in the vapour phase is fixed to 2 %, which corresponds to 20 mbar of toluene in the toluene/nitrogen mixture at atmospheric pressure.

The yield calculation is done for temperature ranging from 300 to 900 K and excitation wavelengths from 266 to 242 nm (cf. top diagram of figure 98).

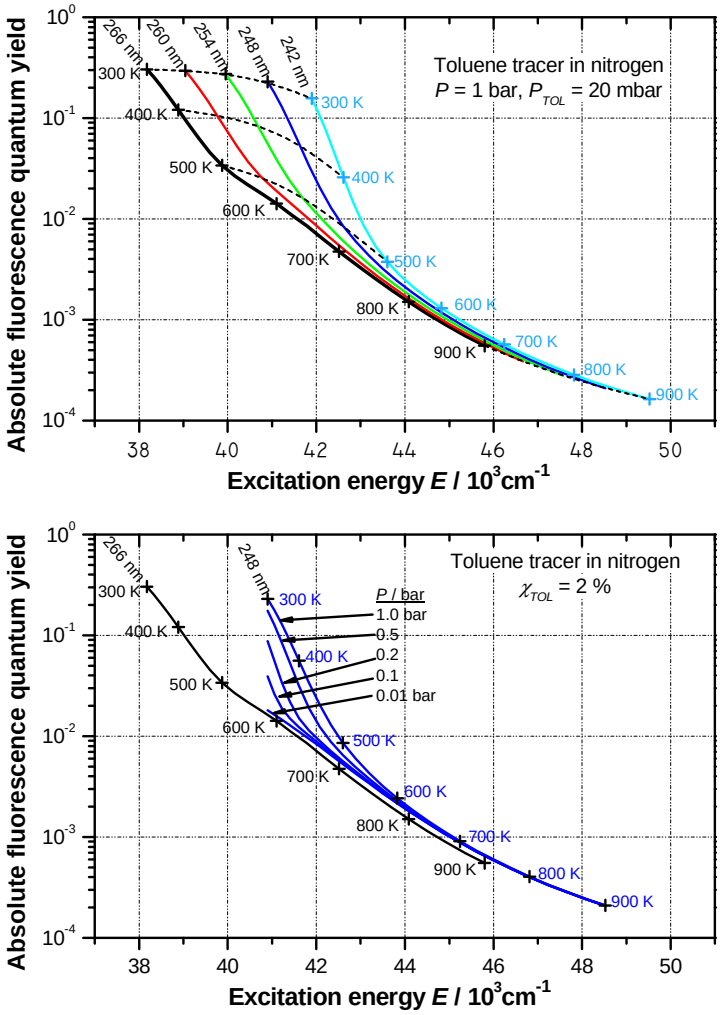

Figure 98: Fluorescence yield simulation from the model adapted to toluene using rates of case (a), cf. text. Top diagram: temperatures varying between 300 and 900 K for different excitation wavelengths between 266 and 242 nm in atmospheric pressure nitrogen. Toluene partial pressure is 20 mbar (2 %). Bottom figure: effect of pressure variation on the yield curves for nitrogen pressure between 10 mbar and 1 bar at 248 nm excitation. The toluene concentration is always 2 % for all pressures. At 266 nm excitation, the same pressure variation produces yield curves, which are practically identical to the atmospheric pressure curve. Though, we know from our experiments, that at this wavelength, yield weakening occurs with increasing pressure. The model is not capable of considering this effect.

For a low excess energy, the excitation energy dependence of the fluorescence yield is obviously split to a thermal and a photon energy effect. If the excitation energy is purely thermally increased, a much stronger yield loss is observed than for an increase in photon energy of the same amount. However, with increasing excess, the photon energy becomes evidently more influential to the yield loss. This is deduced from the fact that, with rising excitation energy, the simulated yield curves for various photon energies converge towards a single trace curve. At high excess energy, an increase of the same amount of thermal or photon energy has a similar effect with respect to the yield loss.

The different influence of thermal and photon energy to the fluorescence yield is related to the pressure-induced stabilisation. For 248 nm excitation wavelength, the theoretical fluorescence yield reveals a decrease with pressure as shown from 1 bar to 10 mbar in the bottom diagram of figure 98. Obviously, with decreasing pressure, the fluorescence yield curves pro-

gressively tends to the trace of the yield curve for 266 nm excitation. The same would be for the other wavelengths shown in the top diagram.

For 266 nm excitation, the fluorescence yield calculated by the model is practically not altered by pressure, whereas our experiments showed a pressure-induced yield reduction. Recall that for excitation of toluene in direct vicinity of the (0,0) band, the model is unable to reproduce the experimentally observed photo-induced cooling and subsequent heating through collisions with the bath gas due to restriction to an unidirectional collisional energy transfer.

Apart from the simulation results presented for the case of solely intramolecular deactivation, the toluene model is also capable of predicting the fluorescence yield when intermolecular deactivation by means of oxygen quenching is considered (cf. section 5.8.2). The combined influence of temperature and oxygen concentration to the toluene fluorescence at atmospheric pressure is depicted in figure 99.

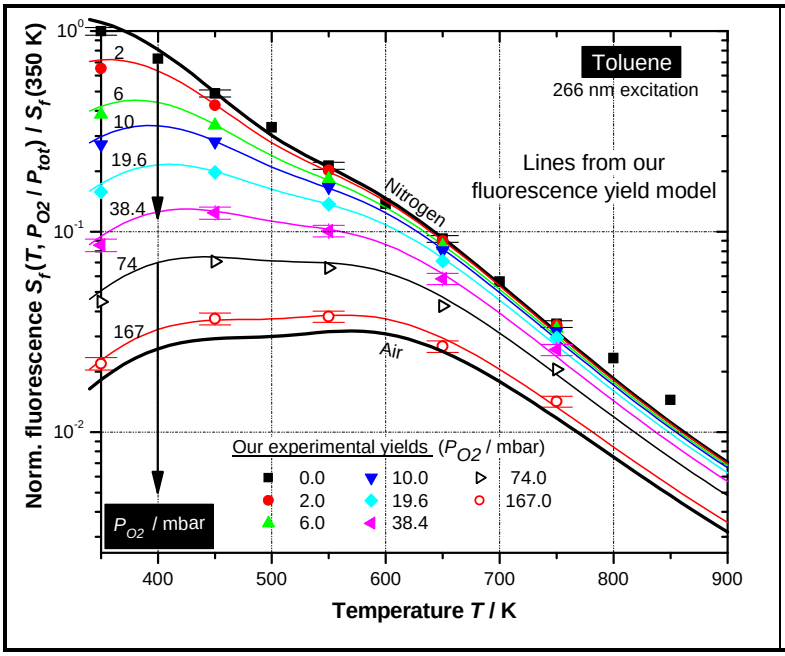

Figure 99: Combined temperature and oxygen influence to toluene fluorescence excited at 266 nm at 1 bar total pressure. Lines are simulated results from our toluene model (the product of modelled yields and the temperature evolution of the absorption cross-section reported in [Koban 2004]). Symbols are our experimental data normalised to 350 K in N_2.

The symbols correspond to our experimental data presented in section 5.6. These are compared in relative value to a simulation from our toluene yield model. The fluorescence intensity is obtained as the product of the simulated yield and the absorption cross-section reported in [Koban 2004]. The experimental fluorescence data is normalised to 350 K in pure nitrogen, while the simulation results are scaled to the experimental data at 450 K in pure nitrogen. The agreement between the experimental data and the simulated results is overall good, except for pure nitrogen at high temperature. Actually, this is where our experimental yield data in pure nitrogen differed most from the yield data reported from [Koban 2004] (cf. figure 65 section 5.6.1(b)). Recall that Koban's data have been used within the parameter optimisation of our toluene yield model (cf. section 5.8.1(c)), since their yields

are provided for two excitation wavelengths, allowing thus to cover a larger domain of excitation energy. Instead, we could have restricted to our own yield data measured at 266 nm. Probably the concordance between the experimental results and the simulation would be enhanced, especially in the high temperature domain, in which the differences between our and Koban's data were observed.

Chapter 6 Spectroscopic fluorescence of kerosene fuel

This chapter is devoted to the characterisation of kerosene fuel (Jet A1) fluorescence properties with temperature, pressure and oxygen concentration in non-quenching and quenching environments. Basically, the kerosene constituents excitable in the middle UV and contributing to the kerosene fluorescence are found among aromatic species. [Baranger 2005] demonstrates that kerosene fluorescence is caused by the fluorescence of mono- and di-aromatics (cf. section 4.8.1). The discussion of the fluorescence behaviour of aromatics presented in the previous chapter will facilitate the interpretation of the kerosene fluorescence measurements reported in the present chapter.

6.1 "Optical fuel" for spectral representation of kerosene fluorescence

As observed in figure 100, the fluorescence spectrum of kerosene is composed of two main spectral bands: a high-frequency band (260 to 310 nm) and a low-frequency band (310 to 420 nm). Furthermore, the dependences of these fluorescence bands with temperature, pressure and oxygen concentration display strong similarities with those revealed for mono- and bicyclic aromatics, respectively.

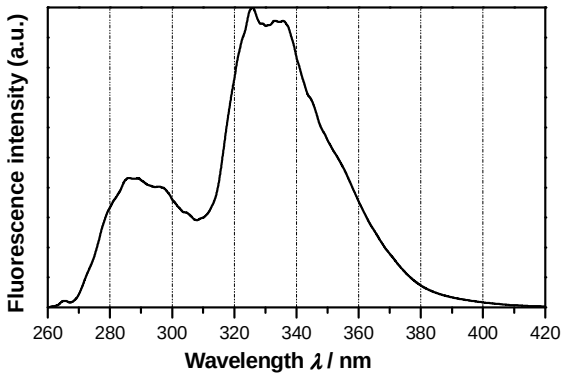

Figure 100: Spectral shape of the kerosene fluorescence spectrum for an excitation wavelength at 266 nm in nitrogen atmosphere at 450 K. Two frequency bands are observed, which correspond to the fluorescence emission of mono- and di-aromatic species contained in the kerosene fuel.

Thus, the tracer molecules at the origin of the kerosene fluorescence can be identified. The procedure adopted for this task consists to compare the fluorescence properties of pure

aromatics tracers with kerosene fluorescence. For that, figure 101 presents a "master series" of fluorescence spectra including all organic species studied in Chapter 5 in non-quenching pure nitrogen environment at 450 K and atmospheric pressure. All the spectra are normalised to the maximum peak of the fluorescence spectrum measured for acetone, establishing then an intensity reference per tracer molecule between the different tracers.

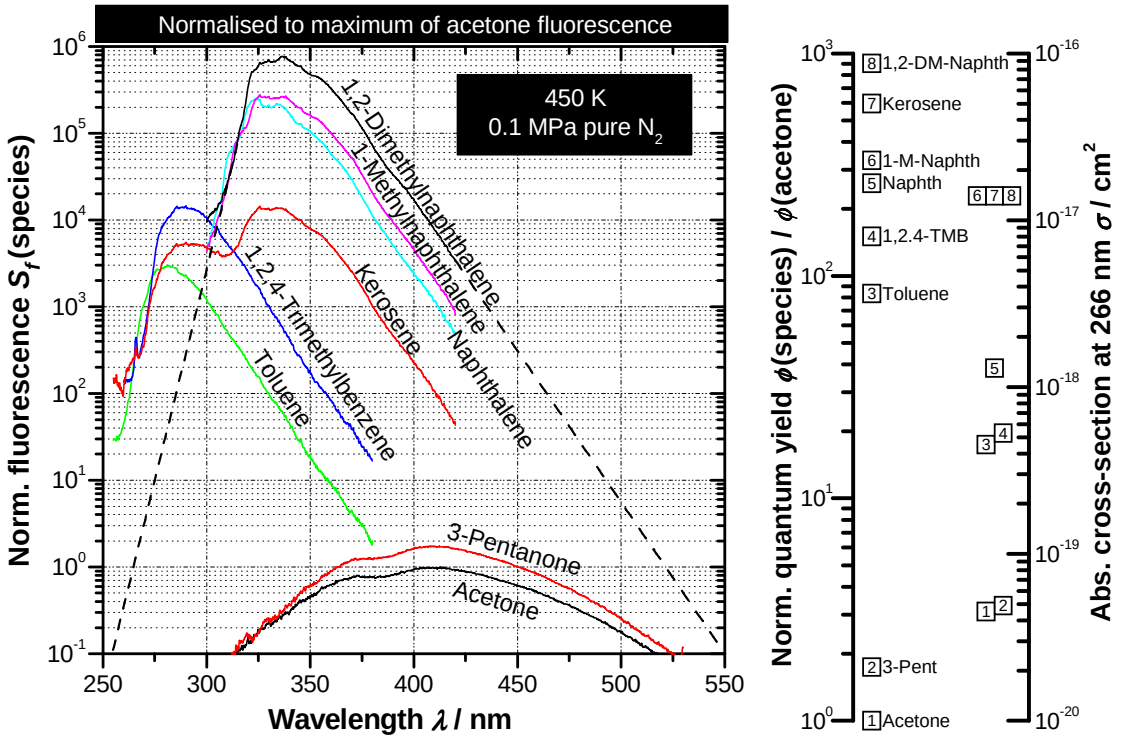

Figure 101: Intensity of fluorescence spectra per tracer molecule for excitation at 266 nm. Comparison of all organic tracers studied in this work. Pure nitrogen atmosphere at ambient pressure and 450 K. All spectra are normalised to the maximum of the fluorescence spectrum measured for acetone. Correction for absorption with Beer-Lambert law. Right hand: fluorescence quantum yields calculated from integrated spectra and respective absorption cross-sections.

For each tracer, the spectral integration of the fluorescence spectra and subsequent division by their respective absorption cross-sections allows to compare the quantum yields of the different species (cf. the diagrams to the right side of figure 101). Fluorescence intensities and yields of each species become further comparable at various environmental conditions by weighting the spectra of the "master" series with the experimental regressions presented in Chapter 5 describing the influence of temperature, pressure and oxygen molar fraction to the integrated fluorescence.

The results presented in figure 101 are used to determine the constituents at the origin of the fluorescence spectrum of the kerosene Jet A1 fuel from the specific bulk used throughout all our measurements. The resulting "optical fuel" composition is presented in

figure 102 for a temperature of 450 K and in an atmospheric pressure nitrogen environment. It is noted that the sum of mass (molar) % values of mono- and di-aromatic constituents are quite similar compared to those of the "optical fuel" composition proposed for a different bulk by [Baranger 2005]. In addition to the species composition of [Baranger 2005] which consists of 1,2,4-trimethylbenzene, naphthalene and the substituted 1-methyl- and 1,3-dimethymnaphthalene, we include also toluene, because our kerosene spectrum showed a wider high frequency band, which is unsuitably fitted by only 1,2,4-trimethylbenzene.

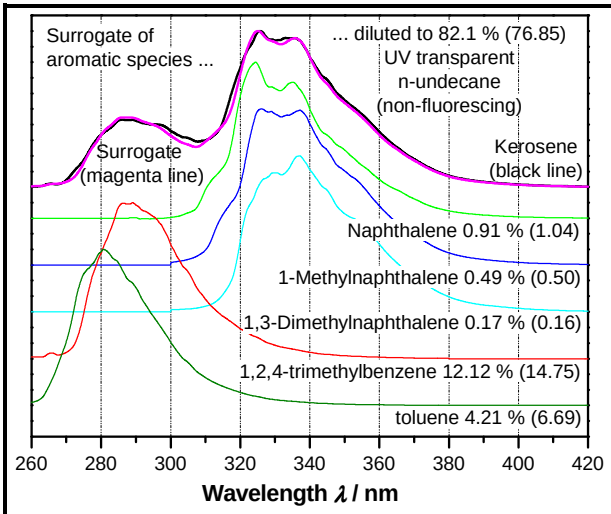

Figure 102: "Optical fuel" for kerosene. Decomposition of kerosene fluorescence spectrum (266 nm excitation at 450 K in atmospheric pressure pure nitrogen) into overlaid spectra from the pure aromatic species studied in Chapter 5. The mass (molar) % of each species have been determined from comparison of fluorescence intensities per tracer molecule for each species normalised to acetone presented in figure 101. Sums of mass (molar) % values of mono- and di-aromatic constituents are quite similar those of the „optical fuel" proposed from [Baranger 2005].

„optical fuel" constituents in mass (molar) %:	mono-aromatics	di-aromatics	n-undecane
this work:	16.33 (21.45)	1.57 (1.70)	82.1 (76.85)
[Baranger 2005]:	16.17 (20.02)	1.73 (1.82)	82.1 (78.16)

6.2 Kerosene fluorescence – comparison to "optical fuel" in non-quenching nitrogen

This section discusses the fluorescence measurements obtained for the multi-component kerosene fuel. The kerosene fluorescence spectrum can be represented by the overlap of fluorescence spectra of mono- and di-aromatic species entering in the species composition of the "optical fuel" as indicated in figure 102. In order to obtain a high level of agreement between the "optical fuel" fluorescence with the kerosene fluorescence, small amounts of methylated naphthalenes have to be considered. Unfortunately, the knowledge of fluorescence properties of methylated naphthalenes is only given at 450 K compared to that of mono-aromatics and naphthalene, which are studied over a large range of temperature and pressure. Thus, the "optical fuel" composition under thermodynamic conditions different from that of the master series have to be defined assuming similar fluorescence properties between the methylated naphthalenes and naphthalene. A weighting factor has then to be

introduced to account for the differences found in spectral shape and intensity of the fluorescence emission within the master series observed between those molecules.

6.2.1 Temperature dependence

The temperature effect to the absorption and fluorescence of vapour kerosene diluted in pure nitrogen at atmospheric pressure and temperature ranging between 450 and 900 K is now presented.

(a) Absorption

The temperature dependence of the kerosene absorption cross-section from measurements at 266 nm excitation wavelength is depicted in figure 103. The red line represents an average value excluding the data recorded at 850 K, where chemical mechanisms might degrade the stability of the fuel composition. An overall fit to a constant absorption cross-section of $5.4 \cdot 10^{-19}\,\mathrm{cm}^2$ within the range of experimental error is then obtained.

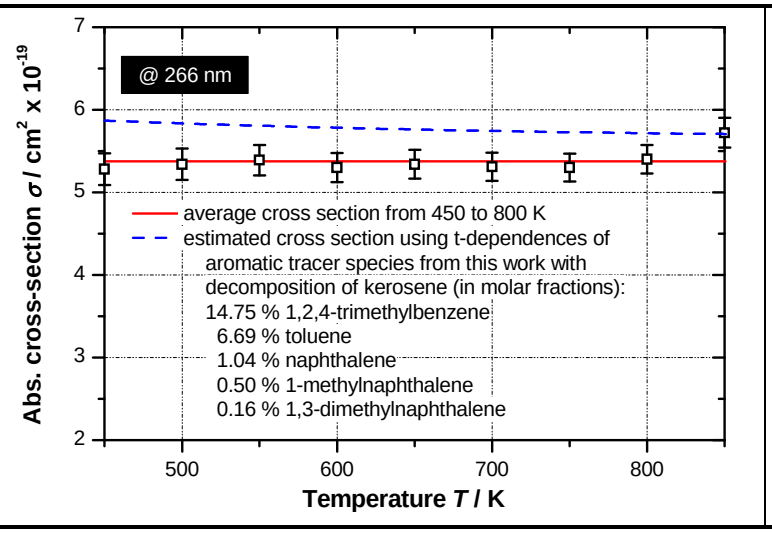

Figure 103: Kerosene absorption cross-section after 266 nm laser excitation as a function of temperature. Kerosene was evaporated from liquid to constant number density of 9.5×10^{16} cm^{-3} (5.9 to 11.1 mbar from 450 to 850 K) in pure nitrogen atmosphere at ambient pressure.

The fluorescence spectrum obtained from the overlap of individual mono- and di-aromatic fluorescence spectra previously selected also allows to estimate the absorption cross-section of the "optical fuel". In this procedure, the non-aromatics kerosene constituents are supposed to be optically transparent in the middle UV and the absorption cross-sections of the methylated naphthalenes are similar to that of naphthalene. The absorption cross-section of the "optical fuel" at 450 K with the species composition defined in section 6.1 is then equal to $5.9 \cdot 10^{-19}\,\mathrm{cm}^2$, exhibiting a slight decrease to $5.7 \cdot 10^{-19}\,\mathrm{cm}^2$ at 850 K, cf. the blue dashed line. Comparison of the cross-sections of the "optical fuel" and kerosene shows high concordance, which reassures about our initial assumptions.

(b) Fluorescence

The temperature effect on kerosene fluorescence spectra in atmospheric pressure nitrogen is presented in figure 105. The peak at 266 nm corresponds to the Rayleigh scattering and stray light at the laser frequency. As observed in this figure, the intensity of the fluorescence emission decreases faster for the high-frequency band (260 to 310 nm) than for the low-frequency band (310 to 420 nm). This is in analogy with the observations made for the mono- and di-aromatics studied in Chapter 5. Thus, it might be presumed, that the change of kerosene fluorescence with temperature are strongly related to the combined temperature effects to the fluorescence of its mono- and di-aromatic constituents. Unfortunately, integrations of kerosene fluorescence over the high- and the low-frequency bands prevent any validation of this assumption because of the overlap of both bands within the spectral range of 290 -350 nm. Inversely, the evaluation of the combined temperature effects of individual aromatic constituents of the "optical fuel" can be compared to the results of kerosene fuel. Therefore, the "optical fuel" is built without methylated naphthalenes, which are replaced by naphthalene. A weighting factor is then introduced for taking into account the variation of physical parameters like the molar fractions of methylated naphthalenes, the fluorescence peaks in the master series shown in figure 104 and the integrated surfaces under their normalised fluorescence spectra.

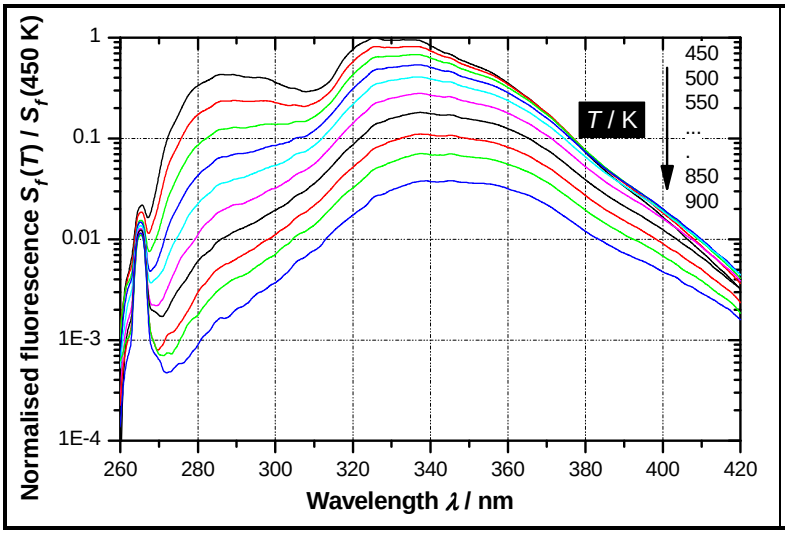

Figure 105: Kerosene fluorescence spectra after 266 nm laser excitation as a function of temperature. Normalised to 450 K. Kerosene was evaporated from liquid to constant number density of 9.5×10^{16} cm^{-3} (5.9 to 11.7 mbar from 450 to 900 K) in pure nitrogen atmosphere at ambient pressure.

The temperature evolution of the integrated kerosene fluorescence from 270 to 420 nm is shown in figure 106 and compared to the temperature behaviour of pure aromatic species studied in Chapter 5 (cf. continuous lines). The temperature-decrease of kerosene fluorescence is more pronounced than that of naphthalene and slower than that of mono-aromatics. The blue broken line in figure 106 displays the temperature decrease of the "optical fuel", which exhibits very good concordance to that of kerosene fuel. A small deviation is observed at temperature higher than 650 K which probably arises from the replacement of

methylated naphthalenes with naphthalene, leading then to a slight underestimation of the kerosene fluorescence intensity fall-off.

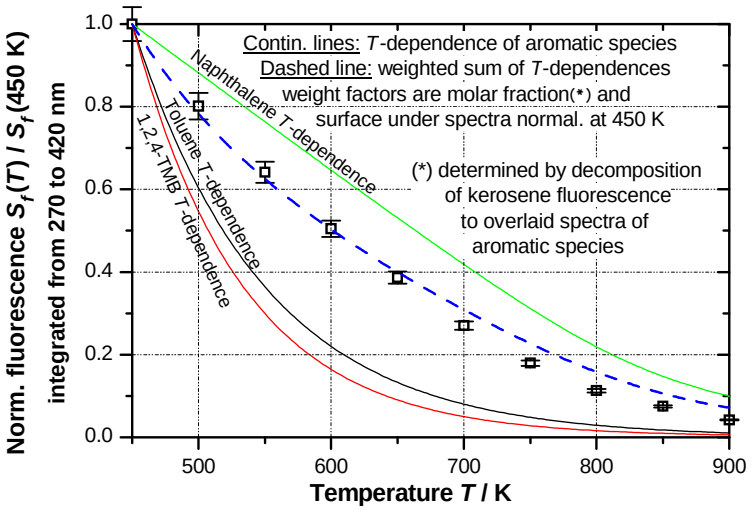

Figure 106: Kerosene fluorescence integrated (270 to 420 nm) and normalised to 450 K. Excitation at 266 nm wavelength in atmospheric pressure nitrogen. Comparison to the temperature regressions of individual aromatic species studied in the previous chapter and further to that of a „optical fuel" with constituents of similar composition like determined in figure 103 (replacing methylated by simple naphthalene), cf. text for detailed information.

6.2.2 Pressure dependence

Pressure effect of kerosene fluorescence in non-quenching nitrogen has been studied at temperature levels of 450 and 700 K from 1 to 30 bar. The results are shown in figure 107. As observed from the aromatics fluorescence in Chapter 5, the spectral shape of the fluorescence is unaltered when increasing the nitrogen pressure. For kerosene fluorescence, differences on fluorescence spectra are noted mainly in the spectral domain of 290 - 350 nm, where the fluorescence spectra of mono-aromatics and di-aromatics overlap.

At 450 K, a monotonous decrease of the fluorescence intensity of the high-frequency band (260 to 310 nm) is observed when increasing pressure. This behaviour corresponds to the one observed for mono-aromatics when excited close to the (0,0) band. As already mentioned, the temperature increase leads to an attenuation of the fluorescence emission, which is much more pronounced for the mono- than for the di-aromatic species. Thus, at 700 K, the fluorescence of mono-aromatics in the kerosene spectrum becomes almost indiscernible due to the existence of di-aromatics fluorescence spectrum presenting a large wing structure in this spectral domain.

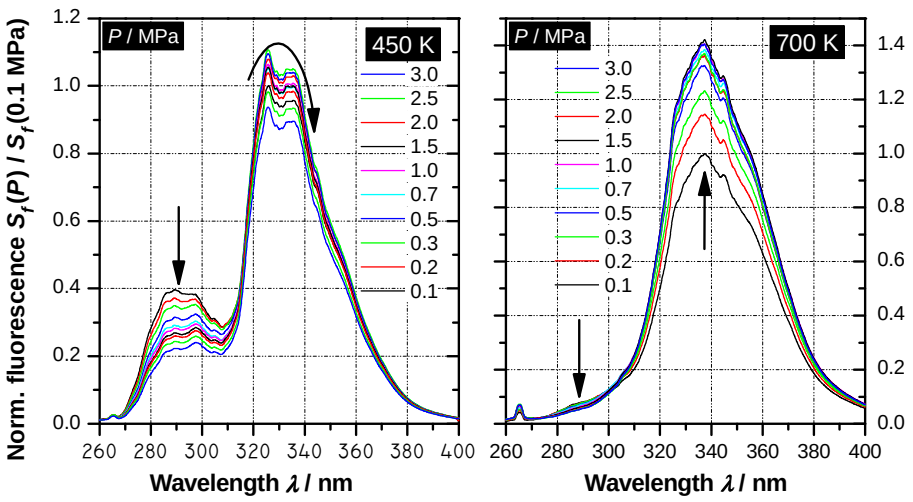

Figure 107: Kerosene fluorescence spectra after 266 nm laser excitation as a function of pressure. Normalised to 0.1 MPa. Kerosene was evaporated to constant number density *n*. Pure nitrogen atmosphere at 450 K (left figure) with $n \approx 2.10\times10^{17}$ cm^{-3} and at 700 K (right figure) with $n \approx 1.35\times10^{17}$ cm^{-3}. Kerosene concentration is about 13 mbar. All spectra are first order Savitzky-Golay smoothed with 2.5 nm window size.

At 450 K, the low-frequency fluorescence band (310 to 420 nm) initially increases with pressure followed by a subsequent decrease, whereas at 700 K it monotonically increases. This result is in complete analogy to what is observed for naphthalene. Recall that this observation is the consequence of the pressure-induced fluorescence stabilisation, which is more pronounced at high temperature.

Figure 108 displays the pressure evolution of the ratio of the integrated fluorescence (270 - 420 nm spectral domain) to the one recorded at atmospheric pressure for the temperature levels of 450 and 700 K. At 450 K, a comparison with the pressure evolutions presented in Chapter 5 shows that the kerosene fluorescence lies between mono-aromatics and naphthalene fluorescence, somewhat closer to the latter (cf. top diagram). The pressure evolution of the "optical fuel" fluorescence is shown for 450 K as blue dashed line graph. Despite the initial increase for low pressure (≤ 0.5 MPa) and the slightly faster decrease at high pressure (≥ 2.5 MPa) observed for the kerosene data, the pressure regression of the "optical fuel" well approximates that of the kerosene fuel. The same as for 450 K, a comparison to the pressure regression of the "optical fuel" is shown at the temperature level of 700 K (cf. bottom diagram). It is somewhat astonishing to observe the kerosene data at higher yields even than the pressure evolution determined for naphthalene at this temperature. The pressure evolution for the "optical fuel" lies naturally between the naphthalene and the mono-aromatics evolutions, and thus even farer from the measured kerosene yields. Two possible explanations can be given for this observation. Firstly, the pressure dependences of the neglected methylated naphthalenes might to some extent cause this behaviour if these deviate more from that of naphthalene as it is the case for the temperature evolutions. Another explanation is given by possible effects of collisions with other (non-fluorescent) species contained in the kerosene

fuel. These collisions are then at the origin of vibrational relaxation and possibly reinforce the fluorescence yield.

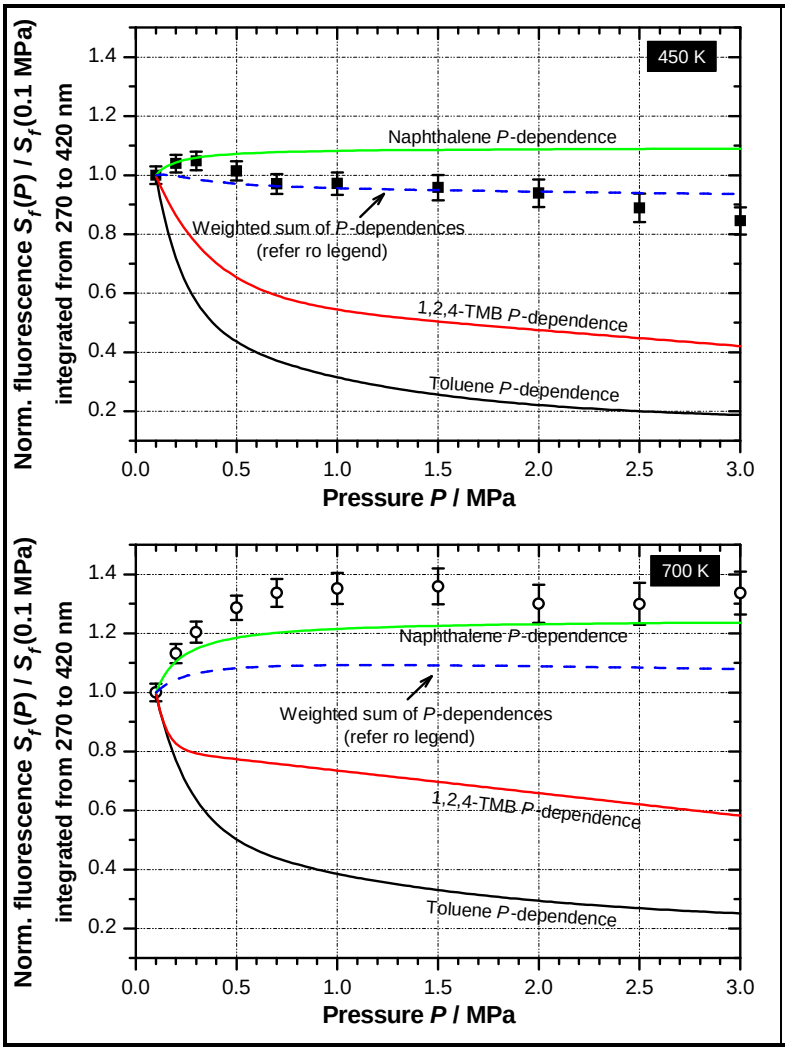

Figure 108: Kerosene fluorescence after 266 nm laser excitation as a function of pressure. Normalised to 0.1 MPa, from integrated fluorescence spectra (270 to 420 nm). Pure nitrogen atmosphere at 450 K and at 700 K.

6.2.3 Oxygen dependence

The sensitivity of kerosene fluorescence towards oxygen quenching was studied at atmospheric pressure. Fluorescence spectra normalised to the condition of pure nitrogen atmosphere are presented in figure 109 for temperature between 450 and 750 K.

The kerosene quenching behaviour is depicted for the entire spectral range of the kerosene fluorescence emission. The intensity fall-off is stronger at the low-frequency than at the high-frequency band, which confirms the observation of a stronger naphthalene quenching compared to that of toluene and 1,2,4-trimethylbenzene.

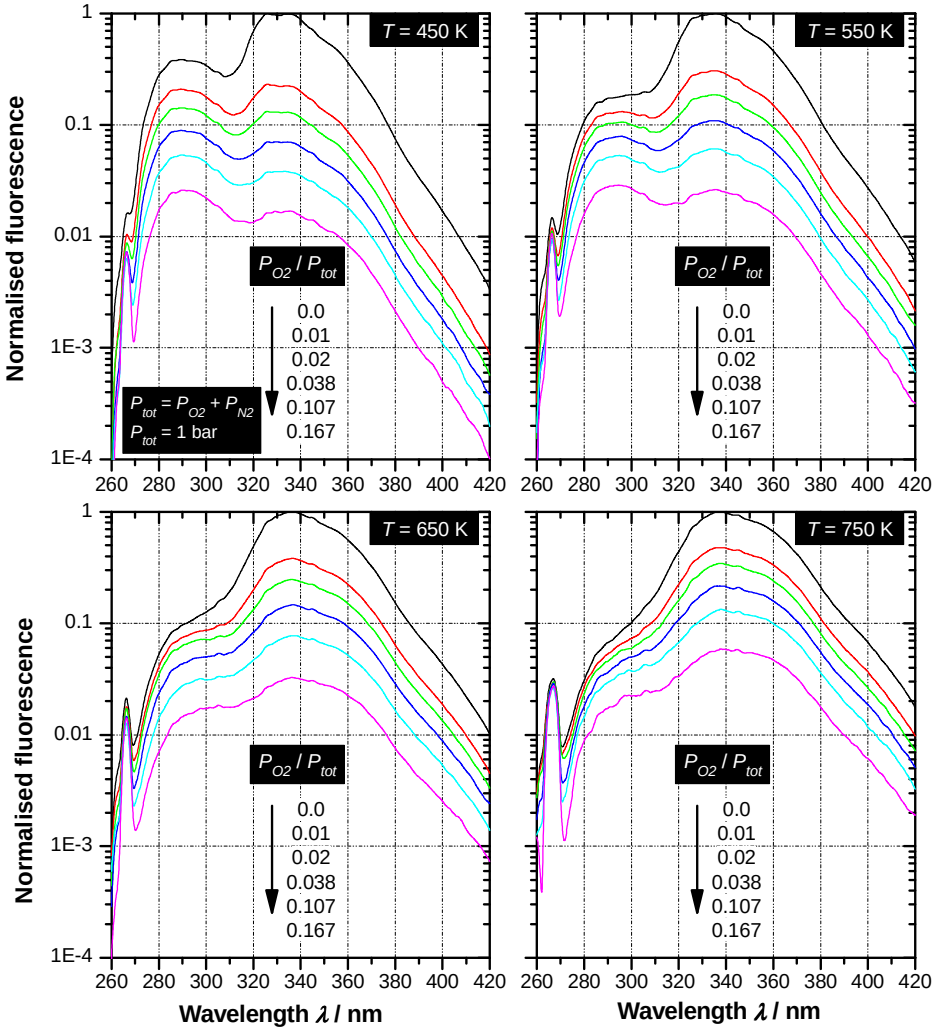

Figure 109: Kerosene fluorescence spectra after 266 nm laser excitation as a function of oxygen partial pressure at 450, 550, 650 and 750 K. The maximum oxygen partial pressure for all measurements is 167 mbar. Kerosene with 2.6 mbar concentration. All spectra are first order Savitzky-Golay smoothed with 2.5 nm window size. Normalised to maximum peak at each temperature for pure nitrogen.

Applying a two-dimensional kerosene PLIF strategy, this untreated fluorescence emission has to be spectrally integrated, and therefore, the specific fluorescence emission behaviour related to the identity of mono- and di-aromatics would be lost. With the aim to preserve this identity, a dual channel filtered detection of the kerosene fluorescence is necessary. A separation of the kerosene fluorescence emission into a contribution of mono- and of di-aromatics constituents by use of appropriately chosen optical filter sets is presented in the following section.

6.3 Dual channel filtered detection of kerosene fluorescence

The principle of the filtering scheme separating the kerosene fluorescence emission into a contribution of mono- and of di-aromatics is depicted in figure 110 in front of exemplary kerosene fluorescence spectra for two temperature levels. A "filter set A" optimised for the detection of the di-aromatics emission is easily established (cf. the green continuous transmission line). An exclusive detection of the mono-aromatics emission is somewhat more difficult. A feasible (and affordable) solution is found by using a "filter set B", which has a transmission curve covering with the "filter set A" towards the low-frequency side, whereas it lets pass the emission of mono-aromatics towards the high-frequency side, excluding stray light and Rayleigh emission at the laser frequency (cf. the red continuous transmission line). The emission of mono-aromatics is then obtained as the signal difference from the filtered detection of "filter set A" and "filter set B". This indirect channel is called "difference A-B" (cf. broken blue transmission line).

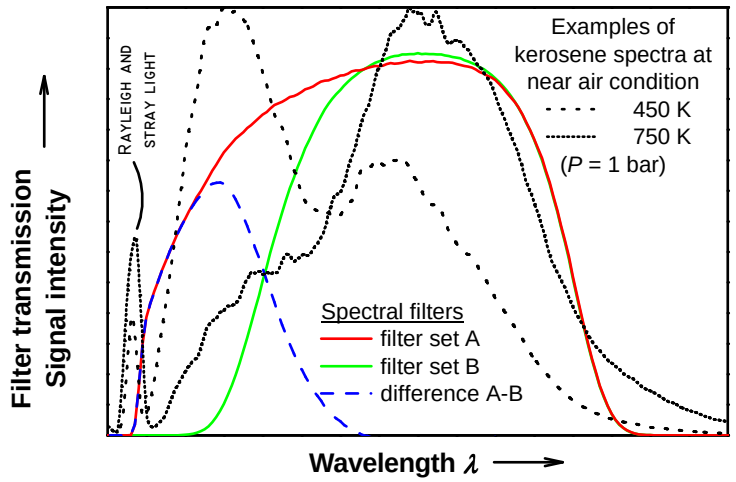

Figure 110: Dual channel filtered detection of kerosene fluorescence. Exemplary kerosene spectra are shown for atmospheric pressure near air condition at 450 and 750 K. The filter set A covers essentially the whole spectral domain of the kerosene fluorescence. For the filter set B, highest transmission is settled at the low-frequency domain corresponding roughly to the fluorescence of di-aromatics.

In non-quenching environment, the fluorescence behaviour of kerosene has been shown to be reproducible by the "optical fuel". The same finding has now to be demonstrated in quenching environment. When defining the "optical fuel", the methylated naphthalenes are again replaced by naphthalene and by introduction of a correction factor. [Baranger 2005] reported that the quenching of 1,3-dimethylnaphthalene is stronger than for naphthalene and 1-methylnaphthalene. Replacing then 1,3-dimethylnaphthalene by naphthalene results in a smaller naphthalene concentration in the "optical fuel". The quenching behaviour of the kerosene fluorescence is now shown in figure 111 as filtered spectra using the different filter sets displayed in figure 110.

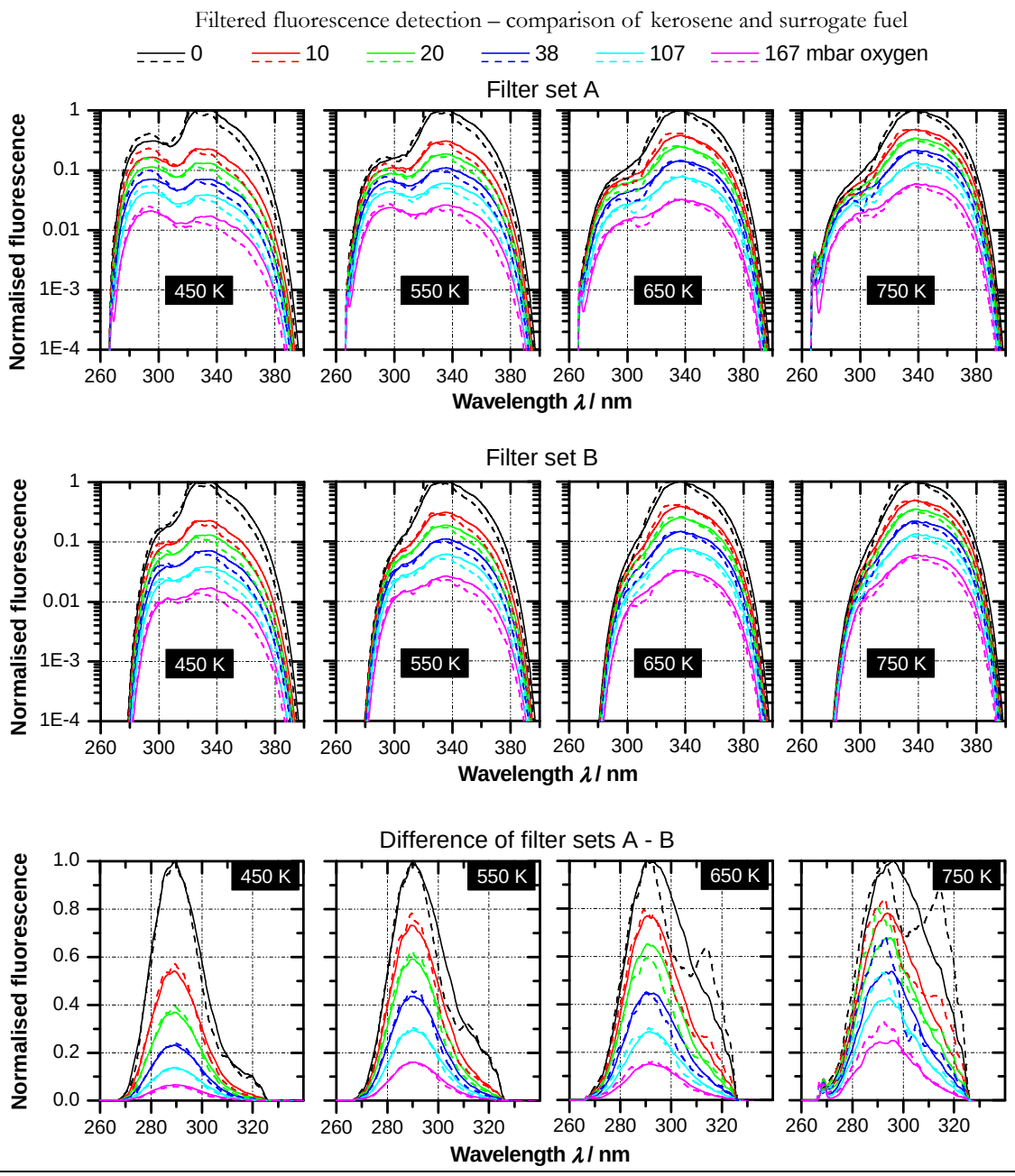

Figure 111: Spectrally filtered kerosene fluorescence (266 nm laser excitation) as a function of oxygen partial pressure at 450, 550, 650 and 750 K (continuous line graphs). A comparison is shown to the filtered fluorescence of an "optical fuel" of aromatic species (broken line graphs) with 14.76 % 1,2,4-trimethylbenzene, 7.39 % toluene, 0.34 % naphthalene, 0.34 % 1-methylnaphthalene and 0.32 % 1,3-dimethylnaphthalene (methylated naphthalenes are replaced with simple naphthalene, introducing a weighting factor for error compensation similar as described in section 6.2.1(b)).
The maximum oxygen partial pressure for all measurements is 167 mbar. Kerosene with 2.6 mbar concentration. All spectra are first order Savitzky-Golay smoothed with 2.5 nm window size. Normalised to maximum peak at each temperature for pure nitrogen.

For the use of "filter set A", an overall good agreement is seen for all temperature levels. The same observation is made for "filter set B". As to the difference of the signals recorded by both filter sets, "difference A-B", an excellent concordance is seen at 450 K. Towards higher temperature and for low oxygen concentration, the low-frequency wing of the "optical fuel" spectrum presents a deviation from the kerosene spectrum. The methylation effect on the naphthalene fluorescence causes a slight spectral shift towards lower frequencies (cf. figure 75 in section 5.7). In the "optical fuel" spectra, the replacement of methylated naphthalenes by naphthalene induces thus a spectral error, which shows as an additional side-peak. Fortunately, this spectral deviation does not alter the agreement of the integrated fluorescence signal between the "optical fuel" and kerosene.

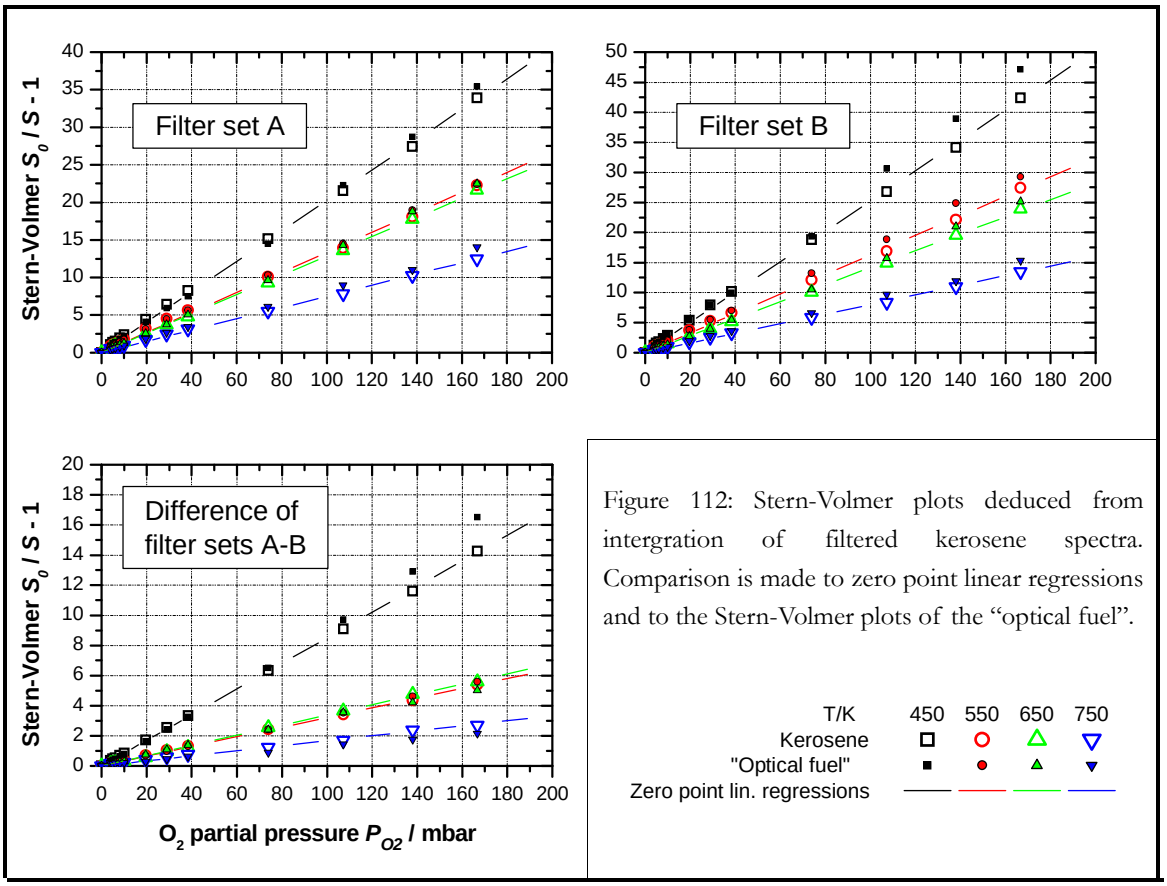

Figure 112: Stern-Volmer plots deduced from intergration of filtered kerosene spectra. Comparison is made to zero point linear regressions and to the Stern-Volmer plots of the "optical fuel".

An integration of the filtered kerosene spectra from figure 111 allows now to show the quenching behaviour of the spectrally separated parts as individual Stern-Volmer relations (cf. figure 112). The measured Stern-Volmer data are highly linear for all filter sets (cf. the vicinity to the zero point linear regressions). A comparison is shown between kerosene and the "optical fuel". At low and medium oxygen concentration, an excellent concordance is observed for all filter situations. The Stern-Volmer relation of the "optical fuel" deviates most from that of kerosene at low temperature and higher oxygen concentration, especially for "filter set B" and the "difference A-B". A comparison of the result obtained for the filter

set difference "A-B" to the Stern-Volmer relation determined earlier for 1,2,4-trimethylbenzene (cf. figure 73 in section 5.6.3) reveals excellent analogy, demonstrating that major mono-aromatics present in kerosene is definitely 1,2,4-trimethylbenzene.

In view of the experimental data detailed in Chapter 5, oxygen quenching is the dominating path of deactivation for all studied aromatic tracer species when oxygen concentration is close to air, i.e. the collisional effect induced by nitrogen pressure is small compared to the effect of oxygen. For naphthalene, the total neglect of intramolecular vibrational relaxation induces only small error to the calculated result when using the naphthalene yield model (cf. figure 97 in section 5.8.3). For strongly quenched aromatic species, a simplified method of fluorescence yield estimation is then possible via an extrapolation of the Stern-Volmer relations measured at atmospheric total pressure to higher total air pressure. The kerosene fluorescence yield is thus estimated similarly by extrapolation of the Stern-Volmer relation.

6.4 Strategy for temperature and fuel-to-air ratio kerosene PLIF measurements

The strategy for quantification of the filtered kerosene fluorescence signals in terms of temperature and concentrations of kerosene and oxygen is based on the application of a dual detection path using "filter set A" and "filter set B" for the kerosene PLIF measurements. This allows for recording physically uncorrelated data corresponding roughly to the mono- and di-aromatic species contained in the kerosene fuel. The quantification approach, which has to be applied at each pixel position of the filtered kerosene PLIF images, implies then the following steps.

- Dual channel filtered fluorescence acquisition:
  Two-dimensional measurements are performed using a simultaneous detection of the fluorescence signals on two ICCD cameras, which exactly image the same area. The filtered fluorescence detection leads to three spectral detection channels defined by "filter set A", "filter set B" and their difference "A-B".
- Signal calibration:
  A kerosene/air mixture at known thermodynamic condition is homogeneously seeded to the measurement volume. Together with the effect of temperature to the fluorescence in nitrogen and the Stern-Volmer data known from the previous measurements, this allows to scale the filtered kerosene fluorescence signals.
- Extrapolation of Stern-Volmer relations to higher than atmospheric pressure:
  When oxygen quenching is the dominating electronic deactivation, the Stern-Volmer data can be extrapolated to higher air pressure. A regression function $k_{SV\#}(T)$ describes the evolution of the Stern-Volmer slope with temperature for each filter set

(#..."A", "B", "A-B"). The respective Stern-Volmer coefficients are then calculated as $\{S_{0\#}/S_{\#}-1\}_{calc\#} = \mathrm{k_{SV\#}(T)} \cdot p_{O_2}/p_{total}$ from a given couple $\{T, p_{O_2}\}$ of temperature and oxygen partial pressure. Since the thermodynamic conditions are unknown, they have to be derived iteratively. To restrain the convergence to meaningful solutions, an initial guess is made for a couple $\{T, p_{O_2}\}$ in the range of the experimental operating conditions.

- Iterative program algorithm:
  A $\{T, p_{O_2}\}$-couple fulfilling the condition $\{S_{0\#}/S_{\#}-1\}_{calc\#} - \{S_{0\#}/S_{\#}-1\}_{meas\#} \leq \varepsilon$ is derived for each filter set (#..."A", "B", "A-B"). $S_{0\#}$ is the respective signal level in pure nitrogen at the given temperature known from the signal calibration above. The $\{T, p_{O_2}\}$-couple is continually changed in the direction of smaller convergence parameter ε, and is valid when the above condition is true for all three filter sets.
- Closure relation for the species concentration:
  With a valid $\{T, p_{O_2}\}$-couple, the oxygen concentration is derived from the known total pressure as $\chi_{O_2} = p_{O_2}/p_{tot}$. It is assumed that the mono- and di-aromatic fractions in the kerosene are unchanged and therefore represent the fuel concentration. This is a reasonable statement for non-reactive parts of the flow. From the closure relation for the species concentrations $\chi_{O_2} + \chi_{N_2} + \chi_{fuel} \equiv 1$, the nitrogen concentration χ_{N_2} and the fuel concentration χ_{fuel} are derived. For known fuel composition, the concentration of di-aromatic species $\chi_{di-arom}$ is then deduced from χ_{fuel}, the same as the concentration of mono-aromatics.
- Inverse control with the determined thermodynamic parameters:
  With the temperature and oxygen partial pressure, the Stern-Volmer ratio can be inversely calculated for the different filter sets. The signal levels in pure nitrogen at a given fuel concentration and temperature can be deduced from the calibration procedure. These are needed to weight the Stern-Volmer ratios in order to obtain a comparison to the measured fluorescence signals. If these are not similar, the determined parameters were not meaningful. The iterative procedure has then to be repeated with new initial guess for the $\{T, p_{O_2}\}$-couple.

Chapter 7 Kerosene and OH PLIF in a high-pressure combustor

Increasingly stringent regulations on pollutant emissions, such as NO_x, CO_x and soot, require to improve combustion efficiency and overall operability of kerosene-fuelled aeronautical gas turbines. The mechanisms of pollution formation in turbine combustion have been reviewed in section 1.1. Concepts for the reduction of pollutant emissions are subject of new engine concepts. Low emission engine concepts like fuel staging have brought significant improvements, but will not be sufficient to fulfil ACARE targets for 2020. Substantial improvements can still be made from further development and application of novel injection strategies for lean combustion such as LDI (multipoint), LP (Lean Premixed) and LPP (Lean Premixed Prevaporised) injectors (cf. section 1.2). These concepts have therefore become an important area of research (cf. section 1.3).

The principle of these injectors is to atomise the liquid fuel into small droplets which evaporate to a large extent, and mix the subsequent fuel vapour with air in a prevaporising/premixing duct, in order to obtain a fairly homogeneous fuel-air mixture before combustion occurs. Many experiments have used laser-based techniques to determine the influence of parameters like droplet size and velocity, air temperature, fuel and air flow rates on the performances of such injectors [Löfström 2000, Greenhalgh 2000]. However, these studies were mainly focused on the spatial distribution of liquid phase in the combustor, and the evolution of droplet size at different locations from the injector exit was used to estimate fuel evaporation [Michou 1999, Becker 2003]. Indeed, only few experiments were performed to characterise fuel vapour phase [Stufflebeam 2002, Galley 2004, Krämer 1999]. In addition, results were typically obtained with surrogate fuels or added tracers, which were not necessarily representative of typical fuels used in aircraft engines (i.e. kerosene). The conclusions drawn from these experiments may therefore be biased by the type of fuel they used, because of the different evaporation behaviour and combustion processes of surrogates or tracers compared to that of real fuels. Only very few examples of studies performed with laser-based diagnostics directly applied to kerosene vapour are available in the literature (cf. section 4.7.2). Unfortunately, these results were only qualitative, because kerosene spectroscopy was not properly established despite the pioneering work of [Löfström 1996].

Recent work of [Baranger 2005] has shown that thorough investigation of kerosene photophysics is beneficial for the identification of the molecular species responsible for its fluorescence emission. Baranger's promising results highlight the importance of mono- and di-aromatic tracers naturally present in the kerosene fuel. Using their fluorescence properties, an "optical fuel" with similar fluorescence characteristics like the kerosene fuel was established. The present thesis work aimed for en extended photophysical study of these identified aromatic species (cf. Chapter 5) as well as of kerosene fuel (cf. Chapter 6). The parameter range covered conditions similar to those encountered in turbine combustion (up to 900 K and 30 bar). Combination of the results from aromatic species and kerosene allowed to define a concept for quantitative measurements of temperature, fuel and oxygen concentration (local equivalence ratio) in kerosene-fuelled gas turbines using a filtered PLIF-kerosene strategy (cf. section 6.4).

The results of the present work provide the necessary physical understanding of kerosene fluorescence to assess fuel vapour concentration at high-pressure in the non-reactive zones of a turbine combustor under firing conditions. Characterising the performances of aircraft injectors also requires the determination of the flame structure and flame reaction rate, which gives information about combustion efficiency depending on operating conditions. This can be classically performed using PLIF applied to OH radical [Hanson 1986] and the technique has already been applied to pressure larger than 1.0 MPa [Frank 1999, Atakan 1997]. However, it is interesting to determine the spatial and temporal correlation between fuel vapour distribution and flame structure. Such information can be obtained by means of simultaneous measurements of kerosene vapour and OH radical in the combustor, and this can be used to evaluate the influence of fuel concentration on local flame reaction rate.

The goal of the present experiments is to combine PLIF-kerosene and PLIF-OH in order to measure simultaneously local equivalence ratio and spatial distribution of OH radical in a high-pressure combustor operating with jet A1 fuel. Apart from qualitative visualisation of the fuel and OH distribution, a major objective of these experiments is to evaluate the feasibility of the quantification of the kerosene PLIF technique in terms of temperature and equivalence ratio within a domain of temperature between 480 and 730 K and pressure up to 2.2 MPa.

7.1 Planar laser-induced fluorescence for kerosene vapour measurements

Detection of fluorescence from aromatics with one excitation wavelength over two specific spectral ranges can provide dual-parameter imaging, yielding for example equivalence ratio in addition to temperature. Collection of kerosene and di-aromatics fluorescence signals on two separate ICCD cameras with appropriate spectral filters may be one of the possibilities be-

cause of their different temperature and oxygen dependencies. Such a strategy of kerosene PLIF quantification was defined in section 6.4. Along with a calibration point in a reference flow where thermodynamic parameters are well known, an iterative processing routine of both instantaneous fluorescence signals, combined with the closure relation for species composition ($\chi_{O_2} + \chi_{N_2} + \chi_{fuel} \equiv 1$) is then used to determine the desired quantities. Note that this data reduction implies that the ratio between mono-aromatics and di-aromatics remains constant during the experiments (χ_{fuel} can be represented by the concentration of mono- or di-aromatic species). This assumption remains valid for temperatures up to 1100-1300 K, where kerosene pyrolysis may be observed.

7.2 Experimental set-up

The combustor with the fuel injector under study is connected to the so-called "M1 test bench", which is the high temperature – high pressure combustion facility from ONERA-Palaiseau dedicated to the investigation of aircraft and helicopter injectors under real operating conditions. This bench consists of a heat exchanger which can preheat air up to 900 K for air flow rates up to 1 kg/s or up to 800 K for air flow rates up to 4 kg/s. The figure 113 gives an impression of the

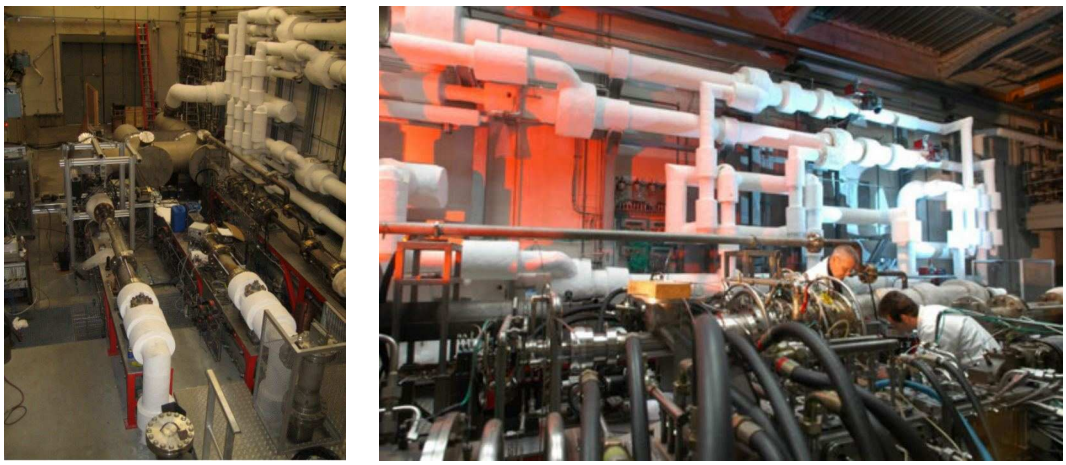

Figure 113: M1 test bench – installation at ONERA-Palaiseau, which allows to reproduce the realistic operating conditions of aeronautic turbine combustion. The combustor with the injector under study is connected to this bench.

7.2.1 Combustor facility

The combustor used in the experiments is represented in figure 114. Preheated air is injected into the combustor together with liquid kerosene via two injectors: a single pilot injector is

located on the combustor axis and it is used to stabilise the flame whereas a multipoint main injector is located at larger radial distance. Fuel flow rate is split between the two injectors and the ratio between equivalence ratio from the pilot and the main injector (Φ_{pilot}/Φ_{main}) lies between 0.1 and 1, except for a condition where only the pilot injector is used (see table 12). The combustor comprises a water-cooled visualisation sector which is equipped with three optical accesses for laser measurements. Optical windows are made of UV-transparent silica. One is used for laser access and the two others for detecting fluorescence from kerosene and OH radical. Optical accesses are specifically designed so that fluorescence can be collected directly at the outlet of the injector. The outlet of the combustor is equipped with a sonic throttle which can be partly obstructed by a water-cooled needle in order to control the pressure inside the combustor. Finally, exhaust gases are collected by a fan. Air inlet temperature varies between 480 and 730 K and pressure inside the combustor is in the range 0.45–2.2 MPa.

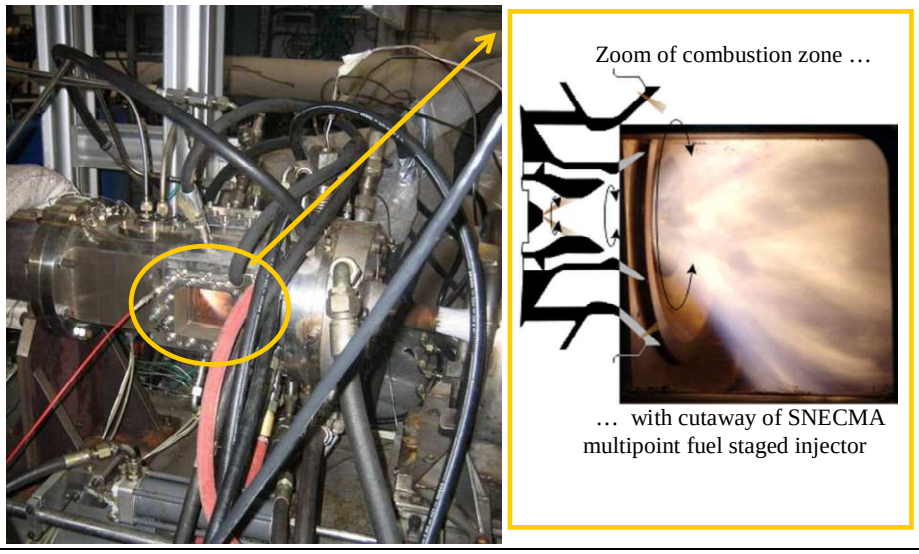

Figure 114: Combustor facility at firing conditions.

Table 12 summarises the operating conditions presented in this article. In the following, Φ_{pilot} is the equivalence ratio of the pilot injector and Φ_{main} refers to the equivalence ratio of the main injector.

Table 12: Operating conditions

Temperature (K)	Pressure (MPa)	Φ_{pilot}/Φ_{main}
480	0.45	Pilot only
590	0.95	1
730	2.2	0.1

7.2.2 Optical set-up

Two pulsed laser systems are used to perform OH and kerosene vapour PLIF measurements simultaneously (figure 115). Both systems are installed in an optical room located close to the test bench. Measurements of OH radical are performed using a frequency-doubled, Q-switched Nd:YAG laser to pump a dye laser. The laser is frequency doubled to deliver wavelengths in the 280–290 nm spectral range, with energy of 20 mJ per pulse. The dye laser is tuned to 282.75 nm to excite the $Q_1(5)$ line of the (1, 0) band of the OH ($X^2\Pi - A^2\Sigma^+$) system. Part of the laser beam is directed to the burnt gases of a reference laminar methane-air flame in order to tune the laser to the aforementioned OH transition. The linewidth is estimated to be approximately 0.1 cm^{-1} by recording the spectral profile of several OH transitions in the reference flame. This OH transition is chosen because of its high intensity, its well-isolated spectral feature and its low dependence upon temperature. Measurements of kerosene fluorescence use a single-excitation scheme which comprises a frequency-quadrupled Nd:YAG laser generating 8 ns, 50 mJ pulses at 266 nm. Energy of both laser beams is controlled during the experiments by means of laser power meters. Time delay between the two laser beams is fixed to 200 ns in order to avoid cross-talks between fluorescence signals of OH and kerosene. This duration is much shorter than the typical flow time-scale, ensuring that images of OH and kerosene fluorescence are representative of the same phenomenon at the time of recording.

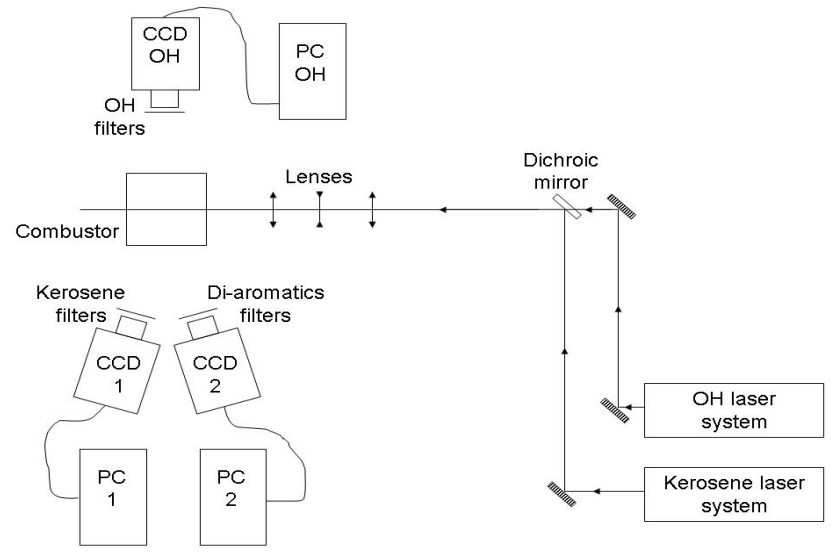

Figure 115: Optical setup for the simultaneous detection of OH radical and kerosene vapour fluorescence.

Both laser beams are transported via optical mirrors around the combustor facility and superimposed with a combination of dichroic mirrors. They are then transformed into two superimposed collimated sheets using a unique set of cylindrical and spherical lenses. The

two cylindrical lenses form a telescope which spreads the beams into collimated sheets. Only the central zone of the laser sheets is used to obtain laser sheet energy profiles as flat as possible, allowing, in a first assumption, proportionality between the fluorescence signals and the probe species concentration. A spherical lens with 1-meter focal length finally focuses the two sheets to a 130 μm waist located in the centre of the combustion chamber. Energy in the laser sheet is maintained to 4 mJ for OH and 25 mJ for kerosene vapour detection, respectively. Fluorescence from OH radicals is recorded with a 16-bit ICCD camera while fluorescence from kerosene vapour and liquid phases are simultaneously recorded by two 16-bit ICCD cameras (figure 115). The camera used for OH visualisation has a CCD array of 1024×1024 pixels, a temporal gate of 40 ns, with a framing rate of 4 Hz and it is equipped with a 105 mm, f/4.5 UV-NIKKOR lens. The cameras used for kerosene detection have a CCD array of 512×512 pixels, a temporal gate of 40 ns, with a framing rate of 4 Hz, and each camera is equipped with a *f*=94 mm, achromatic UV lens. For OH measurements, the camera has a combination of coloured glass filters (WG 295 and UG 5 from Schott) and an interferential filter centred at 310 nm (FWHM = 5.6 nm). For kerosene measurements, the first camera is equipped with a combination of coloured glass filters (WG 280 from Schott and a custom-made bandpass filter collecting fluorescence in the range 260–420 nm) to collect the whole fluorescence of kerosene (i.e. fluorescence from mono- and di-aromatics), whereas the second camera uses a combination of coloured glass filters (WG 305 from Schott and a custom-made bandpass filter collecting fluorescence in the range 260–420 nm) to collect fluorescence from di-aromatics only. Each camera is interfaced to a personal computer used to control the camera and to record images.

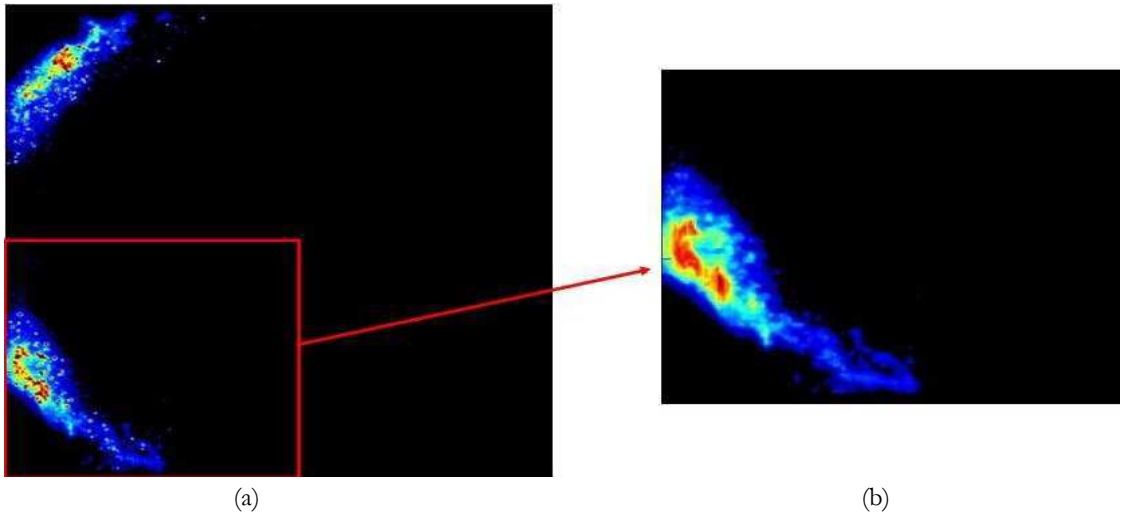

Figure 116: Fluorescence intensity emitted by kerosene vapour and droplets in the combustor (a), example of the removal of droplet fluorescence intensity (b), 480 K and 0.45 MPa (Pilot only).

Figure 116a presents a typical instantaneous raw image of kerosene fluorescence after illumination of the flow in the combustor by the laser sheet from top to bottom. The bright

dots, representing large intensities, correspond to droplets, while fuel vapour is displayed with a false colour scale. The gain of both ICCD cameras is adjusted to keep the energy recorded by the array detector proportional to the fluorescence signal issued from the liquid and gas phases, which prevents the ICCD cameras from local saturation and blooming induced by the liquid kerosene fluorescence. For each flow condition, 200 single-shot images are acquired with each ICCD camera and the maps of mean fluorescence (either from kerosene or OH radical) presented in this article result from the average over these 200 single-shots. Raw fluorescence images are corrected for background luminosity, non-uniformities in the collection optics and inhomogeneity in the laser sheet profile. An average background image is acquired with the laser on in hot air. Subtraction of this image from the fluorescence image accounts for laser scattering and other background luminosity. An average background image is also acquired with the laser off and the flame on in order to remove chemiluminescence emission from the flame. Finally, with the present experiments, it is necessary to add an extra routine which takes account of the presence of kerosene droplets in the flow. Due to the difference of density between the liquid and vapour phases of kerosene, fluorescence signals are significantly larger for the liquid phase. As a result, there is a strong intensity gradient between a droplet and its surrounding vapour. We take advantage of this feature to identify the location of droplets and to eliminate the fluorescence signal from the liquid phase which is initially set to zero. The fluorescence signal at the droplet location is then interpolated over the droplet area using the value of fluorescence intensity from kerosene vapour at the first pixel around the droplet both in the radial and axial directions. Example of this processing is shown in figure 116b. However, considering the difference of density between liquid and vapour phases (typically $\sim 10^2 - 10^3$) and the fact that droplet fluorescence intensity is proportional to its cubic diameter, fluorescence signal from droplets with diameter less than 20 μm cannot be distinguished from fluorescence signal coming from the vapour phase, with the present spatial resolution. This introduces some uncertainty on the maps of local equivalence ratio. The working conditions at higher pressures (cf. table 12) imply also higher levels of air inlet temperature, which reduces the amount of liquid fuel in the measurement volume to an indiscernible level.

7.3 Results

This section presents simultaneous PLIF measurements of kerosene and OH radical at the outlet of the multipoint injector for different operating conditions. Both axial measurements and radial measurements have been performed. In the first part, spatial correlation between kerosene and OH fluorescence is discussed. The second part of the section presents the influence of combustion parameters (temperature, pressure and fuel split between the pilot and the main injectors) on kerosene and OH spatial distributions.

7.3.1 Correlation between OH and kerosene fluorescence

Figure 117 shows a comparison between axial single-shot fluorescence images of OH radical and kerosene for operating condition 590 K and 0.95 MPa ($\Phi_{pilot}/\Phi_{main}=1$). The red contour is used to define the spatial contours of kerosene vapour at the outlet of the injector.

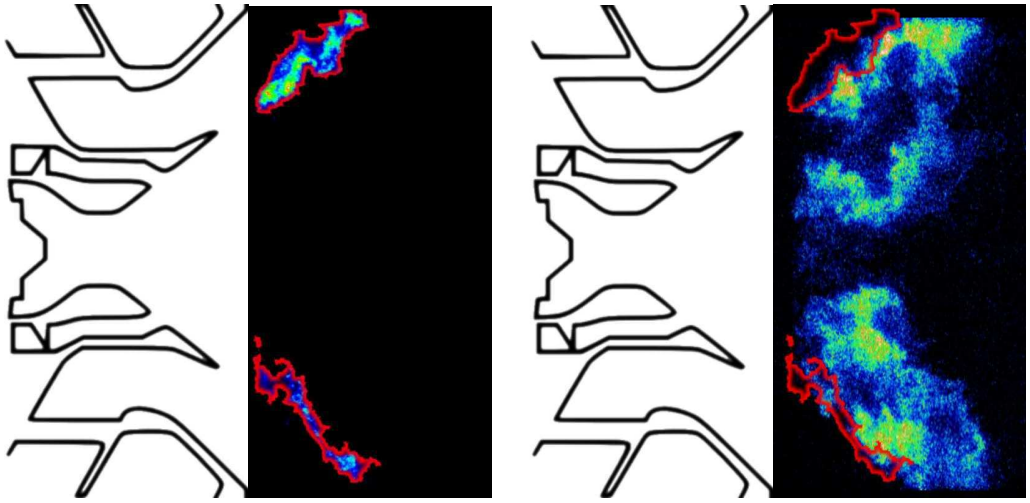

Figure 117: Axial instantaneous image of kerosene (left side) and OH radical (right side) fluorescence for operating condition 590 K and 0.95 MPa ($\Phi_{pilot}/\Phi_{main}=1$).

The main injector has a wide angle and kerosene vapour is mainly located at the edge of the bowl due to swirling effects. As can be seen, a good spatial correlation is obtained between the distribution of kerosene vapour and the location of OH radical, and the respective images can be compared in details. Indeed, for a given condition, small scale structures due to local high levels of turbulence can be observed at the same position on both images. In particular, it is remarkable that kerosene fuel is present at larger distance than OH radical, which suggests that combustion occurs on the inner side of the cone delimitating kerosene. Although OH radical is present both in the flame front and in the region of hot gases, the combined analysis of the simultaneous fluorescence images of kerosene and OH radical allows to determine where the flame front starts. Indeed, it is noticed that the flame front appears at the location where kerosene vapour vanishes, and no "dark zone" is visible. This confirms that, unlike surrogate fuels such as acetone that pyrolyse at significant distance upstream from the flame front, aromatics are consumed within the flame front and their signal remains detectable at temperatures higher than 1000 K. Therefore, in the following, the term "flame front" will refer to the outer edge of the region where OH radical is present.

7.3.2 Influence of combustion parameters

(a) Axial measurements

For axial measurements, the laser sheet propagates from the top to the bottom of the combustor and it is located on its vertical axis.

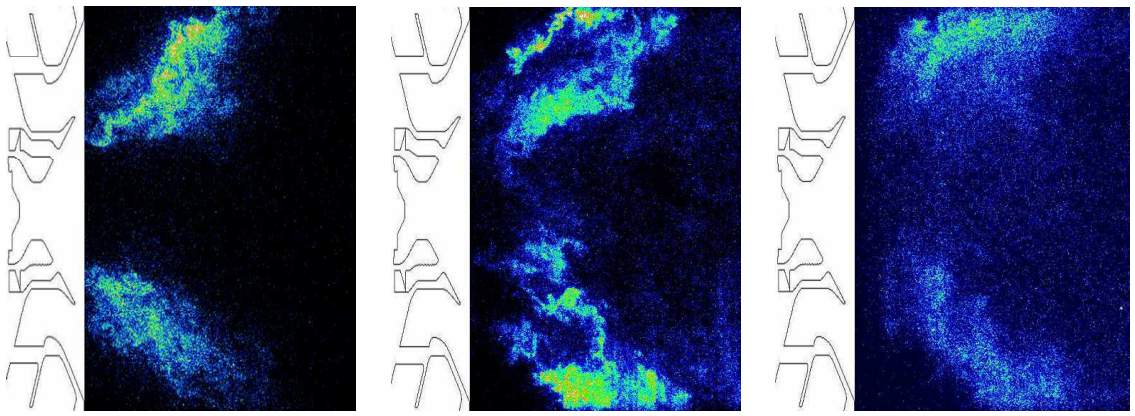

(a) (b) (c)

Figure 118: Axial instantaneous images of OH radical fluorescence for various operating conditions: (a) 480 K and 0.45 MPa (Pilot only), (b) 590 K and 0.95 MPa ($\Phi_{pilot} / \Phi_{main} = 1$), (c) 730 K and 2.2 MPa ($\Phi_{pilot} / \Phi_{main} = 0.1$).

Figure 118 shows axial single-shot images of OH radical fluorescence for various conditions of temperature, pressure and fuel split between the pilot and the main injectors. As can be seen, the flame front is highly stretched by turbulence and wrinkled structures can be clearly identified. In figure 117a, only the pilot injector is used and, therefore, the flame front is located close to the axis of the injector, with a cone-like shape. By contrast, pilot and main injectors are operated with the same equivalence ratio in figure 117b and a double flame structure is noticeable on the image. There are indeed two flame fronts: the one close to the axis comes from the pilot injector, whereas the peripheral flame front can be attributed to the main injector. In figure 118c, kerosene fuel is mainly injected through the main injector and, therefore, the flame front is located at the outer part of the injector.

Figures 119 and 120 show the mean images obtained after average over 200 single laser-shots for the same operating conditions as in figure 118. These images are corrected for laser absorption across the combustor using the classical Beer-Lambert's law, assuming that the flame shape and the spatial distribution of kerosene fuel are axisymmetric.

As can be seen in figure 119, when temperature and pressure increase, the flame tends to slightly move away from the injector. However, in figures 119a and 119b, the pilot injector is

operated, and this injector has a recess of several millimetres compared to the main injector. Therefore, the flame front due to the pilot injector is located at axial locations smaller than the flame front coming from the main injector. Nonetheless, in figure 119c the flame front occurs at larger axial distance from the injector (a few mm) as temperature and pressure increase. Not surprisingly, as the fuel split between the pilot and the main injectors switches from 100 % pilot to ~ 100 % main, the flame front gradually moves to larger radial distance and changes from a cone-like to a bowl-like shape. It is remarkable that the double flame structure remains visible on the average image in figure 119b, which indicates that it is fairly repeatable from one image to the other. In addition, it is noticed that the flame shape is axi-symmetric, which comes from unbalanced airflow through the injector due to the geometry of the kerosene injection strut. Figure 119 also allows to determine flame angle and flame length for the different operating conditions. It is noticed that the flame opens up as pressure and temperature increase and flame angle increases from ~ 95° to ~ 135°. This evolution may be partly attributed to the gradual switch of the repartition of fuel loading between the pilot and the main injectors from 100 % pilot to ~ 100 % main. In addition, flame length also tends to increase from figure 119a to 119c. Nonetheless, fuel split, temperature and air flow rates are different between all these conditions, and it is difficult to determine which parameter most influences the flame length. Finally, very little fluorescence from OH radical is detected on the axis of the combustor, which suggests that OH concentration is very low at that position. Indeed, the recirculation zone located at the outlet of the injector entrains burnt gases and dilution air close to the injector and helps to stabilise the flame. Dilution air quenches chemical reactions in the burnt gases, which reduces OH concentration in the gas mixture recirculating back close to the injector.

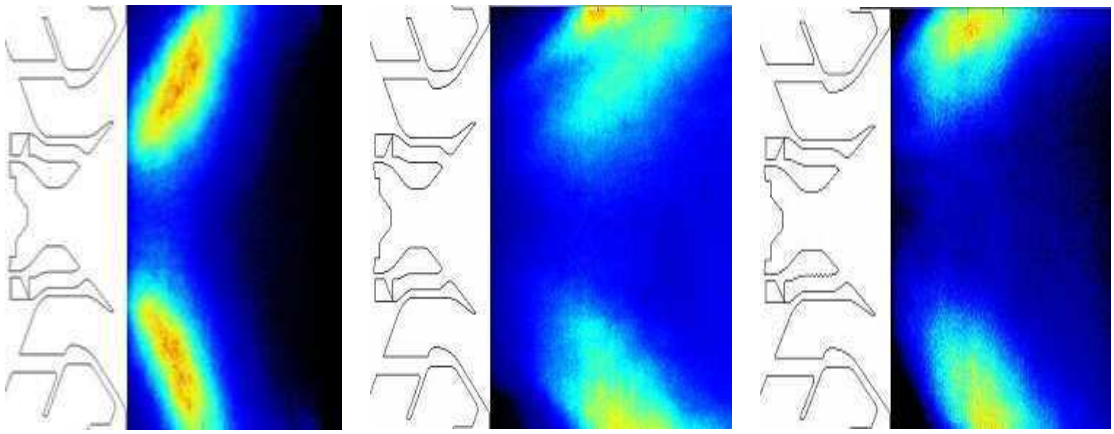

(a) (b) (c)

Figure 119: Axial mean images of OH radical fluorescence for various operating conditions: (a) 480 K and 0.45 MPa (Pilot only), (b) 590 K and 0.95 MPa ($\Phi_{pilot} / \Phi_{main} = 1$), (c) 730 K and 2.2 MPa ($\Phi_{pilot} / \Phi_{main} = 0.1$). Average is performed over 200 instantaneous images.

Similarly to observations with OH radical, figure 120 shows that when fuel injection gradually switches from 100 % pilot to ~ 100 % main, kerosene vapour gradually moves to larger radial distance. In addition, as temperature and pressure increase, the spatial extent of kerosene vapour reduces. Although values of local equivalence ratio are representative of droplet evaporation and mixing efficiency between fuel vapour and air, absolute values displayed in figures 120a to 120c cannot be compared straightforward. Indeed, the operating conditions given in table 1 have different overall equivalence ratio. The exact values cannot be unveiled for confidentiality reasons, but it roughly increases by 50 % from 0.45 to 2.2 MPa. As can be seen in figure 120a, increase of local equivalence ratio is larger than 50 % between figure 120a and 120c. This simply results from higher air inlet temperature at 2.2 MPa, which enhances droplet evaporation.

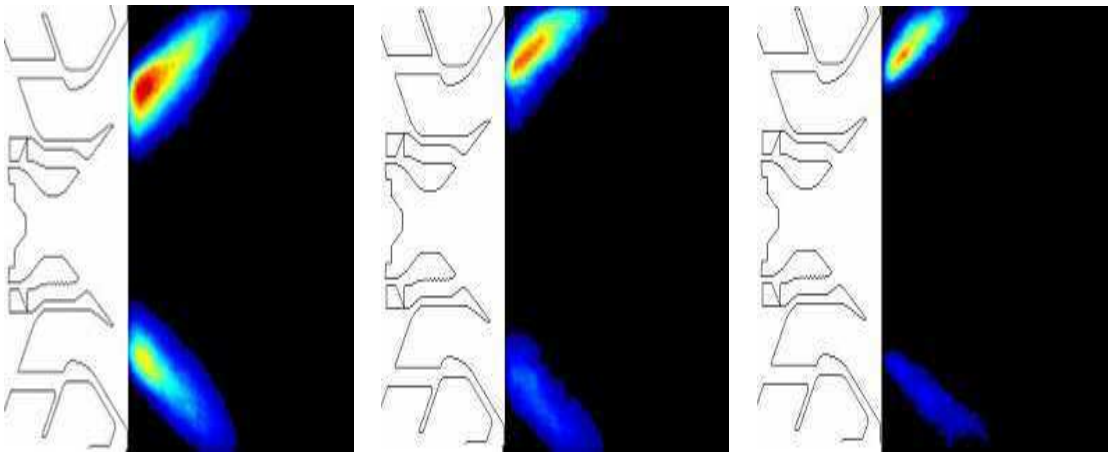

Figure 120: Axial mean images of equivalence ratio for various operating conditions: (a) 480 K and 0.45 MPa (Pilot only), (b) 590 K and 0.95 MPa ($\Phi_{pilot} / \Phi_{main} = 1$), (c) 730 K and 2.2 MPa ($\Phi_{pilot} / \Phi_{main} = 0.1$). Average is performed over 200 instantaneous images.

(b) Radial measurements

For radial measurements, the laser sheet propagates from right to left on the images across the combustor, at different distances downstream from the injector. The focal plane of the images is located on the combustor axis.

Figure 121 shows radial single-shot images of kerosene and OH radical fluorescence for the condition where the pilot and the main injectors are operated with the same equivalence ratio. Images are corrected for distortion due to the angle (~ 30°) between the laser sheet and the ICCD cameras. Figure 122 shows radial mean images corresponding to the same operating conditions, but uncorrected for the distortion.

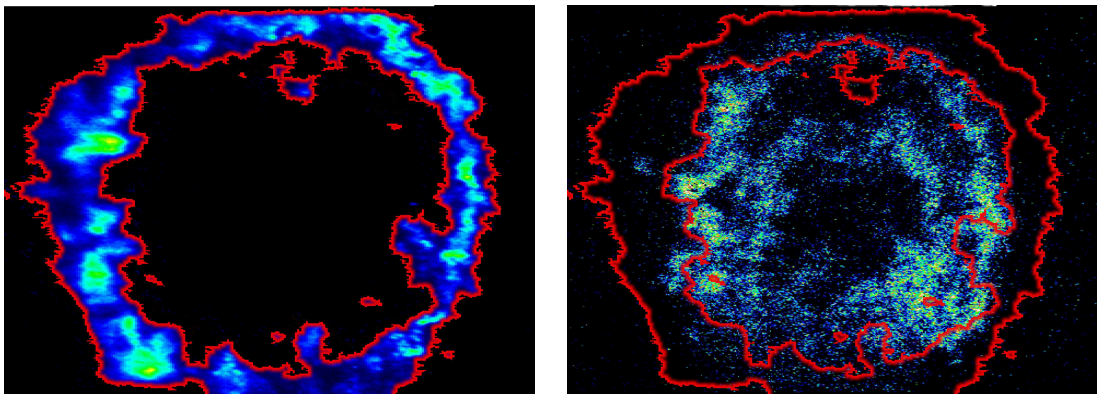

(a) (b)

Figure 121: Radial instantaneous images of kerosene (a) and OH radical (b): 590 K and 0.95 MPa ($\Phi_{pilot} / \Phi_{main} = 1$).

Fluorescence information is missing both on the upper and the lower part for the images, which is due to limited viewing angle of the optical windows. Nor OH or kerosene images have been corrected for absorption of the laser sheet across the combustor, which explains the asymmetry observed between the left and right part of each image. It is noticed that the flame front exhibits a double structure, which is similar to observations from figure 118b. This double structure can also be observed on the average image in figure 122b. Comparison between figures. 121a and 121b (or 122a and 122b) shows that kerosene is located at larger axial distance than OH radical, which indicates that combustion occurs on the inner side of the cone delimitating kerosene. This is in agreement with findings from figure 117.

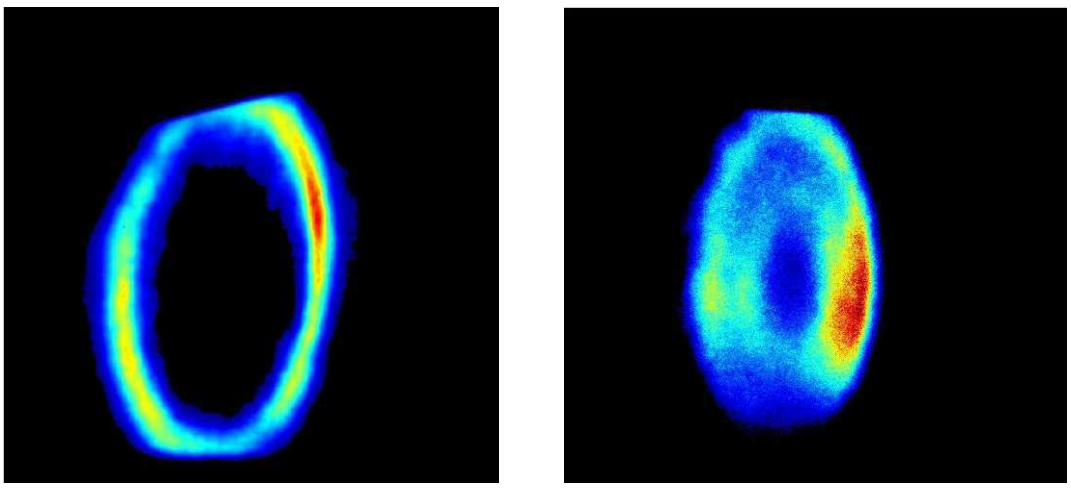

(a) (b)

Figure 122: Radial mean images of kerosene (a) and OH radical (b): 590 K and 0.95 MPa ($\Phi_{pilot} / \Phi_{main} = 1$). Average is performed over 200 instantaneous images.

Finally, the spatial distribution of both kerosene and OH radical are axisymmetric, which confirms results from axial measurements. This suggests that such a multi-point injector can provide a fairly homogeneous repartition of kerosene in the combustor. Therefore, regions with large gradients of fuel concentration should be limited, which may help to achieve stable combustion and low levels of pollutant emissions. In addition, the axisymmetric spatial distributions of kerosene and OH radical obtained with the radial measurements validate the hypothesis used to correct the raw axial images of OH and kerosene fluorescence for laser absorption.

7.4 Conclusion

Simultaneous measurements of planar laser-induced fluorescence applied to OH radical and kerosene were successfully performed at the outlet of a multipoint injector, for various operating conditions (temperature up to 730 K and pressure up to 2.2 MPa). Experiments demonstrate the potential of PLIF technique to visualise simultaneously the flame structure and the spatial distribution of kerosene vapour concentration in a real aeronautical injection system operating at flight conditions. Results can be summarised as follows.

Application of OH-PLIF and kerosene-PLIF to a real aircraft injection system is demonstrated at pressure up to 2.2 MPa. Discrimination of fluorescence of mono-aromatics and di-aromatics is also demonstrated experimentally, which makes possible the quantitative analysis of the present results.

The combined measurements allow the study of the effect of the operating conditions (especially the pressure) on the flame structure as well as the kerosene vapour distribution. Furthermore, the results show good spatial correlation between the repartition of the kerosene vapour and the position of the flame front. The spatial removal of aromatics coincides with the production of OH radicals, which means that aromatics naturally present in kerosene (multi-component fuel) matches the behaviour of the parent fuel. No pyrolysis effect is observed. This result demonstrates the validity of our proposal made for a data processing for kerosene fluorescence, in which kerosene is supposed to be chemically unaltered throughout the measurement zone. This condition is visibly fulfilled as actually the kerosene vapour is observed to diminish exactly where the OH emission occurs.

Chapter 8 Conclusions and recommendations

Nowadays, most of the industrial combustors operate with multi-component liquid fuel sprays (e.g. aircraft engines, gas turbines, internal combustion engine …) in order to improve combustion efficiency by increasing heat and mass transfer surface between fuel and oxidiser. Improving key physical processes such as the evaporation of liquid spray requires the understanding of elementary processes such as droplet evaporation, mixing between fuel and air, interaction with turbulence … The experimental characterization of these processes then requires the use of quantitative non-intrusive laser diagnostics which allow to measure key scalar parameters like the instantaneous spatial distribution of fuel vapour concentration and temperature. Relative to these techniques, Planar Laser-induced Fluorescence (PLIF) is well relevant for measurements of such data in practical combustion systems. This technique based on the excitation of fluorescent tracers requires their selection in regard to their attractive spectroscopic properties (large quantum yield, dependence of their fluorescence upon temperature, pressure, quenching with molecules such as oxygen …). Among possible tracers, aromatics, ketones, di-ketones, other carbonyls and amines that absorb and subsequently fluoresce with broad spectra are attractive candidates. The goal of the present thesis was first to investigate and to compare the fluorescence properties of various ketones (acetone, 3-pentanone) and aromatics (toluene, 1,2,4-trimethylbenzene, naphthalene) versus temperature, pressure and species composition. In a second step, the photophysical data were used to derive strategies for temperature and equivalence ratio measurements. Then, the case of multi-component fuel such as kerosene (Jet A1) was studied in order to explore and exploit the kerosene fluorescence for measurements of temperature and fuel vapour concentration in real combustion engines. For that purpose, a spectroscopic study similar to those performed on pure tracers was reproduced. The data processing of the resulting measurements highlighted the possibility to detect simultaneously the fluorescence of various aromatics (mono- and di-aromatics) naturally present in kerosene for measuring the vapour fuel concentration. A demonstration of the application of kerosene-PLIF on an innovative aeronautic injection system running with liquid kerosene was thus performed in real operating flight conditions (pressure temperature inlet of air inside the combustion chamber up to 2.2 MPa and up to 800 K respectively).

In parallel to this experimental work, a development of a physically-based model of fluorescence yield with empirically-determined parameters was performed for naphthalene and toluene. By the light of the agreement between simulation and experimental data, the fluorescence model developed for both molecules represents, to our knowledge, a significant advance for providing in the future a qualitative and quantitative description of fluorescence behaviour of larger polyatomic tracers.

The following sections summarize the major accomplishments and results on the experimental spectroscopy of the molecular organic species and associated models for probing the fuel vapour. Recommendations for future work in the area of quantitative, high pressure fluorescence measurements in two-phase combustion flows are also discussed.

8.1 Summary and conclusions

8.1.1 High-pressure high-temperature cell

An experimental facility has been specifically developed and applied to investigate laser diagnostic spectroscopic experiments on organic molecules in high-pressure high-temperature gaseous environments. This facility includes: (1) a high pressure cell constructed with standard stainless-steel materials allowing experiments at pressure up to 3.0 MPa; (2) a heating wire allowing the heating of the gaseous molecular species mixture inside the cell at temperatures up to 900 K; (3) optical access with 4 cm clear aperture on three sides. The optical cell and associated flow controls were designed to operate with gaseous organic molecules/O_2/N_2 flows although they can readily accommodate with other gaseous constituents. The gaseous mixture flowing into the cell was produced from a "controller evaporator and mixer" system which guarantees well-defined molar fractions of the probed gaseous mixture. Continuous and constant evaporation is then achieved by forcing the buffer gas and the atomized liquid molecular organic species in a fine heated capillary.

The operating flow conditions inside the high-pressure high-temperature cell were regulated by mass flow transducers for both phases (liquid and gas). A PID temperature regulation was applied to control the heating process of the wire. Finally, temperature and pressure into the cell were controlled respectively by means of thermocouples and pressure transducers.

The fluorescence measurements were performed by exciting fluorescent organic molecules by UV pulses from the frequency-quadrupled output of a Nd:YAG laser at 266 nm. The control of incident beam intensity and the beam attenuation inside the cell (i.e. absorption measurements) were controlled by fast photodiodes placed prior to and after the cell.

The fluorescence spectrum of the illuminated tracer vapour was collected at right angle from the laser beam axis by a spectrograph coupled with an ICCD camera.

The experimental set-up was fully computer controlled via a home-made program written in LABVIEW. Additional specific data processing codes of fluorescence and absorption measurements were also developed to guarantee reliably information and to fulfil the requirements of the tasks performed in the present thesis.

8.1.2 Photophysical properties of pure organic molecules

Fluorescence diagnostics are usually performed on various molecular organic species for temperature and vapour fuel concentration measurements. The choice of a reliable tracer for such measurements is motivated by its photophysical properties which are a trade-off between e.g. oscillator strength of the absorption feature and the accessibility of the transition by an excitation laser source. The fluorescence molecules selected in the present thesis belong to two organic molecules classes. Due to its quasi insensitivity towards oxygen quenching, aliphatic ketones like acetone and 3-pentanone are selected as potential fluorescence markers allowing the indirect measurement of local fuel concentration, when doped to a non fluorescing surrogate fuel. From the monocyclic benzene derivatives, the toluene and 1,2,4-trimethylbenzene have been chosen as fluorescence markers due respectively to its affinity to commercial gasoline and its relevance within the composition of kerosene fuel (Jet A1). Tracers molecules selected from ketones and monocyclic benzene derivatives might also represent the high to medium volatility fraction of petroleum type fuels. The fraction of lower volatility compounds could be addressed by polycyclic aromatic compounds. Since larger tracer compounds are often more stable, they might also be traced nearer to the flame front, where small tracers already have decomposed. Within this study, the naphthalene molecule was also selected for its relevance within the composition of kerosene fuel, based on both a chromatographic fuel analysis and spectroscopic measurements reported in preceding studies. For all the probed molecules, absorption cross-sections, fluorescence quantum yields and fluorescence quenching efficiencies by oxygen after excitation at 266 nm have been systematically measured in the temperature range of 300 – 950 K in nitrogen, and from 300 – 700 K when oxygen was present. Experiments were also performed for pressure ranging between 1 and 3.0 MPa in order to predict their capabilities to be used in real combustion engines.

Several conclusions can be drawn from the experimental data.

Although the experimental challenges of seeding and monitoring the vapour phase concentration of such candidates must be overcome, the photophysical data gathered from such tracers are unique as illustrated by the different observed dependences of fluorescence with temperature, pressure and species composition recorded in the cell.

For all the probed molecules, the fluorescence signals exhibit a decrease with rising temperature. Mono-aromatic molecules like toluene and 1,2,4-trimethylbenzene display the stronger dependence on temperature decreasing by more than one order of magnitude on the explored temperature range. The fluorescence yields exhibit strong dependence on temperature decreasing by three orders of magnitude. Fluorescence is also subject to oxygen quenching as shown by the Stern-Volmer plots displaying large sensitivities of fluorescence with the partial pressure of oxygen. Finally, a decrease of fluorescence is also observed when pressure increases. Note that this effect is less pronounced for 1,2,4-trimethylbenzene what makes it a better candidate for high-pressure experiments. In contrast to mono-aromatics photophysics, ketone molecules display different fluorescence behaviours. Thus, the decrease of the fluorescence yields with increasing temperature is less pronounced (less than one order of magnitude) on the explored temperature range. The effect of pressure on fluorescence is on opposition to the mono-aromatics as illustrated by a significant increase of fluorescence with increasing pressure in the pressure range investigated. Finally, fluorescence is quite insensitive to oxygen excepted at low temperature where the Stern-Volmer factor becomes dependent with the partial pressure of oxygen. Photophysical properties of naphthalene combine the properties of mono-aromatics and ketones, i.e. a fluorescence behaviour with temperature and pressure comparable to the ketone ones and a strong dependence of fluorescence with the partial pressure of oxygen. Note that this effect is largely pronounced for naphthalene in comparison with those observed for mono-aromatics.

Absolute comparison between the photophysical properties of the different tracers highlights their attractive properties for measuring scalar parameters inside a flow. The distinct temperature- and oxygen-dependence of fluorescence for all the tracers probed in the present thesis offers a multitude of possibilities for quantitative measurements of temperature and oxygen concentration in addition to the fuel-to-air ratio. Thus, the use of fluorescence tracers with different boiling points allows now to probe many conventional fuels, including Diesel and jet engines. While the study of single tracers provides a large area for exploration, the use of combinations of tracers also expands the field of investigation even further. The potential use of oxygen-sensitive and oxygen-insensitive tracer combinations for oxygen imaging could be proposed. This approach is also the suitable strategy retained for multi-component fuel like kerosene.

8.1.3 Photophysical properties of a multicomponent fuel (kerosene)

Kerosene fluorescence spectrum presents a double structure arising from the fluorescence of the aromatics naturally present into the fuel. Identification of the main molecular species responsible for this fluorescence was achieved by comparison with the reference spectra of different pre-selected single-ring and two-ring aromatics. The dependence of kerosene vapour fluorescence on temperature, pressure and O_2 partial pressure yields then possibilities

for measuring fuel-to-air ratio in kerosene/air flows using kerosene vapour-PLIF. The experimental method consists to record on two separate detection channels (i.e. two ICCD cameras with adequate optical filters) the fluorescence delivered by mono- and di-aromatics after an excitation at 266 nm. The data processing of both fluorescence signals coupled with the knowledge of the evolution of the fluorescence signals with temperature, pressure and species composition acquired in the high-pressure high-temperature cell allow to measure locally and instantaneously the distribution of temperature and fuel-to-air ratio.

8.1.4 PLIF measurements in an aero-engine combustor

Simultaneous measurements of planar laser-induced fluorescence applied to OH radical and kerosene were performed at the outlet of a multipoint injector, for various operating conditions (temperature up to 800 K and pressure up to 2.2 MPa). The measurements performed in the present thesis under fired operation demonstrate the potential of PLIF technique to visualise simultaneously the flame structure and the spatial distribution of kerosene vapour concentration in a real aeronautical injection system operating at flight conditions. Results can be summarised as follows:

- Application of OH-PLIF and kerosene-PLIF to a real aircraft injection system is demonstrated at pressure up to 2.2 MPa. Discrimination of fluorescence of mono-aromatics and di-aromatics is also demonstrated experimentally, which makes possible the quantitative analysis of the present results.
- Results show good spatial correlation between the distribution of kerosene vapour and the position of the flame front. The spatial removal of aromatics coincides with the production of OH radicals, which means that aromatics naturally present in kerosene (multi-component fuel) matches the behaviour of the parent fuel without any pyrolysis effect.

8.1.5 Generation of fluorescence model for naphthalene and toluene

In parallel to this experimental work, a semi-empirical model based on photophysical considerations has been developed for predicting the fluorescence of naphthalene and toluene that satisfactorily describes the available experimental data. It can predict signal intensities for higher oxygen partial pressures (up to 3.0 MPa of air) within the investigated temperature range (350 – 900 K). The physical mechanisms playing a significant role on the emission of fluorescence (excitation, oxygen quenching, vibrational relaxation, temperature effects …) have been introduced and semi-empirical key parameters relative to the description of these relevant mechanisms have been deduced from the experimental data. In particular, the effects of oxygen quenching over the different deactivation pathways like the vibrational re-

laxation have been properly taken into account. Furthermore, new semi-empirical laws for the excitation energy dependence of radiative and non-radiative decay rates for naphthalene and toluene were established.

8.2 Recommendations for further study

The current study suggests numerous fruitful avenues for further exploration, both in characterizing photophysical behaviour of new PLIF tracers and in extending and applying the tracers PLIF techniques to flows of practical interest.

In complement of measurements of fuel-air mixture fraction and temperature distribution in a variety of applications, potentially for basic fluid and heat transfer studies, but more likely in high pressure combustion engines running with kerosene, organic molecules-PLIF diagnostics could be useful to tackle new problems interesting automotive and aeronautic industries which are faced with growing concerns on pollutant and greenhouse gas emissions. The development of cleaner and more efficient engines therefore requires advanced diagnostics to obtain detailed information on the physical processes occurring inside the combustion chambers and provides pertinent guidelines for combustion chamber design and optimization. One perspective of improvement of combustion in the future is the use of alternative fuels like biofuels which appears to be a straightforward way to reduce combustion generated greenhouse gas emissions. However, the effect of biofuel addition into conventional fuel on the combustion process is not well understood. A better comprehensive understanding could enable improved optimization of combustion engines. However, significant changes of the fuel properties occur when biofuels are mixed with standard fuels or used as pure fuels for instance with regard to the evaporation properties. As a consequence, it is expected that processes of mixture formation, combustion and pollutant formation would be affected. Using organic molecules-PLIF diagnostic would be then useful for the evaluation of the consequence of biofuel addition on mixture formation in both aeronautic and automotive combustion chamber configurations. This experimental approach would require the use of "conventional tracers" like the ones studied in the present thesis but also new organic compounds with boiling points well-matched with the biofuels ones (for instance, boiling point up to 340-380 °C for Ester molecules)

The development of more physically-detailed models would be also useful in the future to extend the understanding and quantifying of photophysics of other classes of organic molecules in larger domains of temperature and pressure. For a better understanding of the excited state dynamics of organic molecules, more sophisticated approaches would be required in addition to a full experimental fluorescence investigation. Fluorescence data could provide useful model benchmarks, for instance, measurements of the fluorescence high pressure limit as a function of temperature. However, fluorescence data alone may not explain

the details of mechanisms required to quantitatively understand the dynamic of energy transfer in the excited state, as illustrating by the multiple possible pathways for oxygen quenching. Simultaneous product formation measurements, e.g., of singlet oxygen, would thus provide additional insight. In addition to studying oxygen-induced decay mechanisms, more direct vibrational energy transfer studies with ultrashort laser pulse would serve to propose a better vibrational energy transfer model.

Appendix

A-1 Parameters used within the naphthalene yield simulation

Table 13: Parameters used in parameterised expression for non-radiative and radiative rates to apply to equation (5.27) and (5.28), section 5.8.1(b). Coefficients were determined within non-linear least square problem while searching the optimal fit of the naphthalene yield simulation to our relative yield data. The proximity to absolute yield data from [Hsieh 1974] and [Hall 1976] was accounted for. The rates are depicted in the top and the resulting yields in the bottom diagram of figure 87, section 5.8.1(b).

k_{nr}	y_0	x_c	A	w	a_3	a_4
equ. (5.27)	$-6.7024 \cdot 10^6$	60203	$7.2144 \cdot 10^{12}$	6675.2	1.4702	1.5029
k_f	α_1	α_2	α_3	α_4	α_5	
equ. (5.28)	6.2365	7.0973	32675	664.87	0.36052	

Table 14: Parameters of collisional energy transfer.

$$\Delta E_{coll} = \frac{1}{k_{coll}} \sum_i \left[Z_i n_i \cdot \alpha_i \left(E - E_{th}\right) \cdot \left(\frac{T}{300}\right)^{\beta_i} \right] \text{ with } T \text{ in K and } k_{coll} = \sum_i Z_i n_i$$

Z_i... collision frequencies from Lennard-Jones parameters from naphthalene, methane and nitrogen:

[Kimura 2004]: $\sigma_{N_2} = 3.74$ Å; $\epsilon_{N_2} / k_B = 82$ K

[Reid 1987]: $\sigma_{Naph} = 6.45$ Å; $\epsilon_{Naph} / k_B = 554.4$ K

[Hippler 1983]: $\sigma_{CH_4} = 3.79$ Å; $\epsilon_{CH_4} / k_B = 153$ K

α_{N_2}	β_{N_2}	α_{Naph}	β_{Naph}	α_{CH4}	β_{CH4}
0.010	1.2212	0.20107	0 *	0.02956	0 *

Parameters with * for naphthalene and methane are set to zero value, since no temperature dependent data was accessible.

A-2 Parameters used within the toluene yield simulation

Table 15: Coefficients α_i used in parameterised rate expression, cf. modified Boltzmann function defined in equation (5.29), section 5.8.1(b). Coefficients were determined within non-linear least square problem while searching the optimal fit of the toluene yield simulation to the relative yield data from [Koban 2004]. The proximity to absolute yield data from [Burton 1968] was accounted for. The rates are depicted in the top and the resulting yields in the bottom diagram of figure 90, section 5.8.1(b).

Rate	Case / Symbol	α_1	α_2	α_3	α_4	α_5
k_{nr}	(a) —	5.78	11.97	37090	824.7	0.1537
	(b) --	6.666	11.76	38860	804.3	0.2207
k_f	(a) —	6.629	7.491	39840	392.6	0.313
	(b) --	6.622	7.717	40910	636.5	0.824

Table 16: Parameters of collisional energy transfer

$$\Delta E_{coll} = \frac{1}{k_{coll}} \sum_i \left[Z_i n_i \cdot \alpha_i (E - E_{th}) \cdot \left(\frac{T}{300} \right)^{\beta_i} \right] \text{ with } T \text{ in K and } k_{coll} = \sum_i Z_i n_i$$

Z_i... collision frequencies from Lennard-Jones parameters from toluene and nitrogen:

[Kimura 2004]: $\sigma_{N_2} = 3.74$ Å; $\epsilon_{N_2} / k_B = 82\,\mathrm{K}$

[Lee 1969]: $\sigma_{Tol} = 5.932$ Å; $\epsilon_{Tol} / k_B = 377\,\mathrm{K}$

case (a) — $\Rightarrow$ $\alpha_{N_2} = 0.042376$; $\beta_{N_2} = 4.716$; $\alpha_{Tol} = 0.3751$; $\beta_{Tol} = 1.6528$

case (b) -- $\Rightarrow$ $\alpha_{N_2} = 0.01903$; $\beta_{N_2} = 9.5365$; $\alpha_{Tol} = 0.59372$; $\beta_{Tol} = -11.022$

References

Amanatidis 2001 — Amanatidis, G.T., European research on the atmospheric effects of aviation and the CORSAIRE project cluster, Air & Space Europe 3, 3-4 (2001), pp.238–240.

Angeli 2005 — Angeli, C.; Borini, S.; Ferrighi, L.; Cimiraglia, R., A CASSCF theoretical study of the vibrational frequencies and structure of formaldehyde, acetaldehyde and acetone valence excited states, Journal of Molecular Structure: THEOCHEM 718, 1-3 (2005), pp.55–69.

Appuhn 1997 — Appuhn, M.; Ruhnke, R.; Moortgat, G.; Meller, R.; Schneider, W. (1997), UV/VIS-Adsorption cross-sections and quantum yields for use in photochemistry and atmospheric modelling, Part 2: Organic substances. (Berichte des Forschungszentrums Jülich, JUEL-3341).

Archer 1973 — Archer, A.S.; Cundall, R.B.; Evans, G.B.; Palmer, T.F., The Effect of Temperature, Pressure, and Excitation Wavelength on the Photoluminescence of Acetaldehyde Vapour, Proceedings of the Royal Society of London. Series A, Mathematical and Physical Sciences 333, 1594 (1973), pp.385–402.

Arnold 1990a — Arnold, A.; Becker, H.; Hemberger, R.; Hentschel, W.; Ketterle, W.; Kollner, M. et al., Laser in situ monitoring of combustion processes, Appl. Opt. 29, 33 (1990), pp.4860–4872.

Arnold 1990b — Arnold, A.; Becker, H.; Suntz, R.; Monkhouse, P.; Wolfrum, J.; Maly, R.; Pfister, W., Flame front imaging in an internal-combustion engine simulator by laser-induced fluorescence of acetaldehyde, Opt. Lett. 15, 15 (1990), pp.831–833.

Arnold 1993 — Arnold, A.; Buschmann, A.; Cousyn, B.; Decker, M.; Vannobel, F.; Sick, V.; Wolfrum, J., Simultaneous imaging of fuel and hydroxyl radicals in an in-line four cylinder SI-engine, SAE Paper 932696 (1993).

Arnold 2000 — Arnold, A.; Bombach, R.; Hubschmid, W.; Inauen, A.; Käppeli, B., Fuel-oil concentration in a gas turbine burner measured with laser-induced fluorescence, Experiments in Fluids 29, 5 (2000), pp.468–477.

Ashpole 1971 — Ashpole, C.W.; Formosinho, S.J.; Porter, G., Pressure Dependence of Intersystem Crossing in Aromatic Vapours, Proceedings of the Royal Society of London. Series A, Mathematical and Physical Sciences 323, 1552 (1971), pp.11–28.

Astholz 1982 — Astholz, D.C.; Croce, A.E.; Troe, J., Temperature dependence of the ozone absorption coefficient in the Hartley continuum, The Journal of Physical Chemistry 86, 5 (1982), pp.696–699.

Atakan 1997 — Atakan, B.; Heinze, J.; Meier, U.E., OH laser-induced fluorescence at high pressures: spectroscopic and two-dimensional measurements exciting the A–X (1,0) transition, Applied Physics B Lasers and Optics 64, 5 (1997), pp.585–591.

Atkins 2008 — Atkins, P.; Friedman, R., Molecular quantum mechanics, Oxford Univ. Press, Oxford (2008).

Avouris 1977 — Avouris, P.; Gelbart, W.M.; El-Sayed, M.A., Nonradiative electronic relaxation under collision-free conditions, Chemical Reviews 77, 6 (1977), pp.793–833.

Baba 1985 — Baba, M.; Hanazaki, I.; Nagashima, U., The $S_1(n, \pi^*)$ states of acetaldehyde and acetone in supersonic nozzle beam: Methyl internal rotation and C=O out-of-plane wagging, J. Chem. Phys. 82, 9 (1985), pp.3938–3947.

Bae 2000 — Bae, S.Y.; Lee, I.-J.; Park, J., Methylation effects on the collisional quenching of vibrationally excited benzene derivatives by unexcited parent molecules, Chemical Physics 255, 1 (2000), pp.103–110.

Baranger 2004 — Baranger, P. (2004), Détection du kérosène par imagerie de fluorescence induite par laser, pour application sur foyer aéronautique, PhD Thesis, University Paris XI.

Baranger 2005 — Baranger, P.; Orain, M.; Grisch, F., Fluorescence spectroscopy of kerosene vapour: Application to gas turbines, 43rd AIAA Aerospace Sciences Meeting and Exhibit - Meeting Papers, AIAA 2005-828 (2005).

Baritaud 1992 — Baritaud, T.A.; Heinze, T.A., Gasoline Distribution Measurements with PLlF in a SI Engine, SAE Technical Paper Series, 922355 (1992).

Barkova 1987 Barkova, L.A.; Gruzinskii, V.V.; Kaputerko, M.N., Quenching and stabilisation of the fluorescence of anthracene vapor by xenon, Journal of Applied Spectroscopy 47, 2 (1987), pp.786-789-789.

Bass 1950 Bass, A.M., Fluorescence Studies of Some Simple Benzene Derivatives in the Near Ultraviolet: II. Toluene and Benzonitrile, J. Chem. Phys. 18, 10 (1950), pp.1403–1410.

Beck 1980 Beck, S.M.; Hopkins, J.B.; Powers, D.E.; Smalley, R.E., Jet-cooled naphthalene. II. Single vibronic level fluorescence spectra, The Journal of Chemical Physics 74, 1 (1980), pp.43–52.

Becker 1969 Becker, R.S.; Dolan, E.; Balke, D.E., Vibronic Effects in Photochemistry – Competition between Internal Conversion and Photochemistry, J. Chem. Phys. 50, 1 (1969), pp.239–245.

Becker 2003 Becker, J.; Hassa, C., Liquid Fuel Placement and Mixing of Generic Aeroengine Premix Module at Different Operating Conditions, Journal of Engineering for Gas Turbines and Power 125, 4 (2003), pp.901–908.

Beddard 1974 Beddard, G.S.; Fleming, G.R.; Gijzeman, O.L.J.; Porter, G., Vibrational Energy Dependence of Radiationless Conversion in Aromatic Vapours, Proceedings of the Royal Society of London. Series A, Mathematical and Physical Sciences 340, 1623 (1974), pp.519–533.

Beddard 1973 Beddard, G.S.; Formosinho, S.J.; Porter, G., Pressure effects on the fluorescence from naphthalene vapour, Chemical Physics Letters 22, 2 (1973), pp.235–238.

Berckmüller 1994 Berckmüller, M.; Tait, N.P.; Lockett, R.D.; Greenhalgh, D.A.; Ishii, K.; Urata, Y. et al., In-cylinder crank-angle-resolved imaging of fuel concentration in a firing spark-ignition engine using planar laser-induced fluorescence, Twenty-Fifth Symposium (International) on Combustion, Symposium (International) on Combustion 25, 1 (1994), pp.151–156.

Bernardi 1996 Bernardi, F.; Olivucci, M.; Robb, M.A., Potential energy surface crossings in organic photochemistry, Chemical Society Reviews 25, 5 (1996), pp.321–328.

Bernath 1995 Bernath, P.F., Spectra of atoms and molecules, Topics in physical chemistry, Oxford university press, New York, Oxford (1995).

Beyer 1973 Beyer, T.; Swinehart, D.F., Algorithm 448: number of multiply-restricted partitions, Communications of the ACM 16, 6 (1973), p.379.

Bilger 1989 — Bilger, R.W., Turbulent Diffusion Flames, Annual Review of Fluid Mechanics 21, 1 (1989), pp.101–135.

Bolovinos 1982 — Bolovinos, A.; Philis, J.; Pantos, E.; Tsekeris, P.; Andritsopoulos, G., The methylbenzenes vis-à-vis benzene, Comparison of their spectra in the valence-shell transitions region, Journal of Molecular Spectroscopy 94, 1 (1982), pp.55–68.

Bowen 1956 — Bowen, E.J.; Veljkovic, S., The Enhancement of the Fluorescence of Vaporus, Proceedings of the Royal Society of London. Series A, Mathematical and Physical Sciences 236, 1204 (1956), pp.1–6.

Brasseur 1998 — Brasseur, G.P.; Cox, R.A.; Hauglustaine, D.; Isaksen, I.; Lelieveld, J.; Lister, D.H. et al., European scientific assessment of the atmospheric effects of aircraft emissions, Atmospheric Environment 32, 13 (1998), pp.2329–2418.

Brockhinke 2006 — Brockhinke, A.; Letzgus, M.; Rinne, S.; Kohse-Hoinghaus, K., Energy Transfer in the $d^3\Pi_g - a^3\Pi_u$ (0−0) Swan Bands of C_2: Implications for Quantitative Measurements, The Journal of Physical Chemistry A 110, 9 (2006), pp.3028–3035.

Brouwer 1985 — Brouwer, L.D.; Hippler, H.; Lindemann, L.; Troe, J., Measurement of internal energies by hot ultraviolet absorption spectroscopy: spectra of excited azulene molecules, The Journal of Physical Chemistry 89, 21 (1985), pp.4608–4612.

Brown 1974 — Brown, R.G.; Phillips, D., Quenching of the first excited singlet state of substituted benzenes by molecular oxygen, Journal of the Chemical Society, Faraday Transactions 2: Molecular and Chemical Physics 70 (1974), pp.630–636.

Brown 1975 — Brown, R.G.; Rockley, M.G.; Phillips, D., Collisional effects on the fluorescence of p-fluorotoluene vapour, Chemical Physics 7, 1 (1975), pp.41–51.

Bruneaux 2010 — Bruneaux, G.; Di Lella, A.; Kashdan, J.; Stark, L.; Ledier, C.; Orain, M.G.F., BIOPTIC: Optical diagnostic techniques for biofuels, 2nd seminar of the Enerbio research fund, Rueil-Malmaison, France, 2010.

Bryant 1997 — Bryant, R.A.; Donbar, J.M.; Driscoll, J.F., Acetone LIF flow visualization at temperatures below 300 K, AIAA, Aerospace Sciences Meeting & Exhibit, 35th, Reno, NV, Jan. 6-9, 1997, AIAA Paper 97-0156 (1997).

Bryant 2000 — Bryant, R.A.; Donbar, J.M.; Driscoll, J.F., Acetone laser induced fluorescence for low pressure/low temperature flow visualization, Experiments in Fluids 28, 5 (2000), pp.471–476.

Burri 2004 Burri, J.; Crockett, R.; Hany, R.; Rentsch, D., Gasoline composition determined by 1H NMR spectroscopy, Fuel 83, 2 (2004), pp.187–193.

Burton 1968 Burton, C.S.; Noyes, A.W.[JR.]., Electronic energy relaxation in toluene vapor, The Journal of Chemical Physics 49, 4 (1968), pp.1705–1714.

Caldeira-Pires 2001 Caldeira-Pires, A., Free radical imaging techniques applied to hydrocarbon flames diagnosis, Journal of Thermal Science 10, 2 (2001), pp.182–187.

Carter 1998 Carter, C.D.; Donbar, J.M.; Driscoll, J.F., Simultaneous CH planar laser-induced fluorescence and particle imaging velocimetry in turbulent non-premixed flames, Applied Physics B: Lasers and Optics 66, 1 (1998), pp.129–132.

Cheng 2002 Cheng, B.-M.; Bahou, M.; Chen, W.-C.; Yui, C.-h.; Lee, Y.-P.; Lee, L.C., Experimental and theoretical studies on vacuum ultraviolet absorption cross-sections and photodissociation of CH_3OH, CH_3OD, CD_3OH, and CD_3OD, Journal of Chemical Physics 117, 4 (2002), p.1633.

Cogan 2007 Cogan, S.; Haas, Y.; Zilberg, S., Intersystem crossing at singlet conical intersections, Theoretical Aspects of Photoinduced Processes in Complex Systems, Journal of Photochemistry and Photobiology A: Chemistry 190, 2-3 (2007), pp.200–206.

Collins 2007 Collins, C.D., Implementing Phytoremediation of Petroleum Hydrocarbons, Phytoremediation, Methods in biotechnology Volume 23, Humana press (2008).

Coulson 1952 Coulson, C.A., Alkyl Shifts in Absorption Spectra of Azulene and other Aromatic Molecules, Proceedings of the Physical Society. Section A 65, 11 (1952), p.933.

Dagaut 2006 Dagaut, P.; Cathonnet, M., The ignition, oxidation, and combustion of kerosene: A review of experimental and kinetic modeling, Progress in Energy and Combustion Science 32, 1 (2006), pp.48–92.

Damm 1991 Damm, M.; Deckert, F.; Hippler, H.; Troe, J., Isomerization and collisional deactivation of highly vibrationally excited azulene molecules after UV excitation at 248 and 193 nm, The Journal of Physical Chemistry 95, 5 (1991), pp.2005–2009.

Dasch 1984 Dasch, C.J., Continuous-wave probe laser investigation of laser vaporization of small soot particles in a flame, Applied Optics 23, 13 (1984), pp.2209–2215.

Davy 2003 — Davy, M.; Williams, P.; Han, D.; Steeper, R., Evaporation characteristics of the 3-pentanone–isooctane binary system, Experiments in Fluids 35, 1 (2003), pp.92–99.

Dawson 1998 — Dawson, M.; Hochgreb, S., Liquid fuel visualization using laser-induced fluorescence during cold start, SAE Technical Paper Series 982466 (1998).

Devillers 2009 — Devillers, R.; Bruneaux, G.; Schulz, C., Investigation of toluene LIF at high pressure and high temperature in an optical engine, Applied Physics B: Lasers and Optics 96, 4 (2009), pp.735–739.

Dexter 1953 — Dexter, D.L., A Theory of Sensitized Luminescence in Solids, J. Chem. Phys. 21, 5 (1953), pp.836–850.

Dietz 1982 — Dietz, T.G.; Duncan, M.A.; Smalley, R.E., Time evolution studies of triplet toluene by two-color photoionization, J. Chem. Phys. 76, 3 (1982), pp.1227–1232.

Dolson 1983 — Dolson, D.A.; Holtzclaw, K.W.; Lee, S.H.; Munchak, S.; Parmenter, C.S.; Stone, B.M.; Knight, A.E.W., Intramolecular Vibrational Redistribution at Low State Densities in S1 Aromatics. Evidence for Rotational Contributions, Laser Chemistry 2, 5-6 (1983), pp.271–283.

Draeger 1985 — Draeger, J.A., The methylbenzenes-I. Vapor-phase vibrational fundamentals, internal rotations and a modified valence force field, Spectrochimica Acta Part A: Molecular Spectroscopy 41, 4 (1985), pp.607–627.

Dreier 2002 — Dreier, T.; Ewart, P., Coherent Techniques for Measurements with Intermediate Concentrations, Book chapter, Applied combustion diagnostics by K. Kohse-Höinghaus and J. B. Jeffries, Combustion, Taylor & Francis, New York (2002).

Dreizler 2002 — Dreizler, A.; Janicka, J., Diagnostic challenges for gas turbine combustor model validation, Book chapter, Applied combustion diagnostics by K. Kohse-Höinghaus and J. B. Jeffries, Combustion, Taylor & Francis, New York (2002).

Dyakov 2005 — Dyakov, Y.A.; Ni, C.K.; Lin, S.H.; Lee, Y.T.; Mebel, A.M., Photodissociation of Azulene at 193 nm: Ab Initio and RRKM Study, The Journal of Physical Chemistry A 109, 39 (2005), pp.8774–8784.

Eckbreth 1977 — Eckbreth, A.C., Effects of laser-modulated particulate incandescence on Raman scattering diagnostics, Journal of Applied Physics 48, 11 (1977), pp.4473–4479.

Eckbreth 1996 — Eckbreth, A.C., Laser diagnostics for combustion temperature and species, Combustion science and technology 3, Gordon & Breach, Amsterdam (1996).

Edwards 2001 — Edwards, T.; Maurice, L.Q., Surrogate mixtures to represent complex aviation and rocket fuels, Journal of Propulsion and Power 17, 2 (2001), pp.461–466.

Einecke 2000 — Einecke, S.; Schulz, C.; Sick, V., Measurement of temperature, fuel concentration and equivalence ratio fields using tracer LIF in IC engine combustion, Applied Physics B: Lasers and Optics 71, 5 (2000), pp.717–723.

Espey 1997 — Espey, C.; Dec, J.E.; Litzinger, T.A.; Santavicca, D.A., Planar laser Rayleigh scattering for quantitative vapor-fuel imaging in a diesel jet, Combustion and Flame 109, 1-2 (1997), pp.65–86.

Etzkorn 1999 — Etzkorn, T.; Klotz, B.; Sørensen, S.; Patroescu, I.V.; Barnes, I.; Becker, K.H.; Platt, U., Gas-phase absorption cross-sections of 24 monocyclic aromatic hydrocarbons in the UV and IR spectral ranges, Atmospheric Environment 33, 4 (1999), pp.525–540.

Eyring 2005 — Eyring, V.; Köhler, H.W.; van Aardenne, J.; Lauer, A., Emissions from international shipping: 1. The last 50 years, J. Geophys. Res. 110 (2005).

Fahr 1994 — Fahr, A.; Nayak, A.K., Temperature dependent ultraviolet absorption cross-sections of 1,3-butadiene and butadiyne, Chemical Physics 189, 3 (1994), pp.725–731.

Faiz 1996 — Faiz, A.; Weaver, C.S.; Walsh, M.P., Air pollution from motor vehicles, Standards and technologies for controlling emissions, World Bank, Washington, DC (1996).

Fansler 1995 — Fansler, T.D.; French, D.T.; Drake, M.C., Fuel distributions in a firing direct-injection spark-ignition engine using laser-induced fluorescence imaging, SAE Technical Paper Series, 950110 (1995).

Fansler 2009 — Fansler, T.D.; Drake, M.C.; Gajdeczko, B.; Düwel, I.; Koban, W. et al., Quantitative liquid and vapor distribution measurements in evaporating fuel sprays using laser-induced exciplex fluorescence, Measurement Science and Technology 20, 12 (2009), pp.125401-125401.

Farmanara 2001 — Farmanara, P.; Stert, V.; Radloff, W.; Hertel, I.V., Ultrafast Internal Conversion in Highly Excited Toluene Monomers and Dimers, The Journal of Physical Chemistry A 105, 23 (2001), pp.5613–5617.

Ferguson 1957 — Ferguson, J.; Reeves, L.W.; Schneider, W.G., Vapor Absorption Spectra and Oscillator Strengths of Naphthalene, Anthracene, and Pyrene, canadian journal of chemistry 35, 10 (1957), pp.1117–1136.

Fischer 1974a — Fischer, S.F.; Lim, E.C., Excitation energy dependence of non-radiative decay rate in isolated large molecules, Chemical Physics Letters 26, 3 (1974), pp.312–317.

Fischer 1974b — Fischer, S.F.; Stanford, A.L.; Lim, E.C., Excess energy dependence of radiationless transitions in naphthalene vapor: Competition between internal conversion and intersystem crossing, J. Chem. Phys. 61, 2 (1974), pp.582–593.

Foldy 1962 — Foldy, L.L., Antisymmetric Functions and Slater Determinants, J. Math. Phys. 3, 3 (1962), pp.531–539.

Förster 1951 — Förster, T., Fluoreszenz organischer Verbindungen, Vandenhoeck and Ruprecht, Göttingen (1951).

Frank 1999 — Frank, J.H.; Miller, M.F.; Allen, M.G., Imaging of laser-induced fluorescence in a high-pressure combustor, AIAA Paper 99-0773 (1999).

Frat 2004 — Frat, F.; Legrix, L.; Vervisch, P.; Dionnet, F.; Dominguès, E., Dependence with pressure and temperature of laser induced fluorescence of toluene for application to fuel/air ration imaging in an optical SI engine, International Conference on Advanced Optical Diagnostics in Fluids, Solids and Combustion, Tokyo, Japan 2004.

Frat 2007 — Frat, F.; Legrix, L.; Vervisch, P.; Dominguès, E., Effects of Pressure and Temperature on the Fluorescence of Toluene excited at 248 nm. Implication to Fuel/Air Ratio Measurements in Engines, Proceedings of the European Combustion Meeting Third European Combustion Meeting ECM (2007).

Frederick 1982 — Frederick, J.E.; Mentall, J.E., Solar Irradiance in the Stratosphere: Implications for the Herzberg Continuum Absorption of O2, Geophysical Research Letters 9, 4 (1982), pp.461–464.

Freed 1974 — Freed, K.F.; Heller, D.F., Pressure dependence of electronic relaxation: A stochastic model, J. Chem. Phys. 61, 10 (1974), pp.3942–3953.

Frerichs 2005 — Frerichs, H.; Lenzer, T.; Luther, K.; Schwarzer, D., Multiplex detection of collisional energy transfer using KCSFI, Phys. Chem. Chem. Phys. 7, 4 (2005), pp.620–626.

Frieden 2002 Frieden, D.; Sick, V.; Gronki, J.; Schulz, C., Quantitative oxygen imaging in an engine, Applied Physics B: Lasers & Optics 75, 1 (2002), p.137.

Frieden 2003 Frieden, D.; Sick, V., A two-tracer LIF strategy for quantitative oxygen imaging in engines applied to study the influence of skip- firing on in-cylinder oxygen contents of an SIDI engine, SAE Technical Paper Series, 2003-01-1114 (2003).

Fujikawa 1998 Fujikawa, T.; Hattori, Y.; Akihama, K.; Koike, M., Quantitative 2-D fuel distribution measurements in a direct-injection gasoline engine using laser-induced fluorescence technique, Fourth International Symposium on Diagnostics and Modeling in Internal Combustion Engineering (COMODIA 98) Kyoto, Japan, 20-23 July 1998 (1998), pp.pp. 317-322.

Fujikawa 2006 Fujikawa, T.; Hattori, Y.; Akihama, K., 2-D Temperature Measurements of Unburned Gas Mixture in an Engine by Two-line Excitation LIF Technique, SAE Technical Paper Series 2006-01-3336 (2006).

Fuyuto 2006 Fuyuto, T.; Kronemayer, H.; Lewerich, B.; Koban, W.; Akihama, K.; Schulz, C., Laser-based temperature imaging close to surfaces with toluene and NO-LIF, Journal of Physics: Conference Series (2006), p.69.

Gaines 1988 Gaines, G.A.; Donaldson, D.J.; Strickler, S.J.; Vaida, V., The (n0-3s) Rydberg state of acetone: absorption spectroscopy of jet-cooled acetone and acetone-d6, The Journal of Physical Chemistry 92, 10 (1988), pp.2762–2766.

Galley 2004 Galley, D.; Pubill Melsio, A.; Ducruix, S.; Lacas, F.; Veynante, D., Experimental study of the dynamics of a LPP injection system, AIAA Paper 2004-4032 (2004).

Gattermann 1977 Gattermann, H.; Stockburger, M., Two-photon and multi-photon excitation of naphthalene in the vapor phase, studied by excitation and fluorescence spectra, Chemical Physics 24, 3 (1977), pp.327–332.

George 1968 George, G.A.; Morris, G.C., The intensity of absorption of naphthalene from 30 000 cm^{-1} to 53 000 cm^{-1}, Journal of Molecular Spectroscopy 26, 1 (1968), pp.67–71.

Geigle 2008 Geigle, K.P.; Zerbs, J.; Guin, C., Laser-induced incandescence for soot measurements in technical flames at increased pressure at the ONERA M1 test rig, ODAS 2008 (9th annual meeting), Chatillon/Paris (France) (2008).

Ghandhi 1996 Ghandhi, J.B.; Felton, P.G., On the fluorescent behavior of ketones at high temperatures, Experiments in Fluids 21, 2 (1996), pp.143–144.

Gibson 1983 Gibson, S.T.; Gies, H.P.F.; Blake, A.J.; McCoy, D.G.; Rogers, P.J., Temperature dependence in the Schumann-Runge photoabsorption continuum of oxygen, Journal of Quantitative Spectroscopy and Radiative Transfer 30, 5 (1983), pp.385–393.

Gilbert 1991 Gilbert, A.; Baggott, J.E., Essentials of molecular photochemistry, Blackwell Scientific Publications, Oxford (1991).

Ginsburg 1946 Ginsburg, N.; Robertson, W.W.; Matsen, F.A., The Near Ultraviolet Absorption Spectrum of Toluene Vapor, J. Chem. Phys. 14, 9 (1946), pp.511–517.

Gradinger 2001 Gradinger, T.B.; Inauen, A.; Bombach, R.; Käppeli, B.; Hubschmid, W.; Boulouchos, K., Liquid-fuel/air premixing in gas turbine combustors: experiment and numerical simulation, Combustion and Flame 124, 3 (2001), pp.422–443.

Greenblatt 1984 Greenblatt, G.D.; Ruhman, S.; Haas, Y., Fluorescence decay kinetics of acetone vapour at low pressures, Chemical Physics Letters 112, 3 (1984/12/7/), pp.200–206.

Greenhalgh 2000 Greenhalgh, D.A., Laser Imaging of Fuel Injection Systems and Combustors, Proceedings of the Institution of Mechanical Engineers -- Part A -- Power & Energy 214, 4 (2000), pp.367–376.

Griffiths 1999 Griffiths, D.J., Introduction to electrodynamics, Prentice Hall, Upper Saddle River, NJ (1999).

Grisch 1997 Grisch, F.; Thurber, M.C.; Hanson, R.K., Mesure de température par fluorescence induite par laser sur la molécule d'acétone, Revue Scientifique et Technique de la Defense 4 (1997), pp.51–60.

Grisch 2001 Grisch, F.; BRESSON, A., Radical imaging and temperature mapping in turbulent gaseous flowfields, Comptes Rendus de l'Académie des Sciences - Series IV - Physics 2, 7 (2001), pp.1037–1047.

Grisch 2008 Grisch, F.; Orain, M.; Rossow, B.; Jourdanneau, E.; Guin, C., Simultaneous Equivalence Ratio and Flame Structure Measurements in Multipoint Injector using PLIF, 44th AIAA/ASME/SAE/ASEE Joint Propulsion Conference and Exhibit, Hartford, CT, July 21-23, 2008, AIAA 2008-4868 (2008).

Grossmann 1996 Grossmann, F.; Monkhouse, P.B.; Ridder, M.; Sick, V.; Wolfrum, J., Temperature and pressure dependences of the laser-induced fluorescence of gas-phase acetone and 3-pentanone, Applied Physics B: Lasers and Optics 62, 3 (1996), pp.249–253.

Grünefeld 1994 — Grünefeld, G.; Beushausen, V.; Andresen, P.; Hentschel, W., Spatially resolved Raman scattering for multi-species and temperature analysis in technically applied combustion systems: Spray flame and four-cylinder inline engine, Applied Physics B: Lasers and Optics 58, 4 (1994), pp.333–342.

Hall 1976 — Hall, L.M.; Hunter, T.F.; Stock, M.G., Absolute fluorescence quantum yields for vapour-phase benzene and naphthalene, and comments on the non-radiative processes, Chemical Physics Letters 44, 1 (1976), pp.145–149.

Han 2002a — Han, D.; Steeper, R.R., An LIF equivalence ratio imaging technique for multicomponent fuels in an IC engine, Proceedings of the Combustion Institute 29, 1 (2002), pp.727–734.

Han 2002b — Han, D.; Steeper, R., Examination of iso-octane/ketone mixtures for quantitative LIF measurements in a DISI engine, SAE Technical Paper Series, 2002-01-0837 (2002).

Hansen 1975 — Hansen, D.A.; Lee, E.K.C., Radiative and nonradiative transitions in the first excited singlet state of symmetrical methyl-substituted acetones, J. Chem. Phys. 62, 1 (1975), pp.183–189.

Hanson 1986 — Hanson, R.K., Combustion diagnostics: Planar imaging techniques, Twenty-First Symposuim (International on Combustion), Symposium (International) on Combustion 21, 1 (1986), pp.1677–1691.

Hassel 2000 — Hassel, E.P.; Linow, S., Laser diagnostics for studies of turbulent combustion, Measurement Science and Technology 11, 2 (2000), pp.R37.

He 2002 — He, Y.; Pollak, E., Theory of fluorescence decay of naphthalene: Was photoinduced cooling observed experimentally?, Journal of Chemical Physics 116, 14 (2002), p.6088.

Herold 2007 — Herold, R.E.; Foster, D.E.; Ghandhi, J.B.; Iverson, R.J.; Eng, J.A.; Najt, P.M., Fuel unmixedness effects in a gasoline homogeneous charge compression ignition engine, International Journal of Engine Research 8, 3 (2007), pp.241–257.

Hickman 1996 — Hickman, C.G.; Gascooke, J.R.; Lawrance, W.D., The S_1–S_0 ($^1B_2$–$^1A_1$) transition of jet-cooled toluene: Excitation and dispersed fluorescence spectra, fluorescence lifetimes, and intramolecular vibrational energy redistribution., Journal of Chemical Physics 104, 13 (1996), p.4887.

Hicks 1997 — Hicks, Y.; Locke, R.; Andersen, R.; Zaller, M.; Schock, H., Imaging fluorescent combustion species in gas turbine flame tubes: On complexities in real systems, NASA/TM-107491 (1997).

Hicks 2000 — Hicks, Y.R.; Locke, R.J.; Anderson, R.C., Optical measurement and visualization in high-pressure, high-temperature, aviation gas turbine combustors, NASA/TM-2000-210377 (2000).

Hicks 2005 — Hicks, Y.R.; Locke, R.J.; Anderson, R.C., Laser-Based Flowfield Imaging in a Lean Premixed Prevaporized Sector Combustor, NASA/TM-2005-213402 (2005).

Hippler 1983a — Hippler, H.; Troe, J.; Wendelken, H.J., UV absorption spectra of vibrationally highly excited toluene molecules, J. Chem. Phys. 78, 9 (1983), pp.5351–5357.

Hippler 1983b — Hippler, H.; Troe, J.; Wendelken, H.J., Collisional deactivation of vibrationally highly excited polyatomic molecules. II. Direct observations for excited toluene, J. Chem. Phys. 78, 11 (1983), pp.6709–6717.

Hippler 1989 — Hippler, H.; Otto, B.; Troe, J., Collisional energy-transfer of vibrationally highly excited molecules 6. energy-dependence of (delta-E) in azulene, Berichte Der Bunsen-Gesellschaft-Physical Chemistry Chemical Physics 93, 4 (1989), pp.428–434.

Hishinuma 1996 — Hishinuma, H.; Urushihara, T.; Kakuho, A.; Itoh, T., Development of a technique for quantifying in-cylinder ratio distribution using LIF image processing, JSAE Review 17, 4 (1996), pp.355–359.

Horowitz 2001 — Horowitz, A.; Meller, R.; Moortgat, G.K., The UV-VIS absorption cross-sections of the α-dicarbonyl compounds: pyruvic acid, biacetyl and glyoxal, Journal of Photochemistry and Photobiology A: Chemistry 146, 1-2 (2001), pp.19–27.

Hsieh 1974 — Hsieh, J.C.; Huang, C.-S.; Lim, E.C., Radiationless singlet deactivation in isolated large molecules. I Naphthalene, naphthol, and naphthylamine, J. Chem. Phys. 60, 11 (1974), pp.4345–4353.

Huang 1976 — Huang, C.-S.; Hsieh, J.C.; Lim, E.C., The energy and isotope dependence of electronic relaxation in dilute vapors of fluorene and β-naphthylamine, Chemical Physics Letters 37, 2 (1976), pp.349–352.

Hückel 1931 — Hückel, E., Quantentheoretische Beiträge zum Benzolproblem, Zeitschrift für Physik A Hadrons and Nuclei 70, 3 (1931), pp.204–286.

Ikeda 1985 — Ikeda, N.; Nakashima, N.; Yoshihara, K., Photochemistry of toluene vapor at 193 nm. Direct measurements of formation of hot toluene and the dissociation rate to benzyl radical, J. Chem. Phys. 82, 11 (1985), pp.5285–5286.

Jacon 1977 — Jacon, M.; Lardeux, C.; Lopez-Delgado, R.; Tramer, A., On the "third decay channel" and vibrational redistribution problems in benzene derivatives, Chemical Physics 24, 2 (1977), pp.145–157.

Jaluria 2010 — Jaluria, Y., Role of experiments in the accurate numerical simulation of thermal processes, AIAA Paper 1999-332 20, 5 (2010), pp.467–491.

Johansson 1995 — Johansson, B.; Neij, H.; Alden, M.; Juhlin, G., Investigations of the influence of mixture preparation on cyclic variations in a SI-Engine, using laser induced fluorescence, SAE Congress Paper 950108, 950108 (1995).

Kaiser 2003 — Kaiser, S.; Kyritsis, D.C.; Dobrowolski, P.; Long, M.B.; Gomez, A., The Electrospray and Combustion at the Mesoscale, Journal of the Mass Spectrometry Society of Japan 51, 1 (2003), pp.42–49.

Kaiser 2005 — Kaiser, S.A.; Long, M.B., Quantitative planar laser-induced fluorescence of naphthalenes as fuel tracers, Proceedings of the Combustion Institute 30, 1 (2005/1), pp.1555–1563.

Kakuho 2006 — Kakuho, A.; Nagamine, M.; Amenomori, Y.; Urushihara, T.; Itoh, T., In-Cylinder Temperature Distribution Measurement and Its Application to HCCI Combustion, SAE Paper 2006-01-1202 (2006).

Kiefer 2008 — Kiefer, J.; Li, Z.S.; Zetterberg, J.; Bai, X.S.; Aldén, M., Investigation of local flame structures and statistics in partially premixed turbulent jet flames using simultaneous single-shot CH and OH planar laser-induced fluorescence imaging, Combustion and Flame 154, 4 (2008), pp.802–818.

Kikuchi 1993 — Kikuchi, K.; Sato, C.; Watabe, M.; Ikeda, H.; Takahashi, Y.; Miyashi, T., New aspects of fluorescence quenching by molecular oxygen, Journal of the American Chemical Society 115, 12 (1993), pp.5180–5184.

Kimura 2004 — Kimura, Y.; Abe, D.; Terazima, M., Vibrational energy relaxation of naphthalene in the S_1 state in various gases, J. Chem. Phys. 121, 12 (2004), pp.5794–5800.

King 1997 — King, G.F.; Lucht, R.P.; Dutton, J.C., Instantaneous dual-tracer PLIF measurements of molecular mixing in axisymmetric jets, AIAA, Aerospace Sciences Meeting & Exhibit, 35th, Reno, NV, Jan. 6-9, 1997, AIAA Paper 97-0152 (1997).

Klessinger 1995 — Klessinger, M.; Michl, J., Excited states and photochemistry of organic molecules, VCH, New York, Weinheim, Cambridge (1995).

Knight 2006 Knight, D.; Rossman, T.; Jaluria, Y., Evaluation of Fluid-Thermal Systems by Dynamic Data Driven Application Systems, Book chapter, Computational Science - ICCS 2006, Lecture Notes in Computer Science 3993, Springer-Verlag GmbH, Berlin Heidelberg (2006).

Koban 2002 Koban, W.; Schorr, J.; Schulz, C., Oxygen-distribution imaging with a novel two-tracer laser-induced fluorescence technique, Applied Physics B: Lasers & Optics 74, 1 (2002), p.111.

Koban 2004 Koban, W.; Koch, J.D.; Hanson, R.K.; Schulz, C., Absorption and fluorescence of toluene vapor at elevated temperatures, Physical Chemistry Chemical Physics 6, 11 (2004), pp.2940–2945.

Koban 2005a Koban, W.; Koch, J.D.; Hanson, R.K.; Schulz, C., Oxygen quenching of toluene fluorescence at elevated temperatures, Applied Physics B: Lasers and Optics 80, 6 (2005), pp.777–784.

Koban 2005b Koban, W.; Schulz, C., FAR-LIF: Myth and reality, Proceedings of the European Combustion Meeting Third European Combustion Meeting ECM (2005).

Koban 2005c Koban, W.; Schulz, C., Toluene Laser-Induced Fluorescence (LIF) Under Engine-Related Pressures,Temperatures and Oxygen Mole Fractions, SAE Technical Paper Series, 2005-01-2091 (2005).

Koban 2005d Koban, W. (2005), Photophysical characterization of toluene and 3 pentanone for quantitative imaging of fuel/air ratio and temperature in combustion systems, PhD Thesis, Heidelberg, University of Heidelberg, Institute of Physical Chemistry.

Koch 2001 Koch, J.D.; Hanson, R.K., Ketone photophysics for quantitative PLIF imaging, AIAA Paper 2001, 413 (2001).

Koch 2003a Koch, J.; Hanson, R.K., A Photophysics Model for 3-pentanone PLIF: Temperature, Pressure, and Excitation Wavelength Dependences, AIAA 2003-403 (2003).

Koch 2003b Koch, J.D.; Hanson, R.K., Temperature and excitation wavelength dependencies of 3-pentanone absorption and fluorescence for PLIF applications, Applied Physics B: Lasers & Optics 76, 3 (2003), p.319.

Koch 2004 Koch, J.D.; Hanson, R.K.; Koban, W.; Schulz, C., Rayleigh-Calibrated Fluorescence Quantum Yield Measurements of Acetone and 3-Pentanone, Appl. Opt. 43, 31 (2004), pp.5901–5910.

Koch 2005 — Koch, J. (2005), Fuel tracer photophysics for quantitative planar laser-induced fluorescence, Report no. TSD-159, PhD Thesis, Stanford, Stanford University.

Koch 2008 — Koch, J.D.; Gronki, J.; Hanson, R.K., Measurements of near-UV absorption spectra of acetone and 3-pentanone at high temperatures, Journal of Quantitative Spectroscopy and Radiative Transfer 109, 11 (2008), pp.2037–2044.

Kohse-Höinghaus 1994 — Kohse-Höinghaus, K., Laser techniques for the quantitative detection of reactive intermediates in combustion systems, Progress in Energy and Combustion Science 20, 3 (1994), pp.203–279.

Kohse-Höinghaus 2002 — Kohse-Höinghaus, K.; Jeffries, J.B., Applied combustion diagnostics, Combustion, Taylor & Francis, New York (2002).

Kohse-Höinghaus 2005 — Kohse-Höinghaus, K.; Barlow, R.S.; Aldén, M.; Wolfrum, J., Combustion at the focus: laser diagnostics and control, Proceedings of the Combustion Institute 30, 1 (2005), pp.89–123.

Krämer 1999 — Krämer, H.; Dinkelacker, F.; Leipertz, A., Optimization of the mixing quality of real size gas turbine burner with instantaneous planer laser-induced fluorescence imaging, American Society of Mechanical Engineers (Paper), 99-GT-135 (1999).

Kühni 2010 — Kühni, M.; Morin, C.; Guibert, P., Fluoranthene laser-induced fluorescence at elevated temperatures and pressures: implications for temperature-imaging diagnostics, Applied Physics B: Lasers and Optics (2010), pp.1–13.

Laor 1971 — Laor, U.; Ludwig, P.K., Fluorescence Lifetimes of Vibronic States of Naphthalene Vapor in the Region of Excitation from 3080--2150 [A-ring], Journal of Chemical Physics 54, 3 (1971), pp.1054–1057.

Lawrenz 1992 — Lawrenz, W.; Köhler, J.; Meier, F.; Stolz, W.; Wirth, R.; Bloss, W.H. et al., Quantitative 2D LIF measurements of air/fuel ratios during the intake stroke in a transparent SI engine, SAE Paper 922320, 922320 (1992).

Lee 2001 — Lee, A.Y.T.; Yung, Y.L.; Cheng, B.-M.; Bahou, M.; Chung, C.-Y.; Lee, Y.-P., Enhancement of Deuterated Ethane on Jupiter, The Astrophysical Journal Letters, 1 (2001), pp.L93.

Lefebvre 1995 — Lefebvre, A.H., The Role of Fuel Preparation in Low-Emission Combustion, Journal of Engineering for Gas Turbines and Power 117, 4 (1995), pp.617–654.

Lefebvre 1999 — Lefebvre, A.H., Gas turbine combustion, Taylor & Francis, Philadelphia, Pa. (1999).

Lenhert 2007 — Lenhert, D.B.; Miller, D.L.; Cernansky, N.P., The oxidation of JP-8, Jet-A, and their surrogates in the low and intermediate temperature regime at elevated pressures, Combustion Science and Technology 179, 5 (2007), pp.845–861.

Lenzer 2000 — Lenzer, T.; Luther, K.; Reihs, K.; Symonds, A.C., Collisional energy transfer probabilities of highly excited molecules from kinetically controlled selective ionization (KCSI). II. The collisional relaxation of toluene: P(E',E) and moments of energy transfer for energies up to 50000 cm^{-1}, J. Chem. Phys. 112, 9 (2000), pp.4090–4110.

Levine 2000 — Levine, I.N., Quantum chemistry, Prentice Hall, Upper Saddle River, NJ (2000).

Liao 1999 — Liao, D.W.; Mebel, A.M.; Hayashi, M.; Shiu, Y.J.; Chen, Y.T.; Lin, S.H., Ab initio study of the n-π^* electronic transition in acetone: Symmetry-forbidden vibronic spectra, J. Chem. Phys. 111, 1 (1999), pp.205–215.

Lim 1972 — Lim, E.C.; Uy, J.O., Excitation Energy and Deuteration Dependence of Fluorescence in Naphthalene Vapor, J. Chem. Phys. 56, 7 (1972), pp.3374–3377.

Lim 1973 — Lim, E.C.; Huang, C.-S., Radiationless transition in large isolated molecules: Variation of excess energy dependence of its decay rate with initially prepared electronic state, J. Chem. Phys. 58, 3 (1973), pp.1247–1248.

Lim 1997 — Lim, E.C., Photophysics of Gaseous Aromatic Molecules: Excess Vibrational Energy Dependence of Radiationless Processes, Advances in Photochemistry 23 (1997), pp.165–211.

Limão-Vieira 2003 — Limão-Vieira, P.; Eden, S.; Mason, N.J.; Hoffmann, S.V., Electronic state spectroscopy of acetaldehyde, CH_3CHO, by high-resolution VUV photoabsorption, Chemical Physics Letters 376, 5-6 (2003), pp.737–747.

Linow 2000 — Linow, S.; Dreizler, A.; Janicka, J.; Hassel, E.P., Comparison of two-photon excitation schemes for CO detection in flames, Applied Physics B: Lasers and Optics 71, 5 (2000), pp.689–696.

List 2008 — List, H.; Eichlseder, H.; Piock, W.F., Grundlagen und Technologien des Ottomotors, Springer-11774 /Dig. Serial], Springer, Heidelberg (2008).

Locke 1998 Locke, R.J.; Hicks, Y.R.; Anderson, R.C.; Zaller, M.M., Fuel Injector Pattern-nation Evaluation in Advanced Liquid-Fueled, High Pressure, Gas Turbine Combustors, Using Nonintrusive Optical Diagnostic Techniques, NASA/TM-1998-206292 (1998).

Locke 1999 Locke, R.J.; Zaller, M.; Hicks, Y.R.; Anderson, R.C., Non-intrusive laser-induced imaging for speciation and patternation in high pressure gas turbine combustors, NASA/TM-1999-209395 (1999).

Löfström 1996 Löfström, C.; Kaaling, H.; Aldén, M., Visualization of fuel distributions in premixed ducts in a low-emission gas turbine combustor using laser techniques, Symposium (International) on Combustion 2 (1996), pp.2787–2793.

Löfström 2000 Löfström, C.; Engström, J.; Richter, M.; Kaminski, C.F.; Johansson, P.; Nyholm, K. et al., Feasibility Studies and Application of Laser/optical Diagnostics for Characterisation of a Practical Low-Emission gas Turbine Combustor, Proceedings of ASME TURBO EXPO 2000, ASME 2000-GT-0124 (2000).

Loper 1972 Loper, G.L.; Lee, E.K.C., Fluorescence decay and radiative lifetimes of fluorinated aromatic molecules, Chemical Physics Letters 13, 2 (1972), pp.140–143.

Lowe 2006 Lowe, J.P.; Peterson, K.A., Quantum chemistry, Elsevier, Amsterdam (2006).

Lozano 1992 Lozano, A. (1992), Laser-Excited Luminescent Tracers for Planar Concentration Measurements in Gaseous Jets, PhD Thesis, Stanford, Stanford University.

Lozano 1994 Lozano, A.; Smith, S.H.; Mungal, M.G.; Hanson, R.K., Concentration measurements in a transverse jet by planar laser-induced fluorescence of acetone, AIAA journal 32, 1 (1994), pp.218–221.

Lu 2004 Lu, H.-C.; Chen, H.-K.; Cheng, B.-M., Analysis of C_2H_4 in C_2H_6 and C_2H_5D with VUV Absorption Spectroscopy and a Method To Remove C_2H_4 from C_2H_6 and C_2H_5D, Analytical Chemistry 76, 19 (2004), pp.5965–5967.

Luong 2006 Luong, M.; Schulz, C., Novel strategies for imaging temperature distribution using Toluene LIF, Journal of Physics: Conference Series (2006), p.133.

Luong 2008 Luong, M.; Zhang, R.; Schulz, C.; Sick, V., Toluene laser-induced fluorescence for in-cylinder temperature imaging in internal combustion engines, Applied Physics B: Lasers & Optics 91, 3/4 (2008), pp.669–675.

Malkin 1992 Malkin, J., Photophysical and photochemical properties of aromatic compounds, CRC, Boca Raton, Ann Arbor, London (1992).

Martinez 1992 Martinez, R.D.; Buitrago, A.A.; Howell, N.W.; Hearn, C.H.; Joens, J.A., The near U.V. absorption spectra of several aliphatic aldehydes and ketones at 300 K, Atmospheric Environment. Part A. General Topics 26, 5 (1992/4), pp.785–792.

Melton 1983 Melton, L.A., Spectrally separated fluorescence emissions for diesel fuel droplets and vapor, Appl. Opt. 22, 14 (1983), pp.2224–2226.

Melton 1984 Melton, L.A., Soot diagnostics based on laser heating, Appl. Opt. 23, 13 (1984), pp.2201–2208.

Michou 1999 Michou, Y.; Carvahlo, I.S.; Chauveau, C.; Gökalp, I., Experimental study of lean premixed and prevaporised turbulent spray combustion, AIAA Paper 1999-332 (1999).

Miles 1992 Miles, R.B.; Forkey, J.N.; Lempert, W.R., Filtered Rayleigh scattering measurements in supersonic/hypersonic facilities, AIAA paper 1992-3894 (1992).

Miles 2001 Miles, R.B.; Lempert, W.R.; Forkey, J.N., Laser Rayleigh scattering, Measurement Science and Technology 12, 5 (2001), pp.R33.

Modica 2007 Modica, V.; Morin, C.; Guibert, P., 3-Pentanone LIF at elevated temperatures and pressures: measurements and modeling, Applied Physics B: Lasers & Optics 87, 1 (2007), pp.193–204.

Mokhov 2005 Mokhov, A.V.; Gersen, S.; Levinsky, H.B., Spontaneous Raman measurements of acetylene in atmospheric-pressure methane/air flames, Chemical Physics Letters 403, 4-6 (2005), pp.233–237.

Moss 2007 Moss, J.B.; Aksit, I.M., Modelling soot formation in a laminar diffusion flame burning a surrogate kerosene fuel, Proceedings of the Combustion Institute 31, 2 (2007), pp.3139–3146.

Naidja 2003 Naidja, A.; Krishna, C.R.; Butcher, T.; Mahajan, D., Cool flame partial oxidation and its role in combustion and reforming of fuels for fuel cell systems, Progress in Energy and Combustion Science 29, 2 (2003), pp.155–191.

Natelson 2008 — Natelson, R.H.; Kurman, M.S.; Cernansky, N.P.; Miller, D.L., Experimental investigation of surrogates for jet and diesel fuels, Fuel 87, 10-11 (2008), pp.2339–2342.

Nau 1996 — Nau, W.M.; Scaiano, J.C., Oxygen Quenching of Excited Aliphatic Ketones and Diketones, The Journal of Physical Chemistry 100, 27 (1996), pp.11360–11367.

Neij 1994 — Neij, H.; Johansson, B.; Aldén, M., Development and demonstration of 2D-LIF for studies of mixture preparation in SI engines, Combustion and Flame 99, 2 (1994), pp.449–457.

Ni 2004 — Ni, C.-K.; Lee, Y.T., Photodissociation of simple aromatic molecules in a molecular beam, International Reviews in Physical Chemistry 23, 2 (2004), pp.187–218.

Nitzan 1972 — Nitzan, A.; Jortner, J., Sequence congestion effects in optical selection studies of electronic relaxation, Chemical Physics Letters 13, 5 (1972), pp.466–472.

Nobre 2008 — Nobre, M.; Fernandes, A.; Ferreira Da Silva, F.; Antunes, R.; Almeida, D.; Kokhan, V. et al., The VUV electronic spectroscopy of acetone studied by synchrotron radiation, Physical Chemistry Chemical Physics 10, 4 (2008), pp.550–560.

North 1995 — North, S.W.; Blank, D.A.; Gezelter, J.D.; Longfellow, C.A.; Lee, Y.T., Evidence for stepwise dissociation dynamics in acetone at 248 and 193 nm, J. Chem. Phys. 102, 11 (1995), pp.4447–4460.

Nyholm 1994 — Nyholm, K.; Fritzon, R.; Aldén, M., Single-pulse two-dimensional temperature imaging in flames by degenerate four-wave mixing and polarization spectroscopy, Applied Physics B: Lasers and Optics 59, 1 (1994), pp.37–43.

Orkin 1997 — Orkin, V.L.; Huie, R.E.; Kurylo, M.J., Rate Constants for the Reactions of OH with HFC-245cb ($CH_3CF_2CF_3$) and Some Fluoroalkenes (CH_2CHCF_3, CH_2CFCF_3, CF_2CFCF_3, and CF_2CF_2), The Journal of Physical Chemistry A 101, 48 (1997), pp.9118–9124.

Ossler 1997 — Ossler, F.; Aldén, M., Measurements of picosecond laser induced fluorescence from gas phase 3-pentanone and acetone: Implications to combustion diagnostics, Applied Physics B: Lasers and Optics 64, 4 (1997), pp.493–502.

Ossler 2001 Ossler, F.; Metz, T.; Aldén, M., Picosecond laser-induced fluorescence from gas-phase polycyclic aromatic hydrocarbons at elevated temperatures. I. Cell measurements, Applied Physics B: Lasers and Optics 72, 4 (2001), pp.465–478.

Otis 1983 Otis, C.E.; Knee, J.L.; Johnson, P.M., The identification of channel three in isolated benzene, J. Chem. Phys. 78, 4 (1983), pp.2091–2092.

Pariser 1953 Pariser, R.; Parr, R.G., A Semi-Empirical Theory of the Electronic Spectra and Electronic Structure of Complex Unsaturated Molecules. I, J. Chem. Phys. 21, 3 (1953), pp.466–471.

Parmenter 1970 Parmenter, C.S.; Schuyler, M.W., Transitions non-radiatives dans Ies molecules, Journal de chimie physique (1970), p.92.

Pastor 2002 Pastor, J.V.; Lopez, J.J.; Julia, J.E.; Benajes, J.V., Planar laser-induced fluorescence fuel concentration measurements in isothermal diesel sprays, Optics Express 10, 7 (2002), pp.309–323.

Penner 1999 Penner, J.E.; Lister, D.H.; Griggs, D.J.; Dokken, D.J.; McFarland, M., Aviation and the global atmosphere, A Special Report of IPCC WGI and III (1999).

Peters 2006 Peters, N., Turbulent combustion, Cambridge monographs on mechanics, Cambridge Univ. Press, Cambridge (2006).

Pople 1953 Pople, J.A., Electron interaction in unsaturated hydrocarbons, Transactions of the Faraday Society 49 (1953), pp.1375–1385.

Pritchard 1986 Pritchard, H.O., Decoupling vibrational relaxation from collisional deactivation in the theory of unimolecular reactions, The Journal of Physical Chemistry 90, 19 (1986), pp.4471–4473.

Rakopoulos 2004 Rakopoulos, C.D.; Hountalas, D.T.; Rakopoulos, D.C.; Levendis, Y.A., Comparative Environmental Evaluation of JP-8 and Diesel Fuels Burned in Direct Injection (DI) or Indirect Injection (IDI) Diesel Engines and in a Laboratory Furnace, Energy & Fuels 18, 5 (2004), pp.1302–1308.

Rao 1969 Rao, T.N.; Collier, S.S.; Calvert, J.G., Quenching reactions of the first excited singlet and triplet states of sulfur dioxide with oxygen and carbon dioxide, Journal of the American Chemical Society 91, 7 (1969), pp.1616–1621.

Reboux 1994 — Reboux, J.; Puechberty, D., A new approach of PLIF applied to fuel/air ratio measurement in the compression stroke of an optical SI engine, SAE Technical Paper Series 941988, (1994).

Reid 1977 — Reid, R.C.; Prausnitz, J.M.; Sherwood, T.K., The properties of gases and liquids, McGraw-Hill chemical engineering series, McGraw-Hill, New York (1977).

Rohatgi-Mukherjee 1978 — Rohatgi-Mukherjee, K.K., Fundamentals of photochemistry, Wiley, New Delhi (1978).

Rothamer 2007 — Rothamer, D.A. (2007), Development and application of infrared and tracer-based planar laser-induced fluorescence imaging diagnostics, Report TSD-174, PhD Thesis, Stanford, Stanford University.

Sacadura 2000 — Sacadura, J.C.; Robin, L.; Dionnet, F.; Gervais, D.; Gastaldi, P.; Ahmed, A., Experimental investigation of an optical direct injection SI engine using FARLIF, SAE Technical Paper Series 2000-01-1794, 2000-01-1794 (2000).

Salazar 2009 — Salazar, V.M.; Kaiser, S.A., Optimizing Precision and Accuracy of Quantitative PLIF of Acetone as a Tracer for Hydrogen Fuel, SAE Technical Paper Series, 2009-01-1534 (2009).

Saleh 2001 — Saleh, B.E.A.; Teich, M.C., Fundamentals of photonics, Wiley series in pure and applied optics, Wiley-Interscience, Hoboken, NJ (2001).

Scholz 2006 — Scholz, J.; Röhl, M.; Wiersbinski, T.; Beushausen, V., Verification and application of fuel-air-ratio-LIF, 13th International Symposium on Applications of Laser Techniques to Fluid Mechanics (2006), pp.26–29.

Schulz 2005 — Schulz, C.; Sick, V., Tracer-LIF diagnostics: quantitative measurement of fuel concentration, temperature and fuel/air ratio in practical combustion systems, Progress in Energy and Combustion Science 31, 1 (2005), pp.75–121.

Schulz 2006 — Schulz, C.; Kock, B.F.; Hofmann, M.; Michelsen, H.; Will, S.; Bougie, B. et al., Laser-induced incandescence: recent trends and current questions, Applied Physics B: Lasers and Optics 83, 3 (2006), pp.333–354.

Sercey 2005 — Sercey, G. de; Awcock, G.; Heikal, M., Use of LIF image acquisition and analysis in developing a calibrated technique for in-cylinder investigation of the spatial distribution of air-to-fuel mixing in direct injection gasoline engines, Machine Vision Special Issue, Computers in Industry 56, 8-9 (2005), pp.1005–1015.

Seyfried 2007 — Seyfried, H.; Brackmann, C.; Lindholm, A.; Linne, M.; Aldén, M.; Barreras, F.; Bank, R.V.D., Optical investigations of the combustion characteristics of gas turbine pilot burner, Collection of Technical Papers - 45th AIAA Aerospace Sciences Meeting 8, AIAA-2007-469 (2007), pp.5630–5641.

Shama 1991 — Shama, S.A.A.E.-A. (1991), Vacuum ultraviolet absorption spectra of organic compounds in gaseous and liquid state, Thesis, Benha, Egypt, Zagazig University, Faculty of Science.

Shimanouchi 1972 — Shimanouchi, T., Tables of Molecular Vibrational Frequencies, Consolidated Volume I, NSRDS–NBS 39 (1972).

Sick 2009 — Sick, V.; Westbrook, C.K., Diagnostic implications of the reactivity of fluorescence tracers, Proceedings of the Combustion Institute 32, 1 (2009), pp.913–920.

Silverstein 1998 — Silverstein, R.M.; Bassler, G.C.; Morrill, T.C., Identification spectrométrique de composés organiques, De Boeck université, Paris, Bruxelles (1998).

Smalley 1983 — Smalley, R.E., Dynamics of Electronically Excited States, Annu. Rev. Phys. Chem. 34, 1 (1983), p.129.

Smith 2007 — Smith, J.D.; Sick, V., Quantitative, dynamic fuel distribution measurements in combustion-related devices using laser-induced fluorescence imaging of biacetyl in iso-octane, Proceedings of the Combustion Institute 31, 1 (2007), pp.747–755.

Soep 1973 — Soep, B.; Michel, C.; Tramer, A.; Lindqvist, L., Study of intersystem crossing in naphthalene and 1-methylnaphthalene in collision-free conditions and pressure effects, Chemical Physics 2, 3 (1973), pp.293–303.

Spadaccini 1982 — Spadaccini, L.J.; Tevelde, J.A., Autoignition characteristics of aircraft-type fuels, Combustion and Flame 46 (1982), pp.283–300.

Sponer 1955 — Sponer, H.; Cooper, C.D., Vapor Absorption Spectra of Light and Heavy Naphthalenes at 2900---2500 A, J. Chem. Phys. 23, 4 (1955), pp.646–651.

Sreeramamurty 1951 — Sreeramamurty, K., The near ultraviolet absorption spectrum of pseudocumene, Proceedings of National Institute of Sciences of India 17, 5 (1951), pp.385–389.

Steer 1978 — Steer, R.P.; Swords, M.D.; Phillips, D., Vibrational relaxation in first electronically excited singlet state of fluorobenzenes, Chemical Physics 34, 1 (1978), pp.95–102.

Stepowski 1992 — Stepowski, D., Laser measurements of scalars in turbulent diffusion flames, Progress in Energy and Combustion Science 18, 6 (1992), pp.463–491.

Stevens 1994 — Stevens, J.K., Three-dimensional confocal microscopy, Volume investigation of biological specimens, Chapter 3 by James B. Pawley: Sources of Noise in Three-Dimensional Microscopical Data Sets, Academic Press, San Diego (1994).

Stockburger 1975 — Stockburger, M.; Gattermann, H.; Klusmann, W., Spectroscopic studies on naphthalene in the vapor phase. II. Fluorescence quantum yields from single vibronic levels in the first excited singlet state - Behavior of higher excited singlet states, The Journal of Chemical Physics 63, 10 (1975), pp.4529–4540.

Strelkova 2008 — Strelkova, M.I.; Kirillov, I.A.; Potapkin, B.V.; Safonov, A.A.; Sukhanov, L.P.; Umanskiy, S.Y. et al., Detailed and Reduced Mechanisms of Jet a Combustion at High Temperatures, Combustion Science and Technology 180, 10 (2008), pp.1788–1802.

Stufflebeam 2002 — Stufflebeam, J.H.; Kendrick, D.W.; Sowa, W.A.; Snyder, T.S., Quantifying Fuel/Air Unmixedness in Premixing Nozzles Using an Acetone Fluorescence Technique, Journal of Engineering for Gas Turbines and Power 124, 1 (2002), pp.39–45.

Suto 1992 — Suto, M.; Wang, X.; Shan, J.; Lee, L.C., Quantitative photoabsorption and fluorescence spectroscopy of benzene, naphthalene, and some derivatives at 106-295 nm, Journal of Quantitative Spectroscopy and Radiative Transfer 48, 1 (1992), pp.79–89.

Tacina 2002 — Tacina, R.; Wey, C.; Laing, P.; Mansour, A., A Low NOx Lean-Direct Injection, Multipoint Integrated Module Combustor Concept for Advanced Aircraft Gas Turbines, NASA/TM-2002-211347 (2002).

Tait 1992 — Tait, N.P.; Greenhalgh, D.A., 2D laser induced fluorescence imaging of parent fuel fraction in nonpremixed combustion, Twenty-Fourth Symposium on Combustion, Symposium (International) on Combustion 24, 1 (1992), pp.1621–1628.

Taylor 1997 — Taylor, J.R., An introduction to error analysis, The study of uncertainties in physical measurements, Univ. Science Books, Sausalito, Calif. (1997).

Tea 2010 — Tea, G.; Bruneaux, G.; Kashdan, J.T.; Schulz, C., Unburned Gas Temperature Measurements in a Diesel Jet via Two-Color Toluene-LIF Imaging, contribution to the 33rd International Symposium on Combustion - Beijing, China August 1-6, 2010, Proceeding of the Combustion Institute, to be published.

Thurber 1998 — Thurber, M.C.; Grisch, F.; Kirby, B.J.; Votsmeier, M.; Hanson, R.K., Measurements and Modeling of Acetone Laser-Induced Fluorescence with Implications for Temperature-Imaging Diagnostics, Appl. Opt. 37, 21 (1998), pp.4963 - 4978.

Thurber 1999a — Thurber, M.C.; Hanson, R.K., Pressure and composition dependences of acetone laser-induced fluorescence with excitation at 248, 266, and 308 nm, Applied Physics B: Lasers & Optics 69, 3 (1999), p.229.

Thurber 1999b — Thurber, M.C. (1999), Acetone laser-induced fluorescence for temperature and multiparameter imaging in gaseous flows, Topical Report TSD-120, PhD Thesis, Stanford, Stanford University.

Tkachenko 2006 — Tkachenko, N.V., Optical spectroscopy, Methods and instrumentations, Elsevier, Amsterdam (2006).

Topal 2004 — Topal, M.H.; Wang, J.; Levendis, Y.A.; Carlson, J.B.; Jordan, J., PAH and other emissions from burning of JP-8 and diesel fuels in diffusion flames, Fuel 83, 17-18 (2004), pp.2357–2368.

Toselli 1991 — Toselli, B.M.; Brenner, J.D.; Yerram, M.L.; Chin, W.E.; King, K.D.; Barker, J.R., Vibrational relaxation of highly excited toluene, J. Chem. Phys. 95, 1 (1991), pp.176–188.

Trentelman 1989 — Trentelman, K.A.; Kable, S.H.; Moss, D.B.; Houston, P.L., Photodissociation dynamics of acetone at 193 nm: Photofragment internal and translational energy distributions, J. Chem. Phys. 91, 12 (1989), pp.7498–7513.

Turro 1991 — Turro, N.J., Modern molecular photochemistry, University science books, Mill Valley Calif. (1991).

Uy 1970 — Uy, J.O.; Lim, E.C., Electronic relaxation in naphthalene vapor, Chemical Physics Letters 7, 2 (1970), pp.306–310.

Valeur 2007 — Valeur, B., Molecular fluorescence, Principles and applications, Wiley-VCH, Weinheim (2007).

Vasu 2008 — Vasu, S.S.; Davidson, D.F.; Hanson, R.K., Jet fuel ignition delay times: Shock tube experiments over wide conditions and surrogate model predictions, Combustion and Flame 152, 1-2 (2008), pp.125–143.

Verma 1971 — Verma, V.N.; Nair, K.P.R.; Rai, D.K., Vibrational Analysis of the 2400–2800 Å Bands of 1,2,3- and 1,3,5-Trimethylbenzenes in Vapour Phase, Bulletin of the Chemical Society of Japan 44, 8 (1971), pp.2031–2035.

Wadi 1999 — Wadi, H.; Pollak, E., Theory of laser cooling of polyatomic molecules in an electronically excited state, The Journal of Chemical Physics 110, 24 (1999), pp.11890–11905.

Wermuth 2005 — Wermuth, N.; Sick, V., Absorption and Fluorescence Data of Acetone, 3-Pentanone, Biacetyl, and Toluene at Engine-Specific Combinations of Temperature and Pressure, SAE Technical Paper Series, 2005-01-2090 (2005).

Whiteside 2005 — Whiteside, P.T.; King, A.K.; Reid, K.L., Photoelectron spectroscopy of S_1 toluene: I. Photoionization propensities of selected vibrational levels in S_1 toluene, J. Chem. Phys. 123, 20 (2005), pp.204316-6.

Wolfrum 1998 — Wolfrum, J., Lasers in combustion: From basic theory to practical devices, Twenty-Seventh Sysposium (International) on Combustion Volume One, Symposium (International) on Combustion 27, 1 (1998), pp.1–41.

Wolfrum 2000 — Wolfrum, J.; Dreier, T.; Ebert, V.; Schulz, C., Laser-Based Combustion Diagnostics, Encyclopedia of Analytical Chemistry, John Wiley & Sons, Ltd (2000).

Wood 1989 — Wood, C.P.; McDonell, V.G.; Smith, R.A.; Samuelsen, G.S., Development and Application of a Surrogate Distillate Fuel, Journal of Propulsion and Power 5, 4 (1989), pp.399–405.

Wulff 1997 — Wulff, A.; Hourmouziadis, J., Technology review of aeroengine pollutant emissions, Aerospace Science and Technology 1, 8 (1997), pp.557–572.

Yan 2007 — Yan, Y.; Gashi, S.; Nouri, J.M.; Lockett, R.D.; Arcoumanis, C., Investigation of spray characteristics in a spray-guided DISI engine using PLIF and LDV, Journal of Physics: Conference Series 85 (2007), p.12036.

Yip 1994 — Yip, B.; Miller, M.F.; Lozano, A.; Hanson, R.K., A combined OH/acetone planar laser-induced fluorescence imaging technique for visualizing combusting flows, Experiments in Fluids 17, 5 (1994), pp.330–336.

Yuen 1997 — Yuen, L.S.; Peters, J.E.; Lucht, R.P., Pressure dependence of laser-induced fluorescence from acetone, Appl. Opt. 36, 15 (1997), pp.3271–3277.

Yujing 2000 — Yujing, M.; Mellouki, A., The near-UV absorption cross sections for several ketones, Journal of Photochemistry and Photobiology A: Chemistry 134, 1-2 (2000), pp.31–36.

Zaslonko 1997 — Zaslonko, I.S., Energy exchange and reactions of highly excited polyatomic molecules, Russian Chemical Reviews 66, 6 (1997), p.483.

Zetterberg 2008 — Zetterberg, J.; Li, Z.; Afzelius, M.; Aldén, M., Two-Dimensional Temperature Measurements in Flames Using Filtered Rayleigh Scattering at 254 nm, Applied Spectroscopy 62, 7 (2008), pp.778–783.

Zhang 2004 — Zhang, R.; Wermuth, N.; Sick, V., Impact of fluorescence tracers on combustion performance in optical engine experiments, SAE Technical Paper Series 2004-01-2975, 2004-01-2975 (2004).

Zhang 2006 — Zhang, R.; Bohac, S.; Sick, V., Stability of isooctane mixtures with 3-pentanone or biacetyl as fluorescence tracers in combustion experiments, Experiments in Fluids 40, 1 (2006), pp.161–163.

Zuckermann 1989 — Zuckermann, H.; Schmitz, B.; Haas, Y., Acetone photophysics in seeded supersonic molecular beams, The Journal of Physical Chemistry 93, 10 (1989), pp.4083–4091.